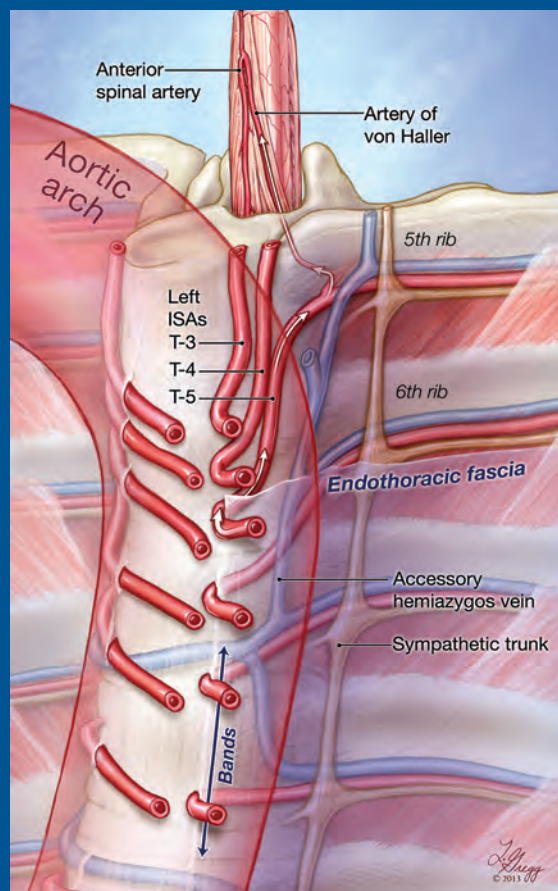# AJNR

AMERICAN JOURNAL OF NEURORADIOLOGY

THE JOURNAL OF DIAGNOSTIC AND
INTERVENTIONAL NEURORADIOLOGY

Activation patterns and intelligence
in children and adolescents

Phlebography shows no difference in patients
with MS and controls

White matter lesions associated with
low serum Vitamin D

Official Journal ASNR • ASFNR • ASHNR • ASPNR • ASSR

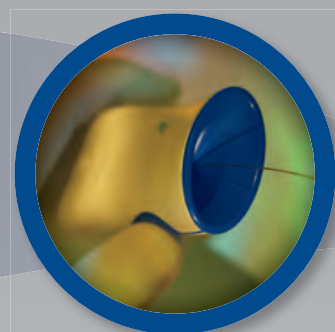![MicroVention TERUMO logo]

Dedicated to the development

The MicroVention family of neuroendovascular products:

DELIVERY & DETACHMENT SYSTEMS

V-Trak® **V-Trak** *Soft*® **V-Grip**®

ACCESS PRODUCTS

Traxcess®
Guidewire

Chaperon®
Guiding Catheter

Headway®
Microcatheter

Headway Duo!
microcatheter

Scepter
Occlusion Balloon Catheter

microvention.com

CE
0297

# of innovative endovascular technologies

HYDROGEL COIL PRODUCTS

HydroFrame®
HydroCoil® Embolic System

HydroSoft®
HydroCoil® Embolic System

HydroFill®
HydroCoil® Embolic System

PLATINUM COIL PRODUCTS

MicroPlex®
coil system

Cosmos®
complex coil

VFC®
Versatile Range Fill Coil

HyperSoft®
finishing coil

Introducing…

HyperSoft® 3D
complex coil

The softness of the HyperSoft® Coil available in Complex Form!

Now you can Frame, Fill and Finish with the softness
you need to match almost any aneurysm morphology.

BARRICADE™
COIL SYSTEM

BLOCKADE
MEDICAL

18 TECHNOLOGY DRIVE #169, IRVINE CA 92618 | **P** 949.788.1443
WWW.BLOCKADEMEDICAL.COM

MADE IN AMERICA

CE
0297
MKTG-020   REV. B

Publication Preview at www.ajnr.org features articles released in advance of print. Visit www.ajnrblog.org to comment on AJNR content and chat with colleagues and AJNR's News Digest at http://ajnrdigest.org to read the stories behind the latest research in neuroimaging.

★ Indicates Editor's Choices selection

✎ Indicates Fellows' Journal Club selection

⚷ Indicates open access to non-subscribers at www.ajnr.org

▤ Indicates article with supplemental on-line table

◧ Indicates article with supplemental on-line photo

▶ Indicates article with supplemental on-line video

EBM 1 Indicates Evidence-Based Medicine Level 1

EBM 2 Indicates Evidence-Based Medicine Level 2
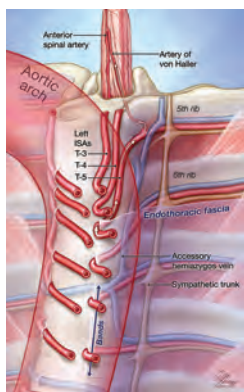
Diagram illustrating the differences in courses of right and left intercostal arteries.
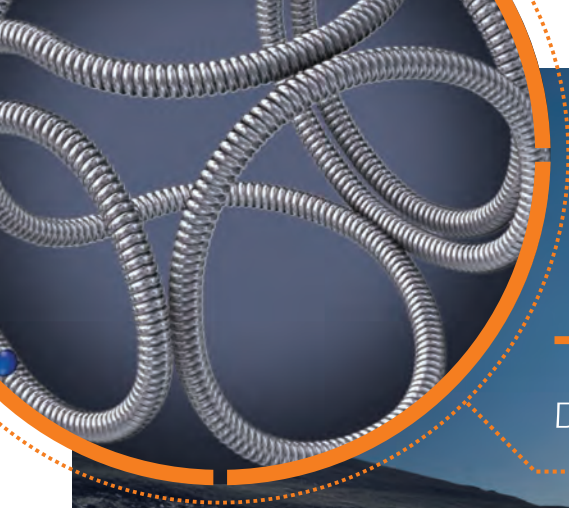
Target®
DETACHABLE COILS

Smooth and Stable

Whether you are framing, filling or finishing, Target Detachable Coils deliver consistently smooth deployment and exceptional microcatheter stability. Focused on design, Target Coils feature a host of advantages to ensure the high-powered performance you demand.

For more information, please visit www.strykerneurovascular.com/Target or contact your local Stryker Neurovascular sales representative.

stryker®
Neurovascular

Stroke: *Our Only Focus. Our Ongoing Promise.*

AJNR

Letter from the President-Elect – Search for New *AJNR* Editor

In June, 2015, Mauricio Castillo, MD, FACR, will complete an eight-year term as the Editor-in-Chief of the *AJNR*. He follows a short list of illustrious neuroradiologists, from Dr. Juan Taveras to Dr. Michael Huckman to Dr. Robert Quencer to Dr. Robert Grossman.

One only has to pick up any random issue of the *AJNR* to realize what a tremendous mark Mauricio has made on the journal. His imprint starts on the first page of content with his column, Perspectives. Probing, erudite, at times very witty, and always brilliant, Mauricio turns out a monthly commentary on the state of neuroradiology, the state of our profession, and, at times, the state of the world. His references and quotations demonstrate a mind not only scientific and exacting but also knowledgeable in realms far beyond medicine.

Having worked with Mauricio very closely at the ASNR for the past two years, I can also attest to the fact that Mauricio is totally dedicated to the journal. At times, it seemed his reason for being. And the journal has benefitted immensely, in turn. From its look to its organization to the quality of the articles, Mauricio has brought the journal into the forefront of all radiology journals and it now ranks #2 in Impact Factor of all radiology journals. *AJNR* is the premier clinical neuroimaging journal with the highest circulation among all imaging-related subspecialty journals, publishing about 350 articles in 12 issues per year. It receives over 1400 original submissions annually and its Web site is accessed over 10 million times a year. In addition to the print version of the Journal, Mauricio also initiated its biannual Special Collections and monthly *AJNR* Digest. Other electronic activities which he began include its popular Case Collection (Case of the Week, Case of the Month, Classic Case, and Clinical Correlation), podcasts (editor's and fellows' journal club selections, travelling journal club, and Special Collections), and Fellows' Portal. With his international background, Mauricio has also been the ideal person to spread the word of the *AJNR* across the world. Finally, he has done all this and kept the journal in sound financial health through a period of difficult economic times.

Mauricio took over leadership of the journal at a time when the concept of the journal was beginning to enter a state of flux. One only has to look at your neighborhood newsstand to realize that this has been a time when many publications have been unable to adjust and have disappeared. In the past eight years, the demands on the journal have changed. Our current expectations are for instant gratification, not a lag time before publication. We require our information in more bite-size pieces, directed at us and easily accessible.

The new editor will face an even more rapidly evolving world. What is the future of radiology journals? We know that the *AJNR* will survive but in what form? What will be the best digital format? There will be an increased demand for electronic access and a further migration to tablets and smartphones. Preserving the brand of the *AJNR* will become more challenging. While in the past, publication was the end point, increasingly, publication today is the starting point, the beginning of an interactive discussion. How will this impact on the financial state of the journal, with decreasing print advertising? How will the *AJNR* respond to the demands of social media?

To assist the Executive Committee in the search for a new editor in these changing times, I will chair a search committee comprised, in part, of Tina Young-Poussaint, Chair of the Publications Committee, Laurie Loevner, Vice-President, Howard Rowley, Robert Quencer, Robert D. Zimmerman, James Barkovich, Tabbassum Kennedy, and some of the Senior Editors of the *AJNR*, Harry J. Cloft, Nancy Fischbein, Pamela W. Schaefer, Jody Tanabe, and Charles M. Strother, as well as James Gantenberg, Karen Halm, and Angelo Artemakis from the ASNR headquarters. The appointment of the new Editor-in-Chief will be announced in the spring of 2015.

All interested physicians are invited to send their curriculum vitae and an introductory letter of intent to Dr. Gordon Sze, American Society of Neuroradiology, 800 Enterprise Drive, Suite 205, Oak Brook, IL, 60523 and via email to gordon.sze@yale.edu and jgantenberg@asnr.org. In addition, we welcome nominations of candidates from the ASNR membership. The deadline for receipt of submissions is August 1, 2014 but earlier submissions are welcome. A position description for the *AJNR* Editor and basic qualifications are posted at: www.ajnr.org/site/misc/eic-search-2015.xhtml.

Gordon Sze, MD, FACR
Chair, Editor-in-Chief Search Committee
President-Elect
American Society of Neuroradiology

BOOK REVIEWS *R.M. Quencer, Section Editor*

Please visit www.ajnrblog.org to read and comment on Book Reviews.

Trevo® XP
PROVUE RETRIEVER

Take Control. Capture More.

48%
Less Delivery Force

Easy to Deliver

- **48% less delivery force** required as demonstrated in bench testing*

Easy to Place

- **Distal FlexCell Design** including softer distal segment,† shorter landing zone‡ and bright radiopaque markers
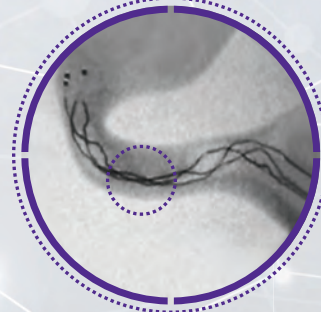
Easy to See

- **Full-length radiopacity**†† for precise placement, visible integration and interactive retrieval

See for Yourself: TrevoXP.com

All photographs taken by Stryker Neurovascular.
Bench test results may not necessarily be indicative of clinical performance.
Testing completed by Stryker Neurovascular. Data on file and available upon request.
  * Compared to Solitaire FR, 4x20mm.
  † Bench testing included Trevo XP ProVue, 4x20mm (n=57) and Solitaire FR, 4x20mm and 4x15mm (n=8).
  ‡ Compared to Trevo® ProVue Retriever.
 †† Bench model photo.
    Solitaire is a trademark of Tyco Healthcare Group LP composed of Covidien, Inc.

Stroke: *Our Only Focus. Our Ongoing Promise.*

Target® Detachable Coils

See package insert for complete indications, contraindications, warnings and instructions for use.

INTENDED USE / INDICATIONS FOR USE

Target Detachable Coils are intended to endovascularly obstruct or occlude blood flow in vascular abnormalities of the neurovascular and peripheral vessels. Target Detachable Coils are indicated for endovascular embolization of:

- Intracranial aneurysms
- Other neurovascular abnormalities such as arteriovenous malformations and arteriovenous fistulae
- Arterial and venous embolizations in the peripheral vasculature

CONTRAINDICATIONS

None known.

POTENTIAL ADVERSE EVENTS

Potential complications include, but are not limited to: allergic reaction, aneurysm perforation and rupture, arrhythmia, death, edema, embolus, headache, hemorrhage, infection, ischemia, neurological/intracranial sequelae, post-embolization syndrome (fever, increased white blood cell count, discomfort), TIA/stroke, vasospasm, vessel occlusion or closure, vessel
perforation, dissection, trauma or damage, vessel rupture, vessel thrombosis. Other procedural complications including but not limited to: anesthetic and contrast media risks, hypotension, hypertension, access site complications.

WARNINGS

- Contents supplied STERILE using an ethylene oxide (EO) process. Do not use if sterile barrier is damaged. If damage is found, call your Stryker Neurovascular representative.
- For single use only. Do not reuse, reprocess or resterilize. Reuse, reprocessing or resterilization may compromise the structural integrity of the device and/or lead to device failure which, in turn, may result in patient injury, illness or death. Reuse, reprocessing or resterilization may also create a risk of contamination of the device and/or cause patient infection or cross-infection, including, but not limited to, the transmission of infectious disease(s) from one patient to another. Contamination of the device may lead to injury, illness or death of the patient.
- After use, dispose of product and packaging in accordance with hospital, administrative and/or local government policy.
- **This device should only be used by physicians who have received appropriate training in interventional neuroradiology or interventional radiology and preclinical training on the use of this device as established by Stryker Neurovascular.**
- Patients with hypersensitivity to 316LVM stainless steel may suffer an allergic reaction to this implant.
- MR temperature testing was not conducted in peripheral vasculature, arteriovenous malformations or fistulae models.
- The safety and performance characteristics of the Target Detachable Coil System (Target Detachable Coils, InZone Detachment Systems, delivery systems and accessories) have not been demonstrated with other manufacturer's devices (whether coils, coil delivery devices, coil detachment systems, catheters, guidewires, and/or other accessories). Due to the potential incompatibility of non Stryker Neurovascular devices with the Target Detachable Coil System, the use of other manufacturer's device(s) with the Target Detachable Coil System is not recommended.

Copyright ©2014 Stryker
NV00006677.AA

- To reduce risk of coil migration, the diameter of the first and second coil should never be less than the width of the ostium.
- In order to achieve optimal performance of the Target Detachable Coil System and to reduce the risk of thromboembolic complications, it is critical that a continuous infusion of appropriate flush solution be maintained between a) the femoral sheath and guiding catheter, b) the 2-tip microcatheter and guiding catheters, and c) the 2-tip microcatheter and Stryker Neurovascular guidewire and delivery wire. Continuous flush also reduces the potential for thrombus formation on, and crystallization of infusate around, the detachment zone of the Target Detachable Coil.
- Do not use the product after the "Use By" date specified on the package.
- Reuse of the flush port/dispenser coil or use with any coil other than the original coil may result in contamination of, or damage to, the coil.
- Utilization of damaged coils may affect coil delivery to, and stability inside, the vessel or aneurysm, possibly resulting in coil migration and/or stretching.
- The fluoro-saver marker is designed for use with a Rotating Hemostatic Valve (RHV). If used without an RHV, the distal end of the coil may be beyond the alignment marker when the fluoro-saver marker reaches the microcatheter hub.
- If the fluoro-saver marker is not visible, do not advance the coil without fluoroscopy.
- Do not rotate delivery wire during or after delivery of the coil. Rotating the Target® Detachable Coil delivery wire may result in a stretched coil or premature detachment of the coil from the delivery wire, which could result in coil migration.
- Verify there is no coil loop protrusion into the parent vessel after coil placement and prior to coil detachment. Coil loop protrusion after coil placement may result in thromboembolic events if the coil is detached.
- Verify there is no movement of the coil after coil placement and prior to coil detachment. Movement of the coil after coil placement may indicate that the coil could migrate once it is detached.
- Failure to properly close the RHV compression fitting over the delivery wire before attaching the InZone® Detachment System could result in coil movement, aneurysm rupture or vessel perforation.
- Verify repeatedly that the distal shaft of the catheter is not under stress before detaching the Target Detachable Coil. Axial compression or tension forces could be stored in the 2-tip microcatheter causing the tip to move during coil delivery. Microcatheter tip movement could cause the aneurysm or vessel to rupture.
- Advancing the delivery wire beyond the microcatheter tip once the coil has been detached involves risk of aneurysm or vessel perforation.
- The long term effect of this product on extravascular tissues has not been established so care should be taken to retain this device in the intravascular space.
- To reduce risk of coil migration, the diameter of the first and second coil should never be less than the width of the ostium.
- In order to achieve optimal performance of the Target Detachable Coil System and to reduce the risk of thromboembolic complications, it is critical that a continuous infusion of appropriate flush solution be maintained between a) the femoral sheath and guiding catheter, b) the 2-tip microcatheter and guiding catheters, and c) the 2-tip microcatheter and Stryker Neurovascular guidewire and delivery wire. Continuous flush also reduces the potential for thrombus formation on, and crystallization of infusate around, the detachment zone of the Target Detachable Coil.
- Do not use the product after the "Use By" date specified on the package.
- Reuse of the flush port/dispenser coil or use with any coil other than the original coil may result in contamination of, or damage to, the coil.

Damaged delivery wires may cause detachment failures, vessel injury or unpredictable distal tip response during coil deployment. If a delivery wire is damaged at any point during the procedure, do not attempt to straighten or otherwise repair it. Do not proceed with deployment or detachment. Remove the entire coil and replace with undamaged product.

- Verify repeatedly that the distal shaft of the catheter is not under stress before detaching the Target Detachable Coil. Axial compression or tension forces could be stored in the 2-tip microcatheter causing the tip to move during coil delivery. Microcatheter tip movement could cause the aneurysm or vessel to rupture.
- After use, dispose of product and packaging in accordance with hospital, administrative and/or local government policy.

CAUTIONS / PRECAUTIONS

- Federal Law (USA) restricts this device to sale by or on the order of a physician.
- Besides the number of InZone Detachment System units needed to complete the case, there must be an extra InZone Detachment System unit as back up.
- Removing the delivery wire without grasping the introducer sheath and delivery wire together may result in the detachable coil sliding out of the introducer sheath.
- Failure to remove the introducer sheath after inserting the delivery wire into the RHV of the microcatheter will interrupt normal infusion of flush solution and allow back flow of blood into the microcatheter.
- Some low level overhead light near or adjacent to the patient is required to visualize the fluoro-saver marker; monitor light alone will not allow sufficient visualization of the fluoro-saver marker.
- Advance and retract the Target Detachable Coil carefully and smoothly without excessive force. If unusual friction is noticed, slowly withdraw the Target Detachable Coil and examine for damage. If damage is present, remove and use a new Target Detachable Coil. If friction or resistance is still noted, carefully remove the Target Detachable Coil and microcatheter and examine the microcatheter for damage.
- If it is necessary to reposition the Target Detachable Coil, verify under fluoroscopy that the coil moves with a one-to-one motion. If the coil does not move with a one-to-one motion or movement is difficult, the coil may have stretched and could possibly migrate or break. Gently remove both the coil and microcatheter and replace with new devices.
- Increased detachment times may occur when:
  – Other embolic agents are present.
  – Delivery wire and microcatheter markers are not properly aligned.
  – Thrombus is present on the coil detachment zone.
- Do not use detachment systems other than the InZone Detachment System.
- Increased detachment times may occur when delivery wire and microcatheter markers are not properly aligned.
- Do not use detachment systems other than the InZone Detachment System.

Trevo® XP ProVue Retrievers

See package insert for complete indications, complications, warnings, and instructions for use.

INDICATIONS FOR USE

The Trevo Retriever is intended to restore blood flow in the neurovasculature by removing thrombus in patients experiencing ischemic stroke within 8 hours of symptom onset. Patients who are ineligible for intravenous tissue plasminogen activator (IV t-PA) or who fail IV t-PA therapy are candidates for treatment.

COMPLICATIONS

Procedures requiring percutaneous catheter introduction should not be attempted by physicians unfamiliar with possible complications which may occur during or after the procedure. Possible complications include, but are not limited to, the following: air embolism; hematoma or hemorrhage at puncture site; infection; distal embolization; pain/headache; vessel spasm, thrombosis, dissection, or perforation; emboli; acute occlusion; ischemia; intracranial hemorrhage; false aneurysm formation; neurological deficits including stroke; and death.

COMPATIBILITY

3x20 mm retrievers are compatible with Trevo® Pro 14 Microcatheters (REF 90231) and Trevo® Pro 18 Microcatheters (REF 90238). 4x20 mm retrievers are compatible with Trevo® Pro 18 Microcatheters (REF 90238). Compatibility of the Retriever with other microcatheters has not been established. Performance of the Retriever device may be impacted if a different microcatheter is used. The Merci® Balloon Guide Catheters are recommended for use during thrombus removal procedures. Retrievers are compatible with the Abbott Vascular DOC® Guide Wire Extension (REF 22260).

Copyright ©2014 Stryker
NV00006807.AA

WARNINGS

- Contents supplied STERILE, using an ethylene oxide (EO) process. Nonpyrogenic.
- To reduce risk of vessel damage, adhere to the following recommendations:
  – Take care to appropriately size Retriever to vessel diameter at intended site of deployment.
  – Do not perform more than six (6) retrieval attempts in same vessel using Retriever devices.
  – Maintain Retriever position in vessel when removing or exchanging Microcatheter.
- To reduce risk of kinking/fracture, adhere to the following recommendations:
  – Immediately after unsheathing Retriever, position Microcatheter tip marker just proximal to shaped section. Maintain Microcatheter tip marker just proximal to shaped section of Retriever during manipulation and withdrawal.
  – Do not rotate or torque Retriever.
  – Use caution when passing Retriever through stented arteries.
- Do not resterilize and reuse. Structural integrity and/or function may be impaired by reuse or cleaning.
- The Retriever is a delicate instrument and should be handled carefully. Before use and when possible during procedure, inspect device carefully for damage. Do not use a device that shows signs of damage. Damage may prevent device from functioning and may cause complications.
- Do not advance or withdraw Retriever against resistance or significant vasospasm. Moving or torquing device against resistance or significant vasospasm may result in damage to vessel or device. Assess cause of resistance using fluoroscopy and if needed resheath the device to withdraw.

- If Retriever is difficult to withdraw from the vessel, do not torque Retriever. Advance Microcatheter distally, gently pull Retriever back into Microcatheter, and remove Retriever and Microcatheter as a unit. If undue resistance is met when withdrawing the Retriever into the Microcatheter, consider extending the Retriever using the Abbott Vascular DOC guidewire extension (REF 22260) so that the Microcatheter can be exchanged for a larger diameter catheter such as a DAC® catheter. Gently withdraw the Retriever into the larger diameter catheter.
- Administer anti-coagulation and anti-platelet medications per standard institutional guidelines.

PRECAUTIONS

- Prescription only – device restricted to use by or on order of a physician.
- Store in cool, dry, dark place.
- Do not use open or damaged packages.
- Use by "Use By" date.
- Exposure to temperatures above 54°C (130°F) may damage device and accessories. Do not autoclave.
- Do not expose Retriever to solvents.
- Use Retriever in conjunction with fluoroscopic visualization and proper anti-coagulation agents.
- To prevent thrombus formation and contrast media crystal formation, maintain a constant infusion of appropriate flush solution between guide catheter and Microcatheter and between Microcatheter and Retriever or guidewire.
- Do not attach a torque device to the shaped proximal end of DOC® Compatible Retriever. Damage may occur, preventing ability to attach DOC® Guide Wire Extension.

AJNR

Writer's Block

M. Castillo, *Editor-in-Chief*

After writing nearly 70 *Perspectives*, it was bound to happen; it seems I have hit "writer's block." This is the first time I sat down to write my monthly essay in over 8 months and I decided to use the occasion to familiarize myself with this condition (and try to liberate myself from it). Writer's block varies in intensity from extreme (abandoning one's career as an author—think Harper Lee and Ralph Ellison) to trivial and temporary (which I hope mine is). Why worry? Most writers have it at one time or another. The most common causes cited for writer's block are lack of inspiration, illness, depression, financial pressure, and a sense of failure. None of these apply to me. In my case, maybe it is just good old academic pressure. With increasing frequency, I hear that the only part of *AJNR* that our subscribers read is my *Perspectives*, to which I say: What about the rest of the *Journal*? That is where most of my energy and time are spent! And, if our readers are paying that much attention to my short essays, should each one be better than the last? Writer's block sounds like the ideal excuse to avoid thinking about what to write (just look at the title of my first reference: "Writer's Block as an Instrument for Remaining in Paradise").[1]

Writer's block is a modern notion, and the term was coined in 1947 by Dr Edmund Bergler, a famous Austrian psychiatrist living in New York City.[2] Today, it is well accepted that the notion of writer's block arose in conjunction with the sudden prestige of psychiatry in the United States after World War II. Dr Bergler, a follower of Freud, blamed writer's block on oral masochism and a milk-denying mother (that gives me something to think about because I know that I was bottle-fed!), in addition to other "phallic and anal" explanations along Freudian lines. Stress leads to panic, and some scientists believe that the reticular activating system in the brain stem will shift higher functions associated with writing from the cortex to the limbic system under duress.[3] Others disagree and think that the creative writing process starts at the level of the limbic system, whereas more technical writing is initially fueled by the frontal cortex. If both were true, all writing would stop as functions shift from one location to the other. However, writer's block can be selective, as it is in my case. That is, I continue to write other articles, chapters, and books, but writing this specific series of essays is my problem. Writer's block is commonly seen in college and university students who consistently fail to turn in their written assignments. In them, procrastination (a behavior specifically called "academic trait procrastination") is a major component of writer's block. Procrastination is learned, so education specialists claim that it can be unlearned.[1] Perfectionism is also blamed for the block; it seems to motivate some procrastination, and together these both promote writer's block.[1]

In academia, the notion of writer's block is disdained by younger members but seems to gain respect at higher levels where it occurs more commonly.[4]

Writer's block is better termed "creative inhibition" or "creative block."[5] It is becoming more prominent: it was little known by the early Romantic writers, became more prominent during the epoch of the French Symbolists, and last, was rampant (and became a recognized entity) during the period of the great American novel. Today, in a manner similar to attention-deficit disorder, writer's block is a nearly unique American affliction (though it occasionally happens in other countries, vide infra).[6]

Agraphia is the ultimate writer's block because it refers to the physiologic inability to write, but, in this case, lesions in the brain, such as those induced by trauma or stroke, are present and explain it. Agraphia results from damage to the Wernicke area and is nearly always accompanied by other language disabilities. In some cases, the inability to write may be physical, such as so-called "writer's cramp." This is a muscle dystonia, and DTI has shown fractional anisotropy changes in the fibers connecting the primary sensorimotor areas with subcortical structures in individuals who suffer from it.[7] In such individuals, fMRI has also shown abnormally low activation of the sensorimotor cortex and supplementary motor areas.[8] The findings of these studies imply that both inhibitory and excitatory mechanisms play a role in writer's cramp and that the pain it causes prevents writing by hand. Writer's cramp can also develop during typing and other activities such as using a screwdriver. Compared with men, women are thought to be better writers; however fMRI does not show significant differences in brain activation for either sex while writing.[9] The same study found significant differences between good and poor writers while handwriting, mostly in brain regions involved with planning for serial finger movements.

The opposite of writer's block is also known to occur, and it can be temporary or affect an individual all of his or her life. Balzac, Hugo, and Dickens probably had "graphorrhea." The problem with calling the obsession to write "graphorrhea" is that this term is also used for manic patients who compose long lists, many times containing only meaningless words, which is not the same as writing many great novels. As psychiatry evolved from an analytic discipline to a chemical science, writer's block came to be blamed on abnormal brain chemistry. More seriously, writer's block can be a manifestation of a dangerous underlying psychiatric disease such as schizophrenia, obsessive compulsive disorder, or substance abuse (think Scott Fitzgerald).

Writer's block has been assessed in individuals who speak languages other than English. Two studies addressed it in Chinese and Spanish native speakers and found that it occurs in those languages as it does in English.[10-12] In other languages, as in English, writer's block appears to be related to premature editing and to a lack of strategies for dealing with complex writing tasks. Developing a strategy before the actual writing helps some individuals. Princeton Professor and author John McPhee tells a related

story in his essay "Structure."[13] For 2 weeks he lay down on a picnic table under the trees looking at them and wondering how to start a piece on pines. After 8 months of work, he was finally able to turn it in. He suggests that having a preplanned structure eases the stress of writing and results in a better organized and flowing article. The ease of cutting and pasting makes attaining the desired structure easier today than in the past.

The use of a computer with word-processing capabilities reduces writer's block for second-language writers but not for native-language writers.[14] Spelling is also intimately related to the ability to write. In one study, disabled spellers showed significantly more activation in clusters of neural networks associated with working memory and executive functions.[15] Computer programs that automatically correct spelling may help these individuals overcome writer's block.

Because writing is intimately related to reading, recognition of the written word is needed for both activities. Alexia is a condition in which patients lose their ability to read and is associated with lesions in the left parietal and occipital lobes.[16] Alexia has been "folklorized" in several accounts by the famous and popular author and neurologist Oliver Sacks. His patients who had this condition were said to have lesions affecting the VWFA (visual word recognition area), which is presumably located in the left midfusiform gyrus (running from temporal to occipital lobe under the parahippocampal gyrus). Because this area is also involved in the recognition of auditory, phonologic, and visual impulses, patients with lesions there have more symptoms than alexia only. Pure alexia caused by a lesion in the VWFA has not been reported. More importantly, a meta-analysis of the literature, including fMRI studies, states that this brain region does not participate in visual word processing, and thus its concept is erroneous.[17] Alexia without agraphia occurs with lesions involving the left-sided splenium of the corpus callosum.

Strategies for coping with (and curing) writer's block include group discussions, brainstorming (I wrote an essay against this), list-making (I have a long list of topics that I have considered, but none seem very attractive now), and engaging with the text (I have no idea what this means). Recalcitrant blockage must be treated with extensive "therapy."[15] Other cures include "automatic writing" in which texts are produced from the subconscious without conscious awareness.[18] Instead of coming directly from the writer's mind, Arthur Conan Doyle believed that automatic writing came from external spirits. Channeling writing from a spirit is called "psychography." Both phenomena may be explained as "ideomotor effects" meaning just an activity of which we are partially or completely unaware. Of course, all of this is nonsense, and fMRI has proved (many times) that ideomotor effects originate in the brain and not outside of it.[19]

At this point, I must say that having finished this *Perspectives*, I feel somewhat liberated. Whether that feeling will be short-lived or last and allow me to write next month's piece, you, kind reader, must wait and see.

REFERENCES

1. Smeets S. **Writer's block as an instrument for remaining in paradise.** *Zeitschrift Schreiben* 2008 Jun 22 [Epub]
2. http://en.wikipedia.org/wiki/Edmund_Bergler#cite_note-Akhtar2009–11. Accessed July 24, 2013
3. Bane R. **The writer's brain: what neurology tells us about teaching creative writing.** http://www.rosannebane.com/newsletters/The_Writer%27%27s_Brain.Rosanne_Bane.41–50%5B1%5D.pdf. Accessed July 24, 2013
4. Gumz A, Brahler E, Erices R. **Burnout experience and work disruptions among clients seeking counseling: an investigation of different groups of academic level.** *Psychother Psychosom Med Psychol* 2012;62:33–39
5. Kantor M. *Understanding Writer's Block: A Therapist's Guide to Diagnosis and Treatment.* Westport, Connecticut: Praeger; 1995
6. Acocella J. **Blocked: why do writers stop writing?** *The New Yorker* June 16, 2004
7. Delmaire C, Vidailhet M, Wassermann D, et al. **Diffusion abnormalities in the primary sensorimotor pathways in writer's cramp.** *Arch Neurol* 2009;66:502–08
8. Oga T, Honda M, Toma K, et al. **Abnormal cortical mechanisms of voluntary muscle relaxation in patients with writer's cramp: an fMRI study.** *Brain* 2002;125:895–903
9. Richards TL, Berninger VW, Stock P, et al. **fMRI sequential-finger movement activation differentiating good and poor writers.** *J Clin Exp Neuropsychol* 2009;31:967–83
10. Lee S, Krashen S. **Writer's block in a Chinese sample.** *Percept Mot Skills* 2003;97:537–42
11. Betancourt F, Phinney M. **Sources of writing block in bilingual writers.** *Written Communications* 1990;7:482–511
12. Phinney M. **Word processing and writing apprehension in first and second language writers.** *Computers Composition* 1991;9:65–82
13. McPhee J. **Structure: beyond the picnic-table crisis.** *The New Yorker* January 14, 2013, pp 46–55
14. Richards TL, Berninger V, Winn W, et al. **Differences in fMRI activation between children with and without spelling disability on 2-back/0-back working memory contrast.** *J Writing Res* 2009; 1:93–123
15. Huston P. **Resolving writer's block.** *Can Fam Physician* 1998; 44:92–97
16. Alexia (condition). http://en.wikipedia.org/wiki/Alexia_(condition). Accessed July 24, 2013
17. Price CJ, Devlin JT. **The myth of the visual word form area.** *NeuroImage* 2003;19:473–81
18. Automatic writing. http://en.wikipedia.org/wiki/Automatic_writing. Accessed July 24, 2013
19. Spengler S, von Cramon DY, Brass M. **Was it me or was it you? How the sense of agency originates from the ideomotor learning revealed by fMRI.** *NeuroImage* 2009;46:290–98

Imaging and Treatment of Patients with Acute Stroke: An Evidence-Based Review

P.C. Sanelli, J.B. Sykes, A.L. Ford, J.-M. Lee, K.D. Vo, and D.K. Hallam

ABSTRACT

SUMMARY: Evidence-based medicine has emerged as a valuable tool to guide clinical decision-making, by summarizing the best possible evidence for both diagnostic and treatment strategies. Imaging plays a critical role in the evaluation and treatment of patients with acute ischemic stroke, especially those who are being considered for thrombolytic or endovascular therapy. Time from stroke-symptom onset to treatment is a strong predictor of long-term functional outcome after stroke. Therefore, imaging and treatment decisions must occur rapidly in this setting, while minimizing unnecessary delays in treatment. The aim of this review was to summarize the best available evidence for the diagnostic and therapeutic management of patients with acute ischemic stroke.

ABBREVIATIONS: DPM = diffusion-perfusion mismatch; IA = intra-arterial; ICH = intracranial hemorrhage; r-proUK = recombinant prourokinase; TIMI = Thrombolysis in Myocardial Infarction

In this era of health care reform and cost containment, major concerns have been raised regarding inappropriate medical expenditures and the lack of data to support the necessity of such high levels of health care spending. It is becoming ever more difficult to justify diagnostic imaging and other medical procedures with anecdotal evidence, expert opinion, or experience. Instead, great emphasis has been placed on the necessity for evidence-based practice to guide clinical decision-making, especially in light of limited financial resources and increased public awareness of imaging-related safety concerns, including risks from radiation and contrast administration.

Evidence-based practice is defined as "integration of the best research evidence with clinical expertise and patient values." This necessitates the balance of scientific evidence, clinical expertise, and judgment. When strong evidence is available and integrated in a methodical fashion, practice guidelines can emerge, eventually shaping new standards of care. However, when strong evidence is not available, clinical expertise and judgment play a major role in medical decision-making.

The aim of this review is to summarize the best available evidence for the diagnostic and therapeutic management of patients with acute ischemic stroke. The first part of this review synthesizes the most current evidence on the appropriate indications and modalities to consider in the diagnostic work-up of patients with acute stroke. The second part examines the efficacy of medical and mechanical interventions in acute stroke. Summary statements along with strength of evidence are provided for each section as a quick reference. Table 1 describes the classification scheme used to determine the strength of evidence in the literature.

EVIDENCE-BASED IMAGING IN ACUTE ISCHEMIC STROKE

Because acute ischemic stroke and intracranial hemorrhage may have similar clinical presentations, the primary imaging goal is to differentiate these 2 entities. Because thrombolysis and endovascular therapy are associated with an increased risk of hemorrhage, an additional imaging goal includes confirming the diagnosis while excluding stroke mimics so that patients are not treated unnecessarily. Finally, for patients who do not meet the criteria for IV thrombolysis but who arrive at the hospital relatively early after stroke onset, emerging imaging goals also include identifying brain tissue that is still viable and identifying the location of vascular occlusion when endovascular therapy is considered.

Imaging Evidence to Assess Intracranial Hemorrhage

CT. Although it is accepted that CT is sensitive in detecting acute ICH, surprisingly few studies have been conducted to support this belief.[1] One of the original studies on a first-generation scanner in the 1970s identified 66 hemorrhages with CT, but the data lacked

From the Departments of Radiology (P.C.S., J.B.S.) and Public Health (P.C.S.), Weill Cornell Medical Center/NewYork-Presbyterian Hospital, New York, New York; Departments of Neurology (A.L.F., J.-M.L.) and Radiology (J.-M.L., K.D.V.), Washington University, School of Medicine, St. Louis, Missouri; and Department of Radiology (D.K.H.), University of Washington Medical Center, Seattle, Washington.

Please address correspondence to Pina C. Sanelli, MD, MPH, Department of Radiology, Weill Cornell Medical College, NewYork-Presbyterian Hospital, 525 East 68th St, Starr 8A, New York, NY 10065; e-mail: pcs9001@med.cornell.edu

Indicates open access to non-subscribers at www.ajnr.org

Table 1: Classification scheme for the strength of evidence

Strength of Evidence	Criteria Used
Strong	Studies with broad generalizability to most patients suspected of having the disease; include prospective, blinded comparison of a diagnostic test with a well-defined final diagnosis in an unbiased sample when assessing diagnostic accuracy or blinded randomized control trials when assessing therapeutic impact or patient outcomes; also included are well-designed meta-analyses
Moderate	Prospective or retrospective studies with narrower spectrum of generalizability, with only a few flaws that are well-described so that their impact can be assessed but still include a blinded study of diagnostic accuracy on an unbiased sample (well-designed cohort or case-control studies) and randomized trials for therapeutic effects or patient outcomes
Limited	Diagnostic accuracy studies with several flaws in research methods, small sample sizes, incomplete reporting, or nonrandomized comparisons for therapeutic impact or patient outcomes
Insufficient	Studies with multiple flaws in research methods, case series, descriptive studies, or expert opinions without substantiating data

postmortem confirmation. Subsequently, in a postmortem series of 79 patients, in 4 of 17 patients, CT missed ICHs—all of which were located in the brain stem.[2] While there is little doubt that the third-generation scanners are far superior today, the precise accuracy of CT for the detection of ICH is unknown.

MR Imaging. MR imaging was reported to detect ICH within 6 hours and as early as 23 minutes from symptom onset.[3,4] One study evaluated 62 patients with ICH within 6 hours of onset and 62 controls, with 3 experienced readers using CT as the reference standard.[5] The readers, blinded to clinical and CT results, identified all acute hemorrhages on MR imaging, yielding 100% sensitivity and specificity. A subsequent study comparing CT and MR imaging for detection of hemorrhagic stroke within 6 hours of onset, using the discharge diagnosis as the reference standard, found 86% sensitivity and 100% specificity for both CT and MR imaging. Of 29 acute hemorrhages on CT, 25 were identified on MR imaging (in 3 of 4 cases, blood was misclassified as chronic instead of acute).[6] Similarly, 4 cases of ICH identified on MR imaging were not seen on CT (all were ischemic infarcts with hemorrhagic transformation). Therefore, it appears that rare cases of early intracranial hemorrhage may be missed on either CT or MR imaging. However, susceptibility-weighted sequences have improved sensitivity in the detection of cerebral microbleeds that are not otherwise detected on CT. Thus far, studies suggest that neither the presence nor number of microbleeds is associated with an increased risk of hemorrhagic transformation in either tPA-treated or untreated patients.[7-9]

Summary of Evidence. In the evaluation of patients with acute stroke for IV thrombolysis, CT has become the technique of choice for exclusion of ICH, based on randomized controlled trials (strong evidence). Recent studies indicate that the accuracy of MR imaging in detecting ICH is likely equivalent to that of CT

even in the hyperacute setting (within 6 hours of ictus) and is even more accurate for detection of chronic cerebral microbleeds (moderate evidence).

Imaging Evidence to Assess Ischemia and Exclude Stroke Mimics

CT. The diagnosis of acute stroke is primarily based on the clinical history and physical examination. At times, patients may present with strokelike symptoms due to nonstroke etiologies. Stroke mimics may account for up to 19% of patients initially diagnosed with stroke and up to 14% of patients treated with IV tPA.[10,11] An additional goal of imaging is to confirm diagnosis and to evaluate the extent of ischemic changes. Large ischemic strokes may demonstrate early signs of ischemia on CT, including loss of gray-white differentiation, hyperattenuated clot in the proximal MCA, sulcal effacement, and local mass effect. Such signs were found in 31% and 81% of patients within 3 and 5 hours after symptom onset, respectively.[12,13] Early CT signs involving more than one-third of the MCA distribution have been associated with large strokes, increased risk of hemorrhagic transformation, and poor outcome.[14-16] The Alberta Stroke Program Early CT Score (ASPECTS), a 10-point scoring system to detect early ischemic changes on NCCT, was developed as a tool that would be more reliable than the MCA rule.[17] While ASPECTS was found to have superior interobserver agreement, it only modestly improved accuracy for predicting functional outcome and performed the same as the MCA rule for predicting symptomatic hemorrhage.[17,18]

MR Imaging. DWI is more sensitive for detecting ischemic changes within minutes of stroke onset and ischemic lesions as small as 4 mm in diameter compared with CT.[19-21] As time from symptom onset increased, the sensitivity of DWI for the diagnosis of ischemic stroke also increased 73%, 81%, and 92% for <3 hours, 3–12 hours, and >12 hours, respectively, whereas CT had only 12%, 20%, and 16% sensitivity at these respective time intervals. The sensitivity for MR imaging to detect ischemia within 6 hours of onset is 81%–91%; therefore, the absence of a DWI lesion does not completely exclude ischemic stroke. DWI may be falsely negative in very early stroke and in patients with small subcortical or vertebrobasilar infarctions or in patients with low stroke severity (NIHSS score < 4).[21-24] Therefore, stroke timing, location, size, and perfusion status contribute to the visualization of a DWI lesion.

Summary of Evidence. DWI is superior to CT for identifying acute ischemic stroke within the first 12 hours of symptom onset (strong evidence). However, MR imaging does not necessarily have a greater influence than CT on decision-making or clinical outcomes in the acute setting, given its limited availability and the need for patient screening. Early CT signs of ischemia involving more than one-third of the MCA distribution have been associated with large strokes, increased risk of hemorrhagic transformation, and poor outcome (strong evidence).

Imaging Evidence to Determine Brain Tissue Viability

MR Imaging. An emerging goal of acute stroke imaging is to identify patients who may benefit from treatment outside the current

Table 2: Clinical studies testing penumbral imaging markers

Study Name	Validation of the Imaging Biomarker	Testing a Treatment on the Basis of Selection of Patients with an Imaging Biomarker
DIAS,[28] DEDAS,[29] DIAS-2,[30] IV tenecteplase,[44,a]	No	Yes
DEFUSE,[31] DEFUSE-2,[32,33]	Yes	No
EPITHET,[34] MR-RESCUE[35]	Yes	Yes

[a] This trial required intracranial vessel occlusion on CTA and CTP mismatch for randomization.

therapeutic window for IV thrombolysis. Thus, identifying tissue that may be rescued with therapy (ie, the ischemic penumbra) has been a major focus of clinical research. Using multimodal MR imaging, DWI is postulated to delineate irreversibly injured tissue (infarct core), and PWI is postulated to delineate critically hypoperfused tissue that will evolve into infarction if not reperfused in a timely manner (ischemic penumbra). When DWI and PWI are superimposed, the nonoverlapping "mismatched" region has been proposed to represent the penumbra.[25,26] Consistent with the idea of an evolving ischemic core, the DWI lesion may grow into a final infarct approximating the early PWI abnormality.[27] The DWI-PWI mismatch has been rapidly translated into clinical trials under 3 categories of study design: 1) to select patients for enrollment in the therapeutic trial, 2) to validate DPM as a biomarker of the penumbra, and 3) both (Table 2).

Within the first category, the Desmoteplase in Acute Ischemic Stroke trial (DIAS),[28] the Dose Escalation for Ischemic Stroke trial (DEDAS),[29] and the DIAS-II[30] have been completed. These trials examined a novel thrombolytic agent, desmoteplase, compared with placebo in patients demonstrating DPM between 3 and 9 hours after stroke onset. While the initial phase-2 studies, DIAS and DEDAS, demonstrated safety and early signs of efficacy for desmoteplase, the phase-3 study, DIAS-II, showed unexpectedly high mortality and no overall clinical benefit. Unfortunately, these negative results did not permit an analysis of which component of the study failed—the therapeutic agent or the DPM criteria.

Within the second category, the Diffusion and Perfusion Imaging Evaluation for Understanding Stroke Evolution (DEFUSE) trial aimed to validate DPM by comparing clinical outcomes in patients with DPM and reperfusion with outcomes in patients without DPM and reperfusion; patients in both groups were treated with tPA between 3 and 6 hours of stroke onset.[31] Of 74 patients enrolled, 75% had DPM and 25% did not. In patients with DPM, reperfusion was associated with better clinical outcome than no reperfusion. However, due to the small number of patients without DPM ($n = 11$), the converse that nonmismatch patients did not improve with reperfusion could not be proved. The high ratio of mismatch to nonmismatch patients made it clear that the definition for DPM was too liberal, resulting in a relatively unselected group of patients with stroke.

On the basis of the DEFUSE results, the DPM definition was refined for the DEFUSE-2 study.[32,33] However, a subset of patients with DPM with "target mismatch" was selected, which excluded patients with a "malignant profile" (large baseline DWI and PWI lesions) because DEFUSE indicated that these patients have worse outcomes. Thus far, selection of patients with the "target mismatch" definition demonstrated improved clinical out-

come and reduced infarct growth compared with the nontarget mismatch group.

Studies giving information about both the utility of the imaging biomarker and the efficacy of treatment include the Echo-Planar Imaging Thrombolytic Evaluation Trial (EPITHET)[34] and MR and Recanalization of Stroke Clots Using Embolectomy (MR-RESCUE).[35] In EPITHET, patients with stroke after 3 hours from symptom onset were serially imaged at 3 time points: 1) before administration of tPA versus placebo, 2) at 3–5 days, and 3) at 90 days after treatment. With its similarity to the DEFUSE protocol, most (86%) of enrolled patients were categorized as having DPM, making conclusions regarding nonmismatch patients difficult. The primary end point showed no difference in geometric mean infarct growth between the tPA and placebo groups. MR-RESCUE,[35] an ongoing study, aims to test both a similar DPM protocol in combination with treatment by using the Merci retriever (Concentric Medical, Mountain View, California) versus placebo up to 8 hours after stroke onset.

Taking advantage of the endogenous susceptibility of deoxyhemoglobin on T2*-weighted images is an active investigation into imaging oxygen metabolism by using MR imaging (eg, MR-oxygen metabolic index),[36-38] a parameter similar to PET-derived cerebral metabolic rate of oxygen. If these physiologic measures of oxygen metabolism accurately delineate the ischemic penumbra, they may yield ischemic thresholds that are time-invariant,[38] unlike diffusion and perfusion thresholds, which vary with elapsed time between stroke onset and imaging.[19,39] These relatively new imaging approaches will require validation in well-designed trials.

CT. Similar to PWI, CTP is capable of providing maps of tissue perfusion. In a prospective multicenter study, patients with acute stroke were imaged <12 hours from stroke onset with CT and MR imaging.[40] The CTP parameter most accurately reflecting the ischemic core (compared with DWI) was absolute CBV < 2 mL/100 g, while the parameter most accurately reflecting the penumbra was a relative mean transit time of >145% of the contralateral hemisphere. However, in more recent studies, relative CBF was found to be more predictive of the ischemic core and final infarct volume than absolute CBV.[41-43] Recently, CTP mismatch with PWI used for both core (CBF) and penumbra (MTT, CBV) in combination with intracranial vessel occlusion on CTA was used to select patients for entry into a randomized controlled trial of IV tenecteplase versus IV tPA administered within 6 hours of stroke onset.[44] This trial was positive for its co-primary end points, improvement in the NIHSS score and percentage reperfusion at 24 hours. However, it is currently unknown whether tenecteplase is superior to tPA in unselected patients because treatment without CTA and CTP screening would save time and perhaps broaden the applicability of tenecteplase.

Summary of Evidence. Determination of tissue viability by using advanced imaging has the potential to individualize therapy and extend the therapeutic time window for some patients with acute stroke. Several imaging modalities, including MR imaging, CT,

and PET, have been examined in this role. Operational hurdles have limited the use of some of these modalities in the acute stroke setting (eg, PET), while others such as MR imaging have been studied in large clinical trials. Randomized controlled trials have not demonstrated a benefit of thrombolytic treatment in patients who are selected by using MR imaging–based criteria such as DPM (moderate evidence); however, studies are ongoing. Clinical trials with positive results will be needed before the use of penumbral imaging techniques in routine clinical decision-making.

Imaging Evidence to Determine the Location of Vascular Occlusion

CTA. An advantage of CTA is that it can be performed immediately after the prerequisite NCCT in patients with stroke. In several small case series, the sensitivity and specificity of CTA for trunk occlusions of the circle of Willis were 83%–100% and 99%–100%, respectively, compared with DSA.[45-48] A study with 2 blinded observers comparing CTA with DSA measured 475 short segments of intracranial arteries in 41 patients.[47] For detection of ≥50% stenosis, CTA had 97.1% sensitivity and 99.5% specificity. A similar study of 672 vessel segments in 28 patients found excellent sensitivity and specificity for intracranial stenosis of 98% and 98%, respectively, with 100% sensitivity and 100% specificity for intracranial occlusion.[48] This study also compared time-of-flight MRA with CTA and found CTA to have significantly higher sensitivity and positive predictive value compared with MRA (see below).

MRA. While MRA appears to be a useful tool for measuring stenosis in large extracranial vessels, its sensitivity decreases for smaller caliber intracranial vessels. For time-of-flight, complete or partial signal voids in regions of high and/or turbulent flow may occur, leading to an overestimation of the extent of stenosis. Therefore, cautious interpretation of the lumen caliber is warranted. In a study of intracranial disease comparing CTA and MRA with DSA in 28 patients (in 672 vessel segments), time-of-flight MRA had a sensitivity of 70% and 81% and a specificity of 99% and 98% for intracranial stenosis and intracranial occlusion, respectively.[48] The Stroke Outcomes and Neuroimaging of Intracranial Atherosclerosis (SONIA) trial was a prospective multicenter study comparing the diagnostic accuracy of transcranial Doppler and MRA with DSA.[49] The SONIA study found that both transcranial Doppler and MRA have high negative predictive values (86% and 91%, respectively) but low positive predictive values (36% and 59%, respectively). Sensitivity and specificity could not be obtained in this study because not every patient underwent DSA.[49]

Summary of Evidence. CTA and MRA have high diagnostic accuracy for detecting large-vessel occlusion compared with DSA (strong evidence). However, evidence supporting these imaging modalities in acute stroke management is lacking (limited evidence). Prospective studies examining the accuracy of acute noninvasive vascular imaging and whether it alters clinical outcome after stroke are needed.

EVIDENCE-BASED TREATMENT IN ACUTE ISCHEMIC STROKE

IV Thrombolytic Therapy

The National Institute of Neurological Disorders and Stroke (NINDS) stroke study proved the efficacy of the use of IV alteplase within 3 hours of stroke onset in patients with MCA stroke and no hemorrhage on NCCT.[50] At 3 months, patients treated with alteplase were at least 30% more likely to have minimal or no disability compared with those treated with a placebo. The benefit occurred despite higher rates of ICH in alteplase-treated patients compared with controls (6.4% versus 0.6%). Treatment with IV alteplase within 3 hours of stroke onset was endorsed early by the Special Writing Group of the Stroke Council, American Heart Association.[51]

A number of studies followed that failed to prove the efficacy of IV alteplase in the 3- to 6-hour time window. More recently, a meta-analysis was undertaken evaluating data from trials with negative results only in the 3- to 4.5-hour time window. The meta-analysis showed the efficacy of treatment with IV alteplase from 3 to 4.5 hours after MCA stroke onset in patients with no hemorrhage and no signs of significant early infarct on NCCT.[52] Multiple registries have been established, and these results further support the safety and efficacy of IV alteplase in the 4.5-hour window.[53-55]

In general, IV thrombolysis is regarded as less effective in recanalizing large occlusive clots, such as those of the terminal ICA or M1 MCA.[56-60] The presence of a hyperdense MCA sign on CT, indicating complete vessel occlusion, bodes poorly for patients treated with IV tPA,[58,59] which yields recanalization rates of 30% for proximal MCA occlusion and 10% for ICA occlusion.[60] On the basis of a subgroup analysis of the NINDS stroke study, despite low rates of recanalization with proximal occlusions, IV tPA improved outcome in large strokes.[61] Presumably, much of the benefit of IV treatment derives from recanalization of smaller more distal branches.

Summary of Evidence. IV thrombolysis is the standard-of-care treatment for acute ischemic stroke in the anterior circulation within 4.5 hours of symptom onset (strong evidence). Larger more proximal clots (ICA, M1 MCA) exhibit lower recanalization rates with IV thrombolytic treatment, and such patients tend to have worse prognosis (strong evidence).

IA Thrombolytic Therapy

Based on preliminary experience with IA therapy, the Prolyse in Acute Cerebral Thromboembolism (PROACT) II trial was implemented to determine the clinical efficacy and safety of intra-arterial r-proUK in patients with acute stroke.[62] Only patients with MCA infarct of <6 hours from onset and no evidence of hemorrhage or early signs of major infarct on CT were included. Angiographic inclusion criteria were either complete occlusion (TIMI 0) or contrast penetration with minimal perfusion (TIMI 1) of either an M1 or M2 division of the MCA. Following angiography, 180 patients met the criteria. These patients were randomized in a 2:1 ratio to receive IA r-proUK plus heparin or heparin only. The results indicated benefit for the treated group with 40% of r-proUK patients compared with 25% of control patients achieving the primary outcome measure of a modified Rankin Scale

score of 0–2, with similar mortality rates. Improved outcome in the treated group was noted despite increased frequency of early symptomatic hemorrhage (within 24 hours, 10% versus 2%). The recanalization rate was 66% for the r-proUK group and 18% for the control group ($P < .001$). Treated and control patients with less severe strokes (NIHSS score ≤ 10) did equally well. Patients with more severe strokes (NIHSS score > 10) were twice as likely as controls to achieve the desired outcome measure. Considering the limitations of this study, many investigators suspect that the demonstrated PROACT II benefit represents a lower limit for IA treatment efficacy.

Combined IV and IA Thrombolysis

Recognizing the trade-offs between IV and IA thrombolytic therapy, researchers have studied combined therapy consisting of IV treatment followed by IA treatment.[63] The Interventional Management of Stroke (IMS) II trial compared combined IV/IA thrombolysis with historical controls of IV thrombolytics alone and placebo from the NINDS stroke study.[64] Eighty-one patients who could be treated with IV alteplase within 3 hours from symptom onset were enrolled. IV treatment consisted of two-thirds the usual alteplase dose administered as a 15% bolus during 1 minute followed by the remainder for 30 minutes. Once IV treatment had been initiated, the patient was transferred to the angiography suite. If an IA treatment-amenable clot was identified, the remaining one-third of the alteplase dose was administered in the clot. If no IA-amenable clot was identified, the remaining one-third of the alteplase dose was administered IV. Of 81 patients, 55 underwent combined treatment with the remainder receiving IV treatment alone. The combined IV/IA-treated patients exhibited a better outcome than the NINDS alteplase-treated subjects by the Barthel Index but not by other outcome measures. The patients with combined treatment had significantly better outcome at 3 months than NINDS patients with placebo on all outcome measures (odds ratio > 2). The 3-month mortality for IMS patients with combined treatment (16%) trended lower than NINDS placebo- (24%) and alteplase-treated subjects (21%). The difference was not statistically significant. A subsequent trial, IMS III, compared combined IV alteplase alone with combined IV/IA treatment including mechanical devices. In April 2012, an independent data safety monitoring board placed the trial on hold because the interim analysis indicated a very low likelihood of improved outcome with combined treatment.

A prospective registry (RECANALISE [REcanalisation using Combined intravenous Alteplase and Neurointerventional ALgorithm for acute Ischemic StrokE] study) compared recanalization rates, 24-hour improvement, and 3-month functional outcome between patients in 2 time intervals who underwent different thrombolytic protocols.[65] In the first time period, patients within 3 hours of symptom onset were treated with IV alteplase according to standard protocol. In the second time interval, patients were treated with a combined technique similar to that in IMS II. Early neurologic recovery (defined as NIHSS 0 or 1 or a 4-point improvement) occurred in 60% of patients with combined treatment compared with 39% of those with IV treatment ($P = .07$); and 3-month functional outcome (mRS 0–2) occurred in 57% of those with combined treatment compared with 44% of those with

IV treatment ($P = .35$). The 90-day mortality and symptomatic intracranial hemorrhage rates were not appreciably different. The most pronounced difference observed was in the recanalization rate: 87% in patients with combined treatment and 52% of those with IV treatment ($P = .0002$).

Mechanical Endovascular Intervention

Mechanical clot removal has not been evaluated in a randomized controlled fashion. The Merci retriever (Concentric Medical) and the Penumbra aspiration system (Penumbra, Alameda, California)[66-69] were evaluated in prospective multicenter single-arm design trials. A historical control from PROACT II was often used, and the patients were treated for up to 8 hours. In the Multi MERCI trial,[67] mechanical thrombectomy was used in large-vessel stroke, in both anterior and posterior circulations, within 8 hours of onset. Patients with persistent large-vessel occlusion after IV alteplase were also included. Successful recanalization was reported in 57.3% (75 of 131) and a higher rate of 69.5% (91 of 131) after adjunctive therapy consisting of IA alteplase. The study also showed improved efficacy in recanalization with the new-generation devices. Significant complications were defined as those procedural complications resulting in an NIHSS decline of ≥4 or death or groin complication necessitating surgery and/or blood transfusion. Such clinically significant complications were observed in 9 patients (5.5%). Symptomatic ICH occurred in 16 patients (9.8%).

In the Penumbra Pivotal trial, patients with treatable large-vessel stroke <8 hours from onset were enrolled.[66] This study observed high recanalization rates (TIMI 2 or 3) of 81.6%. However, 12.8% of patients (18 of 125) endured procedural complications with 2.4% (3 patients) considered serious, resulting in a significant negative impact on the patient.

Two stent retrievers have been developed and compared with the Merci system (Solitaire FR Revascularization Device; Covidien, Irvine, California; and Trevo Pro Retrieval System; Stryker, Kalamazoo, Michigan). Patients treated with both retriever systems showed markedly improved rates of recanalization and reasonable safety.[70,71] As with the MERCI and Penumbra studies, safety was demonstrated along with high rates of recanalization; however, the clinical efficacy data are lacking. Both devices received FDA approval in 2012.

Summary of Evidence. IA thrombolysis may be used at a qualified stroke center to treat patients with major stroke due to MCA occlusion in <6 hours who cannot receive IV alteplase (strong evidence). The FDA has approved several mechanical devices for intracranial clot removal in appropriately selected patients up to 8 hours from symptom onset (strong evidence). Although considered appropriate for emergency stroke treatment, the effect on outcomes has not been established.

CONCLUSIONS

CT has been used as the first-line imaging to assess ICH in patients with acute stroke. Although MR imaging has equivalent accuracy in detecting ICH and is superior to CT within the first 24 hours for detection of ischemia, it should be used only if treatment is not delayed because the time from stroke-symptom onset to treatment is a strong predictor of long-term functional outcome. Non-

invasive vascular imaging (CTA, MRA) to assess the location and extent of clot and perfusion imaging to assess viable tissue are promising imaging techniques that may be used to select patients for novel thrombolytic agents and interventional devices. Therefore, further studies assessing their accuracy and impact on clinical outcomes are greatly needed. Regarding treatment of acute ischemic stroke, strong evidence exists proving the efficacy of IV and IA thrombolysis up to 4.5 and 6 hours, respectively, from stroke symptom onset. Mechanical thrombectomy has been approved in selected patients up to 8 hours.

REFERENCES

1. Culebras A, Kase CS, Masdeu JC, et al. **Practice guidelines for the use of imaging in transient ischemic attacks and acute stroke: a report of the Stroke Council, American Heart Association.** *Stroke* 1997;28:1480–97

2. Jacobs L, Kinkel WR, Heffner RR Jr. **Autopsy correlations of computerized tomography: experience with 6,000 CT scans.** *Neurology* 1976;26:1111–18

3. Schellinger PD, Jansen O, Fiebach JB, et al. **A standardized MRI stroke protocol: comparison with CT in hyperacute intracerebral hemorrhage.** *Stroke* 1999;30:765–68

4. Patel MR, Edelman RR, Warach S. **Detection of hyperacute primary intraparenchymal hemorrhage by magnetic resonance imaging.** *Stroke* 1996;27:2321–24

5. Fiebach JB, Schellinger PD, Gass A, et al. **Stroke magnetic resonance imaging is accurate in hyperacute intracerebral hemorrhage: a multicenter study on the validity of stroke imaging.** *Stroke* 2004;35:502–06

6. Kidwell CS, Chalela JA, Saver JL, et al. **Comparison of MRI and CT for detection of acute intracerebral hemorrhage.** *JAMA* 2004;292:1823–30

7. Fiehler J, Albers GW, Boulanger JM, et al. **Bleeding risk analysis in stroke imaging before thromboLysis (BRASIL): pooled analysis of T2*-weighted magnetic resonance imaging data from 570 patients.** *Stroke* 2007;38:2738–44

8. Lee SH, Kang BS, Kim N, et al. **Does microbleed predict haemorrhagic transformation after acute atherothrombotic or cardioembolic stroke?** *J Neurol Neurosurg Psychiatry* 2008;79:913–16

9. Kakuda W, Thijs VN, Lansberg MG, et al. **Clinical importance of microbleeds in patients receiving IV thrombolysis.** *Neurology* 2005;65:1175–8

10. Libman RB, Wirkowski E, Alvir J, et al. **Conditions that mimic stroke in the emergency department. Implications for acute stroke trials.** *Arch Neurol* 1995;52:1119–22

11. Chernyshev OY, Martin-Schild S, Albright KC, et al. **Safety of tPA in stroke mimics and neuroimaging-negative cerebral ischemia.** *Neurology* 2010;74:1340–45

12. Patel SC, Levine SR, Tilley BC, et al. **Lack of clinical significance of early ischemic changes on computed tomography in acute stroke.** *JAMA* 2001;286:2830–38

13. von Kummer R, Meyding-Lamade U, Forsting M, et al. **Sensitivity and prognostic value of early CT in occlusion of the middle cerebral artery trunk.** *AJNR Am J Neuroradiol* 1994;15:9–15, discussion 6–8

14. Hacke W, Kaste M, Fieschi C, et al. **Intravenous thrombolysis with recombinant tissue plasminogen activator for acute hemispheric stroke: the European Cooperative Acute Stroke Study (ECASS).** *JAMA* 1995;274:1017–25

15. Larrue V, von Kummer R, del Zoppo G, et al. **Hemorrhagic transformation in acute ischemic stroke: potential contributing factors in the European Cooperative Acute Stroke Study.** *Stroke* 1997;28:957–60

16. Larrue V, von Kummer RR, Muller A, et al. **Risk factors for severe hemorrhagic transformation in ischemic stroke patients treated with recombinant tissue plasminogen activator: a secondary analysis of the European-Australasian Acute Stroke Study (ECASS II).** *Stroke* 2001;32:438–41

17. Barber PA, Demchuk AM, Zhang J, et al. **Validity and reliability of a quantitative computed tomography score in predicting outcome of hyperacute stroke before thrombolytic therapy: ASPECTS Study Group—Alberta Stroke Programme Early CT Score.** *Lancet* 2000;355:1670–74

18. Coutts SB, Demchuk AM, Barber PA, et al. **Interobserver variation of ASPECTS in real time.** *Stroke* 2004;35:e103–e105

19. Fiebach JB, Schellinger PD, Jansen O, et al. **CT and diffusion-weighted MR imaging in randomized order: diffusion-weighted imaging results in higher accuracy and lower interrater variability in the diagnosis of hyperacute ischemic stroke.** *Stroke* 2002;33:2206–10

20. González RG, Schaefer PW, Buonanno FS, et al. **Diffusion-weighted MR imaging: diagnostic accuracy in patients imaged within 6 hours of stroke symptom onset.** *Radiology* 1999;210:155–62

21. Chalela JA, Kidwell CS, Nentwich LM, et al. **Magnetic resonance imaging and computed tomography in emergency assessment of patients with suspected acute stroke: a prospective comparison.** *Lancet* 2007;369:293–98

22. Kidwell CS, Alger JR, Di Salle F, et al. **Diffusion MRI in patients with transient ischemic attacks.** *Stroke* 1999;30:1174–80

23. Ay H, Buonanno FS, Rordorf G, et al. **Normal diffusion-weighted MRI during stroke-like deficits.** *Neurology* 1999;52:1784–92

24. An H, Ford AL, Vo K, et al. **Signal evolution and infarction risk for apparent diffusion coefficient lesions in acute ischemic stroke are both time- and perfusion-dependent.** *Stroke* 2011;42:1276–81

25. Neumann-Haefelin T, Wittsack HJ, Wenserski F, et al. **Diffusion- and perfusion-weighted MRI: the DWI/PWI mismatch region in acute stroke.** *Stroke* 1999;30:1591–97

26. Schwamm LH, Koroshetz WJ, Sorensen AG, et al. **Time course of lesion development in patients with acute stroke: serial diffusion- and hemodynamic-weighted magnetic resonance imaging.** *Stroke* 1998;29:2268–76

27. Baird AE, Benfield A, Schlaug G, et al. **Enlargement of human cerebral ischemic lesion volumes measured by diffusion-weighted magnetic resonance imaging.** *Ann Neurol* 1997;41:581–89

28. Hacke W, Albers G, Al-Rawi Y, et al. **The Desmoteplase in Acute Ischemic Stroke Trial (DIAS): a phase II MRI-based 9-hour window acute stroke thrombolysis trial with intravenous desmoteplase.** *Stroke* 2005;36:66–73

29. Furlan AJ, Eyding D, Albers GW, et al. **Dose Escalation of Desmoteplase for Acute Ischemic Stroke (DEDAS): evidence of safety and efficacy 3 to 9 hours after stroke onset.** *Stroke* 2006;37:1227–31

30. Hacke W, Furlan AJ, Al-Rawi Y, et al. **Intravenous desmoteplase in patients with acute ischaemic stroke selected by MRI perfusion-diffusion weighted imaging or perfusion CT (DIAS-2): a prospective, randomised, double-blind, placebo-controlled study.** *Lancet Neurol* 2009;8:141–50

31. Albers GW, Thijs VN, Wechsler L, et al. **Magnetic resonance imaging profiles predict clinical response to early reperfusion: the diffusion and perfusion imaging evaluation for understanding stroke evolution (DEFUSE) study.** *Ann Neurol* 2006;60:508–17

32. Albers G. **Results of DEFUSE 2: imaging endpoints.** In: *Proceedings of the International Stroke Conference*, New Orleans, Louisiana. February 1–3, 2012

33. Lansberg MG. **Results of DEFUSE 2: clinical endpoints.** In: *Proceedings of the International Stroke Conference*, New Orleans, Louisiana. February 1–3, 2012

34. Davis SM, Donnan GA, Parsons MW, et al. **Effects of alteplase beyond 3 h after stroke in the Echoplanar Imaging Thrombolytic Evaluation Trial (EPITHET): a placebo-controlled randomised trial.** *Lancet Neurol* 2008;7:299–309

35. Davis SM, Donnan GA, Butcher KS, et al. **Selection of thrombolytic therapy beyond 3 h using magnetic resonance imaging.** *Curr Opin Neurol* 2005;18:47–52

36. Lee JM, Vo KD, An H, et al. **Magnetic resonance cerebral metabolic**

rate of oxygen utilization in hyperacute stroke patients. *Ann Neurol* 2003;53:227–32

37. Lu H, Xu F, Grgac K, et al. **Calibration and validation of TRUST MRI for the estimation of cerebral blood oxygenation.** *Magn Reson Med* 2012;67:42–49

38. Read SJ, Bladin CF, Yasaka M, et al. **How time dependent is the threshold for cerebral infarction?** *Stroke* 1996;27:1918–20

39. Butcher K, Parsons M, Baird T, et al. **Perfusion thresholds in acute stroke thrombolysis.** *Stroke* 2003;34:2159–64

40. Wintermark M, Flanders AE, Velthuis B, et al. **Perfusion-CT assessment of infarct core and penumbra: receiver operating characteristic curve analysis in 130 patients suspected of acute hemispheric stroke.** *Stroke* 2006;37:979–85

41. Mayer TE, Hamann GF, Baranczyk J, et al. **Dynamic CT perfusion imaging of acute stroke.** *AJNR Am J Neuroradiol* 2000;21:1441–49

42. Bivard A, McElduff P, Spratt N, et al. **Defining the extent of irreversible brain ischemia using perfusion computed tomography.** *Cerebrovasc Dis* 2011;31:238–45

43. Tan JC, Dillon WP, Liu S, et al. **Systematic comparison of perfusion-CT and CT-angiography in acute stroke patients.** *Ann Neurol* 2007;61:533–43

44. Parsons M, Spratt N, Bivard A, et al. **A randomized trial of tenecteplase versus alteplase for acute ischemic stroke.** *N Engl J Med* 2012;366:1099–107

45. Hirai T, Korogi Y, Ono K, et al. **Prospective evaluation of suspected stenoocclusive disease of the intracranial artery: combined MR angiography and CT angiography compared with digital subtraction angiography.** *AJNR Am J Neuroradiol* 2002;23:93–101

46. Katz DA, Marks MP, Napel SA, et al. **Circle of Willis: evaluation with spiral CT angiography, MR angiography, and conventional angiography.** *Radiology* 1995;195:445–49

47. Nguyen-Huynh MN, Wintermark M, English J, et al. **How accurate is CT angiography in evaluating intracranial atherosclerotic disease?** *Stroke* 2008;39:1184–88

48. Bash S, Villablanca JP, Jahan R, et al. **Intracranial vascular stenosis and occlusive disease: evaluation with CT angiography, MR angiography, and digital subtraction angiography.** *AJNR Am J Neuroradiol* 2005;26:1012–21

49. Feldmann E, Wilterdink JL, Kosinski A, et al. **The Stroke Outcomes and Neuroimaging of Intracranial Atherosclerosis (SONIA) trial.** *Neurology* 2007;68:2099–106

50. **Tissue plasminogen activator for acute ischemic stroke: the National Institute of Neurological Disorders and Stroke rt-PA Stroke Study Group.** *N Engl J Med* 1995;333:1581–87

51. Adams HP Jr, Brott TG, Furlan AJ, et al. **Guidelines for thrombolytic therapy for acute stroke: a supplement to the guidelines for the management of patients with acute ischemic stroke—a Statement for Healthcare Professionals From a Special Writing Group of the Stroke Council, American Heart Association.** *Circulation* 1996;94:1167–74

52. Lansberg MG, Bluhmki E, Thijs VN. **Efficacy and safety of tissue plasminogen activator 3 to 4.5 hours after acute ischemic stroke.** *Stroke* 2009;40:2438–41

53. Wahlgren N, Ahmed N, Dávalos A, et al. **Thrombolysis with alteplase 3–4·5 h after acute ischaemic stroke (SITS-ISTR): an observational study.** *Lancet* 2008;372:1303–09

54. Topakian R, Brainin M, Eckhardt R, et al, for the SITS-Austria group. **Thrombolytic therapy for acute stroke in Austria: data from the Safe Implementation of Thrombolysis in Stroke (SITS) register.** *Eur J Neurol* 2011;18:306–11

55. Ahmed N, Wahlgren N, Grond M, et al, for the SITS investigators. **Implementation and outcome of thrombolysis with alteplase 3–4.5 h after an acute stroke: an updated analysis from SITS-ISTR.** *Lancet Neurol* 2010;9:866–74

56. Demchuk AM, Tanne D, Hill MD, et al, for the Multicentre tPA Stroke Survey Group. **Predictors of good outcome after intravenous tPA for acute ischemic stroke.** *Neurology* 2001;57:474–80

57. Sekoranja L, Loulidi J, Yilmaz H, et al. **Intravenous versus combined (intravenous and intra-arterial) thrombolysis in acute ischemic stroke: a transcranial color-coded duplex sonography–guided pilot study.** *Stroke* 2006;37:18050–59

58. Tomsick T, Brott T, Barsan W, et al. **Prognostic value of the hyperdense middle cerebral artery sign and stroke scale score before ultraearly thrombolytic therapy.** *AJNR Am J Neuroradiol* 1996;17:79–85

59. Agarwal P, Kumar S, Hariharan S, et al. **Hyperdense middle cerebral artery sign: can it be used to select intra-arterial versus intravenous thrombolysis in acute ischemic stroke?** *Cerebrovasc Dis* 2004;17:182–90

60. Wolpert SM, Bruckmann H, Greenlee R, et al. **Neuroradiologic evaluation of patients with acute stroke treated with recombinant tissue plasminogen activator: the rt-PA Acute Stroke Study Group.** *AJNR Am J Neuroradiol* 1993;14:3–13

61. **Generalized efficacy of t-PA for acute stroke: subgroup analysis of the NINDS t-PA Stroke Trial.** *Stroke* 1997;28:2119–25

62. Furlan A, Higashida R, Wechsler L, et al. **Intra-arterial prourokinase for acute ischemic stroke: the PROACT II study—a randomized controlled trial. Prolyse in Acute Cerebral Thromboembolism.** *JAMA* 1999;282:2003–11

63. The IMS Study Investigators. **Combined intravenous and intra-arterial recanalization for acute ischemic stroke: the Interventional Management of Stroke Study.** *Stroke* 2004;35:904–11

64. The IMS II Trail Investigators. **The Interventional Management of Stroke (IMS) II Study.** *Stroke* 2007;38:2127–35

65. Mazighi M, Serfaty JM, Labreuche J, et al. **Comparison of intravenous alteplase with a combined intravenous-endovascular approach in patients with stroke and confirmed arterial occlusion (RECANALISE study): a prospective cohort study.** *Lancet Neurol* 2009;8:802–09

66. The Penumbra Pivotal Stroke Trial Investigators. **The Penumbra Pivotal Stroke Trial: safety and effectiveness of a new generation of mechanical devices for clot removal in intracranial large vessel occlusive disease.** *Stroke* 2009;40:2761–68

67. Smith WS, et al. **Mechanical thrombectomy for acute ischemic stroke: final results of the Multi MERCI trial.** *Stroke* 2008;39:1205–12

68. Smith WS, Sung G, Starkman S, et al. **Safety and efficacy of mechanical embolectomy in acute ischemic stroke: results of the MERCI trial.** *Stroke* 2005;36:1432–38

69. Smith WS. **Safety of mechanical thrombectomy and intravenous tissue plasminogen activator in acute ischemic stroke: results of the multi Mechanical Embolus Removal in Cerebral Ischemia (MERCI) trial, Part I.** *AJNR Am J Neuroradiol* 2006;27:1177–82

70. Saver JL, Jahan R, Levy EI, et al. **Solitaire flow restoration device versus the Merci retriever in patients with acute ischaemic stroke (SWIFT): a randomised, parallel-group, non-inferiority trial.** *Lancet* 2012;380:1241–49

71. Nogueira RG, Lutsep HL, Gupta R, et al. **Trevo versus Merci retrievers for thrombectomy revascularisation of large vessel occlusions in acute ischaemic stroke (TREVO 2): a randomised trial.** *Lancet* 2012;380:1231–40

Dynamic MR Imaging Patterns of Cerebral Fat Embolism: A Systematic Review with Illustrative Cases

K.-H. Kuo, Y.-J. Pan, Y.-J. Lai, W.-K. Cheung, F.-C. Chang, and J. Jarosz

ABSTRACT

SUMMARY: Different MR imaging patterns of cerebral fat embolism have been reported in the literature without a systematic review. Our goal was to describe the patterns, explore the relationship between disease course and the imaging patterns, and discuss the underlying mechanism. We reveal 5 distinctive MR imaging patterns: 1) scattered embolic ischemia occurring dominantly at the acute stage; 2) confluent symmetric cytotoxic edema located at the cerebral white matter, which mainly occurs at the subacute stage; 3) vasogenic edematous lesions also occurring at the subacute stage; 4) petechial hemorrhage, which persists from the acute to the chronic stage; and 5) chronic sequelae, occurring at late stage, including cerebral atrophy, demyelinating change, and sequelae of infarction or necrosis. Underlying mechanisms of these imaging patterns are further discussed. Recognition of the 5 evolving MR imaging patterns of cerebral fat embolism may result in adjustment of the appropriate management and improve the outcome.

ABBREVIATION: CFE = cerebral fat embolism

Since its first emergence in Zenker in 1862,[1] fat embolism syndrome has been known to be associated with displaced long bone fracture of the lower extremities and is characterized by respiratory disability, petechial skin rash, and neurologic symptoms, typically seen between 12 and 72 hours after the injury. The incidence of cerebral fat embolism (CFE) has been reported to be 0.9%–2.2%.[2] Although CFE is usually self-limiting, it may be fatal. In comparison with the respiratory presentations, diagnosis of CFE in the brain may be more challenging because the symptoms are more variable (headache, confusion, seizure to coma). Moreover, the presentations of CFE can be further complicated by the frequent co-occurrence of brain contusion or hypoxic-ischemic injury caused by traumatic insults.

MR imaging of the brain by using T2-weighted, diffusion-weighted, gadolinium contrast-enhanced images, and susceptibility-weighted imaging has been applied to CFE and has improved the ability to make a diagnosis.[3-5] However, the image diagnosis of CFE remains a challenge because it has various presentations: Reversibility and distribution of the brain lesions in the different reported series and timing have been confusing.[4-6] The explanations for these diverse results include the small number of reported cases and MR imaging examinations performed at different stages of CFE. These segmented observations clearly limit the understanding of the whole disease entity.

In this systematic review, we aimed to describe and summarize the MR imaging patterns from the existing literature and explore the relationship between the disease time course and the image patterns. We hypothesized that CFE involves a dynamic process with time and may present with different dominant image patterns in each specific time window. The associated mechanisms are also discussed.

MATERIALS AND METHODS

We included all articles written in English in the PubMed database up to April 30, 2012, by searching approximately 20 MeSH terms and keywords such as "fat emboli" or "embolism," "MR image," "diffusion-/susceptibility-weighted image," and their derivatives. Reference lists of included articles were hand-searched for published reports missed by the electronic search. Articles published earlier than 1996 (no proper DWI image) or without satisfying image quality were later excluded. In addition, we searched the Far Eastern Memorial Hospital image database for additional CFE cases. Finally, all identified cases were summarized; images were reread by 2 neuroradiologists, assigned to patterns, and correlated with the timing in the disease course (Fig 1). The course was

separated into 3 stages: acute (within 24 hours to 4 days after the fracture), subacute (5–14 days after the fracture), and late (>14 days after the fracture).

RESULTS

There were 21 case reports identified from the literature search, which included 25 cases. Additionally, we identified 2 cases from the Far Eastern Memorial Hospital image database (all images provided in this article are from these 2 cases). There were, in total, 27 cases and 44 MR imaging examinations reviewed for this article. Among the 38 MR images with recorded timing of examinations, 13 were obtained in the acute stage; 11, in the subacute stage; and 14, in the late stage. The longest follow-up duration for a single case was 152 days. In Fig 2, both the number of cases of

each imaging pattern and the proportion of cases with each pattern against time are illustrated. The analysis shows that the image patterns did evolve with time and could be separated into 3 major types. In addition, the type 2 pattern could be further divided into 3 subtypes. The patterns are summarized in the On-line Table and described below in detail.

Type 1: Scattered Cytotoxic Edema

Type 1 is the most well-known pattern of CFE, which was first named the "starfield pattern" by Parizel et al in 2001.[6] It is also the most common pattern in this review (61.5% of 44 MR examinations). The pattern is actually a nonspecific feature seen in all kinds of embolic events; in CFE, it tends to be reversible, with reversibility resulting in a better clinical outcome. The MR imaging findings are scattered spot lesions with restricted diffusion on DWI sequences. The signal of T2WI may be iso- or hyperintense. The lesions are distributed bilaterally in watershed zones and deep gray matter, such as the centrum semiovale, basal ganglia, and thalami (Fig 3). Of all the acute-stage MR imaging examinations, 84.6% were shown to have a type 1 pattern, while it is much less frequently seen in the subacute and late stages (18% and 0%) (Fig 2).

Type 2A: Confluent Cytotoxic Edema in White Matter

Although the type 2A pattern is often ignored, it is also a common (57.7% of 44 MR imaging examinations) and characteristic finding of CFE. The MR imaging feature is confluent symmetric lesions with restricted diffusion on DWI in periventricular and subcortical white matter bilaterally. The cerebellar peduncles, corpus callosum, and posterior internal capsule may be involved (Fig 4A–F). On T2WI, lesions are usually faintly hyperintense or occasionally have no obvious signal change. In this review, the pattern was noted dominantly at the subacute stage with an 81.8% positive rate among all the reported subacute stage MR imaging examinations (Fig 2). Differential diagnoses included hypoglyce-
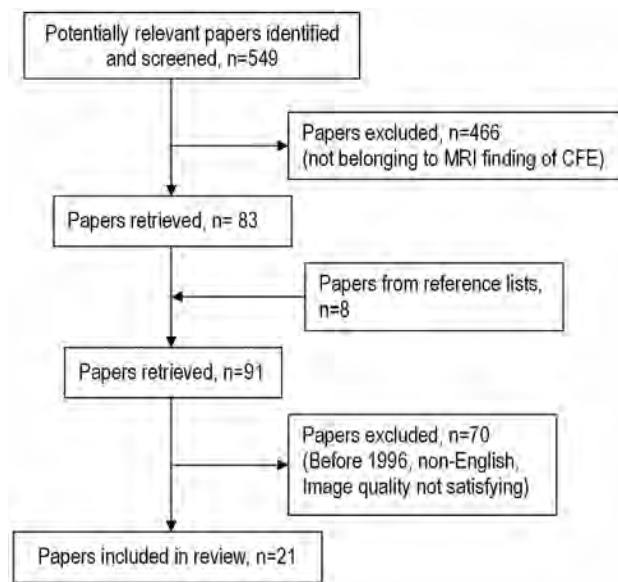
FIG 1. Quality of Reporting of Meta-analysis standards (QUOROM) flow diagram of articles included in this systematic review.

$$\text{Positive rate of image pattern} = \frac{\text{Number of cases positive of specific pattern}}{\text{Number of cases with MR examinations}}$$
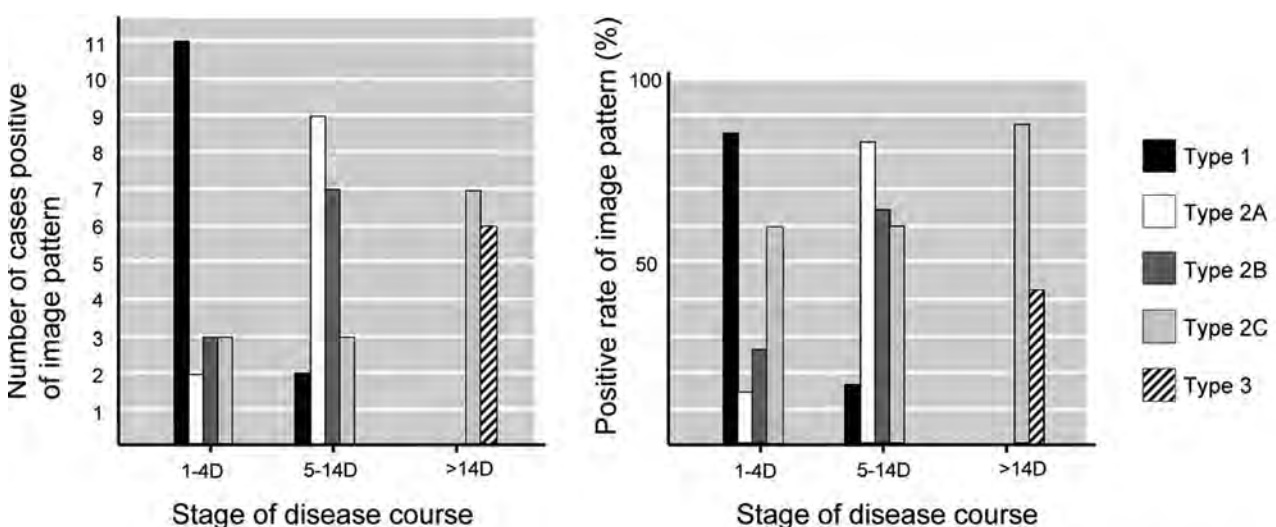
FIG 2. Bar graph of case numbers and positive proportion of each pattern against time.

mic encephalopathy, delayed posthypoxic leukoencephalopathy, and toxic leukoencephalopathy. Detailed history-taking and laboratory examinations may help to achieve a correct diagnosis.

Type 2B: Vasogenic Edema Lesions That May Enhance

During the subacute stage, another commonly found MR imaging feature (64% of 11 MR examinations) in this review was type 2B, with hyperintense lesions on T2WI. The difference is that these lesions usually have a small dot or patch shape, and the signal on the DWI image shows increased diffusion instead. The

lesions lie in both gray and white matter (Fig 4). In the 4 cases with contrast injection in this review, 3 demonstrated enhancement of the lesions (On-line Table).

Type 2C: Petechial Hemorrhage of White Matter

T2* sequences, such as gradient-echo images or SWI, are sensitive for detecting vascular structures, blood products, and changes in iron content. Previous reports have mentioned that it is common to detect tiny petechial hemorrhages of the perivascular space in CFE.[3,7-9] Suh et al[3] mentioned that SWI is better at detecting hemorrhages of CFE than gradient-echo images. In this review, the type 2C pattern was noted in all stages (60%, 60%, and 88% in acute, subacute, and late stages, respectively; Fig 2). Petechiae were noticed as early as the first day of the long bone fracture and could last through the whole course without significant change (Fig 5). Differential diagnoses included diffuse axonal injury, which presents with petechial hemorrhage as well. However, diffuse axonal injury mainly occurs in the gray-white matter interface of the frontotemporal lobes and corpus callosum, while CFE petechial hemorrhage is located predominantly in the white matter and shares the same distribution as the confluent white matter cytotoxic edema pattern (type 2A). In our opinion, the high positive rate with early-onset and persistent, specific MR imaging characteristics indicating petechiae hem-
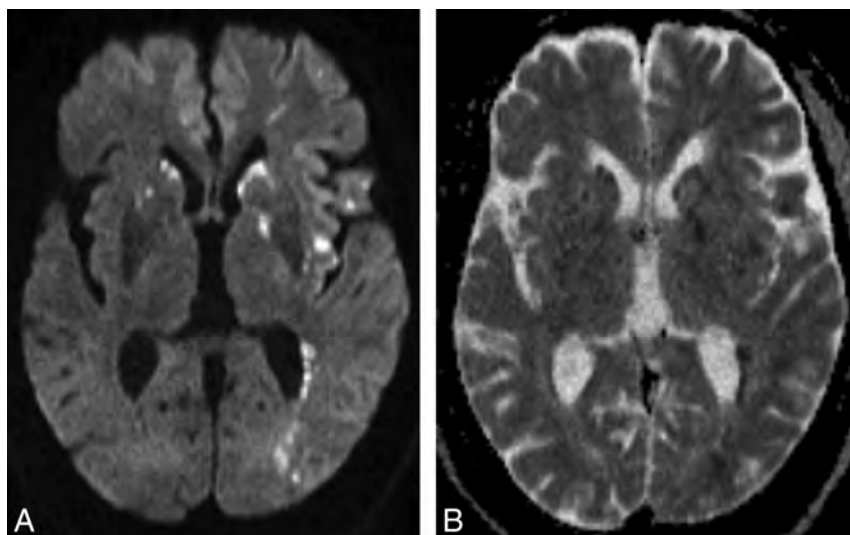
FIG 3. A 25-year-old man with a traumatic tibial bone fracture. Rapid consciousness decline was noted at postfracture day 1, and the brain MR imaging was performed at postfracture day 2. Axial DWI (A) and corresponding axial ADC image (B) demonstrate scattered spot diffusion-restricted lesions in the bilateral striatum, left posterior internal capsule, insula, operculum, and periventricular white matter (type 1 pattern).
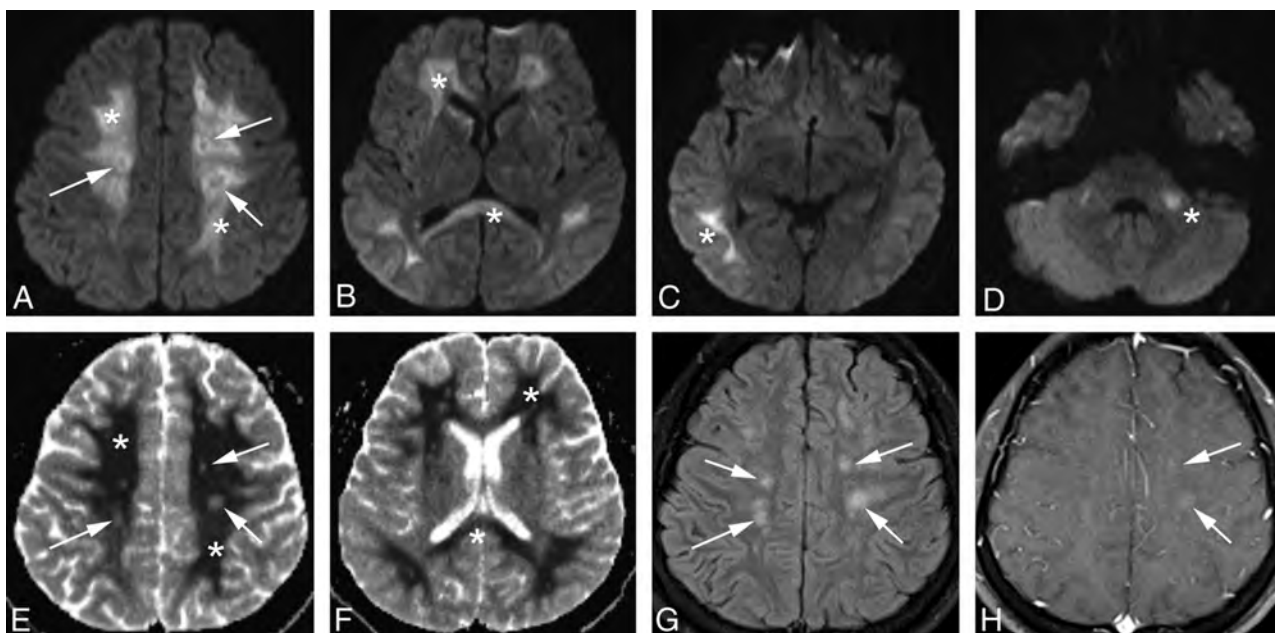
FIG 4. Another 19-year-old man with a traumatic tibial bone fracture. Stupor was noted at postfracture day 1, and the brain MR imaging was delayed to postfracture day 7 due to unstable vital signs. Serial axial DWI (A–D) and axial ADC images (E and F) demonstrate confluent cytotoxic edematous lesions in periventricular and subcortical white matter of the frontal, parietal, and temporal lobes; corpus callosum; and cerebellar peduncle bilaterally, which are type 2A patterns (asterisks). Axial ADC (E), corresponding FLAIR (G), and contrast-enhanced T1WI (H) demonstrate dot-shaped vasogenic edema with faint enhancement, which is a type 2B pattern (arrows).
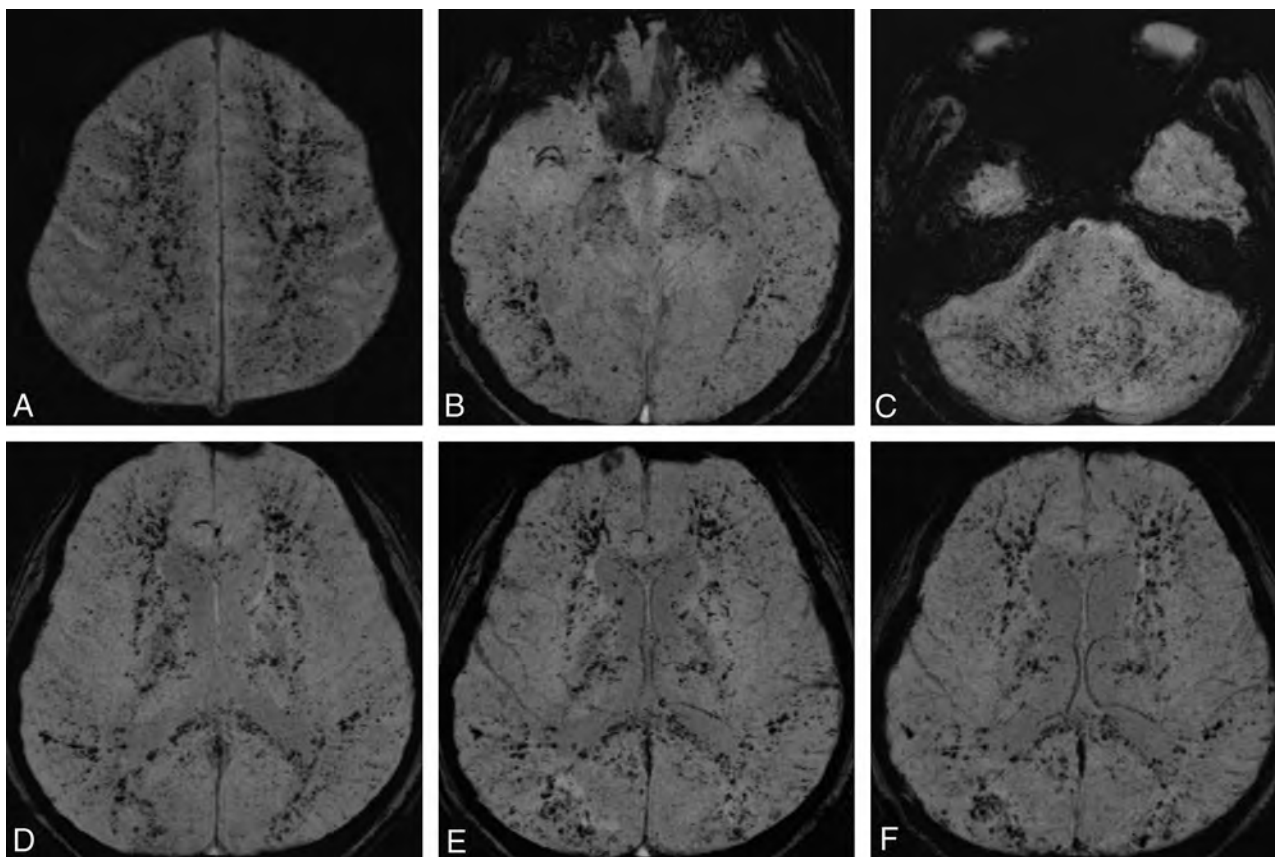
FIG 5. Serial axial SWI images of the second case at postfracture week 3 (*A–D*) demonstrate numerous petechial hemorrhages in the subcortical and periventricular white matter, cerebellar hemisphere and peduncle, and posterior corpus callosum bilaterally. Corresponding images of the same level at postfracture week 5 (*E*) and 3 months (*F*) demonstrate no significant interval change (type 2C pattern).
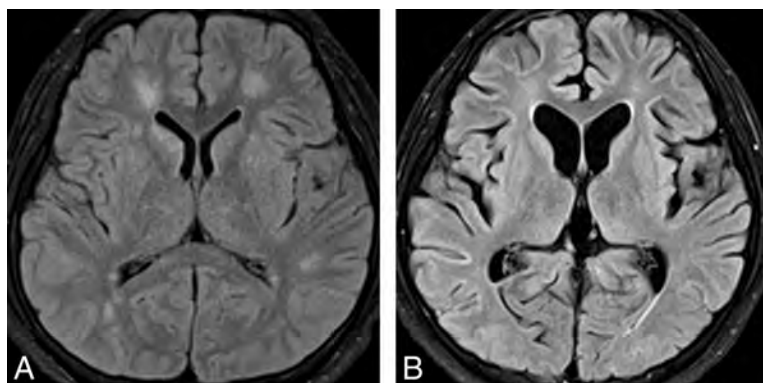
FIG 6. Axial FLAIR images of the second case at postfracture day 7 (*A*) and 3 months (*B*) demonstrate brain volume loss and demyelination change at the late stage of CFE (type 3 pattern).

orrhage and unique distribution in white matter could make this pattern a pathognomonic feature of CFE.

Type 3: Chronic Sequelae
At the late stage, most of the above lesions were resolving while brain atrophy was beginning to be noted (Fig 6). Although the presence of chronic sequelae was not emphasized in the existing CFE literature, this feature suggests an incomplete lesion resolution rather than a true recovery. Besides, there is a group of other abnormal findings. Most are hyperintense on T2WI without restricted diffusion on DWI. Some are in a dot/nodule shape, and some have a large amorphous shape. These may represent sequelae of infarction, cavitation, scar formation, gliosis, or chronic demyelination. The type 3 findings may be the best correlation with the final clinical prognosis.

DISCUSSION
To date, CFE has been thought to result from an initial mechanical obstruction of arterial circulation by neutral fat, followed by a delayed extensive biochemical toxic injury from free fatty acids.

It is claimed that because long bone fracture occurs at the lower extremity, a large amount of disseminated bone marrow fat tissue may flow into the pulmonary circulation and, in the presence of right-to-left shunts, can later pass into the systemic circulation.[10] However, most reported cases in this review failed to demonstrate this shunt; the presence of an alternative mechanism may be a better explanation. A study on orthopedic surgery with dogs has shown that fat vacuoles smaller than 5 μm still could directly pass through the pulmonary capillary bed.[11] Subsequently, showers of microemboli flow into the brain sporadically, getting lodged in capillaries, which may result in ischemic injury and present as a "starfield" (type 1) pattern seen on DWI at an early stage. The size of the impacted intravascular fat

vacuole was further identified as approximately 4–42 μm in another animal study.[12]

Nevertheless, because the fat vacuoles, mainly the triglyceride triolein, are in liquid form in the human body (freezing point of 40°C), they could deform, split into smaller globules, and recycle into the pulmonary circulation.[13,14] Reperfusion of the brain then salvages the damaged tissue; this possibility may explain the transient imaging change and clinically better outcome than other embolic events.

Fat embolism in the lung is hydrolyzed to free fatty acids by the action of local pulmonary lipase-oleic acid as its major component.[15] Oleic acid and the triglyceride triolein both are toxic to the lungs and brain, and the former is more toxic and may induce cerebral cytotoxic edema reported in the cat model of CFE experiments.[16-18] Microcystic change of the neutrophil matrix and swelling of neuronal and glial cells were prominent in electron microscopy.[17] DWI can detect cytotoxic edema and reveal the corresponding evidence as confluent symmetric diffusion-restricted lesions, which usually occur in the subacute stage (type 2A pattern). Clinically, despite the fact that fat emboli are small, the lesions tend to be distributed in white matter rather than gray matter. Sevitt[18] proposed that rich vascularity in the gray matter could have sufficient anastomotic potential to protect against the injury, and Kamenar and Burger[19] suggested that white matter lesions are indirectly produced by the cortical emboli through venous sludging and white matter edema. However, myelin has a high lipid content and a slow turnover; all the myelinated tracts are particularly vulnerable to the accumulation of lipophilic substances and to lipid peroxidation. Therefore, cerebral white matter may be selectively vulnerable due to its lipophilic property.

The type 2A pattern is quite similar to images of delayed posthypoxic leukoencephalopathy, usually caused by carbon monoxide or heroin intoxication. Although the exact mechanism of this leukoencephalopathy is not clear, the hypothesis of "leukotoxin" inducing delayed leukoencephalopathy was proposed.[20,21] Future research to explore potential relationships between "leukotoxin" and the mechanism underlying CFE image changes in the subacute stage is warranted.

In addition to cerebral cytotoxic edema, it seems that the toxicity of free fatty acids also causes vasogenic edema at an early phase of disease by opening the blood-brain barrier. In a cat study, as early as 30 minutes after oleic acid was injected into the internal carotid artery, electron microscopy revealed discontinuity of the cerebral capillary endothelium with a gap of approximately 1–3 μm. Small fat vacuoles, red blood cells, and plasma fluid were leaked into the perivascular interstitial space.[17] This process could explain the type 2B and 2C MR imaging patterns, such as the appearance of hyperintensity on T2WI and ADC maps and numerous tiny low intensities seen on T2* images.

Although the damage seems to occur within minutes in animal studies,[16,17] a time lag of neurologic symptoms after fracture is commonly seen in clinical settings—the passage between the pulmonary and systemic circulation (the filter effect) may play a key role in determining the lag. Furthermore, this filter effect could also be a major determinant of the extent and pattern of arterial mechanical obstruction. Without the existence of the "filter" (eg, in the presence of a patent foramen ovale), the onset of neurologic symptoms would

have been much earlier and the lesions, larger; there could have been more territorial infarctions in cases of CFE as well.

Last, reversible image change was proposed in several previous reports,[4] whereas complete recovery was seldom seen in clinical presentations. After reviewing these cases in detail, brain atrophy and demyelinating changes were the most common anomaly found in the late stage of disease (type 3 pattern). Normalization of signal, instead of reversible change, would be a better explanation of the MR imaging attenuation recovery. In fact, some residual lacunar infarction and necrosis were also noted. It seems likely that the brain volume loss may correlate with prognosis.

CONCLUSIONS

In this review, 5 distinct image patterns were identified through the 3 different stages of CFE; this finding suggests dynamic patterns of CFE with time. Scattered cytotoxic edema mainly occurred in the acute stage, while in the subacute stage, confluent cytotoxic edema or vasogenic edema or both were identified. In the late stage, chronic sequelae including brain atrophy or demyelination were recognized. Petechial hemorrhage in a confluent shape was seen in the examined images from all stages; this pattern in SWI may be a pathognomonic feature of CFE. Early recognition of the proper pattern may help determine appropriate management and improve the outcome.

Because all cases in this review were discovered because they were recognized and described as CFE, there is an inherent selection bias against previously unrecognized or atypical patterns. Further studies with CFE cases involving a series of imaging changes with time may be required to provide further support for the current findings. Correlation with clinical outcome is also needed.

REFERENCES

1. Zenker FA. Beitrage zur normalen und pathologischen Anatomie der Lunge. Dresden, Germany: Schonfeld; 1862
2. Eguia P, Medina A, Garcia-Monco JC, et al. **The value of diffusion-weighted MRI in the diagnosis of cerebral fat embolism.** J Neuroimaging 2007;17:78–80
3. Suh SI, Seol HY, Seo WK, et al. **Cerebral fat embolism: susceptibility-weighted magnetic resonance imaging.** Arch Neurol 2009;66:1170
4. Butteriss DJ, Mahad D, Soh C, et al. **Reversible cytotoxic cerebral edema in cerebral fat embolism.** AJNR Am J Neuroradiol 2006;27:620–23
5. Simon AD, Ulmer JL, Strottmann JM. **Contrast-enhanced MR imaging of cerebral fat embolism: case report and review of the literature.** AJNR Am J Neuroradiol 2003;24:97–101
6. Parizel PM, Demey HE, Veeckmans G, et al. **Early diagnosis of cerebral fat embolism syndrome by diffusion-weighted MRI (starfield pattern).** Stroke 2001;32:2942–44
7. Lee J. **Gradient-echo MRI in defining the severity of cerebral fat embolism.** J Clin Neurol 2008;4:164–66
8. Chen JJ, Ha JC, Mirvis SE. **MR imaging of the brain in fat embolism syndrome.** Emerg Radiol 2008;15:187–92
9. Metting Z, Rödiger LA, Regtien JG, et al. **Delayed coma in head injury: consider cerebral fat embolism.** Clin Neurol Neurosurg 2009;111:597–600
10. Bardana D, Rudan J, Cervenko F, et al. **Fat embolism syndrome in a patient demonstrating only neurologic symptoms.** Can J Surg 1998;41:398–402
11. Byrick RJ, Mullen JB, Mazer CD, et al. **Transpulmonary systemic fat**

embolism. Studies in mongrel dogs after cemented arthroplasty. *Am J Respir Crit Care Med* 1994;150:1416–22

12. Kim HJ, Lee CH, Kim HG, et al. **Reversible MR changes in the cat brain after cerebral fat embolism induced by triolein emulsion.** *AJNR Am J Neuroradiol* 2004;25:958–63

13. Takahashi M, Suzuki R, Osakabe Y, et al. **Magnetic resonance imaging findings in cerebral fat embolism: correlation with clinical manifestations.** *J Trauma* 1999;46:324–27

14. Brown WR, Moody DM, Challa VR. **Cerebral fat embolism from cardiopulmonary bypass.** *J Neuropathol Exp Neurol* 1999;58:109–19

15. Boyd HM, Peltier LF, Sott JR. **Fat embolism. II. The chemical composition of fat obtained from human long bones and subcutaneous tissue.** *Surgery* 1956;40:661–64

16. Kim HJ, Lee JH, Lee CH, et al. **Experimental cerebral fat embolism: embolic effects of triolein and oleic acid depicted by MR imaging and electron microscopy.** *AJNR Am J Neuroradiol* 2002;23:1516–23

17. Kim HJ, Lee CH, Lee SH, et al. **Early development of vasogenic edema in experimental cerebral fat embolism in cats: correlation with MRI and electron microscopic findings.** *Invest Radiol* 2001;36:460–69

18. Sevitt S. **The significance and pathology of fat embolism.** *Ann Clin Res* 1977;9:173–80

19. Kamenar E, Burger PC. **Cerebral fat embolism: a neuropathological study of a microembolic state.** *Stroke* 1980;11:477–84

20. Molloy S, Soh C, Williams TL. **Reversible delayed posthypoxic leukoencephalopathy.** *AJNR Am J Neuroradiol* 2006;27:1763–65

21. Kim JH, Chang KH, Song IC, et al. **Delayed encephalopathy of acute carbon monoxide intoxication: diffusivity of cerebral white matter lesions.** *AJNR Am J Neuroradiol* 2003;24:1592–97

22. Kumar S, Gupta V, Aggarwal S, et al. **Fat embolism syndrome mimicker of diffuse axonal injury on magnetic resonance imaging.** *Neurol India* 2012;60:100–02

23. Rojo E, Villarón S, Cítores R, et al. **Magnetic resonance and ophthalmoscopy in a case of fat embolism syndrome.** *Neurologia* 2011;26:436–38

24. Liu HK, Chen WC. **Images in clinical medicine: fat embolism syndrome.** *N Engl J Med* 2011;364:1761

25. You JS, Kim SW, Lee HS, et al. **Use of diffusion-weighted MRI in the emergency department for unconscious trauma patients with negative brain CT.** *Emerg Med J* 2010;27:131–32

26. Shaikh N, Parchani A, Bhat V, et al. **Fat embolism syndrome: clinical and imaging considerations: case report and review of literature.** *Indian J Crit Care Med* 2008;12:32–36

27. Guillevin R, Vallée JN, Demeret S, et al. **Cerebral fat embolism: usefulness of magnetic resonance spectroscopy.** *Ann Neurol* 2005;57:434–39

28. Marshall GB, Heale VR, Herx L, et al. **Magnetic resonance diffusion weighted imaging in cerebral fat embolism.** *Can J Neurol Sci* 2004;31:417–21

29. Jenkins K, Chung F, Wennberg R, et al. **Fat embolism syndrome and elective knee arthroplasty.** *Can J Anaesth* 2002;49:19–24

30. Ott MC, Meschia JF, Mackey DC, et al. **Cerebral embolization presenting as delayed, severe obtundation in the postanesthesia care unit after total hip arthroplasty.** *Mayo Clin Proc* 2000;75:1209–13

31. Honda S, Inatomi Y, Yonehara T, et al. **A case report of serial MRI findings of cerebral fat embolism** [in Japanese]. *Rinsho Shinkeigaku* 2010;50:566–71

32. Buskens CJ, Gratama JW, Hogervorst M, et al. **Encephalopathy and MRI abnormalities in fat embolism syndrome: a case report.** *Med Sci Monit* 2008;14:CS125–29

33. Yanagawa Y, Kaneko N, Sakamoto T, et al. **Fat embolism syndrome with multiple hypointensity signals detected by head magnetic resonance imaging demonstrating a favorable outcome: a case report.** *Am J Emerg Med* 2007;25:217–18

34. de Feiter PW, van Hooft MA, Beets-Tan RG, et al. **Fat embolism syndrome: yes or no?** *J Trauma* 2007;63:429–31

A Meta-Analysis on the Diagnostic Performance of ^{18}F-FDG and ^{11}C-Methionine PET for Differentiating Brain Tumors

C. Zhao, Y. Zhang, and J. Wang

ABSTRACT

SUMMARY: ^{18}F-FDG-PET has been widely used in patients with brain tumors. However, the reported sensitivity and specificity of ^{18}F-FDG-PET for brain tumor differentiation varied greatly. We performed this meta-analysis to systematically assess the diagnostic performance of ^{18}F-FDG-PET in differentiating brain tumors. The diagnostic performance of ^{11}C-methionine PET was assessed for comparison. Relevant studies were searched in PubMed/MEDLINE, Scopus, and China National Knowledge Infrastructure (until February 2013). The methodologic quality of eligible studies was evaluated, and a meta-analysis was performed to obtain the combined diagnostic performance of ^{18}F-FDG and ^{11}C-methionine PET with a bivariate model. Thirty eligible studies, including 5 studies with both ^{18}F-FDG and ^{11}C-methionine PET data were enrolled. Pooled sensitivity, pooled specificity, and area under the receiver operating characteristic curve of ^{18}F-FDG-PET ($n = 24$) for differentiating brain tumors were 0.71 (95% CI, 0.63–0.78), 0.77 (95% CI, 0.67–0.85), and 0.80. Heterogeneity was found among ^{18}F-FDG studies. Subsequent subgroup analysis revealed that the disease status was a statistically significant source of the heterogeneity and that the sensitivity in the patients with recurrent brain tumor was markedly higher than those with suspected primary brain tumors. Pooled sensitivity, pooled specificity, and area under the receiver operating characteristic of ^{11}C-methionine PET ($n = 11$) were 0.91 (95% CI, 0.85–0.94), 0.86 (95% CI, 0.78–0.92), and 0.94. No significant statistical heterogeneity was found among ^{11}C-methionine studies. This meta-analysis suggested that ^{18}F-FDG-PET has limited diagnostic performance in brain tumor differentiation, though its performance may vary according to the status of brain tumor, whereas ^{11}C-methionine PET has excellent diagnostic accuracy in brain tumor differentiation.

ABBREVIATIONS: AUC = area under receiver operating characteristic curve; ^{18}F-FDOPA = 3,4-dihydroxy-6-^{18}F-fluoro-L-phenylalanine; ^{18}F-FET = O-(2-[^{18}F]fluoroethyl)-L-tyrosine; ^{18}F-FLT = 3′-deoxy-3′-^{18}F-fluorothymidine; HSROC = hierarchic summary receiver operating characteristics; LR = likelihood ratio; MET = methionine; SPBT = suspected primary brain tumor; SRBT = suspected recurrence of brain tumor after treatment

^{18}F-FDG-PET has been widely used in brain tumor differentiation. Commonly the glucose use in malignant brain tumors is increased, and ^{18}F-FDG-PET performs well in identifying high-grade gliomas.[1] However, because of the high physiologic glucose metabolism in normal brain tissue, the diagnostic accuracy of ^{18}F-FDG-PET in brain tumors is reduced, especially in low-grade brain tumors, which typically have lower levels of glucose metabolism.[2,3] Moreover, ^{18}F-FDG uptake in brain tumors demonstrates great variety and might not be closely associated with the

malignant grade,[3] making ^{18}F-FDG-PET unreliable in differentiating brain tumors.[4]

A number of ^{18}F-FDG-PET studies for differentiating brain tumors, including suspected primary brain tumor (SPBT) and/or suspected recurrence of brain tumors after treatment (SRBT), have shown a wide range of sensitivity and specificity, from 0.25 to 1.00 and 0.22 to 1.00, respectively.[1,2,5-27] This great disparity of diagnostic values causes confusion on the application of ^{18}F-FDG-PET for brain tumor differentiation. Therefore, although ^{18}F-FDG-PET remains the dominant approach for brain tumor imaging, a systematic assessment of the diagnostic performance of ^{18}F-FDG-PET for brain tumor differentiation is imperative.

In view of the limitation of ^{18}F-FDG, amino acid and amino acid analog PET tracers have been developed. PET imaging with these tracers improved the ability to differentiate brain tumors due to high tumor uptake and low uptake in normal brain tissue.[28] Among these tracers, ^{11}C-methionine (MET) is one of the most extensively investigated. ^{11}C-MET accumulates extensively in proliferating tumors by the mechanism of increased amino acid

From the Department of Nuclear Medicine (C.Z., J.W.), Hangzhou First People's Hospital, Hangzhou Cancer Hospital, Hangzhou, China; and Department of Nuclear Medicine (Y.Z.), Second Affiliated Hospital of Zhejiang University School of Medicine, Hangzhou, China.

Please address correspondence to Ying Zhang, MD, Department of Nuclear Medicine, Second Affiliated Hospital, School of Medicine, Zhejiang University, 88 Jie-Fang Rd, Hangzhou, Zhejiang 310009, China; e-mail: zhy-lly@126.com

transport and protein synthesis. Several reports confirmed that ^{11}C-MET PET differentiated brain tumors with high sensitivity and specificity.[29,30]

A recent meta-analysis concluded that ^{18}F-FDG and ^{11}C-MET PET have moderately good overall accuracy for diagnosing recurrent glioma.[31] However, other types of brain tumors with high clinical incidence, such as SPBTs and nongliomas, have not been well studied so far. A thorough understanding of the diagnostic effectiveness of ^{18}F-FDG and ^{11}C-MET PET for differentiating brain tumors could be highly referential in clinical practice. Therefore, we performed a meta-analysis to comprehensively investigate the diagnostic performance of ^{18}F-FDG and ^{11}C-MET PET for differentiating brain tumors with various statuses and histologic types.

MATERIALS AND METHODS
Identification and Eligibility of Studies
A systematic search was performed in MEDLINE, Scopus, and the China National Knowledge Infrastructure data bases from January 1991 to February 2013, restricted to human studies in English and Chinese. The detailed search strategies are presented in the On-line Appendix. To search for more potential studies, we also screened references of the retrieved studies.

Studies using ^{18}F-FDG or/and ^{11}C-MET for the assessment of SPBT or SRBT were enrolled. Inclusion criteria were the following: 1) the purpose of the study was to differentiate SPBT or SRBT, 2) the study population consisted of a minimum of 10 patients, 3) histology or clinical follow-up was used as a reference standard, and 4) the reported primary data were sufficient to calculate both sensitivity and specificity. Exclusion criteria were the following: 1) the PET tracer not being ^{18}F-FDG or ^{11}C-MET; 2) animal or in vitro studies; 3) abstracts, systematic reviews, editorials, letters, comments, and case reports; and 4) studies for staging, searching for metastasis, and evaluating the therapeutic response of definitely diagnosed brain tumors.

Data Extraction and Study Quality
Two experienced nuclear medicine physicians (C.Z., Y.Z.) screened titles, abstracts, and full texts of eligible studies independently. Characteristics of eligible studies were extracted to 2 predefined forms, including the first author's name, year of publication, study country of origin, study design, sample size, mean or median age of patients, male to female ratio, type of brain tumor, disease status, PET tracers, prior imaging tests, reference standard, clinical or radiologic follow-up after PET, PET scanner type, injected dose, time of scanning after injection, scan time, analysis method for diagnostic performance, positive criteria of visual assessment, and cutoff value of quantitative parameters. After data extraction, discrepancies were resolved by consensus and discussion.

The methodologic quality of eligible studies was assessed by using 14 items of the Quality Assessment of Diagnostic Accuracy Studies.[32] Each item of the Quality Assessment of Diagnostic Accuracy Studies was described as yes (score = 2), unclear (score = 1), and no (score = 0). The total score was summarized from all the items with a range of 0–28. Two experienced reviewers (C.Z., Y.Z.) independently evaluated

the quality of selected studies, and disagreements were resolved by discussion.

True-positive, false-positive, true-negative, and false-negative values for ^{18}F-FDG or ^{11}C-MET PET in differentiating brain tumors were extracted for each eligible study to construct a contingency table.

Data Analysis
Pooled estimates for sensitivity, specificity, likelihood ratios (LRs) with corresponding 95% confidence intervals, and area under receiver operating characteristic curve (AUC) for ^{18}F-FDG and ^{11}C-MET PET were analyzed for the primary meta-analysis on the basis of the bivariate mixed-effects regression model.[33] The bivariate model uses a random effects approach for both sensitivity and specificity, which allows heterogeneity beyond chance as a result of clinical and methodologic differences between studies, and the bivariate model is a more valid statistical model for a diagnostic meta-analysis.[34] The LRs indicate by how much a given test would raise or lower the probability of having a disease. Generally, a good diagnostic test may have LR+ above 5 and LR− below 0.2. The AUC is the average true-positive rate over the entire range of false-positive rate values and serves as a global measure of test performance. The guidelines for the interpretation of intermediate AUC values are the following: low accuracy, $0.5 \leq AUC \leq 0.7$; moderate accuracy, $0.7 < AUC \leq 0.9$; or high accuracy, $0.9 < AUC \leq 1$.[35]

To graphically describe the results, we plotted the hierarchic summary receiver operating characteristic (HSROC) curves. The HSROC curve is a recommended standard method for diagnostic meta-analysis.[36] Heterogeneity among the studies was checked by using the χ^2-based Q-test and the I^2 statistic.[37,38] The existence of significant heterogeneity was assumed with a P value < .05 for the Q-test and/or an I^2 statistic $\geq 50\%$. If significant heterogeneity was observed, subgroup analysis by using meta-regression was adopted to explore a potential source of heterogeneity by calculating the I^2 statistics. The covariates investigated included study design, imaging method, analysis method for diagnostic performance, malignant grade of brain tumor, disease status, and histology. The malignant grades of brain tumors in the studies were assigned according to the classification of World Health Organization.[39] The stability of our analysis model was tested by 1-way sensitivity analysis if heterogeneity existed. We excluded each study in turn and checked how the new summary diagnostic values could be influenced by the removed one.

We also performed direct comparison of the diagnostic values of ^{18}F-FDG and ^{11}C-MET PET from the 5 studies with the same population of the patients[22-26] to diminish the potential bias induced by pooling data from all the studies, though the data subset was smaller.

Publication bias was tested by using the linear regression method and funnel plot of Deeks et al.[40] A P value < .05 in this linear regression indicates potential publication bias.

Statistical analyses were performed with STATA 12.0 (StataCorp, College Station, Texas). The commands used are presented in the On-line Appendix. A P value < .05 was considered statistically significant. All P values were 2-sided.
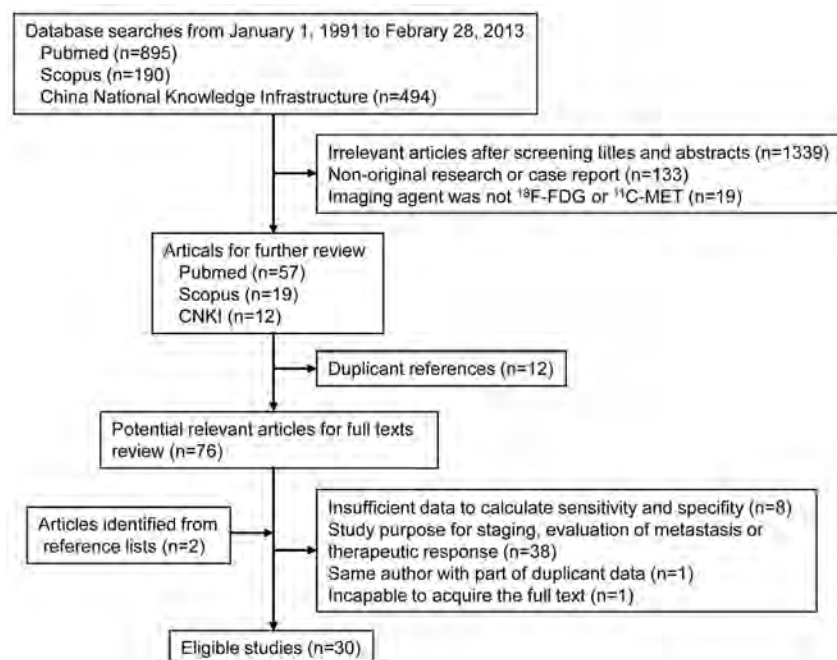
FIG 1. Flow chart of identification of eligible studies.

RESULTS

Study Characteristics, Quality, and Publication Bias

According to the search strategies, the electronic search yielded 1579 articles: 895 from PubMed, 190 from Scopus, and 494 from the China National Knowledge Infrastructure. After we screened article types, titles, and abstracts, 76 studies remained and the full-text versions were reviewed. After we reviewed full texts, 48 studies were excluded and 2 studies identified from the reference lists of other eligible studies were included (Fig 1). Finally 30 eligible studies were enrolled, including 19 for ^{18}F-FDG-PET,[1,2,5-21] 6 for ^{11}C-MET PET,[29,30,41-44] and 5 for both.[22-26] The characteristics of the studies are summarized in On-line Tables 1 and 2.

The quality of included studies was assessed on the basis of the Quality Assessment of Diagnostic Accuracy Studies (On-line Table 3). The overall quality of the included studies was considered acceptable for most of the items. The total score varied from 13 to 24 in ^{18}F-FDG studies and from 18 to 22 in ^{11}C-MET studies. The proportion of studies with a total score of >20 in ^{18}F-FDG studies (11/24) was apparently lower than that in ^{11}C-MET studies (9/11); this difference indicated the overall higher quality of ^{11}C-MET studies. A common poor-quality item (item 6) in most studies was the failure to use the same reference standard.

We found no significant evidence of publication bias in both ^{18}F-FDG ($P = .07$, On-line Fig 1) and ^{11}C-MET ($P = .26$, On-line Fig 2) studies by using the linear regression method of Deeks et al.[40]

Heterogeneity of ^{18}F-FDG-PET Studies and Sensitivity Analysis

The sensitivity and specificity of ^{18}F-FDG-PET for brain tumor differentiating across 24 eligible studies ranged from 0.25 to 1.00 and 0.22 to 1.00, respectively. The test of heterogeneity revealed significant statistical heterogeneity (Q-value for sensitivity = 83.23, $P = .00$, $I^2 = 72.37\%$; Q-value for specificity = 57.11, $P = .00$, $I^2 = 59.73\%$).

We excluded 1 study from the overall pooled analysis each time to check the influence of the removed dataset on the summary estimates. When a single study was excluded, the new pooled sensitivity and specificity remained close to those obtained with all eligible studies (On-line Table 4).

Diagnostic Values and HSROC Curve of ^{18}F-FDG-PET Studies

When all twenty-four ^{18}F-FDG studies were pooled, the sensitivity, specificity, and AUC for differentiating brain tumors were 0.71 (95% CI, 0.63–0.78), 0.77 (95% CI, 0.67–0.85), and 0.8. The overall LR+ and LR− were 3.13 (95% CI, 2.11–4.64) and 0.37 (95% CI, 0.29–0.48). The HSROC curve is shown in Fig 2.

In 5 studies with the same population of the patients for both ^{18}F-FDG and ^{11}C-MET PET, the pooled sensitivity, pooled specificity, and AUC for ^{18}F-FDG-PET were 0.70 (95% CI, 0.50–0.85), 0.78 (95% CI, 0.59–0.90), and 0.81. The overall LR+ and LR− of ^{18}F-FDG-PET were 3.17 (95% CI, 1.73–5.82) and 0.38 (95% CI, 0.22–0.65).

Heterogeneity of ^{11}C-MET PET Studies

The sensitivity and specificity of ^{11}C-MET PET for brain tumor differentiation across 11 eligible studies ranged from 0.75 to 1.00 and 0.6 to 1.00, respectively. The test of heterogeneity indicated no significant statistical heterogeneity (Q-value for sensitivity = 12.81, $P = .23$, $I^2 = 21.92\%$; Q-value for specificity = 10.98, $P = .36$, $I^2 = 8.89\%$).

Diagnostic Values and HSROC Curve of ^{11}C-MET PET Studies

When all eleven ^{11}C-MET studies were pooled, the sensitivity, specificity, and AUC for differentiating brain tumors were 0.91 (95% CI, 0.85–0.94), 0.86 (95% CI, 0.78–0.92), and 0.94. The overall LR+ and LR− were 6.60 (95% CI, 3.93–11.07) and 0.11 (95% CI, 0.07–0.18). The HSROC curve is shown in Fig 3.

In 5 studies with the same population of the patients for both ^{18}F-FDG and ^{11}C-MET PET, the pooled sensitivity, pooled specificity, and AUC for ^{11}C-MET PET were 0.94 (95% CI, 0.88–0.97), 0.87 (95% CI, 0.76–0.93), and 0.96. The overall LR+ and LR− of ^{11}C-MET PET were 7.28 (95% CI, 3.81–13.92) and 0.07 (95% CI, 0.04–0.14).

Subgroup Analyses of ^{18}F-FDG and ^{11}C-MET PET Studies

Metaregression was performed for ^{18}F-FDG-PET studies to explore the potential source of heterogeneity. The results of subgroup meta-analyses are shown in Table 1. The source of the heterogeneity among ^{18}F-FDG-PET studies was not observed with respect to study design, imaging method, malignant grade of brain tumor, and histology ($P > .05$). However, the disease status had a statistically significant influence on the heterogeneity ($I^2 =$
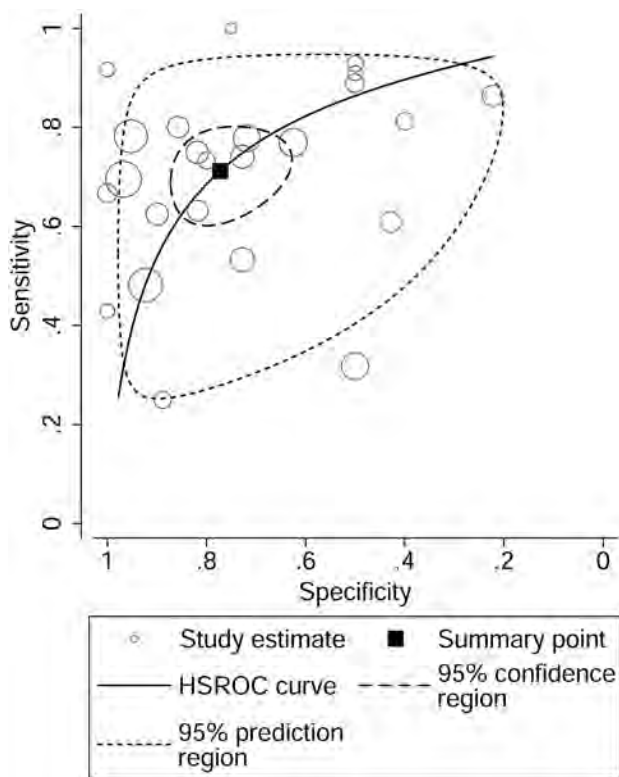
FIG 2. HSROC curve of ^{18}F-FDG-PET for differentiating brain tumors.
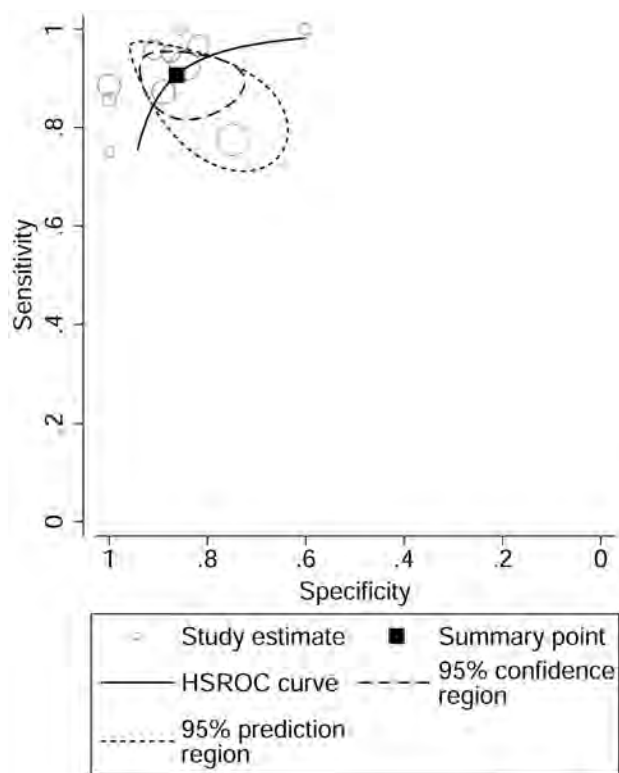
FIG 3. HSROC curve of ^{11}C-MET PET for differentiating brain tumors.

77.72; $P = .01$). The sensitivity in SPBT (0.43; 95% CI, 0.28–0.59) was markedly lower than that in SRBT (0.75; 95% CI, 0.67–0.81).

Metaregression was not performed for ^{11}C-MET PET studies

because no statistically significant heterogeneity was found. However, the sensitivity, specificity, and LRs in subgroups by study design, PET measurement, imaging method, malignant grade, disease status, and histologic finding were also calculated and are listed in Table 2. No apparent difference was observed among the subgroups.

DISCUSSION

We analyzed 24 ^{18}F-FDG-PET studies with an accumulated population of 857 patients for differentiating brain tumors, including SPBT and/or SRBT. The meta-analysis showed that ^{18}F-FDG-PET has moderately good pooled sensitivity (0.71; 95% CI, 0.63–0.78) and specificity (0.77; 95% CI, 0.67–0.85) for differentiating brain tumors. In the assessment of intracranial masses and the recurrence of brain tumors with ^{18}F-FDG-PET, a positive ^{18}F-FDG lesion without the presence of tumor (false-positive) often indicates inflammatory tissue or other nontumor tissues and thus limits the specificity.[3,45] On the other hand, absent or decreased ^{18}F-FDG uptake in pathologically identified brain tumors (false-negative) reflects the lower levels of glucose metabolism and is usually highly influenced by the high physiologic glucose metabolism in surrounding normal brain tissue, leading to a decrease of sensitivity.[11] The relatively low pooled sensitivity and specificity of ^{18}F-FDG-PET for differentiating brain tumors demonstrated in our meta-analysis indicates a considerably high incidence of both false-positives and false-negatives.

In the subgroup analyses of ^{18}F-FDG studies, the disease status was identified as the only possible source of heterogeneity. We found that the sensitivity of ^{18}F-FDG-PET was the worst (0.43; 95% CI, 0.3–0.58) when applied to the patients with SPBT. However, because no study on only SPBT was found, the SPBT data were extracted from 3 eligible studies on brain tumors with various statuses. As a result, the number of patients with SPBTs in subgroup analysis was limited, and the reliability of the subgroup analysis might be impaired to some extent. In subgroup analysis by malignant grade, low-grade brain tumors showed slightly less sensitivity (0.60; 95% CI, 0.35–0.81) compared with high-grade ones (0.74; 95% CI, 0.68–0.80). These results were consistent with those in previous reports by other investigators indicating that ^{18}F-FDG-PET was less effective in low-grade brain tumors,[2,29] though this difference was not a statistically significant source of heterogeneity ($P = .46$) in our analysis. In subgroup analysis by histology, the patients with glioma showed sensitivity and specificity similar to that of pooled data, suggesting that the type of brain tumor has no apparent influence on the diagnostic performance of ^{18}F-FDG-PET in brain tumor differentiation, regardless of the grading of glioma.

Qualitative assessment was used for image interpretation in most of the eligible ^{18}F-FDG studies, but there were various criteria for visual assessment as shown in On-line Table 2. These different criteria for visual assessment in ^{18}F-FDG studies may inevitably bring bias to our pooled data. Moreover, Tripathi et al[24] reported that even within the same ^{18}F-FDG study, interobserver agreement for visual interpretation was not good. The difficulty in discriminating the lesion and surrounding normal brain tissue in some patients and the subjectivity of visual assessment of the interpreter may together contribute to the low diagnostic ac-

Table 1: Metaregression analyses and diagnostic performance of ^{18}F-FDG-PET in subgroups of brain tumors

Analysis	No. of Studies (pts)	I² of Metaregression (95% CI, P Value)	Independent Estimates (95% CI)		LR (95% CI)	
			Sensitivity	Specificity	LR+	LR-
Design						
Retrospective	9 (333)	0.00 (0–100, .86)	0.71 (0.58–0.81)	0.73 (0.57–0.85)	2.63 (1.68–4.13)	0.40 (0.29–0.55)
Prospective	15 (524)		0.71 (0.60–0.79)	0.80 (0.66–0.89)	3.45 (1.96–6.07)	0.37 (0.26–0.52)
PET or PET/CT						
PET	17 (511)	0.00 (0–100, .38)	0.74 (0.64–0.81)	0.74 (0.60–0.84)	2.82 (1.74–4.55)	0.36 (0.25–0.51)
PET/CT	7 (346)		0.65 (0.50–0.78)	0.84 (0.68–0.92)	3.97 (2.09–7.54)	0.42 (0.29–0.59)
PET measurement						
Qualitative	19 (757)	57.87 (4.96–100, .09)	0.69 (0.60–0.76)	0.79 (0.67–0.87)	3.24 (2.00–5.24)	0.40 (0.30–0.52)
Quantitative	4 (85)		0.86 (0.71–0.94)	0.67 (0.43–0.84)	2.59 (1.40–4.81)	0.21 (0.09–0.45)
Malignant grade						
Low	14 (330)[a]	0.00 (0–100, .46)	0.60 (0.35–0.81)	0.79 (0.64–0.89)	2.87 (1.52–5.41)	0.50 (0.27–0.92)
High	17 (473)[a]		0.74 (0.68–0.80)	0.78 (0.65–0.87)	3.35 (2.09–5.38)	0.33 (0.26–0.42)
NS	7 (192)		0.70 (0.50–0.84)	0.70 (0.54–0.82)	2.33 (1.47–3.67)	0.44 (0.26–0.74)
Disease status						
SPBT	3 (127)[b]	77.72 (51.54–100, .01)	0.43 (0.28–0.59)	0.74 (0.49–0.90)	1.67 (0.59–4.76)	0.77 (0.48–1.24)
SRBT	20 (643)[b]		0.75 (0.67–0.81)	0.79 (0.66–0.88)	3.51 (2.17–5.66)	0.32 (0.25–0.41)
Histology						
Glioma	17 (609)[c,d]	0.00 (0–100, .47)	0.75 (0.64–0.83)	0.78 (0.64–0.87)	3.36 (2.02–5.59)	0.33 (0.23–0.47)
Nonglioma or NS	8 (250)[c]		0.64 (0.52–0.75)	0.75 (0.63–0.84)	2.58 (1.69–3.94)	0.48 (0.35–0.65)

Note:—NS indicates not separable; pts, patients.
[a] Patients with nonneoplastic lesions in 14 studies[2,6-8,11,12,15,16,18,19,21,23-25] were used for both low- and high-grade subgroups.
[b] Patients with nonneoplastic lesions in 2 studies[8,25] were used for both SPBT and SRBT subgroups.
[c] Five patients with nonneoplastic lesions from Hong et al 2011[16] were used for both glioma and nonglioma subgroups.
[d] One patient with lymphoma in Pauleit et al 2009[8] and 2 patients with esthesioblastoma and renal cell metastasis in Kahn et al 1994[12] were excluded from subgroup analysis.

Table 2: Diagnostic performance of ^{11}C-MET PET in subgroups of brain tumors

Analysis	No. of Studies (pts)	Independent Estimates (95% CI)		LR (95% CI)	
		Sensitivity	Specificity	LR+	LR-
Design					
Prospective	4 (156)	0.91 (0.84–0.95)	0.92 (0.78–0.97)	11.49 (3.87–34.08)	0.10 (0.06–0.18)
Retrospective	7 (260)	0.91 (0.81–0.96)	0.84 (0.73–0.90)	5.50 (3.18–9.51)	0.11 (0.05–0.24)
PET measurement					
Qualitative	5 (189)	0.93 (0.87–0.96)	0.85 (0.73–0.92)	6.10 (3.34–11.15)	0.08 (0.04–0.16)
Quantitative	6 (227)	0.89 (0.79–0.94)	0.89 (0.74–0.96)	8.38 (3.07–22.88)	0.13 (0.07–0.25)
PET or PET/CT					
PET	7 (232)	0.86 (0.78–0.91)	0.89 (0.72–0.96)	7.96 (2.75–23.00)	0.16 (0.10–0.26)
PET/CT	4 (184)	0.95 (0.89–0.97)	0.86 (0.74–0.93)	6.62 (3.48–12.59)	0.06 (0.03–0.13)
Malignant grade					
Low	5 (97)[a]	0.90 (0.76–0.96)	0.88 (0.77–0.94)	7.44 (3.68–15.02)	0.12 (0.05–0.30)
High	7 (132)[a]	0.98 (0.75–1.00)	0.88 (0.75–0.95)	8.51 (3.78–19.17)	0.02 (0.00–0.34)
NS	4 (153)	0.87 (0.79–0.93)	0.87 (0.69–0.96)	6.93 (2.52–19.04)	0.15 (0.08–0.26)
Disease status					
SPBT	2 (85)	0.95 (0.85–0.98)	0.83 (0.65–0.93)	5.49 (2.47–12.21)	0.07 (0.02–0.20)
SRBT	8 (238)	0.92 (0.83–0.97)	0.87 (0.75–0.93)	6.81 (3.39–13.69)	0.09 (0.04–0.21)
NS	2 (93)	0.88 (0.78–0.94)	0.95 (0.71–0.99)	16.69 (2.47–112.66)	0.13 (0.07–0.24)
Histology					
Glioma	9 (292)[b]	0.92 (0.85–0.95)	0.87 (0.76–0.93)	7.01 (3.67–13.38)	0.10 (0.05–0.18)
Nonglioma and NS	4 (182)[b]	0.88 (0.79–0.93)	0.83 (0.66–0.92)	5.07 (2.39–10.79)	0.14 (0.08–0.28)

Note:—NS indicates not separable; pts, patients.
[a] Patients with non-neoplastic lesions in 5 studies[23-25,30,43] were used for both low and high grade subgroups.
[b] Patients with non-neoplastic lesions in 2 studies[29,41] were used for both glioma and non-glioma subgroups.

curacy and require us to explain the pooled results prudently when using qualitative evaluation in ^{18}F-FDG-PET. Quantitative assessments were adopted in four ^{18}F-FDG-PET studies[20,22,24,26] that used a lesion-to–normal tissue ratio or standard uptake value as the criterion and showed better sensitivity but worse specificity than qualitative assessment. However, this difference was not a statistically significant source of heterogeneity ($P = .09$) in our analysis. The setting of the cutoff value in quantitative assessment may greatly influence the results of diagnostic estimates and consequently affect the reliability of direct comparison of the diag-

nostic values by quantitative and qualitative assessment. The limited number of patients analyzed with quantitative methods may also bring bias to the subgroup analysis by the method of assessment. In addition, due to the lack of the ability to distinguish lesion and normal brain tissue in ^{18}F-FDG-PET, the veracity of quantitative or semiquantitative methods for the interpretation of ^{18}F-FDG-PET images for evaluating brain tumor was also unreliable and could not provide additional information compared with visual assessment.[1,10,27] On the basis of the results of our meta-analysis, ^{18}F-FDG-PET does not appear to be an ideal ap-

proach for differentiating brain tumors, and we do not recommend its routine use for this purpose because a rather large number of diseases would be missed.

On the other hand, the meta-analysis in 11 ^{11}C-MET PET studies demonstrated excellent pooled sensitivity (0.91; 95% CI, 0.85–0.94) and specificity (0.86; 95% CI, 0.78–0.92) for differentiating brain tumors. The overall high diagnostic accuracy of ^{11}C-MET PET (AUC = 0.94) over ^{18}F-FDG-PET (AUC = 0.80) for brain tumor differentiation is likely due to the high uptake in tumor and low accumulation in normal brain tissue.[25,41] The sensitivity and specificity of ^{11}C-MET PET for differentiating brain tumors in the subgroups by various conditions showed higher values than those in pooled and subgroup ^{18}F-FDG-PET analyses, indicating the superiority of ^{11}C-MET PET over ^{18}F-FDG-PET and the stability of the diagnostic effectiveness of ^{11}C-MET PET in patients with various tumor types. This result was further verified by the direct comparison of the diagnostic values of ^{18}F-FDG and ^{11}C-MET PET from the 5 studies.[22-26] After removing the potential bias caused by pooling all the data, the overall diagnostic accuracy of ^{11}C-MET PET (AUC = 0.96) in the pooled data of the 5 studies was much higher than that of ^{18}F-FDG-PET (AUC = 0.81). Although there were 4 eligible ^{11}C-MET PET studies that included patients with different types of brain tumors,[23,29,41,42] no heterogeneity was observed. Therefore, the results of meta-analysis in ^{11}C-MET PET studies are more convincing, though there were fewer patients in ^{11}C-MET PET studies than in ^{18}F-FDG-PET studies. On the basis of our meta-analysis, it is always preferable to use ^{11}C-MET PET instead of ^{18}F-FDG-PET for differentiating brain tumors if possible.

However, although ^{11}C-MET PET appears to be a promising tracer for brain tumor differentiation, the use of ^{11}C-MET PET is restricted to the PET centers with a cyclotron due to the short half-life of [11]C (20 minutes) and the rapid catabolism of ^{11}C-MET.[25] As substitutes for ^{11}C-MET and ^{18}F-FDG, [18]F (half-life = 110 minutes) labeled PET tracers such as O-(2-[^{18}F]fluoroethyl)-L-tyrosine (^{18}F-FET),[8] 3,4-dihydroxy-6-^{18}F-fluoro-L-phenylalanine (^{18}F-FDOPA),[46] and 3′-deoxy-3′-^{18}F-fluorothymidine (^{18}F-FLT)[18,20] have been developed and applied in brain tumor imaging. Among these ^{18}F-labeled tracers, ^{18}F-FET and ^{18}F-FDOPA show superiority over ^{18}F-FDG in brain tumor differentiation, especially in low-grade brain tumors,[1,47] on the basis of the advantage of their high uptake in tumor tissue and low uptake in normal brain tissue. A meta-analysis with ^{18}F-FET PET studies in patients with SPBT has demonstrated the high performance of ^{18}F-FET PET with a pooled sensitivity and specificity of 0.82 and 0.76, respectively.[48] However, these values were not as good as our results for ^{11}C-MET PET. As for the ^{18}F-FLT PET, Choi et al[7] reported that although ^{18}F-FLT PET is useful for evaluating tumor grade and cellular proliferation in brain tumors, it is not useful enough for differentiating tumors from non-tumorous lesions. Because the PET studies using ^{18}F-FDOPA for brain tumor differentiation are still insufficient, further systematic evaluation using this tracer is expected in the future.

The recent meta-analysis by Nihashi et al[31] on the diagnostic accuracy of PET for recurrent glioma reported that ^{18}F-FDG-PET had moderately good sensitivity and specificity in either pooled glioma with different grades (sensitivity = 0.77, specificity = 0.78) or high-grade glioma (sensitivity = 0.79, specificity = 0.70).

The subgroup analysis in our study showed similar sensitivity and specificity of ^{18}F-FDG-PET in the glioma group. However, Nihashi et al reported a pooled sensitivity as low as 0.7 for ^{11}C-MET PET for high-grade gliomas, which is considerably different from our results. We believe our results are more reliable because we enrolled more eligible studies with more abundant data and investigated more brain tumor types.

However, a few limitations should be addressed in this study. First, although the overall sample size was as much as 857 in ^{18}F-FDG-PET and 416 in ^{11}C-MET PET settings, there was still incomplete data collection as reflected by the failure to access the full text of an eligible study.[49] In addition, the insufficient data in certain subtypes of brain tumors may impair the reliability of the analysis. We searched potential sources for heterogeneity in ^{18}F-FDG-PET studies and found that disease status was a significant source. Although the use of the bivariate model could at least correct this issue to some extent, the results should be interpreted cautiously. Second, methodologic quality might be a source of heterogeneity in ^{18}F-FDG-PET studies. We found that some included studies had low methodologic quality with few Y scores (≤6 items) in the Quality Assessment of Diagnostic Accuracy Studies.[5,10,13] In addition, a number of eligible studies included patients with various types of brain tumors.[1,7,9,10,14,16,17,23] Because the characteristics of different brain tumors may vary greatly (eg, brain lymphoma usually presents with higher ^{18}F-FDG uptake than normal brain tissue),[50] the composition of different brain tumors might bring bias by a nonrepresentative patient spectrum in ^{18}F-FDG-PET studies. Third, some characteristics of the eligible studies were not in good agreement. For example, the starting time of PET imaging after tracer injection differed widely, especially in the ^{18}F-FDG-PET studies. The differences of study characteristics may also contribute to the heterogeneity of our meta-analysis.

CONCLUSIONS

Our meta-analysis shows that ^{18}F-FDG-PET has limited diagnostic performance in brain tumor differentiation. However, ^{11}C-MET PET has excellent diagnostic performance in brain tumor differentiation and should be considered as a preferential approach for this purpose if available. Due to the inconvenience of the supply of ^{11}C, other ^{18}F-labeled tracers such as ^{18}F-FDOPA could be considered as potential alternatives for brain tumor differentiation and deserve future systematic evaluation after accumulating relevant studies in the future.

ACKNOWLEDGMENTS

REFERENCES

1. Chen W, Silverman DH, Delaloye S, et al. **18F-FDOPA PET imaging of brain tumors: comparison study with 18F-FDG-PET and evaluation of diagnostic accuracy.** J Nucl Med 2006;47:904–11
2. Ricci PE, Karis JP, Heiserman JE, et al. **Differentiating recurrent tumor from radiation necrosis: time for re-evaluation of positron emission tomography?** AJNR Am J Neuroradiol 1998;19:407–13
3. Wong TZ, van der Westhuizen GJ, Coleman RE. **Positron emission**

tomography imaging of brain tumors. *Neuroimaging Clin N Am* 2002;12:615–26

4. Sasaki M, Kuwabara Y, Yoshida T, et al. **A comparative study of thallium-201 SPET, carbon-11 methionine PET and fluorine-18 fluorodeoxyglucose PET for the differentiation of astrocytic tumours.** *Eur J Nucl Med* 1998;25:1261–69

5. Zuo C, Liu Y, Guan Y, et al. **Clinical application of FDG-PET for the diagnosis of recurrent glioma.** [in Chinese] *Nuclear Techniques* 2001;24:899–902

6. Gómez-Río M, Rodriguez-Fernandez A, Ramos-Font C, et al. **Diagnostic accuracy of 201Thallium-SPECT and 18F-FDG-PET in the clinical assessment of glioma recurrence.** *Eur J Nucl Med Mol Imaging* 2008;35:966–75

7. Choi SJ, Kim JS, Kim JH, et al. **[18F]3′-deoxy-3′-fluorothymidine PET for the diagnosis and grading of brain tumors.** *Eur J Nucl Med Mol Imaging* 2005;32:653–59

8. Pauleit D, Stoffels G, Bachofner A, et al. **Comparison of (18)F-FET and (18)F-FDG-PET in brain tumors.** *Nucl Med Biol* 2009; 36:779–87

9. Lau EW, Drummond KJ, Ware RE, et al. **Comparative PET study using F-18 FET and F-18 FDG for the evaluation of patients with suspected brain tumour.** *J Clin Neurosci* 2010;17:43–49

10. Estrada G, Gonzalez-Maya L, Celis-Lopez MA, et al. **Diagnostic approach in suspected recurrent primary brain tumors using (18)FDG-PET/MRI, perfusion MRI, visual and quantitative analysis, and three dimensional stereotactic surface projections: first experience in Mexico.** *Rev Esp Med Nucl* 2008;27:329–39

11. McCarthy M, Yuan JB, Campbell A, et al. **18F-fluorodeoxyglucose positron emission tomography imaging in brain tumours: the Western Australia positron emission tomography/cyclotron service experience.** *J Med Imaging Radiat Oncol* 2008;52:564–69

12. Kahn D, Follett KA, Bushnell DL, et al. **Diagnosis of recurrent brain tumor: value of 201Tl SPECT vs 18F-fluorodeoxyglucose PET.** *AJR Am J Roentgenol* 1994;163:1459–65

13. Thompson TP, Lunsford LD, Kondziolka D. **Distinguishing recurrent tumor and radiation necrosis with positron emission tomography versus stereotactic biopsy.** *Stereotact Funct Neurosurg* 1999;73:9–14

14. Sun A, Sun L, Wang R, et al. **Value of 18F-FDG-PET in differentiation of brain tumor recurrence from radiation necrosis after radiotherapy.** [in Chinese] *Chin J Med Imaging Technol* 2004;20:1484–86

15. Santra A, Kumar R, Sharma P, et al. **18F-FDG-PET-CT in patients with recurrent glioma: comparison with contrast enhanced MRI.** *Eur J Radiol* 2012;81:508–13

16. Hong IK, Kim JH, Ra YS, et al. **Diagnostic usefulness of 3′-deoxy-3′-[18F]fluorothymidine positron emission tomography in recurrent brain tumor.** *J Comput Assist Tomogr* 2011;35:679–84

17. Tan H, Chen L, Guan Y, et al. **Comparison of MRI, 18F-FDG, and 11C-choline PET/CT for their potentials in differentiating brain tumor recurrence from brain tumor necrosis following radiotherapy.** *Clin Nucl Med* 2011;36:978–81

18. Enslow MS, Zollinger LV, Morton KA, et al. **Comparison of 18F-fluorodeoxyglucose and 18F-fluorothymidine PET in differentiating radiation necrosis from recurrent glioma.** *Clin Nucl Med* 2012;37:854–61

19. Belohlávek O, Klener J, Vymazal J, et al. **The diagnostics of recurrent gliomas using FDG-PET: still questionable?** *Nucl Med Rev Cent East Eur* 2002;5:127–30

20. Spence AM, Muzi M, Link JM, et al. **NCI-sponsored trial for the evaluation of safety and preliminary efficacy of 3′-deoxy-3′-[18F]fluorothymidine (FLT) as a marker of proliferation in patients with recurrent gliomas: preliminary efficacy studies.** *Mol Imaging Biol* 2009;11:343–55

21. Janus TJ, Kim EE, Tilbury R, et al. **Use of [18F]fluorodeoxyglucose positron emission tomography in patients with primary malignant brain tumors.** *Ann Neurol* 1993;33:540–48

22. Kim YH, Oh SW, Lim YJ, et al. **Differentiating radiation necrosis from tumor recurrence in high-grade gliomas: assessing the effi-**

23. Cai L, Gao S, Li DC, et al. **Value of 18F-FDG and 11C-MET PET-CT in differentiation of brain ringlike-enhanced neoplastic and non-neoplastic lesions on MRI imaging** [in Chinese]. *Zhonghua Zhong Liu Za Zhi* 2009;31:134–38

24. Tripathi M, Sharma R, Varshney R, et al. **Comparison of F-18 FDG and C-11 methionine PET/CT for the evaluation of recurrent primary brain tumors.** *Clin Nucl Med* 2012;37:158–63

25. Li DL, Xu YK, Wang QS, et al. **¹¹C-methionine and ¹⁸F-fluorodeoxyglucose positron emission tomography/CT in the evaluation of patients with suspected primary and residual/recurrent gliomas.** *Chin Med J (Engl)* 2012;125:91–96

26. Ye C, Pan M, Li Y, et al. **11C-MET PET/CT in the detection of recurrent cerebral glioma.** [in Chinese] *Chin J Stereotact Funct Neurosurg* 2009;22:229–31

27. Hustinx R, Smith RJ, Benard F, et al. **Can the standardized uptake value characterize primary brain tumors on FDG-PET?** *Eur J Nucl Med* 1999;26:1501–09

28. Jager PL, Vaalburg W, Pruim J, et al. **Radiolabeled amino acids: basic aspects and clinical applications in oncology.** *J Nucl Med* 2001;42:432–45

29. Chung JK, Kim YK, Kim SK, et al. **Usefulness of 11C-methionine PET in the evaluation of brain lesions that are hypo- or isometabolic on 18F-FDG-PET.** *Eur J Nucl Med Mol Imaging* 2002;29:176–82

30. Nakajima T, Kumabe T, Kanamori M, et al. **Differential diagnosis between radiation necrosis and glioma progression using sequential proton magnetic resonance spectroscopy and methionine positron emission tomography.** *Neurol Med Chir (Tokyo)* 2009;49:394–401

31. Nihashi T, Dahabreh IJ, Terasawa T. **Diagnostic accuracy of PET for recurrent glioma diagnosis: a meta-analysis.** *AJNR Am J Neuroradiol* 2013;34:944–50

32. Whiting P, Rutjes AW, Reitsma JB, et al. **The development of QUADAS: a tool for the quality assessment of studies of diagnostic accuracy included in systematic reviews.** *BMC Med Res Methodol* 2003;3:25

33. Arends LR, Hamza TH, van Houwelingen JC, et al. **Bivariate random effects meta-analysis of ROC curves.** *Med Decis Making* 2008;28:621–38

34. Reitsma JB, Glas AS, Rutjes AW, et al. **Bivariate analysis of sensitivity and specificity produces informative summary measures in diagnostic reviews.** *J Clin Epidemiol* 2005;58:982–90

35. Swets JA. **Measuring the accuracy of diagnostic systems.** *Science* 1988;240:1285–93

36. Harbord RM, Whiting P, Sterne JA, et al. **An empirical comparison of methods for meta-analysis of diagnostic accuracy showed hierarchical models are necessary.** *J Clin Epidemiol* 2008;61:1095–103

37. Higgins JP, Thompson SG, Deeks JJ, et al. **Measuring inconsistency in meta-analyses.** *BMJ* 2003;327:557–60

38. Higgins JP, Thompson SG. **Quantifying heterogeneity in a meta-analysis.** *Stat Med* 2002;21:1539–58

39. Louis DN, Ohgaki H, Wiestler OD, et al. **The 2007 WHO classification of tumours of the central nervous system.** *Acta Neuropathol* 2007;114:97–109

40. Deeks JJ, Macaskill P, Irwig L. **The performance of tests of publication bias and other sample size effects in systematic reviews of diagnostic test accuracy was assessed.** *J Clin Epidemiol* 2005;58:882–93

41. Terakawa Y, Tsuyuguchi N, Iwai Y, et al. **Diagnostic accuracy of 11C-methionine PET for differentiation of recurrent brain tumors from radiation necrosis after radiotherapy.** *J Nucl Med* 2008;49:694–99

42. Galldiks N, Kracht LW, Berthold F, et al. **[11C]-L-methionine positron emission tomography in the management of children and young adults with brain tumors.** *J Neurooncol* 2010;96:231–39

43. Sonoda Y, Kumabe T, Takahashi T, et al. **Clinical usefulness of 11C-MET PET and 201Tl SPECT for differentiation of recurrent glioma from radiation necrosis.** *Neurol Med Chir (Tokyo)* 1998;38:342–47, discussion 347–48

22. ...**cacy of 18F-FDG-PET, 11C-methionine PET and perfusion MRI.** *Clin Neurol Neurosurg* 2010;112:758–65

44. Tsuyuguchi N, Takami T, Sunada I, et al. **Methionine positron emission tomography for differentiation of recurrent brain tumor and radiation necrosis after stereotactic radiosurgery–in malignant glioma.** *Ann Nucl Med* 2004;18:291–96

45. Chen W. **Clinical applications of PET in brain tumors.** *J Nucl Med* 2007;48:1468–81

46. Schiepers C, Chen W, Cloughesy T, et al. **18F-FDOPA kinetics in brain tumors.** *J Nucl Med* 2007;48:1651–61

47. Floeth FW, Pauleit D, Sabel M, et al. **Prognostic value of O-(2–18F-fluoroethyl)-L-tyrosine PET and MRI in low-grade glioma.** *J Nucl Med* 2007;48:519–27

48. Dunet V, Rossier C, Buck A, et al. **Performance of 18F-fluoro-ethyl-tyrosine (18F-FET) PET for the differential diagnosis of primary brain tumor: a systematic review and Metaanalysis.** *J Nucl Med* 2012;53:207–14

49. Ozsunar Y, Mullins ME, Kwong K, et al. **Glioma recurrence versus radiation necrosis? A pilot comparison of arterial spin-labeled, dynamic susceptibility contrast enhanced MRI, and FDG-PET imaging.** *Acad Radiol* 2010;17:282–90

50. Kosaka N, Tsuchida T, Uematsu H, et al. **18F-FDG-PET of common enhancing malignant brain tumors.** *AJR Am J Roentgenol* 2008;190:W365–69

The Independent Payment Advisory Board

J.A. Hirsch, W.D. Donovan, R.M. Barr, G.N. Nicola, D.A. Rosman, P.W. Schaefer, and L. Manchikanti

ABBREVIATIONS: IPAB = Independent Payment Advisory Board; ACA = Patient Protection and Affordable Care Act; PCORI = Patient Centered Outcomes Research Institute; MedPAC = Medicare Payment Advisory Commission

The Independent Payment Advisory Board (IPAB) is considered the most potent cost-cutting measure of the Patient Protection and Affordable Care Act (ACA), which was signed into law in March 2010. Together with the Patient Centered Outcomes Research Institute (PCORI), it is 1 of 2 independent boards established as part of the sweeping health care reform bill and is one of the bill's most controversial measures.

The IPAB, when complete, will be composed of 15 members charged with holding Medicare spending growth within specified limits. Whenever projected Medicare spending exceeds determined target levels, the IPAB is required to present recommendations to control costs, and the Health and Human Services Secretary is required to implement those changes unless Congress specifically takes action to override the recommendations and replace them with alternatives that achieve similar savings.

Neuroradiologists should be informed about the existence and purpose of the IPAB because their reimbursement may be significantly affected by its actions in the foreseeable future.

The Affordable Care Act represents a generational change in the provision of health care in the United States.[1-3] It includes a monumental expansion of Medicaid as well as the development of a system of State-Based Health Insurance Exchanges for those citizens who do not qualify for the expanded Medicaid system. There are mandates for people to purchase insurance and for businesses to provide insurance to avoid penalties. To help fund this expansion, there are reductions in funding for programs such as Medicare Advantage; and there are new tax programs, such as the Medicare Tax Rate Increase, the Net Investment Income Tax, and the Cadillac Insurance Tax.[2-4]

The ACA is divided into 10 titles with elements that went into effect as early as June 21, 2010.[1-3,5] There have been multiple attempts by House Republicans to revoke this law.[6] Although small portions of the law have been enforced since the passage of the ACA, 2014 and 2015 will mark the implementation of some of its principal components.[4,5,7,8]

Two independent boards have been established as part of the law. The first is the Patient Centered Outcomes Research Institute. PCORI moves the agenda of comparative effectiveness research forward; given the limited work that has been done in this area, PCORI provides an opportunity for neuroradiologists to obtain funding to investigate practices that will improve patient care.[8] Its formation has enjoyed the support of the American College of Radiology, as well as much of organized medicine, though there are notable exceptions.[8,9] As part of the legislation, PCORI cannot be used for denial of coverage nor may it consider the cost of providing care.[2,8,9,10]

The second of the 2 boards is the Independent Payment Advisory Board. As opposed to PCORI, IPAB has drawn criticism from much of organized medicine, including the American College of Radiology and the American Society of Neuroradiology. The raison d'être for the IPAB is to facilitate statutory Medicare budget limits.[7] This vignette will focus on the IPAB.

HISTORY

During the administration of President Lyndon B. Johnson, Congress created Medicare as part of a series of social reforms known as the "Great Society." This landmark legislation occurred in 1965 as part of Title XVIII of the Social Security Act. Its purpose was to provide health insurance to people age 65 years and older, regardless of income or medical history.

The growth in cost during the past 45 years of the US health care endeavor, including Medicare, has been striking.[5,10] In 2011, total US health care spending was $2.7 trillion; this represented 17.9% of gross domestic product, the highest percentage of any

industrialized nation. The average industrialized nation spends 9.5% of gross domestic product on health care. The countries with the second and third highest percentages are the Netherlands at 12%, and France at 11.6% (2010 Organisation for Economic Co-operation and Development Health Data, reported in 2012). Most agree that this trend is unsustainable.[11]

Recent publications[11,12] have documented a slowing of growth in US health care spending. In 2011, US health care spending grew 3.9%, marking the third consecutive year of relatively slow growth. Growth in national health spending closely tracked growth in nominal gross domestic product in 2010 and 2012, and health spending as a share of gross domestic product remained stable from 2009 through 2011. However, although growth in spending at the national level has remained stable, personal health care spending growth accelerated in 2011 from 3.7%–4.1%, in part because of faster growth in spending for prescription drugs and physician and clinical services. A recent Medicare trustees report[13] postulated with cautious optimism that the slowdown in health spending that has extended the trust fund's life is here to stay, and not a reflection of the slow economy of the past few years. However, in this estimation, it was assumed that the Sustainable Growth Rate cuts would be implemented. If the Sustainable Growth Rate were replaced, this would likely increase costs of Medicare and more rapidly deplete the Medicare trust fund.[7,13,14]

During the years there have been a variety of proposals to create an independent entity, analogous to the United Kingdom's National Institute for Health and Clinical Excellence of the National Health Service, that would be charged with curbing growth in federal health care spending.[15] Theoretically, this independent status would insulate these policy makers from special-interest groups and lobbyists.[15-17]

Along those lines, the IPAB is an independent board within the executive branch. This is in direct contrast to the Medicare Payment Advisory Commission (MedPAC), an existing panel that reports to the legislative branch.[1-3,7,8] MedPAC was enacted as part of the Balanced Budget Act of 1997 by merger of the Prospective Payment Assessment Commission and the Physician Payment Review Commission.[18] Composed of 17 appointed members, it generates 2 formal reports per year to Congress on policy and payment issues affecting Medicare.

However, MedPAC's role is purely advisory; Congress has frequently declined to follow its recommendations.

The IPAB is composed of 15 full-time members to be appointed by the President, and approved by the Senate. As most of the members are required to be nonproviders, as mandated by the legislation, Board membership is a full-time job so as to limit any possibility of conflict of interest.

The IPAB would have the authority to make both mandatory and advisory recommendations.

IPAB RECOMMENDATIONS
The IPAB is mandated to submit recommendations whenever Medicare per capita spending growth is projected to exceed statutory targets. The timelines are defined in the legislation.[5,19] The recommendation requires an explanation and rationale, as well as an estimate of the necessary administrative funding. The Center for Medicare & Medicaid Services Actuary must certify that the recommendations will result in the legislatively mandated savings and will not result in any increase in Medicare spending during the subsequent 10-year period starting with the implementation year.

In addition to the mandatory recommendations above, the IPAB can make advisory recommendations on far-ranging health care policy issues, including recommendations to slow the growth of private health care expenditures—much like MedPAC.

As part of a common theme of the ACA (ie, more care at less cost), the mandatory recommendations are required to maintain or enhance beneficiary access to quality care. Moreover, the law prohibits certain recommendations that could negatively affect beneficiaries or certain providers. The IPAB may not recommend anything that could be construed as rationing health care, increase Medicare beneficiary costs, or otherwise restrict benefits.

FAST-TRACK PROCEDURES
The extraordinary powers of the IPAB, in part, derive from unique congressional fast-track procedures for its mandatory recommendations. The board's proposals *must be* introduced to both the House and the Senate on the same day. Once introduced, these mandatory recommendations must be sent to the committees with relevant jurisdiction. The committees must report those recommendations, with any changes, within 3 months, or the proposals are formally discharged from the committees. Of note, the committees and the full House and Senate cannot consider any amendment that would change or repeal the IPAB's recommendations unless those changes meet the same fiscal criteria under which the board operates. A supermajority in the Senate is required to waive this restriction.

LIMITATIONS ON JUDICIAL OR ADMINISTRATIVE REVIEW
In addition to the severe constraints placed on Congress, the ACA explicitly disallows review by either the administration or the judiciary. Although this move sounds aggressive, it is in keeping with the policy goal of moving forward with the mandatory recommendations of the IPAB. Specifically, the Secretary of Health and Human Services is required to implement the IPAB recommendations, or an alternative of a similar revenue-saving effect.

DISCUSSION
The ACA represents a paradigm shift in how health care will be delivered for millions of Americans.[1-3] Its key programs of mandated insurance, elimination of pre-existing conditions, and children's coverage until age 26 years have been widely reviewed.

Less known to the broad audience who has interest in the ACA are the particulars of the IPAB.[1-3,7,8] The IPAB has remarkable power to affect the reimbursement of physicians in general and neuroradiologists in particular.[1-3,7,19,20] This is particularly true in early implementation of the ACA, as hospitals and nursing homes are insulated from IPAB authority until 2020, leaving the physician providers in the crosshairs.

There have been a multitude of arguments for and against IPAB, including arguments for expansion on the one hand, and repeal on the other. Aaron[17] considered the IPAB akin to Congress good deed for the country. He pursued a fascinating line of

thinking, that is, that among the most important attributes of legislative statesmanship is self-abnegation—the willingness of legislators to abstain from meddling in matters they are poorly equipped to manage. The Federal Reserve Board embodies that virtue. Essentially, Congress recognized the temptation to use monetary policy for political ends and realized that it would, at times, prove irresistible.[17] Consequently, to save themselves from this possibility, legislators created an organization whose funding and operations were largely beyond the reach of normal legislative controls. When one begins to process these concepts, one appreciates the fundamental similarities with the Federal Reserve in the construct of the IPAB.

Going even further, some advocates think it should be extended to include Medicaid, exchanges, and all types of payers.[21,22] In testimony before the House Budget Committee in 2011, Feder[21] argued that given Medicare's relative success with cost controls, the expertise and authority of the IPAB should be applied to all payers—with a system wide spending target. Kathleen Sebelius,[22] the Secretary of the US Department of Health and Human Services, stated that experts across the country, including independent economists and the Congressional Budget Office, believe that the IPAB is a needed safeguard.

In contrast, Holtz-Eakin[23] is a detractor. He described the IPAB as a dramatic policy error that will fail to deliver meaningful reform to the Medicare program. In fact, he believes that it may well exacerbate existing reimbursement problems that already limit access to care for Medicare beneficiaries and stifle US-led medical innovation.

In a balanced perspective piece in the *New England Journal of Medicine*, Oberlander and Morrison[11] note that the IPAB is hailed by supporters as the most important institutional change in the ACA, and a crucial component of health care cost containment. Specifically, many health policy analysts applaud the vision of a nonpartisan board, insulated from political pressures, that can formulate a more cohesive Medicare policy, analogous to the National Institute for Health and Clinical Excellence of the National Health Service.[15] These authors also report that supporters praise it as fail-safe, ensuring that growth in Medicare spending is moderated, regardless of congressional inaction. On the other hand, the authors also discuss the viewpoints of various IPAB critics. For instance, constraints prohibit the IPAB from making recommendations that raise revenues, increase cost sharing of Medicare beneficiaries, or restrict benefits and eligibility. It is expected to focus on savings from medical providers.[11] A broad coalition of health care industry groups, fearful that the boards' proposals will result in reduced Medicare payments, fiercely opposes the IPAB. Furthermore, Republicans also view it as an instrument of rationing and bureaucratic intrusion into medicine.

One of the most telling points in the article by Oberlander and Morrison[11] is their ironic observation that the first major milestone in the Board's operation passed with scant public notice, despite the political storm surrounding the IPAB.[11] The April 2013 report of the Chief Actuary of the Center for Medicare & Medicaid Services projected that Medicare spending per person will grow at an average rate of 1.15% during 2011–2015, far below the target growth rate set by the ACA—the average of the consumer price index and the medical consumer price index. Conse-

quently, this level of spending growth will not necessitate IPAB to propose reductions in Medicare reimbursement. If low Medicare spending growth continues, then the most controversial feature of the IPAB— congressional consideration of IPAB proposals under expedited procedures—will not come into play. It is, however, mandated that the target growth rate set by the ACA will be a rolling annual calculation, allowing the IPAB to act at the very hint of return of health care inflation.

The IPAB is supposed to begin its work in 2014, with recommendations due for the 2015 Medicare budget cycle. Of note, 3 years after the ACA's enactment, the President has yet to nominate a single member for the Board.[11] Filling positions on the IPAB may itself be a monumental task, as these presidential appointments will require Senate approval—a daunting challenge given the current political climate.

It has been commonly noted that President Obama described the IPAB as "MedPAC on steroids." Considered in that vein, MedPAC might provide insight on how the regulatory and advisory roles of IPAB may affect neuroradiologists. Recent MedPAC proposals include the application of a multiple procedure payment reduction to the professional component of advanced imaging services, an approach that the American Society of Neuroradiology vehemently opposes along with the American College of Radiology, other imaging societies, and the American Medical Association. Page 40 of the June 2011 MedPAC report[24] states, "CMS should calculate the payment reduction for second and subsequent professional component services performed in the same session by analyzing efficiencies in physician work associated with multiple services." In addition, and as a separate data point, we note that MedPAC has included specific information regarding radiologist compensation in its reports to Congress. Although we list only these 2 data points, it is reasonable to conclude from multiple data points that are beyond the scope of this article that MedPAC takes issue with the role that imaging plays in the global health care expenditure.

Neuroradiologists may hope that congressional review would deflect any intemperate IPAB recommendations and would never allow Congress to be marginalized by a nonlegislative independent board, given Medicare's popularity. Unfortunately, the track record of Congress with sequestration, the debt ceiling, and the multiyear failure to repeal the Sustainable Growth Rate formula argue against its ability to find a supermajority on any issue, particularly one promising revenue savings.

Arguably, the most compelling evidence marginalizing the potential power of the IPAB in the near future is the recent slowing in health care spending growth. The IPAB may be deprioritized until Medicare expenditures hit their legislatively defined targets.

CONCLUSIONS

The IPAB is a critical and controversial element of the ACA. Congress has ceded much of its own authority over Center for Medicare & Medicaid Services spending to this independent board. Further, it has limited its own ability to affect the actions of the board through the fast-track process. The IPAB has the potential to significantly affect neuroradiologists' reimbursement.

ACKNOWLEDGMENTS

We would like to thank Mike Morrow, American Society of Neuroradiology staff, for his review of this manuscript. We would also like to thank Cynthia Hynes for her assistance with the manuscript.

REFERENCES

1. Public Law No: 111-48: H.R. 3590. **Patient Protection and Affordable Care Act.** March 23, 2010
2. Manchikanti L, Hirsch JA. **Patient Protection and Affordable Care Act of 2010: a primer for neurointerventionalists.** *J Neurointerv Surg* 2012;4:141–46
3. Manchikanti L, Hirsch JA. **Obamacare 2012: prognosis unclear for interventional pain management.** *Pain Physician* 2012;15:E629–40
4. Meltzer CC. **Summary of the Affordable Care Act.** *AJNR Am J Neuroradiol* 2011;32:1165–66
5. Manchikanti L, Singh V, Caraway DL, et al. **Proposed physician payment schedule for 2013: guarded prognosis for interventional pain management.** *Pain Physician* 2012;15:E615–27
6. S. 668 (112th). **Health Care Bureaucrats Elimination Act.** March 29, 2011
7. Manchikanti L, Hirsch JA. **The Independent Payment Advisory Board: impact on neurointerventionalists.** *J Neurointerv Surg* 2012;4:468–72
8. Manchikanti L, Helm S, Hirsch JA. **The evolution of the Patient-Centered Outcomes Research Institute.** *J Neurointerv Surg* 2012;4:157–62
9. Manchikanti L, Falco FJ, Benyamin RM, et al. **The impact of comparative effectiveness research on interventional pain management: evolution from Medicare Modernization Act to Patient Protection and Affordable Care Act and the Patient-Centered Outcomes Research Institute.** *Pain Physician* 2011;14:E249–82
10. Manchikanti L, Falco FJE, Benyamin RM, et al. **Value-based interventional pain management: a review of Medicare national and local coverage determination policies.** *Pain Physician* 2013;16: E145–80
11. Oberlander J, Morrison M. **Failure to launch? The Independent Payment Advisory Board's uncertain prospects.** *N Engl J Med* 2013;369:105–07
12. Hartman M, Martin AB, Benson J, et al. **National health spending in 2011: overall growth remains low, but some payers and services show signs of acceleration.** *Health Aff* 2013;32:87–99
13. **Centers for Medicare and Medicaid Services, Trustees Report shows reduced cost growth, longer Medicare solvency, May 31, 2013.** http://www.cms.gov/Newsroom/MediaReleaseDatabase/Press-Releases/2013-Press-Releases-Items/2013–05-31.html. Accessed June 25, 2013
14. Hirsch JA, Rosman DA, Liu RW, et al. **Sustainable growth rate 2013: time for definitive intervention.** *J Neurointerv Surg* 2013;5:382–86
15. **National Institute for Health and Clinical Excellence (NICE).** http://www.nice.org.uk/. Accessed June 25, 2013
16. Terry K. **Should MedPAC be given authority over Medicare payments?** BNET, June 4, 2009. http://www.bnet.com/blog/healthcare-business/should-medpac-be-given-authorityover-medicare-payments/414 Blog on CBS Interactive Business Network. Accessed June 25, 2013
17. Aaron HJ. **The Independent Payment Advisory Board – Congress's "good deed."** *N Engl J Med* 2011;364:2377–79
18. H.R. 2015. **Balanced Budget Act of 1997. P.L. 105e33.** House Bill, 5 August 1997
19. Ebeler J, Neuman T, Cubanski J. **The Independent Payment Advisory Board: a new approach to controlling Medicare spending.** The Kaiser Family Foundation Program on Medicare Policy, April 13, 2011. http://kff.org/health-reform/issue-brief/the-independent-payment-advisory-board-a-new/. Accessed June 25, 2013
20. Ellenbogen PH. **Independent Payment Advisory Board: beware–danger!** *J Am Coll Radiol* 2013;10:307
21. **Testimony by Judith Feder, PhD, Professor and former Dean, Georgetown Public Policy Institute, and Urban Fellow Institute before the United States House of Representatives, Committee on the Budget RE: Medicare's future: An examination of the Independent Payment Advisory Board.** July 12, 2011
22. **Statement of Kathleen Sebelius, Secretary, U.S. Department of Health and Human Services, before the United States House of Representatives, Committee on the Budget RE: Medicare's future: An examination of the Independent Payment Advisory Board.** July 12, 2011
23. **Testimony by Douglas Holtz-Eakin, President, American Action Forum, before the United States House of Representatives, Committee on the Budget RE: Medicare's future: An examination of the Independent Payment Advisory Board.** July 12, 2011
24. Medicare Payment Advisory Commission. Report to the Congress. **Medicare and the Health Care Delivery System.** Washington, DC: MedPAC. June 2012. http://www.medpac.gov/documents/Jun12_EntireReport.pdf. Accessed June 25, 2013

Genetics of Huntington Disease

S. Mahalingam and L.M. Levy

ABBREVIATIONS: HD = Huntington disease; CAG = cytosine-adenine-guanine

Huntington disease (HD) is an autosomal dominant genetic condition that can affect movement and cognition and is progressive and fatal. It results from genetic mutations involving trinucleotide repeats of the *huntingtin* gene, which encodes the huntingtin protein.

HD is presently the most widely studied genetic neurodegenerative disease that has diagnostic and predictive genetic testing, with the possibility of gene-targeted therapy in the near future.

Neuroimaging can play an important diagnostic and prognostic role in HD by evaluating affected regions of the brain by using techniques such as MR imaging, FDG-PET, MR spectroscopy, and diffusion tensor imaging.

HISTORY OF HUNTINGTON DISEASE

Huntington disease is a neurodegenerative genetic condition that can affect movement and cognition and is progressive and fatal. While it has been known by various names previously, it obtained its eponym after George Huntington presented an exhaustive description of the clinical manifestation of the disease in 1872.[1] Although it was called Huntington's chorea for nearly a century, it is now more accurately referred to as Huntington disease, because chorea is neither a constant nor a particularly dominant feature of the disease. HD is an autosomal dominant disease that exhibits complete penetrance, so that all individuals carrying the defective gene will manifest the disease.[2] The largest number of closely related affected patients comes from interrelated families from Lake Maracaibo in Venezuela.[1] An extensive project studying these families led to mapping of the gene to the short arm of chromosome 4 at locus 16.3.[3] The huntingtin protein was later isolated 1993.[4] HD holds a unique position in the field of medical genetics because it has largely contributed to the understanding of the

gene: This was the first genetic disorder to be mapped to a specific locus in the chromosome without prior knowledge of the gene location and one of the first diseases to have prenatal genetic testing made available.[1] HD is more common in whites, with an estimated prevalence of 4–10 per 10,000,[2] and much lower in Asian and African populations.[5]

WHAT ARE THE CLINICAL MANIFESTATIONS OF HUNTINGTON DISEASE?

Huntington disease has 3 subtypes, with the adult-onset being the most common and the juvenile and infantile varieties being far less prevalent. In adult-onset HD, the disease is characterized by a triad of behavioral, cognitive, and motor features.[2] Behavioral symptoms often present early as increased irritability, agitation, loss of inhibition, and increased aggression. In a patient without a definite family history, definitive diagnosis with these symptoms is often delayed. However, diagnosis is often easier with evidence of motor symptoms. These include chorea, which can become less pronounced with the onset of rigidity and dyskinesia; motor impersistence (the inability to maintain a sustained voluntary muscle contraction); and loss of fine and gross motor skills, which respectively occur in the early and late phase of the disease.[5] In general, HD is a devastating and relentlessly progressive disease, which is fatal within 15–20 years of onset.[2]

Juvenile-onset HD and infantile HD account for <10% of the disease prevalence.[6] Rigidity and dyskinesia along with cognitive decline are dominant features with chorea rarely seen.[6] Regression of motor milestones and poor performance in school are often present at the time of diagnosis.

WHAT ARE THE FUNCTIONS OF THE *HUNTINGTIN* GENE?

Although the gene map for *huntingtin* was discovered many years ago, the exact function of the protein has yet to be confirmed. Given its location in both the cytoplasm and nucleus and its numerous interactions with other proteins, it has been postulated that the huntingtin protein has a regulatory role in transcription

and intracellular transport.[4] It is widely expressed in many cell types, with a preferential expression in the brain and testis and, to a lesser, extent in the liver and lungs.[7] Its distribution in the brain is variable, with high amounts present in the corpus striatum and the cerebral and cerebellar cortices. This protein also has an anti-apoptotic role, and cells with mutant or decreased expression of *huntingtin* undergo early cell dysfunction and death. Expansion of the cytosine-adenine-guanine (CAG) repeats causes increased polyglutamine in the *huntingtin* gene, with CAG corresponding to the 3 DNA bases, cytosine-adenine-guanine. This leads to the formation of abnormal nuclear and cytoplasmic intracellular inclusions or aggregates, which dysregulate cell homeostasis and promote cell death[4,8]

WHAT IS THE SIGNIFICANCE OF THE HUNTINGTIN PROTEIN?

The normal huntingtin protein has fewer than 27 CAG repeats that encode for polyglutamine. Individuals with CAG repeats of 27–35 (intermediate alleles)[9] will not manifest the disease, though intermediate alleles possess the potential to expand into an allele range of ≥36 in subsequent generations. Those with ≥36 CAG repeats are affected with HD and will manifest the disease.

The greater the number of the CAG repeats, the earlier is the onset of the disease. With each generation, there is an increase in the CAG triplet expansion, leading to "anticipation" of the disease.[5] Thus, patients with infantile- and juvenile-onset HD will possess a large number of repeats in their alleles and earlier onset compared with their parents, from whom they inherited the disease.[10]

WHAT IS THE SIGNIFICANCE OF THE INTERMEDIATE ALLELE AND THE ROLE OF SEX?

The intermediate allele containing the CAG repeat of 27–35 shows a greater degree of instability and a propensity for expansion during spermatogenesis compared with oogenesis.[9] Thus a male with the intermediate allele has a higher probability of producing an offspring with the HD allele containing ≤36 CAG repeats than a female with an intermediate allele. In addition, juvenile-onset HD and infantile HD have a higher percentage of paternal inheritance compared with maternal inheritance.[6]

DIAGNOSTIC TESTING

In individuals with a strong family history of HD and evidence of appropriate symptoms, genetic testing is often unnecessary. However, in situations in which the diagnosis is not apparent or a positive family history is unavailable, negative testing results can conclusively rule out the disease and allow the pursuit of alternative differential diagnoses.

IS THERE PREDICTIVE TESTING AVAILABLE FOR HUNTINGTON DISEASE?

Considering the prolonged and difficult course of this fatal disease, obtaining genetic testing is a significant decision for the patient. Presently, predictive testing is offered after due review of the individual's mental status and available psychological support to prevent any adverse outcomes.[5] In general, predictive testing is used by a person with a family history of HD before significant life-changing events such as marriage or pregnancy.[3] Prenatal diagnostic testing is also available to determine the HD allele status of the fetus. However, predictive testing cannot be used to forecast the age at onset because it has a high degree of variability.[2] Thus, even though individuals with larger numbers of repeats have earlier onset, the number of repeats cannot predict the age of onset.[3]

WHAT ARE THE ROLES OF STRUCTURAL AND FUNCTIONAL NEUROIMAGING IN HD?

Neuroradiology can play a diagnostic and prognostic role in the evaluation of HD. In individuals with a strong family history of HD, MR volumetric analysis can predict loss of striatal volume as early as 20 years before the appearance of motor symptoms.[11] In the clinical symptomatic phase, MR imaging and CT can identify caudate atrophy and the consequent dilation of the frontal horns. Cortical and subcortical atrophy are heterogeneous and appear later than striatal atrophy. Loss of striatal volume can serve as a biomarker for predicting the course of the disease because it is constant throughout.[2] FDG-PET can reveal a decrease in the metabolism of glucose in the striatum in the early phase of the disease, and subsequently in the cortex. A recent study suggested that glucose hypometabolism in the cortex can serve as a marker for faster disease progression.[12] MR spectroscopy can be used to detect decreases in *N*-acetylaspartate and creatine in the caudate and putamen along with decreased putaminal glutamate during the preclinical phase. Also, MR spectroscopy has demonstrated a correlation between disease severity and levels of *N*-acetylaspartate, creatine, and glutamate, and these may be useful as future biomarkers.[13] Diffusion tensor imaging has also been useful in demonstrating the degeneration of white matter tracts, which can occur early in the course of the disease.[14,15]

CONCLUSIONS

Huntington disease is the most widely studied genetic neurodegenerative disease that has available diagnostic and predictive genetic testing, with the possibility of gene-targeted therapy in the near future. Valuable insights provided by genetic research in HD have also strengthened the understanding of other neurodegenerative disorders such as Alzheimer disease, with increased hope for more definitive therapeutic strategies.

REFERENCES

1. Bates GP. **History of genetic disease: the molecular genetics of Huntington disease: a history.** *Nat Rev Genet* 2005;6:766–73
2. Ross CA, Tabrizi SJ. **Huntington's disease: from molecular pathogenesis to clinical treatment.** *Lancet Neurol* 2011;10:83–98
3. Myers RH. **Huntington's disease genetics.** *NeuroRx* 2004;1:255–62
4. Borrell-Pagès M, Zala D, Humbert S, et al. **Huntington's disease: from huntingtin function and dysfunction to therapeutic strategies.** *Cell Mol Life Sci* 2006;63:2642–60
5. Walker FO. **Huntington's disease.** *Lancet* 2007;369:218–28
6. Koutsis G, Karadima G, Kladi A, et al. **The challenge of juvenile Huntington disease: to test or not to test.** *Neurology* 2013;80:990–96
7. Trottier Y, Devys D, Imbert G, et al. **Cellular localization of the Huntington's disease protein and discrimination of the normal and mutated form.** *Nat Genet* 1995;10:104–10
8. Bates G. **Huntingtin aggregation and toxicity in Huntington's disease.** *Lancet* 2003;361:1642–44
9. Semaka A, Creighton S, Warby S, et al. **Predictive testing for Hun-**

tington disease: interpretation and significance of intermediate alleles. *Clin Genet* 2006;70:283–94

10. Tabrizi SJ, Langbehn DR, Leavitt BR, et al. **Biological and clinical manifestations of Huntington's disease in the longitudinal TRACK-HD study: cross-sectional analysis of baseline data.** *Lancet Neurol* 2009;8:791–801

11. Klöppel S, Henley SM, Hobbs NZ, et al. **Magnetic resonance imaging of Huntington's disease: preparing for clinical trials.** *Neuroscience* 2009;164:205–19

12. Shin H, Kim MH, Lee SJ, et al. **Decreased metabolism in the cerebral cortex in early-stage Huntington's disease: a possible biomarker of disease progression?** *J Clin Neurol* 2013;9:21–25

13. Versluis MJ, van der Grond J, van Buchem MA, et al. **High-field imaging of neurodegenerative diseases.** *Neuroimaging Clin N Am* 2012;22:159–71, ix

14. Bohanna I, Georgiou-Karistianis N, Sritharan A, et al. **Diffusion tensor imaging in Huntington's disease reveals distinct patterns of white matter degeneration associated with motor and cognitive deficits.** *Brain Imaging Behav* 2011;5:171–80

15. Rosas HD, Tuch DS, Hevelone ND, et al. **Diffusion tensor imaging in presymptomatic and early Huntington's disease: selective white matter pathology and its relationship to clinical measures.** *Mov Disord* 2006;21:1317–25

Radiation Doses of Cerebral Blood Volume Measurements Using C-Arm CT: A Phantom Study

W.F. Chu, C.J. Lin, W.S. Chen, S.C. Hung, C.F. Chiu, T.H. Wu, and W.Y. Guo

ABSTRACT

BACKGROUND AND PURPOSE: Parenchymal blood volume measurement by C-arm CT facilitates in-room peritherapeutic perfusion evaluation. However, the radiation dose remains a major concern. This study aimed to compare the radiation dose of parenchymal blood volume measurement using C-arm CT with that of conventional CTP using multidetector CT.

MATERIALS AND METHODS: A biplane DSA equipped with C-arm CT and a Rando-Alderson phantom were used. Slab parenchymal blood volume (8-cm scanning range in a craniocaudal direction) and whole-brain parenchymal blood volume with identical scanning parameters, except for scanning ranges, were undertaken on DSA. Eighty thermoluminescent dosimeters were embedded into 22 organ sites of the phantom. We followed the guidelines of the International Commission on Radiation Protection number 103 to calculate the effective doses. For comparison, 8-cm CTP with the same phantom and thermoluminescent dosimeter distribution was performed on a multidetector CT. Two repeat dose experiments with the same scanning parameters and phantom and thermoluminescent dosimeter settings were conducted.

RESULTS: Brain-equivalent dose in slab parenchymal blood volume, whole-brain parenchymal blood volume, and CTP were 52.29 ± 35.31, 107.51 ± 31.20, and 163.55 ± 89.45 mSv, respectively. Variations in the measurement of an equivalent dose for the lens were highest in slab parenchymal blood volume (64.5%), followed by CTP (54.6%) and whole-brain parenchymal blood volume (29.0%). The effective doses of slab parenchymal blood volume, whole-brain parenchymal blood volume, and CTP were 0.87 ± 0.55, 3.91 ± 0.78, and 2.77 ± 1.59 mSv, respectively.

CONCLUSIONS: The dose measurement conducted in the current study was reliable and reproducible. The effective dose of slab parenchymal blood volume is about one-third that of CTP. With the advantages of on-site and immediate imaging availability and saving procedural time and patient transportation, slab parenchymal blood volume measurement using C-arm CT can be recommended for clinical application.

ABBREVIATIONS: PBV = parenchymal blood volume; s-PBV = slab parenchymal blood volume; w-PBV = whole-brain parenchymal blood volume; TLD = thermoluminescent dosimeter

CTP is an imaging technique commonly used in conjunction with CT angiography to evaluate the cerebral perfusion status of patients with cerebrovascular disorders.[1,2] It serves as an excellent patient triage tool for strategy planning in patients with acute ischemic stroke by its quantitative delineation of the extent of ischemic core and penumbra.[1,3,4] It is also used to evaluate therapeutic effects and detect complications such as hyperperfusion syndrome or hemorrhagic transformation for subsequent management.[5-7] Nevertheless, CT cannot demonstrate intracranial territorial hemodynamics. It is not feasible either to serve as imaging guidance for neurovascular intervention or to provide immediate information without patient transportation to scanners. Recent advances in flat panel detector technology render a C-arm system capable of providing projection radiography, fluoroscopy, DSA, and CT-like images in 1 imaging suite. Due to the versatile applications, C-arm CT equipped with a flat detector has gained wide popularity in current imaging practice.[8-10]

C-arm CT also allows functional imaging of parenchymal blood volume (PBV) with either intravenous or intra-arterial contrast injection.[11,12] It is highly correlated with CBV from CTP and has shown promising initial results in treating acute middle cerebral artery occlusions.[13] It can be used to access the extent of

Table 1: Number and distributions of TLD-100Hs in the Rando-Alderson phantom for the experiments

Site Number	Organ	TLD No.
1	Brain	21
2	Salivary gland	4
3	Thyroid	4
4	Esophagus	3
5	Lung	3
6	Heart	3
7	Liver	3
8	Stomach	3
9	Kidney	2
10	Small intestine	4
11	Colon	2
12	Bladder	2
13	Gonad (surface)	4
14	Rib	2
15	Thoracic spine	3
16	Lumbar spine	3
17	Pelvis	2
18	Skin (eye)	4
19	Skin (thorax)	4
20	Skin (abdomen)	4
	Total	80

the ischemic core and detect hyperperfusion phenomena peritherapeutically in the angiography suite, facilitating endovascular therapy without the transfer of patients to the CT room.[10-15] In a recent study, Royalty et al[16] showed the feasibility of using C-arm CT to measure perfusion parameters in an animal model. Nevertheless, the combination of DSA and flat panel parenchymal blood volume raises concerns related to radiation exposure.[17,18] Unintentional adverse effects due to overexposure to x-rays in CT rooms or angiography suites should be avoided.[17,19] Before the one-stop imaging from diagnosis to imaging-guided endovascular treatment and posttherapeutic evaluation is widely adopted in clinical service, the dose measurement of C-arm CT in perfusion parameter evaluation should be investigated. We, therefore, present the current study.

MATERIALS AND METHODS
Radiation Dose Measurement
A radiation experiment by using an anthropomorphic phantom (Rando-Alderson phantom; Radiology Support Devices, Long Beach, California) was used for both PBV and CTP. The phantom consisted of 35 sections of 2.5-cm thickness each. It simulated the body of a 170-cm tall, 70-kg man. The phantom was composed of a natural human skeleton embedded in a mass with the properties of human soft tissue (mass attenuation, $\rho = 0.985$ kg/dm^3, effective atomic number, $Z_{eff} = 7.3$). The thorax of the phantom was made of foam ($\rho = 0.32$ kg/dm^3; $Z_{eff} = 7.3$) to simulate human lung tissue. Eighty lithium fluoride thermoluminescent dosimeters (TLD-100H; Bicron-Harshaw, Solon, Ohio) divided across 22 organ sites were embedded in the phantom (Table 1). Those TLD-100Hs with coefficients of variation >3% were excluded. The TLDs were made of a tissue-equivalent material with high sensitivity and a linear response to radiation doses. Moreover, after an adequate annealing process, the TLDs could be recycled, which made them suitable for monitoring the delivery of radiation with PBV and CTP imaging techniques. We followed the

guidelines of the International Commission on Radiation Protection number 103 to calculate the effective dose (ED)[20] as follows:

$$1) \qquad ED = \sum D_T \cdot w_R \cdot w_T,$$

where D_T is the mean absorbed dose to the target organ, W_R is the radiation-weighting factor, and W_T is the tissue-weighting factor. Accordingly, the W_R for x-ray was 1. The absorbed dose obtained from TLD in each specific organ was multiplied by the W_R to yield the equivalent doses in each individual organ.

The values of the entrance skin dose/dose-area product of C-arm CT and the dose-length product of multidetector CT as shown by the consoles were recorded for comparison, while both scanners were regularly calibrated following standard clinical service requirements.

CT Perfusion
For comparison, CT scans on the same phantom and TLD distribution were obtained on a 256-section multidetector CT scanner (Brilliance iCT; Philips Healthcare, Best, the Netherlands). A clinical CTP scanning protocol was used in accordance with the American Association of Physicists in Medicine (AAPM).[21] The acquisition parameters were 8-cm scan coverage identical to slab PBV (s-PBV), 5-mm section thickness, 64 × 1.25 mm collimation, 20 × 20 cm FOV, 80 kV(peak), and 250-mA tube current with a rotation time of 0.4 seconds, equivalent to effective 100 mAs. The scan interval was 1.5 seconds, with a 1-minute duration. No patient table movement was encountered throughout the CTP data acquisition.

Parenchymal Blood Volume
PBV dose measurement was conducted with a biplane flat panel detector–DSA suite (Axiom-Artis; Siemens, Erlangen, Germany). A routine clinical imaging protocol (one 8-second rotational mask run with 60 frames/second followed by another 8-second rotational contrast-medium-filled run with the same frame rate) for cerebral PBV measurement (syngo DynaPBV Neuro; Siemens) was used. The scanning parameters were 73 kV, 483–555 mA, rotation angle of 200°, 0.5° per frame, and a 616 × 480 matrix. Two FOVs, full-size (30 × 40 cm) and slab (8 cm at the isocenter in a craniocaudal direction × 40 cm in a right-left direction), were used. The PBV measurements obtained were respectively called whole-brain PBV (w-PBV) and slab PBV (ranging from the sella turcica to high convexity). A repeat dose measurement with same imaging protocol and scanning parameters was conducted.

RESULTS
The dose-area product and entrance skin dose were 2574.6 μGym^2/222 mGy and 6850.4 μGym^2/238 mGy for s-PBV and w-PBV, respectively. As a comparison, the CTP dose-length product was 1177.3–1232.9 mGy·cm, equivalent to an effective dose of 2.47–2.59 mSv calculated by the American Association of Physicists in Medicine of k factor (k = 0.0021 mSv·mGy^{-1}·cm^{-1}). The equivalent doses of different tissue organs in s-PBV, w-PBV, and CTP measured from TLDs are listed in Table 2. Most TLDs were located in the head, followed by the salivary glands and thyroid glands in all 3 protocols. s-PBV demonstrated a 62.5% ab-

Table 2: Radiation doses of individual organs/tissues in CTP, s-PBV, and w-PBV protocols measured from 2 repeated TLD exposure experiments[a]

Tissue or Organ	CTP	s-PBV	w-PBV
Brain	163.55 ± 89.45	52.29 ± 35.31	107.51 ± 34.20
Salivary gland	13.94 ± 1.35	3.03 ± 0.61	137.75 ± 16.77
Thyroid	4.44 ± 1.64	1.20 ± 0.28	12.68 ± 2.48
Thymus	0.23 ± 0.08	0.10 ± 0.07	0.46 ± 0.15
Esophagus	1.18 ± 0.36	0.60 ± 0.08	2.61 ± 0.36
Breast	0.61 ± 0.17	0.19 ± 0.07	1.16 ± 0.17
Lung	0.50 ± 0.12	0.28 ± 0.09	1.19 ± 0.20
Stomach	0.06 ± 0.04	0.07 ± 0.06	0.16 ± 0.08
Liver	0.08 ± 0.03	0.05 ± 0.03	0.19 ± 0.07
Kidney	0.64 ± 0.74	0.05 ± 0.02	0.18 ± 0.03
Small intestine	0.03 ± 0.05	0.03 ± 0.05	0.04 ± 0.05
Colon	0.00 ± 0.00	0.01 ± 0.00	0.01 ± 0.01
Bladder	0.05 ± 0.03	0.05 ± 0.03	0.08 ± 0.05
Gonads	0.06 ± 0.03	0.03 ± 0.03	0.07 ± 0.04
Bone marrow	0.43 ± 0.15	0.32 ± 0.13	1.12 ± 0.36
Skin	0.45 ± 0.29	0.12 ± 0.06	0.65 ± 0.11
Bone surface	0.42 ± 0.15	0.32 ± 0.15	1.12 ± 0.50
Effective dose[b]	2.77 ± 1.59	0.87 ± 0.55	3.91 ± 0.78

[a] Unless otherwise specified, data are in millisieverts.

[b] The sum of organ doses are weighted by the tissue-weighting factor recommended in the International Commission on Radiation Protection number 103.

sorbed dose reduction compared with w-PBV across all organ/tissue sites. In addition to head and neck regions, w-PBV showed a higher dose than s-PBV in the remaining organs.

Brain-equivalent doses in s-PBV, w-PBV, and CTP were 52.29 ± 35.31, 107.51 ± 31.20, and 163.55 ± 89.45 mSv, respectively. The variation of doses in brain areas was the largest in s-PBV (67.5%), followed by CTP (54.7%) and then by w-PBV (31.8%) (Fig 1). The equivalent dose of the lens was highest in CTP (157 ± 141 mSv), followed by w-PBV (104 ± 25 mSv) and then s-PBV (37 ± 39 mSv). Variation in the measurement of equivalent dose for the lens was larger in CTP (54.6%) and s-PBV (64.5%) and lower in w-PBV (29.0%) (Fig 2). The equivalent dose of salivary glands was largest in w-PBV followed by CTP and s-PBV (Fig 3). For the remaining organs below the thyroid, there were no dramatic variations in individual scanning protocols.

The effective dose was lowest in s-PBV (0.87 ± 0.55 mSv), followed by CTP (2.77 ± 1.59 mSv) and w-PBV (3.91 ± 0.78 mSv), according to International Commission on Radiation Protection number 103.

DISCUSSION

The effective dose of CTP in the current study measured by TLD (2.77 ± 1.59 mSv) is close to that estimated from the dose-length product (2.47–2.59 mSv), calculated by the American Association of Physicists in Medicine of k factor, the reference effective dose estimation in a clinical setting. Nevertheless, we found some heterogeneity of dose distribution in the current TLD dose readouts. The heterogeneity is caused by multifactorial mechanisms. The elliptic shape of the Rando-Alderson phantom and limited rotation angles of the tube (200 °) make the attenuation distance of individual TLDs on the ventral side of the phantom longer than those on the dorsal side. Moreover, in the same section of the Rando-Alderson phantom, the attenuation distance of individual TLDs in the center is longer than that in the periphery. Therefore, dose values read in the ventral side and center are lower (Fig 1). This phenomenon is more profound in the area of the primary beam, such as in the brain and salivary glands. Narrower scan ranges (ie, s-PBV and CTP) cause higher dose variations than those in w-PBV. The latter received both primary and scatter beams of irradiation (Fig 3). Due to the vicinity of the inferior margin of the scanning range and lens in CTP and s-PBV modes, the lenses were partly within the primary beams and resulted in a large variation of equivalent dose (Fig 2). In a clinical scenario, we can adjust the patient's head into the chin-
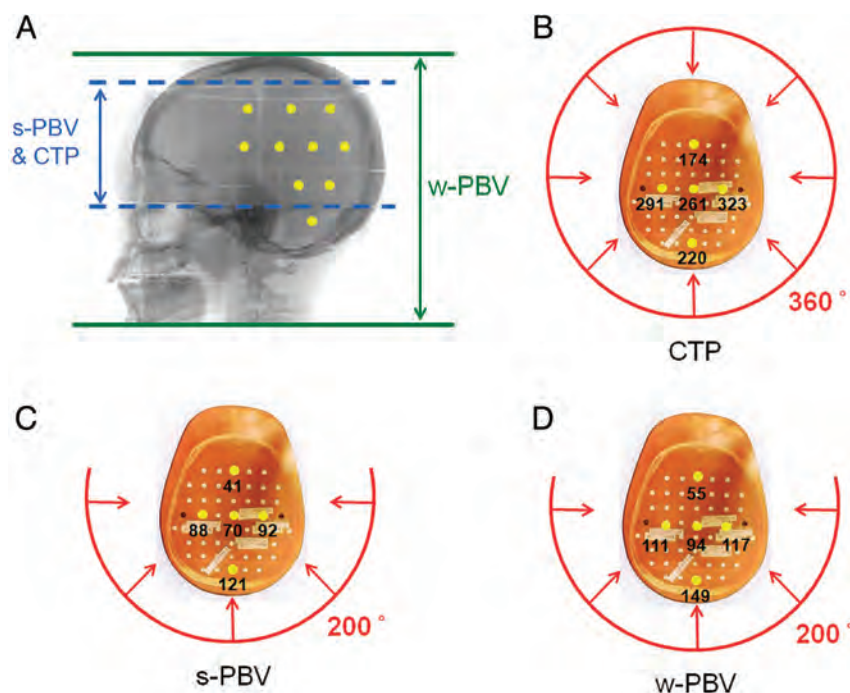
FIG 1. *A*, Ten yellow dots simulating TLDs are placed on a lateral skull view of the Rando-Alderson phantom. The scanning ranges of s-PBV and CTP are both 8 cm at the isocenter in a craniocaudal direction (*blue dashed lines*), while that of w-PBV is 30 cm (*green solid lines*). *B*, Eight-centimeter CTP is performed with a 360° rotation of the x-ray source in CT, and both s-PBV and w-PBV (*C* and *D*) are obtained with a 200° rotation of the x-ray source in DSA from the dorsal side of the Rando-Alderson phantom. The red arrows indicate x-ray beams. The 5 yellow dots placed on transaxial sections of the phantom indicate the TLDs placed on a phantom section. The numbers indicate the equivalent dose of each TLD in millisieverts. The elliptic head configuration of the phantom makes the dose heterogeneous (ie, the attenuation distance of TLDs on the ventral side of the phantom is longer than that on the dorsal side and the attenuation distance of the center one is longer than that of the peripheral one). The geometry makes the overall variation of the dose in the brain area the largest in s-PBV (67.5%), followed by CTP (54.7%) and then w-PBV (31.8%).
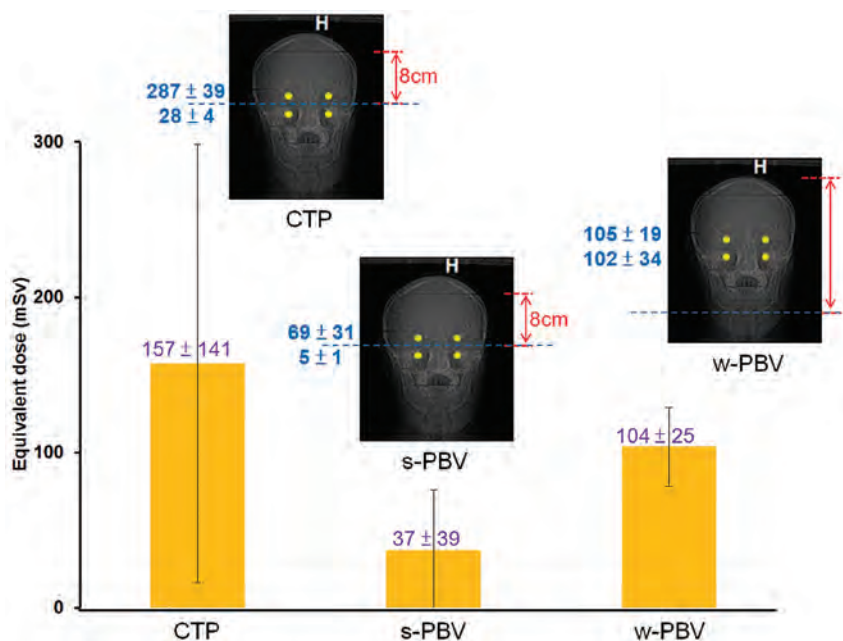
FIG 2. Equivalent dose (millisieverts) of the lens for CTP, s-PBV, and w-PBV. Variation in the measurement of the equivalent dose for the lens is larger in CTP (54.6%) and s-PBV (64.5%) and lower in w-PBV (29.0%). Two TLDs are within the primary beams, and the other 2 TLDs are within the secondary beams in CTP and s-PBV, while in w-PBV, all TLDs are within the primary beam.
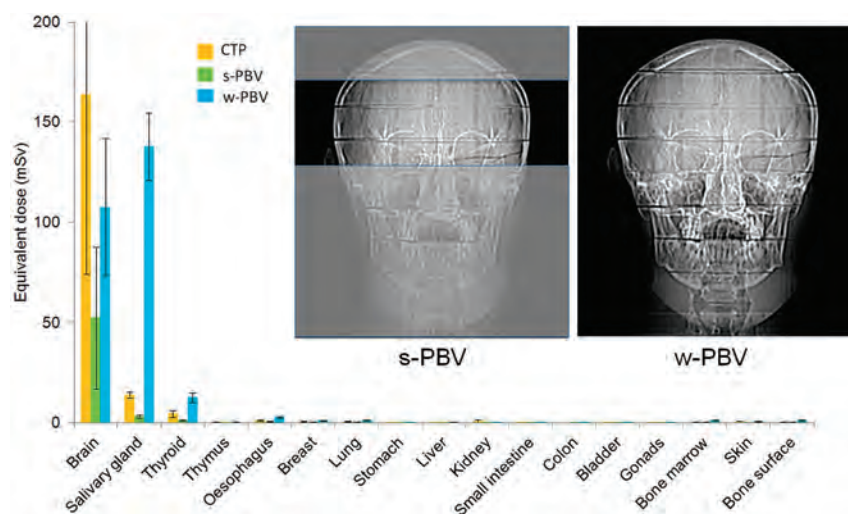
FIG 3. Anteroposterior views of the Rando-Alderson phantom for s-PBV and w-PBV. For the brain region, CTP received the largest equivalent dose followed by w-PBV and s-PBV. For the salivary and thyroid gland regions, the equivalent dose of w-PBV is higher than that of s-PBV and CTP due to larger x-ray beam z-axial coverage.

tuck position to avoid the lenses falling within the scan ranges in CTP or s-PBV.

CTP acquisition protocols were related to the scan interval, scan range, and tube potential. These variables were different across different brands and platforms of CT scanners. The effective doses, therefore, can range from 2.5 to 10 mSv.[22-25] We chose the latest CT technique in our institution for the comparative study. The s-PBV (8-cm scanning range at the isocenter) was conducted for direct and equal comparison of radiation doses with CTP (8-cm coverage). Nevertheless, in contrast to the fixed and limited coverage of the brain for most CTPs, the scan range for

PBV can be adjusted according to the operator's preference. For example, coverage of the infratentorium is not mandatory for a patient with known acute MCA stroke, not only because of suboptimal quality infratentorially but also because of irrelevant vascular territory.[26] In real practice, the coverage can be individually tailored to an optimal range on the basis of clinical needs. Although the s-PBV did not include the whole brain, it sufficiently covered most regions of interest, which are important for neurointerventional procedures. For example, vascular pathology that involves the distal anterior cerebral artery and MCA tributaries was usually too distal for endovascular intervention in acute stroke settings.[26] Similarly, the imaging quality of infratentorium perfusion imaging was suboptimal due to beam-hardening artifacts; thus, its role in guiding thrombolytic therapy is limited.[27]

The comprehensive acute stroke imaging work-up usually includes noncontrast CT, CT angiography, and CT perfusion.[28] Their main contributions are to exclude hemorrhage and large-territory infarction and to further quantify the thrombus burden and collateral circulations.[1,29,30] Modern flat panel detector–CT imaging, to some extent, has a spatial and contrast resolution equivalent to that of multidetector CT.[14,31] For those patients eligible for intra-arterial thrombolysis, DSA is far superior to CT angiography for evaluating vasculatures, occluded length, and collaterals. In addition to PBV, in-room assessment of the ischemic core and thrombus condition was feasible, thus reducing the door-to-puncture time and improving recanalization rates.[10,32]

Further reduction of the radiation dose is possible by lowering tube currents in CTP.[33] A similar strategy might be applied in PBV. The optimal tube voltage of the PBV system among individuals was beyond the scope of our study. The radiation dose from fluoroscopy required to put patients into an appropriate scan position before PBV differs between operators. Although its contribution to the overall dose is trivial, it can be further reduced with improving skill in scanning practice. Wearing lens protection while undergoing PBV may be an alternative to further reduce the dose to the lens.

s-PBV decreases the radiation dose and keeps an efficient coverage for peritherapeutic monitoring of cerebral hemody-

namics. If combined with faster and multiple rotations, it is possible to obtain cerebral blood flow with reasonable radiation exposure.[16] Because the arterial input function was determined by histogram rather than vessels, the measurements were relatively constant as long as most of the brain was included in the scanning range.[11,12]

CONCLUSIONS

The radiation dose measurement presented in this study is reliable and reproducible. Cerebral PBV measurement by using flat panel detector–DSA is a dose-saving imaging protocol. The effective dose with s-PBV is about one-third that of CTP. If one takes into account the advantages of on-site and immediate morphologic imaging availability and saving procedural time and patient transportation, flat panel DSA s-PBV may be recommended as an alternative peri-interventional imaging for evaluating intracranial hemodynamics of neurovascular disorders.

REFERENCES

1. Konstas AA, Wintermark M, Lev MH. **CT perfusion imaging in acute stroke.** *Neuroimaging Clin N Am* 2011;21:215–38, ix
2. Waaijer A, van Leeuwen MS, van Osch MJ, et al. **Changes in cerebral perfusion after revascularization of symptomatic carotid artery stenosis: CT measurement.** *Radiology* 2007;245:541–48
3. Xue J, Gao P, Wang X, et al. **Ischemic lesion typing on computed tomography perfusion and computed tomography angiography in hyperacute ischemic stroke: a preliminary study.** *Neurol Res* 2008;30:337–40
4. Olivot JM, Mlynash M, Thijs VN, et al. **Optimal Tmax threshold for predicting penumbral tissue in acute stroke.** *Stroke* 2009;40:469–75
5. Fukuda T, Ogasawara K, Kobayashi M, et al. **Prediction of cerebral hyperperfusion after carotid endarterectomy using cerebral blood volume measured by perfusion-weighted MR imaging compared with single-photon emission CT.** *AJNR Am J Neuroradiol* 2007;28:737–42
6. Cheng B, Golsari A, Fiehler J, et al. **Dynamics of regional distribution of ischemic lesions in middle cerebral artery trunk occlusion relates to collateral circulation.** *J Cereb Blood Flow Metab* 2011;31:36–40
7. Molina CA, Montaner J, Abilleira S, et al. **Timing of spontaneous recanalization and risk of hemorrhagic transformation in acute cardioembolic stroke.** *Stroke* 2001;32:1079–84
8. Kyriakou Y, Struffert T, Dorfler A, et al. **Basic principles of flat detector computed tomography (FD-CT)** [in German]. *Radiologe* 2009;49:811–19
9. Jaffray DA, Siewerdsen JH. **Cone-beam computed tomography with a flat-panel imager: initial performance characterization.** *Med Phys* 2000;27:1311–23
10. Hung SC, Lin CJ, Guo WY, et al. **Toward the era of a one-stop imaging service using an angiography suite for neurovascular disorders.** *Biomed Res Int* 2013;2013:873614
11. Struffert T, Deuerling-Zheng Y, Engelhorn T, et al. **Feasibility of cerebral blood volume mapping by flat panel detector CT in the angiography suite: first experience in patients with acute middle cerebral artery occlusions.** *AJNR Am J Neuroradiol* 2012;33:618–25
12. Struffert T, Deuerling-Zheng Y, Kloska S, et al. **Cerebral blood volume imaging by flat detector computed tomography in comparison to conventional multislice perfusion CT.** *Eur Radiol* 2011;21:882–89
13. Struffert T, Deuerling-Zheng Y, Kloska S, et al. **Flat detector CT in the evaluation of brain parenchyma, intracranial vasculature, and cerebral blood volume: a pilot study in patients with acute symptoms of cerebral ischemia.** *AJNR Am J Neuroradiol* 2010;31:1462–69
14. Dörfler A, Struffert T, Engelhorn T, et al. **Rotational flat-panel computed tomography in diagnostic and interventional neuroradiology.** *Rofo* 2008;180:891–98
15. Orth RC, Wallace MJ, Kuo MD, et al. **C-arm cone-beam CT: general principles and technical considerations for use in interventional radiology.** *J Vasc Interv Radiol* 2008;19:814–20
16. Royalty K, Manhart M, Pulfer K, et al. **C-arm CT measurement of cerebral blood volume and cerebral blood flow using a novel high-speed acquisition and a single intravenous contrast injection.** *AJNR Am J Neuroradiol* 2013 May 23. [Epub ahead of print]
17. Amis ES Jr, Butler PF, Applegate KE, et al. **American College of Radiology white paper on radiation dose in medicine.** *J Am Coll Radiol* 2007;4:272–84
18. Wintermark M, Lev MH. **FDA investigates the safety of brain perfusion CT.** *AJNR Am J Neuroradiol* 2010;31:2–3
19. Staniszewska M. **Evaluation of patient exposure in computerised tomography in Poland.** *Radiat Prot Dosimetry* 2002;98:437–40
20. International Commission on Radiological Protection. The 2007 recommendations of the International Commission on Radiological Protection. ICRP Publication 103. *Ann ICRP* 37 (2–4). http://www.icrp.org/publication.asp?id=ICRP%20Publication%20103. Accessed October 11, 2013
21. Adult Brain Perfusion CT Protocols. Version 1.1. May 22, 2012. http://www.aapm.org/pubs/CTProtocols/documents/AdultBrainPerfusionCT.pdf. Accessed October 11, 2013
22. Siebert E, Bohner G, Dewey M, et al. **320-slice CT neuroimaging: initial clinical experience and image quality evaluation.** *Br J Radiol* 2009;82:561–70
23. Abels B, Klotz E, Tomandl BF, et al. **CT perfusion in acute ischemic stroke: a comparison of 2-second and 1-second temporal resolution.** *AJNR Am J Neuroradiol* 2011;32:1632–39
24. Smith AB, Dillon WP, Gould R, et al. **Radiation dose-reduction strategies for neuroradiology CT protocols.** *AJNR Am J Neuroradiol* 2007;28:1628–32
25. Hirata M, Murase K, Sugawara Y, et al. **A method for reducing radiation dose in cerebral CT perfusion study with variable scan schedule.** *Radiat Med* 2005;23:162–69
26. Furtado AD, Lau BC, Vittinghoff E, et al. **Optimal brain perfusion CT coverage in patients with acute middle cerebral artery stroke.** *AJNR Am J Neuroradiol* 2010;31:691–95
27. Lee DH, Jo KD, Kim HG, et al. **Local intraarterial urokinase thrombolysis of acute ischemic stroke with or without intravenous abciximab: a pilot study.** *J Vasc Interv Radiol* 2002;13:769–74
28. Cohnen M, Wittsack HJ, Assadi S, et al. **Radiation exposure of patients in comprehensive computed tomography of the head in acute stroke.** *AJNR Am J Neuroradiol* 2006;27:1741–45
29. Olivot JM, Mlynash M, Thijs VN, et al. **Relationships between infarct growth, clinical outcome, and early recanalization in diffusion and perfusion imaging for understanding stroke evolution (DEFUSE).** *Stroke* 2008;39:2257–63
30. Arnold M, Schroth G, Nedeltchev K, et al. **Intra-arterial thrombolysis in 100 patients with acute stroke due to middle cerebral artery occlusion.** *Stroke* 2002;33:1828–33
31. Söderman M, Babic D, Holmin S, et al. **Brain imaging with a flat detector C-arm: technique and clinical interest of XperCT.** *Neuroradiology* 2008;50:863–68
32. Mishra NK, Albers GW, Davis SM, et al. **Mismatch-based delayed thrombolysis: a meta-analysis.** *Stroke* 2010;41:e25–33
33. Lin CJ, Wu TH, Lin CH, et al. **Can iterative reconstruction improve imaging quality for lower radiation CT perfusion? Initial experience.** *AJNR Am J Neuroradiol* 2013;34:1516–21

Combined Low-Dose Contrast-Enhanced MR Angiography and Perfusion for Acute Ischemic Stroke at 3T: A More Efficient Stroke Protocol

K. Nael, A. Meshksar, B. Ellingson, M. Pirastehfar, N. Salamon, P. Finn, D.S. Liebeskind, and J.P. Villablanca

ABSTRACT

BACKGROUND AND PURPOSE: There is need to improve image acquisition speed for MR imaging in evaluation of patients with acute ischemic stroke. The purpose of this study was to evaluate the feasibility of a 3T MR stroke protocol that combines low-dose contrast-enhanced MRA and dynamic susceptibility contrast perfusion, without additional contrast.

METHODS: Thirty patients with acute stroke who underwent 3T MR imaging followed by DSA were retrospectively enrolled. TOF-MRA of the neck and brain and 3D contrast-enhanced MRA of the craniocervical arteries were obtained. A total of 0.1 mmol/kg of gadolinium was used for both contrast-enhanced MRA (0.05 mmol/kg) and dynamic susceptibility contrast perfusion (0.05 mmol/kg) (referred to as half-dose). An age-matched control stroke population underwent TOF-MRA and full-dose (0.1 mmol/kg) dynamic susceptibility contrast perfusion. The cervicocranial arteries were divided into 25 segments. Degree of arterial stenosis on contrast-enhanced MRA and TOF-MRA was compared with DSA. Time-to-maximum maps (>6 seconds) were evaluated for image quality and hypoperfusion. Quantitative analysis of arterial input function curves, SNR, and maximum T2* effects were compared between half- and full-dose groups.

RESULTS: The intermodality agreements (*k*) for arterial stenosis were 0.89 for DSA/contrast-enhanced MRA and 0.63 for DSA/TOF-MRA. Detection specificity of >50% arterial stenosis was lower for TOF-MRA (89%) versus contrast-enhanced MRA (97%) as the result of overestimation of 10% (39/410) of segments by TOF-MRA. The DWI-perfusion mismatch was identified in both groups with high interobserver agreement (*r* = 1). There was no significant difference between full width at half maximum of the arterial input function curves (*P* = .14) or the SNR values (0.6) between the half-dose and full-dose groups.

CONCLUSIONS: In patients with acute stroke, combined low-dose contrast-enhanced MRA and dynamic susceptibility contrast perfusion at 3T is feasible and results in significant scan time and contrast dose reductions.

ABBREVIATIONS: AIF = arterial input function; CE-MRA = contrast-enhanced MRA; FWHM = full width at half maximum; GRAPPA = generalized autocalibrating partially parallel acquisition; Tmax = time-to-maximum

S troke is a common and serious disorder, with an annual incidence of approximately 795,000.[1] It has been estimated that for every minute in which ischemic stroke is left untreated, approximately 1.9 million neurons are lost.[2] Therefore, both the speed of diagnosis and efficacy of treatment are desirable.

MRA to evaluate the status of both cervical and intracranial arteries and dynamic susceptibility contrast perfusion imaging to determine the presence of hypoperfused tissue at risk have been used in comprehensive stroke protocols.

Although the concept of applying contrast-enhanced MRA (CE-MRA) in the evaluation of both neck and intracranial arterio-occlusive disease has been explored in the literature,[3-5] CE-MRA has not been widely adopted into acute stroke protocols for several reasons. First, CE-MRA generally has a lower spatial resolution relative to TOF-MRA because the competing requirements of coverage and acquisition speed require a compromise in CE-MRA spatial resolution. A second potential limitation to the incorporation of CE-MRA into clinical stroke protocols is the extra contrast dose required, which is in addition to the intravenous contrast bolus normally used for perfusion imaging. Promising results on low-dose CE-MRA of the supra-aortic arteries have been reported with contrast dose as low as 0.05 mmol/kg.[6,7] The effects of contrast dose reduction on DSC perfusion have been evaluated by several investigators,[8,9] and

contrast dosages as low as 0.05 mmol/kg have been used with promising results.[10,11]

The purpose of this study was to prospectively evaluate the feasibility of a combined low-dose CE-MRA and DSC perfusion acute stroke protocol at 3T that requires no additional contrast during diagnostic assessment and to compare the results with a routine stroke protocol that employs TOF-MRA. Two hypotheses were tested: 1) low-dose CE-MRA provides comparable or superior diagnostic performance in the detection of both extracranial and intracranial arterio-occlusive disease in comparison with TOF-MRA, with potential for significant reduction in acquisition time; 2) DSC perfusion by use of half of the conventional dose is feasible with comparable image quality.

MATERIALS AND METHODS

This retrospective study was conducted between August 2011 and April 2013. All examinations were performed in accordance with institutional review board guidelines with an approved study protocol. Inclusion criteria included 1): patients with clinical suspicion of acute ischemic stroke who presented within the first 9 hours from symptom onset; 2) acquisition of 3T MR imaging as the initial imaging test; and 3) DSA within 24 hours after symptom onset. DSA was performed either because of failed response to conventional treatment, including IV tPA ($n = 4$), or detection of a proximal clot and major arterial occlusion requiring further endovascular treatment ($n = 26$). Exclusion criteria included patients with severe contrast allergy, MR-incompatible implants, glomerular filtration rates <30 mL/min/1.73 m^2, and severe claustrophobia. The baseline NIHSS scores and median time from stroke onset to MR imaging were documented for each patient.

Image Acquisition

All MR examinations were performed on a 3T (Trio) clinical MR scanner (Siemens, Erlangen, Germany). A combination 12-channel head ($n = 8$) and neck coil ($n = 4$) was used for radiofrequency signal reception. All patients underwent routine MR stroke protocol, which included DWI, FLAIR, gradient refocused echo, brain 3D TOF-MRA and 2D TOF-MRA of the neck, and DSC perfusion imaging.

MRA sequence parameters were brain TOF-MRA: 3D multislab gradient-echo sequence (TR/TE: 25/3.8 ms, flip angle: 18°, 5 slabs each with 30 partitions, FOV: 200 × 200 mm, matrix: 256 mm, section thickness: 0.7 mm, generalized autocalibrating partially parallel acquisition (GRAPPA) × 2, acquisition time: 5:50 minutes); neck TOF-MRA: 2D gradient-echo sequence (TR/TE: 21/5.9 ms, flip angle: 45°, 110 partitions, section thickness: 2 mm, FOV: 250 × 180 mm, matrix: 256 mm, GRAPPA × 2, acquisition time: 3:30 minutes).

A high spatial resolution 3D CE-MRA with centric k-space ordering was performed just before the perfusion imaging by use of a fast spoiled–gradient refocused echo sequence in the coronal plane: (TR/TE: 3/1.2 ms, flip angle: 25°, FOV: 340 × 280 mm, matrix: 448 mm). One hundred twenty sections with a thickness of 0.8 mm were acquired in the coronal plane, providing arterial coverage from the aortic arch to the cranial vertex. With the use of a GRAPPA algorithm[12] with an acceleration factor of 4, a near

isotropic sub-millimeter voxel size 3D dataset ($0.8 \times 0.9 \times 0.8$ mm^3) was achieved during a 22-second acquisition. A modified 2-phase contrast injection scheme[13] was used to perform CE-MRA and DSC perfusion imaging, without need for additional contrast. To accomplish this, a total of 0.1 mmol/kg of gadolinium (MultiHance, Bracco Diagnostics, Princeton, New Jersey) that is normally used routinely for MR perfusion was diluted with normal saline to a total volume of 50 mL. Three mL of contrast solution was injected and flushed with 20 mL of saline to determine the transit time from the arm vein to the cervical carotid arteries. A total of 22 mL of contrast solution was then injected and flushed with 20 mL of saline for the CE-MRA acquisition. The contrast injection rate for timing run and CE-MRA was 1.5 mL/s. Subsequently, the remaining 25 mL of contrast solution was injected and flushed with 20 mL of saline at 5 mL/s for the MR perfusion scan, which was performed last. The DSC perfusion was performed by use of a single-shot, gradient echo-planar sequence (TR/TE: 1920/32 ms, flip angle: 90°, 25 partitions, 5-mm section thickness, and an in-plane voxel size of 1.7×1.7 mm^2). With the use of GRAPPA × 2, 45 dynamic frames were obtained over a 90-second acquisition time.

Image Analysis

MRA. The source data and reconstructed MRA images by use of MIP were used for image analysis. The cervicocranial arteries were divided into 25 segments, including 1,2: bilateral common carotid arteries; 3,4: bilateral cervical ICAs; 5,6: bilateral petrocavernous ICAs; 7,8: bilateral supraclinoid ICAs; 9–12:bilateral anterior cerebral arteries (A1 and A2 segments); 13–16: bilateral MCAs (M1 and M2 segments); 17,18: bilateral cervical vertebral arteries; 19,20: bilateral intradural segments of vertebral arteries; 21: basilar artery; and 22–25: bilateral posterior cerebral arteries (P1 and P2 segments).

Arterial segments were examined for stenoses independently by 2 neuroradiologists by use of the CE-MRA and TOF-MRA datasets during separate sessions. Datasets were presented in random order to avoid recall bias. Observers were blinded to results of other imaging. The severity of arterial disease was evaluated by use of a 1–4 grading scale: 1, no stenosis; 2, mild stenosis with ≤50% luminal narrowing; 3, significant stenosis with luminal narrowing >50 and <99%; and 4, occlusion. When 2 or more stenoses were detected in the same vessel segment, the most severe stenosis was used for grading and analysis. Finally, if necessary, discordant reads on both the CE-MRA and TOF-MRA datasets evaluated for arterial stenosis or occlusion were resolved by consensus review and used to determine the diagnostic accuracy of each technique by use of preprocedural DSA as the reference standard.

DSC Perfusion Analysis. DSC perfusion datasets were processed by use of FDA-approved software (Olea Sphere; Olea Medical, La Ciotat, France). DSC analysis consisted of the following steps: 1) truncation of the first 5 time points in the DSC time-series, 2) calculation of prebolus signal intensity on a voxel wise basis, followed by 3) conversion of truncated DSC time-series to a concentration-time curve on the basis of the T2* relaxivity of the contrast agent. The change in signal intensity with respect to baseline was
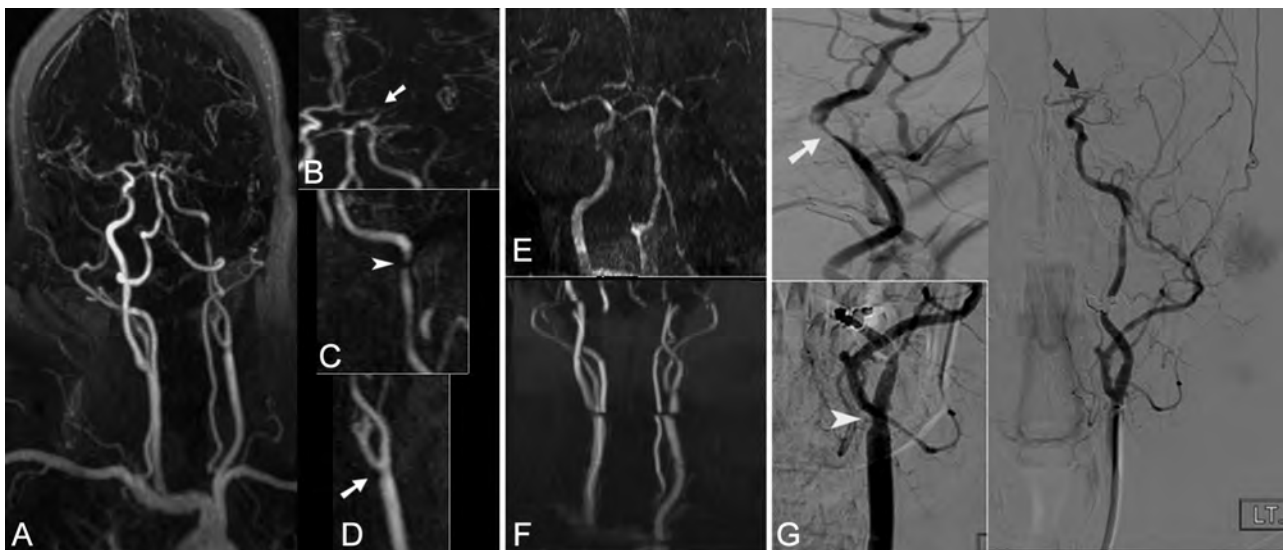
FIG 1. A 55-year-old woman presented with acute onset aphasia; NIHSS score 20. Full-thickness MIP of the entire supra-aortic arteries *(A)* and focused oblique reformatted *(B, C,* and *D)* thin MIP images from CE-MRA, coronal MIP images from TOF-MRA of the brain *(E)* and neck *(F)*, and focused oblique views from DSA *(G)* after left common and ICA injections are demonstrated. Both CE-MRA and DSA demonstrate mild stenosis of the left distal common carotid artery (arrow in *D* and arrowhead in *G*), high-grade stenosis of the distal left ICA near the petrous segment (arrow on *C* and *G*), and occlusion of the ICA bifurcation with extension into the left M1 (arrow in *B* and black arrow in *G*). Because of longer acquisition time, both TOF-MRA of the neck *(F)* and brain *(E)* are degraded by motion artifact. The mild stenosis at the left common carotid artery is not clearly seen. In addition, because of distal occlusion and sluggish flow, the entire left high cervical, petrocavernous, and supracliniod ICA segments appear to be occluded.

converted to the change in tissue T2* as a result of contrast agent injection, taken with respect to precontrast baseline time points. The arterial input function (AIF) was selected automatically by the perfusion software, and the deconvoluted perfusion parameters were calculated by use of a block-circulant singular value decomposition technique.[14] Quantitative analysis of the AIF curves was performed to determine the peak and full width at half maximum (FWHM). The infarction volume was automatically calculated by means of the software, by use of ADC threshold $<600 \times 10^{-6}$ mm^2/s. The time-to-maximum maps, with the use of a threshold of >6 seconds, were evaluated by observers independently in each group to determine the presence of hypoperfusion and DWI-perfusion mismatch by use of a 3-scale scoring system: 1, mismatch present, confident; 2, mismatch may be present, less confident; 3, no mismatch present.

The volumes of DWI abnormality, hypoperfused region by use of Tmax >6 seconds, and DWI-diffusion mismatch ratios were generated automatically by the software. These values were used as reference to compare the accuracy of subjective mismatch scores (Fig 2).

Quantitative analysis of the SNR values and maximum T2* effect was performed by use of an ROI-based analysis. ROIs approximately 1 cm in diameter were placed on the normal contralateral postcentral gyrus and corresponding subcortical white matter. The signal intensity of these ROIs was calculated over the entire 45 sequential dynamic perfusion frames, and the mean $\pm$ SD of the signal intensity was noted for each perfusion scan. Maximum T2* effect, which is the maximum signal intensity drop during the intracerebral passage of an intravenous contrast bolus, was also calculated for each scan. To minimize the nonuniform distribution of noise across the field of view caused by parallel imaging, 2 ROIs were placed in the extracranial space (1 at the top

and 1 at the bottom of field of view) to determine the background noise. The standard deviation of the mean of these background ROIs in all 45 dynamic frames (90 ROIs) was defined as image noise and was used to calculate the SNR. The baseline SNR was also evaluated by use of the precontrast perfusion images, which were available during the first 4 dynamic frames (initial 8 seconds) before contrast arrival. This was performed to investigate whether the half-dose perfusion scans obtained after CE-MRA were contaminated with recirculating contrast agent and/or had a reduced baseline signal in comparison to the full-dose control perfusion group.

Statistical Analysis

Statistical analysis was performed by use of MedCalc (Version 12.2.1, MedCalc Software Mariakerke, Belgium). The degree of interobserver and intermodality agreement for estimation of arterial stenosis was determined by kappa (κ) coefficients and calculation of 95% CI. The sensitivity and specificity of CE-MRA and TOF-MRA for stenosis >50% was calculated for each observer, by use of preprocedural DSA images as the standard of reference. Spearman-Rank correlation coefficient was used to evaluate the qualitative scores of perfusion maps and interobserver confidence. The SNR values, maximum T2* effects, and peak and FWHM of the AIF curves were plotted as mean $\pm$ SD, and the differences between the full- and half-dose groups were evaluated by means of a *t* test. The significance level was defined as $P < .05$ (2-sided).

Cohort Controlled Group

To perform a comparative analysis for the DSC perfusion parameters, an age-matched control population of 30 patients (12 women, 18 men; age range, 43–90 years; average, 69 years) with
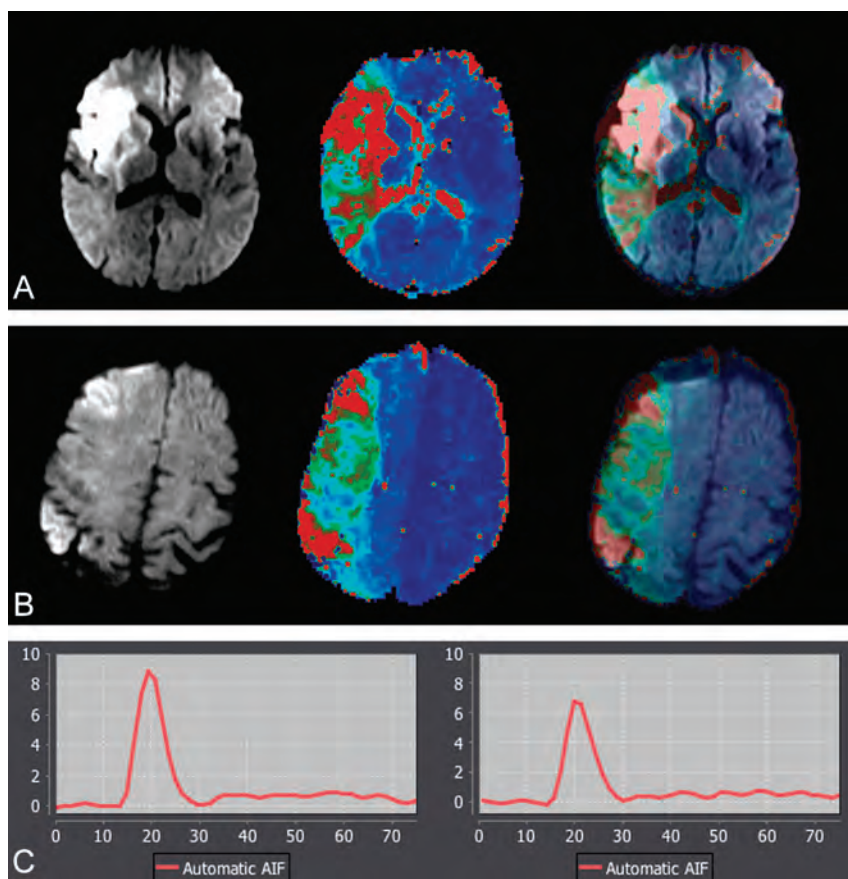
FIG 2. *A,* 62-year-old man with acute stroke; NIHSS score, 14. MR imaging was performed at 3T, 5 hours after the onset (from cohort group: 0.1 mmol/kg of gadolinium used for dynamic susceptibility contrast perfusion). *B,* 58-year-old man with acute stroke; NIHSS score, 16. MR imaging was performed at 3T, 3 hours after the onset (from study group: 0.05 mmol/kg gadolinium was used for dynamic susceptibility contrast perfusion). Serial DWI, Tmax, and superimposed DWI-Tmax demonstrate diagnostic image quality in both patients. A large perfusion-diffusion mismatch was identified with high confidence in both patients. The corresponding arterial input function curves are shown. There is approximately 24% lower arterial peak in half dose (6.7) compared with full dose (8.9). There is only small difference between the full width at half maximum of full dose (13) versus half dose (15).

stenoses were identified by CE-MRA: mild ($\leq$50%): $n = 14$; high-grade ($>$50–99%): $n = 18$; and occlusion: $n = 20$. Eighty-two segmental arterial stenoses were identified by TOF-MRA: mild ($\leq$50%): $n = 20$; high-grade ($>$50–99%): $n = 22$; and occlusion: $n = 40$. The interobserver agreements were $k = 0.78$; 95% CI, 0.65–0.90 for CE-MRA; $k = 0.86$; 95% CI, 0.78–0.92 for TOF-MRA.

Preprocedural DSA images were available for 410 arterial segments, and identified 50 arterial stenoses: mild ($\leq$50%): $n = 19$; high-grade ($>$50%–99%): $n = 12$; and occlusion: $n = 19$. Table 1 shows the distribution of arterial stenoses detected by TOF-MRA and CE-MRA in comparison to DSA. Table 2 shows the diagnostic performance and agreement of CE-MRA and TOF-MRA in comparison with DSA as the standard of reference. Compared with DSA, by use of CE-MRA, 1 arterial segment with high-grade stenosis was graded as occlusion and 8 arterial segments with mild stenosis were graded high-grade stenoses. This resulted in a sensitivity and specificity of 100% and 97%, respectively, for the detection of high-grade arterial stenosis ($>$50%). With the use of TOF-MRA, 21 arterial segments with varying degrees of stenosis were graded as occluded and 18 arterial segments with no to mild stenosis were graded as high-grade stenosis. This resulted in sensitivity and specificity of 100% and 89%, respectively, for the detection of high-grade arterial stenosis ($>$50%).

acute stroke who had undergone full-dose contrast (0.1 mmol/kg) DSC perfusion was selected. The available NIHSS score in the control group ranged from 5–18. In this population, MRA was acquired by use of TOF-MRA only. No CE-MRA was performed before DSC imaging. The studies were performed on an identical 3T scanner. The DSC perfusion sequence parameters were equivalent to our study population. A total of 17 patients from the control group had proximal arterial occlusion (internal carotid artery, $n = 5$, proximal MCA, $n = 12$).

RESULTS

A total of 30 patients (18 men; age range, 38–84 years; average, 62 years) met our inclusion criteria. Baseline NIHSS scores ranged from 4–24, with a median of 16. The median time from presentation to MR imaging was 5 hours (range, 1–8 hours).

All studies were completed successfully. In 2 patients (7%), evaluation of the aortic arch and proximal aspects of supra-aortic arteries on CE-MRA was degraded by motion artifact. In 15 studies (50%), the image quality of TOF-MRA of the neck was degraded by motion artifact (Fig 1). A total of 52 segmental arterial

DSC Perfusion

The mean $\pm$ SD of the volume of infarction on DWI and hypoperfusion with Tmax $>$6 seconds were 16.5 $\pm$ 7.6 (mL)/120 $\pm$ 48 (mL) for the full-dose group and 18 $\pm$ 9 (mL)/137 $\pm$ 70 (mL) for the half-dose group ($P = .2$). The mismatch ratios calculated automatically by the software demonstrated DWI-perfusion mismatch in all patients in both groups. DWI-perfusion mismatch was identified in 100% of the full-dose group and 90% of the half-dose group by both observers, with high confidence ($r = 1$).

There was no statistically significant difference in the SNR and background noise values between half- and full-dose groups (Table 3). When the baseline SNR of the initial phase of the perfusion study before arrival of contrast was evaluated, there was no significant difference ($P = .6$) between the mean baseline SNR of the full-dose (342 $\pm$ 101) and half-dose groups (330 $\pm$ 67), indicating an absence of significant recirculation effects. The maximum T2* signal drop values were higher in the full-dose group ($P = .01$). There was statistically significant higher AIF peak in the full-dose group ($P = .002$). There was however, no statistically significant

Table 1: Distribution of arterial stenoses detected by TOF-MRA and CE-MRA in comparison with DSA (total arterial segments available for comparison = 410)

	TOF-MRA			CE-MRA			DSA		
	Stenosis Severity			Stenosis Severity			Stenosis Severity		
Arterial Segment	≤50%	>50, <99%	Occlusion	≤50%	>50, <99%	Occlusion	≤50%	>50, <99%	Occlusion
Common carotid artery	3	2	3	5	1	0	3	0	0
Cervical ICA	2	1	6	4	4	4	7	5	4
Pretrocavernous ICA	2	3	4	1	1	1	0	2	1
Supraclinoid ICA	3	4	6	1	5	3	1	1	3
MCA	3	6	14	1	2	11	2	1	10
Anterior cerebral artery	2	2	2	0	1	0	2	1	0
Cervical vertebral artery	0	0	1	1	0	1	2	0	1
Intradural vertebral artery	3	0	3	1	0	0	0	1	0
Basilar artery	2	1	0	0	0	0	0	0	0
Posterior cerebral artery	0	3	1	0	2	0	2	1	0
Total	20	22	40	14	18	20	19	12	19

Table 2: Diagnostic performance and agreement of CE-MRA and TOF-MRA for arterial stenosis and occlusion in comparison with DSA

	No Disease		Mild Stenosis (≤50%)		High Grade (>50%, <99%)		Occlusion	
DSA	CE-MRA	TOF-MRA	CE-MRA	TOF-MRA	CE-MRA	TOF-MRA	CE-MRA	TOF-MRA
No disease	353	324	7	17	0	14	0	5
Mild stenosis (≤50%)	5	4	7	3	7	4	0	8
High grade (>50%, <99%)	0	0	0	0	11	4	1	8
Occlusion	0	0	0	0	0	0	19	19

Note:—$n = 410$ arterial segments. DSA served as reference standard.
Intermodality agreement for CE-MRA: $k = 0.89$; 95% CI, 0.84−0.92.
Intermodality agreement for TOF-MRA, $k = 0.63$; 95% CI, 0.60−0.72.

Table 3: Comparative quantitative analysis of DSC perfusion between full dose (0.1 mmol/kg) and half dose (0.05 mmol/kg)

Image Parameter Evaluated	Full Dose	Half Dose	t Test
SNR	342 ± 101	330.3 ± 67	0.6
Max T2* signal drop	120 ± 54	81.6 ± 48	0.01
Background noise	2.5 ± 0.6	2.7 ± 0.9	0.4
Peak of AIF	9.1 ± 2.4	7.2 ± 2.0	0.002
FWHM of AIF	16.8 ± 2.6	18.2 ± 2.8	0.14

Note:—Data presented as mean ± standard deviation.
Max indicates maximum.

difference between the FWHM of the AIF curves among the full-dose and half-dose groups ($P = .1$) (Table 3).

DISCUSSION

Our results suggest that the described protocol combining low-dose CE-MRA and DSC perfusion imaging is feasible in the evaluation of patients with acute stroke, without the need for additional contrast. With the use of the described low-dose protocol, near isotropic sub-millimeter voxel sizes of neck and brain arteries were obtained with diagnostic accuracy equal or superior to TOF-MRA when compared with DSA. DSC perfusion imaging with reduced contrast dose was feasible at 3T with comparable qualitative results to a full-dose control group. Importantly, the presence of contrast in the circulating blood of the CE-MRA half-dose group did not negatively affect the image quality nor the quantitative analysis of perfusion data when compared with the control full-dose group.

MRA is used not only to detect the presence of intracranial arterio-occlusive disease but also to detect extracranial tandem stenosis to characterize the stroke mechanism. Despite its broad use in stroke protocols, TOF-MRA requires long acquisition times in the order of 8−11 minutes for the neck and brain arteries.

In addition, spin saturation and phase dispersion caused by slow, in-plane, turbulent, or complex flow[15,16] can result in overestimation of arterial stenosis and occlusion and increase false-positive rates. It is not uncommon to notice the complete absence of flow signal in intracranial branches distal to a sub-occlusive thrombus or clot (Fig 1).

CE-MRA has not been widely incorporated into routine stroke protocols because of its relatively lower spatial resolution for evaluation of intracranial stenosis and need for extra contrast dose, which, until now, has been required in addition to the contrast used for DSC perfusion imaging. Introduction of multi-coil technology with inherent improved SNR and fast imaging techniques such as GRAPPA[12] have significantly improved the speed and spatial resolution of CE-MRA[17,18] while also permitting use of very low contrast doses.[6,7]

With the use of the proposed CE-MRA protocol, sub-millimeter voxel sizes of cervicocranial arteries were obtained by use of 0.05 mmol/kg of gadolinium contrast. The specificity of CE-MRA was higher than TOF-MRA because of more frequent overestimation of arterial stenosis on TOF-MRA, predominantly caused by slow flow and phase dispersion in arterial segments at or distal to a high-grade stenosis or occlusion. Acquisition time required for MR stroke protocol including DWI, FLAIR, gradient refocused echo, and DSC perfusion is approximately 10 minutes with the use CE-MRA as compared with approximately 20 minutes if TOF-MRA is used. Therefore, the use of CE-MRA instead of TOF-MRA can cut total scan time in half and result in a time savings of approximately 10 minutes.

Although the role of DSC perfusion in the acute stroke setting is still being defined,[19,20] it is being used with increasing frequency in multiple prospective clinical trials and has become an important component of acute MR stroke protocols in large stroke cen-

ters. The main application of DSC perfusion in patients with acute ischemic stroke is to identify a perfusion-diffusion mismatch. This is performed in most stroke centers with the use of a perfusion time map such as Tmax, as supported by the current literature.

Our study found that by use of a split dose of contrast and after applying contrast for CE-MRA, diagnostic DSC Tmax perfusion images can be obtained with comparable results to a full-dose control group with acceptable interobserver agreement, consistent with reported literature.[10,11] Furthermore, we showed that despite a lower AIF peak in the half-dose group, the width of AIF was not significantly different between 2 groups ($P = .14$). As a result, one can assume that the delay time for the occurrence of the peak value (Tmax) would also not differ significantly. This is consistent with the effects of contrast dose reduction on time variables such as MTT and Tmax, as previously noted by Alger et al.[9] It is important to recognize that the quantitative values of CBV and CBF probably varied between the full-dose and half-dose groups.

The influence of dose reduction on tissue relaxivity ($\Delta R2^*$) and deconvoluted values such as rCBF has been evaluated by several investigators.[8-10] A systematic evaluation of the relationship between contrast dose reduction and deconvoluted values was beyond the scope of this report. Reducing the contrast dose can result in a decrease in $\Delta R2^*$ and thus a drop in peak of AIF as shown by us and others, including Alger et al.[9] This drop in peak AIF amplitude can possibly lead to inaccuracies in quantitative parameters calculated from deconvolution through additional noise contamination.

General consensus suggests an increase in injection length at a fixed rate, or increase in contrast concentration, leads to a higher peak concentration in the brain. We did not compare the quantitative measure of bolus width between the full- and half-dose groups because these were 2 different populations with possibly different hemodynamic characteristics. However, to minimize the effect of contrast bolus length, we used a similar injection rate (5 mL/s) and injection volume for both groups by dilution with saline.

One of the other potential disadvantages of the reduced contrast dose is increase in the noise level, which can certainly lead to inaccuracies in AIF and subsequently affects the deconvoluted perfusion parameters. Although not directly evaluated in this report, the image quality and high confidence in defining the perfusion abnormality between 2 groups indicate that noise was not a major limiting factor for the diagnostic interpretation. Importantly, in our study, the quantitative evaluation of SNR between half- and full-dose groups did not reveal a significant difference. In addition, the mean baseline SNR of 2 groups before arrival of contrast bolus was not statistically significant, suggesting that neither recirculation effects nor baseline signal intensity shifts are of concern during analysis of half-dose data when a contrast dose has been administered for CE-MRA before DSC perfusion.

Our study has several limitations. First is a possible selection bias introduced by the inclusion of patients who also underwent DSA. Usually, DSA is considered when there is an intention to treat major proximal arterio-occlusive disease. Therefore, the results and performance of CE-MRA should be interpreted in this context. Second, the 50% cutoff used for hemodynamic significant arterial stenosis is somewhat arbitrary because there are no firm guidelines to determine the threshold of hemodynamic significance for the intracranial circulation. Third, the full-dose control group for DSC perfusion analysis was different from our patient population, with differences in underlying hemodynamic status, which can potentially complicate direct comparisons of image quality and quantitation. However, the limitation imposed by total contrast dose precludes the use of the same patients as their own control group. By matching the age, sex, and sequence parameters, we attempted to control for these potential confounding factors. Nevertheless, the comparison of image quality scores between 2 different groups should be interpreted with some caution. The choice of a longer TR (1.9 seconds) used in the current study is less ideal for DSC perfusion. This value was chosen to compensate for a possible SNR penalty that may result when reducing contrast dose.[21] It is possible that this choice of TR could have resulted in undersampling of the AIF and therefore overestimation of perfusion parameters. Finally, the combination of parallel acquisition (GRAPPA) and contrast dose reduction may accentuate the effect of noise on image quality and DSC quantitative values, though higher SNR at 3T can help to mitigate this effect. Larger-scale clinical studies with concurrent use of different contrast dosage in the same individuals would help to validate our results.

CONCLUSIONS

Combining low-dose CE-MRA and DSC perfusion at 3T is feasible, with diagnostic image quality and without the need for additional contrast. The proposed protocol is significantly faster and more accurate than is the routine stroke protocol by use of TOF-MRA and may be adopted into routine clinical practice to streamline the treatment of patients with acute stroke. Our study demonstrates the clinical feasibility of performing DSC perfusion by use of a lower dose of contrast with qualitative measures comparable to a conventional dose group.

REFERENCES

1. Lloyd-Jones D, Adams RJ, Brown TM, et al. **Heart disease and stroke statistics–2010 update: a report from the American Heart Association.** *Circulation* 2010;121:e46–e215
2. Saver JL. **Time is brain–quantified.** *Stroke* 2006;37:263–66
3. Sohn CH, Sevick RJ, Frayne R. **Contrast-enhanced MR angiography of the intracranial circulation.** *Magn Reson Imaging Clin N Am* 2003;11:599–614
4. Bernstein MA, Huston J 3rd, Lin C, et al. **High-resolution intracranial and cervical MRA at 3.0T: technical considerations and initial experience.** *Magn Reson Medicine* 2001;46:955–62
5. Takano K, Utsunomiya H, Ono H, et al. **Dynamic contrast-enhanced subtraction MR angiography in intracranial vascular abnormalities.** *Eur Radiol* 1999;9:1909–12
6. Tomasian A, Salamon N, Lohan DG, et al. **Supraaortic arteries: contrast material dose reduction at 3.0-T high-spatial-resolution MR angiography–feasibility study.** *Radiology* 2008;249:980–90

7. Nael K, Moriarty JM, Finn JP. **Low dose CE-MRA.** *Eur J Radiol* 2011;80:2–8

8. Heiland S, Reith W, Forsting M, et al. **How do concentration and dosage of the contrast agent affect the signal change in perfusion-weighted magnetic resonance imaging? A computer simulation.** *Magn Reson Imaging* 2001;19:813–20

9. Alger JR, Schaewe TJ, Lai TC, et al. **Contrast agent dose effects in cerebral dynamic susceptibility contrast magnetic resonance perfusion imaging.** *J Magn Reson Imaging* 2009;29:52–64

10. Manka C, Traber F, Gieseke J, et al. **Three-dimensional dynamic susceptibility-weighted perfusion MR imaging at 3.0 T: feasibility and contrast agent dose.** *Radiology* 2005;234:869–77

11. Alger JR, Schaewe TJ, Liebeskind DS, et al. **On the feasibility of reduced dose dynamic susceptibility contrast perfusion MRI for stroke.** *Paper presented at International Society of Magnetic Resonance Medicine*, Montréal, Québec, Canada. May 7–13, 2011

12. Griswold MA, Jakob PM, Heidemann RM, et al. **Generalized autocalibrating partially parallel acquisitions (GRAPPA).** *Magn Reson Med* 2002;47:1202–10

13. Habibi R, Krishnam MS, Lohan DG, et al. **High-spatial-resolution lower extremity MR angiography at 3.0 T: contrast agent dose comparison study.** *Radiology* 2008;248:680–92

14. Wu O, Ostergaard L, Weisskoff RM, et al. **Tracer arrival timing-insensitive technique for estimating flow in MR perfusion-weighted imaging using singular value decomposition with a block-circulant deconvolution matrix.** *Magn Reson Med* 2003;50:164–74

15. Lin W, Tkach JA, Haacke EM, et al. **Intracranial MR angiography: application of magnetization transfer contrast and fat saturation to short gradient-echo, velocity-compensated sequences.** *Radiology* 1993;186:753–61

16. Isoda H, Takehara Y, Isogai S, et al. **MRA of intracranial aneurysm models: a comparison of contrast-enhanced three-dimensional MRA with time-of-flight MRA.** *J Comput Assist Tomogr* 2000;24:308–15

17. Nael K, Villablanca JP, Pope WB, et al. **Supraaortic arteries: contrast-enhanced MR angiography at 3.0 T– highly accelerated parallel acquisition for improved spatial resolution over an extended field of view.** *Radiology* 2007;242:600–09

18. Phan T, Huston J 3rd, Bernstein MA, et al. **Contrast-enhanced magnetic resonance angiography of the cervical vessels: experience with 422 patients.** *Stroke* 2001;32:2282–86

19. Butcher KS, Parsons M, MacGregor L, et al. **Refining the perfusion-diffusion mismatch hypothesis.** *Stroke* 2005;36:1153–59

20. Sobesky J, Zaro Weber O, Lehnhardt FG, et al **Does the mismatch match the penumbra? Magnetic resonance imaging and positron emission tomography in early ischemic stroke.** *Stroke* 2005;36:980–85

21. Carpenter TK, Armitage PA, Bastin ME, et al. **DSC perfusion MRI: quantification and reduction of systematic errors arising in areas of reduced cerebral blood flow.** *Magn Reson Med* 2006;55:1342–49

MR Quantitative Susceptibility Imaging for the Evaluation of Iron Loading in the Brains of Patients with β-Thalassemia Major

D. Qiu, G.C.-F. Chan, J. Chu, Q. Chan, S.-Y. Ha, M.E. Moseley, and P.-L. Khong

ABSTRACT

BACKGROUND AND PURPOSE: Patients with β-thalassemia require blood transfusion to prolong their survival, which could cause iron overload in multiple organs, including the heart, liver, and brain. In this study, we aimed to quantify iron loading in the brains of patients with β-thalassemia major through the use of MR quantitative susceptibility imaging.

MATERIALS AND METHODS: Thirty-one patients with thalassemia with a mean (± standard deviation) age of 25.3 (±5.9) years and 33 age-matched healthy volunteers were recruited and underwent MR imaging at 3T. Quantitative susceptibility images were reconstructed from a 3D gradient-echo sequence. Susceptibility values were measured in the caudate nucleus, putamen, globus pallidus, red nucleus, substantia nigra, dentate nucleus, and choroid plexus. General linear model analyses were performed to compare susceptibility values of different ROIs between the patients with thalassemia and healthy volunteers.

RESULTS: Of the 31 patients, 27 (87.1%) had abnormal iron deposition in one of the ROIs examined. Significant positive age effect on susceptibility value was found in the putamen, dentate nucleus, substantia nigra, and red nucleus ($P = .002$, $P = .017$, $P = .044$, and $P = .014$, respectively) in the control subjects. Compared with healthy control subjects, patients with thalassemia showed significantly lower susceptibility value in the globus pallidus ($P < .001$) and substantia nigra ($P = .003$) and significantly higher susceptibility value in the red nucleus ($P = .021$) and choroid plexus ($P < .001$).

CONCLUSIONS: A wide range of abnormal susceptibility values, indicating iron overloading or low iron content, was found in patients with thalassemia. MR susceptibility imaging is a sensitive method for quantifying iron concentration in the brain and can be used as a potentially valuable tool for brain iron assessment.

ABBREVIATIONS: QSM = quantitative susceptibility mapping; GP = globus pallidus; DN = dentate nucleus; SN = substantia nigra; CP = choroid plexus; DFO = deferoxamine; L1 = deferiprone

Beta-thalassemia major is a disease caused by genetic defects that lead to reduced production of hemoglobin. The patients require blood transfusion to prolong their survival, which could cause iron overload in multiple organs, including the heart, liver,

From the Departments of Diagnostic Radiology (D.Q, P.-L.K.) and Pediatrics and Adolescent Medicine (G.C.-F.C., S.-Y.H.), The University of Hong Kong, Hong Kong, China; Department of Radiology and Imaging Sciences (D.Q.), Emory University, Atlanta, Georgia; Department of Radiology (J.C.), First Affiliated Hospital of Sun Yat Sen University, Guangzhou, China; Philips Healthcare Hong Kong (Q.C.), Hong Kong, China; and Department of Radiology (M.E.M.), Stanford University, Stanford, California.

Please address correspondence to Deqiang Qiu, PhD, Emory University, Department of Radiology and Imaging Sciences, 1364 Rd, Clifton, CG06, Atlanta, GA 30322; e-mail: qiudeqiang@gmail.com or Pek-Lan Khong, MD, The University of Hong Kong, Department of Diagnostic Radiology, Room 406, Blk. K, Queen Mary Hospital, 102 Pokfulam Rd, Hong Kong; e-mail: plkhong@hkucc.hku.hk

Evidence-Based Medicine Level 2.

and brain.[1] Iron chelation therapy is administrated to clear the excess iron. Whereas iron overload in the heart and liver may cause death, alterations of iron content in the brain may contribute to cognitive impairment, as observed in some patients with thalassemia,[2,3] which has not been found to correlate with age and blood ferritin levels. Accurate assessment of iron content in the brains of patients with thalassemia could provide valuable information for individualized patient treatment. Conventionally, MR relaxometry on the basis of methods that use T2 and T2* mapping has been used to quantify iron in the brain.[4] Recently, the application of measuring brain iron by use of phase value of MR imaging with SWI[5,6] and quantitative susceptibility mapping (QSM)[7-12] has been evaluated for the quantification of iron content in patients with Parkinson disease.[13] QSM is an MR imaging technique that measures the magnetic susceptibility of tissues, such as blood or iron content, through mathematically modeling their induced effects on the phase of signal. Although the derivation of a magnetic susceptibility image from the phase informa-

tion obtained from MR imaging is an ill-posed problem, techniques have been established to overcome this by imposing smoothness or sparseness constraints on the susceptibility images.[9-11] QSM has been successfully applied in multiple sclerosis, Parkinson disease, and so forth. A recent study[14] has also established positive correlation between magnetic susceptibility values measured by use of QSM and iron content measured by x-ray fluorescence imaging and inductively coupled plasma mass spectrometry. In the present study, we quantified the brain iron content in a cohort of patients with β-thalassemia major and compared this with healthy age-matched subjects. We hypothesize that there are significant differences in iron loading between patients with thalassemia and healthy control subjects as measured by QSM.

MATERIALS AND METHODS
Subjects
Thirty-one (14 male) patients with β-thalassemia major were recruited for the study and 33 (17 male) age-matched healthy volunteers were recruited from the local community. The mean $\pm$ standard deviation (SD) age of the patient group was 25.3 ± 5.9 years (range, 15.2–34.3 years); the mean $\pm$ SD age of the control group was 26.1 ± 4.1 years (range 19.9–34.9 years). The study was approved by the institutional review board, and written informed consent was obtained from the subjects and/or their parent as appropriate. Among the 31 patients, 7 had hepatitis C, 16 had hypogonadism, and 7 had diabetes. The mean $\pm$ SD number of years of transfusion for the patients was 24.6 ± 5.9 years, and average hemoglobin level of the patients before transfusion was 96.3 ± 6.1 g/L.

Chelation Therapy
The patients received iron chelation therapy for an average of 20.9 ± 5.2 years. All 31 patients began their chelation therapy with deferoxamine (DFO). Of these 31 patients, 8 continued to receive DFO up to the dates of their MR imaging (DFO group), 6 changed treatment to deferiprone (L1; L1 group), 12 received additional treatment with L1, that is, combined DFO and L1 treatment (L1+DFO group), and 5 changed treatment to deferasirox (Exjade group). The mean $\pm$ SD treatment durations for the DFO, L1, L1+DFO, and Exjade groups with their current chelation agents at the time of MR imaging were 16.2 ± 8.2, 4.6 ± 2.3, 2.8 ± 1.3, and 1.6 ± 1.4 years, respectively.

Blood Ferritin Level
Blood ferritin level was taken regularly every 2 months. The last reading before the MR imaging, the first reading after the MR imaging, and 1-year average were obtained for correlation with MR findings in patients with thalassemia. The mean $\pm$ SD ferritin levels before and after MR imaging and the 1-year average were 4687.2 ± 2715.8 (range, 1119–111,062) μmol/mL, 4910.3 ± 2853.9 (range, 1166–14,200) μmol/mL, and 4868.5 ± 2575.8 (range, 1295–11,059) μmol/mL, respectively.

Image Acquisition
The MR imaging scan was performed with the use of an Achieva 3T scanner (Philips, Best, the Netherlands), and the protocol included a 3D gradient-echo sequence for susceptibility imaging (FOV = 230 mm, matrix = 256×256, section thickness = 2 mm, TR/TE = 16/23 ms). A T1-weighted image was acquired with the use of either MPRAGE (FOV = 250 mm, matrix = 252×240, section thickness = 1 mm) or 2D inversion recovery turbo spin-echo sequence (IR = 800 ms, TR/TE = 2000/20 ms, FOV = 230 mm, matrix = 296×252, section thickness/gap = 4 /1 mm) for anatomic identification and image normalization.

Image Processing
Image processing was performed by use of Matlab (MathWorks, Natick, Massachusetts). The phase images were first unwrapped by use of PRELUDE (part of FSL [http://www.fmrib.ox.ac.uk/fsl]) and the background field was removed by means of the spherical mean filtering technique.[15] The background-removed phase image was then subject to an L1-norm constrained iterative reconstruction algorithm[16] to calculate the magnetic susceptibility image from phase image. In the Fourier space, the relationship between magnetic field $f(\vec{k})$ (Fourier transformation of $f(\vec{r})$) and susceptibility distribution $\chi(\vec{k})$ (Fourier transformation of $\chi(\vec{r})$) is point-wise multiplication with a kernel $C(\vec{k})$:

$$1) \qquad f(\vec{k}) = \chi(\vec{k}) \cdot C(\vec{k})$$

$$2) \qquad C(\vec{k}) = \left(\frac{1}{3} - \frac{k_z^2}{|\vec{k}|^2} \right),$$

The relative magnetic field map $f(\vec{r})$ can be calculated from the processed phase map $\varphi(\vec{r})$ as:

$$3) \qquad f(\vec{r}) = -\frac{\varphi(\vec{r})}{\text{TE} \cdot B_0},$$

where TE is the echo time of the image and B_0 is the main magnetic field of the scanner. Reconstruction of magnetic susceptibility distribution $\chi(\vec{r})$ from the magnetic field map $f(\vec{r})$ is an ill-posed deconvolution problem because the convolution kernel $C(\vec{k})$ is zero at the cone surface $|\vec{k}^2| = 3 \cdot k_z^2$. One approach to solving this problem is to condition the problem by imposing sparsity constraints on the susceptibility map and recast the problem as the following optimization problem:

$$4) \qquad \chi(\vec{r}) = \arg\min_X(|A \cdot X(\vec{r}) - f(\vec{r})|_2 + \rho \cdot |W \cdot X(\vec{r})|_1)$$

where $A = ifft \cdot C(\vec{k}) \cdot fft$ is the forward transformation from susceptibility map to field map according to Equations 1 and 2, $f(\vec{r})$ is the relative field map calculated from the processed phase map according to Equation 3, W is a sparse transformation, that is, wavelet transformation, and ρ is a tuneable parameter that controls the balance between the data consistency and solution sparsity in the transformed domain given by W. This algorithm is similar to the method previously proposed, except that wavelet transformation was used in this study instead of total variation as regularization term[10] because wavelet transformation can provide a better sparsity of the images.[17] An optimal ρ was determined by a previously described method,[18] in which the normalized mean square error of the reconstructed susceptibility map was plotted against different ρ values, and the optimal ρ was chosen to be a turning point of the curve.

We adopted a semi-automatic approach for the analysis of susceptibility value of multiple brain regions. With the use of
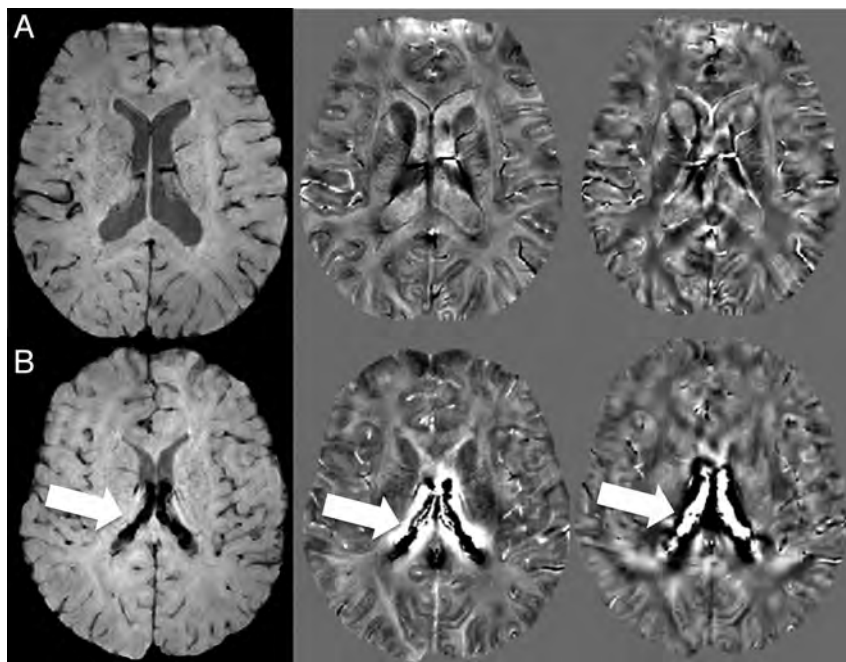
FIG 1. Left to right: Magnitude image, filtered phase image, and susceptibility image for *(A)* a healthy volunteer and *(B)* patient with thalassemia. For the patient with thalassemia, overloading of iron content in the choroid plexus can be observed as low signal intensity on the magnitude image and filtered phase image and high signal intensity in the susceptibility image *(arrows)*.

pected normal susceptibility value (SV_{exp}) for each ROI of each individual was calculated by use of $SV = a + b \times age + c \times sex$, in which the coefficients *a, b,* and *c* were determined from regression analysis from the healthy subjects. The age- and sex-corrected susceptibility value (cSV) was then calculated as $cSV = SV - SV_{exp}$. The susceptibility value was defined to be low susceptibility value if $cSV < -3*SD$, in which SD indicates standard deviation of the residuals from the regression analysis from the healthy control subjects, and this suggests iron "underloading"; conversely, the susceptibility value was defined to be high susceptibility value if $cSV > 3*SD$, and this suggests iron overloading. On the basis of the cSV of the ROIs, the patients were then categorized as iron overloaded if at least 1 of the ROIs had high susceptibility value while no ROI had low susceptibility value; iron underloaded if at least 1 of the ROIs had low susceptibility value while none had high susceptibility value; "mixed" findings if low susceptibility value was found in 1 ROI and high susceptibility value was found in another ROI; and normal if no ROI had low susceptibility value or high susceptibility value.

Pearson correlation was performed between susceptibility values of each ROI with blood ferritin levels taken within 2 months before and after the MR image as well as its average over 1 year. General linear model analysis was performed to compare susceptibility value of each ROI between patients receiving different types of chelation therapy after controlling for the effect of age. A value of $P < .05$ was considered statistically significant.

RESULTS
Qualitative Observations
Qualitatively, QSM was able to show regions of high iron deposition at the expected locations in the brain. Subcortical structures including putamen, GP, SN, and red nucleus can be nicely depicted in QSM images (Fig 1*A*). In some patients, a high amount of iron deposition was shown as high signal intensity in susceptibility imaging in regions including the CP (Fig 1*B*). Figure 2 shows the placement of ROIs on the mean susceptibility image.

Relationship between Susceptibility Value and Age and Sex among Control Subjects
Table 1 shows the result of linear regression of the susceptibility value on the control group with age and sex as independent variables. A significant positive effect of age on susceptibility value was found in the putamen, DN, SN, and red nucleus, suggesting higher level of iron concentration with increasing age in these regions ($P = .002, .017, .044,$ and $.014$, respectively). In the DN, significantly higher susceptibility value was found in the women as compared with men after controlling for the effect of age ($P = .018$). In other regions except for the SN, the susceptibility value

SPM8 (Wellcome Department of Imaging Neuroscience, London, UK), the susceptibility image from every subject was normalized to Montreal Neurological Institute space by use of the respective magnitude image and the T1WI as medium. ROIs were then manually outlined on the group mean image of the normalized susceptibility maps and included bilateral caudate nucleus, putamen, globus pallidus (GP), red nucleus, substantia nigra (SN), dentate nucleus (DN) and the choroid plexus (CP). The generated ROIs were then copied to each subject for measurement of susceptibility values and the mean susceptibility value was calculated as the mean value of all non-negative voxels within an ROI as defined above. We excluded voxels with negative susceptibility value to avoid the boundary effects and the inclusion of neighboring white matter voxels. The susceptibility values of left and right ROIs were then averaged for each anatomic region for further statistical analysis.

Statistical Analysis
Statistical analysis was performed with the use of SPSS (IBM, Armonk, New York). The Mann-Whitney *U* test was performed to determine differences in age between patients and control subjects. A χ^2 test was performed to determine difference in sex ratio between patients and control subjects. First, to evaluate the dependence of susceptibility values on age and sex among healthy control subjects, linear regression was performed by use of sex as a factor and age as a covariate. Second, general linear model analysis was performed to determine susceptibility value difference for different ROIs between patients and control subjects, controlling for the effect of age.

To further characterize the iron loading status of each patient, each ROI from each patient was classified according to the regression analysis result from the healthy control subjects. The ex-

FIG 2. Mean susceptibility map on *(A)* axial, *(B)* coronal, and *(C)* sagittal plane and *(D–G)* placement of ROIs on the mean susceptibility map, including the caudate nucleus (CN), putamen (PT), globus pallidus (GP), red nucleus (RN), substantia nigra (SN), dentate nucleus (DN) and choroid plexus (CP).

Table 1: Results of linear regression of the susceptibility value on the control group with age and sex as independent variables

ROI	Intercept /10^{-2} ppm	Age /10^{-3} ppm	Sex /10^{-3} ppm	*P* Value of Age	*P* Value of Sex
PT	0.45	0.51	1.15	.002	.346
GP	7.22	0.18	8.26	.729	.057
CN	1.55	0.18	0.30	.338	.837
DN	1.60	1.10	8.68	.017	.018
SN	4.35	1.22	−3.49	.044	.455
RN	1.26	1.72	1.07	.014	.841
CP	3.83	−0.341	9.75	.763	.284

Note:—Significant positive age effect on susceptibility value was found in PT, DN, SN, and RN, suggesting higher level of iron concentration with increasing age. In the DN, significantly higher susceptibility value was found in women compared with men after controlling for the effect of age. In other regions except for the SN, the susceptibility value was also higher in women, though these differences were not statistically significant. These findings suggest that in the majority of brain regions, iron concentration increases with age and is higher among women.
SD indicates standard deviation; PT, putamen; GP, globus pallidus; CN, caudate nucleus; DN, dentate nucleus; SN, substantia nigra; RN, red nucleus; CP, choroid plexus.

was also higher in women, though these differences were not statistically significant. These findings suggest that in most of the brain regions, iron concentration increases with age and is higher among women.

Iron Deposition in Patients with Thalassemia
Table 2 shows mean and SDs of susceptibility values of different ROIs between healthy control subjects and patients with thalassemia, as well as the *P* value for group effect by use of the general linear model after controlling for the effect of age. Significantly lower susceptibility value was found in patients with thalassemia compared with healthy control subjects in the GP ($P < .001$) and the SN ($P = .003$); significantly higher susceptibility value was found in patients with thalassemia in the red nucleus ($P = .021$) and the CP ($P < .001$).

Classification of Patients
On the basis of the results from the linear regression analysis on healthy control subjects, we established a normal range of the susceptibility value by use of 3 times the SD of the residues as

cutoff points. Out of the 31 patients, 27 (87.1%) had abnormal iron deposition in at least 1 of the ROIs. Six had low susceptibility value in at least 1 of the ROIs and normal susceptibility value in other ROIs. Thirteen of the patients had high susceptibility values in at least 1 of the ROIs and normal susceptibility value in other ROIs, 12 of which involved the CP. Eight of the patients had mixed abnormal susceptibility value, with at least 1 of the ROIs having higher susceptibility value and at least 1 other ROI having lower susceptibility values.

Table 3 shows the number of patients with thalassemia with iron overloading or underloading in each ROI. The largest number of patients was found to have abnormal susceptibility value in the CP ($n = 20$), followed by the GP ($n = 12$). As a control analysis, the same analysis was performed on healthy volunteers, and the results showed that all ROIs had normal susceptibility value.

Correlation between Blood Ferritin Level and Susceptibility Value
There was no significant correlation between measures of ferritin level and susceptibility value of the ROIs.

Susceptibility Value and Chelation Agents
Table 4 shows means and SDs of susceptibility values in the brain regions among patients receiving different chelation agents. No significant differences between patients receiving different chelation agents were found.

DISCUSSION
In this study, we applied QSM in studying brain iron loading in a group of patients with thalassemia and age-matched control subjects. The prevalence of "abnormal" iron concentration was 87.1% in our patient cohort, and we found large variations of iron concentration among the patients. Approximately two-thirds of the patients had high susceptibility value in the CP (20/31), suggesting overloaded iron content in this region, whereas reduced or "underloaded" iron concentration was found in the GP in approximately one-third of the patients (11/31).

Among the control subjects, higher susceptibility value was found with increasing age in multiple brain regions, which is consistent with the literature.[19] The landmark work of Hallgren and Sourander,[20] whose data still provide the largest quantitative survey of brain iron content with age, indicates that iron typically increases rapidly from birth until approximately 20 years of age

Table 2: Mean (standard deviation) of susceptibility values of different ROIs between healthy control subjects and patients with thalassemia and *P* values for group effect with the use of the general linear model after controlling for effects of age and sex

	PT	GP	CN	DN	SN	RN	CP
Control subjects (10^{-2} ppm)	1.82 (0.40)	8.23 (1.24)	2.04 (0.41)	4.94 (1.19)	7.42 (1.35)	5.75 (1.63)	3.00 (0.63)
Patients (10^{-2} ppm)	1.91 (0.63)	6.58 (2.23)	2.04 (0.62)	4.55 (1.81)	6.33 (1.37)	6.67 (2.52)	7.17 (4.55)
P value	.248	<.001	.842	.246	.003	.021	<.001

Note:—Significantly lower susceptibility value was found in patients with thalassemia compared with healthy control subjects in GP and SN; significantly higher susceptibility value was found in patients with thalassemia in RN and CP.
PT indicates putamen; GP, globus pallidus; CN, caudate nucleus; DN, dentate nucleus; SN, substantia nigra; RN, red nucleus; CP, choroid plexus.

Table 3: Number of patients with thalassemia with iron overloading or underloading in each ROI

	PT	GP	CN	DN	SN	RN	CP
Iron overload	1	0	2	1	0	3	20
Iron underload	0	11	0	2	1	0	0

Note:—PT indicates putamen; GP, globus pallidus; CN, caudate nucleus; DN, dentate nucleus; SN, substantia nigra; RN, red nucleus; CP, choroid plexus.

Table 4: Susceptibility values among patients receiving different chelation agents

	Mean (SD) /10^{-2} ppm				
	DFO	L1	DFO+L1	Exjade	P Value
PT	1.82 (0.69)	2.09 (0.50)	1.81 (0.59)	2.07 (0.85)	.201
GP	7.64 (2.07)	6.69 (3.50)	5.62 (1.73)	7.06 (1.06)	.296
CN	2.37 (0.60)	1.66 (0.49)	1.98 (0.54)	2.09 (0.80)	.232
DN	4.95 (1.53)	3.50 (1.57)	4.44 (2.08)	5.44 (1.55)	.064
SN	6.87 (1.77)	5.89 (1.61)	6.28 (1.15)	6.08 (0.86)	.573
RN	6.01 (3.23)	7.26 (1.85)	6.86 (1.90)	6.55 (3.68)	.801
CP	7.38 (4.28)	7.03 (3.63)	7.47 (6.09)	6.24 (1.75)	.955

Note:—No significant difference was found in susceptibility values between patients receiving different chelation agents.
DFO indicates deferoxamine; L1, deferiprone; SD, standard deviation; PT, putamen; CN, caudate nucleus; RN, red nucleus.

for nearly all brain regions. After this age, brain iron increases less rapidly and in some regions approaches a distinct plateau in middle age.

Iron overload in β-thalassemia occurs through multiple pathways, including extensive destruction of senescent native and transfused red blood cells, increased intestinal iron absorption caused by tissue hypoxia, apoptosis of defective erythroid precursors, and peripheral hemolysis.[21] Whether abnormal systemic iron level directly leads to changes in the brain iron level is unclear. It is expected that the brain's iron levels would be well regulated and maintained according to its own mechanism and metabolic needs, and the existence of the blood-brain barrier would further reduce the influence of blood iron levels on brain iron level. Nonetheless, it is conceivable that blood iron levels may have some degree of modulation effect on the brain iron levels. It is interesting to note that mixed levels of abnormal brain iron content were observed among the patients with thalassemia in the present study, with some regions having excessive iron concentration such as the CP and less so, the red nucleus, and some regions having low iron concentration such as the GP and less so, the SN and DN. Also, the dynamic interactions between the effects of regular blood transfusion and iron chelation therapy may contribute to the regional variations in brain iron level among the different regions. It has been shown that the CP, which forms the blood-CSF barrier, is an important interface for brain iron homeostasis and has abundant proteins related to iron transportation,[22] which may contribute to the excessive iron content in this region among patients with thalassemia. It is noteworthy that iron content in brain regions increases with age among healthy subjects.[23] Because of disruption of sex hormone production,[24] patients with β-thalassemia have delayed maturation, which may contribute to the observed lower iron content in the GP and the DN among patients with β-thalassemia. Moreover, patients with β-thalassemia are prone to chronic systemic illnesses, including hypogonadism, hepatitis C, diabetes, and so forth. All these may be contributory to the effects on the brain and cognition. Thus, the exact physiologic mechanism underlying the abnormal iron distribution in patients with thalassemia is complex and remains to be fully elucidated.

Although the effects of iron overload on heart and liver dysfunction have been extensively studied because of their early impact on survival, the effect of alteration of iron content in the central nervous system remains unclear and the literature to date is limited. It has been found that patients with thalassemia have neuropsychological impairment in the domains of abstract reasoning, attention, and memory.[2] Hemosiderosis, toxicity from chelating agents, and chronic hypoxia have been postulated to be the contributory factors of these cognitive dysfunctions. In our current study, we found that most patients had either higher or lower levels of iron in at least 1 region evaluated, but with variations across regions and subjects. Previous study with the use of T2 mapping showed higher brain iron loading in patients with β-thalassemia.[25] Although the exact cause of the abnormal brain iron level is still unclear, the presence of these brain iron level abnormalities as shown in the current study may have implications in cognitive functioning. High brain iron level is associated with high oxidative stress, and this has been implicated in many neurologic diseases including Parkinson disease, Alzheimer disease, multiple sclerosis, and so forth.[4] On the other hand, low iron content has been shown to adversely affect the dopaminergic-opiate system and the cholinergic system[26] and thus may also affect cognition. In addition, factors associated with chronic illness leading to regular school absence, physical and social restrictions, abnormal mental state, rather than the disease per se, could also play a potential role in the development of cognitive dysfunction in patients with thalassemia.[2,3]

It would have been interesting to evaluate the effect of the various chelation agents on iron deposition. Although our preliminary results showed no significant differences, this retrospective study was limited by the confounding variable of different treatment times and the small sample size. However, it is interest-

ing to note that patients treated with L1 had the lowest iron loads in the DN, and the ANOVA analysis approached statistical significance. L1, which crosses the blood-brain barrier, has been found useful in lowering iron levels in the DN of patients with Friedreich ataxia.[27]

Other limitations of the current study are that we did not acquire quantitative liver or cardiac iron measures or neuropsychological assessments. Future controlled studies with a larger cohort including these measures are warranted. Finally, although susceptibility values obtained in our study are generally lower than what was reported previously,[28] this is possibly caused by the combination of differences in subject cohort, ROI placements, and the selection of regularization parameters in the dipole deconvolution. However, because the parameters used were the same between patients and control subjects, the susceptibility values obtained are directly comparable.

Conclusions

We have shown that quantitative susceptibility mapping is sensitive to iron deposition in the brain. The nature of abnormal iron content varies across different anatomic regions in patients with thalassemia. QSM is potentially a valuable tool for iron assessment, both on an individual basis for which treatment may be tailored and for use in clinical trials.

REFERENCES

1. Olivieri NF, Brittenham GM. **Iron-chelating therapy and the treatment of thalassemia.** *Blood* 1997;89:739–61
2. Economou M, Zafeiriou DI, Kontopoulos E, et al. **Neurophysiologic and intellectual evaluation of beta-thalassemia patients.** *Brain Dev* 2006;28:14–18
3. Monastero R, Monastero G, Ciaccio C, et al. **Cognitive deficits in beta-thalassemia major.** *Acta Neurol Scand* 2000;102:162–68
4. Brass SD, Chen NK, Mulkern RV, et al. **Magnetic resonance imaging of iron deposition in neurological disorders.** *Topics Magn Reson Imaging* 2006;17:31–40
5. Haacke EM, Mittal S, Wu Z, et al. **Susceptibility-weighted imaging: technical aspects and clinical applications, part 1.** *Am J Neuroradiol* 2009;30:19–30
6. Mittal S, Wu Z, Neelavalli J, et al. **Susceptibility-weighted imaging: technical aspects and clinical applications, part 2.** *AJNR Am J Neuroradiol* 2009;30:232–52
7. de Rochefort L, Brown R, Prince MR, et al. **Quantitative MR susceptibility mapping using piece-wise constant regularized inversion of the magnetic field.** *Magn Reson Med* 2008;60:1003–09
8. Kressler B, de Rochefort L, Liu T, et al. **Nonlinear regularization for per voxel estimation of magnetic susceptibility distributions from MRI field maps.** *IEEE Trans Med Imaging* 2010;29:273–81
9. Li W, Wu B, Liu C. **Quantitative susceptibility mapping of human brain reflects spatial variation in tissue composition.** *NeuroImage* 2011;55:1645–56
10. Liu T, Liu J, de Rochefort L, et al. **Morphology enabled dipole inversion (MEDI) from a single-angle acquisition: comparison with COSMOS in human brain imaging.** *Magn Reson Med* 2011;66:777–83
11. Shmueli K, de Zwart JA, van Gelderen P, et al. **Magnetic susceptibility mapping of brain tissue in vivo using MRI phase data.** *Magn Reson Med* 2009;62:1510–22
12. Wharton S, Bowtell R. **Whole-brain susceptibility mapping at high field: a comparison of multiple- and single-orientation methods.** *NeuroImage* 2010;53:515–25
13. Lotfipour AK, Wharton S, Schwarz ST, et al. **High resolution magnetic susceptibility mapping of the substantia nigra in Parkinson's disease.** *J Magn Res Imaging* 2012;35:48–55
14. Zheng W, Nichol H, Liu S, et al. **Measuring iron in the brain using quantitative susceptibility mapping and X-ray fluorescence imaging.** *NeuroImage* 2013;78:68–74
15. Schweser F, Deistung A, Lehr BW, et al. **Quantitative imaging of intrinsic magnetic tissue properties using MRI signal phase: an approach to in vivo brain iron metabolism?** *NeuroImage* 2011;54:2789–807
16. Qiu D, Zaharchuk G, Feng S, et al. **Quantitative Susceptibility Imaging using L1 regularized reConstruction with sparsity promoting transformation: SILC.** *Proceedings of International Society of Magnetic Resonance in Medicine Annual Meeting* 2011;19:4470
17. Chui CK. *An Introduction to Wavelets.* San Diego: Academic Press; 1992
18. Wu B, Li W, Guidon A, et al. **Whole brain susceptibility mapping using compressed sensing.** *Magn Reson Med* 2012;67:137–47
19. Pfefferbaum A, Adalsteinsson E, Rohlfing T, et al. **MRI estimates of brain iron concentration in normal aging: comparison of field-dependent (FDRI) and phase (SWI) methods.** *NeuroImage* 2009;47:493–500
20. Hallgren B, Sourander P. **The effect of age on the non-haemin iron in the human brain.** *J Neurochem* 1958;3:41–51
21. Rund D, Rachmilewitz E. **Beta-thalassemia.** *N Engl J Med* 2005;353:1135–46
22. Rouault TA, Zhang DL, Jeong SY. **Brain iron homeostasis, the choroid plexus, and localization of iron transport proteins.** *Metab Brain Dis* 2009;24:673–84
23. Li W, Wu B, Batrachenko A, et al. **Differential developmental trajectories of magnetic susceptibility in human brain gray and white matter over the lifespan.** *Hum Brain Mapp* 2014;35:2698–713
24. Moshtaghi-Kashanian GR, Razavi F. **Ghrelin and leptin levels in relation to puberty and reproductive function in patients with beta-thalassemia.** *Hormones* 2009;8:207–13
25. Metafratzi Z, Argyropoulou MI, Kiortsis DN, et al. **T(2) relaxation rate of basal ganglia and cortex in patients with beta-thalassaemia major.** *Br J Radiol* 2001;74:407–10
26. Youdim MB. **Brain iron deficiency and excess; cognitive impairment and neurodegeneration with involvement of striatum and hippocampus.** *Neurotox Res* 2008;14:45–56
27. Pandolfo M, Hausmann L. **Deferiprone for the treatment of Friedreich's ataxia.** *J Neurochem* 2013;126(Suppl 1):142–46
28. Lim IA, Faria AV, Li X, et al. **Human brain atlas for automated region of interest selection in quantitative susceptibility mapping: application to determine iron content in deep gray matter structures.** *NeuroImage* 2013;82:449–69

Imaging the Effects of Oxygen Saturation Changes in Voluntary Apnea and Hyperventilation on Susceptibility-Weighted Imaging

K. Chang, S. Barnes, E.M. Haacke, R.I. Grossman, and Y. Ge

ABSTRACT

BACKGROUND AND PURPOSE: Cerebrovascular oxygenation changes during respiratory challenges have clinically important implications for brain function, including cerebral autoregulation and the rate of brain metabolism. SWI is sensitive to venous oxygenation level by exploitation of the magnetic susceptibility of deoxygenated blood. We assessed cerebral venous blood oxygenation changes during simple voluntary breath-holding (apnea) and hyperventilation by use of SWI at 3T.

MATERIALS AND METHODS: We performed SWI scans (3T; acquisition time of 1 minute, 28 seconds; centered on the anterior commissure and the posterior commissure) on 10 healthy male volunteers during baseline breathing as well as during simple voluntary hyperventilation and apnea challenges. The hyperventilation and apnea tasks were separated by a 5-minute resting period. SWI venograms were generated, and the signal changes on SWI before and after the respiratory stress tasks were compared by means of a paired Student t test.

RESULTS: Changes in venous vasculature visibility caused by the respiratory challenges were directly visualized on the SWI venograms. The venogram segmentation results showed that voluntary apnea decreased the mean venous blood voxel number by 1.6% ($P < .0001$), and hyperventilation increased the mean venous blood voxel number by 2.7% ($P < .0001$). These results can be explained by blood CO_2 changes secondary to the respiratory challenges, which can alter cerebrovascular tone and cerebral blood flow and ultimately affect venous oxygen levels.

CONCLUSIONS: These results highlight the sensitivity of SWI to simple and noninvasive respiratory challenges and its potential utility in assessing cerebral hemodynamics and vasomotor responses.

ABBREVIATIONS: ACPC = anterior/posterior commissure; SD = standard deviation

Blood oxygen supply and metabolism are critical to maintaining normal brain function and are dependent on neurovascular coupling, a unique characteristic of the brain that ensures adequate CBF in response to neuronal activity. This mechanism is thought to be associated with intrinsic changes in the caliber of cerebral arteries secondary to neuronal-induced vasoactive stimuli. These vasoactive agents and metabolites include K^+, nitric oxide, adenosine, and CO_2 and have been shown to cause vasodilation of cerebral blood vessels and an increase in CBF.[1,2] External vasoactive stimuli such as intravenous acetazolamide, ingestion of caffeine, and inhaled CO_2 have also been shown to modulate CBF, leading to the appropriate downstream effect on blood oxygenation.[3-8] These external hemodynamic modulators are of clinical interest because they are often used to evaluate cerebral hemodynamics and vasomotor responses, which can be impaired in many neurologic diseases such as stroke,[9] Alzheimer disease,[10] and multiple sclerosis.[11,12]

In line with the interest in cerebral vasomotor response in numerous neurologic diseases, respiratory challenges that can induce systemic changes in CO_2 have been introduced as simple modulators of CBF because they do not require complicated equipment for gas delivery setup and can be easily repeated.[13-16] Voluntary apnea, or breath-holding, results in a hypercapnic state, which has been shown to cause vasodilation and an increase in CBF. Conversely, voluntary hyperventilation results in a hypocapnic state, which decreases CBF by vasoconstriction.[17,18] Because there is constant oxygen metabolism, increases in CBF

will eventually lead to increases in venous blood oxygenation, whereas the opposite holds true for decreases in CBF.[16]

SWI uses venous blood oxygenation or deoxyhemoglobin as an intrinsic contrast agent to enhance venous vessel visibility and provides an opportunity to directly visualize the vasomotor response to stimuli. Although recent works have demonstrated that oxygen saturation changes caused by breathing carbogen or pure oxygen or ingesting caffeine can be visualized on SWI venography,[6,19] few studies have addressed the sensitivity of SWI to simple and fast respiratory stresses.[16] Fushimi et al[16] demonstrated that SWI tissue signal changes reflected decreases in CBF and associated blood oxygenation changes as a result of hyperventilation. The venous conspicuity changes on SWI venograms related to simple alteration in respiratory pattern have not yet been directly defined. Thus, the aim of the present study is to quantitatively assess the sensitivity and degree of cerebral venous blood oxygenation changes in response to both voluntary breath-holding (apnea) and hyperventilation on SWI venous conspicuity.

MATERIALS AND METHODS

Ten healthy male volunteers (mean age, 34.7 ± 10.2 years) participated in the study. According to the institutional guidelines, all subjects gave informed written consent to the study approved by our institutional review board at New York University School of Medicine before MR imaging.

Experimental Design

All experiments were performed on a clinical 3T system (Tim Trio; Siemens, Erlangen, Germany) by use of a 12-channel array head coil. Axial T2- and T1-weighted images were acquired first and used as anatomic reference parallel to the line running through the anterior commissure and the posterior commissure (ACPC). SWI is a 3D, radiofrequency-spoiled fast low-angle shot gradient-echo sequence with flow compensation in all 3 directions. This gradient moment nulling in all 3 orthogonal directions reduces signal loss in blood attributable to flow dephasing. To avoid the susceptibility artifacts near the skull base, SWI was performed solely at the lateral ventricle level with the first section going through the ACPC line. The SWI scans were performed with the following parameters: TR/TE = 29/20 ms, flip angle = 15°, resolution = 0.4×0.4 mm^2, section thickness = 1.2 mm, section number = 16, bandwidth = 120 Hz/pixel, and 1 acquisition. The total acquisition time of each SWI scan was 88 seconds without the use of parallel imaging.

The experimental design included 3 SWI scans with different breathing patterns: normal, breath-hold, and hyperventilation. Each subject was instructed by an investigator on how to perform these baseline and respiratory challenges before the start of the study. The participants were also instructed not to ingest caffeine for 6 hours before the scan. The baseline SWI with normal breathing was performed first, followed by the breath-holding scan. The subjects were instructed to start the breath-hold 10 seconds into the SWI scan. The breath-holding challenge was followed by a recovery period of 5 minutes with normal breathing and the head kept still. The third SWI scan was then started, at which point the participants were instructed to begin the hyperventilation challenge. Hyperventilation lasted throughout the entirety of the scan.

Each scan (baseline, breath-hold, and hyperventilation) was obtained with the same imaging parameters, section number, orientation, and localization. The periods for breath-hold and hyperventilation were 30~45 seconds and approximately 90 seconds (duration of scan), respectively, which were well tolerated in all participants. In addition to the constraint headphones and a cushion used to prevent movement during imaging, the subjects were instructed to keep the head still during the respiratory tasks for motion artifact control. A few participants complained of dizziness immediately after the experiment; however, none of the subjects had any procedure-related side effects 20 minutes after the scan.

Image Processing and Analysis

SWI is designed to enhance susceptibility contrast by use of phase information. The raw magnitude and phase from each SWI scan were obtained and used to generate an SWI venogram. As had been previously described,[20] all phase images were reconstructed and corrected for field inhomogeneities by use of a 32×32 high-pass filter with the use of an in-house image-processing software (SPIN). Because the current Siemens system uses a left-handed system, the phase mask is defined such that the mask runs from unity to zero for positive phase values from 0 to 180° and unity for negative phase values from −180° to 0°. The original magnitude image was multiplied by this phase mask 4 times to enhance the visibility of venous structures. Finally, SWI venograms were created by use of an MIP performed over 8 sections, creating a total of 9.6-mm coverage centered around the ventricular body between the ACPC line and upper centrum semiovale to maintain consistency between subjects.

Quantification of the venous blood voxels was performed on the basis of these 12 SWI MIP images with enhanced venous visibility. A statistical thresholding algorithm,[21] similar to what has been used to segment arteries,[22] was used to isolate venous structures on the basis of their contrast with surrounding brain tissue. This algorithm involves first applying a threshold to remove background noise and structures (ie, skull).[23] A shape-filtering noise removal algorithm was then used to remove falsely identified venous structures from the threshold-generated map. Further filtering of false-positives was performed by removal of clusters of connected voxels below a certain size.[21] The compactness[24] and relative anisotropy of connected voxels were then assessed by means of shape analysis to highlight clusters of venous structures. These clusters were displayed on color-coded venous vasculature maps, and the voxel number of each venous cluster was then finally quantified.[25]

One limitation to note is that very small veins that were visualized on the SWI MIP venogram may not have been identified by the thresholding algorithm because of signal attenuation from partial volume effects that limit the available contrast. However, because the thresholding parameters, imaging parameters, and position setting were consistent across all 3 SWI scans, the low contrast vessels were treated in a consistent manner, and we assumed that the difference in number of venous blood voxels between scans was caused by oxygenation changes associated with the respiratory challenges. The differences of segmentation results of venous blood on SWI venography between SWI scans were
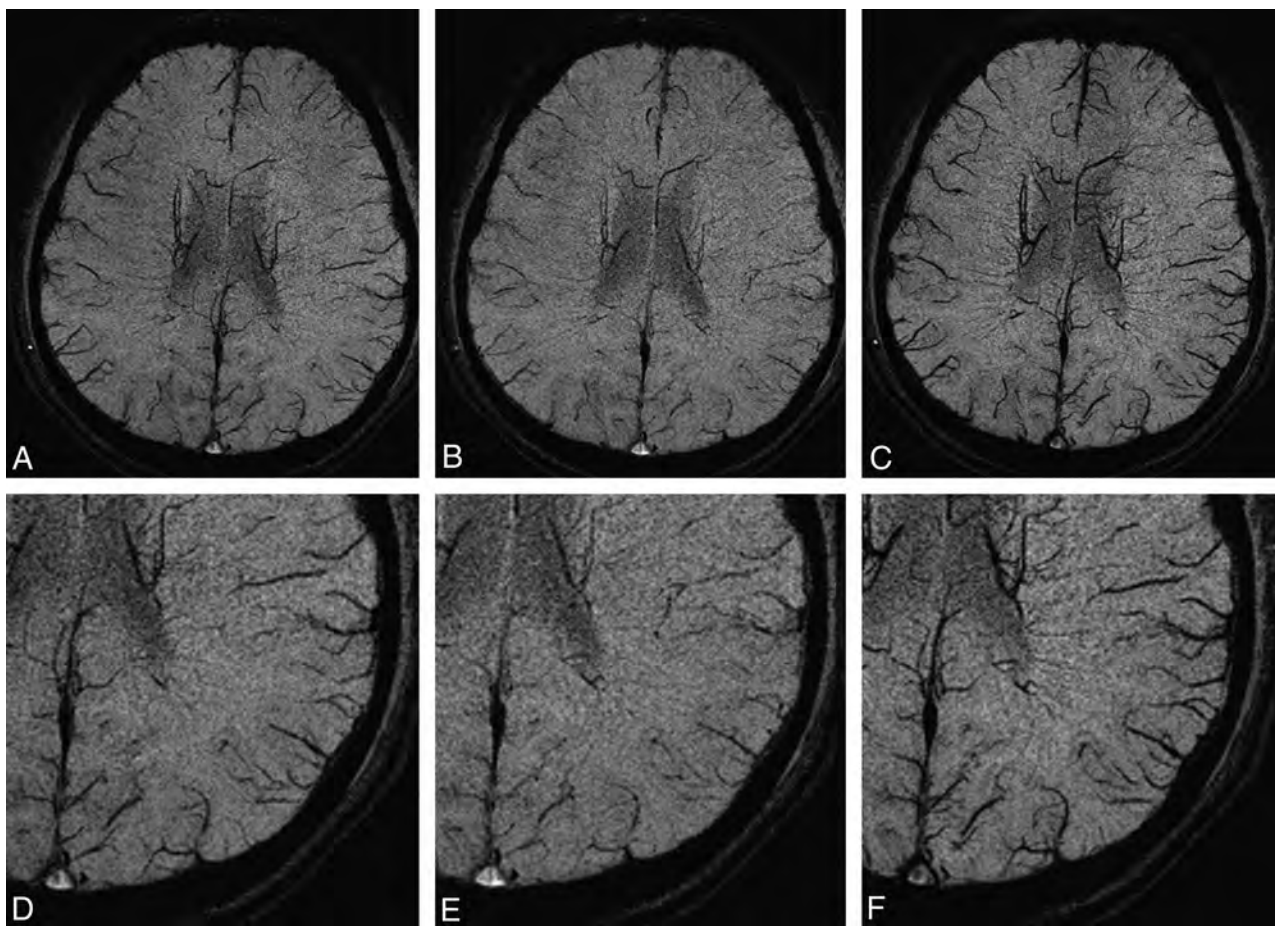
FIG 1. Axial SWI MIP venogram at baseline *(A)*, breath-holding *(B)*, and hyperventilation *(C)* in a healthy subject. *D–F*, Magnified portions of the SWI venogram at baseline, breath-holding, and hyperventilation, respectively. The signal intensity changes in the venous architecture are caused by oxygenation level alterations during the respiratory challenges. There is a slight increase in signal intensity within venous structures during breath-holding *(B)* and marked signal decrease during hyperventilation *(C)* as a result of different responses of vascular tone to changes of blood CO_2, which is a vasoactive modulator.

assessed by use of the paired *t* test, with a value of $P < .05$ considered statistically significant.

RESULTS

Changes in oxygenation level as indicated by venous blood signal change caused by alteration in the concentration of deoxyhemoglobin in the veins was clearly seen on SWI in all volunteers. Figure 1 shows the SWI MIP venogram for a typical subject at baseline and during apnea and hyperventilation respiratory challenges. Compared with the baseline scan with normal breathing, the venous architecture is slightly attenuated during breath-holding and is amplified during hyperventilation. Figure 2 shows the total venous voxel number for all 10 subjects during baseline, apnea, and hyperventilation. Although there were variations in SWI venous voxels from subject to subject, the behavior of these signal changes in response to apnea and hyperventilation were consistent across all 10 subjects.

The paired *t* test showed significant decrease of venous voxel numbers during breath-hold ($P < .0001$) and significant increase during hyperventilation ($P < .0001$) compared with baseline. The mean and standard deviation (SD) of venous voxel numbers were $24,427 \pm 936$, $24,032 \pm 962$, and $25,081 \pm 959$ at baseline, apnea, and hyperventilation SWI, respectively. Relative to baseline, there

was a significant percent change in venous blood voxel number during breath-holding (mean/SD: $-1.6 \pm 0.46\%$) and a significant increase during hyperventilation (mean/SD: $2.7 \pm 0.41\%$).

DISCUSSION

Although many in vivo human studies have demonstrated MR imaging signal changes with vascular stimuli (eg, hypercapnia, carbogen, or caffeine) on the basis of gradient-echo or blood oxygen level–dependent type techniques, few studies have investigated changes in venous conspicuity on SWI venograms when there is an alteration of respiratory pattern. Our data indicate that venous blood oxygenation level is higher during voluntary breath-holding and lower during hyperventilation. As a result, venous vasculature visibility on SWI venograms is enhanced for hyperventilation and diminished for apnea. Therefore, SWI may afford a noninvasive and relatively simple and quick method to assess underlying blood flow changes or oxygen metabolic pathophysiology in various disease states.

Hyperventilation is a physiologic mechanism by which CO_2 is expelled from the body in response to acidotic states secondary to the pathologic conditions. Voluntary hyperventilation will also cause the same decrease in blood CO_2,[26] which leads to vasoconstriction and a corresponding decrease in CBF. The mechanism
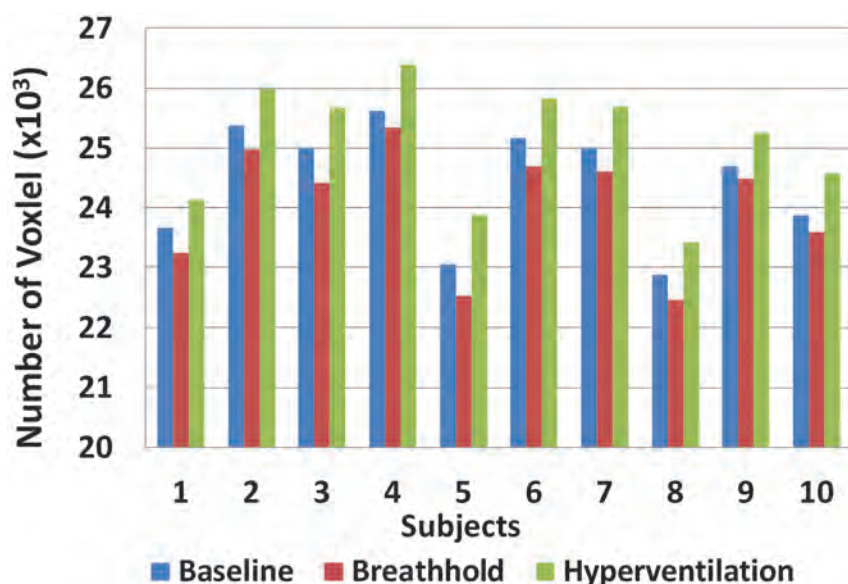
FIG 2. Number of venous blood voxels for each of the 10 subjects at baseline, breath-hold, and hyperventilation. There is a decrease in venous blood voxel number during breath-holding and an increase in venous voxel number during hyperventilation, and such changes are consistent across subjects.

by which this vasoconstriction occurs is mediated by the local increase in blood pH or reduction in $[H^+]$.[27,28] Because cerebral oxygen consumption remains unchanged in healthy persons,[29] the reduction in CBF means less overall oxygen delivery, and this will eventually result in a more deoxygenated venous blood. The local susceptibility effects of deoxyhemoglobin lead to a decrease in MR signal intensity, which translates to the observed increase in venous visibility on the SWI venogram. These results are consistent with the enhanced venous contrast on the SWI caused by hyperventilation, as reported by Fushimi et al,[16] as well as the decrease in MR signal intensity on SWI due to caffeine ingestion, as reported by Sedlacik et al.[6] Opposite to hyperventilation, breath-holding leads to the accumulation of blood CO_2 and a resultant cerebrovascular smooth muscle relaxation. This vasodilation decreases the resistance to blood flow, allowing for an increase in CBF and thus oxygen delivery to the brain. More oxygenated venous blood with decreased deoxyhemoglobin concentration will cause an increase in signal intensity. This translates to a decrease in venous vasculature visibility on the SWI venogram and a decrease in venous voxel number. These results are consistent with the decrease in venous contrast on SWI caused by carbogen breathing, as reported in Rauscher et al.[19] Whereas venous deoxyhemoglobin concentration plays an important role in modulating SWI signal, the venous vasculature visibility can also be influenced by its caliber size changes. However, unlike arterial vasculature, venous vasculature has thin walls, lacks vasomotor smooth muscle, and is insensitive to vasoactive stimuli. Therefore, the observed SWI venous conspicuity changes during respiratory stress in this study are probably caused by $PaCO_2$ alteration and subsequent oxygenation changes, which outweigh venous caliber changes (if any).

The SWI venous voxel change during apnea (1.6%) was observed to be smaller than that during hyperventilation (2.7%). This difference, which can be partly attributed to the greater uniformity among subjects in the ability to hyperventilate (with task

performed lasting 90 seconds) compared with breath-hold (with task performed around 30~45 seconds). The baseline SWI venous voxel numbers were also observed to be variable from subject to subject, as shown in Fig 2. These variations probably are representative of the normal anatomic variation in venous structures, which have been documented to be less conserved than their corresponding arterial structures. In addition, this intersubject variation in SWI venous voxel numbers can also be explained by the slight differences in brain coverage during the SWI scan. Some of the variance seen may also be caused by changing partial volume effects from scan to scan and variability in the small vasculature from person to person. Although anatomic landmarks were used to maintain consistency in brain coverage across subjects, slight inconsistencies were still possible. Nevertheless, the observed intersubject variations do not affect the results of our study because comparisons of SWI venous vasculature between baseline, apnea, and hyperventilation were performed within each individual subject and not across subjects.

There are several limitations of note. First, perfusion imaging (ie, arterial spin-labeling) was not performed because of the potential for increased subject distress during the prolonged respiratory challenges or longer scan times required for perfusion imaging. Measurement of CBF would have provided direct validation that the observed changes in SWI venous contrast resulted from alterations to CBF in response to the respiratory challenges. In addition, we do not have $PaCO_2$ measurements in this study. Measurement of end-tidal CO_2, a representation of $PaCO_2$, would have confirmed that the respiratory challenges of apnea and hyperventilation were actually inducing changes in blood CO_2 levels. Second, because of the limitations placed on acquisition times, whole-brain imaging with SWI was not performed. Whole-brain imaging, however, was not necessary because the aim of the study was to simply evaluate the sensitivity of SWI to respiratory challenges. The region of the central brain that was scanned included both small white matter medullary veins and large peripheral cortical veins and was therefore sufficient for our purposes in observing changes in CBF and venous oxygenation. Last, the resolution of the SWI venogram was also limited by the shortened acquisition time. Although this was not a problem for this current study, future resolution limitations can be resolved with ultra-high field MR imaging (eg, 7T), and enhanced venous visibility would be possible as the result of the stronger susceptibility effect at higher magnetic fields. Recent advances in the use of phase to create quantitative susceptibility maps may make this type of evaluation even easier because this technique will provide positive contrast and possibly a direct measure of changes in oxygen saturation.[30,31]

CONCLUSIONS

Our study shows that changes in venous blood oxygenation in response to simple respiratory challenges can be imaged by SWI on 3T. Because of its noninvasiveness and sensitivity, SWI probably will play a role in the assessment of the cerebral vasomotor response for various cerebrovascular and neurodegenerative diseases such as stroke, multiple sclerosis, and Alzheimer disease.

ACKNOWLEDGMENTS

The authors thank Jens H. Jensen and Leon Axel for the helpful discussion of the experiment design.

REFERENCES

1. Attwell D, Iadecola C. **The neural basis of functional brain imaging signals.** *Trends Neurosci* 2002;25:621–25
2. Lauritzen M. **Reading vascular changes in brain imaging: is dendritic calcium the key?** *Nat Rev Neurosci* 2005;6:77–85
3. Derdeyn CP, Grubb RL Jr, Powers WJ. **Cerebral hemodynamic impairment: methods of measurement and association with stroke risk.** *Neurology* 1999;53:251–59
4. Bruhn H, Kleinschmidt A, Boecker H, et al. **The effect of acetazolamide on regional cerebral blood oxygenation at rest and under stimulation as assessed by MRI.** *J Cereb Blood Flow Metab* 1994;14:742–48
5. Kleinschmidt A, Steinmetz H, Sitzer M, et al. **Magnetic resonance imaging of regional cerebral blood oxygenation changes under acetazolamide in carotid occlusive disease.** *Stroke* 1995;26:106–10
6. Sedlacik J, Helm K, Rauscher A, et al. **Investigations on the effect of caffeine on cerebral venous vessel contrast by using susceptibility-weighted imaging (SWI) at 1.5, 3 and 7 T.** *NeuroImage* 2008;40:11–18
7. Rostrup E, Larsson HB, Toft PB, et al. **Susceptibility contrast imaging of CO2-induced changes in the blood volume of the human brain.** *Acta Radiol* 1996;37:813–22
8. Rostrup E, Larsson HB, Toft PB, et al. **Functional MRI of CO2 induced increase in cerebral perfusion.** *NMR Biomed* 1994;7:29–34
9. Webster MW, Makaroun MS, Steed DL, et al. **Compromised cerebral blood flow reactivity is a predictor of stroke in patients with symptomatic carotid artery occlusive disease.** *J Vasc Surg* 1995;21:338–44
10. Glodzik L, Randall C, Rusinek H, et al. **Cerebrovascular reactivity to carbon dioxide in Alzheimer's disease.** *J Alzheimers Dis* 2013;35:427–40
11. Ge Y, Lu H, Zhou Y, et al. **Impaired regulation of the blood supply to the brain in multiple sclerosis measured with hypercapnia BOLD MRI.** *Proc. Intl. Soc. Mag. Reson. Med.* 2013:43
12. Ge Y, Zhou Y, Lu H, et al. **Cerebrovascular reactivity defect in multiple sclerosis.** *Proc. Intl. Soc. Mag. Reson. Med.* 2013:3601
13. Markus HS, Harrison MJ. **Estimation of cerebrovascular reactivity using transcranial Doppler, including the use of breath-holding as the vasodilatory stimulus.** *Stroke* 1992;23:668–73
14. de Boorder MJ, Hendrikse J, van der Grond J. **Phase-contrast magnetic resonance imaging measurements of cerebral autoregulation with a breath-hold challenge: a feasibility study.** *Stroke* 2004;35:1350–54
15. Posse S, Olthoff U, Weckesser M, et al. **Regional dynamic signal changes during controlled hyperventilation assessed with blood oxygen level-dependent functional MR imaging.** *AJNR Am J Neuroradiol* 1997;18:1763–70
16. Fushimi Y, Miki Y, Mori N, et al. **Signal changes in the brain on susceptibility-weighted imaging under reduced cerebral blood flow: a preliminary study.** *J Neuroimaging* 2010;20:255–59
17. Wasserman AJ, Patterson JL Jr. **The cerebral vascular response to reduction in arterial carbon dioxide tension.** *J Clin Invest* 1961;40:1297–303
18. Matta BF, Lam AM, Mayberg TS. **The influence of arterial oxygenation on cerebral venous oxygen saturation during hyperventilation.** *Can J Anaesth* 1994;41:1041–46
19. Rauscher A, Sedlacik J, Barth M, et al. **Noninvasive assessment of vascular architecture and function during modulated blood oxygenation using susceptibility weighted magnetic resonance imaging.** *Magn Reson Med* 2005;54:87–95
20. Haacke EM, Xu Y, Cheng YC, et al. **Susceptibility weighted imaging (SWI).** *Magn Reson Med* 2004;52:612–18
21. Barnes SR, Haacke EM, Ayaz M, et al. **Semiautomated detection of cerebral microbleeds in magnetic resonance images.** *Magn Reson Imaging* 2011;29:844–52
22. Wilson DL, Noble JA. **An adaptive segmentation algorithm for time-of-flight MRA data.** *IEEE Trans Med Imaging* 1999;18:938–45
23. Pandian DS, Ciulla C, Haacke EM, et al. **Complex threshold method for identifying pixels that contain predominantly noise in magnetic resonance images.** *J Magn Reson Imaging* 2008;28:727–35
24. Bribiesca E. **A measure of compactness for 3D shapes.** *Comput Math Applications* 2000;40:1275–84
25. Ge Y, Zohrabian VM, Osa EO, et al. **Diminished visibility of cerebral venous vasculature in multiple sclerosis by susceptibility-weighted imaging at 3.0 Tesla.** *J Magn Reson Imaging* 2009;29:1190–94
26. Richardson DW, Wasserman AJ, Patterson JL Jr. **General and regional circulatory responses to change in blood pH and carbon dioxide tension.** *J Clin Invest* 1961;40:31–43
27. Traystman RJ. In: Caplan LR, Reis DJ, Siesjo BK, et al, eds. *Regulation of Cerebral Blood Flow by Carbon Dioxide.* New York: Academic Press; 1997:55–58
28. Kontos HA, Wei EP, Raper AJ, et al. **Local mechanism of CO2 action of cat pial arterioles.** *Stroke* 1977;8:226–29
29. van Rijen PC, Luyten PR, van der Sprenkel JW, et al. **1H and 31P NMR measurement of cerebral lactate, high-energy phosphate levels, and pH in humans during voluntary hyperventilation: associated EEG, capnographic, and Doppler findings.** *Magn Reson Med* 1989;10:182–93
30. Haacke EM, Tang J, Neelavalli J, et al. **Susceptibility mapping as a means to visualize veins and quantify oxygen saturation.** *J Magn Reson Imaging* 2010;32:663–76
31. Tang J, Liu S, Neelavalli J, et al. **Improving susceptibility mapping using a threshold-based K-space/image domain iterative reconstruction approach.** *Magn Reson Med* 2013;69:1396–407

A Prognostic Model Based on Preoperative MRI Predicts Overall Survival in Patients with Diffuse Gliomas

A. Hilario, J.M. Sepulveda, A. Perez-Nuñez, E. Salvador, J.M. Millan, A. Hernandez-Lain, V. Rodriguez-Gonzalez, A. Lagares, and A. Ramos

ABSTRACT

BACKGROUND AND PURPOSE: Diffuse gliomas are classified as grades II–IV on the basis of histologic features, with prognosis determined mainly by clinical factors and histologic grade supported by molecular markers. Our aim was to evaluate, in patients with diffuse gliomas, the relationship of relative CBV and ADC values to overall survival. In addition, we also propose a prognostic model based on preoperative MR imaging findings that predicts survival independent of histopathology.

MATERIALS AND METHODS: We conducted a retrospective analysis of the preoperative diffusion and perfusion MR imaging in 126 histologically confirmed diffuse gliomas. Median relative CBV and ADC values were selected for quantitative analysis. Survival univariate analysis was made by constructing survival curves by using the Kaplan-Meier method and comparing subgroups by log-rank probability tests. A Cox regression model was made for multivariate analysis.

RESULTS: The study included 126 diffuse gliomas (median follow-up of 14.5 months). ADC and relative CBV values had a significant influence on overall survival. Median overall survival for patients with ADC $< 0.799 \times 10^{-3}$ mm^2/s was <1 year. Multivariate analysis revealed that patient age, relative CBV, and ADC values were associated with survival independent of pathology. The preoperative model provides greater ability to predict survival than that obtained by histologic grade alone.

CONCLUSIONS: ADC values had a better correlation with overall survival than relative CBV values. A preoperative prognostic model based on patient age, relative CBV, and ADC values predicted overall survival of patients with diffuse gliomas independent of pathology. This preoperative model provides a more accurate predictor of survival than histologic grade alone.

ABBREVIATION: rCBV = relative cerebral blood volume

Diffuse gliomas are the second most common primary CNS neoplasms, behind meningiomas, and account for roughly 80% of primary malignant brain tumors.[1-3]

Diffuse gliomas are a heterogeneous group of neoplasms classified according to the World Health Organization system as grades II–IV on the basis of histologic features, including cell density nuclear atypia, mitotic activity, endothelial proliferation, and necrosis.[3,4] The prognosis for these tumors is determined mainly by histologic grade,[3] with a median survival of approximately 3 years for anaplastic astrocytoma and 1 year for glioblastoma.[5] However, it has been shown that histologic classification of gliomas remains insufficient due to its lack of precision in terms of prognosis.[6] This classification for phenotype determination and grade is also subjective due to the fact that 1 histologic subtype could comprise different molecular subtypes with different prognoses.[6] In recent years, extensive molecular studies[7] have identified diagnostic and prognostic markers in gliomas that support the World Health Organization histologic classification.[4] 1p19q codeletion, methylation of the O^6-methylguanine DNA methyltransferase gene promoter, and *isocitrate dehydrogenases 1* and *2* gene mutations are the 3 most important markers in diffuse gliomas and may influence the sensitivity of these tumors to treatment.[4]

The role of neuroimaging has been widely studied in the literature, not only in the preoperative grading of diffuse gliomas[8] but also in the determination of tumor response to treatment or tu-

mor progression.[9] However, the results about the utility of imaging techniques have been mixed, especially those in diffusion and perfusion MR imaging, in the determination of the prognosis of diffuse gliomas. The purposes of our study were as follows: 1) to evaluate the relationship of relative cerebral blood volume (rCBV) and ADC values to overall survival in a group of patients with histologically confirmed diffuse gliomas, and 2) to establish a prognostic model based on preoperative MR imaging findings that could predict overall survival regardless of histology.

MATERIALS AND METHODS
Study Population
We conducted a retrospective analysis of the preoperative MR imaging findings of 126 diffuse gliomas, which were histologically confirmed by surgical resection or stereotactic biopsy.

The patients were selected from a larger group of 162 consecutive patients with diffuse gliomas admitted to our hospital during a 4-year period (2006–2010). Inclusion criteria were preoperative diffusion and perfusion MR imaging data suitable for evaluation and histologic diagnosis. Thirteen patients were excluded for incomplete follow-up (they did not continue at our institution). Another 23 patients were rejected because they underwent radiation therapy or chemotherapy before inclusion in the study. For histopathologic diagnosis, the samples were analyzed individually by 2 neuropathologists and were classified as low-grade (grade II) and high-grade (grades III and IV) according to the *2007 World Health Organization Classification of Tumors of the Central Nervous System*.[10] In all cases, patient treatment after histologic diagnosis was decided in the multidisciplinary neuro-oncology unit of our hospital on the basis of standard management (National Comprehensive Cancer Network guidelines for the treatment of the CNS cancers; www.nccn.org).

Perfusion MR Imaging Protocol and Processing
All patients were examined with the same imaging acquisition protocol on a 1.5T MR imaging system (Signa Excite; GE Healthcare, Milwaukee, Wisconsin) by using an 8-channel head coil. After an initial loading dose of 2-mL gadobutrol[11] (Gadovist, 1 mmol/mL; Berlex Laboratories, Wayne, New Jersey), dynamic contrast-enhanced T2*-weighted perfusion MR imaging was performed by using a gradient-echo echo-planar imaging acquisition during the first pass of a bolus of gadobutrol. Nineteen sections were selected for perfusion MR imaging to cover the tumor on the basis of T2-weighted fast spin-echo (TR = 4100 ms, TE = 85 ms) or FLAIR (TR = 8000 ms, TE = 120 ms, TI = 2000 ms) images. Imaging parameters were as follows: TR/TE = 2000/21.1 ms, FOV = 26 × 26 cm, section thickness = 4 mm with a 0.4-mm skip, matrix =128 × 128, flip angle = 90°. A series of 40 multisection acquisitions was acquired at 0.2-second intervals; the total acquisition time was 1 minute 21 seconds. The first 8 acquisitions were performed before the contrast agent injection to establish a precontrast baseline. At the eighth acquisition, 0.1 mmol/kg of body weight of gadobutrol was injected with a power injector (Spectris Solaris EP; Medrad, Indianola, Pennsylvania) at a rate of 5 mL/s through an 18-gauge intravenous catheter, immediately followed by a bolus injection of saline at the same rate for a total of 20 mL.

The dynamic susceptibility-weighted contrast-enhanced MR perfusion images were processed on an Advantage Workstation by using FuncTool software (GE Healthcare). CBV maps were generated by calculating the change in relaxation rate ($\Delta R2^*$) by using the following equation: $\Delta R2^*(t) = -\log$ neperien$(S(t) / S_0) /$ time-echo, where $S(t)$ is the signal intensity at time t and S_0 is the baseline (precontrast) signal intensity. Because the CBV must be expressed relative to an internal reference, we normalized it by expressing ratios relative to values measured in the normal white matter of the contralateral lobe. We have referred to these relative values as rCBV. On the color-coded rCBV maps, 2 neuroradiologists (5 and 9 years of clinical experience in perfusion MR imaging) placed multiple ROIs to cover the entire tumor area, which was defined on the basis of T2/FLAIR or postgadolinium abnormality. The maximum rCBV value was therefore selected for quantitative analysis by consensus between the 2 neuroradiologists. The standardized region of interest was 2–3 mm², which was used for most of the tumor and white matter measurements. Care was taken not to include large intra- or peritumoral vessels because these can confound perfusion measurements. This method has been demonstrated to provide the most optimal interobserver and intraobserver reproducibility.[12]

Diffusion MR Imaging Protocol and Data Evaluation
The diffusion-weighted imaging included an axial single-shot spin-echo echo-planar sequence with the following parameters: TR/TE = 8000/78.2 ms, section thickness = 5 mm, number of sections = 26, acquisition matrix = 128 × 128, FOV = 26 × 26 cm, b-values of 0 and 1000 s/mm², diffusion gradient encoding in 6 orthogonal directions, and a total scanning time of 1 minute 4 seconds.

Postprocessing of ADC maps was performed by using commercially available FuncTool software (Advantage Workstation). ADC measurements were obtained by placing multiple ROIs (area ranging from 1 to 2 mm²) over the whole tumor, which was defined on the basis of FLAIR/T2 or postgadolinium abnormality. By visual inspection, ROIs were placed on areas showing the lowest intratumoral ADC, and then the minimum ADC value was selected for quantitative analysis by consensus between the 2 neuroradiologists. In comparison with susceptibility imaging, care was taken not to include intralesional blood products that would significantly decrease ADC values. ADC values were expressed as 10^{-3} mm²/s.

Statistical Analysis
The end point of the study was overall survival, which was evaluated from the date of initial diagnosis to death or, for living patients, from diagnosis to the last available follow-up. Median maximum rCBV and minimum ADC values were selected as the cutoff values for quantitative analysis. Histology, rCBV, and ADC values were first evaluated univariately by constructing probability curves according to the Kaplan-Meier method and by comparing them with the log-rank test. A P value < .05 indicated a statistically significant difference.

Radiologic variables achieving a P value < .05 in the univariate analysis, together with age and histology, were subsequently introduced in a multivariable stepwise proportional hazards regression analysis (Cox model) to identify a set of features indepen-

dently associated with survival. From the data obtained from multivariable analysis, we proposed a preoperative prognostic model based on patient age and MR imaging findings that could predict overall survival in diffuse gliomas.

Furthermore, the predictive power of survival models built with preoperative factors (age and MR imaging findings), postoperative factors (age, MR imaging findings, and histologic grade), and histologic grade alone was compared for obtaining Harrell C and Somers D parameters.[13] These parameters were proposed as measures of the general predictive power of general regression models by Harrell et al.[14] The Somers D is the probability that when 1 of 2 subjects is observed to survive another, the survivor has the lower of the 2 hazard ratios predicted by the model, rather than the survivor having the higher of the 2 predicted hazard ratios. The Harrell C is the probability that the survivor has the lower hazard ratio plus half the probability that the 2 subjects have equal hazard ratios. Univariate and multivariate analyses were both performed for the whole series ($n = 126$). All calculated P values were 2-sided. Statistical analysis was performed by using the Statistical Package for the Social Sciences, Version 12 software (IBM, Armonk, New York) and by using STATA 12 (StataCorp, College Station, Texas).

RESULTS
Patient Population
The study included 80 male and 46 female patients. Within this group of 126 diffuse gliomas, the median age at diagnosis was 53.4 years. Samples for histologic diagnosis were obtained by surgical resection in 84 patients (66.7%) and by stereotactic biopsy in the remaining 33.3% ($n = 42$). According to histologic analysis, our series comprised 26 low-grade (20.6%) and 100 high-grade gliomas (79.4%). We included 95 astrocytomas and 31 oligodendroglial tumors. The histopathologic diagnoses are presented in Table 1. The median follow-up was 14.5 months (range, 0–76 months between January 2006 and February 2012, with a median follow-up of 36 months for living patients). Four patients died

within the first 3 weeks after surgery as a result of cerebral edema ($n = 3$) and multiple organ dysfunction syndrome ($n = 1$). Tables 2 and 3 summarize the treatment of patients classified according to tumor grade, rCBV, and ADC values.

Univariate Survival Analysis
The Kaplan-Meier overall survival curves for diffuse gliomas classified by tumor grade are shown in Fig 1. Histologic diagnosis had a significant influence on survival, with a median survival of 50 months for patients with grade III gliomas and 10 months (95% CI, 6.87–13.12 months) for grade IV tumors. At the end of follow-up, patients with grade II gliomas had not reached median overall survival. Significant differences were observed among the 3 tumor grades ($P < .001$).

Median maximum rCBV and minimum ADC values were 5.195 and 0.799×10^{-3} mm^2/s, respectively. Relative cerebral blood volume correlated significantly with survival as shown in Fig 2: Median survival was 11 months (95% CI, 7.543–14.457 months) for tumors with rCBV $\geq$ 5.195 and 50 months (95% CI, 13.869–86.131 months) for tumors with perfusion values lower than the median maximum rCBV ($P < .001$). Kaplan-Meier estimates of survival indicated that patients with an rCBV < 5.195 had a significantly better overall survival.

The Kaplan-Meier overall survival curves for diffuse gliomas classified by ADC are shown in Fig 3. Apparent diffusion coefficient had a significant influence on survival, even better than rCBV. The group of gliomas with minimum ADC < 0.799×10^{-3} mm^2/s had a median survival time of 8 months (95% CI, 5.194–10.806 months). At the end of the follow-up, patients with ADC $\geq 0.799 \times 10^{-3}$ mm^2/s had not reached median overall survival. Significant differences in overall survival were observed in diffuse gliomas classified by median minimum ADC ($P < .001$). Our results also predicted that the median survival for diffuse gliomas with ADC values lower than 0.799×10^{-3} mm^2/s is <12 months. Table 4 summarizes the P values for all variables evaluated by the univariate analysis.

As can be seen in Table 5, we also evaluated the median overall survival for the different histologic grades classified according to the rCBV and ADC values. In patients with low-grade tumors, ADC had a stronger correlation to survival than rCBV.

Table 1: Histopathologic diagnosis distributed by tumor grade

Histology	Grade II	Grade III	Grade IV	Total
Astrocytomas	15 (11.9%)	7 (5.6%)	73 (57.9%) (GBM)	95 (75.4%)
Oligodendrogliomas	8 (6.3%)	10 (7.9%)		18 (14.2%)
Oligoastrocytomas	3 (2.4%)	3 (2.4%)	7 (5.6%) (GBM-O)	13 (10.4%)
Total	26 (20.6%)	20 (15.9%)	80 (63.5%)	126 (100%)

Note:—GBM indicates glioblastoma multiforme; GBM-O, glioblastoma with oligoastrocytoma grade IV.

Table 2: Treatment of patients classified by histologic grade, rCBV, and ADC values

Histologic Grade	No Adjuvant Therapy	Radiotherapy	Chemotherapy (TMZ)	Chemoradiotherapy	Total
Grade II	7 (5.6%)	2 (1.6%)	14 (11.2%)	7 (5.6%)	24%
Grade III	1 (0.8%)	0 (0%)	6 (4.8%)	11 (8.8%)	14.4%
Grade IV	13 (10.4%)	0 (0%)	2 (1.6%)	63 (49.6%)	61.6%
Total	16.8%	1.6%	17.6%	64%	100%
rCBV values					
rCBV $\geq$ 5.195	11 (8.7%)	0 (0.0%)	4 (3.2%)	48 (38.1%)	50%
rCBV < 5.195	11 (8.7%)	2 (1.6%)	18 (14.3%)	32 (25.4%)	50%
Total	17.5%	1.6%	17.5%	63.5%	100%
ADC values					
ADC < 0.799×10^{-3} mm^2/s	13 (10.3%)	0 (0.0%)	3 (2.3%)	47 (37.4%)	50%
ADC $\geq 0.799 \times 10^{-3}$ mm^2/s	8 (6.4%)	2 (1.6%)	19 (15%)	34 (27%)	50%
Total	16.7%	1.6%	17.3%	64.4%	100%

Note:—TMZ indicates temozolomide.

Table 3: Salvage therapy classified by histologic grade, ADC and rCBV values

	Salvage Surgery	Additional Chemotherapy
Grade II	6 (4.8%)	1 (0.8%)
Grade III	2 (1.6%)	2 (1.6%)
Grade IV	11 (8.7%)	15 (12%)
Total	19 (15.1%)	18 (14.4%)
rCBV $\geq$ 5.195	8 (6.3%)	11 (8.7%)
rCBV < 5.195	11 (8.7%)	7 (5.7%)
Total	19 (15.1%)	18 (14.4%)
ADC < 0.799×10^{-3} mm²/s	10 (8%)	12 (9.6%)
ADC $\geq$ 0.799×10^{-3} mm²/s	9 (7.1%)	6 (4.8%)
Total	19 (15.1%)	18 (14.4%)
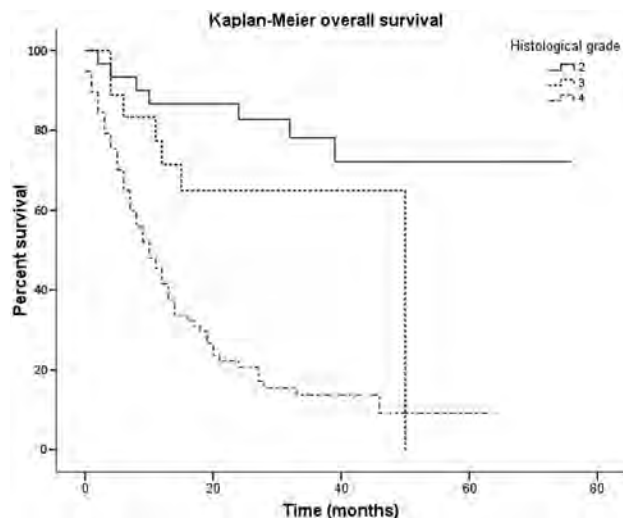
FIG 1. Kaplan-Meier survival curves of 126 diffuse gliomas show overall survival to be concordant with histologic grade. Low-grade gliomas had the longest overall survival, followed by grade III and IV tumors.

Multivariate Survival Analysis

We also combined the favorable imaging variables ($P < .05$) with patient age and histology in a multivariate Cox regression analysis, which demonstrated that age, ADC, and rCBV values were independent predictors of survival. Determining imaging characteristics that may predict survival is a challenge in neuro-oncology. We can then set a preoperative prognostic model for diffuse gliomas based on ADC, rCBV, and patient age that predicts overall survival independent of pathology. Table 6 summarizes the multivariate associations of variables with survival in the whole series. Table 7 compares the predictive value of different possible multivariate Cox regression models built with pre- and postoperative factors. The preoperative model had a similar predictive power to that obtained postoperatively by using histologic information. Preoperative information presents greater predictive ability of survival than that obtained by histologic grade alone.

DISCUSSION

The management of diffuse gliomas has undergone many changes during the past 2 decades, with novel approaches to surgery, radiation, and chemotherapy improving survival and quality of life for patients.[2] With regard to surgery, a more extensive surgical resection has been associated with longer life expectancy for both low- and high-grade newly diagnosed gliomas.[15] On the other
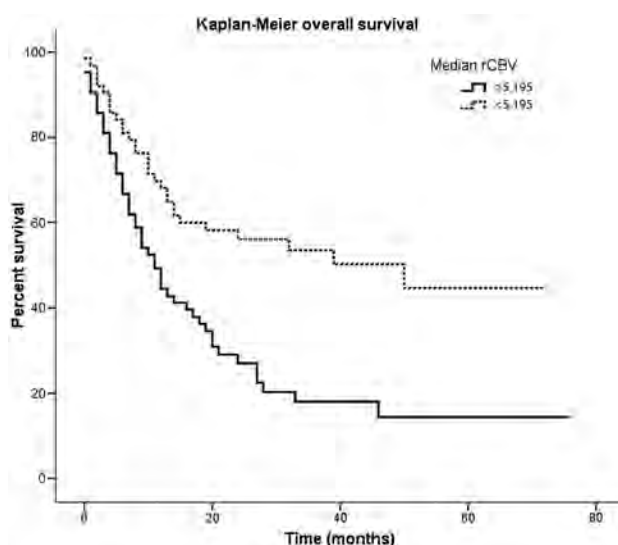
FIG 2. Kaplan-Meier survival curves of 126 patients with diffuse gliomas. Survival curves are plotted according to the classification based on median rCBV values. Relative cerebral blood volume has a significant influence on overall survival, with a median survival of 11 months for tumors with perfusion values lower than the median rCBV.
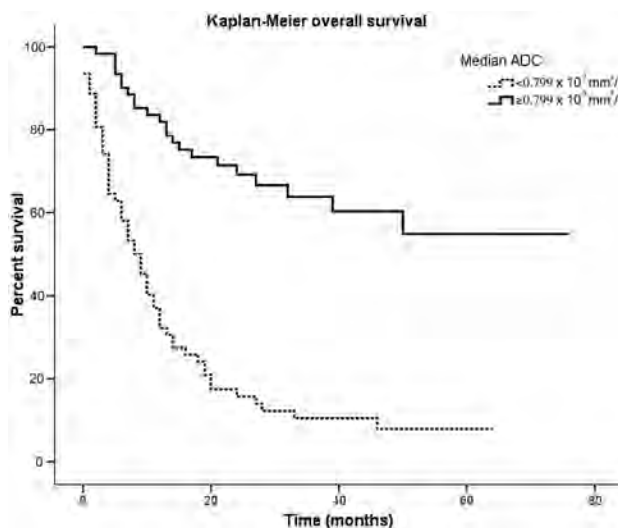
FIG 3. Overall survival calculated by using Kaplan-Meier curves for all patients stratified by median ADC values. Apparent diffusion coefficient has a significant influence on survival, even better than rCBV. In our series, the median survival for diffuse gliomas with ADC values lower than 0.799×10^{-3} mm²/s was <12 months.

hand, knowledge about the molecular biology of CNS gliomas has provided a dynamic classification of tumors that helps determine prognosis and the likelihood of a therapeutic response.[2]

The role of imaging techniques has also changed significantly during the past few years. First, several studies[8,16] have demonstrated that ADC and rCBV values could serve as a noninvasive method of approximating tumor grade in diffuse gliomas. Second, researchers in several studies[17,18] have proved the utility of rCBV in the prediction of median time to progression and propensity for malignant transformation. In view of the findings of these studies, we have gone a step further by evaluating the relationship between rCBV and ADC values and overall survival in a large group of 126 histologically confirmed diffuse gliomas. In this article, we have also

attempted to create a preoperative prognostic model able to predict overall survival independent of pathology.

When selecting the rCBV and ADC cutoff values, we found discrepancies among previously published reports. Those differences found in rCBV values may be due to the use of a loading dose of contrast, the preload-postprocessing algorithm, and the use of sophisticated tools of segmentation instead of the region-of-interest-approach.[19,20] Traditional region-of-interest measurements of rCBV remain the preferred technique for perfusion analysis in that they show the highest correlation to tumor grade.[21] However, it has been demonstrated that the histogram method has an advantage over the region-of-interest-approach, an operator-dependent method, in the assessment of tumor response to treatment, especially with angiogenesis inhibitors.[21] Law et al[18] used an rCBV value of 1.74 to predict median time to progression in a group of 189 diffuse gliomas. On the other hand, Zacharaki et al[5] performed a survival analysis of patients with high-grade gliomas based on mean rCBV and ADC values. For the MR imaging analysis, the threshold values selected in our study were median rCBV and ADC, similar to those used by Saraswathy et al,[22] for assessing MR imaging markers that predict survival in patients with glioblastoma before adjuvant therapy.

In our series, we have confirmed the relationship between histologic diagnosis and survival in diffuse gliomas. The median survival of 50 months for the grade III gliomas and 10 months for the grade IV tumors is similar to that published previously in the literature by Labussiere al[4] and DeAngelis.[23]

We have also demonstrated that perfusion and diffusion imaging have a significant influence on the survival of patients with diffuse gliomas. The overall survival of those patients with tumors differed significantly depending on the ADC and rCBV values. Not only did the lower ADC and higher rCBV values correlate with a worse prognosis but the median overall survival for patients with ADC $< 0.799 \times 10^{-3}$ mm^2/s was <1 year.

However, the most important conclusion that can be drawn from our data is that minimum ADC and maximum rCBV values predict overall survival regardless of histologic grade. This finding represents an advance in the understanding of gliomas, postulating ADC and rCBV as potential biomarkers for survival.

The relationship of ADC to survival is based on the assumption that water diffusivity within the extracellular component is inversely related to the content and attenuation of the intracellular space.[24] Quantitative information of the restriction of water molecule movement can be observed by calculating the ADC values from DWI.[25] Thus, brain neoplasms with higher cellularity or with higher grades show a significant reduction in ADC values.[26] These results support the findings, in a group of 39 high-grade gliomas, previously published by Hamstra et al,[27] who reported that tumor assessment based on functional diffusion maps provides an early biomarker for response, time to progression, and overall survival in patients in malignant gliomas. Recently, Pope et al[28,29] demon-

Table 4: Summary of univariate associations with survival in the whole series

Prognostic Factor	Univariate Analysis		
	Hazard Ratio	95% CI	P Value
Patient age	1.062	1.042–1.082	<.001
rCBV median ≥ 5.195	2.238	1.419–3.531	.001
ADC median < 0.799 × 10^{-3} mm^2/s	4.766	2.882–7.883	<.0001
Histologic grade (ref grade II)			<.0001
Grade III	2.411	0.838–6.934	.0103
Grade IV	7.611	3.418–16.944	<.0001

Note:—ref indicates reference.

Table 5: Median overall survival for histologic grades classified according to the rCBV and ADC values

	No. (%)	Median Overall Survival (mo)	95% CI
Grade II + ADC < 0.799 × 10^{-3} mm^2/s	3 (2.4)	4	0.799–7.201
Grade II + ADC ≥ 0.799 × 10^{-3} mm^2/s	23 (18.2)	–	–
Grade III + ADC < 0.799 × 10^{-3} mm^2/s	7 (5.6)	6	1.706–10.294
Grade III + ADC ≥ 0.799 × 10^{-3} mm^2/s	13 (10.3)	50	–
Grade IV + ADC < 0.799 × 10^{-3} mm^2/s	58 (46)	9	6.307–11.693
Grade IV + ADC ≥ 0.799 × 10^{-3} mm^2/s	22 (17.5)	17	6.152–27.848
Grade II + rCBV ≥ 5.195	0 (0)	–	–
Grade II + rCBV < 5.195	26 (20.6)	–	–
Grade III + rCBV ≥ 5.195	5 (4)	11	–
Grade III + rCBV < 5.195	15 (11.9)	50	–
Grade IV + rCBV ≥ 5.195	59 (46.8)	10	6.301–13.699
Grade IV + rCBV < 5.195	21 (16.7)	10	5.639–14.361

Note:— – indicates that at the end of follow-up, patients had not reached median overall survival.

Table 6: Summary of multivariate associations with survival in the whole series ($n = 126$)

Prognostic Factor	Multivariate Analysis		
	Hazard Ratio	95% CI	P Value
Patient age	1.054	1.031–1.077	<.001
rCBV median ≥ 5.195	1.608	0.928–2.784	.090
ADC median < 0.799 × 10^{-3} mm^2/s	2.339	1.291–4.240	.005
Histologic grade (ref grade II)			.027
Grade III	1.484	0.495–4.449	.481
Grade IV	3.538	1.328–9.427	.012

Note:—ref indicates reference.

Table 7: Comparison of predictive performance of different Cox survival models built with prognostic factors obtained pre- and postoperatively

Prognostic Models	Harrell C	95% CI	Somers D	95% CI
Preoperative (age, rCBV median ≥ 5.195, ADC median < 0.799 × 10^{-3} mm^2/s)	0.77	0.71–0.83	0.61	0.45–0.77
Postoperative (age, rCBV median ≥ 5.195, ADC median < 0.799 × 10^{-3} mm^2/s, histologic grade)	0.78	0.72–0.84	0.64	0.48–0.81
Histologic grade	0.67	0.61–0.73	0.35	0.22–0.48

strated the relevance of ADC values in the management of gliomas. These authors showed that pretreatment ADC histogram analysis could stratify progression-free and overall survival in patients with newly diagnosed and recurrent glioblastomas treated with bevacizumab. Regarding these articles,[27-29] our work contributes, as an innovation, the inclusion of low- and high-grade tumors in evaluating the relationship between ADC values and overall survival.

The association of rCBV with survival is based on the theory that vascular proliferation defines the biologic aggressiveness of gliomas and is considered a very important factor in histopathologic grading.[24,30] CBV measurements correlate with tumor grade and histologic findings of increased tumor vascularity. Because higher vascularity corresponds to a higher tumor grade, as the grade of astrocytoma increases, the maximal tumor CBV tends to increase.[24,31] Law et al[18] demonstrated in 2008 that dynamic susceptibility-weighted contrast-enhanced MR perfusion imaging could be used to predict median time to progression in patients with gliomas, independent of pathology. However, in that series, it was found that rCBV was not significantly associated with overall survival ($P > .63$). Our results differ from those published by Law et al,[18] demonstrating that rCBV has a significant influence on overall survival of patients with gliomas. Both series comprised a large number of patients (126 versus 189), but the reason for the opposite results may be the inclusion of a greater percentage of grade II tumors in the series of Law et al.[18] Our results are also in disagreement with those published by Zacharaki et al,[5] who reported that region of interest–based characteristics in rCBV were not among the top-ranked variables for predicting survival in high-grade gliomas. An explanation for the differing results could be differences in the study population. Zacharaki et al included only high-grade tumors, which have generally increased rCBV on perfusion MR imaging.

As seen above, ADC and rCBV values may be considered MR imaging markers that predict survival in diffuse gliomas, which may be important for stratifying patients to different treatment protocols. For this reason, one of the goals of our study was the design of a preoperative model able to predict prognosis in diffuse gliomas. Zacharaki et al[5] reported recently that prediction models based on machine-learning algorithms provide a more accurate predictor of prognosis in malignant gliomas than does histopathologic classification alone. Our research is similar to that of Zacharaki et al and presented, in a larger series (126 versus 67), the design of a more simple prognostic model based on patient age, ADC, and rCBV values capable of predicting survival in diffuse gliomas independent of pathology. We have also demonstrated that the preoperative model provides greater predictive ability of survival than that obtained by histologic grade alone.

There are some limitations to our study. First, the major one is that it was performed retrospectively in a heterogeneous group that included astrocytomas and oligodendroglial tumors of any grade. A second potential limitation was the possible subjectivity and reproducibility of a region of interest–based technique for rCBV and ADC measurements. Finally, it is likely that improvement in the current World Health Organization classification with incorporation of molecular markers, as well as imaging biomarkers of outcome, will predict future understanding of glioma biology and therapy.

CONCLUSIONS

ADC values had a significant influence on overall survival, even better than rCBV, with a median time of 8 months for the group of gliomas with ADC $< 0.799 \times 10^{-3}$ mm^2/s. A preoperative prognostic model based on patient age, rCBV, and ADC values predicts overall survival of diffuse gliomas independent of pathology. This preoperative model provides greater predictive ability of survival than does histologic grade alone.

REFERENCES

1. Bondy ML, Scheurer ME, Malmer B, et al. **Brain tumor epidemiology: consensus from the brain tumor epidemiology consortium (BTEC).** *Cancer* 2008;113:1953–68
2. Jansen M, Yip S, Louis DN. **Molecular pathology in adult gliomas: diagnostic, prognostic and predictive markers.** *Lancet Neurol* 2010;9:717–26
3. Theeler BJ, Yung WK, Fuller GN, et al. **Moving toward molecular classification of diffuse gliomas in adults.** *Neurology* 2012;79: 1917–26
4. Labussiere M, Wang XW, Idbaih A, et al. **Prognostic markers in gliomas.** *Future Oncol* 2010;6:733–39
5. Zacharaki EI, Morita N, Bhatt P, et al. **Survival analysis of patients with high-grade gliomas based on data mining of imaging variables.** *AJNR Am J Neuroradiol* 2012;33:1065–71
6. Ducray F, El Hallani S, Idbaih A. **Diagnostic and prognostic markers in gliomas.** *Curr Opin Oncol* 2009;21:537–42
7. Yan H, Parsons DW, Jin G, et al. **IDH1 and IDH2 mutations in gliomas.** *N Engl J Med* 2009;360:765–73
8. Hilario A, Ramos A, Perez-Nuñez A, et al. **The added value of apparent diffusion coefficient to cerebral blood volume in the preoperative grading of diffuse gliomas.** *AJNR Am J Neuroradiol* 2012;33:701–07
9. Caroline I, Rosenthal MA. **Imaging modalities in high-grade gliomas: pseudoprogression, recurrence, or necrosis?** *J Clin Neurosci* 2012;19:633–37
10. Louis DN, Ohgaki H, Wiestler OD, et al, eds. *2007 WHO Classification of Tumours of the Central Nervous System.* 4th ed. Lyon, France: IARC Press; 2007
11. Lacerda S, Law M. **Magnetic resonance perfusion and permeability imaging in brain tumors.** *Neuroimaging Clin N Am* 2009;19:527–57
12. Wetzel SG, Cha S, Johnson G, et al. **Relative cerebral blood volume measurements in intracranial mass lesions: interobserver and intraobserver reproducibility study.** *Radiology* 2002;224:797–803
13. Newson R. **Confidence intervals for rank statistics: Somers's D and extensions.** *Stata J* 2006;6:308–34
14. Harrell FE Jr, Lee KL, Mark DB. **Multivariate prognostic models: issues in developing models, evaluating assumptions and adequacy, and measuring and reducing errors.** *Stat Med* 1996;15:361–87
15. Hardesty DA, Sanai N. **The value of glioma extent of resection in the modern neurosurgical era.** *Front Neurol* 2012;3:140–47
16. Law M, Yang S, Babb JS, et al. **Comparison of cerebral blood volume and vascular permeability from dynamic susceptibility contrast-enhanced perfusion MR imaging with glioma grade.** *AJNR Am J Neuroradiol* 2004;25:746–55
17. Law M, Oh S, Babb JS, et al. **Low-grade gliomas: dynamic suscepti-**

bility-weighted contrast-enhanced perfusion MR imaging: prediction of patient clinical response. *Radiology* 2006;238:658–67

18. Law M, Young RJ, Babb JA, et al. **Gliomas: predicting time to progression or survival with cerebral blood volume measurements at dynamic susceptibility-weighted contrast-enhanced perfusion MR imaging.** *Radiology* 2008;247:490–98

19. Boxerman JL, Prah DE, Paulson ES, et al. **The role of preload and leakage correction in gadolinium-based cerebral blood volume estimation determined by comparison with MION as a criterion standard.** *AJNR Am J Neuroradiol* 2012;33:1081–87

20. Paulson ES, Schmainda KM. **Comparison of dynamic susceptibility-weighted contrast-enhanced MR methods: recommendations for measuring relative cerebral blood volume in brain tumors.** *Radiology* 2008;249:601–13

21. Law M, Young R, Babb J, et al. **Histogram analysis versus region of interest analysis of dynamic susceptibility contrast perfusion MR imaging data in the grading of cerebral gliomas.** *AJNR Am J Neuroradiol* 2007;28:761–66

22. Saraswathy S, Crawford FW, Lamborn KR, et al. **Evaluation of MR markers that predict survival in patients with newly diagnosed GBM prior to adjuvant therapy.** *J Neurooncol* 2009;91:69–81

23. DeAngelis LM. **Brain tumors.** *N Engl J Med* 2001;344:114–23

24. Cha S. **Update on brain tumor imaging: from anatomy to physiology.** *AJNR Am J Neuroradiol* 2006;27:475–87

25. Kono K, Inoue Y, Nakayama K, et al. **The role of diffusion-weighted imaging in patients with brain tumors.** *AJNR Am J Neuroradiol* 2001;22:1081–88

26. Sugahara T, Korogi Y, Kochi M, et al. **Usefulness of diffusion-weighted MRI with echo-planar technique in the evaluation of cellularity in gliomas.** *J Magn Reson Imaging* 1999;9:53–60

27. Hamstra DA, Chenevert TL, Moffat BA, et al. **Evaluation of the functional diffusion map as an early biomarker of time-to-progression and overall survival in high-grade glioma.** *Proc Natl Acad Sci U S A* 2005;102:16759–64

28. Pope WB, Lai A, Mehta R, et al. **Apparent diffusion coefficient histogram analysis stratifies progression-free survival in newly diagnosed bevacizumab-treated glioblastoma.** *AJNR Am J Neuroradiol* 2011;32:882–89

29. Pope WB, Qiao XJ, Kim HJ, et al. **Apparent diffusion coefficient histogram analysis stratifies progression-free and overall survival in patients with recurrent GBM treated with bevacizumab: a multicenter study.** *J Neurooncol* 2012;108:491–98

30. Hakyemez B, Erdogan C, Ercan I, et al. **High-grade and low- grade gliomas: differentiation by using perfusion MR imaging.** *Clin Radiol* 2005;60:493–502

31. Sadeghi N, D'Haene N, Decaestecker C, et al. **Apparent diffusion coefficient and cerebral blood volume in brain gliomas: relation to tumor cell density and tumor microvessel density based on stereotactic biopsies.** *AJNR Am J Neuroradiol* 2008;29:476–82

Glioma: Application of Histogram Analysis of Pharmacokinetic Parameters from T1-Weighted Dynamic Contrast-Enhanced MR Imaging to Tumor Grading

S.C. Jung, J.A. Yeom, J.-H. Kim, I. Ryoo, S.C. Kim, H. Shin, A.L. Lee, T.J. Yun, C.-K. Park, C.-H. Sohn, S.-H. Park, and S.H. Choi

ABSTRACT

BACKGROUND AND PURPOSE: The usefulness of pharmacokinetic parameters for glioma grading has been reported based on the perfusion data from parts of entire-tumor volumes. However, the perfusion values may not reflect the entire-tumor characteristics. Our aim was to investigate the feasibility of glioma grading by using histogram analyses of pharmacokinetic parameters including the volume transfer constant, extravascular extracellular space volume per unit volume of tissue, and blood plasma volume per unit volume of tissue from T1-weighted dynamic contrast-enhanced perfusion MR imaging.

MATERIALS AND METHODS: Twenty-eight patients (14 men, 14 women; mean age, 49.75 years; age range, 25–72 years) with histopathologically confirmed gliomas (World Health Organization grade II, $n = 7$; grade III, $n = 8$; grade IV, $n = 13$) were examined before surgery or biopsy with conventional MR imaging and T1-weighted dynamic contrast-enhanced perfusion MR imaging at 3T. Volume transfer constant, extravascular extracellular space volume per unit volume of tissue, and blood plasma volume per unit volume of tissue were calculated from the entire-tumor volume. Histogram analyses from these parameters were correlated with glioma grades. The parameters with the best percentile from cumulative histograms were identified by analysis of the area under the curve of the receiver operating characteristic analysis and were compared by using multivariable stepwise logistic regression analysis for distinguishing high- from low-grade gliomas.

RESULTS: All parametric values increased with increasing glioma grade. There were significant differences among the 3 grades in all parameters ($P < .01$). For the differentiation of high- and low-grade gliomas, the highest area under the curve values were found at the 98th percentile of the volume transfer constant (area under the curve, 0.912; cutoff value, 0.277), the 90th percentile of extravascular extracellular space volume per unit volume of tissue (area under the curve, 0.939; cutoff value, 19.70), and the 84th percentile of blood plasma volume per unit volume of tissue (area under the curve, 0.769; cutoff value, 11.71). The 98th percentile volume transfer constant value was the only variable that could be used to independently differentiate high- and low-grade gliomas in multivariable stepwise logistic regression analysis.

CONCLUSIONS: Histogram analysis of pharmacokinetic parameters from whole-tumor volume data can be a useful method for glioma grading. The 98th percentile value of the volume transfer constant was the most significant measure.

ABBREVIATIONS: AUC = area under the curve; DCE = dynamic contrast-enhanced; K^{trans} = volume transfer constant; ROC = receiver operating characteristic analysis; Ve = extravascular extracellular space volume per unit volume of tissue; Vp = blood plasma volume per unit volume of tissue

The growth of tumors beyond a certain size depends on the development of a vascular supply that meets the metabolic requirements of the neoplastic tissue.[1-4] Newly developed vascular networks of tumors show increased tortuosity, lack of maturity, and increased permeability to macromolecules due to the presence of large endothelial cell gaps.[5,6] In particular, high-grade gliomas are associated with a higher proportion of immature and hyperpermeable vessels.[7,8]

Angiogenesis and the microvascular system of gliomas have recently been the focus of grading before treatment and for evaluating posttherapy status with perfusion MR imaging. With con-

trast media, the dynamic change of signal intensity can be measured and converted into an analysis of perfusion changes. From the signal-time curves, many pharmacokinetic parameters can be extracted for the characterization of gliomas. Cerebral blood volume and cerebral blood flow, vascular permeability, and extravascular extracellular volume have been proposed as representative parameters derived from T1-weighted dynamic contrast-enhanced (DCE) perfusion-weighted imaging in the differentiation of glioma grades.[8-16] More recently, many reports based on T1-weighted DCE-PWI MR imaging have introduced volume transfer constant K^{trans}, extravascular extracellular space volume per unit volume of tissue (Ve), and blood plasma volume per unit volume of tissue (Vp) as feasible parameters for glioma grading.[8,10,17,18] K^{trans} and Ve are pharmacokinetic parameters well-known for reflecting permeability. K^{trans} is the volume transfer constant between the plasma and extravascular extracellular space. Ve is the extravascular extracellular space per unit volume of tissue and is known as leakage space.[19,20] Vp is defined as the blood plasma volume per unit volume of tissue, which may be a marker of angiogenic activity in a tumor.[13] However, previous studies collected the perfusion data from parts of entire-tumor volumes. Therefore, the presented values may not have reflected the entire tumor characteristics.

In this study, we obtained the pharmacokinetic parameters from the entire-tumor volume by using T1-weighted DCE MR images. We hypothesized that a histogram-based analysis of the pharmacokinetic parameters from the entire-tumor volume would be helpful for glioma grading because high-grade gliomas have a wide spectrum of histologic features, ranging from grade II to IV; this wide spectrum may account for sampling biases. The purposes of this study were to investigate the feasibility of using a histogram analysis of pharmacokinetic parameters, including K^{trans}, Ve, and Vp, for glioma grading and to explore the diagnostic performance of the histogram analysis of these parameters.

MATERIALS AND METHODS
This retrospective study was approved by our institutional review board. Patient informed consent was waived.

Patients
Between January 2010 and October 2012, fifty patients with initial DCE MR imaging at our institution (Seoul National University Hospital) were diagnosed with astrocytic tumors on the basis of the World Health Organization classification for tumors of the central nervous system. This study included 28 patients with the following inclusion criteria: 1) MR imaging was performed with a 3T scanner before treatment or biopsy; and 2) grade II, III, and IV gliomas were diagnosed. There were 14 male and 14 female patients enrolled (mean age, 49.75 years; age range, 25–72 years). In the enrolled patients, there were 28 gliomas (grade II, 7 gliomas; grade III, 8 gliomas; grade IV, 13 gliomas). Grade II gliomas were classified as low-grade, and grades III and IV were classified as high-grade.

MR Imaging Protocol
The MR imaging protocol consisted of conventional MR imaging and DCE MR imaging by using a 3T scanner with a 32-channel head coil (Magnetom Verio; Siemens, Erlangen, Germany). Conventional MR imaging included the following: T1-weighted imaging, such as transverse spin-echo imaging, before and after contrast enhancement; multiplanar reconstructed transverse, coronal imaging with a sagittal 3D magnetization-prepared rapid acquisition of gradient echo sequence, before and after contrast enhancement; transverse fluid-attenuated inversion recovery; and transverse T2-weighted imaging with turbo spin-echo sequences. Contrast-enhanced T1WI was performed after the intravenous administration of gadobutrol (Gadovist; Bayer Schering Pharma, Berlin, Germany), at a dose of 0.1 mmol/kg of body weight. Transverse spin-echo T1WI was performed with the following parameters: TR, 558 ms; TE, 9.8 ms; flip angle, 70°; matrix, 384 × 187; FOV, 175 × 220 mm; section thickness, 5 mm; and NEX, 1. We obtained the 3D-MPRAGE sequences by using the following parameters: TR, 1500 ms; TE, 1.9 ms; flip angle, 9°; matrix, 256 × 232; FOV, 220 × 250; section thickness, 1 mm; and NEX, 1. The parameters in axial FLAIR imaging were the following: TR, 9000 ms; TE, 97 ms; TI, 2500 ms; flip angle, 130°; matrix, 384 × 348; FOV, 199 × 220; and section thickness, 5 mm. The parameters of the transverse T2WI were as follows: TR, 5160 ms; TE, 91 ms; flip angle, 124°-130°; matrix, 640 × 510–580; FOV, 175–199 × 220; section thickness, 5 mm; and NEX, 3.

DCE MR imaging was performed with 3D gradient-echo T1WI after the intravenous administration of gadobutrol (0.1 mmol/kg of body weight) at a rate of 4 mL/s by using a power injector (Spectris MR injector; MedRad, Indianola, Pennsylvania). A 30-mL bolus injection of saline followed at the same injection rate. For each section, 40 images were acquired at intervals equal to the TR. The parameters were as follows: TR, 2.8 ms; TE, 1.0 ms; flip angle, 10°; matrix, 192 × 192; section thickness, 3 mm; FOV, 240 × 240 mm; voxel size, 1.25 × 1.25 × 3 mm³; pixel bandwidth, 789 Hz; total acquisition time, 1 minute 30 seconds.

Image Analysis
DCE MR images were processed by using the MR perfusion analysis method (nordicICE; Nordic Neuro Lab, Bergen, Norway), in which FLAIR or T2WI was used for structural imaging. On the basis of the 2-compartment pharmacokinetic model proposed by Tofts and Kermode,[21] we used the perfusion analysis method to calculate pharmacokinetic parameters, including K^{trans}, Ve, and Vp.[21] Deconvolution with the arterial input function was performed in the pharmacokinetic model. For each tumor, the arterial input function was determined in intracranial tumor-supplying arteries near the tumor. Perfusion analysis was able to generate an arterial input function curve and a concentration-time curve of the tumor for each tumor-supplying artery in a region of interest. Two neuroradiologists (S.C.J. and S.H.C.) manually defined the ROIs by consensus. They chose an appropriate arterial input function curve to show the ideal relationship between the input function curve and the concentration-time curve. The arterial input function curves had higher values than the concentration-time curves and showed rapid wash-in and slow washout patterns, whereas the concentration-time curves showed a steady increase in the wash-in slope. The baseline T1 value was fixed at 1000 ms in this study.[22]
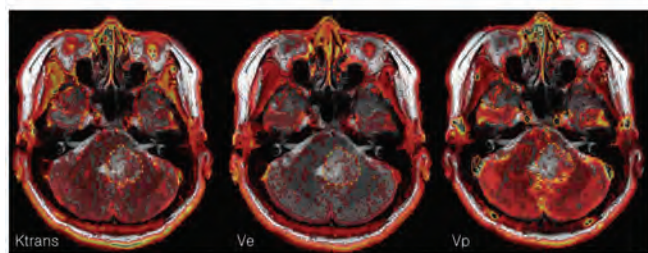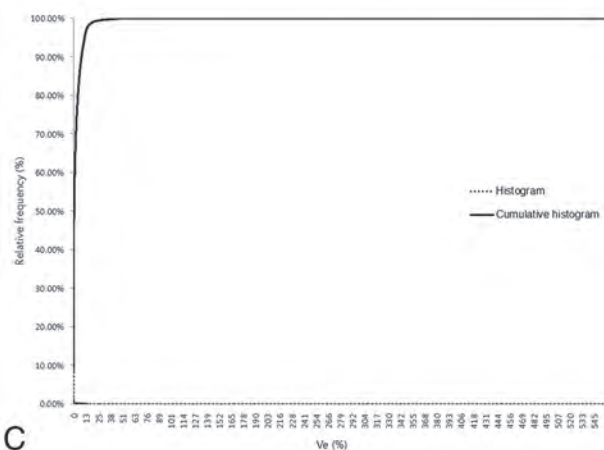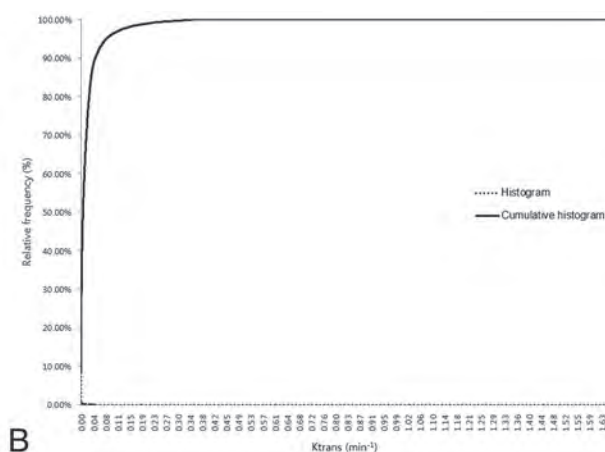
FIG 1. ROIs manually defined on axial T2WI coregistered with parametric maps in a 43-year-old woman with a grade II glioma (*A*) and the histogram and cumulative histogram from the entire-tumor volume (*B–D*) are presented.

Pharmacokinetic parameters, including K^{trans}, Ve, and Vp, were measured from each region of interest by a neuroradiologist (S.C.J.). The perfusion analysis method was used to calculate the pharmacokinetic parameters and to present these parameters as parametric maps. The coregistration between the structural images and parametric maps (color overlay) was accomplished automatically by using mutual information based on an algorithm that facilitated the search for an optimal rigid transformation aligning the 2 datasets.[23-25] The 2 reviewers defined the margins of the tumors on each axial plane by consensus, manually outlining the margins on the T2WI or FLAIR image by using the perfusion analysis workstation. The outline of the tumor region of interest was defined excluding the cystic or necrotic regions and intralesional macrovessels (Figs 1*A*, 2*A*, and 3*A*). On a pixel-by-pixel basis, all values of the parameters were calculated from an outline (region of interest) on an axial plane. The overall values for each tumor were obtained by summing the values from every plane. Finally, the total parametric values from the entire-tumor volume were acquired and recorded for each tumor.

Statistical Analysis
Commercially available software (MedCalc for Windows, Version 11.1.1.0; MedCalc Software, Mariakerke, Belgium) was used for the analysis. The Kolmogorov-Smirnov test was used to determine whether values were normally distributed. For all statistical analyses, a 2-tailed *P* value < .05 was considered indicative of a statistically significant difference.

The mean and SD of the parametric values were calculated for each parameter. The values were compared according to the grade by using the unpaired *t* test.

The histograms were plotted with the parametric values on the x-axis, with a bin size of 1×10^{-4} min^{-1} for K^{trans}, 1×10^{-2} for Ve, and 1×10^{-2} for Vp. The relative frequency was plotted on the y-axis of the histograms as a percentage of the total tumor volume, calculated by dividing the frequency in each bin by the total number of pixels.[26] The ranges of the bins were chosen as 0–1.66 in K^{trans}, 0–5.5765 in Ve, and 0–0.7201 in Vp because 1.66, 5.5765, and 0.7201 were the highest values for each parameter, respectively. The cumulative histograms were built from the aforementioned histograms. The relative cumulative frequency on the y-axis was expressed as a percentage summating the relative frequency from the first bin to a specified bin, and the parametric values were plotted on the x-axis (Figs 1*B–D*, 2*B–D*, and 3*B–D*).

A corresponding parametric value to a specific one from the 50th percentile (C50) to the 100th percentile (C100) was calcu-
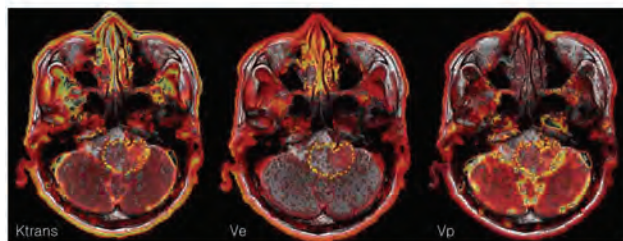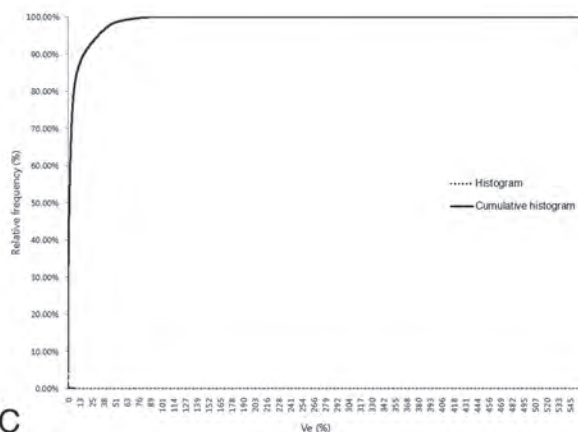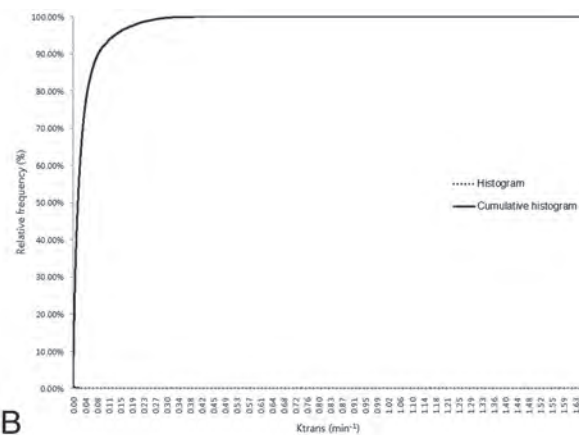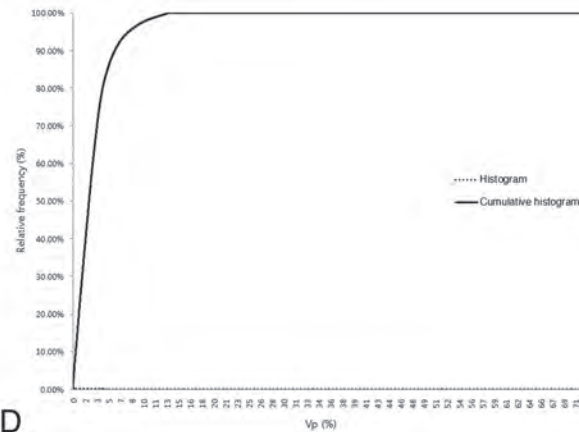
FIG 2. ROIs manually defined on axial T2WI coregistered with parametric maps in a 61-year-old man with a grade III glioma (*B*) and the histogram and cumulative histogram from the entire-tumor volume (*B–D*) are presented.

lated in each tumor and parameter. Receiver operating characteristic (ROC) curves were generated to determine the optimum cutoff percentile for distinguishing high-grade from low-grade gliomas and differentiating grade III and IV tumors. The area under the curve (AUC), obtained from ROC analysis according to a specific percentile from C50 to C100, was analyzed. The percentiles with the highest AUC and the cutoff values with the best diagnostic performances (highest sensitivity and specificity) were presented in each parameter. The parameters with the best percentile values were compared by using a multivariable stepwise logistic regression model to determine the best predictors for differentiating high- and low-grade gliomas.[27]

RESULTS

Mean K^{trans}, Ve, and Vp values are presented according to the tumor grade in Table 1. The pharmacokinetic parameters increased with increasing glioma grade. There were significant differences among the grades for all parameters ($P < .01$).

Histogram Analysis

The histograms and cumulative histograms from the entire-tumor volume showed that low-grade gliomas presented a higher relative frequency at low parametric values and a lower relative frequency at high parametric values compared with high-grade gliomas in all parameters. These characteristics resulted in substantial divergence according to grades in the cumulative histogram (Fig 4).

Optimal Cutoff Values of K^trans, Ve, and Vp for the Differentiation of High- and Low-Grade Gliomas

Between the C50 (median value) and C99 values from the cumulative K^{trans}, Ve, and Vp histograms, the K^{trans} of C98, Ve of C90, and Vp of C84 exhibited the highest AUCs—0.912, 0.939, and 0.769—for differentiating high- from low-grade gliomas.

We applied each cutoff value of K^{trans}, Vp, and Ve for the differentiation of high- and low-grade gliomas, so that tumors with values greater than or equal to the cutoff values were regarded as high-grade gliomas. In terms of K^{trans}, the cutoff value of C98 was 0.277 minute^{-1} and showed a sensitivity of 76.19% (16 of 21 high-grade gliomas) and a specificity of 100% (7 of 7 low-grade gliomas). The Ve cutoff value at C90 was 19.70% and had a sensitivity and a specificity of 85.7% (18 of 21 high-grade gliomas) and 100% (7 of 7 low-grade gliomas), respectively. We found that the Vp cutoff value at C84 was 11.71% and showed a sensitivity of 61.9% (13 of 21 high-grade gliomas) and a specificity of 100% (7 of 7 low-grade gliomas) (Table 2).

Optimal Cutoff Values of K^trans, Ve, and Vp for Differentiation of Grade II and III Gliomas

Between the C50 and C99 values from the cumulative K^{trans}, Vp, and Ve histograms, only Ve showed a significant parameter ($P < .05$) for differentiating grade III from grade II gliomas and the Ve C90 exhibited the highest AUCs: 0.839. The Ve C90 cutoff value was 19.7% with a sensitivity of 62.5% (5 of 8 grade III gliomas)
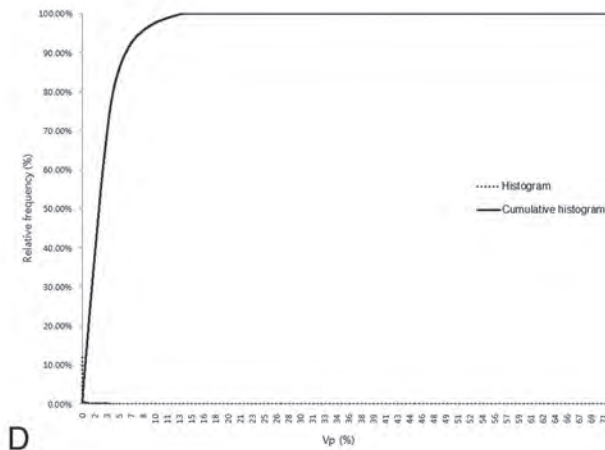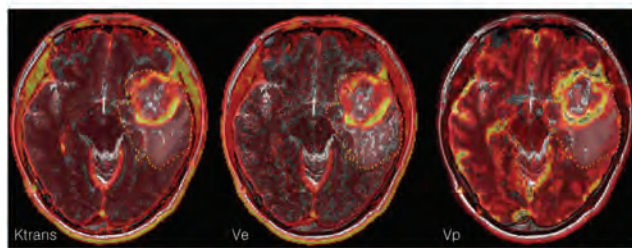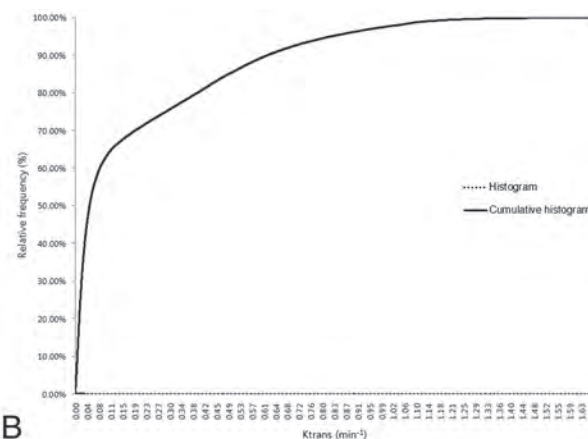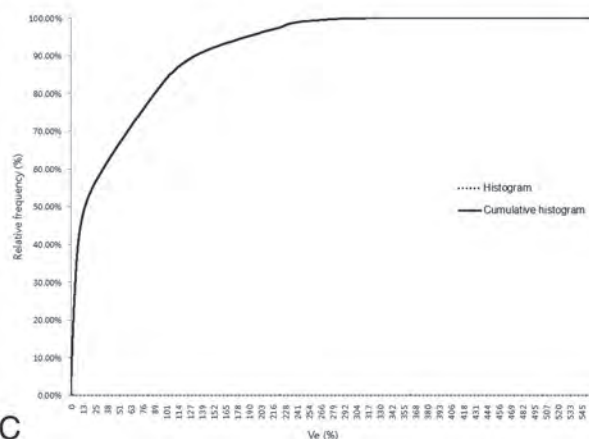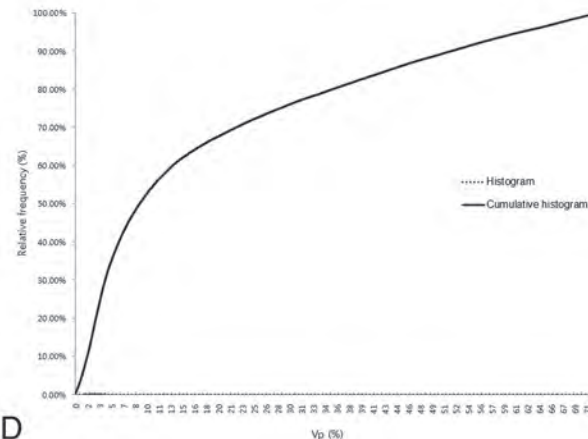
FIG 3. ROIs manually defined on axial T2WI coregistered with parametric maps in a 37-year-old woman with a grade IV glioma (*C*) and the histogram and cumulative histogram from the entire-tumor volume (*B–D*) are presented.

Table 1: The pharmacokinetic parameters in each grade of glioma[a]

	Grade II[b]/ Low-Grade[c]	Grade III[b]	Grade IV[b]	High-Grade[c]
K^{trans} [d]	0.027 ± 0.041	0.057 ± 0.091	0.158 ± 0.226	0.122 ± 0.195
Ve[e]	5.809 ± 10.381	15.469 ± 26.165	45.103 ± 63.888	35.059 ± 55.920
Vp[e]	3.858 ± 3.958	5.735 ± 5.772	10.624 ± 12.396	8.826 ± 10.723

[a] All data are means.

[b] There were statistically significant differences among grades ($P < .01$).

[c] There were statistically significant differences between low- and high-grade ($P < .01$).

[d] Data for K^{trans} are in units of minute^{-1}.

[e] Data for Ve and Vp are percentages.

and a specificity of 100% (7 of 7 grade III gliomas). We applied each cutoff so that tumors with values equal to or greater than the cutoff values were regarded as grade III gliomas.

Optimal Cutoff Values of K^trans, Ve, and Vp for the Differentiation of Grade III and IV Gliomas

Between the C50 and C99 values from the cumulative K^{trans}, Vp, and Ve histograms, the K^{trans} C97, Ve C66, and Vp C92 exhibited the highest AUCs for differentiating grade IV from grade III gliomas: 0.971, 0.885, and 0.798, respectively. The K^{trans} C97 cutoff value was 0.412 minute^{-1} with a sensitivity of 92.31% (12 of 13 grade IV gliomas) and a specificity of 100% (8 of 8 grade III gliomas). The Ve C66 cutoff value was 8.37% with a sensitivity of 92.31% (12 of 13 grade IV gliomas) and a specificity of 75% (6 of 8 grade III gliomas). We found that the Vp

C92 cutoff value was 19.33% and showed a sensitivity of 76.92% (10 of 13 grade IV gliomas) and a specificity of 87.50% (7 of 8 grade III gliomas). We applied each cutoff so that tumors with values equal to or greater than the cutoff values were regarded as grade IV gliomas.

Multivariable Stepwise Logistic Regression Analysis

The AUCs corresponding to profiles with the highest diagnostic accuracy showed significant differences between low- and high-grade gliomas ($P < .05$). However, multivariable stepwise logistic regression analysis showed that the K^{trans} C98 value was the most significant variable, with a parameter estimate of 16.64 and a standard error of 8.17 ($P < .05$). K^{trans} C97 was the most significant variable with a parameter estimate of 17.96 and a standard error of 8.38 in differentiating grade IV from grade III gliomas, but there was no significant variable in differentiating grade III from grade II gliomas ($P < .05$).

DISCUSSION

Histogram analysis of pharmacokinetic parameters including K^{trans}, Ve, and Vp obtained from the entire-tumor volume based on T1-weighted DCE perfusion MR imaging was useful for glioma grading. The best percentiles for differentiating high- and low-grade gliomas, in terms of the highest area under the curve of the receiver operating characteristic curves, were K^{trans} C98, Ve
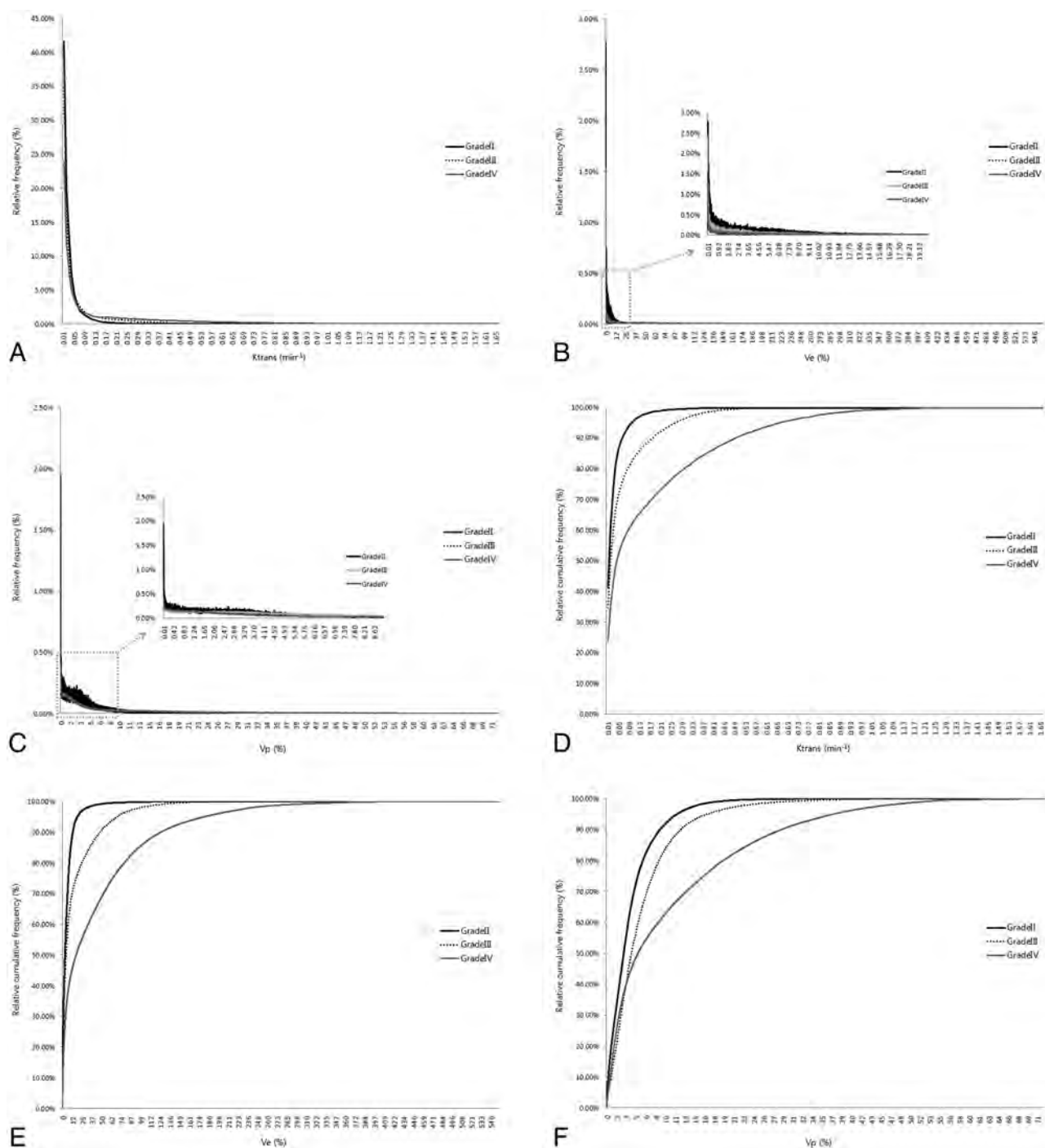
FIG 4. A histogram and cumulative histogram were derived from the total parametric values of all masses ($n = 28$) according to each grade. $A–F$, The histogram and cumulative histogram show that lower grade gliomas present a higher relative frequency at low parametric values and a lower relative frequency at high parametric values compared with higher grade gliomas for all of the parameters. C and F, However, in the Vp histogram, the relative frequency of grade IV gliomas is higher than that of grade III gliomas at a number of low values.

C90, and Vp C84. K^{trans} C98 was the most significant parameter for distinguishing high- from low-grade gliomas.

A number of studies on glioma grading by using pharmacokinetic parameters from DCE MR imaging—in particular, K^{trans}, Ve, and Vp—have been published.[8,10-13,15,18,28] Using ROC curve analyses, Jia et al[8] showed that K^{trans} and Ve were significantly lower in low-grade gliomas than in high-grade gliomas, with cutoff values of K^{trans} and Ve of 0.035 minutes^{-1} and 0.13, respectively. Awasthi et al[10] presented a discriminant function for

differentiating low- and high-grade gliomas and a correlation with immunohistochemical markers by using relative CBV, elimination rate of contrast agent or Kep, and Ve derived from DCE MR imaging. Zhang et al[29] concluded that K^{trans} was the most sensitive and specific parameter among the 5 available parameters (K^{trans}, Kep, rate constant of contrast agent reflux to plasma or Kel, Ve, and Vp) in distinguishing high-grade from low-grade gliomas on the basis of DCE MR imaging. These studies calculated parameters in portions of the entire-tumor volumes. The ROIs

Table 2: ROC results of the percentiles with the best AUC for glioma grading

Parameter	AUC[a]	Sensitivity (%)[b]	Specificity (%)[b]	Cutoff Value[c]	P Value
K^{trans}					
C98	0.912 (0.742–0.985)	76.19 (16/21)	100 (7/7)	0.277	<.01
Ve					
C90	0.939 (0.779–0.994)	85.71 (18/21)	100 (7/7)	19.70	<.01
Vp					
C84	0.769 (0.572–0.906)	61.9 (13/21)	100 (7/7)	11.71	<.01

[a] Data in parentheses are 95% confidence intervals.
[b] Sensitivity and specificity for identifying high-grade tumors. Data in parentheses are the numbers used to calculate the percentages.
[c] Data for K^{trans} are in units of minute^{-1}, and data for Ve and Vp are percentages.

included smaller portions of the tumor margins on each section and were mostly used to show the highest parametric values.[8,10,29] In comparison, we collected and analyzed whole-pixel values from the entire-tumor volume. In addition, we evaluated the parameters on the basis of T2WI or FLAIR, whereas previous studies used contrast- enhanced T1WI. T2-weighted high-signal-intensity lesions, excluding definite cystic or necrotic regions around gliomas, were generally considered to be tumor-involved lesions. We believe that the methods used in the present study could reflect whole-tumor characteristics.

The previous studies presented the parametric values with cutoff values to differentiate low- and high-grade gliomas. The presented values in the previous studies were not consistent with one another. The inconsistency in parametric values may be caused by different MR imaging protocols, pharmacokinetic models, or perfusion-analysis software. However, histogram analysis from the entire-tumor volume could be an alternative method for grading gliomas. The percentiles, which were generated from relative rankings based on the analyzed parametric values from the analysis, directly apply to other clinical or research settings.

Baseline T1 was fixed at 1000 ms in this study, whereas an estimate for the baseline T1 has been generally derived from a fitting process by using the precontrast T1 field-echo signal at multiple flip angles.[20,30,31] The estimation of the baseline T1 is very sensitive to noise that is present in multiple flip angle and DCE images, and this sensitivity results in the broadening of the baseline T1. The fixed baseline T1 can contribute to obtaining more consistent results and can protect dynamic data from incorrect scale factors or patient movements during DCE data collection. In addition, the effort to estimate the actual baseline T1 could be reduced. If one assumed that the purpose of the DCE analysis is to determine the relative vascular change, the analysis by using the fixed baseline T1 may be sufficient to draw correct conclusions, even though the fixed baseline T1 is not physiologic.[22] However, these characteristics may result in Ve values of >100% in our study.

Although there were a number of methodologic differences, the results from this study were in agreement with those in previous studies. The parametric values increased as the grades increased, and K^{trans} was the most significant parameter in glioma grading.

This study had a number of limitations. A retrospective analysis was performed, and a small number of patients were enrolled. In particular, only 7 cases of low-grade glioma were included because of their low incidence. Second, although the determination of the arterial input function was performed in terms of the best

optical shape and in relation to the concentration-time curve of the tumor, it might be insufficient for objective and reproducible selection. Third, the drawing of the regions of interest was performed manually on T2WI or FLAIR images. Because infiltrative tumors show particularly poor margins, differentiating the tumor from the surrounding normal brain tissue may not be easy, and this difficulty may result in low reproducibility. However, the volume of data from the entire-tumor volume was high enough that small erroneous data were not thought to cause severe bias. Fourth, we assumed that significant differences in parameters among the glioma grades would be identified in higher percentiles over the range C50 to C100. This assumption was based on the characteristic vascular system of gliomas (ie, higher grade gliomas have more permeability and abundant vascularity). Although the AUC curves also supported the validity of the assumption, the analysis was not completely free from limitations. Fifth, multicolinearity was detected in the multivariable stepwise logistic regression analysis because the variables were highly correlated with one another. The percentiles were extracted from one parameter, and the parameters were originally dependent on one another. Sixth, fixed-baseline T1 was used for the calculation of contrast concentration in tissue, even though it was not physiologic. Finally, the histogram analysis of the data from the entire-tumor volume could present entire profiles of glioma grades on the basis of the calculated parameters, but this may not be practical in terms of time effectiveness for application to real clinical settings.

CONCLUSIONS

Histogram analysis of the pharmacokinetic parameters K^{trans}, Ve, and Vp obtained from the entire-tumor volume data can be useful for grading gliomas. K^{trans} C98 was the most significant parameter. We expect our results to contribute to perfusion analyses in diverse clinical and research settings.

REFERENCES

1. Kargiotis O, Rao JS, Kyritsis AP. **Mechanisms of angiogenesis in gliomas.** J Neurooncol 2006;78:281–93
2. Folkman J. **What is the evidence that tumors are angiogenesis dependent?** J Natl Cancer Inst 1990;82:4–6
3. Folkman J. **The role of angiogenesis in tumor growth.** Semin Cancer Biol 1992;3:65–71
4. Wesseling P, Ruiter DJ, Burger PC. **Angiogenesis in brain tumors; pathobiological and clinical aspects.** J Neurooncol 1997;32:253–65
5. Less JR, Skalak TC, Sevick EM, et al. **Microvascular architecture in a mammary carcinoma: branching patterns and vessel dimensions.** Cancer Res 1991;51:265–73
6. Wesseling P, van der Laak JA, de Leeuw H, et al. **Quantitative immunohistological analysis of the microvasculature in untreated human glioblastoma multiforme: computer-assisted image analysis of whole-tumor sections.** J Neurosurg 1994;81:902–09
7. Tate MC, Aghi MK. **Biology of angiogenesis and invasion in glioma.** Neurotherapeutics 2009;6:447–57
8. Jia Z, Geng D, Xie T, et al. **Quantitative analysis of neovascular permeability in glioma by dynamic contrast-enhanced MR imaging.** J Clin Neurosci 2012;19:820–23

9. Hakyemez B, Erdogan C, Ercan I, et al. **High-grade and low-grade gliomas: differentiation by using perfusion MR imaging.** *Clin Radiol* 2005;60:493–502

10. Awasthi R, Rathore RK, Soni P, et al. **Discriminant analysis to classify glioma grading using dynamic contrast-enhanced MRI and immunohistochemical markers.** *Neuroradiology* 2012;54:205–13

11. Provenzale JM, York G, Moya MG, et al. **Correlation of relative permeability and relative cerebral blood volume in high-grade cerebral neoplasms.** *AJR Am J Roentgenol* 2006;187:1036–42

12. Zhang Y, Wang J, Wang X, et al. **Feasibility study of exploring a T(1)-weighted dynamic contrast-enhanced MR approach for brain perfusion imaging.** *J Magn Reson Imaging* 2012;35:1322–31

13. Harrer JU, Parker GJ, Haroon HA, et al. **Comparative study of methods for determining vascular permeability and blood volume in human gliomas.** *J Magn Reson Imaging* 2004;20:748–57

14. Lüdemann L, Grieger W, Wurm R, et al. **Quantitative measurement of leakage volume and permeability in gliomas, meningiomas and brain metastases with dynamic contrast-enhanced MRI.** *Magn Reson Imaging* 2005;23:833–41

15. Mills SJ, Patankar TA, Haroon HA, et al. **Do cerebral blood volume and contrast transfer coefficient predict prognosis in human glioma?** *AJNR Am J Neuroradiol* 2006;27:853–58

16. Aref M, Chaudhari AR, Bailey KL, et al. **Comparison of tumor histology to dynamic contrast enhanced magnetic resonance imaging-based physiological estimates.** *Magn Reson Imaging* 2008;26:1279–93

17. Patankar TF, Haroon HA, Mills SJ, et al. **Is volume transfer coefficient (K^{trans}) related to histologic grade in human gliomas?** *AJNR Am J Neuroradiol* 2005;26:2455–65

18. Roberts HC, Roberts TP, Brasch RC, et al. **Quantitative measurement of microvascular permeability in human brain tumors achieved using dynamic contrast-enhanced MR imaging: correlation with histologic grade.** *AJNR Am J Neuroradiol* 2000;21:891–99

19. Tofts PS, Brix G, Buckley DL, et al. **Estimating kinetic parameters from dynamic contrast-enhanced T(1)-weighted MRI of a diffusable tracer: standardized quantities and symbols.** *J Magn Reson Imaging* 1999;10:223–32

20. Haroon HA, Buckley DL, Patankar TA, et al. **A comparison of Ktrans measurements obtained with conventional and first pass pharmacokinetic models in human gliomas.** *J Magn Reson Imaging* 2004;19:527–36

21. Tofts PS, Kermode AG. **Measurement of the blood-brain barrier permeability and leakage space using dynamic MR imaging. 1. Fundamental concepts.** *Magn Reson Med* 1991;17:357–67

22. Haacke EM, Filleti CL, Gattu R, et al. **New algorithm for quantifying vascular changes in dynamic contrast-enhanced MRI independent of absolute T1 values.** *Magn Reson Med* 2007;58:463–72

23. Sundar H, Shen D, Biros G, et al. **Robust computation of mutual information using spatially adaptive meshes.** *Med Image Comput Comput Assist Interv* 2007;10(pt 1):950–58

24. Pluim JP, Maintz JB, Viergever MA. **Mutual-information-based registration of medical images: a survey.** *IEEE Trans Med Imaging* 2003;22:986–1004

25. Bjornerud A. **The ICE software package: direct co-registration of anatomical and functional datasets using DICOM image geometry information.** *Proc Hum Brain Mapping* New York, New York, June 19–22, 2003;19

26. Kang Y, Choi SH, Kim YJ, et al. **Gliomas: histogram analysis of apparent diffusion coefficient maps with standard- or high-b-value diffusion-weighted MR imaging– correlation with tumor grade.** *Radiology* 2011;261:882–90

27. Hauck WW, Miike R. **A proposal for examining and reporting stepwise regressions.** *Stat Med* 1991;10:711–15

28. Mills SJ, Soh C, O'Connor JP, et al. **Enhancing fraction in glioma and its relationship to the tumoral vascular microenvironment: a dynamic contrast-enhanced MR imaging study.** *AJNR Am J Neuroradiol* 2010;31:726–31

29. Zhang N, Zhang L, Qiu B, et al. **Correlation of volume transfer coefficient Ktrans with histopathologic grades of gliomas.** *J Magn Reson Imaging* 2012;36:355–63

30. Li KL, Zhu XP, Waterton J, et al. **Improved 3D quantitative mapping of blood volume and endothelial permeability in brain tumors.** *J Magn Reson Imaging* 2000;12:347–57

31. Zhu XP, Li KL, Kamaly-Asl ID, et al. **Quantification of endothelial permeability, leakage space, and blood volume in brain tumors using combined T1 and T2* contrast-enhanced dynamic MR imaging.** *J Magn Reson Imaging* 2000;11:575–85

Arterial Spin-Labeling Evaluation of Cerebrovascular Reactivity to Acetazolamide in Healthy Subjects

Y. Inoue, Y. Tanaka, H. Hata, and T. Hara

ABSTRACT

BACKGROUND AND PURPOSE: Arterial spin-labeling MR imaging permits safe, repeated CBF measurement. We investigated the potential and technical factors of arterial spin-labeling imaging in assessing cerebrovascular reactivity to acetazolamide.

MATERIALS AND METHODS: The regional CBF was measured in 8 healthy volunteers by use of a 3D pseudocontinuous arterial spin-labeling sequence. Arterial spin labeling imaging was performed at rest and every 2 minutes after intravenous acetazolamide injection. To evaluate repeatability, regional CBF measurements were repeated without acetazolamide within an imaging session and on a separate day. Additionally, arterial spin-labeling imaging was performed at rest and after acetazolamide injection with different postlabeling delays, and regional cerebrovascular reactivity was calculated.

RESULTS: The regional CBF started to increase immediately after acetazolamide injection and peaked at approximately 10 minutes, followed by a slow decrease. Favorable intrasession repeatability was demonstrated, especially when scanner tuning was omitted between scans. Rest regional CBF was slightly lower with a postlabeling delay of 2525 ms than with a postlabeling delay of 1525 ms, and the postlabeling delay–dependent difference was more evident for regional CBF after acetazolamide injection and regional cerebrovascular reactivity.

CONCLUSIONS: Arterial spin-labeling imaging allows evaluation of the distribution, magnitude, and time course of cerebrovascular response to acetazolamide. The influence of the postlabeling delay on the estimated cerebrovascular reactivity should be noted.

ABBREVIATIONS: ACZ = acetazolamide; ant-MCA = anterior part of the territory of the MCA; ASL = arterial spin-labeling; CVR = cerebrovascular reactivity; PLD = postlabeling delay; post-MCA = posterior part of the territory of the MCA; rCBF = regional CBF; rCVR = regional cerebrovascular reactivity

MR imaging with an arterial spin-labeling (ASL) technique permits evaluation of cerebral perfusion with neither radiation exposure nor the administration of an exogenous contrast agent.[1,2] Arterial water in the neck is labeled with a radiofrequency pulse, and the brain is imaged after a fixed time interval, termed postlabeling delay (PLD). Cerebral perfusion is estimated on the basis of signal changes caused by an influx of magnetically labeled water into brain tissues, and absolute values of CBF are calculated. The 3D ASL MR imaging by use of a pseudocontinuous arterial spin-labeling technique for magnetic labeling offers contiguous CBF images covering the whole brain with a favorable signal-to-noise ratio[3] and is expected to enhance the utility of ASL imaging.

In occlusive cerebrovascular diseases, the cerebral vessels dilate to compensate for decreased cerebral perfusion pressure and to maintain CBF in areas with compromised cerebral hemodynamics.[4] Such areas are presumably vulnerable to ischemic brain injury after further reduction in perfusion pressure and are considered to have decreased cerebral perfusion reserve. CBF measurements at rest and after acetazolamide (ACZ) injection allow evaluation of compensatory vasodilation and reveal impaired cerebral hemodynamics even when rest CBF is preserved.[5,6] ACZ is a potent dilator of cerebral vessels and increases CBF after intravenous injection. In brain regions in which decreased cerebral perfusion pressure has already caused compensatory vasodilation, cerebrovascular response to ACZ diminishes. Comparison of rest and post-ACZ CBFs demonstrates compromised cerebral hemodynamics as decreased cerebrovascular reactivity (CVR) to ACZ.

CVR is commonly assessed with the use of SPECT measurements of CBF at rest and after ACZ injection.[5,6] This method is well established but requires radiation exposure and long examination times. CBF and CVR can be assessed by ASL MR imaging

with ACZ.[7-12] The ASL technique allows estimation of rest and post-ACZ CBFs, in addition to morphologic assessments by conventional MR imaging, in one imaging session. In the present study, we used 3D pseudocontinuous ASL imaging to evaluate CVR to ACZ in healthy volunteers. We acquired ASL images after ACZ injection repeatedly with high temporal resolution and investigated the time course of CBF changes for each vascular territory. Intrasession and interday repeatabilities were assessed to evaluate the capability of ASL imaging to detect changes in CBF. The magnitude and distribution of ASL signals depends on the time after labeling, and thus the PLD is the key parameter of ASL imaging.[2,13] ASL signals may originate from labeled water in blood vessels in addition to that in brain tissues. Prolongation of the PLD facilitates labeled water entering brain tissues and appears to be beneficial for evaluation of tissue perfusion. However, magnetic labeling decays rapidly with T1 relaxation, and a longer PLD may result in weaker signals. In the present study, we examined the effect of the PLD on rest CBF, post-ACZ CBF, and CVR. The aim of this study was to investigate the potential and technical factors of the ASL assessment of CVR.

MATERIALS AND METHODS

Subjects
This study included 8 healthy adult volunteers (7 men and 1 woman), ages 30.1 ± 4.6 (mean ± SD) years. The volunteers had no history of chronic diseases and no contraindications to MR imaging. No abnormalities were found in the brain on T2-weighted FSE images. The study protocol was approved by the institutional review board of the host institute, and written informed consent was obtained from all subjects before participation.

3D ASL Imaging
All imaging studies were performed in the evening on a 1.5T clinical scanner (Signa HDxt; GE Healthcare, Milwaukee, Wisconsin) with the 12-channel head component of the head-neck-spine coil. ASL imaging of the whole brain was performed by use of a 3D pseudocontinuous ASL sequence, which consisted of a pseudocontinuous ASL labeling sequence and a 3D spiral FSE acquisition sequence,[3] with background suppression and no vascular suppression. Each spiral arm contained 512 sampling points in the k-space, and 4 arms (interleaves) were acquired. The PLD was set at 1525 or 2525 ms. Other imaging parameters were as follows: TR = 4608 ms, TE = 10.5 ms, flip angle = 155°, bandwidth = ±62.5 kHz, FOV = 24 × 24 cm^2, section numbers = 36, section thickness = 4 mm, NEX = 2 or 6. A pair of label and control image sets covering the whole brain was acquired for 40 seconds, and the acquisition was repeated as indicated by NEX. ASL perfusion images were generated by subtraction of the label and control image sets and averaging. Immediately after the completion of acquisition of the label and control image sets, a reference proton attenuation image set was obtained by means of a fluid saturation pulse to determine the spatial distribution of signal sensitivity. In total, acquisition times were 1 minute, 42 seconds for a NEX of 2 and a PLD of 1525 ms; 4 minutes, 10 seconds for a NEX of 6 and a PLD of 1525 ms; and 4 minutes, 48 seconds for a NEX of 6 and a PLD of 2525 ms. Quantitative CBF images were created

from the ASL perfusion images and proton attenuation images by use of the software on the MR scanner.[14]

Calculation of Regional CBF Values
ROIs were determined by means of automated software (3D stereotactic region of interest template, 3D-SRT; Fujifilm RI Pharama, Tokyo, Japan)[15] to calculate regional CBF (rCBF) values. The quantitative CBF images obtained in the study subject were registered anatomically to the standard brain atlas. Parameters for anatomic standardization were determined with the use of proton attenuation images but not CBF images because the margin was clearer in the proton attenuation images. The 3D-SRT software has ROIs predefined on the standard brain atlas and provides rCBF values for each of the right and left sides of the following 12 regions: callosomarginal, precentral, central, parietal, angular, temporal, posterior cerebral, pericallosal, basal ganglia, thalamus, hippocampus, and cerebellum. In the present study, we determined rCBF in the territory of the anterior cerebral artery through the use of callosomarginal and pericallosal ROIs; rCBF in the anterior part of the territory of the middle cerebral artery (ant-MCA) through the use of precentral and central ROIs; rCBF in the posterior part of the territory of the middle cerebral artery (post-MCA) through the use of parietal, angular, and temporal ROIs; and rCBF in the territory of the posterior cerebral artery through the use of a posterior cerebral ROI.

Time Course after ACZ Injection
The time course of cerebrovascular response to ACZ was evaluated by means of serial ASL imaging. The subjects underwent ASL imaging with a NEX of 2 and a PLD of 1525 ms twice at rest. Thereafter, 1000 mg of ACZ in 20 mL of saline was injected intravenously for 30 seconds by use of an autoinjector, followed by a 20-mL saline flush for 30 seconds. ASL imaging was started at the beginning of ACZ injection and repeated every 2 minutes for 32 minutes, yielding 16 post-ACZ image sets. Although scanner tuning consisting of shimming and auto prescan is commonly performed before each imaging to adjust scanner settings, it was performed before the first rest imaging and omitted thereafter. Such omission was made only in this time course study. The rCBF value for each brain region, that is, the anterior cerebral artery, ant-MCA, post-MCA, or posterior cerebral artery region, was calculated as the average of the right and left values obtained by ROI analysis. The normalized rCBF at each time point was determined as a percentage of the average of the 2 rest values, and its temporal change was evaluated.

Repeatability of Rest rCBF Measurement
The repeatability of rest rCBF measurement by ASL imaging was assessed by use of 4 measurements in each subject. Two rest measurements performed for the evaluation of the time course after ACZ injection without intervening scanner tuning were also used for the assessment of repeatability. On another day, with an interval of approximately 3 months, ASL imaging was performed twice in 1 imaging session. Unlike the time course study, scanner tuning was performed between the 2 data acquisitions. The NEX was 2 and the PLD was 1525 ms in all 4 measurements.

The rCBF values were obtained by the automated ROI method, and data for the right and left sides were analyzed sepa-
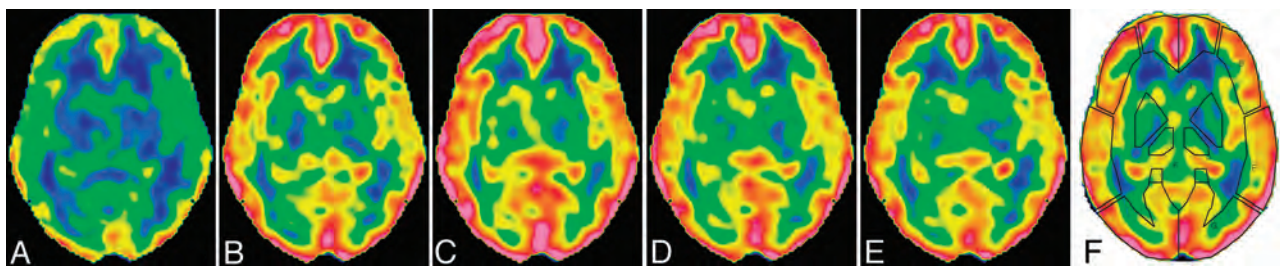
FIG 1. CBF images at the level of the basal ganglia in a 28-year-old woman. Data were acquired with a NEX of 2 and a postlabeling delay of 1525 ms at rest *(A)* and 3 minutes *(B)*, 9 minutes *(C)*, 15 minutes *(D)*, and 31 minutes *(E)* after acetazolamide injection. The time indicates the mid time of data acquisition. The upper and lower limits of the color scale are set at 110 and 0 mL/min per 100 g, respectively. *F*, ROIs placed automatically by the 3D-SRT software.
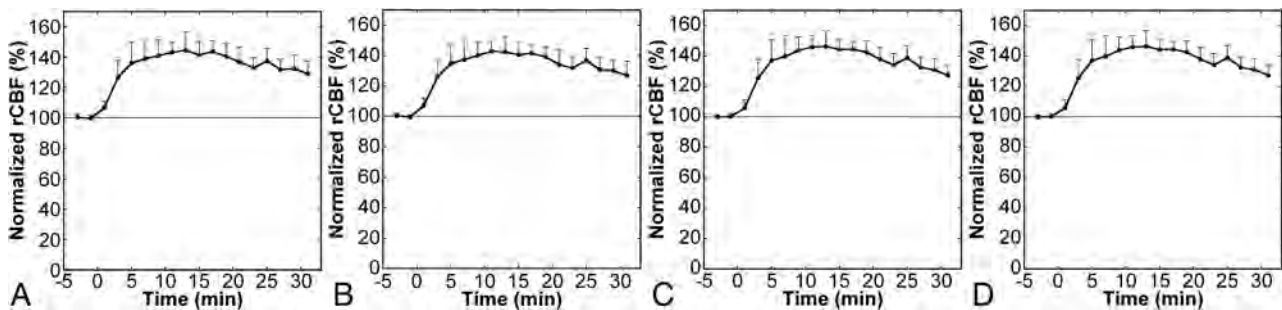
FIG 2. Time courses of normalized regional CBF after acetazolamide injection in the anterior cerebral artery *(A)*, anterior MCA *(B)*, posterior MCA *(C)*, and posterior cerebral artery *(D)* regions. Error bars indicate SDs. ACZ was injected at time 0, and plots with negative *x* values represent data of rest imaging.

rately for this repeatability study, yielding 8 brain regions for analysis. The coefficient of variance was calculated from 2 corresponding rCBF values in each subject and was regarded as an indicator of variation of rest measurement. The coefficient of variance between the 2 serial measurements of the time course study was calculated to assess intrasession variation without tuning. The coefficient of variance between the 2 serial measurements performed on the other day was used to assess intrasession variation with tuning. The coefficient of variance was also calculated between the preceding measurements on separate days and was used as an indicator of interday variation.

rCBF and Regional Cerebrovascular Reactivity with Different PLDs

ASL imaging before and after ACZ injection was performed with different PLDs, and the effects of the PLD on rCBF and regional cerebrovascular reactivity (rCVR) were investigated. The PLDs studied were 1525 and 2525 ms, and the NEX was set at 6. ASL imaging was performed twice at rest: initially with a PLD of 1525 ms and then with a PLD of 2525 ms. After the completion of imaging at rest, 1000 mg of ACZ was injected intravenously, similarly to the time course study. ASL imaging with a PLD of 1525 ms was started 8 minutes after the start of ACZ injection, followed by imaging with a PLD of 2525 ms. This order of imaging with different PLDs was applied to 4 subjects, and imaging with a PLD of 2525 ms was performed before that with a PLD of 1525 ms in the remaining 4 subjects for both rest and post-ACZ imaging. Scanner tuning preceded each ASL acquisition.

The rCVR was defined as percent increase in rCBF and was calculated by the equation rCVR = (post-ACZ rCBF/rest rCBF − 1) × 100 for each of the 8 brain regions. The rCBF and rCVR were

compared between regions and between PLDs. The CVR image was created by pixel-by-pixel calculation of the percent increase in CBF after noise reduction by use of a 3D Gaussian filter of 8-mm full width at half maximum.

Statistical Analysis

Values are expressed as mean ± SD. Paired comparisons between PLDs were performed by Wilcoxon signed rank tests, and brain regions were compared by use of the Kruskal-Wallis test followed by the Steel-Dwass test. A value of $P < .05$ was deemed to indicate statistical significance.

RESULTS

Time Course after ACZ Injection

CBF images with acceptable qualities were obtained serially after ACZ injection, and augmentation of CBF was noted visually (Fig 1). ROIs were successfully placed by use of the 3D-SRT software, providing an absolute rCBF value for each brain region. The mean rest rCBF calculated from the first scan was 51.9 ± 4.5, 52.4 ± 5.0, 51.6 ± 5.3, and 50.1 ± 8.0 mL/min per 100 g in the anterior cerebral artery, ant-MCA, post-MCA, and posterior cerebral artery regions, respectively. The rCBF started to increase just after ACZ injection, peaked at approximately 10 minutes, and then decreased slowly (Fig 2). The temporal patterns of cerebrovascular response were similar among the brain regions.

Repeatability of Rest rCBF Measurement

Mean coefficients of variance of rCBF measurements representing intrasession variation without tuning were generally small, ranging from 1.7–2.7%, depending on the brain regions (Table 1). Insertion of tuning, consisting of shimming and auto prescan, between 2 measurements increased variation in rCBF definitely. The mean coefficients of variance representing intrasession variation with tuning ranged from

Table 1: Coefficients of variance for repeated measurements

| Region | Side | Coefficient of Variance (%) | | |
		Intrasession Tuning−	Intrasession Tuning+	Interday
Anterior cerebral artery	R	2.2 (1.1)	3.8 (3.6)	7.7 (5.9)
	L	2.3 (1.6)	3.9 (2.2)	8.1 (5.0)
Anterior MCA	R	2.7 (1.2)	3.3 (2.1)	6.2 (5.2)
	L	1.8 (1.7)	4.8 (2.4)	9.4 (6.3)
Posterior MCA	R	1.7 (1.3)	4.1 (2.7)	6.5 (5.1)
	L	1.7 (1.9)	5.7 (2.6)	8.7 (6.2)
Posterior cerebral artery	R	1.9 (1.5)	4.3 (4.5)	6.8 (5.3)
	L	1.8 (1.5)	5.7 (5.4)	7.9 (6.3)

Note:—Values are presented as mean (SD).
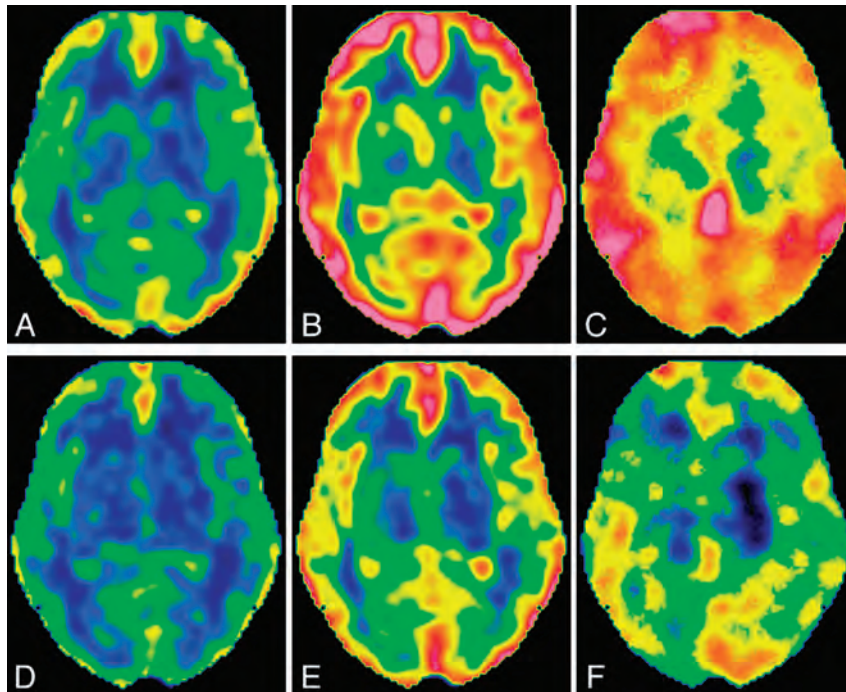
FIG 3. CBF and cerebrovascular reactivity images with different postlabeling delays at the level of the basal ganglia in the same subject as presented in Fig 1. *A–C*, Rest CBF image, post-acetazolamide CBF image, and CVR image, respectively, with a PLD of 1525 ms. *D–F*, Rest CBF image, post-ACZ CBF image, and CVR image, respectively, with a PLD of 2525 ms. The upper and lower limits of the color scale are set at 110 and 0 mL/min per 100 g, respectively, for CBF images, and the upper and lower limits for CVR images are set at 70% and 0%, respectively.

3.3–5.7%. Interday variation was still larger, with mean coefficients of variance ranging from 6.2–9.4%. There were no significant differences in coefficients of variance among the brain regions.

rCBF and rCVR with Different PLDs

The rest and post-ACZ CBF images as well as the CVR images are illustrated in Fig 3, and numeric values obtained by automated ROI analysis are presented in Table 2. Significant differences were not found in rest rCBF, post-ACZ rCBF, or rCVR among the brain regions, irrespective of the PLD. With a PLD of 1525 ms, mean rest rCBF and mean post-ACZ rCBF ranged, depending on the brain regions, from 45.9–50.1 mL/min per 100 g and from 67.3–72.7 mL/min per 100 g, respectively, resulting in mean rCVR values ranging from 42.5–46.4%. Despite negligible differences in mean values, the standard deviations of rCVR among subjects were obviously different among the brain regions and were

the smallest in the anterior cerebral artery region, followed by the ant-MCA, post-MCA, and posterior cerebral artery regions.

Rest rCBF values were significantly lower with a PLD of 2525 ms (44.3–47.8 mL/min per 100 g) than with a PLD of 1525 ms; however, the differences were small. Post-ACZ rCBF values were also significantly lower with a PLD of 2525 ms (58.0–62.4 mL/min per 100 g), and the PLD-dependent difference was more evident. As a result, rCVR was significantly and largely lower with a PLD of 2525 ms (26.9–32.5%).

DISCUSSION

Although SPECT measurements of CBF at rest and after ACZ injection are commonly used for the assessment of CVR,[5,6] they require radiation exposure and long examination times. ASL MR imaging is a safe, rapid method of measuring CBF and is applicable to the assessment of CVR.[7-12] In the present study, we evaluated cerebrovascular response to ACZ by 3D pseudocontinuous ASL MR imaging. Repeated ASL imaging after ACZ injection demonstrated a CBF increase in the whole brain visually and quantitatively. The number of arms and the NEX determine the acquisition time, and we selected relatively small numbers (4 arms and a NEX of 2) to shorten the acquisition time and attain high temporal resolution. With the use of these imaging parameters, ASL images with acceptable qualities were obtained during an acquisition time of 1 minute, 42 seconds. In ASL assessment of CBF with no vascular suppression, magnetically labeled water in the cerebral vessels may lead to erroneously high CBF values in the superficial areas of the brain.[2,16] The position and size of the ROI may affect calculated rCBF values, depending on the degree of inclusion of superficial high values in the ROI. We used automated software for the ROI setting to avoid operator-dependent variations in rCBF estimates and to improve reproducibility. This software was developed to analyze CBF SPECT[15]; however, it was applicable to the analysis of ASL imaging. ROIs determined by use of the reference proton attenuation images for anatomic standardization were visually judged to be appropriate and provided CBF values for each region.

Quantitative analysis of rCBF after ACZ injection showed a rapid increase in CBF, with a peak at approximately 10 minutes and a subsequent slow decrease. Such a detailed assessment of the time course of CBF changes is difficult with the use of methods

Table 2: Regional CBF and regional cerebrovascular reactivity values with acetazolamide injection

Region	Side	Rest rCBF, mL/min per 100 g		Post-Acetazolamide rCBF, mL/min per 100 g		rCVR, %	
		1525 ms	2525 ms	1525 ms	2525 ms	1525 ms	2525 ms
Anterior cerebral artery	R	48.5 (5.3)	47.0 (3.3)	71.1 (9.8)	62.0 (6.3)	46.2 (6.2)	31.6 (6.9)
	L	50.0 (5.0)	47.5 (3.9)	72.1 (8.8)	62.4 (5.7)	43.8 (5.3)	31.3 (5.4)
Anterior MCA	R	49.3 (5.7)	46.5 (4.2)	71.1 (10.9)	59.2 (6.1)	43.8 (7.8)	27.2 (5.8)
	L	50.1 (4.5)	46.5 (4.1)	71.5 (8.6)	58.9 (5.3)	42.5 (6.6)	26.9 (6.8)
Posterior MCA	R	48.4 (5.5)	47.3 (4.9)	71.1 (12.0)	61.8 (7.4)	46.4 (10.3)	30.6 (7.7)
	L	50.1 (4.5)	47.8 (4.5)	72.7 (10.4)	62.3 (6.3)	44.8 (10.8)	30.6 (7.9)
Posterior cerebral artery	R	45.9 (5.9)	44.3 (5.5)	67.3 (12.9)	58.0 (7.9)	45.9 (13.0)	30.9 (10.0)
	L	47.9 (6.2)	45.0 (6.5)	69.8 (13.2)	59.5 (8.9)	45.1 (13.5)	32.5 (11.7)

Note:—Values are presented as mean (SD); 1525 ms and 2525 ms indicate postlabeling delays of 1525 ms and 2525 ms, respectively.

requiring administration of exogenous contrast agents or radio-tracers. Doppler ultrasonography[17,18] and phase-contrast MR imaging[19] have been used to assess the time course of cerebrovascular response to ACZ and have shown temporal changes in blood flow or velocity in the major cerebral arteries that are consistent with temporal changes in rCBF observed in the current study. Planar dynamic imaging after radio-labeled albumin has also revealed similar temporal patterns in alterations of cerebral blood volume representing intravascular volume.[20] The present study confirmed the time course of cerebrovascular response to ACZ by assessing brain tissue perfusion instead of an approach from the vessels. CBF SPECT after ACZ injection is commonly performed assuming peak CBF response at 10–15 minutes after injection on the basis of Doppler measurement of the major cerebral arteries; the validity of this timing is supported by the present rCBF measurement.

The PLD is an essential parameter in ASL imaging. The use of a short PLD may diminish labeled water that reaches the brain tissues by the time of data acquisition, whereas the use of a long PLD causes decreased signals caused by relaxation of labeled water. We evaluated the effect of the PLD on the assessment of cerebrovascular response to ACZ by ASL imaging. Although rest rCBF did not differ largely, post-ACZ rCBF and rCVR were definitely lower with a PLD of 2525 ms than with a PLD of 1525 ms. CBF measurement by use of ASL MR imaging is dependent on the arterial arrival time, the time for water labeled in the neck to reach the brain tissues, and this dependence is more pronounced with a short PLD.[2,13] Previous studies with the use of Doppler ultrasonography demonstrated increased blood velocity after ACZ injection in the MCA[17] and internal carotid artery.[18] The administration of ACZ may shorten the arrival time as a result of increased blood velocity and aid early influx of labeled water into the brain tissues, which may enhance ASL signals with a short PLD preferentially and consequently cause overestimation of CVR. The mean CVR values reported in normal subjects range from 25–31% with the use of ^{133}Xe inhalation SPECT,[18,21-23] from 33.5–35% with the use of ^{15}O-water positron-emission tomography,[24,25] and from 37.7–54.2% with the use of ASL MR imaging.[9-11] Although the CVR values obtained with the use of a PLD of either 1525 ms (43.8–46.4%, depending on the region) or 2525 ms (26.9–32.5%) in the present study are in the range of the reported values, those obtained with a PLD of 1525 ms as well as those previously reported by use of ASL MR imaging are relatively high; thus, ASL MR imaging probably leads to overestimation of CVR. The method that provides more accurate CVR cannot be

concluded because of the lack of a standard reference; however, our results indicate that the influence of the PLD on CVR estimates should be taken into consideration.

Regional differences were not apparent in the temporal patterns of cerebrovascular response to ACZ among cortical regions. Systematic differences among regions were not demonstrated for rest rCBF, post-ACZ rCBF, or rCVR. However, rCVR was more variable among subjects in the posterior cerebral artery region than in the other regions, as indicated by a large SD. A long arrival time has been reported in the posterior cerebral artery region,[26] and such difference between carotid and vertebro-basilar circulations may be related to the variability in rCVR in the posterior cerebral artery region. Although the actual cause of the variability in CVR is unclear, our results raise caution in the assessment of CVR in the posterior cerebral artery region by use of ASL imaging.

High repeatability is crucial for evaluation of true changes from 2 measurements. Several reports have focused on the repeatability of CBF measurement by ASL imaging.[11,14,27-30] Interday repeatability indicates the capability of detecting alterations in CBF in the longitudinal assessment of disease status. CVR can be assessed by ASL imaging before and after ACZ injection in 1 imaging session, and intra-session repeatability is essential for this assessment. Differences in the positioning of the subject, physiologic fluctuations, and instability of the instruments are major factors causing interday variation but not intrasession variation. In the present study, we evaluated intrasession repeatability in addition to interday repeatability. Naturally, intrasession variation was smaller than intersession variation, as shown in a previous study.[27] Scanner tuning is commonly performed before each imaging and consists of shimming of the magnetic field, adjustment of the transmit gain, adjustment of the receive gain, and determination of the resonant frequency. It is noteworthy that omission of the tuning between scans reduced the coefficients of variance in rCBF measurement by a factor of 2. Tuning appears to be a major factor in intrasession variation. The peak response to ACZ is attained at approximately 10 minutes after injection. In clinical practice, imaging other than ASL would be performed during the waiting period before the commencement of post-ACZ ASL imaging, resulting in a need for tuning between rest and post-ACZ ASL imaging. Recording the tuning parameters for rest ASL imaging and application of the same parameters to post-ACZ ASL imaging may be helpful to improve the accuracy of assessing CVR to ACZ.

CONCLUSIONS

We performed 3D pseudocontinuous ASL imaging before and after ACZ injection to assess cerebrovascular response to ACZ. The observed time course in rCBF changes supports the previous reports of flow and velocity in the major cerebral arteries and cerebral blood volume. The magnitude of CVR was comparable to that in previous studies. The PLD influenced rest rCBF mildly and post-ACZ rCBF and rCVR severely. It was also suggested that attention should be paid in assessing CVR abnormalities in the posterior cerebral artery region. Intrasession repeatability was favorable, especially when the scanner settings were not changed by tuning between scans. The 3D pseudocontinuous ASL imaging allows evaluation of the distribution, magnitude, and time course of cerebrovascular response without radiation exposure or administration of exogenous contrast agents and is expected to serve as a tool for investigating in vivo physiology and assessing impaired hemodynamics in pathologic conditions.

REFERENCES

1. Hendrikse J, Petersen ET, Golay X. **Vascular disorders: insights from arterial spin labeling.** *Neuroimaging Clin North Am* 2012;22:259–69
2. Pollock JM, Tan H, Kraft RA, et al. **Arterial spin-labeled MR perfusion imaging: clinical applications.** *Magn Reson Imaging Clin North Am* 2009;17:315–38
3. Dai W, Garcia D, de Bazelaire C, et al. **Continuous flow-driven inversion for arterial spin labeling using pulsed radio frequency and gradient fields.** *Magn Reson Med* 2008;60:1488–97
4. Powers WJ, Raichle ME. **Positron emission tomography and its application to the study of cerebrovascular disease in man.** *Stroke* 1985;16:361–76
5. Hirano T, Minematsu K, Hasegawa Y, et al. **Acetazolamide reactivity on ^{123}I-IMP single photon emission computed tomography in patients with major cerebral artery occlusive disease: correlation with positron emission tomography parameters.** *J Cereb Blood Flow Metab* 1994;14:763–70
6. Yudd AP, Van Heertum RL, Masdeu JC. **Interventions and functional brain imaging.** *Semin Nucl Med* 1991;21:153–58
7. Uchihashi Y, Hosoda K, Zimine I, et al. **Clinical application of arterial spin-labeling MR imaging in patients with carotid stenosis: quantitative comparative study with single-photon emission CT.** *AJNR Am J Neuroradiol* 2011;32:1545–51
8. Zaitsu Y, Kudo K, Terae S, et al. **Mapping of cerebral oxygen extraction fraction changes with susceptibility-weighted phase imaging.** *Radiology* 2011;261:930–36
9. Bokkers RP, van Osch MJ, Klijn CJ, et al. **Cerebrovascular reactivity within perfusion territories in patients with an internal carotid artery occlusion.** *J Neurol Neurosurg Psychiatry* 2011;82:1011–16
10. Bokkers RP, van Osch MJ, van der Worp HB, et al. **Symptomatic carotid artery stenosis: impairment of cerebral autoregulation measured at the brain tissue level with arterial spin-labeling MR imaging.** *Radiology* 2010;256:201–08
11. Yen YF, Field AS, Martin EM, et al. **Test-retest reproducibility of quantitative CBF measurements using FAIR perfusion MRI and acetazolamide challenge.** *Magn Reson Med* 2002;47:921–28
12. Detre JA, Samuels OB, Alsop DC, et al. **Noninvasive magnetic resonance imaging evaluation of cerebral blood flow with acetazolamide challenge in patients with cerebrovascular stenosis.** *J Magn Reson Imaging* 1999;10:870–75
13. Wu WC, St Lawrence KS, Licht DJ, et al. **Quantification issues in arterial spin labeling perfusion magnetic resonance imaging.** *Top Magn Reson Imaging* 2010;21:65–73
14. Xu G, Rowley HA, Wu G, et al. **Reliability and precision of pseudo-continuous arterial spin labeling perfusion MRI on 3.0 T and comparison with ^{15}O-water PET in elderly subjects at risk for Alzheimer's disease.** *NMR Biomed* 2010;23:286–93
15. Takeuchi R, Yonekura Y, Matsuda H, et al. **Usefulness of a three-dimensional stereotaxic ROI template on anatomically standardised ^{99m}Tc-ECD SPET.** *Eur J Nucl Med Mol Imaging* 2002;29:331–41
16. Petersen ET, Zimine I, Ho YC, et al. **Non-invasive measurement of perfusion: a critical review of arterial spin labelling techniques.** *Br J Radiol* 2006;79:688–701
17. Dahl A, Russell D, Rootwelt K, et al. **Cerebral vasoreactivity assessed with transcranial Doppler and regional cerebral blood flow measurements: dose, serum concentration, and time course of the response to acetazolamide.** *Stroke* 1995;26:2302–06
18. Hauge A, Nicolaysen G, Thoresen M. **Acute effects of acetazolamide on cerebral blood flow in man.** *Acta Physiol Scand* 1983;117:233–39
19. Hartkamp NS, Hendrikse J, van der Worp HB, et al. **Time course of vascular reactivity using repeated phase-contrast MR angiography in patients with carotid artery stenosis.** *Stroke* 2012;43:553–56
20. Inoue Y, Momose T, Machida K, et al. **An approach to cerebral vasodilatory capacity in unilateral and bilateral cerebrovascular diseases using radiolabeled human serum albumin.** *Clin Nucl Med* 1995;20:340–45
21. Sorteberg W, Lindegaard KF, Rootwelt K, et al. **Effect of acetazolamide on cerebral artery blood velocity and regional cerebral blood flow in normal subjects.** *Acta Neurochir (Wien)* 1989;97:139–45
22. Bonte FJ, Devous MD, Reisch JS. **The effect of acetazolamide on regional cerebral blood flow in normal human subjects as measured by single-photon emission computed tomography.** *Invest Radiol* 1988;23:564–68
23. Vorstrup S, Brun B, Lassen NA. **Evaluation of the cerebral vasodilatory capacity by the acetazolamide test before EC-IC bypass surgery in patients with occlusion of the internal carotid artery.** *Stroke* 1986;17:1291–98
24. Endo H, Inoue T, Ogasawara K, et al. **Quantitative assessment of cerebral hemodynamics using perfusion-weighted MRI in patients with major cerebral artery occlusive disease: comparison with positron emission tomography.** *Stroke* 2006;37:388–92
25. Okazawa H, Yamauchi H, Sugimoto K, et al. **Effects of acetazolamide on cerebral blood flow, blood volume, and oxygen metabolism: a positron emission tomography study with healthy volunteers.** *J Cereb Blood Flow Metab* 2001;21:1472–79
26. MacIntosh BJ, Filippini N, Chappell MA, et al. **Assessment of arterial arrival times derived from multiple inversion time pulsed arterial spin labeling MRI.** *Magn Reson Med* 2010;63:641–47
27. Chen Y, Wang DJ, Detre JA. **Test-retest reliability of arterial spin labeling with common labeling strategies.** *J Magn Reson Imaging* 2011;33:940–49
28. Pfefferbaum A, Chanraud S, Pitel AL, et al. **Volumetric cerebral perfusion imaging in healthy adults: regional distribution, laterality, and repeatability of pulsed continuous arterial spin labeling (PCASL).** *Psychiatry Res* 2010;182:266–73
29. Wu WC, Jiang SF, Yang SC, et al. **Pseudocontinuous arterial spin labeling perfusion magnetic resonance imaging: a normative study of reproducibility in the human brain.** *Neuroimage* 2011;56:1244–50
30. Jahng GH, Song E, Zhu XP, et al. **Human brain: reliability and reproducibility of pulsed arterial spin-labeling perfusion MR imaging.** *Radiology* 2005;234:909–16

Diffusion-Weighted Imaging Score of the Brain Stem: A Predictor of Outcome in Acute Basilar Artery Occlusion Treated with the Solitaire FR Device

I. Mourand, P. Machi, E. Nogué, C. Arquizan, V. Costalat, M.-C. Picot, A. Bonafé, and D. Milhaud

ABSTRACT

BACKGROUND AND PURPOSE: The prognosis for ischemic stroke due to acute basilar artery occlusion is very poor: Early recanalization remains the main factor that can improve outcomes. The baseline extent of brain stem ischemic damage can also influence outcomes. We evaluated the validity of an easy-to-use DWI score to predict clinical outcome in patients with acute basilar artery occlusion treated by mechanical thrombectomy.

MATERIALS AND METHODS: We analyzed the baseline clinical and DWI parameters of 31 patients with acute basilar artery occlusion, treated within 24 hours of symptom onset by using a Solitaire FR device. The DWI score of the brain stem was assessed with a 12-point semiquantitative score that separately considered each side of the medulla, pons, and midbrain. Clinical outcome was assessed at 180 days by using the mRS. According to receiver operating characteristic analyses, the cutoff score determined the optimal positive predictive value for outcome. The Spearman rank correlation coefficient assessed the correlation between the DWI brain stem score and baseline characteristics.

RESULTS: Successful recanalization (Thrombolysis in Cerebral Infarction 3–2b) was achieved in 23 patients (74%). A favorable outcome (mRS $\leq$ 2) was observed in 11 patients (35%). An optimal DWI brain stem score of <3 predicted a favorable outcome. The probability of a very poor outcome (mRS $\geq$ 5) if the DWI brain stem score was $\geq$5 reached 80% (positive predictive value) and 100% if this score was $\geq$6. Interobserver reliability of the DWI brain stem score was excellent, with an intraclass correlation coefficient of 0.97 (95% CI, 0.96–0.99). The DWI brain stem score was significantly associated with baseline tetraplegia ($P = .001$) and coma ($P = .005$).

CONCLUSIONS: In patients with acute basilar artery occlusion treated by mechanical thrombectomy, the baseline DWI brain lesion score seems to predict clinical outcome.

ABBREVIATIONS: ABAO = acute basilar artery occlusion; BSS = brain stem score; IQR = interquartile range; pc-ASPECT = posterior circulation Alberta Stroke Program Early CT Score; PPV = positive predictive value; ROC = receiver operating characteristic

A cute basilar artery occlusion (ABAO) is an uncommon cause of stroke, accounting for only 6%–10% of large-vessel strokes.[1] Its prognosis is very poor, with a mortality rate of up to 85%[2] and severe residual deficits in >65% of survivors.[3]

Early recanalization remains the main important factor that can improve outcome.[4-6] However, even though the best recanalization rate is achieved by using a newer stent retriever, such as a

Solitaire FR Device (Covidien, Irvine, California) (up to 100%),[7-10] stent retriever impact on functional outcome is not as clear-cut as expected and has not been documented in a randomized trial.

The extent of baseline brain stem ischemic damage can also influence outcome. DWI and perfusion-weighted imaging have demonstrated prognostic value in acute anterior ischemic stroke.[11,12] In previous studies on vertebrobasilar ischemic stroke, the acute global DWI lesion volume did not correlate with the baseline NIHSS score.[13,14] More recently, investigators have studied the functional outcome and extent of lesions in patients with a posterior circulation infarction by diffusion-weighted MR imaging.[15-17] Because of the high attenuation of the anatomic architecture in the brain stem, lesion location rather than lesion volume can be critical in determining functional outcome after a posterior circulation infarction, especially when the brain stem is involved.[18]

The aim of our study was to test the reproducibility and validity of a novel baseline and easy-to-use prethrombectomy DWI brain stem score (BSS) in 31 consecutive patients with proved ABAO and treated within 24 hours of symptom onset, by using mechanical thrombectomy. This score may predict functional outcomes and help determine the indications for an optimal recanalization approach.

MATERIALS AND METHODS

From November 2009 to May 2011, consecutive patients who underwent MR imaging before a mechanical thrombectomy, with or without IV thrombolysis for ABAO, in our academic center were included in this prospective monocenter study.

Inclusion criteria were the following: 1) acute stroke in the posterior circulation within 24 hours of symptom onset, 2) MR imaging that included DWI before treatment, 3) acute basilar ischemia assessed on MR imaging matching clinical symptoms, and 4) ABAO confirmed by intra-arterial DSA and treated by using mechanical thrombectomy. Patients were excluded under the following conditions: 1) ineligibility for MR imaging; 2) pregnancy; 3) younger than 18 years of age; 4) cerebral imaging revealing an intracranial hemorrhage, a tumor, or a subacute infarct; and 5) life expectancy of <3 months.

The study was approved by the local ethics committee; informed consent was obtained from all patients or their relatives before treatment. The NIHSS score and the Glasgow Coma Scale were assessed by a stroke neurologist at admission and just before thrombectomy. An NIHSS score of 38 was assigned to an unconscious/comatose patient. Demographic characteristics, stroke presentation and severity, time of symptom onset, and imaging data were prospectively collected.

Imaging Protocol

MR imaging was performed as soon as possible after admission, by using a 1.5T scanner (Intera, Release 10; Philips Healthcare, Best, the Netherlands) with 33-mT/m hypergradients. MR imaging was available during the study period 24 hours per day, including outside workings hours. The MR imaging protocols, acquired in an axial section that covered the whole brain, included the following: 1) a T2*-weighted gradient-echo sequence (to screen for intracranial hemorrhage); 2) a DWI sequence ($b=0$, $b=500$, and 1000 s/mm^2 to identify the necrotic core) with apparent diffusion coefficient map reconstruction; 3) fluid-attenuated inversion recovery (to corroborate information about the time from symptom onset); and 4) the time-of-flight sequence that focused on the circle of Willis (to screen for large-vessel occlusion). Collateral flow of the distal basilar artery was evaluated by CTA or MRA according to the classification of Archer and Horenstein.[19]

Image Analyses: DWI Brain Stem Score

A 12-point semiquantitative BSS evaluated the extent of the DWI brain stem lesions by using prethrombectomy MR imaging. Our new score was based on direct visual interpretation of the DWI. To assess the score, we analyzed each brain stem level (medulla, pons, and midbrain) separately and considered the right side and the left side separately. One point was given for each unilateral high-intensity lesion at the brain stem level (medulla, pons, and midbrain) that occupied less than one-half of the area; 2 points were given if the lesion occupied more than one-half of the area. To obtain higher interobserver reproducibility, we chose the slide on which the lesion was more evident and more extended. The brain stem DWI lesion score ranged from 0 to 12. A DWI BSS of zero indicated the absence of visible brain stem ischemia, whereas a score of 12 indicated ischemic lesions in all the brain stem territories. Two examples of scoring are given in Figs 1 and 2.

To assess interobserver reproducibility, a neuroradiologist (P.M.) and 2 neurologists (D.M., I.M.), blinded to the clinical outcomes, each independently read each patient's diffusion-weighted MR images and assessed the DWI BSS. Moreover, a neuroradiologist (P.M.) and a neurologist (I.M.) assessed the posterior circulation Alberta Stroke Program Early CT Score (pc-ASPECTS) on DWI according to the method described by Tei et al[17] and the DWI score proposed by Renard et al.[15]

Therapeutic Regimens

Selective diagnoses and therapeutic DSA were performed in all cases with the patient under general anesthesia. Treatment of ABAO involved either a mechanical thrombectomy after IV thrombolysis (as a bridging therapy [$n = 19$] at a full dose 0.9 mg/kg, with a loading dose of 10%) or a mechanical thrombectomy alone ($n = 12$) in patients with a contraindication for IV thrombolysis according to the European Cooperative Acute Stroke Study (ECASS) III.[20] Mechanical thrombectomy was performed by using a Solitaire FR device, which was certified through the Conformité Européenne for thrombectomy. It is a laser-cut, self-expanding, and fully retrievable split-design nitinol device. The TICI scale was used to assess recanalization of the basilar artery. Antiplatelet drugs were started 24 hours after IV thrombolysis and after CT or MR imaging.

Outcome Measures

Successful recanalization was defined as a TICI grade of 2b or 3. Symptomatic intracranial hemorrhage was defined as a documented hemorrhage associated with a decline of ≥4 points in the NIHSS score. Device-related complications included vessel perforation, arterial dissection, or distal embolization of a previously uninvolved region. Clinical follow-up was assessed at 30, 90, and 180 days. Because outcome tends to be better for patients with ABAO after a longer follow-up, clinical outcome was assessed by using the ≥180-day NIHSS score, the mRS, the Barthel Index, and mortality rates. A favorable outcome was defined as a ≥180-day mRS score of 0–2. A very poor outcome, including death and total dependency, was defined as a mRS score of 5–6.

Statistical Analyses

The intraclass correlation coefficient was used to assess the intraobserver reproducibility of the DWI BSS. Statistical associations between DWI BSS and baseline characteristics were evaluated by using the Spearman rank correlation coefficient and the Fisher exact test. For the 3 scores, receiver operating characteristic analysis (ROC) curves were drawn by plotting sensitivity against the 1-specificity of each possible cutoff point of the score. The area under the ROC curve was calculated along with its 95% confi-
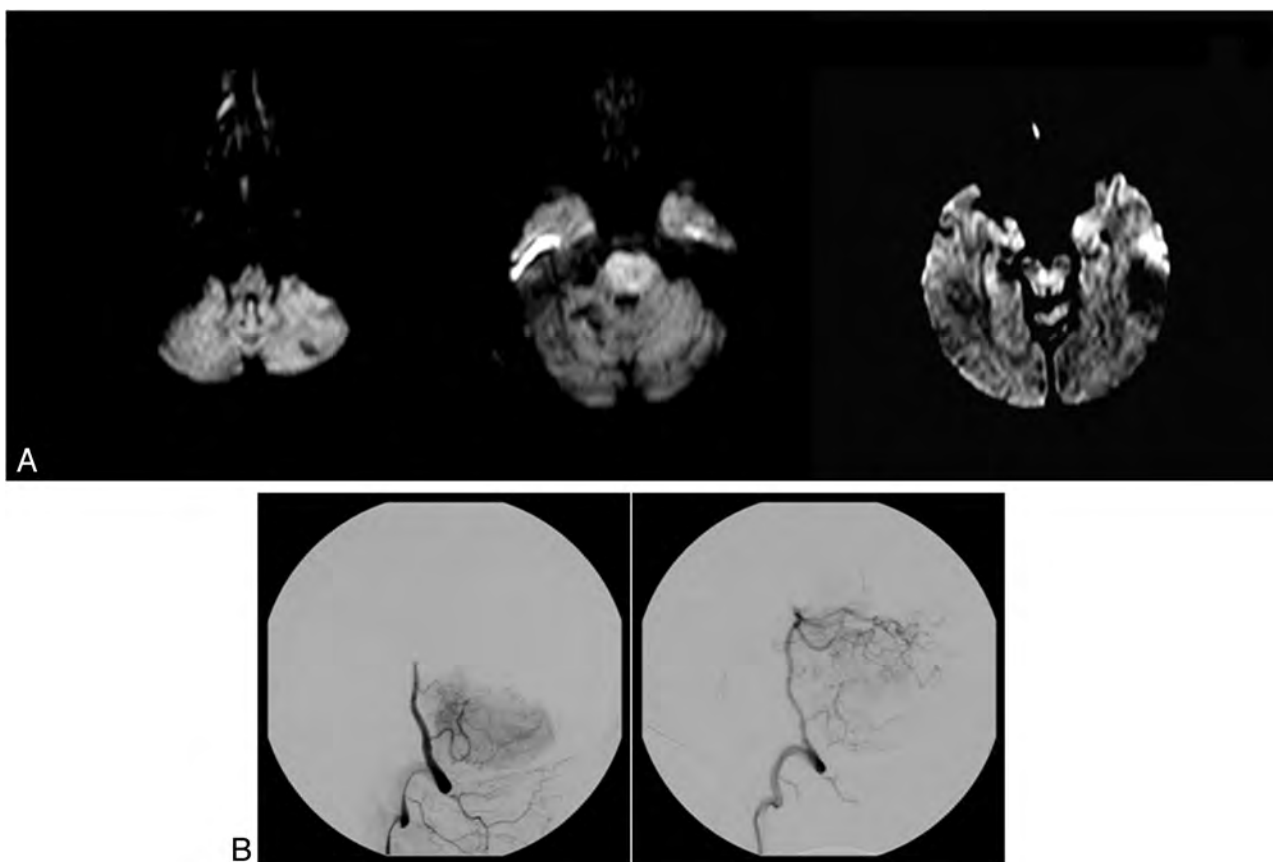
FIG 1. Prethrombectomy DWI (*A*) of a 54-year-old woman with tetraplegia in a coma. The DWI shows extensive bilateral lesions in the pons and limited bilateral lesions in the midbrain (brain stem score, 2 + 2 +1 + 1 = 6). DSA shows a midbasilar occlusion (*B*) successfully recanalized after IV thrombolysis and a thrombectomy (TICI 3). Time from symptom onset to recanalization was 283 minutes (4 hours 43 minutes). The outcome was unfavorable by day 180 (mRS 5).

dence interval and was compared among the 3 scores by using the method of DeLong et al.[21] The optimal cutoff point was determined to increase to a maximum to the Youden Index (the difference between the true-positive and the false-positive rates), and the positive predictive value (PPV), to predict a favorable outcome (mRS 0–2) and a very poor outcome (mRS 5–6). Potential independent predictors were tested in a multivariate logistic regression including the DWI BSS. The OR and its 95% CI were reported. The statistically significance threshold was set at 5%. Statistical analyses were conducted by using SAS software, Version 9.1 (SAS Institute, Cary, North Carolina).

RESULTS

Thirty-one consecutive patients with ABAO met the inclusion criteria of our study. Their prethrombectomy clinical status was severe, with a median NIHSS score of 38 (interquartile range [IQR] = 9–38).

Baseline characteristics, recanalization rates, procedural complications, and clinical outcomes are summarized in Tables 1 and 2.

The median time interval from symptom onset to MR imaging was 334 minutes (IQR = 160–480 minutes). Patients had a lesion detected by DWI in the following locations: 1 (3.2%) in the medulla, 27 (8.7%) in the pons, 14 (45.2%) in the midbrain, 8 (25.8%) in the temporo-occipital area, 7 (22.6%) in the thalamus,

and 17 (54.8%) in the cerebellum. All patients, except 1, presented with at least 1 lesion of the brain stem, including 16 patients with a bilateral lesion of the pons and 4 patients with a bilateral lesion of the midbrain. Twenty-one patients (67.7%) had multiple lesions.

The median DWI BSS was 4 (IQR = 2–4; range, 0–8). Twenty-one patients had a score of ≥3 (68%); no patient had a score >8. The mean time to assess the DWI BSS was 136 seconds (range, 16–300 seconds). On the DWI, the median pc-ASPECTS was 6 (IQR = 4–8; range = 2–10) and the median Renard et al[15] score was 3 (IQR = 2–4.5; range = 0–6).

All patients showed complete occlusion of the basilar artery (TICI 0). Only 1 patient presented with a distal vertebral artery occlusion and a proximal basilar occlusion. For patients with a bridging therapy, the median door-to-needle time was 97.5 minutes (IQR = 89–150 minutes) and the median time from the start of intravenous thrombolysis to groin puncture was 40 minutes (IQR = 20–103). The mean time from symptom onset to recanalization was 512 ± 258 minutes.

Among the 10 embolic infarcts observed in a new territory, 2 patients had severe neurologic deterioration or death and 5 patients experienced mild-to-moderate clinical sequelae (gait ataxia, abnormal visual field). One patient among the 5 with symptomatic intracranial hemorrhages died from a large symp-
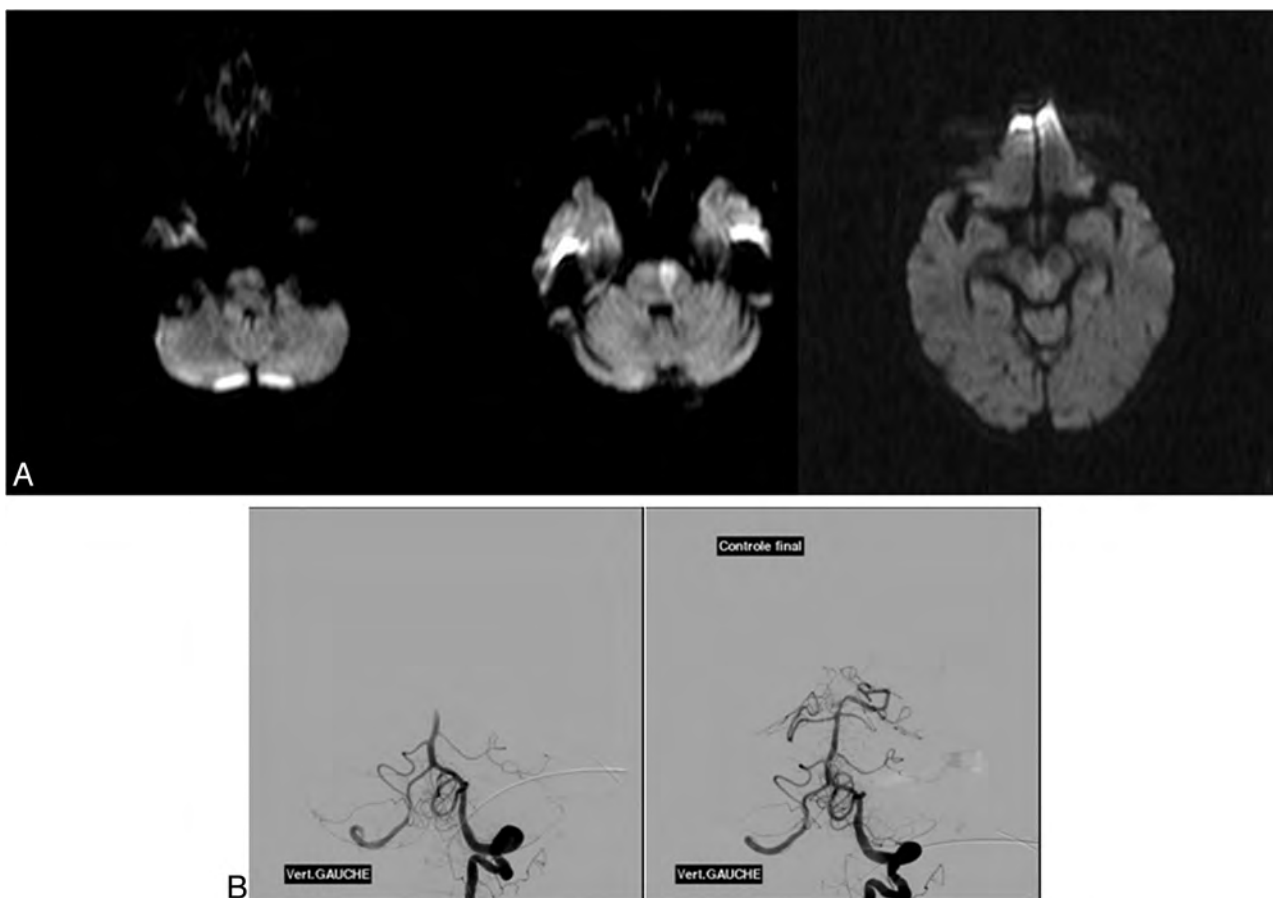
FIG 2. An 88-year-old woman who had right hemiparesis, vertigo, dysarthria, and vomiting. Pretreatment DWI (*A*) shows an extensive lesion in the left pons (brain stem score, 2) with a distal basilar clot on DSA (*B*) recanalized after IV thrombolysis and a thrombectomy (TICI 3). The time from symptom onset to recanalization was 336 minutes (4 hours 63 minutes). At day 180, the outcome was favorable (mRS 0).

Table 1: Baseline clinical and radiologic characteristics of 31 patients

Clinical Characteristics		Radiologic Characteristics (No.) (%)	
Mean age (yr)	61 ± 17	Site of basilar artery occlusion	
Men (No.) (%)	15 (48)	Proximal	4 (13)
Median NIHSS[a] (IQR)	38 (9–38)	Mid	8 (26%)
Median Glasgow Coma Scale[a] (IQR)	7 (4–14)	Distal	19 (61%)
Tetraplegia (No.) (%)	11 (35.5)	Presence of collateral flow	19 (61)
Coma (GCS ≤8) (No.) (%)	19 (61)		
Cardioembolic infarct (No.) (%)	16 (52)		

Note:—GCS indicates Glasgow Coma Scale.
[a] Prethrombectomy.

Table 2: Outcome characteristics (recanalization rate, procedural complications, and clinical outcome) of 31 patients

Recanalization rate (TICI 3–2b)	23 (74%)	Clinical outcome ≥180 days	
		Median NIHSS (IQR)	3 (2–6)
Procedural complications		Median Barthel Index (IQR)	100 (45–100)
New embolic infarcts	10 (32%)	Median mRS (IQR)	4 (2–6)
Intracranial hemorrhage symptomatic	5 (16%)	mRS 0–2	11 (35%)
		mRS 3–5	10 (32%)
Other	0	mRS 6	10 (32%)

tomatic posterior fossa hematoma. Only 1 device-related complication occurred, a postprocedural vertebral dissection with posterior inferior cerebellar artery infarction.

Predictive Factors for Clinical Outcome

Univariate analysis failed to demonstrate any statistical significance among coma, tetraplegia, and the clinical outcome. Only 18% of patients presenting with tetraplegia had a favorable outcome (mRS ≤ 2), while 82% of patients presenting without tetraplegia had a favorable outcome (OR = 4.05 [0.69–23.95]; *P* = .12). Furthermore, 68% of patients presenting with coma had an unfavorable outcome, while 32% of patients presenting without coma had unfavorable outcome (OR = 1.80 [0.39–8.35], *P* = .45).

Table 3: Statistical measures of the cutoff performance for the 3 scores

Scores	AUC (95% CI)	Cutoff	Sensitivity	Specificity	PPV	NPV
Favorable outcome (mRS ≤2)						
DWI BSS	0.76 (0.58–0.95)	<3	64%	85%	70%	81%
pc-ASPECTS	0.63 (0.41–0.84)	≥7	55%	65%	46%	72%
Renard et al[15]	0.73 (0.53–0.92	<3.5	82%	65%	56%	87%
Very poor outcome (mRS ≥5)						
DWI BSS	0.80 (0.63–0.96)	≥2	100%	41%	58%	100%
		≥3	93%	53%	62%	90%
		≥4	79%	65%	65%	79%
		≥5	29%	94%	80%	62%
		≥6	21%	100%	100%	61%

Note:—NPV indicates negative predictive value.

Table 4: Functional outcome according to the categorized diffusion-weighted imaging brain stem score

DWI BSS	No.	mRS 0–2	mRS 3–4	mRS 5–6	P Value[a]
0–2	10	7 (70%)	2 (20%)	1 (10%)	.05
3–5	18	4 (22%)	6 (33%)	8 (44%)	
6–12	3	0 (0%)	0 (0%)	3 (100%)	
Total	31	11 (35%)	6 (19%)	14 (45%)	

[a] Fisher P value.

Table 5: Predictors of favorable outcome (mRS ≤2) analyzed by univariate regression logistic

	OR	95% CI	P Value
Age (yr)	0.96	0.91–1.01	.08
DWI BSS <3	9.92	1.75–56.30	.01
pc-ASPECTS ≥7	2.23	0.50–10.00	.30
Renard et al[15] <3.5	8.36	1.40–49.88	.02

Patients with successful recanalization showed a nonsignificant trend toward a better outcome ($P = .20$). Moreover, the mean time from symptom onset to recanalization tended to be lower in our patients with a poor outcome compared with patients with a favorable outcome ($P = .03$). New embolic infarcts ($P = 1$) or symptomatic intracranial hemorrhage ($P = .13$) did not reach significance to predict clinical outcome.

Correlation between Scores and Clinical Variables

The DWI BSS was moderately correlated with the score of Renard et al[15] ($r = 0.63$) and was weakly correlated with the pc-ASPECTS ($r = -0.38$), whereas a strong correlation appeared between the pc-ASPECTS and the score of Renard et al ($r = -0.88$).

The DWI BSS was significantly higher in the presence of tetraplegia ($P = .001$) or coma ($P = .005$) at admission. No relation was found between this score and age, the baseline NIHSS and Glasgow Coma Scale scores, time interval from symptom onset to MR imaging, presence of collateral flow, use of IV thrombolysis, the recanalization rate, new embolic infarct, or symptomatic intracranial hemorrhage.

Predictors

Brain stem DWI lesion measurements demonstrated a good reproducibility with an intraclass correlation coefficient of 0.98 (95% CI, 0.96–0.99). The area under the curve, which approximated the chance that the DWI BSS correctly predicted a favorable outcome (mRS < 2), was 0.76 (95% CI, 0.60–0.93). It was better but not significantly different ($P = .25$) from the score of Renard et al[15] (area under the curve = 0.73) and the pc-ASPECTS (area under the curve = 0.63). According to the ROC, the optimal cutoff score to predict a favorable outcome was 3 for DWI BSS, 3.5 for the score of Renard et al, and 7 for pc-ASPECTS. Associated performances are presented in Table 3. In fact, the probability of having a favorable outcome reached 70% if the DWI BSS was <3 (PPV). The functional outcomes, according to the DWI BSS, are presented in Table 4.

In a univariate model, a DWI BSS of <3 and a lesion score of

Renard et al[15] of <3.5 were predictors of a good outcome (mRS < 2), whereas a pc-ASPECTS of ≥7 was not statistically relevant (Table 5). In the multivariate analysis, age, the baseline Glasgow Coma Scale score, DWI BSS of <3, Renard et al[15] score <3.5, and IV thrombolysis were tested. Only a DWI BSS of <3 and age were considered predictive of favorable outcome ($OR_{DWI<3}$ = 18.4[95% CI, 2.1–162.4] and $OR_{Age} = 0.93$ [95% CI, 0.97–0.10]).

Last, the probability of having a very poor outcome (mRS > 5) if the DWI BSS was >5 reached 80% (PPV) and 100% if this score was >6 (Table 3). With these properties associated with an area under the curve of 0.80, the DWI BSS appeared more relevant than the score of Renard et al[15] (area under the curve = 0.71) and the pc-ASPECTS (area under the curve = 0.59) for predicting very poor outcome.

DISCUSSION

This study reports the largest baseline DWI data available on ABAO and shows that our new BSS could predict clinical outcome without needing additional time-consuming postprocessing.

In posterior circulation stroke, previous studies have failed to detect a correlation between lesion volume detected by DWI and the neurologic scale at onset[13] or functional outcome.[18] More recently, authors[15-17] have studied patients with a posterior circulation stroke by using various neuroradiologic scales of DWI. In 2010, Tei et al[17] evaluated the usefulness of the pc-ASPECTS on DWI to predict functional outcome in 132 patients with a posterior circulation infarction. They found that the pc-ASPECTS was an independent predictor of functional outcome ($P < .001$). According to the ROC, the optimal cutoff score that predicted a favorable outcome was a pc-ASPECTS of ≥7 and an NIHSS score of ≤5. Renard et al[15] reported 16 patients with ABAO who received intra-arterial thrombolysis. Using a 10-point semiquantitative DWI score, they found that in univariate analyses, all patients with a lesion score of >3 had a worse outcome or died ($P = .026$). Cho et al[16] analyzed 29 patients treated with endovascular procedures for ABAO and found that the brain stem score was the only independent baseline predictor of clinical outcome. In contrast to previous studies[13,14] on vertebrobasilar ischemic stroke,

they found a significant association between the DWI brain stem lesion score and the baseline NIHSS score, as well as between the presence and length of a coma before treatment.

The results of Cho et al[16] support the use of sectorial scoring of DWI lesions in ABAO rather than global volume assessment. However, these previous reports have some limitations. The Renard et al[15] score and the pc-ASPECTS[17] included more items than our score (ie, they included an infarction in the cerebellum, thalamus, or temporo-occipital lobe). These lesions are less involved in functional prognoses than those in the brain stem. Effectively, small strategic brain stem infarcts can cause devastating clinical syndromes, whereas large cerebellar infarcts may cause minimal symptoms and attenuate the strength of the relationship between lesion volume and clinical functional status.[14] For instance, with the pc-ASPECTS, a patient with a large bilateral pontine infarction has the same lesion score (of 2) as a patient with a small bilateral cerebellar infarction, but the former condition is likely to have a worse prognosis.[15] Moreover, patients lose the same number of points if they present with an extensive lesion of the structure as well as a punctiform infarct. To improve correlations with mRS, which is essentially based on motor function, Renard et al[15] gave a higher score in lesion structures that contain a pyramidal tract. These findings suggest that the main benefit of DWI analysis remains the brain stem, essentially because involvement of the brain stem, in particular the pons and midbrain, is critical to functional outcome.

The use of a brain stem score to identify a predictor of clinical outcome had been tested by Cho et al.[16] Their score is based on arterial territory segmentation of the medulla, pons, and midbrain, as described by Tatu et al.[22] However, they did not determine the optimal cutoff score, according to ROC, to predict outcome. Moreover, MR imaging analysis of the exact volume of a lesion in a brain stem score appears difficult to assess routinely as a standard score in an acute phase, especially by using DWI sequences, which have poor spatial resolution.

In our population of patients with ABAO, a pc-ASPECTS of ≥7 was not statistically associated with the favorable clinical outcome. However, our population did have specific differences. In the study of Tei et al,[17] all the arteries within the posterior territory were involved and there was no exclusive ABAO, acute arterial occlusion was not proved, and no patients received acute revascularization therapy. In addition, their patients had less severe symptoms, and the pc-ASPECTS was evaluated within 12–36 hours after stroke onset.[17] This time window is very long compared with that in current thrombolytic therapies.

The use of DWI BSS may help to identify patients who could benefit from recanalization therapy. Our aim was to simplify the decision-making algorithm, focusing on the DWI BSS, evaluated only at the level of the brain stem, because it seems to be the most critical area for functional outcome. DWI BSS is a rapid and easy-to-use score, with an excellent interobserver reliability. Furthermore, in comparison with previous scores published in the literature, the DWI BSS appeared to relate better to good and poor outcomes, respectively. Looking at the results of our study, we can state that patients with ABAO and a DWI BSS of <3 are good candidates for mechanical revascularization. Conversely, basilar artery recanalization of patients with DWI BSS of ≥6 is not re-

lated to good clinical outcome. Hence, patients in this group should not be considered for mechanical treatment.

The size of our sample is relatively small. Further studies are required in a larger ABAO population to evaluate whether the DWI BSS is a reliable predictor for clinical outcome or to evaluate other MR imaging parameters to identify patients who can benefit from recanalization therapy.

CONCLUSIONS

This report shows that a DWI BSS is useful in predicting outcomes in ABAO treated by thrombectomy and may simplify the decision-making algorithm. However, further evaluation is needed before it can be used as a routine treatment strategy.

REFERENCES

1. Mortimer AM, Bradley M, Renowden SA. **Endovascular therapy for acute basilar artery occlusion: a review of the literature.** *J Neurointervent Surg* 2012;4:266–73

2. Mattle HP, Arnold M, Lindsberg PJ, et al. **Basilar artery occlusion.** *Lancet Neurol* 2011;10:1002–14

3. Schonewille WJ, Algra A, Serena J, et al. **Outcome in patients with basilar artery occlusion treated conventionally.** *J Neurol Neurosurg Psychiatry* 2005;76:1238–41

4. Eckert B, Kucinski T, Pfeiffer G, et al. **Endovascular therapy of acute vertebrobasilar occlusion: early treatment onset as the most important factor.** *Cerebrovasc Dis* 2002;14:42–50

5. Arnold M, Nedeltchev K, Schroth G, et al. **Clinical and radiological predictors of recanalisation and outcome of 40 patients with acute basilar artery occlusion treated with intra-arterial thrombolysis.** *J Neurol Neurosurg Psychiatry* 2004;75:857–62

6. Lutsep HL, Rymer MM, Nesbit GM. **Vertebrobasilar revascularization rates and outcomes in the MERCI and multi-MERCI trials.** *J Stroke Cerebrovasc Dis* 2008;17:55–57

7. Andersson T, Kuntze Soderqvist A, Soderman M, et al. **Mechanical thrombectomy as the primary treatment for acute basilar artery occlusion: experience from 5 years of practice.** *J Neurointerv Surg* 2013;5:221–25

8. Espinosa de Rueda G, Parrilla J, Zamarro B, et al. **Treatment of acute vertebrobasilar occlusion using thrombectomy with stent retrievers: initial experience with 18 patients.** *AJNR Am J Neuroradiol* 2013;34:1044–48

9. Mordasini P, Brekenfeld C, Byrne JV, et al. **Technical feasibility and application of mechanical thrombectomy with the Solitaire FR revascularization device in acute basilar artery occlusion.** *AJNR Am J Neuroradiol* 2013;34:159–63

10. Roth C, Mielke A, Siekmann R, et al. **First experiences with a new device for mechanical thrombectomy in acute basilar artery occlusion.** *Cerebrovasc Dis* 2011;32:28–34

11. Albers GW, Thijs VN, Wechsler L, et al, for the DEFUSE investigators. **Magnetic resonance imaging profiles predict clinical response to early reperfusion: the diffusion and perfusion imaging evaluation for understanding stroke evolution (DEFUSE) study.** *Ann Neurol* 2006;60:508–17

12. Nezu T, Koga M, Kimura K, et al. **Pretreatment ASPECTS on DWI predicts 3-month outcome following rt-PA: SAMURAI rt-PA registry.** *Neurology* 2010;75:555–61

13. Linfante I, Llinas RH, Schlaug G, et al. **Diffusion-weighted imaging and National Institutes of Health Stroke Scale in the acute phase of posterior-circulation stroke.** *Arch Neurol* 2001;58:621–28

14. Ostrem JL, Saver JL, Alger JR, et al. **Acute basilar artery occlusion: diffusion-**

perfusion MRI characterization of tissue salvage in patients receiving intra-arterial stroke therapies. *Stroke* 2004;35:e30–e34

15. Renard D, Landragin N, Robinson A, et al. **MRI-based score for acute basilar artery thrombosis.** *Cerebrovasc Dis* 2008;25:511–16

16. Cho TH, Nighoghossian N, Tahon F, et al. **Brain stem diffusion-weighted imaging lesion score: a potential marker of outcome in acute basilar artery occlusion.** *AJNR Am J Neuroradiol* 2009; 30:194–98

17. Tei H, Uchiyama S, Usui T, et al. **Posterior circulation ASPECTS on diffusion-weighted MRI can be powerful marker for predicting functional outcome.** *J Neurol* 2010;257:767–73

18. Engelter ST, Wetzel SG, Radue EW, et al. **The clinical significance of diffusion-weighted MR imaging in infratentorial strokes.** *Neurology* 2004;62:574–80

19. Archer CR, Horenstein S. **Basilar artery occlusion: clinical and radiological correlation.** *Stroke* 1977;8:383–90

20. Hacke W, Markku K, Bluhmki E, et al, for the ECASS Investigators. **Thrombolysis with alteplase 3 to 4.5 hours after acute ischemic stroke.** *N Engl J Med* 2008;359:1317–29

21. DeLong ER, DeLong DM, Clarke-Pearson DL. **Comparing the areas under two or more correlated receiver operating characteristic curves: a nonparametric approach.** *Biometrics* 1988;44:837–45

22. Tatu L, Moulin T, Bougousslavsky J, et al. **Arterial territories of human brain: brainstem and cerebellum.** *Neurology* 1996;47:1125–35

Clinical and Angiographic Features and Stroke Types in Adult Moyamoya Disease

D.-K. Jang, K.-S. Lee, H.K. Rha, P.-W. Huh, J.-H. Yang, I.S. Park, J.-G. Ahn, J.H. Sung, and Y.-M. Han

ABSTRACT

BACKGROUND AND PURPOSE: This study was conducted to elucidate the association between clinical and angiographic characteristics and stroke types in adult Moyamoya disease that has been rarely evaluated.

MATERIALS AND METHODS: We analyzed the clinical and radiologic data obtained from a retrospective adult Moyamoya disease cohort with acute strokes, which were classified into 7 categories: large-artery infarct, hemodynamic infarct, perforator infarct, deep intracerebral hemorrhage, lobar intracerebral hemorrhage, intraventricular hemorrhage, and SAH. With conventional angiography, which was performed in the hemispheres with acute strokes, the Suzuki angiographic stage, intracranial aneurysm, major artery occlusion, and collateral vessel development were confirmed within 1 month of stroke onset.

RESULTS: This study included 79 patients with acute ischemic stroke and 96 patients with acute hemorrhagic stroke. The angiographic stage had a strong tendency to be more advanced in the hemorrhagic than the ischemic patients ($P = .061$). Intracranial aneurysms were more frequently found in the hemorrhagic than ischemic or control hemispheres ($P = .002$). Occlusions of the anterior cerebral artery and development of fetal-type posterior cerebral artery were more frequently observed in the hemorrhagic than the ischemic ($P = .001$ and .01, respectively) or control hemispheres ($P = .011$ and .013, respectively). MCA occlusion ($P = .039$) and collateral flow development, including the ethmoidal Moyamoya vessels ($P = .036$) and transdural anastomosis of the external carotid artery ($P = .022$), occurred more often in the hemorrhagic than the ischemic hemispheres. Anterior cerebral artery occlusion occurred more frequently in patients with deep intracerebral hemorrhage or intraventricular hemorrhage than with lobar intracerebral hemorrhage ($P = .009$).

CONCLUSIONS: In adult Moyamoya disease, major artery occlusion and collateral compensation occurred more often in the hemorrhagic than in the ischemic hemispheres. Thus, anterior cerebral artery occlusion with or without MCA occlusion and intracranial aneurysms may be the main contributing factors to hemorrhagic stroke in adult patients with Moyamoya disease.

ABBREVIATIONS: ACA = anterior cerebral artery; ECA = external carotid artery; HI = hemodynamic infarct; IVH = intraventricular hemorrhage; LAI = large-artery infarct; MMD = Moyamoya disease; PCA = posterior cerebral artery; PI = perforator infarct

Moyamoya disease (MMD) is a chronic, progressive cerebrovascular disorder with bilateral stenosis or occlusion of the supraclinoid ICA and its major branches at the surrounding area of the circle of Willis.[1] MMD exhibits diverse symptoms, such as TIA, recurrent TIAs, cerebral infarct, intracranial hemorrhage, headache, seizure, cognitive decline, ataxia, or choreiform movements; it can also be asymptomatic. In adult MMD, approximately half of the patients have intracranial hemorrhage, and the rest of the patients have TIA or cerebral infarct.[2,3] Recently, MMD was reported to exhibit a bimodal peak of symptom onset in the ischemic type and a unimodal peak in the hemorrhagic type.[4] However, the cause of differential onset and the distinct presentation in MMD are not completely understood. Although angio-

graphic factors causing intracranial hemorrhage in adult MMD, such as dilation and branch extension of the anterior choroidal artery or posterior communicating artery have also been reported,[5-7] direct comparison studies on the angiographic features according to stroke type in adult MMD have been limited.

We hypothesized that there may be differences in major artery occlusion and collateral patterns according to stroke type. Because understanding differences in the angiographic characteristics of ischemic and hemorrhagic stroke types may be helpful to prevent future strokes and make a good prognosis in adult patients with MMD, this study aimed to compare the angiographic features of adult MMD with ischemic and hemorrhagic stroke.

MATERIALS AND METHODS

From 2002–2011, a retrospective adult MMD cohort in 8 hospitals was recruited. The study protocol was approved by the Institutional Review Board of Catholic Medical Center at the Catholic University of Korea. The inclusion criteria were as follows: 1) age ≥18 years, 2) compatible with the Japanese MMD diagnosis guideline,[1] 3) radiologically proven symptomatic acute stroke, 4) digital subtraction angiography that had been performed within 1 month of the acute stroke, and 5) newly diagnosed MMD. Patients with Moyamoya syndrome or probable MMD, ethnicity other than Korean, incomplete radiologic data, or a term between acute stroke and DSA longer than 1 month were excluded. Those who had had repeat strokes at diagnosis or new strokes after surgical treatment were also excluded. The baseline characteristics were scrutinized, such as age at the initial diagnosis of MMD; sex; the presence of hypertension or antihypertensive medication history; the presence of diabetes mellitus or antidiabetic medication history; clinical symptoms, including headaches, weakness, sensory changes, visual disturbances, seizures, and decreased consciousness; initial Glasgow coma scale score; and mRS.

An ischemic stroke was confirmed by use of MR DWI, and a hemorrhagic stroke was identified by means of CT, T2WI, or gradient-echo MR imaging of abnormal lesions, with a low signal indicating a hemosiderin rim that was larger than 0.5 cm. Acute ischemic strokes were categorized into 6 groups, as suggested by Mugikura et al[8] and Kim et al[9]: anterior cerebral artery (ACA) infarct; anterior watershed infarct between the ACA and MCA territories; anterior half of the MCA territory infarct; posterior half of MCA territory infarct; posterior watershed infarct between the MCA and posterior cerebral artery (PCA) territories; PCA infarct; and perforator infarct (PI). Acute cerebral hemorrhages were classified as follows: frontal lobe hemorrhage, temporal lobe hemorrhage, parietal lobe hemorrhage, occipital lobe hemorrhage, basal ganglia hemorrhage, thalamic hemorrhage, intraventricular hemorrhage (IVH), and SAH.

Angiographic details of all the hemispheres included the following: angiographic stage as suggested by Suzuki and Takaku[10]; ACA, MCA, and PCA occlusions; fetal PCA development (enlargement of the posterior communicating artery); ethmoidal Moyamoya development; leptomeningeal collateral from the PCA to the ACA or MCA territories; collateral flow through the posterior communicating artery from the PCA to the ICA; transdural anastomosis from the external carotid artery (ECA); and cerebral aneurysm (Fig 1). Two independent

neurologic physicians reviewed all the radiologic data. When a disagreement regarding the diagnosis and measurement between reviewers occurred, a consensus was drawn after a thorough discussion.

There were 372 adult patients with MMD from 2002–2011. Sixty-four patients (17.2%) were excluded because of incomplete radiologic data ($n = 60$) and other ethnicity ($n = 4$; 3 Chinese and 1 Japanese). Among the remaining 308 study entrants, 130 (42.2%) were excluded because of presenting symptoms of chronic or recurrent stroke ($n = 71$, 23.1%), TIA ($n = 40$, 12.9%), headache ($n = 9$, 2.9%), dizziness ($n = 4$, 1.3%), seizure ($n = 1$, 0.3%), and an absence of symptoms ($n = 5$, 1.6%). Finally, 178 patients (57.8%) who had acute stroke and underwent DSA within 1 month from ictus were included. One patient with ruptured basilar apex aneurysm, 1 patient with pure IVH, and 1 patient with nonaneurysmal SAH were excluded from the final analysis because of an inability to define the laterality of the bleeding site.

Statistics

To compare the angiographic characteristics between acute ischemic stroke and hemorrhagic stroke in adult MMD, the stroke subtypes were grouped as follows: ACA infarct, anterior or posterior half of an MCA infarct and a PCA infarct into a large-artery infarct; PI; anterior watershed and posterior watershed infarct into a hemodynamic infarct (HI); basal ganglia or thalamic hemorrhage into a deep intracerebral hemorrhage; frontal, temporal, or parietal lobe hemorrhage into a lobar intracerebral hemorrhage; IVH; and SAH. To confirm the laterality of strokes, in cases of pure IVH, the stroke hemisphere was defined as the side of the lateral ventricle with the larger hemorrhage volume. The baseline characteristics and angiographic parameters between the ischemic and hemorrhagic hemispheres were compared by means of the χ^2 or Fisher exact tests for categoric variables and the t test for continuous variables. The Mann-Whitney U test was performed for non-normally distributed continuous variables. Two-tailed tests were used in all statistical analyses. Statistical significance was established at a value of $P \leq .05$. All statistical analyses were performed by use of SAS version 9.2 (SAS Institute, Cary, North Carolina).

RESULTS

Patient Characteristics

The demographic data of 175 adult patients with MMD with acute stroke at diagnosis are summarized in Table 1. The median age at diagnosis was 43 years (range, 18–78 years). The male-to-female ratio was 1 to 1.57. Of the 175 patients, 44 (25.1%) had a history of hypertension, and 20 (11.4%) had diabetes. The most common symptoms of stroke were weakness (40.6%), decreased consciousness (35.4%), headache (29.7%), speech disturbance (23.4%), visual disturbance (9.1%), sensory change (5.1%), and seizure (2.9%). An initial Glasgow Coma Scale score >12 was observed in 133 patients (76%), and an initial mRS <3 was observed in 100 patients (57.1%). The angiographic stages were as follows: stage 1 in 29 hemispheres (8.3%), stage 2 in 87 hemispheres (24.9%), stage 3 in 137 hemispheres (39.1%), stage 4 in 65 hemispheres (18.6%), stage 5 in 29 hemispheres (8.3%), and stage 6 in 3 hemispheres (0.9%). Nine intracranial aneurysms were identified (5 ruptured and 4 unruptured). Seventy-nine patients (45.1%) had ischemic stroke and 96 patients
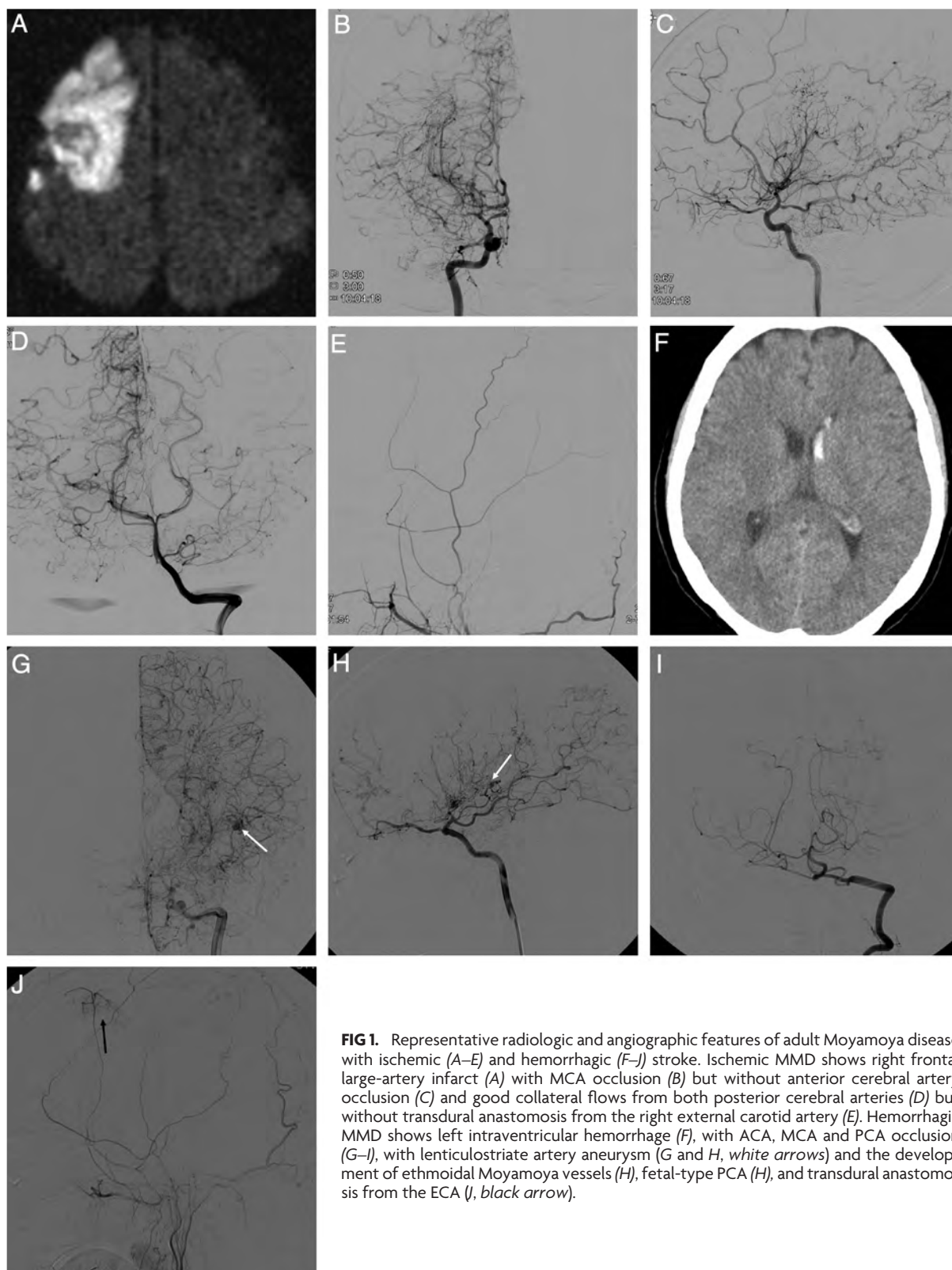
FIG 1. Representative radiologic and angiographic features of adult Moyamoya disease with ischemic *(A–E)* and hemorrhagic *(F–J)* stroke. Ischemic MMD shows right frontal large-artery infarct *(A)* with MCA occlusion *(B)* but without anterior cerebral artery occlusion *(C)* and good collateral flows from both posterior cerebral arteries *(D)* but without transdural anastomosis from the right external carotid artery *(E)*. Hemorrhagic MMD shows left intraventricular hemorrhage *(F)*, with ACA, MCA and PCA occlusion *(G–I)*, with lenticulostriate artery aneurysm *(G and H, white arrows)* and the development of ethmoidal Moyamoya vessels *(H)*, fetal-type PCA *(H)*, and transdural anastomosis from the ECA *(J, black arrow)*.

(54.9%) had hemorrhagic stroke. Between the ischemic and hemorrhagic stroke groups, there was no significant difference regarding hypertension; however, diabetes occurred more frequently in the ischemic stroke group (17.7%) than in the hemorrhagic stroke group (6.3%) ($P = .018$). With respect to symptom presentation, headache and consciousness deterioration occurred more frequently in the hemorrhagic stroke group than in the ischemic stroke group ($P = .002$ and $P < .001$, respectively). However, sensory changes as well as speech and visual disturbances were more frequently observed in the ischemic stroke group than in the hemorrhagic stroke group ($P = .012$, $P < .001$, and $P < .001$, respectively). The prevalence rates for weakness and seizure were not different between the 2 groups. The

Table 1: Clinical summary of 175 adult patients with Moyamoya disease with acute ischemic or hemorrhagic stroke

Variables	Total (n = 175)	Infarct group (n = 79)	Hemorrhage Group (n = 96)	P Value
Demographics				
Age, y (mean ± SD)	42.2 ± 11.3	41.2 ± 11.2	43.1 ± 11.3	.28
Female	107 (61.1)	46 (58.2)	61 (63.5)	.47
Family history	1 (0.6)	1 (1.3)	0	.45
Vascular risk factors				
Hypertension	44 (25.1)	22 (27.8)	22 (22.9)	.45
Diabetes	20 (11.4)	14 (17.7)	6 (6.3)	.018
Symptoms				
Headache	52 (29.7)	14 (17.7)	38 (39.6)	.002
Weakness	71 (40.6)	33 (41.8)	38 (39.6)	.76
Sensory change	9 (5.1)	8 (10.1)	1 (1.0)	.012
Speech disturbance	41 (23.4)	30 (38.0)	11 (11.5)	<.001
Visual disturbance	16 (9.1)	15 (19.0)	1 (1.0)	<.001
Seizure	5 (2.9)	1 (1.3)	4 (4.2)	.38
Decreased consciousness	62 (35.4)	4 (5.1)	58 (60.4)	<.001
Initial neurology				
Initial GCS (>12)	133 (76.0)	78 (98.7)	55 (57.3)	<.001
Initial mRS (<3)	100 (57.1)	55 (69.6)	45 (46.9)	.002
Suzuki stage (350 hemispheres)				.061
1	29 (8.3)	19 (12.0)	10 (5.2)	
2	87 (24.9)	46 (29.1)	41 (21.4)	
3	137 (39.1)	53 (33.5)	84 (43.8)	
4	65 (18.6)	26 (16.5)	39 (20.3)	
5	29 (8.3)	13 (8.2)	16 (8.3)	
6	3 (0.9)	1 (0.6)	2 (1.0)	

Note:—SD indicates standard deviation; GCS, Glasgow Coma Scale.

Table 2: Distribution of intracranial aneurysms[a] according to acute stroke subtype in 350 Moyamoya hemispheres

	Ischemic Stroke (n = 85)	Hemorrhagic Stroke (n = 96)	Silent Stroke (n = 36)	None (n = 133)	P Value
Bleeding					.002
Ruptured	0	5	0	0	
Suzuki stage					
2		2			
3		3			
Unruptured	1	3	0	0	
Suzuki stage					
3		1			
5	1	2			
Location					
Anterior circulation		5	0	0	
Posterior circulation		4	0	0	

[a] One aneurysm was identified in the infarct hemisphere (unruptured anterior falx artery aneurysm), and 8 aneurysms were identified in the hemorrhage hemispheres, consisting of 5 ruptured aneurysms (1 at the splenial artery, 2 at the anterior choroidal artery, 1 at the lenticulostriate artery, and 1 at the posterior cerebral artery) and 3 unruptured aneurysms (2 at the basilar apex and 1 at the superior cerebellar artery).

initial neurologic status (Glasgow Coma Scale and mRS) was better in the ischemic stroke group than in the hemorrhagic stroke group (P < .001 and .002, respectively).

Stroke and Angiographic Profiles

Acute strokes were identified in 181 hemispheres with 85 ischemic strokes (6 bilateral) and 96 hemorrhagic strokes among 350 hemispheres in 175 patients. In addition, 36 hemispheres with silent strokes with abnormal signal changes on T1 or T2 MR imaging were observed, and the remaining 133 hemispheres (control hemispheres) did not show any symptoms or abnormal lesions on brain MR or CT. Representative adult patients with MMD with acute ischemic or hemorrhagic stroke are illustrated in Fig 1. There were significantly more intracranial aneurysms in the hemorrhagic

hemisphere than the control or ischemic hemisphere (P = .002) (Table 2). The proportions of acute stroke were as follows: LAI in 37 hemispheres (20.4%), HI in 35 hemispheres (19.3%), PI in 13 hemispheres (7.2%), deep intracerebral hemorrhage in 50 hemispheres (27.6%), IVH in 32 hemispheres (17.7%), and lobar intracerebral hemorrhage in 14 hemispheres (7.7%) (Fig 2A). The ratio of LAI to HI or PI was 1:1.3, and the ratio of deep intracerebral hemorrhage or IVH to lobar intracerebral hemorrhage was 5.9:1 (Tables 3 and 4). The angiographic stage was significantly more advanced in the hemorrhagic than the control hemispheres and markedly tended to be more progressed in the hemorrhagic than the ischemic hemispheres (Fig 2C). In the hemorrhagic hemispheres, ACA occlusion was more frequently observed compared with the ischemic and control hemispheres (P = .001 and .01, respectively) (Fig 3A, -C). MCA occlusion was also more frequent in the hemorrhagic than the ischemic hemisphere (.039). Hemorrhagic hemispheres were more advanced than ischemic or control hemispheres with regard to ACA and MCA occlusion patterns (P = .034 and .001, respectively) (Fig 3C). In addition, collateral flows, including ethmoidal Moyamoya and transdural anastomosis from the ECA, were more common in the hemorrhagic hemisphere than in the ischemic hemisphere (P = .036 and .022, respectively) (Fig 3E, -I). Fetal PCA was also more frequently observed in the hemorrhagic hemisphere than in the control and ischemic hemispheres (P = .001 and .011, respectively) (Fig 3F).

For the subgroup analysis, according to the topographic patterns of acute stroke, acute ischemic strokes were dichotomized into LAI (37) and HI or PI (48), and acute hemorrhagic strokes were classified into deep intracerebral hemorrhage or IVH (82) and lobar intracerebral hemorrhage (14). ACA, MCA, and PCA occlusions were found more frequently in the LAI group than in the HI or PI group (P = .009, .031, and .003, respectively), but leptomeningeal collateral flow from the PCA to the ACA or MCA occurred more frequently in the HI or PI group than in the LAI group (P = .001) (Table 3). ACA occlusion, PCA occlusion, ethmoidal Moyamoya, and transdural anastomosis from the ECA occurred more often in posterior circulation than in anterior circulation ischemic strokes (P = .027, P < .001, P = .026, and P < .001, respectively) (Table 3). In the hemorrhagic hemispheres, only an ACA occlusion was observed more frequently in the deep intracerebral hemorrhage or
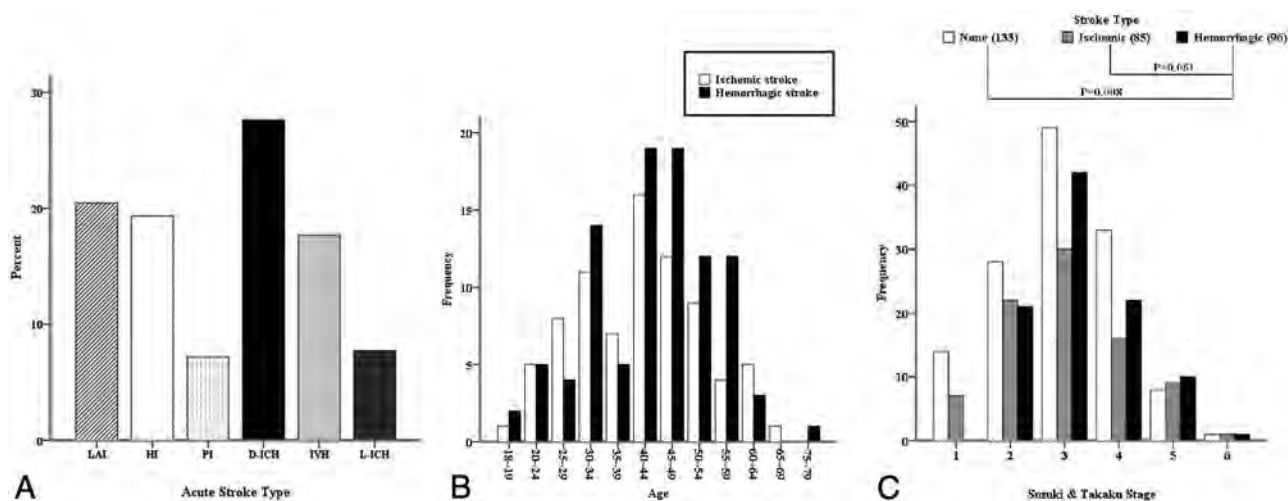
FIG 2. Topographic patterns of acute stroke (A), age distribution of adult Moyamoya disease according to stroke type (B, P = .28), and angiographic distribution of stroke type (C).

Table 3: Angiographic differences according to topographic patterns of acute infarct in adult Moyamoya disease

| | LAI Versus HI or PI | | | Anterior Versus Posterior | | |
| | | | | Anterior Circulation | Posterior Circulation | |
Variables	LAI (n = 37)	HI or PI (n = 48)	P Value	(n = 57)	(n = 28)	P Value
ACA occlusion	30 (81.1)	26 (54.2)	.009	33 (57.9)	23 (82.1)	.027
MCA occlusion	31 (83.8)	30 (62.5)	.031	39 (68.4)	22 (78.6)	.32
PCA occlusion	18 (48.6)	9 (18.8)	.003	11 (19.3)	16 (57.1)	<.001
Ethmoidal Moyamoya	12 (32.4)	14 (29.2)	.74	13 (22.8)	13 (46.4)	.026
Fetal-type PCA	12 (32.4)	18 (37.5)	.63	21 (36.8)	9 (32.1)	.67
PCA collateral	23 (62.2)	44 (91.7)	.001	47 (82.5)	20 (71.4)	.24
PcomA collateral	3 (8.1)	2 (4.2)	.65	3 (5.3)	2 (7.1)	.72
ECA collateral	16 (43.2)	13 (27.1)	.12	12 (21.1)	17 (60.7)	<.001

Note:—Ethmoidal Moyamoya, fetal-type PCA, PCA collateral, PcomA collateral, and ECA collateral indicate the development of ethmoidal Moyamoya vessels, enlargement of PcomA or showing blood supply to PCA territories through PcomA, leptomeningeal collateral vessels from PCA to ACA or MCA territories, collateral flow from PCA to ICA through PcomA, and transdural anastomosis from ECA to ICA, respectively.
PcomA indicates posterior communicating artery.

Table 4: Angiographic difference according to the location of the acute hemorrhage in adult MMD

| | D-ICH or IVH | L-ICH | |
Variables	(n = 82)	(n = 14)	P Value
ACA occlusion	74 (90.2)	9 (64.3)	.009
MCA occlusion	70 (85.4)	11 (78.6)	.45
PCA occlusion	18 (22.0)	3 (21.4)	.99
Ethmoidal Moyamoya	39 (47.6)	5 (35.7)	.41
Fetal-type PCA	46 (56.1)	6 (42.9)	.36
PCA collateral	69 (84.1)	11 (78.6)	.69
PcomA collateral	6 (7.3)	1 (7.1)	.99
ECA collateral	44 (53.7)	5 (35.7)	.21
Aneurysm[a]	5 (6.1)	2 (14.3)	.27

Note:—Ethmoidal Moyamoya, fetal-type PCA, PCA collateral, PcomA collateral, and ECA collateral indicate the development of ethmoidal Moyamoya vessels, enlargement of PcomA or showing blood supply to PCA territories through PcomA, leptomeningeal collateral vessels from PCA to ACA or MCA territories, collateral flow from PCA to ICA through PcomA, and transdural anastomosis from ECA to ICA, respectively.
D-ICH indicates deep intracerebral hemorrhage; L-ICH, lobar intracerebral hemorrhage; PcomA, posterior communicating artery.
[a] Two aneurysms were identified simultaneously in 1 patient in the D-ICH or IVH group.

IVH group than in the lobar intracerebral hemorrhage group (P = .009) (Table 4).

DISCUSSION

This study demonstrated that the hemorrhagic hemisphere in adult MMD was associated more with intracranial aneurysms,

ACA occlusion, and fetal-type PCA development than the ischemic or control hemispheres. MCA occlusion and collateral flow, such as ethmoidal Moyamoya vessels and transdural anastomosis from the ECA, were detected more often in the hemorrhagic than ischemic hemispheres. ACA occlusion was associated with deep intracerebral hemorrhage or IVH.

As independent risk factors for hemorrhagic stroke in MMD, anterior choroidal artery and posterior communicating artery dilation or extension have been described.[5-7] Moreover, cerebral microbleeds in adult patients with MMD were reported to be probable predictors of subsequent hemorrhage, and dilation and extension of the anterior choroidal artery or posterior communicating artery were independent risk factors of cerebral microbleeds in deep and periventricular white matter.[11] In our study, fetal-type PCA development was more commonly observed in the hemorrhagic hemispheres than in the ischemic or control hemispheres. In addition, we newly described the association of ACA occlusion and hemorrhagic stroke (Fig 3A, -C). Intracranial aneurysms were also proven to be an independent risk factor for hemorrhagic stroke in adult patients with MMD (Table 2). The more common prevalence of transdural anastomosis from ECA and ethmoidal Moyamoya vessel development in hemorrhagic hemispheres represent newly detected findings in our study (Fig 3E, -I). In the subgroup analysis, ACA occlusion and deep intra-
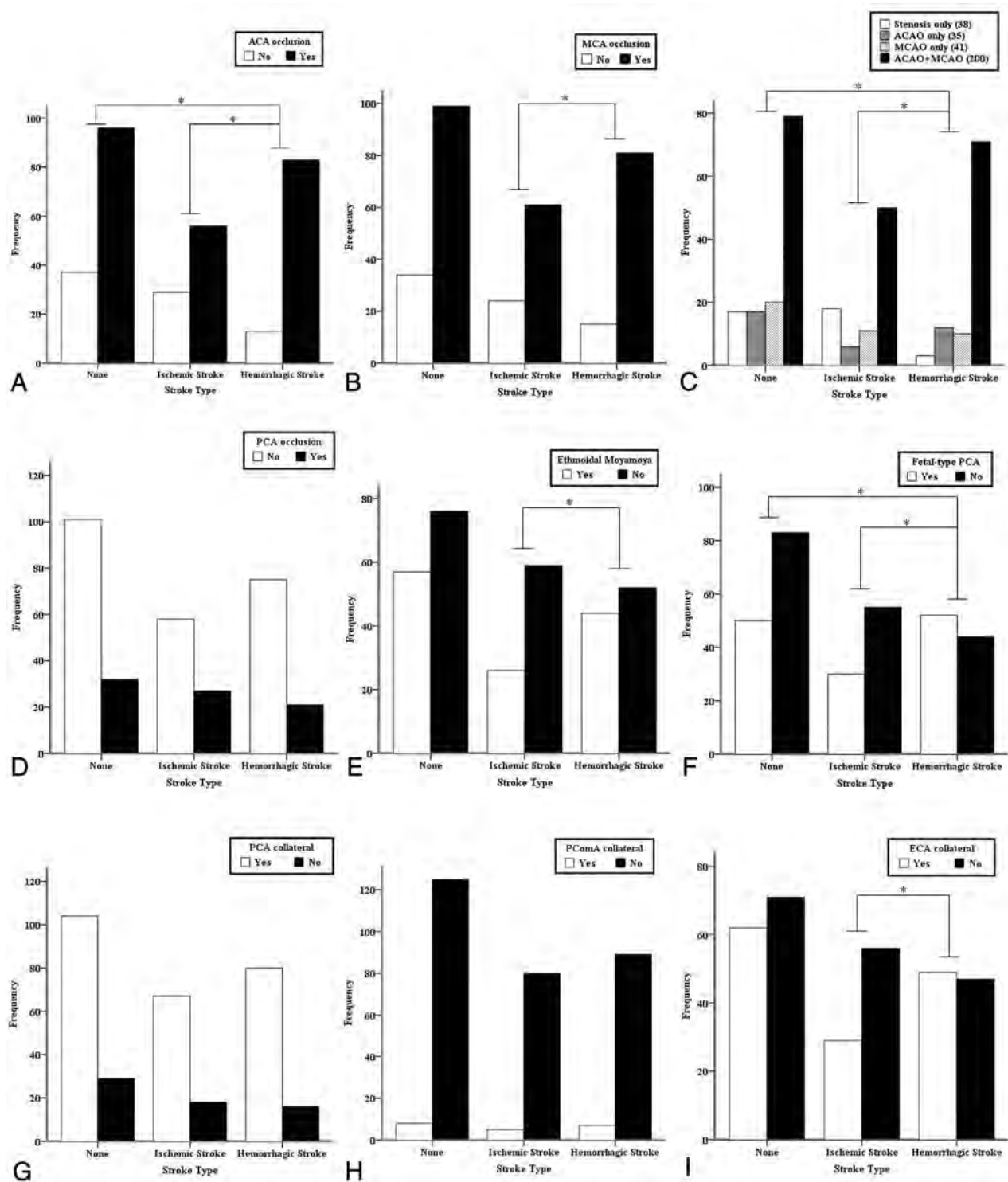
FIG 3. Angiographic patterns according to acute stroke type of 314 hemispheres in 175 adult patients with Moyamoya disease. Asterisks indicate statistical significances between the respective hemispheres (*A–C, E, F*, and *I*).

cerebral hemorrhage or IVH occurrence were associated with each other (Table 4). Taken together, these findings may show important differences between ischemic and hemorrhagic adult MMD.

However, some researchers have reported that ischemic childhood MMD and most ischemic strokes might be associated with the degree of steno-occlusive changes in the ICA and PCA.[8,12] In

ischemic adult MMD, major artery occlusion, including ACA, MCA, and PCA occlusions, was associated more with LAI and posterior circulation ischemic stroke than with HI or PI and with anterior circulation ischemic stroke (Table 3). Therefore, adult ischemic MMD may have angiographic characteristics similar to those in pediatric MMD with ischemic stroke.

The hemorrhagic hemispheres in adult MMD showed more

advanced angiographic stages (Fig 2*C*) than did the control hemispheres and demonstrated more progressive features (Fig 3) than did the ischemic hemispheres, particularly for ACA occlusion, MCA occlusion, ethmoidal Moyamoya, fetal-type PCA, and transdural anastomosis from the ECA. These characteristics may be important angiographic factors in adult MMD and are consistent with the findings of previous studies.[5,13] Specifically, Morioka et al[5] demonstrated that in MMD, ischemic and hemorrhagic hemispheres in both pediatric and adult patients differed at the site of supraclinoid ICA occlusion or stenosis from the ophthalmic segment to the ICA bifurcation. The present study suggests that hemodynamic stress may differ between the ischemic and hemorrhagic hemispheres in adult MMD. Independent of MCA occlusion, ACA occlusion was more frequently detected in the hemorrhagic hemisphere than in the ischemic hemisphere (Fig 3*C*), and intracranial aneurysms were more frequently detected in hemorrhagic MMD. According to the stroke subtype, the hemorrhagic hemispheres also had more bleeding sites near the midline structure or deep brain area than in the subcortical and cortical areas (Table 4).

Such angiographic differences in ischemic and hemorrhagic MMD might originate from genetic differences. With the identification of the first MMD gene, *RNF213*, rapid progress has been made in genetic research on MMD.[14] Miyatake et al[13] revealed that in the homozygote c.14576G>A variant of *RNF213*, 60% of patients were diagnosed with MMD before the age of 4 years, and all had ischemic strokes. They also showed that patients with homozygotes had a significantly earlier age at onset than those of the heterozygote or wild-type c.14576G>A variants. According to their results, there may be large proportion of heterozygote (GA) or wild-type (GG) c.14576G>A variants in *RNF213* in patients with adulthood-onset MMD.[13] Unfortunately, there is still no report on the c.14576G>A variant of *RNF213* with MMD in Korea. Further genetic correlation studies with the angiographic and clinical findings of patients with Moyamoya in Korea may help us to understand the causes of different stroke types. Regarding the stroke risk factors in our cohort, there was a high incidence of diabetes but not of hypertension in ischemic MMD compared with hemorrhagic MMD (Table 1). A future study on whether general risk factors, such as diabetes, affect stroke occurrence in adult patients with MMD is necessary. Although our results did not reveal a difference in the age distribution between ischemic and hemorrhagic strokes in adult MMD (Table 1 and Fig 2*B*), there have been few studies reporting adult MMD in which the symptoms cross over. In addition, most of the symptoms occurred in the ischemic stroke after a hemorrhagic stroke.[9,15,16] These findings suggest that different stroke presentations in adult MMD may be associated with inherent factors.

Bypass surgery may be helpful in reducing the risk of stroke development in adulthood-onset ischemic MMD, similar to childhood-onset MMD, whereas the effectiveness of bypass surgery for stroke prevention is still controversial in adult MMD with intracranial hemorrhage.[17-19] An additional study should be performed on whether a difference in the surgical efficacy between the ischemic and hemorrhagic hemispheres in adult patients with MMD may be associated with any respective angiographic differences.

Our study is limited by the representativeness of ischemic MMD, which included only ischemic stroke cases and no TIA cases. Thus, sampling bias may influence the results of this study. Furthermore, the dilation of the anterior choroidal artery was not assessed as a predictor of hemorrhagic stroke in adult MMD. An additional weakness of this study was that it only demonstrated an association and not causality between the angiographic differences and stroke types.

CONCLUSIONS

Most hemorrhagic strokes in adult MMD occurred near the midline or deep brain structures, in contrast to ischemic strokes. The angiographic status of an acute stroke hemisphere was more advanced in the hemorrhagic than in the ischemic group in adult patients with MMD. Major artery occlusion and collateral compensation occurred more often in the hemorrhagic than in the ischemic hemispheres. Thus, ACA occlusion with or without MCA occlusion and intracranial aneurysms may be main contributing factors to hemorrhagic stroke in adult patients with MMD. We suggest that there may be a potential phenotypic difference between patients with ischemic and hemorrhagic stroke in adult MMD.

APPENDIX

Participating hospitals included Bucheon St Mary's Hospital, Daejeon St Mary's Hospital, Incheon St Mary's Hospital, St Paul's Hospital, St Vincent's Hospital, Seoul St Mary's Hospital, Uijeongbu St Mary's Hospital, and Youido St Mary's Hospital (all hospitals were affiliated with the Catholic University of Korea, College of Medicine).

REFERENCES

1. Fukui M. **Guidelines for the diagnosis and treatment of spontaneous occlusion of the circle of Willis ('Moyamoya' disease): Research Committee on Spontaneous Occlusion of the Circle of Willis (Moyamoya Disease) of the Ministry of Health and Welfare, Japan.** *Clin Neurol Neurosurg* 1997;99(Suppl 2):S238–40

2. Han DH, Kwon OK, Byun BJ, et al. **A co-operative study: clinical characteristics of 334 Korean patients with Moyamoya disease treated at neurosurgical institutes (1976–1994): The Korean Society for Cerebrovascular Disease.** *Acta Neurochir (Wien)* 2000;142:1263–73

3. Fukui M, Kono S, Sueishi K, et al. **Moyamoya disease.** *Neuropathology* 2000;20(Suppl):S61–64

4. Research Committee on the Pathology and Treatment of Spontaneous Occlusion of the Circle of Willis; Health Labour Sciences Research Grant for Research on Measures for Intractable Diseases. **Guidelines for diagnosis and treatment of Moyamoya disease (spontaneous occlusion of the circle of Willis).** *Neurol Med Chir (Tokyo)* 2012;52:245–66

5. Morioka M, Hamada J, Kawano T, et al. **Angiographic dilatation and branch extension of the anterior choroidal and posterior commu-**

nicating arteries are predictors of hemorrhage in adult Moyamoya patients. *Stroke* 2003;34:90–95

6. Liu W, Zhu S, Wang X, et al. **Evaluation of angiographic changes of the anterior choroidal and posterior communicating arteries for predicting cerebrovascular lesions in adult Moyamoya disease.** *J Clin Neurosci* 2011;18:374–78

7. Irikura K, Miyasaka Y, Kurata A, et al. **A source of haemorrhage in adult patients with Moyamoya disease: the significance of tributaries from the choroidal artery.** *Acta Neurochir (Wien)* 1996;138:1282–86

8. Mugikura S, Takahashi S, Higano S, et al. **The relationship between cerebral infarction and angiographic characteristics in childhood Moyamoya disease.** *AJNR Am J Neuroradiol* 1999;20:336–43

9. Kim DS, Jang DK, Huh PW, et al. **Ischaemic stroke after acute intracranial haemorrhage in patients with Moyamoya disease: six new cases and a short literature review.** *Acta Neurochir (Wien)* 2011;153:1253–61

10. Suzuki J, Takaku A. **Cerebrovascular "Moyamoya" disease: disease showing abnormal net-like vessels in base of brain.** *Arch Neurol* 1969;20:288–99

11. Sun W, Yuan C, Liu W, et al. **Asymptomatic cerebral microbleeds in adult patients with Moyamoya disease: a prospective cohort study with 2 years of follow-up.** *Cerebrovasc Dis* 2013;35:469–75

12. Mugikura S, Higano S, Shirane R, et al. **Posterior circulation and high prevalence of ischemic stroke among young pediatric patients with Moyamoya disease: evidence of angiography-based differences by age at diagnosis.** *AJNR Am J Neuroradiol* 2011;32:192–98

13. Miyatake S, Miyake N, Touho H, et al. **Homozygous c. 14576G>A variant of RNF213 predicts early-onset and severe form of Moyamoya disease.** *Neurology* 2012;78:803–10

14. Kamada F, Aoki Y, Narisawa A, et al. **A genome-wide association study identifies RNF213 as the first Moyamoya disease gene.** *J Hum Genet* 2011;56:34–40

15. Hishikawa T, Tokunaga K, Sugiu K, et al. **Clinical and radiographic features of Moyamoya disease in patients with both cerebral ischaemia and haemorrhage.** *Br J Neurosurg* 2013;27:198–201

16. Nagasaka T, Hayashi S, Naito T, et al. **Concomitant cerebral infarction and intraventricular hemorrhage in Moyamoya disease: case report.** *J Neurosurg* 2007;106:388–90

17. Starke RM, Komotar RJ, Hickman ZL, et al. **Clinical features, surgical treatment, and long-term outcome in adult patients with Moyamoya disease.** *J Neurosurg* 2009;111:936–42

18. Roach ES, Golomb MR, Adams R, et al. **Management of stroke in infants and children: a scientific statement from a Special Writing Group of the American Heart Association Stroke Council and the Council on Cardiovascular Disease in the Young.** *Stroke* 2008;39:2644–91

19. Aoki N. **Cerebrovascular bypass surgery for the treatment of Moyamoya disease: unsatisfactory outcome in the patients presenting with intracranial hemorrhage.** *Surg Neurol* 1993;40:372–77

Stenotic Transverse Sinus Predisposes to Poststenting Hyperperfusion Syndrome as Evidenced by Quantitative Analysis of Peritherapeutic Cerebral Circulation Time

C.-J. Lin, F.-C. Chang, F.-Y. Tsai, W.-Y. Guo, S.-C. Hung, D.Y.-T. Chen, C.-H. Lin, and C.-Y. Chang

ABSTRACT

BACKGROUND AND PURPOSE: Hyperperfusion syndrome is a devastating complication of carotid stent placement. The shortening of cerebral circulation time after stent placement is seen as a good indicator of the development of hyperperfusion syndrome. The purpose of our study was to evaluate whether patients with ipsilateral transverse sinus stenosis are prone to having shortened cerebral circulation time after stent placement, subsequently leading to the possible development of hyperperfusion syndrome.

MATERIALS AND METHODS: Forty-nine patients with >70% unilateral carotid stenosis undergoing stent placement were recruited for analysis. Group A consisted of patients with a stenotic ipsilateral transverse sinus >50% greater than the diameter of the contralateral transverse sinus; the remaining patients were in group B. Quantitative DSA was used to calculate cerebral circulation time. Cerebral circulation time was defined as the time difference between the relative time to maximal intensity of ROIs in the proximal internal carotid artery and the internal jugular vein. ΔCCT was defined as cerebral circulation time before stent placement minus cerebral circulation time after stent placement. ΔCCT, white matter hyperintensity signals, and sulcal effacement in MR imaging were compared between the 2 groups.

RESULTS: ΔCCT was significantly shorter in group A (0.65 ± 1.3) than in group B (-0.12 ± 1.4). Three patients had white matter hyperintensity signals in group A, and 1 developed hyperperfusion syndrome. Group B showed no MR imaging signs of hyperperfusion syndrome.

CONCLUSIONS: Ipsilateral hypoplastic transverse sinus was associated with prolonged cerebral circulation time before stent placement and greatly shortened cerebral circulation time after stent placement. Inadequate venous drainage might play a role in impaired cerebral autoregulation and might influence the development of poststenting hyperperfusion syndrome.

ABBREVIATIONS: CCT = cerebral circulation time; ΔCCT = CCT after stent placement minus CCT before stent placement; HPS = hyperperfusion syndrome; TS = transverse sinus

Carotid stent placement restores cerebral perfusion to the ischemic area to prevent further ischemic insults. The normalized cerebral circulation after stent placement also correlates with improved neurologic functional outcomes.[1-3] Although carotid stent placement has been proved a safe therapy for those with significant extracranial stenosis, complications do occur, including thromboembolic events and hyperperfusion syndrome.[4] Hyperperfusion syndrome has a characteristic triad (headache, seizure, and focal neurologic deficits) and typically occurs within several hours or days after the procedure.[5-7] Risk factors for hyperperfusion have been proposed, including high-grade stenosis, poor collateral circulation, high blood pressure, age, and blood-brain barrier breakdown.[7-11]

Nevertheless, the underlying pathophysiology of HPS has not been well evaluated due to its low incidence (0.7%–3%).[7,9,12] The generally accepted explanation emphasizes a failure of autoregulation after sudden augmentation of cerebral blood inflow following carotid stent placement. To assess cerebral perfusion objectively and immediately within the angiography suite, we used quantitative color-coded DSA to evaluate the changes in cerebral circulation time before and after the procedures.[13,14] CCT is defined as the time required for blood to traverse through the brain, and it can serve as a surrogate for cerebral perfusion during angiography.[15] Obtaining immediate cerebral hemodynamic mea-

surements can help detect HPS early and facilitate immediate, aggressive postprocedural blood pressure control.

Despite careful patient selection and postprocedural care, we have nonetheless encountered unexpected cases of HPS after carotid stent placement. A recent study has shown that shortened CCT after carotid stent placement carries higher risks for HPS.[12] After reviewing our cases, we found that those patients with HPS usually had ipsilateral hypoplastic or atretic transverse sinuses. The purpose of our study was to determine the impact of venous stenosis on CCT after stent placement and to determine whether venous stenosis is a risk factor for HPS.

MATERIALS AND METHODS
Patient Selection
We retrospectively reviewed 60 patients who underwent carotid stent placement from June 2011 to December 2012 in our hospital. The inclusion criterion for this study was having unilateral carotid stenosis of >70% according to the NASCET criteria. Three patients with tandem intracranial stenosis or contralateral extracranial stenosis were excluded; 2 cases of dissection and 2 cases with suboptimal DSA imaging quality due to motion artifacts were also excluded. Respiratory problems or congestive heart failure can also alter the waveforms and subsequent CCTs, so we also excluded 4 patients with known heart disease. Forty-nine patients were available for analysis and were divided into 2 groups according to the caliber of the ipsilateral transverse sinus based on measurements taken from their DSA images. Group A consisted of patients with hypoplastic TS (degree of stenosis at least 50% greater than on the contralateral side) or atretic TS (nonmeasurable, with stenosis assumed to be total). Group B consisted of patients with no stenosis (the degree of stenosis identical to that of the contralateral TS) or mild narrowing (greater degree of stenosis than on the contralateral side but <50% greater). Before assessing CCT, 1 neuroradiologist objectively measured the degree of stenosis on the anteroposterior view when the TS was optimally visualized. HPS was defined as abnormally high signal intensity involving periventricular or subcortical white matter or sulcal effacement on FLAIR sequences of posttreatment MR imaging, in combination with ipsilateral headache with or without nausea and vomiting, focal seizure, and neurologic deficits.[9]

Peri-Carotid Stent Placement Management
All patients were premedicated with aspirin, 100 mg/day, and clopidogrel, 75 mg/day, for at least 2 weeks before stent placement. Stent placement was performed with the patient under general anesthesia. Intraoperative heparin was given to maintain an activated thrombin time of >200 seconds. The end point of the successful procedure was defined as residual stenosis of <10%. The patients were transferred to a stroke intensive care unit for strict blood pressure control below 130 mm Hg for 24 hours.

DSA
Quantitative color-coded cerebral angiography was performed to measure changes in cerebral circulation time during carotid stent placement between the 2 groups. The procedures were performed by using 1 flat panel angiography system (Axiom Artis; Siemens,
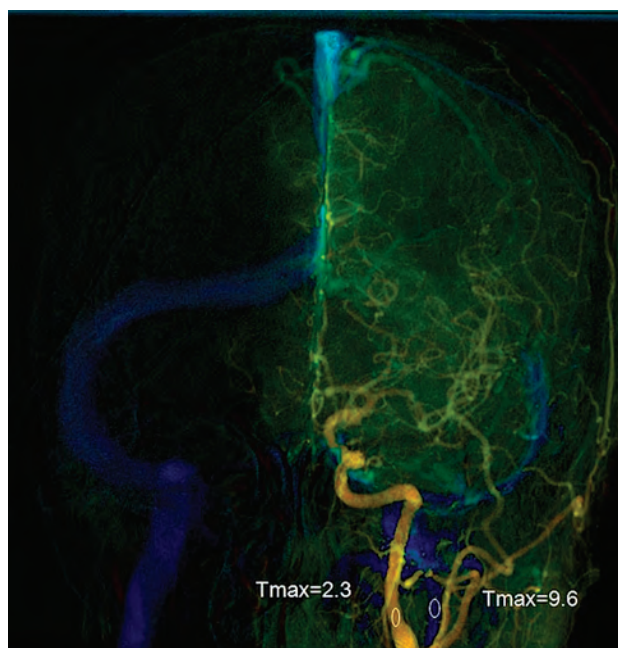
FIG 1. Anteroposterior view of quantitative brain DSA of a 51-year-old woman. The midpoint of the cervical portion of the internal carotid artery was selected for the arterial region of interest. The midpoint of the ipsilateral internal jugular vein was selected for venous region of interest. Cerebral circulation time was the time difference between the 2 ROIs.

Erlangen, Germany). A 4F angiocatheter was placed at the level of the C4 vertebral body for DSA. The fixed acquisition protocol was performed on all patients according to Lin et al.[13] All patients were told to breath-hold during the DSA acquisition. Postprocessing software (syngo iFlow; Siemens) was used to quantify the selected ROIs according to their time to maximal intensity in seconds.[14] The time to maximal intensity of any selected region of interest was defined as the time point when the attenuation of the x-ray reached its maximum along the angiographic frames. An anteroposterior view was used to determine CCT. It was defined as the difference in time to maximal intensity between arterial ROIs in the proximal internal carotid artery and the internal jugular vein (Fig 1). The diameters of all ROIs were intended to cover the calibers of the selected vessels without overlapping other vessels. ΔCCT is equal to CCT after stenting minus CCT before stenting.

MR Imaging
All peritherapeutic MR imaging was conducted in the same scanner (Signa Excite HD; GE Healthcare, Milwaukee, Wisconsin). Presenting MRA with time-of-flight technique (TR = 28 ms, TE = 7 ms, flip angle = 20°, matrix size = 384 × 224) was used to assess collaterals. Lack of collateral circulation was considered as the absence of either the anterior or posterior communicating artery according to the original reports. Selective angiography does not always demonstrate the anterior and posterior cerebral arteries well because of the competing flow from contralateral noniodinated blood flow. This phenomenon is more profound when there is an ipsilateral proximal carotid stenosis. FLAIR sequences (TR = 9000 ms, TE = 120 ms, TI = 2250 ms, section

thickness = 5 mm, matrix size = 288 × 224) of the brain before and after stent placement were used to compare the white matter changes and the gyral effacement, by the consensus of the same 2 experienced neuroradiologists who analyzed the DSA datasets, but in different sessions.

Statistics

The ΔCCT between 2 groups was analyzed by using *t* tests. The white matter changes and incidences of HPS were determined by using the Fisher exact test. $P < .05$ was considered significant. Statistical analysis was performed by using the Statistical Package for the Social Sciences, Version 20 (IBM, Armonk, New York). Diagnostic tests performed with the Youden index, and the ROCs for both present CCT and ΔCCT versus HPS were evaluated.

Table 1: Patient characteristics between those with an ipsilateral stenotic transverse sinus (group A) and those with a normal transverse sinus (group B)

	Group A (*n* = 15)	Group B (*n* = 34)
Age (yr)	74.5 + 10.2	73.9 + 10.3
Sex (M/F)	12:3	31:5
Hypertension	5 (33%)	13 (38%)
MR imaging evidence of prior stroke	6 (40%)	16 (47%)
Stenosis degree	82%	81%
Lack of collaterals in MRA	2 (13%)	6 (18%)

Table 2: Peritherapeutic circulation times and MR imaging findings between those with an ipsilateral stenotic transverse sinus (group A) and those with a normal transverse sinus (group B)

	Group A (*n* = 15)	Group B (*n* = 34)	*P* Value
DSA			
Prestent CCT	6.9 ± 1.2	6.2 ± 1.1	.14
Poststent CCT	6.2 ± 1.5	6.2 ± 1.5	.98
ΔCCT	0.65 ± 1.3	−0.12 ± 1.4	.045[a]
MR imaging			
High SI in periventricular white matter	3	0	<.001[a]
Gyral effacement	2	0	<.001[a]

Note:—SI indicates signal intensity.
[a] Statically significant.

FIG 2. Receiver operating characteristic analysis of present CCT (*A*) and ΔCCT (*B*).

Pre stent CCT — AUC=0.62 (0.21-1.00); Δ CCT — AUC=0.74 (0.58-0.90). Axes: Sensitivity vs 1-Specificity.

RESULTS

All procedures were successful. There were 15 patients in group A (hypoplastic or atretic TS) and 34 patients in group B (normal ipsilateral venous drainage). Patient characteristics are shown in Table 1. No significant differences in age, sex, degree of stenosis, incidences of prior stroke, or hypertension between the 2 groups were found. Peritherapeutic CCTs are listed in Table 2. The prestent CCTs of group A (6.9 ± 1.2) were longer than those of group B (6.2 ± 1.2), but they failed to achieve statistical significance. There were equivalent poststent CCTs between the 2 groups. However, the ΔCCT was significantly shortened in group A (0.65 ± 1.3) compared with group B (0.12 ± 1.4). Figure 2 demonstrates the receiver operating characteristic analysis for both present CCT and ΔCCT versus HPS, respectively. The cutoff time of 7.1 seconds for present CCT predicted HPS in MR imaging with 67% sensitivity and 61% specificity. The cutoff time of 0.4 seconds for ΔCCT predicted HPS in MR imaging with 100% sensitivity and 40% specificity.

There were 3 patients in group A with increased signal intensities of white matter on MR images. One patient developed headache with nausea and vomiting 8 hours after the procedure (Table 3). A poststenting MR image demonstrated increased high signal intensity in the ipsilateral occipital subcortical white matter (Fig 3). Strict blood pressure control below 130 mm Hg was implemented for 3 days, and the clinical follow-up was uneventful. None of the patients in group B showed abnormally high signal intensities of white matter or hyperperfusion syndrome clinically.

DISCUSSION

Regardless of the degree of stenosis of the ipsilateral TS, the CCTs of both groups returned to 6.2 seconds after treatment, consistent with the CCTs of normal populations in the literature.[13] One previous study has also shown that the increased arterial flow after stent placement only shortened the circulation time in arterial ROIs, but not in venous ROIs.[13] Therefore, it is likely that the prolonged CCT in group A before stent placement was caused by coexistent carotid stenosis and ipsilateral TS stenosis. The carotid stenosis caused impeded arterial flow superimposed on the stenotic venous outlet, and the overall venous outflow also decreased and led to prolonged CCT in group A. The differences in ΔCCT between the 2 groups were likely caused in part by the normalization of prolonged CCT in the stenotic group.

In contrast to our results, Narita et al[12] found shortening of the CCT after carotid stent placement. This is likely the result of the ROIs that were measured. Narita et al defined CCT by differences of time to maximal intensity between the cavernous portion of the internal carotid artery and the parietal vein. To assess the venous outflow, we used the internal carotid artery and in-
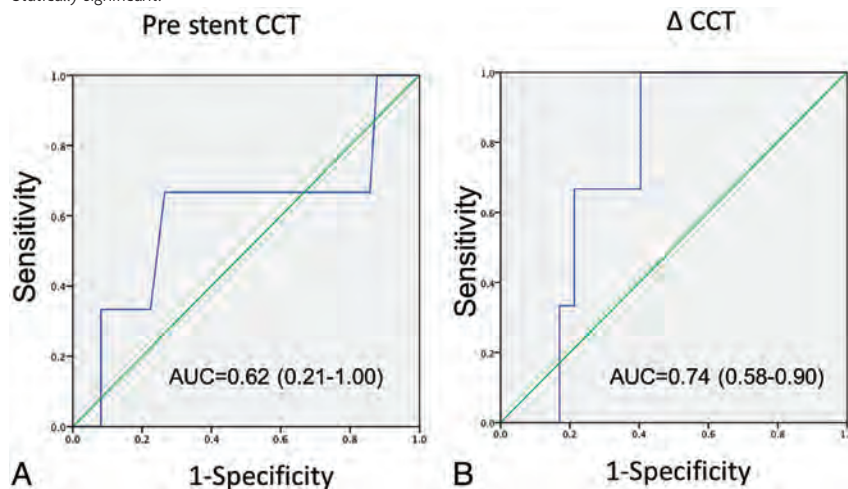
Table 3: Characteristics of 3 patients with high SI in the white matter in FLAIR sequences

Patient	Recent Infarct	HPS	Age (yr)	Sex	Complications	Stenotic Degree	Pre-CCT (sec)	Post-CCT (sec)	ΔCCT (sec)
1	No	Headache	51	F	No	85%	7.5	5.84	1.66
2	No	No	79	F	No	77%	5.5	5.03	0.47
3	No	No	81	M	No	78%	10.0	9.0	1.0

Note:—SI indicates signal intensity.
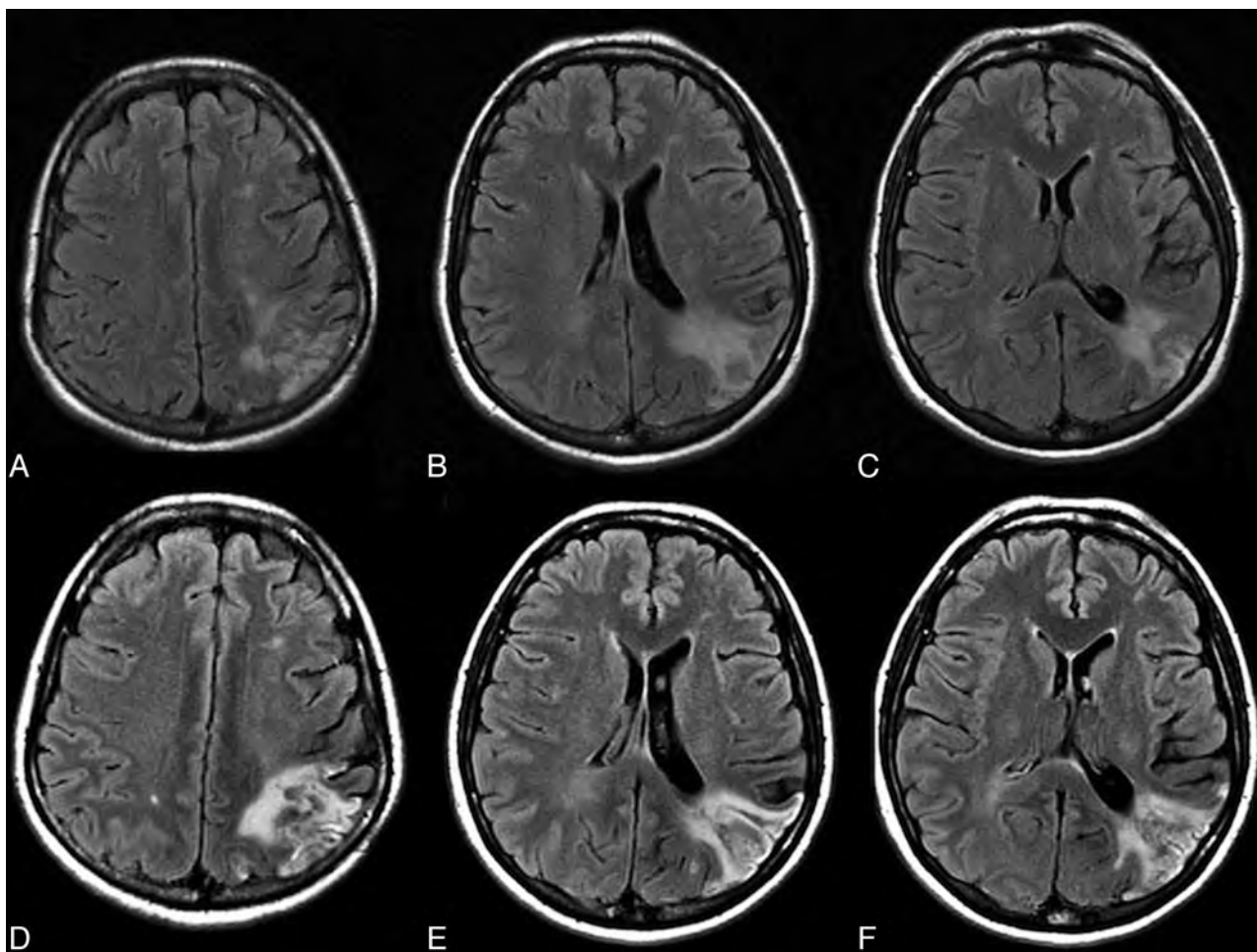
FIG 3. A 51-year-old woman with 90% left internal carotid artery stenosis. Color-coded cerebral DSA demonstrated an ipsilateral atretic transverse sinus in Fig 1. *A–C,* Present MR imaging shows an old infarct in the occipital subcortical white matter. She had headache with nausea 8 hours after the procedure. *D–F,* MR imaging 12 hours after the procedure shows increased signal intensity over the left occipital subcortical white matter.

ternal jugular vein as reference points. A possible mechanism of unchanged CCT after stent placement is autoregulation of the brain occurring at the capillary level, which may have somehow neutralized the benefits of increased upstream arterial flow after stent placement, which could then not be detected at the downstream venous level.

The prolonged CCT before stent placement in the stenotic group indicated a greater degree of hemodynamic impairment. Given that the number of cases of poor collateral circulation did not differ significantly between the 2 groups (13% versus 18%), we speculated that inadequate venous drainage in the stenotic group might have been associated with a dysfunction of autoregulation. Previous literature has shown good correlations between angiography CCT and MTT from perfusion studies.[16,17] Longer MTT indicated pre-existing hemodynamic impairment and predisposed the patient to HPS.[18,19]

The high signal intensity of subcortical white matter on FLAIR imaging represented edematous change and implied impaired dysautoregulation, likely potentiated by the venous stasis. If one reviewed the 3 patients with abnormal MR imaging findings, no incidences of contralateral stenosis or poor collaterals were seen, their mean age was 70 years, and strict postoperation blood pressure control was also performed.[7,17] Thus, shortened ΔCCT combined with venous stenosis seems to cause an increase in cerebral blood flow. Note, however, that blood-brain barrier breakdown is another possible cause, which was not explored in our study.[11]

Asymmetry of the dural sinus is common and does not generally lead to clinical symptoms. Once increased cerebral blood flow has developed following successful recanalization, however, better venous drainage may be required to relieve the sudden increase in cerebral blood flow. All our patients who experienced HPS had severe venous outlet anomalies. Perhaps hyperperfusion

following carotid stent placement in patients with ipsilateral poor venous drainage may follow a similar mechanism as that found in sinus thrombosis with hemorrhage complications: increased venous pressure from acute thrombosis or outlet obstruction precipitating venous hypertension and congestion.[17,20,21]

There were several limitations in our study. First, our study population was fairly small due to the low incidence of hyperfusion, and larger scale studies are needed to confirm our hypothesis. Second, the determination of time to maximal intensity in venous ROIs is vulnerable to waveform changes. The difference between the arrival time of arterial and venous ROIs might be a better surrogate to designate CCT. Unfortunately, this parameter was not available with the current version of the software. Although the mean ΔCCTs were significantly different in the 2 groups, the wide overlapping ranges of presenting CCT and ΔCCT in both groups handicapped these parameters as predictors for HPS in clinical practice. The definition of white matter change was subjective and thus was challenging for cases with mild venous congestion. Future volumetric MR images can potentially quantify the measurement.[22] Finally, the autoregulation of cerebral perfusion after stent placement was dynamic; the most appropriate timing of examinations to predict hyperfusion deserves more detailed investigation.

CONCLUSIONS

Ipsilateral hypoplastic TSs were associated with prolonged CCT before stent placement and greatly shortened CCT after stent placement. Inadequate venous drainage might play a role in the development of poststenting hyperperfusion syndrome.

REFERENCES

1. Chen YH, Lin MS, Lee JK, et al. **Carotid stenting improves cognitive function in asymptomatic cerebral ischemia.** *Int J Cardiol* 2012;157:104–07
2. Lal BK. **Cognitive function after carotid artery revascularization.** *Vasc Endovascular Surg* 2007;41:5–13
3. Mas JL, Chatellier G, Beyssen B, et al. **Endarterectomy versus stenting in patients with symptomatic severe carotid stenosis.** *N Engl J Med* 2006;355:1660–71
4. Sixt S, Rastan A, Schwarzwalder U, et al. **Long term outcome after balloon angioplasty and stenting of subclavian artery obstruction: a single centre experience.** *Vasa* 2008;37:174–82
5. Meyers PM, Higashida RT, Phatouros CC, et al. **Cerebral hyperperfusion syndrome after percutaneous transluminal stenting of the craniocervical arteries.** *Neurosurgery* 2000;47:335–43, discussion 43–45
6. Rezende MT, Spelle L, Mounayer C, et al. **Hyperperfusion syndrome after stenting for intracranial vertebral stenosis.** *Stroke* 2006;37:e12–14
7. Ogasawara K, Sakai N, Kuroiwa T, et al. **Intracranial hemorrhage associated with cerebral hyperperfusion syndrome following carotid endarterectomy and carotid artery stenting: retrospective review of 4494 patients.** *J Neurosurg* 2007;107:1130–36
8. Ascher E, Markevich N, Schutzer RW, et al. **Cerebral hyperperfusion syndrome after carotid endarterectomy: predictive factors and hemodynamic changes.** *J Vasc Surg* 2003;37:769–77
9. Abou-Chebl A, Yadav JS, Reginelli JP, et al. **Intracranial hemorrhage and hyperperfusion syndrome following carotid artery stenting: risk factors, prevention, and treatment.** *J Am Coll Cardiol* 2004;43:1596–601
10. Kawamata T, Okada Y, Kawashima A, et al. **Postcarotid endarterectomy cerebral hyperperfusion can be prevented by minimizing intraoperative cerebral ischemia and strict postoperative blood pressure control under continuous sedation.** *Neurosurgery* 2009;64:447–53, discussion 53–54
11. Ivens S, Gabriel S, Greenberg G, et al. **Blood-brain barrier breakdown as a novel mechanism underlying cerebral hyperperfusion syndrome.** *J Neurol* 2010;257:615–20
12. Narita S, Aikawa H, Nagata S, et al. **Intraprocedural prediction of hemorrhagic cerebral hyperperfusion syndrome after carotid artery stenting.** *J Stroke Cerebrovasc Dis* 2013;22:615–19
13. Lin CJ, Hung SC, Guo WY, et al. **Monitoring peri-therapeutic cerebral circulation time: a feasibility study using color-coded quantitative DSA in patients with steno-occlusive arterial disease.** *AJNR Am J Neuroradiol* 2012;33:1685–90
14. Strother CM, Bender F, Deuerling-Zheng Y, et al. **Parametric color coding of digital subtraction angiography.** *AJNR Am J Neuroradiol* 2010;31:919–24
15. Greitz T. **A radiologic study of the brain circulation by rapid serial angiography of the carotid artery.** *Acta Radiol Suppl* 1956;1–123
16. Aikawa H, Kazekawa K, Tsutsumi M, et al. **Intraprocedural changes in angiographic cerebral circulation time predict cerebral blood flow after carotid artery stenting.** *Neurol Med Chir (Tokyo)* 2010;50:269–74
17. Lee KW, Tsai FY, Cheng CY. **Venous hypertension may be a factor in aneurysmal rupture.** *Neuroradiol J* 2013;26:311–14
18. Rim NJ, Kim HS, Shin YS, et al. **Which CT perfusion parameter best reflects cerebrovascular reserve?: correlation of acetazolamide-challenged CT perfusion with single-photon emission CT in Moyamoya patients.** *AJNR Am J Neuroradiol* 2008;29:1658–63
19. Hosoda K, Kawaguchi T, Shibata Y, et al. **Cerebral vasoreactivity and internal carotid artery flow help to identify patients at risk for hyperfusion after carotid endarterectomy.** *Stroke* 2001;32:1567–73
20. Tsai FY, Nguyen B, Lin WC. **Endovascular procedures for cerebrovenous disorders.** *Acta Neurochir Suppl* 2008;101:83–86
21. Tsai FY, Wang AM, Matovich VB, et al. **MR staging of acute dural sinus thrombosis: correlation with venous pressure measurements and implications for treatment and prognosis.** *AJNR Am J Neuroradiol* 1995;16:1021–29
22. Artzi M, Aizenstein O, Jonas-Kimchi T, et al. **FLAIR lesion segmentation: application in patients with brain tumors and acute ischemic stroke.** *Eur J Radiol* 2013;82:1512–18

Transition into Driven Equilibrium of the Balanced Steady-State Free Precession as an Ultrafast Multisection T2-Weighted Imaging of the Brain

Y.-C.K. Huang, T.-Y. Huang, H.-C. Chiu, T.-S. Kuo, C.-J. Hsueh, H.-W. Kao, C.-W. Wang, H.-H. Hsu and C.-J. Juan

ABSTRACT

BACKGROUND AND PURPOSE: Current T2-weighted imaging takes >3 minutes to perform, for which the ultrafast transition into driven equilibrium (TIDE) technique may be potentially helpful. This study qualitatively and quantitatively evaluates the imaging of transition into driven equilibrium of the balanced steady-state free precession (TIDE) compared with TSE and turbo gradient spin-echo on T2-weighted MR images.

MATERIALS AND METHODS: Thirty healthy volunteers were examined with T2-weighted images by using TIDE, TSE, and turbo gradient spin-echo sequences. Imaging was evaluated qualitatively by 2 independent observers on the basis of a 4-point rating scale regarding contrast characteristics and artifacts behavior. Image SNR and contrast-to-noise ratio were quantitatively assessed.

RESULTS: TIDE provided T2-weighted contrast similar to that in TSE and turbo gradient spin-echo with only one-eighth of the scan time. TIDE showed gray-white matter differentiation and iron-load sensitivity inferior that of TSE and turbo gradient spin-echo, but with improved motion artifacts reduction on qualitative scores. Nonmotion ghosting artifacts were uniquely found in TIDE images. The overall SNRs of TSE were 1.9–2.0 times those of turbo gradient spin-echo and 1.7–2.2 times of those of TIDE for brain tissue ($P < .0001$). TIDE had a higher contrast-to-noise ratio than TSE ($P = .169$) and turbo gradient spin-echo ($P < .0001$) regarding non-iron-containing gray matter versus white matter. TIDE had a lower contrast-to-noise ratio than turbo gradient spin-echo and TSE ($P < .0001$) between iron-containing gray matter and white matter.

CONCLUSIONS: TIDE provides T2-weighted images with reduced scan times and reduced motion artifacts compared with TSE and turbo gradient spin-echo with the trade-off of reduced SNR and poorer gray-white matter differentiation.

ABBREVIATIONS: CNR = contrast-to-noise ratio; TGSE = turbo gradient spin-echo; TIDE = transition into driven equilibrium

T2-weighted MR images are commonly used to depict gross pathologic changes of the brain, including tumor, infarction, ischemia, white matter demyelination, inflammation, edema, and so forth.[1-4] The turbo spin-echo sequence is a method currently used for routine T2WI examination in the brain and in other extracranial regions.[5,6] In daily practice, it often takes >3 minutes to obtain 1 set of 2D TSE T2WIs on a certain plane.[5-7] Accordingly, it might take as long as 10 minutes to obtain T2WI on 3 orthogonal planes by using TSE. Although 3D imaging techniques have been developed to acquire T2WI, they still take as long as 6–8 minutes of acquisition time,[8-10] which makes them prone to motion artifacts and hampers their clinical application in daily practice.

There is an increasing need for a fast imaging technique to acquire T2WI of the brain in patients with motion during MR imaging. In 2000, Chung et al[11] demonstrated the advantage of a fast imaging with steady-state free precession to freeze the fetal motion during MR imaging. However, true fast imaging with steady-state precession carries a contrast known as T2/T1 rather than T2-weighted. The transition into driven equilibrium is a variant of the balanced steady-state free precession technique, inheriting characteristics of balanced steady-state free precession like high SNR efficiency and flow compensation. Different from

the T2/T1 contrast of conventional balanced steady-state free pre-cession,[11,12] pure T2 contrast or T2-weighted contrast with fat suppression can be rendered by transition into driven equilibrium (TIDE) theoretically, depending on the sampling strategy of the contrast-determining central *k*-space.[13-17] The typical scan time of TIDE for a single section is approximately 1 second, which is desirable, especially when 3-plane multisection T2WIs are considered for clinical practice, such as for rapid screening or diagnosis. Before applying them to daily practice, however, the imaging quality and characteristics of TIDE need to be evaluated.

We assume that TIDE could also provide T2-weighted imaging contrast similar to that in other pulse sequences, including TSE and turbo gradient spin-echo (TGSE). In this study, we aimed to qualitatively and quantitatively evaluate TIDE compared with TSE and TGSE in T2-weighted brain MR images.

MATERIALS AND METHODS

This prospective study was approved by the institutional review board of Tri-Service General Hospital. Written informed consent was obtained from all subjects. For assessment of imaging quality, the inclusion criteria were that the volunteers had no history of brain disease such as tumor, hemorrhage, infarction, infection, or inflammation (none were excluded); had no history of brain surgery or radiation therapy (none were excluded); and had not received chemotherapy for systemic malignancy (1 was excluded before MR imaging). Accordingly, 30 healthy volunteers, including 10 men (mean age, 40.7 ± 9.3 years) and 20 women (mean age, 41.5 ± 8.9 years) were enrolled. In addition to qualitative and quantitative analyses of brain images from these healthy volunteers, 2 patients, including a 57-year-old woman with stroke history and a 9-day-old neonate with a seizure history, were also scanned for demonstration only.

MR Imaging Protocols

All MR imaging examinations were conducted on a 1.5T whole-body MR imaging unit (Magnetom Vision Plus; Siemens, Erlangen, Germany) by using a standard circularly polarized head coil with a maximal amplitude of 25 mT/m and a slew rate of 83.3 T/m/s for the gradient system. For anatomic localization, gradient-echo MR imaging was used to acquire 3-plane orthogonal images. Subsequently, whole brain images were acquired by using 3 protocols. The first protocol used a conventional fat-saturated dual-echo turbo spin-echo sequence (hereafter termed the TSE method) with parameters as follows: TR/TE1/TE2, 3800/22/90 ms; number of signals acquired, 1; echo-train length, 5; FOV, 240 × 240 mm; matrix, 250 × 256 (interpolated into 256 × 256 on the MR imaging console); receiver bandwidth, 62.5 kHz; section thickness, 4 mm; and intersection space, 1 mm. Twenty sections covered the brain from the vertex to the level of the upper cervical spinal cord in an axial orientation. In the second protocol, a turbo gradient spin-echo sequence (hereafter termed the TGSE method) was used with all imaging parameters identical to those used with the TSE method. The third protocol used the transition into the driven equilibrium sequence (hereafter termed the TIDE method) (TR/TE, 6.46/3.23 ms; matrix size, 256 × 256; receiver bandwidth, 125 kHz) with all other imaging parameters identical to those used with the TSE and TGSE methods.

Qualitative Analysis of Brain Imaging

The quality of TSE, TGSE, and TIDE images was rated by 2 neuroradiologists (C.-J.J. and C.-J.H., both with 10 years of experience in brain image interpretation) on the basis of a 4-point (0–3) rating scale regarding 5 items: gray-white matter differentiation, iron-load sensitivity, CSF motion artifacts, eyeball motion artifacts, and nonmotion ghosting artifacts. For gray-white matter differentiation, a score of 0, 1, 2, or 3 represented poor, fair, good, and excellent performance in differentiating the gray matter from white matter structures, respectively. For iron-load sensitivity, scores of 0, 1, 2, and 3 represented poor, fair, good, and excellent performance in detecting iron-related low signal intensity, respectively. As for the CSF, eyeball, and ghosting artifacts, scores of 0, 1, 2, and 3 indicated severe, moderate, mild, and without artifacts, respectively. The mean scores of the 2 raters were used when comparing the quality of different imaging techniques.

Image Processing and Quantitative Data Analysis

All image data were transferred from the MR imaging console to a personal computer, where all data were processed with software programs developed (by Y.-C.K.H.) by using Matlab (MathWorks, Natick, Massachusetts). All image processing, region-of-interest drawing, and data analyses were performed by a single author (Y.-C.K.H.). Regions of interest were manually drawn with about 50–100 pixels on the white matter, non-iron-containing gray matter, and iron-containing gray matter. For white matter, the centrum semiovale, corona radiata, and periventricular white matter were chosen. For gray matter, the head of the caudate nucleus, putamen, and thalamus were selected. As for iron-containing gray matter, the globus pallidus was adopted. An additional region of interest was placed outside the head to represent background noise.

The signal-to-noise ratio was calculated for each region of interest. The SNR was defined as the mean signal intensity of the region of interest divided by the SD of the background region of interest (ie, noise). In addition to SNR, the contrast-to-noise ratio (CNR) between gray matter and white matter was also calculated. The CNR was defined as the difference in signal intensities between gray matter and white matter divided by the SD of the background noise. In the calculation of CNRs, the thalamus, globus pallidus, and centrum semiovale were used to represent non-iron-containing gray matter, iron-containing gray matter, and white matter, respectively.

Statistical Analyses

Statistical analyses were performed by using a statistics plug-in, SigmaXL (SigmaXL, Toronto, Ontario, Canada), of the Microsoft Excel program (Microsoft, Redmond, Washington). Interobserver reliability for assessing image quality was evaluated by linearly weighted κ statistics,[18] in which a κ value of 0 represented poor agreement; 0.1–0.2, slight agreement; 0.21–0.40, fair agreement; 0.41–0.60, moderate agreement; 0.61–0.80, substantial agreement; and 0.81–1.00, almost perfect agreement, respectively. The 2-tailed paired Student *t* test was applied to determine the significance of the difference between any 2 of the 3 sequences regarding the imaging quality, SNR, and CNR. For correction of multiple comparisons, *P* values < .05/15 = .0033 (ie, 15 comparisons) for qualitative study and <.05/30 = .0017 (ie, 30 compar-
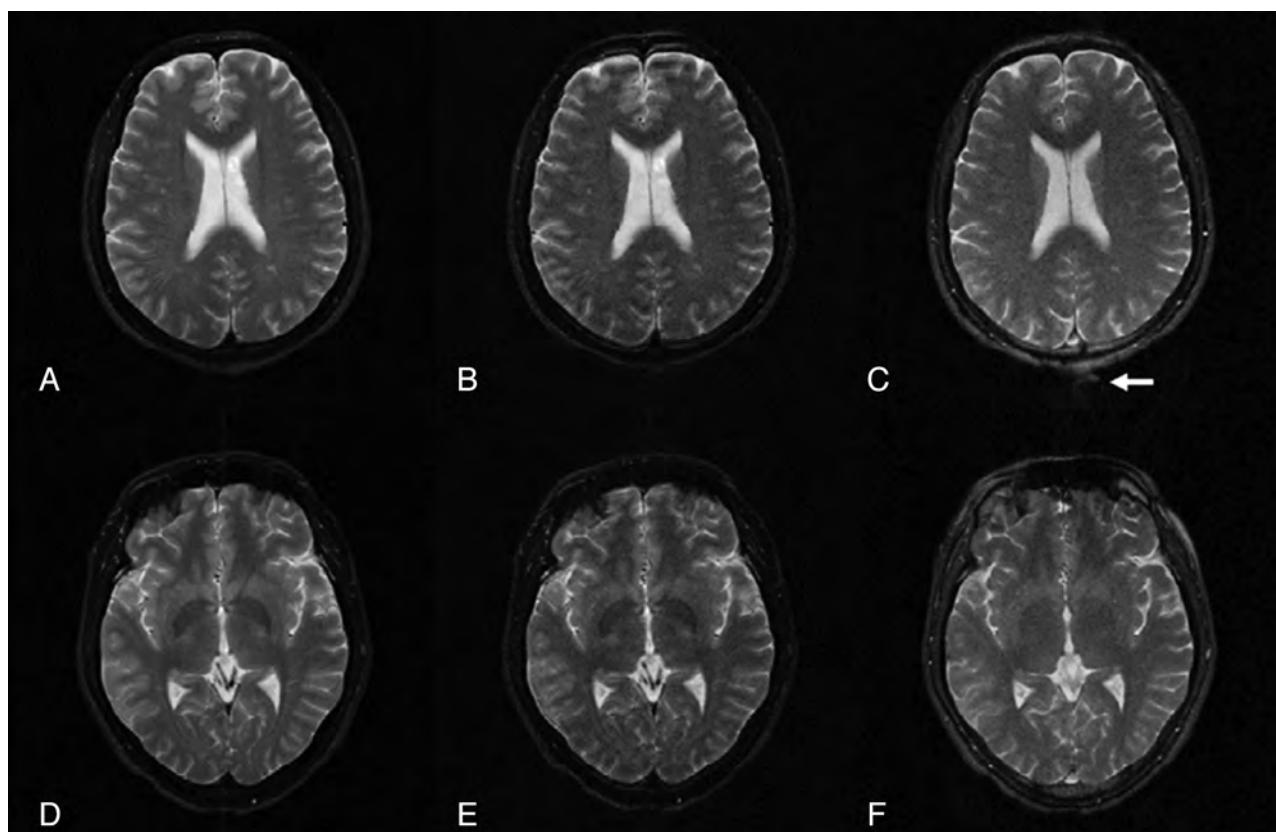
FIG 1. TSE (*A*, *D*), TGSE (*B*, *E*), and TIDE (*C*, *F*) images of a 38-year-old healthy man. The results show similar T2 contrast of the neocortex (*A–C*). At the basal ganglia, iron-containing gray matter (eg, globus pallidus) has a much higher intensity in the TIDE image compared with the other 2 results (*D–F*). Ghosting artifacts appear in the TIDE image (*arrow* in *C*).

isons) for quantitative study were considered statistically significant.

RESULTS
Scan Times
The total scan times for the 20 sections covering the whole brain plus the prescan adjustment were 193, 193, and 24 seconds for TSE, TGSE, and TIDE methods with a ratio of 8:8:1, respectively. With 48 more seconds, TIDE provided additional coronal and sagittal images.

Perceptive Imaging Contrast and Noise of TSE, TGSE, and TIDE Images
Both raters considered all images of TIDE, TSE, and TGSE as T2-weighted in perception (Fig 1). As shown in the axial images at the level of lateral ventricles (Fig 1*A–C*), TSE, TGSE, and TIDE images all showed a similar T2-weighted contrast (ie, higher signal intensity of the superficial cortex and non-iron-containing deep gray matter and lower signal intensity of white matter). While TSE and TGSE images showed lower signal intensity of the iron-containing gray matter than white matter, TIDE images showed isointensity between the iron-containing gray matter and white matter (Fig 1*D–F*).

TSE, TGSE, and TIDE images were susceptible to variable noises, including ghost artifacts, magnetic susceptibility artifacts, and motion artifacts related to eyeball movements and pulsation of CSF and blood flow (Figs 1 and 2). While TSE and TGSE images were more susceptible to motion artifacts (Figs 2*A*, *B*, *D* and *E*),

TIDE seemed to be more susceptible to nonmotion ghost artifacts (Fig 1*C, -F*) and magnetic susceptibility artifacts (Fig 2*C*).

Qualitative Analysis of TSE, TGSE, and TIDE Images
Assessment scores of TSE, TGSE, and TIDE images regarding the 5 imaging quality items rated by 2 neuroradiologists are listed in the On-line Table. Analysis of interobservor agreement by using linearly weighted κ showed substantial agreement for gray-white matter differentiation, iron-load sensitivity, CSF motion artifacts, and nonmotion ghosting artifacts (with linearly weighted κ values of 0.773, 0.671, 0.646, and 0.739, respectively) and fair agreement for eyeball motion artifacts (with a linearly weighted κ value of 0.398).

A significant difference ($P < .003$) was observed between any 2 of TSE, TGSE, and TIDE sequences for all imaging quality items with exceptions regarding nonmotion ghosting artifacts and CSF motion artifacts, in which the difference between TSE and TGSE was insignificant ($P = .573$ and .0034, respectively). The average scores of gray-white matter differentiation were highest on TSE (2.98 ± 0.09), followed by TGSE (2.13 ± 0.22) and TIDE (1.15 ± 0.23) in decreasing order ($P < .0001$). Similarly, the average scores of iron-load sensitivity were also highest on TSE (2.90 ± 0.20), followed by TGSE (2.07 ± 0.22) and TIDE (0.47 ± 0.22) in decreasing order ($P < .0001$). TIDE was less susceptible to CSF and eyeball motion artifacts compared with TSE and TGSE. The average scores of CSF motion artifacts were 2.98 ± 0.09, $1.23 \pm$
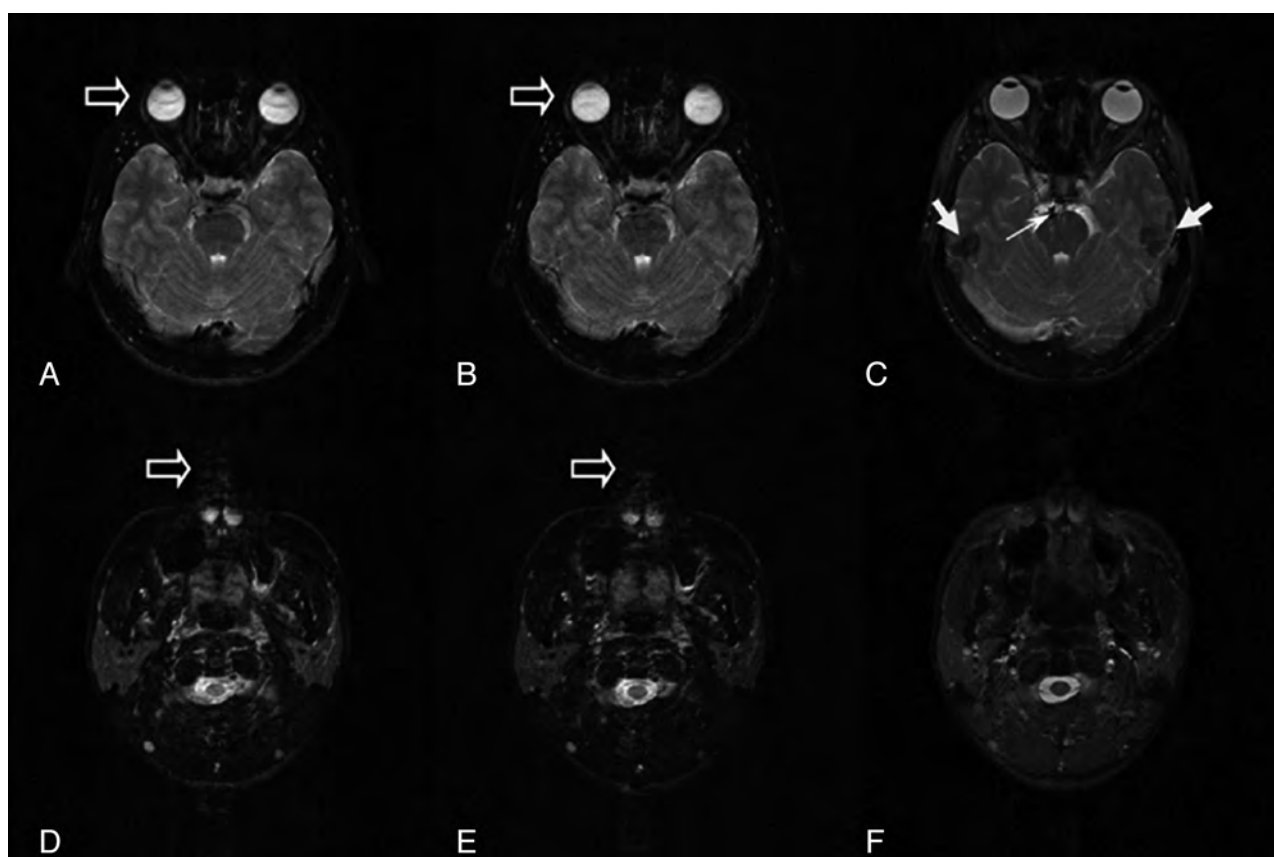
FIG 2. TSE (*A*, *D*), TGSE (*B*, *E*), and TIDE (*C*, *F*) images of a 25-year-old healthy man. Motion artifacts can be found in the TSE and TGSE images, due to eyeball movement (*open arrows* in *A* and *B*) and CSF flow (*open arrows* in *D* and *E*). Magnetic susceptibility artifacts appear in the TIDE image (*solid arrows* in *C*). Occasional basilar artery flow artifacts are seen in the TIDE image (*thin arrow* in *C*).

SNRs and CNRs of TSE, TGSE, and TIDE sequences

	TSE	TGSE	TIDE	$P_{TSE,TGSE}$	$P_{TGSE,TIDE}$	$P_{TSE,TIDE}$
SNR						
WM						
CSO	56.14 ± 8.05	29.29 ± 4.36	25.02 ± 3.70	–	–	–
CR	56.48 ± 8.05	29.71 ± 4.28	25.86 ± 3.63	–	–	–
aPVWM	52.54 ± 6.94	27.35 ± 3.57	24.12 ± 3.25	–	–	–
pPVWM	58.58 ± 7.48	31.05 ± 3.85	28.20 ± 3.59	–	–	–
GM						
CH	68.38 ± 9.35	35.80 ± 4.69	32.39 ± 4.34	–	–	–
PUT	61.97 ± 8.52	32.11 ± 4.25	32.58 ± 4.35	–	.364	–
THA	61.09 ± 8.18	32.03 ± 4.18	30.71 ± 3.76	–	.031	–
GP	48.47 ± 6.58	24.80 ± 3.42	28.30 ± 3.95	–	–	–
CNR						
NICGM-WM, THA-CSO	4.95 ± 3.64	2.74 ± 1.85	5.69 ± 1.37	–	–	.169
ICGM-WM, GP-CSO	−7.67 ± 3.98	−4.494 ± 2.35	3.275 ± 1.70	–	–	–

Note:—CSO indicates centrum semiovale; CR, corona radiata; aPVWM, anterior periventricular white matter; pPVWM, posterior periventricular white matter; CH, head of caudate nucleus; PUT, putamen; THA: thalamus; GP, globus pallidus; NICGM, non-iron-containing gray matter; ICGM, iron-containing gray matter; –, $P < .0001$.

0.39, and 0.98 ± 0.09 for TIDE, TSE, and TGSE, respectively ($P <$ .0001, except $P = .0034$ between TSE and TGSE). The average scores of eyeball motion artifacts were 2.62 ± 0.34, 2.18 ± 0.52, and 1.88 ± 0.36 for TIDE, TSE, and TGSE, respectively ($P <$ .003). TIDE was more susceptible to nonmotion ghosting artifact, while TSE and TGSE were not. The average scores of nonmotion ghosting artifacts were 1.78 ± 0.34, 2.98 ± 0.09, and 2.97 ± 0.13 for TIDE, TSE, and TGSE, respectively ($P <$ .0001, except $P =$ .572 between TSE and TGSE).

Quantitative Region-of-Interest Analysis of SNRs and CNRs

The SNRs of gray matter (head of the caudate nucleus, putamen, thalamus, and globus pallidus) and white matter (centrum semiovale, corona radiata, anterior periventricular white matter, and posterior periventricular white matter) and the CNRs between gray matter (thalamus and globus pallidus) and white matter (centrum semiovale) are listed in the Table. The SNRs of non-iron-containing gray matter were significantly higher than those
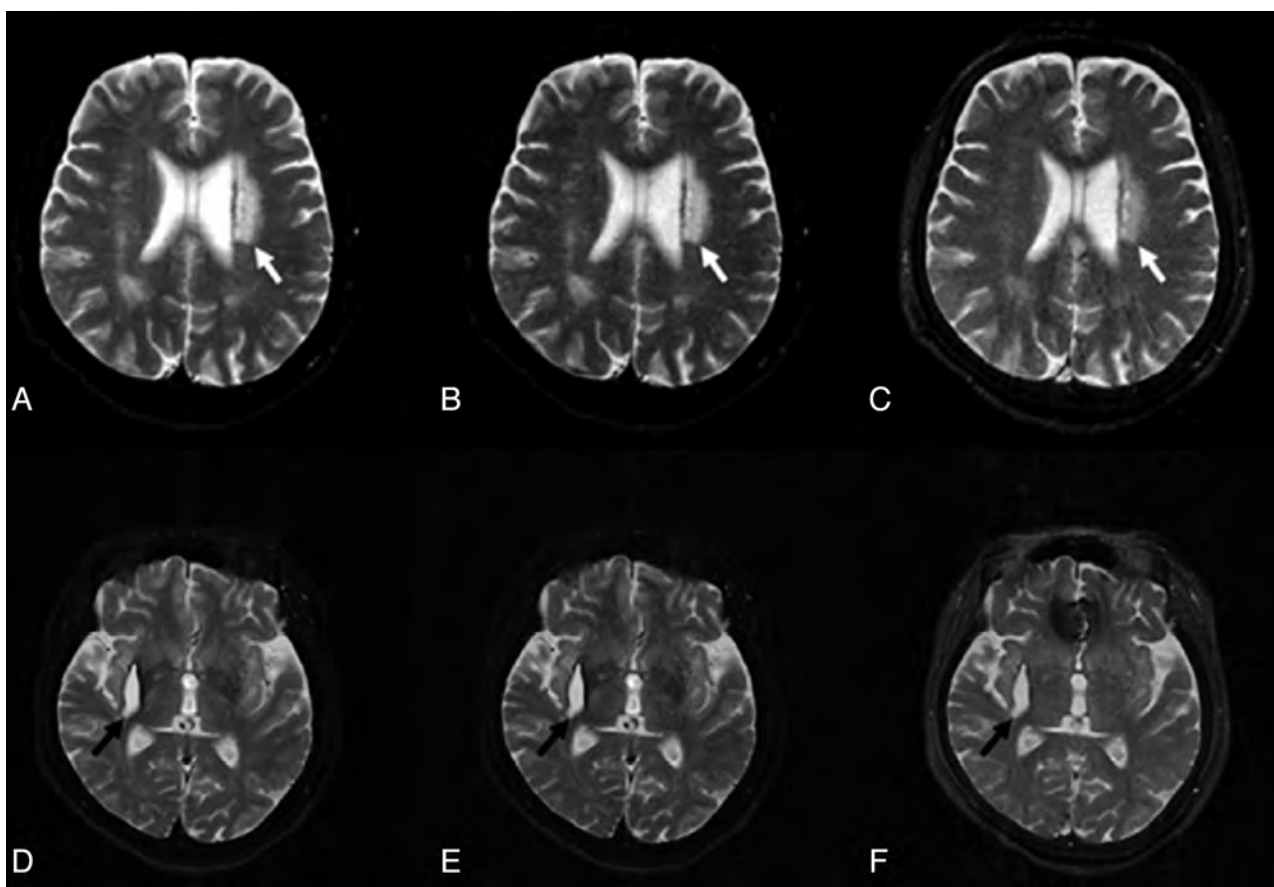
FIG 3. TSE (*A*, *D*), TGSE (*B*, *E*), and TIDE (*C*, *F*) images of a 57-year-old woman with stroke history. A hyperintense lesion appears near the left lateral ventricle (*white arrows* in *A–C*). The degrees of hyperintensity are different in these images. Similar contrast of a late subacute hematoma involving the right corpus striatum is found in all sequences (*black arrows* in *D–F*).

of white matter in images acquired from all pulse sequences ($P <$ .001). The SNRs of iron-containing gray matter were significantly lower than those of white matter in TSE and TGSE ($P <$ .001) but significantly higher than those of white matter in TIDE ($P <$ .001). TSE had significantly higher SNRs than TGSE and TIDE regarding all regions of gray matter and white matter ($P <$ .001). The overall mean SNRs of TSE were 1.9–2.0 times those of TGSE and 1.7–2.2 times those of TIDE for brain tissue, respectively. The SNRs in TIDE images were significantly lower than those in the TGSE images regarding all regions of white matter and the head of the caudate nucleus ($P <$ .001) but not significantly different regarding the putamen ($P =$ .364) and thalamus ($P =$ .031). As for iron-containing gray matter such as the globus pallidus, the SNRs of TIDE images were significantly higher than those of TGSE images ($P <$ .001) but were significantly lower than those of TSE images ($P <$ .001).

The CNR of non-iron-containing gray matter (thalamus) versus the centrum semiovale was highest in TIDE, followed by TSE and TGSE in decreasing order, with statistical significance between TSE and TGSE ($P <$ .0001) and between TIDE and TGSE ($P <$ .0001). The difference in the CNR of non-iron-containing gray matter (thalamus) versus the centrum semiovale between TIDE and TSE, however, was not significant ($P =$ .169). The CNR of iron-containing gray matter (globus pallidus) versus the centrum semiovale was highest in TSE, followed by TGSE and TIDE

in decreasing order, with statistical significance between any 2 pulse sequences ($P <$ .0001). While the CNR was of negative value in TSE and TGSE, it was of positive value in TIDE.

Case Demonstration

A 57-year-old woman with a stroke history was scanned by using TSE, TGSE, and TIDE pulse sequences. An axial TSE image at the level of the lateral ventricles showed an old infarction with high signal intensity involving the left corona radiata (Fig 3*A*). The lesion appeared similarly hyperintense on the TGSE image (Fig 3*B*) but was somewhat less hyperintenese on the TIDE image (Fig 3*C*). In addition, an intracerebral hematoma at the late subacute stage was also found at the right corpus striatum, showing hyperintensity on images acquired by using all pulse sequences, with a dark rim, which was more conspicuous on TSE (Fig 3*D*) and TGSE (Fig 3*E*) and less obvious on TIDE (Fig 3*F*), anteromedially. Notable hypointense magnetic susceptibility artifacts involving the anteromedial frontal region were observed on the TIDE image (Fig 3*F*) but not on TSE or TGSE images.

A second example regarding motion artifacts was demonstrated on coronal TSE T2WI (Fig 4*A*) in a 9-day-old neonate, in which severe motion degraded the imaging quality, hampering the delineation of brain contour and blurring the cerebral sulci and ventricles (Fig 4*A*). Such motion artifacts were avoided by using TIDE imaging (Fig 4*B*), in which the contour of the brain

was clearly demonstrated, the cerebral sulci and ventricles were conspicuously depicted, and the superficial cortex and subcortical white matter were successfully differentiated.

DISCUSSION

Our results show that TIDE is superior to TSE and TGSE through a shortening of the scan time to one-eighth (from 193 to 24 seconds) of the time used in TSE and TGSE acquisitions. The short scan time of TIDE makes it less susceptible to CSF and eyeball motion artifacts compared with TSE and TGSE (Fig 2). While TSE and TGSE were susceptible to CSF motion artifacts (average score = 1.23 and 0.98, respectively), TIDE is almost free of CSF motion artifacts (average score = 2.98). Likewise, TIDE is less susceptible to eyeball motion artifacts (average score = 2.62) than TSE (average score = 2.18) and TGSE (average score = 1.88). In a 26-year-old female volunteer, for example, the trigeminal nerves are blurred on TSE and TGSE partially due to CSF motion artifacts and eyeball motion artifacts (Fig 5A, -B). The TIDE image, which is free of CSF motion artifacts and eyeball motion artifacts, clearly demonstrates the trigeminal nerves (Fig 5C). The rapid

imaging acquisition of TIDE (1 image per second) also makes it free from other motion artifacts. While the initial TSE shows severe motion artifacts in a 9-day-old neonate due to his involuntary head movement during the MR imaging, TIDE provides satisfactory imaging quality without the aforementioned motion artifacts (Fig 4). Nevertheless, TIDE is more susceptible to non-motion ghosting artifacts (average score = 1.78) compared with TSE (average score = 2.98) and TGSE (average score = 2.97). These ghostings are commonly seen on TIDE at certain anatomic regions, including the extracranial region (Fig 1C) and the bases of the middle cranial (Fig 2C) and anterior cranial fossae (Fig 3F) as demonstrated. The origin is related to oscillatory signals in every other phase-encoding arising from the alternative ascending and descending acquisitions in balanced steady-state free precession.[17,19]

Regarding the gray-white matter differentiation, our study shows that TIDE provides poorer gray-white matter differentiation (average score = 1.15) than TGSE (average score = 2.13) and TSE (average score = 2.98) on qualitative analysis. Quantitative analysis of CNRs between gray matter and white matter shows a discrepant result from the aforementioned qualitative analysis. TIDE has a higher CNR (average value = 5.69) between the thalamus (gray matter) and centrum semiovale (white matter) than TSE (average value = 4.95) and TGSE (average value = 2.74). On the other hand, our study shows that TIDE has lower SNRs than TSE and TGSE regarding both gray matter and white matter. The discrepant results suggest that SNR is the dominant factor, compared with CNR, influencing the neuroradiologists' perceptions while judging gray-white matter differentiation in images acquired by using different pulse sequences. In a 40-year-old male volunteer, for example (Fig 6), the SNRs are highest on TSE and lowest on TIDE, while the CNR is highest
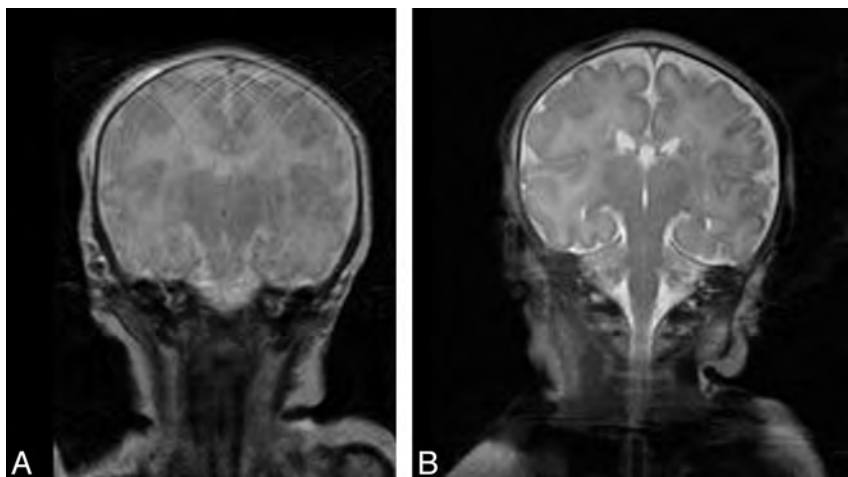
FIG 4. A 9-day-old neonate with seizures, presenting with involuntary movements, was imagined with TSE (A) and TIDE (B) sequences. A motion artifacts-free T2-weighted image can be acquired with TIDE, depicting a clear brain anatomy.
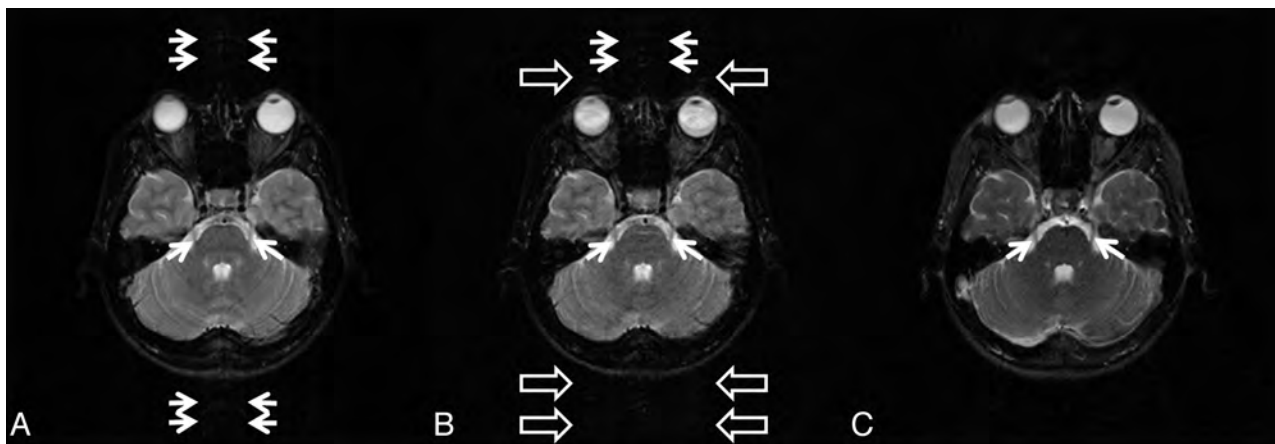
FIG 5. TSE (A), TGSE (B), and TIDE (C) images of a 26-year-old female volunteer. CSF motion artifacts (*double arrows*) are seen on TSE and TGSE images, while eyeball motion artifacts (*open arrows*) are seen on the TGSE image. The trigeminal nerves (*arrows*) are clearly demonstrated on TIDE, which is free of the aforementioned motion artifacts but are somewhat blurred on TSE and TGSE.
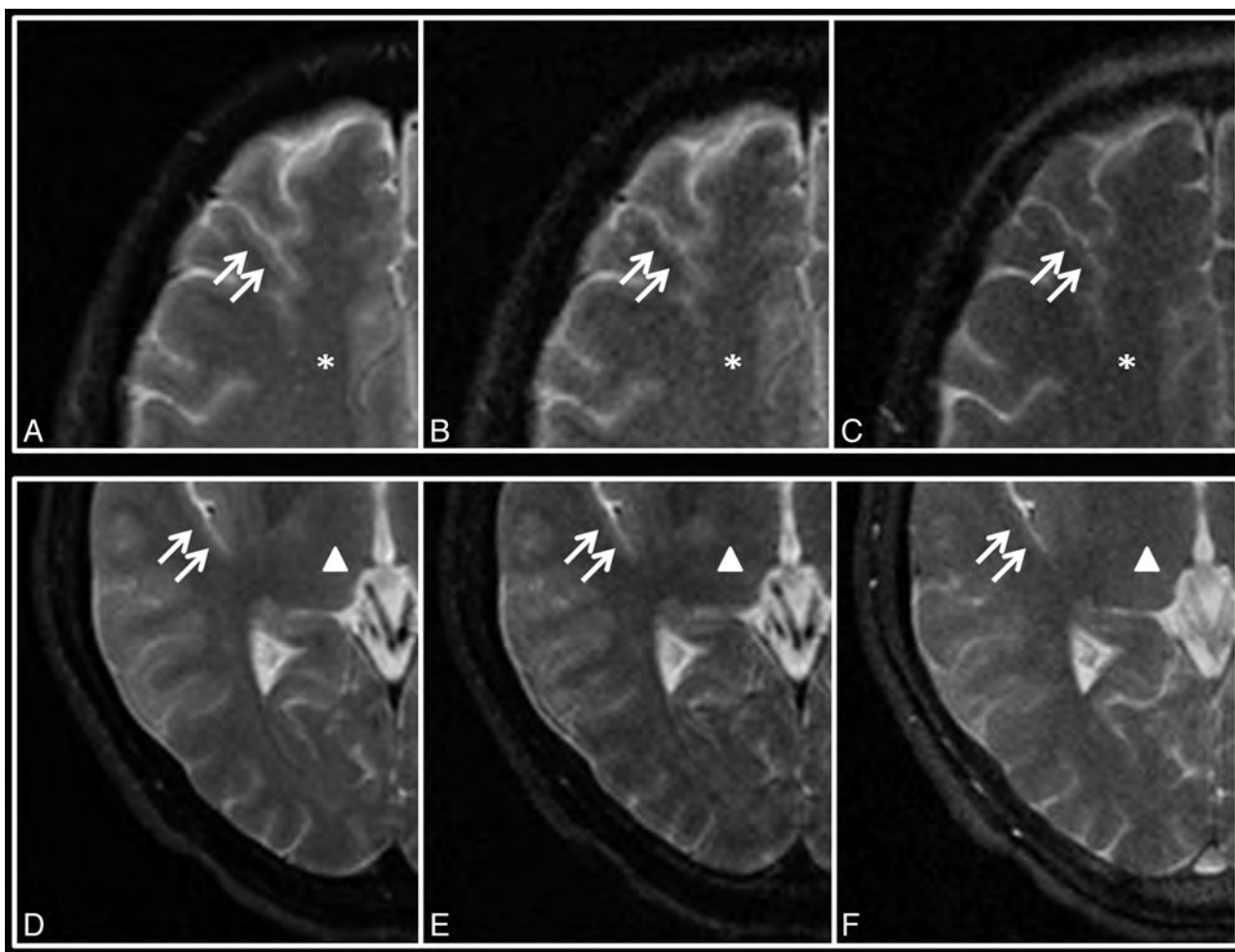
FIG 6. TSE (*A, D*), TGSE (*B, E*), and TIDE (*C, F*) images of a 40-year-old male volunteer at the levels of the centrum semiovale (*star, A–C*) and thalamus (*triangle, D–F*). The gray-white matter junctions (*double arrows*) are clearly demonstrated on TSE but are blurred on TGSE and TIDE.

on TIDE, followed by TSE and TGSE in decreasing order. The gray-white matter junctions are clearly demonstrated on TSE, but blurred on TGSE and TIDE.

In our study, the SNR of TIDE is approximately one-half (0.45–0.58) that for TSE. The lower SNR of TIDE might be due to 2 factors, including the half-Fourier acquisition and a higher readout bandwidth used in TIDE. The use of the half-Fourier function in TIDE, with 8 additional *k*-space lines acquired for Hermitian symmetry calibration, reduces the SNR to 71.84% of the full-Fourier mode value.[20] The readout bandwidth used for TIDE (125 kHz) in our study was 2 times of that used for TSE (62.5 kHz), which further explains another ~0.707 reduction in SNR for TIDE.[21] If one takes both of the above effects into account, the overall SNR in TIDE is thus expected to be approximately one-half that in TSE, as shown in our results. The lower SNRs of TIDE might explain the lower qualitative scores of gray-white matter differentiation of TIDE compared with TSE.

TIDE performs worst in detecting iron deposition in the iron-containing gray matter. Our results show that TIDE has the poorest iron-load sensitivity (average score = 0.47) compared with TGSE (average score = 2.07) and TSE (average score = 2.90) on qualitative analysis. The low signal intensity of the globus pallidus on TSE and TGSE has been attributed to the accumulation of

nonheme iron, ferritin, which has been shown to cause marked T2 shortening.[22] The study of Yamada et al[23] has shown that the iron-related susceptibility has caused underestimation of relative cerebral blood flow and relative cerebral blood volume in the globus pallidus. Our results show that TIDE has positive CNRs (average value = 3.28) rather than the negative CNRs of TGSE (average value = −4.49) and TSE (average value = −7.67). The rapid imaging acquisition of TIDE makes it least susceptible to the iron-related signal loss.

Fast imaging methods by using parallel imaging techniques, including sensitivity encoding, simultaneous acquisition of spatial harmonics, and array spatial sensitivity encoding technique, have been shown to reduce the scan time.[24-26] However, the reduction of scan time by using parallel imaging techniques is achieved at the cost of reduced SNR, which is inversely proportional to the square root of the acceleration factor.[25,27] For example, if an acceleration factor of 8 was used for TSE to achieve a scan time similar to that of TIDE in our study, the SNR would drop to approximately 35.4% of the original value, which is even worse than the SNR performance of TIDE (45%–58%).

There are several limitations in our study. First, we did not acquire coronal and sagittal images on TSE and TGSE sequences. To do that, we would have needed an additional 12 minutes 52

seconds. Thus, the results of our study design only validate the imaging quality on the basis of axial images. Second, qualitative evaluation of imaging was reported on the basis of only 2 experienced raters. Yet since the linearly weighted κ statistics showed substantial interobserver agreement, visual perception from additional neuroradiologists should supposedly yield similar results. Third, we did not collect certain brain pathology for statistical analysis. In our preliminary study, only 2 patients were scanned for demonstration purposes with no statistical analysis performed. Whether TIDE is helpful in lesion detection in patients with involuntary movements (Parkinson disease, tics, neonates, infants, and so forth) deserves further study. On the basis of the limited observations from our study, conspicuity of lesions whose magnetic susceptibility differs from that in surrounding parenchyma, such as iron-containing tissues, hemorrhage, hematoma, or calcification, may need to be paid special attention because of the reduced iron-load sensitivity of the TIDE sequence. On the other hand, regions prone to motion artifacts interferences, such as those adjacent to large vessels, rapid flowing CSF, and the eyeballs, might potentially benefit from the fast scanning characteristics in TIDE imaging.

CONCLUSIONS

TIDE provides T2-weighted images with reduced scan times and reduced motion artifacts compared with TSE and TGSE at the trade-off of reduced SNR and poorer gray-white matter differentiation. The fast-scan nature of TIDE might provide a rapid survey, especially in patients with involuntary movements.

REFERENCES

1. Bauer CM, Jara H, Killiany R. **Whole brain quantitative T2 MRI across multiple scanners with dual echo FSE: applications to AD, MCI, and normal aging.** Neuroimage 2010;52:508–14
2. Juan CJ, Chen CY, Liu YJ, et al. **Acute putaminal necrosis and white matter demyelination in a child with subnormal copper metabolism in Wilson disease: MR imaging and spectroscopic findings.** Neuroradiology 2005;47:401–05
3. Forsting M. **MR imaging of the brain: metabolic and toxic white matter diseases.** Eur Radiol 1999;9:1061–65
4. Patel MR, Klufas RA, Shapiro AW. **MR imaging of diseases of the brain: comparison of GRASE and conventional spin-echo T2-weighted pulse sequences.** AJR Am J Roentgenol 1995;165:963–66
5. Hennig J, Nauerth A, Friedburg H. **RARE imaging: a fast imaging method for clinical MR.** Magn Reson Med 1986;3:823–33
6. Fellner F, Schmitt R, Trenkler J, et al. **True proton density and T2-weighted turbo spin-echo sequences for routine MRI of the brain.** Neuroradiology 1994;36:591–97
7. Chen F, Suzuki Y, Nagai N, et al. **Delayed perfusion phenomenon in a rat stroke model at 1.5 T MR: an imaging sign parallel to spontaneous reperfusion and ischemic penumbra?** Eur J Radiol 2007;61:70–78
8. Kitajima M, Hirai T, Shigematsu Y, et al. **Comparison of 3D FLAIR, 2D FLAIR, and 2D T2-weighted MR imaging of brain stem anatomy.** AJNR Am J Neuroradiol 2012;33:922–27
9. Tubridy N, Barker GJ, Macmanus DG, et al. **Three-dimensional fast fluid attenuated inversion recovery (3D fast FLAIR): a new MRI sequence which increases the detectable cerebral lesion load in multiple sclerosis.** Br J Radiol 1998;71:840–45
10. Kazawa N, Togashi K, Ito J. **The anatomical classification of AICA/ PICA branching and configurations in the cerebellopontine angle area on 3D-drive thin slice T2WI MRI.** Clin Imaging 2013;37:865–70
11. Chung HW, Chen CY, Zimmerman RA, et al. **T2-weighted fast MR imaging with true FISP versus HASTE: comparative efficacy in the evaluation of normal fetal brain maturation.** AJR Am J Roentgenol 2000;175:1375–80
12. Hennig J, Speck O, Scheffler K. **Optimization of signal behavior in the transition to driven equilibrium in steady-state free precession sequences.** Magn Reson Med 2002;48:801–09
13. Paul D, Markl M, Fautz HP, et al. **T2-weighted balanced SSFP imaging (T2-TIDE) using variable flip angles.** Magn Reson Med 2006; 56:82–93
14. Paul D, Hennig J, Zaitsev M. **Intrinsic fat suppression in TIDE balanced steady-state free precession imaging.** Magn Reson Med 2006;56:1328–35
15. Huang YC, Huang TY, Chung HW, et al. **Modified T2-TIDE sequence: a preliminary result.** In: Proceedings of the 14th Scientific Meeting and Exhibition of the International Society for Magnetic Resonance in Medicine, Seattle, Washington. May 6–12, 2006
16. Huang YC, Huang TY, Chung HW. **T_2-TIDE-bSSFP imaging with simple and robust fat suppression.** In: Proceedings of the 14th Scientific Meeting and Exhibition of the International Society for Magnetic Resonance in Medicine, Seattle, Washington. May 6–12, 2006
17. Bieri O, Scheffler K. **Fundamentals of balanced steady state free precession MRI.** J Magn Reson Imaging 2013;38:2–11
18. Sim J, Wright CC. **The kappa statistic in reliability studies: use, interpretation, and sample size requirements.** Phys Ther 2005;85: 257–68
19. Park SH, Duong TQ. **Brain MR perfusion-weighted imaging with alternate ascending/descending directional navigation.** Magn Reson Med 2011;65:1578–91
20. Santa-Marta C, Lafuente J, Vaquero JJ, et al. **Resolution recovery in turbo spin echo using segmented half Fourier acquisition.** Magn Reson Imaging 2004;22:369–78
21. Li T, Mirowitz SA. **Fast T2-weighted MR imaging: impact of variation in pulse sequence parameters on image quality and artifacts.** Magn Reson Imaging 2003;21:745–53
22. Bartzokis G, Mintz J, Sultzer D, et al. **In vivo MR evaluation of age-related increases in brain iron.** AJNR Am J Neuroradiol 1994;15: 1129–38
23. Yamada K, Gonzalez RG, ØStergaard L, et al. **Iron-induced susceptibility effect at the globus pallidus causes underestimation of flow and volume on dynamic susceptibility contrast-enhanced MR perfusion images.** AJNR Am J Neuroradiol 2002;23:1022–29
24. Sodickson DK, Manning WJ. **Simultaneous acquisition of spatial harmonics (SMASH): fast imaging with radiofrequency coil arrays.** Magn Reson Med 1997;38:591–603
25. Pruessmann KP, Weiger M, Scheidegger MB, et al. **SENSE: sensitivity encoding for fast MRI.** Magn Reson Med 1999;42:952–62
26. Griswold MA, Jakob PM, Heidemann RM, et al. **Generalized autocalibrating partially parallel acquisitions (GRAPPA).** Magn Reson Med 2002;47:1202–10
27. Sodickson DK, Griswold MA, Jakob PM, et al. **Signal-to-noise ratio and signal-to-noise efficiency in SMASH imaging.** Magn Reson Med 1999;41:1009–22

Association of White Matter Hyperintensities with Low Serum 25-Hydroxyvitamin D Levels

J.M. Prager, C. Thomas, W.J. Ankenbrandt, J.R. Meyer, Y. Gao, A. Ragin, S. Sidharthan, R. Hutten, and Y.G. Wu

ABSTRACT

BACKGROUND AND PURPOSE: Vitamin D deficiency is associated with cognitive impairment in the elderly and with increased white matter T2 hyperintensities in elderly debilitated patients. We investigated the relationship between serum vitamin D and brain MR findings in adult outpatients.

MATERIALS AND METHODS: Brain MR studies of 56 patients ages 30−69 years were selected when vitamin D level had been obtained within 90 days of the MRI. White matter T2 hyperintensities were characterized by size and location by two neuroradiologists. Manual volumetric analysis was assessed in patients more than 50 years of age.

RESULTS: The entire cohort showed a significant negative relationship between serum 25-hydroxyvitamin D and the number of confluent juxtacortical white matter T2 hyperintensities ($P = .047$). The cohort ages 50 years and older showed stronger correlation between confluent white matter T2 hyperintensities and serum 25-hydroxyvitamin D in the juxtacortical region; number ($P = .015$) and size of white matter T2 hyperintensities ($P = .048$). Atrophy was not significantly related to serum 25-hydroxyvitamin D by radiologist visual analysis or by the bicaudate ratio.

CONCLUSIONS: We found a significant relationship between vitamin D and white matter T2 hyperintensities in independent adult outpatients, especially over the age of 50 years.

ABBREVIATIONS: Vit D = serum 25-hydroxyvitamin D; WMH = white matter T2 hyperintensities

There is accumulating scientific evidence that vitamin D supplements can be protective against some chronic diseases.[1-6] The National Institutes of Health supports a large ongoing study to test for such effects.[2] Investigators have begun to test for brain imaging findings that correlate with serum vitamin D levels.[6-8]

The January 2010 issue of *Neurology* contained 3 studies that evaluated hundreds of elderly subjects to test for a relationship between vitamin D status and dementia or cognitive impairment.[4,8,9] The Annweiler and Buell studies evaluated women only and both women and men, respectively; both showed a significant relationship between low vitamin D and dementia or cognitive impairment. The Slinin report only evaluated men and showed a

trend for a relationship between vitamin D and cognitive impairment. A later study by Annweiler et al,[10] with male and female subjects, showed lower serum 25-hydroxyvitamin D (Vit D) in patients with mild cognitive impairment compared with cognitively healthy individuals. A prospective study with 6-year follow-up involving more than 800 elderly patients showed significant increased risk of cognitive decline in those with low Vit D compared with sufficient levels.[11]

Studies have begun to examine the relationship between Vit D and brain MR findings in mice and in humans with significant disease. In 2010, Fernandes de Abreu et al[7] examined the offspring of maternal vitamin D deficient mice by MR. The mice had smaller ventricles at the age of 30 weeks, which normalized by 70 weeks. Hippocampal volume significantly decreased from weeks 30−70. Young mice also showed learning deficits.[7] The Buell study evaluated 318 dependent, elderly patients with a mean age of 73 years and found a significant negative relationship between Vit D and white matter T2 hyperintensities (WMH) volume.[8] Weinstock-Guttman et al[6] published a 2011 study examining the relationship between Vit D and brain MR in 193 patients with multiple sclerosis. Their patients had a mean age of 46 years. They

did not find a significant relationship between Vit D and WMH. However, a more recent longitudinal study showed a significant correlation between Vit D and the subsequent development of lesions in patients with multiple sclerosis.[12] The Buell and Weinstock-Guttman studies did not account for dietary vitamin D supplementation.

The purpose of this study was to determine if Vit D levels are associated with white matter abnormalities in an outpatient population by MR imaging.

MATERIALS AND METHODS

With the use of our hospital information system, we identified patients 30–69 years of age who had been tested for Vit D and also had a routine MR brain study within a 90-day period for our pilot study. From each decade of age we then selected the 7 patients with the highest and the 7 with the lowest Vit D levels for review. Vit D level, age, race (black or white), history of hypertension, diabetes, and use of dietary vitamin D supplementation were evaluated. All MR images were de-identified in compliance with Health Insurance Portability and Accountability Act regulations. Our institutional review board approved the study.

Image Acquisition and Analysis

MR imaging studies were all performed on 1.5T Siemens Espree and Avanto or GE LX2 and Excite magnets by use of standard institutional protocols and included T1 sagittal/axial, T2 axial, FLAIR axial, and diffusion-weighted sequences. They were evaluated separately by 2 subspecialty-certified neuroradiologists, with more than 20 years (J.R.M.) and 16 years (W.J.A.) of experience interpreting brain imaging, for presence of infarction, atrophy (graded 1–4), and perivascular spaces. White matter T2 hyperintensities were evaluated for type: punctate, defined as 5 mm or less, versus confluent, greater than 5 mm in diameter; confluent lesions were further quantified by number and greatest diameter (mm). White matter T2 hyperintensities were also evaluated for location; juxtacortical within 3 mm of cortex, periventricular within 3 mm of ventricle, or central (neither juxtacortical nor periventricular). When there was less than 7 mm between cortex and the ventricle, the distance was divided into thirds for localization.

Atrophy was further quantified by use of the bicaudate ratio, (minimum intercaudate distance divided by brain width along the same line), which reflects subcortical atrophy (Fig 1).[13]

MR imaging scans from the 25 participants more than 50 years of age were assessed for total WMH volume by use of MRIcro software (http://www.mccauslandcenter.sc.edu/mricro/mricro/mricro.html). Rater W.J.A., an experienced neuroradiologist, performed manual volumetric measurement by use of axial 5-mm FLAIR images.

Statistical Analysis

We used Pearson and Spearman correlations to test for a significant relationship between MR findings and serum vitamin D levels. For analysis, we divided the patients into 3 groups: 1) the entire cohort; 2) those aged 50 and above; and 3) only those not taking supplements. The neuroradiologists' findings were evaluated for strength of agreement; their MR findings were evaluated separately and together. The punctate and confluent white matter changes were evaluated separately and in various combinations, for example, periventricular plus central plus juxtacortical punctate foci.

RESULTS

Patient profiles are shown in Table 1. Nine subjects were excluded because of incomplete MR imaging or confounding pathology (eg, brain tumor). Note the much higher incidence of black subjects in the low Vit D group and the marked increase in subjects taking dietary vitamin D supplementation in the higher Vit D group, 15 compared with 2 in the low Vit D group. There is also a larger ratio of women to men in the higher Vit D group, 22:4 compared with the low Vit D group, 14:7. Four of the 22 patients younger than 50 years of age had WMH compared with 20 of the 25 patients ages 50 and above. The incidence of hypertension (including uncontrolled, blood pressure >140/90) and diabetes (including uncontrolled, fasting glucose >109) was similar in both groups.

Statistical Analysis

Initial review by the combined readers of the entire cohort by use of Spearman correlation showed a significant nega-

FIG 1. FLAIR image just above ventricles shows punctuate and confluent white matter T2 hyperintensities. From left to right: juxtacortical punctate, juxtacortical confluent, periventricular punctate, and central punctate.

Table 1: Demographics and clinical profiles

Age, Years	n	Vit D <20	Vit D ≥20
31–49; mean, 38.2	22	10 (7 female, 3 male)	12 (11 female, 1 male)
		7 white, 3 black	12 white
		1 hypertensive, 1 diabetic	2 hypertensive, 2 diabetic
		1 supplemental vitamin D	8 supplemental vitamin D
50–69; mean, 59.5	25	11 (7 female, 4 male)	14 (11 female, 3 male)
		7 white, 4 black	13 white, 1 black
		8 hypertensive (2 uncontrolled)	10 hypertensive (2 uncontrolled)
		4 diabetic (1 uncontrolled)	3 diabetic (1 uncontrolled)
		1 supplemental vitamin D	7 supplemental vitamin D

FIG 2. Probability value of correlation between Vitamin D level and white matter T2 hyperintensities in subjects without vitamin D supplementation by lesion location and type ($n = 17$, age >50 years). Bar height represents P value of relationship between WMH and serum 25-hydroxyvitamin D. Bars lower than the horizontal line are less than .05 and are significant. Correlation coefficient (r) value is shown above each bar. Red bars are punctate lesions, green bars are confluent lesions by size, and blue bars are confluent lesion number. J indicates juxtacortical; C, central; and P, periventricular.

Table 2: Pearson correlation of patients with migraine and WMH ($n = 47$)

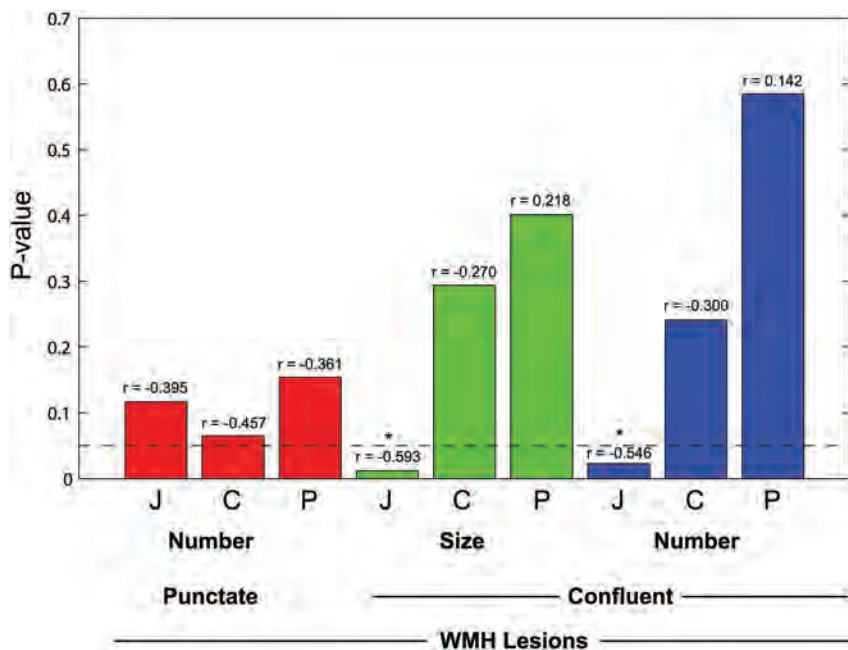|	WMH Region	Correlation Coefficient	P Value
Punctate lesions	Juxtacortical	−0.283	.054
	Central	−0.409	.004
	Periventricular	−0.359	.013
Confluent lesions	Juxtacortical	−0.235	.112
	Central	−0.214	.148
	Periventricular	−0.321	.028
No. of lesions	Juxtacortical	−0.199	.180
	Central	−0.228	.123
	Periventricular	−0.301	.040

tive relationship between Vit D and the number of confluent juxtacortical WMH, $\rho = -0.292$, $P = .047$; reader 2 showed significant relationship with confluent juxtacortical WMH number, $\rho = -0.295$, $P = .044$ and size, $\rho = -0.298$, $P = .042$. Combined readers of the cohort age 50 years and above showed a significant correlation between confluent WMH and Vit D in the juxtacortical region (number of WMH, $\rho = -0.481$, $P = .015$; size of WMH, $\rho = -0.399$, $P = .048$). When subjects taking dietary vitamin D supplementation were excluded, there were 17 subjects 50 years of age and above. The combined readers showed significant relationship between Vit D and juxtacortical confluent WMH number ($\rho = -0.546$; $P = .023$); and size ($\rho = -0.593$; $P = .012$) (Fig 2). In addition, reader 1 showed a relationship with central and combined central and periventricular punctate WMH ($\rho = -0.490$, $P = .046$ and $\rho = -0.506$, $P = .038$, respectively); reader 2 showed a relationship with combined central and periventricular WMH ($\rho = -0.482$, $P = .05$). There was no significant relationship between total WMH score and Vit D by vi-

sual or manual volumetric analysis. There was no significant relationship in the cohort of those ages younger than 50 years. Atrophy was not significantly related to Vit D by radiologist evaluation or by the bicaudate ratio.

Patients with migraine showed strong relationships with punctate WMH (periventricular $P = .013$, central $P = .004$). A significant relationship was also seen with size and number of confluent WMH in the periventricular region ($P = .028$ and .04, respectively) (Table 2).

Significant relationships were identified between all location punctate WMH and hypertension (juxtacortical, $P = .023$; central, $P = .001$; periventricular, $P = .018$). The number of juxtacortical confluent WMH was significantly related ($P = .049$); periventricular confluent WMH were related by number and size ($P = .008$ and $P = .001$, respectively) (Table 3). The relationship between WMH and Vit D is attenuated when controlling for hypertension.

There was fair to moderate agreement between the 2 neuroradiologist evaluators. Interobserver κ values ranged from 0.206–0.532 except for central confluent lesion number when κ value was 0.125. The P value for all WMH by type and location was <.001 except for central and juxtacortical maximum size confluent lesions when $P = .031$ and $P = .003$, respectively (Table 4).

DISCUSSION

We found a significant relationship between WMH and low Vit D in healthy outpatients ages 50 years and above. The relationship is stronger and more extensive when the patients taking supplemental vitamin D are excluded. We were further able to characterize the significant WMH as confluent in the juxtacortical white matter and punctate in the combined periventricular/central white matter.

The presence of WMH is concerning because of the known strong association with reduced cognition.[14-19] The Austrian Stroke Prevention Study showed that baseline grading of WMH was a better predictor for progression of cognitive difficulties than age or the presence of hypertension.[20] However, the presence of hypertension and diabetes are also associated with cognitive decline.[21,22] The exact mechanism by which low vitamin D might be related to reduced cognition or the development of WMH is not known. It has been proposed that the cognitive dysfunction seen with low Vit D is more specifically caused by impaired mental shifting and information updating involving the dorsolateral circuit of the frontosubcortical neuronal circuit.[23] Possible explanations may involve modulation of neurotrophins, calcium binding growth factors, and inflammatory cytokines.[1] It has been suggested that Vit D has an important role in the differentiation and

Table 3: Pearson correlations: WMH versus age, diabetes, and hypertension (n = 47)

		Age		Diabetes		Hypertension	
	WMH Region	Correlation Coefficient	P Value	Correlation Coefficient	P Value	Correlation Coefficient	P Value
Punctate lesions	Juxtacortical	0.364	.012	0.129	.389	0.331	.023
	Central	0.540	0	0.317	.03	0.476	.001
	Periventricular	0.468	.001	0.324	.026	0.345	.018
Confluent lesions	Juxtacortical	0.277	.06	0.297	.042	0.274	.062
	Central	0.410	.004	0.185	.212	0.226	.127
	Periventricular	0.536	0	0.226	.126	0.467	.001
No. of lesions	Juxtacortical	0.205	.168	0.113	.451	0.289	.049
	Central	0.353	.015	0.269	.067	0.263	.074
	Periventricular	0.471	.001	0.232	.117	0.385	.008

Table 4: Correlation between readers (n = 47)

		κ	
	WMH Region	Value	P Value
Punctate lesions	Juxtacortical	0.399	<.001
	Central	0.394	<.001
	Periventricular	0.215	<.001
Confluent lesions	Juxtacortical	0.261	<.001
	Central	0.125	.031
	Periventricular	0.305	<.001
No. of lesions	Juxtacortical	0.532	<.001
	Central	0.206	.003
	Periventricular	0.44	<.001

axonal adhesion of oligodendrogliocytes in the developing brain, with low Vit D increasing oligodendroglial apoptosis. This would prime an appropriate individual for the subsequent development of multiple sclerosis.[24]

Our findings concur with the 2 prior studies that investigated the relationship of Vit D and MR findings. The Buell study[8] found a significant relationship between Vit D and WMH volume in older debilitated patients with average age of 73 years. Our patients are healthier and younger, with an average age of 59 years. This increases the range of patients in whom low Vit D should be considered in the differential of WMH. The Weinstock-Guttman study[6] evaluated patients with MS for a relationship with Vit D and WMH. They did not find a significant relationship, but their patients were younger, with an average age of 46 years. We also did not find a relationship in younger patients. Furthermore, having a higher baseline volume of WMH in patients with multiple sclerosis, a larger number of subjects would be necessary to establish a significant relationship with a small number of additional causes for WMH.

A more recent 5-year longitudinal study of relapsing MS evaluated changes in MRI and clinical status relative to vitamin D levels. The study included 469 patients with 2362 3T MR examinations; the average age was 42 years. They correlated baseline and subsequent vitamin D levels with the development of WMH, gadolinium enhancement, clinical disability, and relapses. There were significant reductions in new WMH, gadolinium-enhancing lesions, and disability correlating with each 10 ng/mL increase in vitamin D level. The clinical relapse rate was lower but not statistically significant.[12]

Our analysis is most limited by measurement of the vitamin D level, which represents a single point in a dynamic process. When one considers the clinical factors that influence the blood level of vitamin D and the clinical profile of WMH, it is apparent why statistical analysis needs to adjust for dietary vitamin D supplementation. Measured vitamin D changes with the season and with individual exposure to sunlight and it is stored in the body for up to 2 months. Vitamin D production decreases in darker skinned individuals and with age.[3,25] The vitamin D level of an older patient taking a supplement does not reflect levels before taking supplements when WMH appeared. White matter T2 hyperintensities accumulate over a lifetime as they are only rarely reversible and then associated with acute illness such as Posterior Reversible Encephalopathy Syndrone or hepatic encephalopathy. Our patients probably had WMH years before they were examined with the use of MR and before they supplemented their diet with vitamin D. We did not control the patient selection process regarding the reason for medical and imaging evaluation, which could lead to unforeseen bias.

Potentially problematic in our patient population is the presence of hypertension and diabetes mellitus, which are closely related confounders known to increase WMH.[26-29] There is a similar incidence of controlled and uncontrolled hypertension (8 of 11, 73%; 10 of 14, 71%) and diabetes (4 of 11, 36%; 3 of 14, 21%) in the low and high Vit D groups.

This is a cross-sectional pilot study with a limited number of subjects and can only establish association but not causation. Future studies should consider including a larger cohort with more rigorous patient selection, especially patients who do not supplement their diet with vitamin D.

White matter T2 hyperintensities are a pathologic end point. Other MR techniques such as magnetization transfer, mean diffusivity, fractional anisotropy, perfusion, and MR spectroscopy have shown abnormalities in normal-appearing white matter in patients with MS.[30] Diffusion abnormalities are also seen in Alzheimer disease.[31] Maillard et al,[19] in a study of elderly subjects with cognitive health, cognitive impairment, and Alzheimer disease, showed an increased risk for white matter conversion to WMH in patients with lower fractional anisotropy and higher FLAIR signal in normal-appearing white matter. Optimized future studies should be longitudinal and use these MR techniques.

CONCLUSIONS
This study shows a previously unreported significant relationship between low Vit D levels and white matter injury evidenced by increased juxtacortical confluent WMH in healthy outpatients between the ages of 50–69 years. There was no relationship in our

patients ages 31–49 years. We showed a more powerful relationship in patients who did not take vitamin D supplements because normal Vit D in such patients could disguise a history of chronic low Vit D before the onset of supplementation. This pilot study has significant limitations including a small number of subjects and patient selection factors. Longitudinal studies with a greater number and control of subjects and additional MR metrics are indicated to establish a more definitive relationship.

REFERENCES

1. Miller JW. **Vitamin D and cognitive function in older adults: are we concerned about vitamin D-mentia?** *Neurology* 2012;74:13–15
2. Brody J. **Reasons that vitamin D may matter.** *The New York Times.* March 13, 2012; D7
3. Holick MF. **Vitamin D deficiency**. *N Engl J Med* 2007;357:266–81
4. Annweiler C, Schott AM, Allali G, et al. **Association of vitamin D deficiency with cognitive impairment in older women: cross-sectional study.** *Neurology* 2010;74:27–32
5. Niino M. **Vitamin D metabolites and multiple sclerosis.** *J Neurol Neurosurg Psychiatry* 2011;82:121
6. Weinstock-Guttman B, Zivadinov R, Qu J, et al. **Vitamin D metabolites are associated with clinical and MRI outcomes in multiple sclerosis patients.** *J Neurol Neurosurg Psychiatry* 2011;82:189–95
7. Fernandes de Abreu DA, Nivet E, Baril N, et al. **Developmental vitamin D deficiency alters learning in C57B1/6J mice.** *Behav Brain Res* 2010;208:603–08
8. Buell JS, Dawson-Hughes B, Scott TM, et al. **25-Hydroxyvitamin D, dementia, and cerebrovascular pathology in elders receiving home services.** *Neurology* 2010;74:18–26
9. Slinin Y, Paudel ML, Taylor BC, et al. **25-Hydroxyvitamin D levels and cognitive performance and decline in elderly men.** *Neurology* 2010;74:33–41
10. Annweiler C, Fantino B, Schott AM, et al. **Vitamin D insufficiency and mild cognitive impairment: cross-sectional association.** *Eur J Neurol* 2012;19:1023–29
11. Llewellyn DJ, Lang IA, Langa KM, et al. **Vitamin D and risk of cognitive decline in elderly persons.** *Arch Intern Med* 2010 170:1135–41
12. Mowry E, Waubant E, McCulloch C, et al. **Vitamin D status predicts new brain MRI activity in multiple sclerosis.** *Ann Neurol* 2012;72:234–40
13. van den Heuvel DM, ten Dam VH, de Craen AJ, et al. **Increase in periventricular white matter hyperintensities parallels decline in mental processing speed in a non-demented elderly population.** *J Neurol Neurosurg Psychiatry* 2006;77:149–53
14. Yoshita M, Fletcher E, Harvey D, et al. **Extent and distribution of white matter hyperintensities in normal aging, MCI, and AD.** *Neurology* 2006;67:2192–98
15. Inzitari D, Simoni M, Pracucci G, et al. **Risk of rapid global functional decline in elderly patients with severe cerebral age-related white matter changes: the LADIS study.** *Arch Intern Med* 2007;167:81–88
16. Gouw AA, van der Flier WM, Fazekas F, et al. **Progression of white matter hyperintensities and incidence of new lacunes over a 3-year period: the Leukoaraiosis and Disability Study.** *Stroke* 2008;39:1414–20
17. Debette S, Bombois S, Bruandet A, et al. **Subcortical hyperintensities are associated with cognitive decline in patients with mild cognitive impairment.** *Stroke* 2007;38:2924–30
18. Vannorsdall TD, Waldstein SR, Kraut M, et al. **White matter abnormalities and cognition in a community sample.** *Arch Clin Neuropsychol* 2009;24:209–17
19. Maillard P, Carmichael O, Harvey D, et al. **FLAIR and diffusion MRI signals are independent predictors of white matter hyperintensities.** *AJNR Am J Neuroradiol* 2013;34:54–61
20. Schmidt R, Enzinger C, Ropele S, et al. **Progression of cerebral white matter lesions: 6-year results of the Austrian Stroke Prevention Study.** *Lancet* 2003;361:2046–48
21. Knopman D, Boland LL, Mosley T, et al. **Cardiovascular risk factors and cognitive decline in middle-aged adults**. *Neurology* 2001;6:42–48
22. Akisaki T, Sakurai T, Takata T, et al. **Cognitive dysfunction associates with white matter hyperintensities and subcortical atrophy on magnetic resonance imaging: Japanese Elderly Diabetes Intervention Trial (J-EDIT).** *Diabetes Metab Res Rev* 2006;22:376–84
23. Annweiler C, Montero-Odasso M, Muir SW, et al. **Vitamin D and brain imaging in the elderly: should we expect some lesions specifically related to hypovitaminosis D?** *Open Neuroimaging Journal* 2012;6:16–18
24. Chaudhuri A. **Why we should offer routine vitamine D supplementation in pregnancy and childhood to prevent multiple sclerosis**. *Med Hypotheses* 2005;64:608–18
25. Rajakumar K, Greenspan SL, Thomas SB, et al. **Solar ultraviolet radiation and vitamin D: a historical perspective.** *Am J Public Health* 2007;97:1746–54
26. Murray AK, Staff RT, Shenkin SD, et al. **Brain white matter hyperintensities: relative importance of vascular risk factors in nondemented elderly people.** *Neurology* 2005;237:251–57
27. Swan GE, DeCarli C, Miller BL, et al. **Association of midlife blood pressure to late-life conngitive decline and brain morphology.** *Neurology* 1998;51:986–93
28. Valdés Hernández MC, Piper RJ, Bastin ME, et al. **Morphologic, distributional, volumetric, and intensity characterization of ventricular hyperintensities.** *AJNR Am J Neuroradiol* 2014;35:55–62
29. Knopman DS, Penman AD, Catellier DJ, et al. **Vascular risk factors and longitudinal changes on brain MRI**. *Neurology* 2011;76:1879–85
30. Filippi M, Rocca MA. **MR imaging of multiple sclerosis**. *Radiology* 2011;259:659–81
31. Stahl R, Dietrich O, Teipel SJ, et al. **White matter damage in Alzheimer disease and mild cognitive impairment: assessment with diffusion-tensor MR imaging and parallel imaging techniques.** *Radiology* 2007;243:483–92

Association between Resting-State Coactivation in the Parieto-Frontal Network and Intelligence during Late Childhood and Adolescence

C. Li and L. Tian

ABSTRACT

BACKGROUND AND PURPOSE: A number of studies have associated the adult intelligence quotient with the structure and function of the bilateral parieto-frontal networks, whereas the relationship between intelligence quotient and parieto-frontal network function has been found to be relatively weak in early childhood. Because both human intelligence and brain function undergo protracted development into adulthood, the purpose of the present study was to provide a better understanding of the development of the parieto-frontal network–intelligence quotient relationship.

MATERIALS AND METHODS: We performed independent component analysis of resting-state fMRI data of 84 children and 50 adolescents separately and then correlated full-scale intelligence quotient with the spatial maps of the bilateral parieto-frontal networks of each group.

RESULTS: In children, significant positive spatial-map versus intelligence quotient correlations were detected in the right angular gyrus and inferior frontal gyrus in the right parieto-frontal network, and no significant correlation was observed in the left parieto-frontal network. In adolescents, significant positive correlation was detected in the left inferior frontal gyrus in the left parieto-frontal network, and the correlations in the frontal pole in the 2 parieto-frontal networks were only marginally significant.

CONCLUSIONS: The present findings not only support the critical role of the parieto-frontal networks for intelligence but indicate that the relationship between intelligence quotient and the parieto-frontal network in the right hemisphere has been well established in late childhood, and that the relationship in the left hemisphere was also established in adolescence.

ABBREVIATIONS: IQ = intelligence quotient; FSIQ = full-scale intelligence quotient; PFN = parieto-frontal network; RS-fMRI = resting-state fMRI; TC-GICA = temporal-concatenation group independent component analysis; R.PFN = right PFN; L.PFN = left PFN; IFG = inferior frontal gyrus

The brain basis of intelligence has been widely investigated for many years.[1] A range of neuroimaging paradigms, including MR imaging, EEG, DTI, PET, and task-based fMRI, have been used to investigate the neural basis of intelligence quotient (IQ).[2] A large percentage of these studies reported that individual differences in IQ are related to the structure or function of the parieto-frontal regions in adults.[3-6] For instance, Haier et al[3] reported that more gray matter in the parieto-frontal regions was associated with higher IQ on the basis of the MR imaging scans of adults. On the basis of MR imaging of young adults, Colom et al[5,6] reported that the structural features of gray matter in the frontal lobes supported fluid, crystallized, and spatial intelligence. Jung and Haier[2] reviewed 37 modern neuroimaging studies associated with intelligence and advanced the parieto-frontal integration theory, which indicated the importance of the parieto-frontal regions, along with some temporal and occipital regions, for intelligence.

Resting-state fMRI (RS-fMRI) is rapidly emerging as a powerful tool for in vivo mapping of neural circuitry in the human brain. Several recent studies investigated the neural basis of IQ in adults by use of RS-fMRI.[7-10] Song et al[7] analyzed the functional connectivities (FCs) associated with the bilateral dorsal lateral prefrontal cortex and reported that the FCs between parieto-frontal regions were particularly associated with intelligence. Van den Heuvel et al[8] examined the RS-fMRI data from a complex network perspective and reported that the characteristic path length in parieto-frontal regions was longer in subjects with lower IQ. Wang et al[9] reported the association between IQ and regional homogeneity of RS-fMRI signals in the parieto-frontal and other

regions in adults. Cole et al[10] reported a highly selective relationship between the global brain connectivity of left lateral prefrontal cortex and individual differences in fluid intelligence.

It should be noted that all these brain-intelligence relationship analyses were based on adults. Both mental abilities and brain function have been reported to undergo protracted development from early childhood into adulthood,[11] and the higher-order association areas, including the parieto-frontal regions, have been reported to mature last.[12,13] This indicates that the association between intelligence and function of the parieto-frontal regions might not have been established in children. Langeslag et al[14] noticed this and analyzed the correlation between IQ and the FCs within the parieto-frontal networks (PFNs) across children 6–8 years old. On the basis of RS-fMRI, a significant functional connectivity-versus-IQ correlation was observed only in the right parieto-frontal network (R.PFN) at a relatively loose threshold ($P <$ .05, false discovery rate–corrected for 10 comparisons), and this correlation in the left parieto-frontal network (L.PFN) was not significant ($P <$ .05, false discovery rate–corrected for 3 comparisons) in their study. To date, the developmental route of the PFN-IQ relationship has not been well depicted, with a relatively weak relationship in early childhood,[14] well-established relationship in adulthood, and unknown relationship in late childhood and adolescence.

To provide a better understanding of the development of PFN-IQ relationship, we analyzed the association between Wechsler full-scale IQ (FSIQ) and resting-state coactivation in the bilateral PFNs obtained by independent component analysis of RS-fMRI data. Independent component analysis is a powerful data-driven approach for finding independent patterns in multivariate data and one of the strongest statistical computational approaches in the detection of resting state networks.[15,16] As compared with the extensively used seed-based functional connectivity analyses, independent component analysis needs no definition of seed regions and thus any possible bias caused by seed-selection in seed-based functional connectivity analyses could be avoided by use of independent component analysis. We performed the study as follows: 1) on the basis of publicly released RS-fMRI data, temporal-concatenation group independent component analysis (TC-GICA) was performed to acquire the group independent component maps for the child group (84 subjects) and adolescent group (50 subjects) separately. Dual regression was then performed to find individual subject-level versions of the network spatial maps; 2) for each group, the components corresponding to the R.PFN and the L.PFN were identified by means of visual inspection, and voxelwise correlations with FSIQ were performed on the spatial maps of both the R.PFN and the L.PFN across subjects.

MATERIALS AND METHODS
Subjects
Data were selected from a large sample RS-fMRI dataset publicly released as "The ADHD-200 Sample" in the "1000 Functional Connectomes Project."[17] Subjects who satisfied the following 4 criteria were included in the present study: 1) typically developing subjects: the subjects had no lifetime history of head trauma with loss of consciousness and no history of neurologic illness or serious physical disease; 2) subjects enrolled at and data collected by

Beijing Normal University. As compared with those from other centers, the Beijing dataset included the largest sample size of typically developing subjects. We did not use data from multiple centers in consideration of avoiding any possible center-related variations,[18] and the present sample size was relatively large (84 children and 50 adolescents); 3) head motion <2.0 mm displacement in any of the x, y, or z directions and 2.0° of any angular motion throughout the resting-state scan; 4) subjects were right-handed, which was evaluated by the 10-item handedness inventory designed by The National Cooperative Research Team for Handedness of China. According to these 4 criteria, 134 subjects were included in this study, and were divided into 1 child group (84 subjects, 44 girls, 8.00–11.99 years old, with a mean age of 10.22 ± 1.11 years) and 1 adolescent group (50 subjects, 14 girls, 12.00–15.99 years old, with a mean age of 13.47 ± 0.81 years).

Dataset
MR imaging data were obtained by use of a Trio 3T scanner (Siemens, Erlangen, Germany). Functional images were collected axially by use of an echo-planar imaging sequence sensitive to blood oxygen level–dependent contrast with the following parameters: 33 sections, 2000/30 ms (TR/TE), 90° (flip angle), 220 × 220 mm (FOV), 64 × 64 (resolution), 3.5/0.7 mm (thickness/gap). The resulting nominal voxel size was 3.44 × 3.44 × 4.50 mm. The functional imaging lasted for 480 seconds. Whole-brain 3D T1-weighted images were then obtained sagittally with the following parameters: 128 sections, 2530/3.39 ms (TR/TE), 1.33/0 mm (thickness/gap), 256 × 256 (resolution), 240 × 240 mm (FOV), 7° (flip angle). The resulting nominal voxel size was 1.07 × 1.07 × 1.33 mm.

Subject FSIQ scores were assessed by use of the Wechsler Intelligence Scale for Chinese Children-Revised. Because the raw test scores were tailored to exact age, the FSIQ scores used in this study were independent of age. The mean FSIQ score of the 84 children was 119.4 (standard deviation [SD] = 13.4) and the range was 84–153. The mean FSIQ score of the 50 adolescents was 115.2 (SD = 12.7) and the range was 81–135.

RS-fMRI Data Preprocessing
RS-fMRI data preprocessing was performed by use of FSL (http://www.fmrib.ox.ac.uk/fsl). The following processing steps were applied to the RS-fMRI data of each subject: 1) removing the first 5 volumes; 2) correcting for head motion by use of the MCFLIRT tool in FSL; 3) removing the nonbrain tissues with the Brain Extraction Tool; 4) spatial smoothing by use of a Gaussian kernel of full width at half maximum 5 mm; 5) high-pass temporal filtering to remove slow drift (cutoff frequency = 0.01 Hz); 6) registering the subject's RS-fMRI data to his or her high-resolution structural image and then to Montreal Neurological Institute 152 standard space by use of the FLIRT and FNIRT tools in FSL and resampling the subject's registered RS-fMRI data to 2 × 2 × 2-mm resolution. Because the effects associated with head motion and other noise could be ameliorated through the use of independent component analysis and dual regression, no denoising was performed.

TC-GICA and Dual Regression
TC-GICA was carried out on the datasets of the child group and adolescent group separately by use of MELODIC in FSL. Given
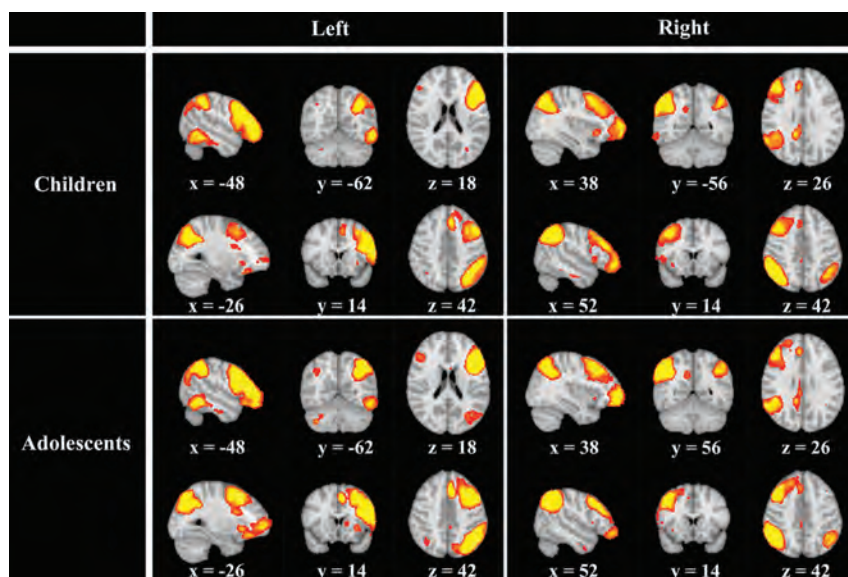
FIG 1. Spatial maps representing the parieto-frontal networks on the basis of temporal-concatenation group independent component analyses.

computational resource limitations, we performed a 2-stage TC-GICA, as was used in the study by Biswal et al,[18] as follows: 1) TC-GICA was performed 10 times, each with 20 randomly selected subjects, and the number of components was fixed at 20.[16,18] 2) A second-stage independent component analysis was then carried out across the 10 runs to extract the 20 spatial maps consistently identified across the 10 runs. Dual regression was then applied to each subject's preprocessed RS-fMRI data to build individual-subject-level spatial maps.[19-21] Specifically, for each subject (separately): 1) the formerly obtained 20 group-independent component analysis spatial maps (based on his or her own group dataset) were used as spatial regressors against the subject's 4D RS-fMRI data to estimate the network time-series of each component. Before being fed into the model, each component map was demeaned and normalized. 2) The resulting 20 time-series were then used as temporal regressors against each subject's preprocessed 4D RS-fMRI data, resulting in 1 individual-subject-level spatial map for each component, reflecting how closely the functional data temporally resembled the component time-series at each voxel. Again, each time-series was demeaned and normalized before entering into the regression model.

PFN-IQ Relationship Analyses

PFN-IQ relationship analyses were performed on the spatial maps of the bilateral PFNs of the child group and adolescent group separately. To do this, we first identified the R.PFN and the L.PFN on the basis of visual inspection of the spatial maps generated by TC-GICA: the obviously right-lateralized network covering mainly the right parieto-frontal regions was identified as the R.PFN, and the network covering mainly the parieto-frontal regions in the left hemisphere was identified as the L.PFN. The spatial maps corresponding to the R.PFN/L.PFN were then collected across subjects into a 4D file (the fourth dimension was subject number). Five thousand permutations were finally performed within the corresponding PFN-mask obtained by thresholding the spatial map of the network on the basis of TC-GICA at

5, to test for significant spatial map–versus–FSIQ correlations by use of the randomize command in FSL. Age, sex, and gray matter attenuation (acquired by voxel-based morphometry analysis of the 3D T1-weighted data, as a voxelwise covariate) were taken as covariates and removed. The results were thresholded at $P < .05$ (threshold-free cluster enhanced in FSL, family-wise error–corrected).[22] To provide a comprehensive perspective about the PFN-IQ relationship at the 2 developmental stages, marginally significant correlations that survived a looser threshold of $P < .005$ (uncorrected) and cluster size >200 mm^3 (25 resampled voxels) were also reported.

To test whether the spatial map–versus–FSIQ correlations were specific to the bilateral PFNs, the medial visual network, the auditory-motor network, and the default mode network were selected as control RSNs, and 5000 permutations were also performed on the 3 control networks within the corresponding mask.

RESULTS

The R.PFN of the child group was similar to that of the adolescent group, and the L.PFNs of the 2 groups were also similar (Fig 1). The R.PFN and the L.PFN of each group appeared to be symmetrical. In each PFN, in addition to the ipsilateral parieto-frontal regions, small clusters were also observed in the presupplementary motor area and posterior cingulate cortex, the ipsilateral fusiform, as well as the contralateral parieto-frontal regions and cerebellum. Spatial maps of all 20 components of children and adolescents are shown in On-line Figs 1 and 2, respectively.

In the R.PFN of children, significant positive spatial map–versus–FSIQ correlations were found in the right angular gyrus and inferior frontal gyrus (IFG) ($P < .05$, threshold-free cluster enhanced, family-wise error–corrected), and positive correlations in left cerebellum and another right angular gyrus region were marginally significant (uncorrected $P < .005$ and cluster size >200 mm^3) (Fig 2a–d and Table). No marginally significant negative correlation was found in the R.PFN of children. In the L.PFN of children, no marginally significant correlation (either positive or negative) was found.

In adolescents, significant positive correlations with the spatial map of the L.PFN were found in left IFG ($P < .05$, threshold-free cluster enhanced, family-wise error–corrected), and the positive correlation in the left frontal pole was marginally significant (uncorrected $P < .005$ and cluster size >200 mm^3) (Fig 2e,-f and Table). Marginally significant positive correlation on the basis of the R.PFN was detected in the right frontal pole (Fig 2g and Table). No marginally significant negative correlation was found in the 2 PFNs of adolescents.

No marginally significant spatial map–versus–FSIQ correlation (uncorrected $P < .005$ and cluster size >200 mm^3), either positive or negative, was detected in any of the 3 control RSNs of
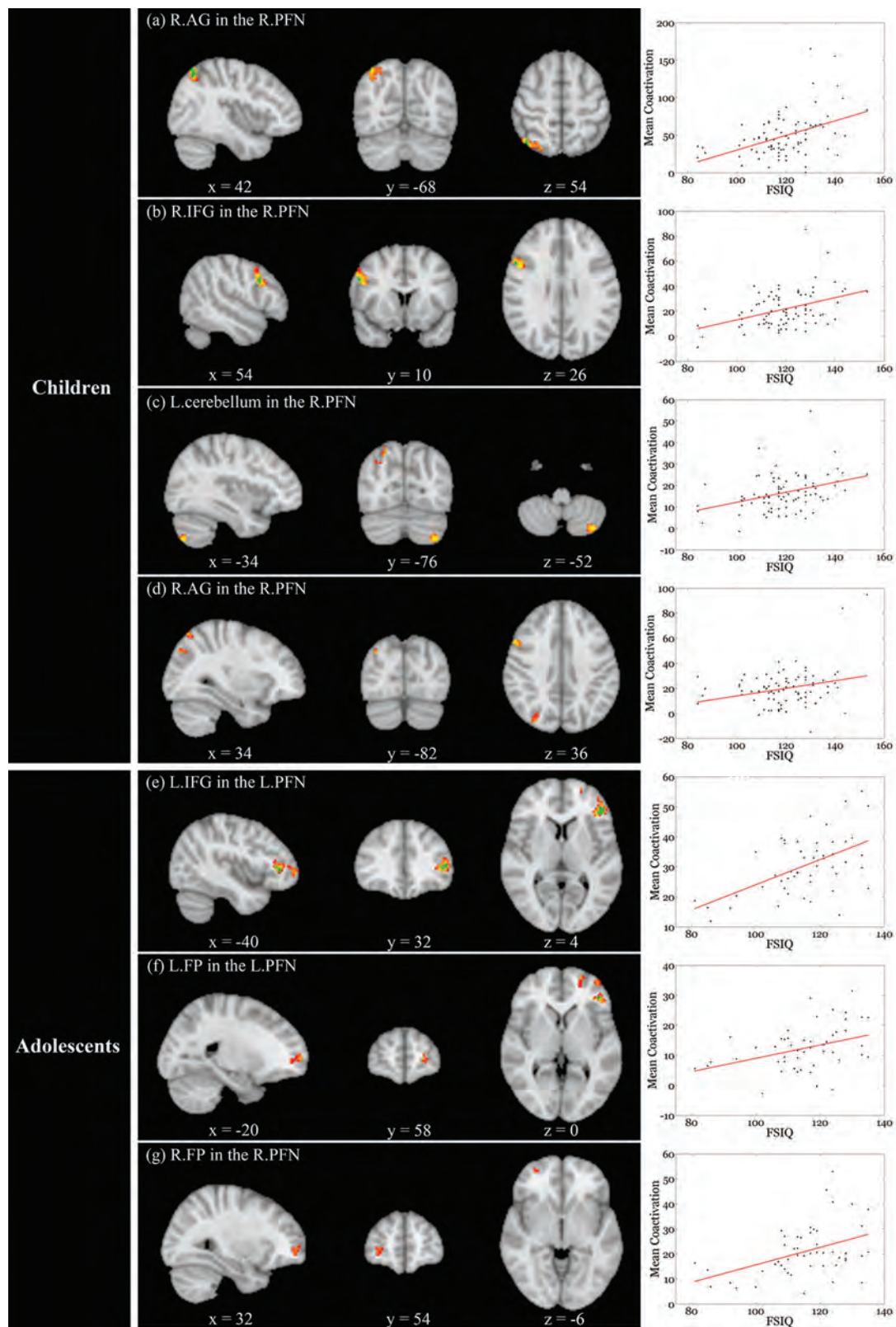
FIG 2. Positive correlations with full-scale intelligence quotient (FSIQ) across subjects. In the right parieto-frontal network (R.PFN) of children, significant correlations were observed in the right angular gyrus (AG) *(a)* and inferior frontal gyrus (IFG) *(b)*, and marginally significant correlations were observed in the left cerebellum *(c)* and another right AG region *(d)*. In adolescents, significant correlations were observed in the left IFG in the left PFN (L.PFN) *(e)*, and marginally significant correlations were observed in the left frontal pole (FP) in the L.PFN *(f)* and right FP in the R.PFN *(g)*. Green color indicates significant correlations and red-yellow color indicates marginally significant correlations. In the scatterplots, the *y*-coordinate indicates the mean coactivation of voxels exhibiting significant spatial map–versus–FSIQ correlations.

Positive correlations with FSIQ across subjects

Region	Brodmann Area	Cluster Size, mm³	MNI Coordinate (Peak)	*r* Value (mean)
Children:				
Correlations with FSIQ in the R.PFN				
R AG	39	184	40, −66, 56	0.45
		1656[b]		
R IFG	44	128	52, 12, 28	0.41
		1616[b]		
L cerebellum[a]		536[b]	−36, −74, −50	0.37
R AG[a]	39	280[b]	32, −80, 38	0.27
Adolescents:				
Correlations with FSIQ in the L.PFN				
L IFG	45	256	−42, 34, 6	0.54
		2416[b]		
L FP[a]	10	360[b]	−22, 60, 2	0.37
Correlations with FSIQ in the R.PFN				
R FP[a]	11	528[b]	30, 56, −4	0.43

Note:—Threshold was *P* < .05 (threshold-free cluster enhanced, family-wise error–corrected).
[a] Marginally significant correlations (uncorrected *P* < .005 and cluster size >200 mm³); [b] represents the cluster size at this threshold. No marginally significant correlation was found in the L.PFN of children.
R indicates right; L, left; IFG, inferior frontal gyrus; AG, angular gyrus; FP, frontal pole; MNI, Montreal Neurological Institute.

any group (children and adolescents). This indicates that the spatial map–versus–FSIQ correlations were specific to the PFNs.

DISCUSSION

In this study, we obtained spatial maps by use of independent component analysis decomposition of RS-fMRI data of 84 older children and 50 adolescents and examined whether the PFN-IQ relationship had been established in each group. Only positive spatial map–versus–FSIQ correlations were detected in this study, and the correlations were specific to the PFNs. In children, significant/marginally significant positive correlations were found in the right angular gyrus and IFG and left cerebellum in the R.PFN (Fig 2*a–d* and Table). In adolescents, significant positive correlations were found in the left IFG in the L.PFN, and the positive correlations in the frontal pole in the 2 PFNs were marginally significant (Fig 2*e–g* and Table).

The importance of the PFN for IQ has been reported in many pioneering studies by use of diverse neuroimaging techniques.[1-4,7,8,23] Specifically, more gray matter in the bilateral parieto-frontal regions has been reported to be associated with higher IQ.[3,24] The fractional anisotropy within the bilateral frontal and occipito-parietal regions has been reported to be positively correlated with IQ.[25] With task-based fMRI/PET, the parieto-frontal regions have been reported to be active during working memory[26] and a variety of reasoning tasks,[23] both of which are important for intelligence. On the basis of graph-theoretical network analyses of EEG data, the degree centralities of parieto-frontal regions have been reported to be significantly correlated with intelligence.[27] On the basis of RS-fMRI, IQ has been reported to be associated with functional connectivity between parieto-frontal regions,[7] regional homogeneity of RS-fMRI signals in parieto-frontal regions,[9] global brain connectivity of the left lateral prefrontal cortex,[10] and the normalized characteristic path length of parieto-frontal regions.[8] In this study, significant/marginally significant spatial map–versus–FSIQ correlations were found in the right angular gyrus and IFG in the R.PFN of children (Fig 2*a, b, and d* and Table), left IFG and frontal pole in the L.PFN, and right frontal pole in the R.PFN of adolescents (Fig 2*e–g* and Table). The right IFG has been reported to play important roles in environ-

ment monitoring, action planning, numerical ordering, and symbolic arithmetic.[28,29] The left IFG has been repeatedly reported to be involved in phonological processing.[30,31] Angular gyrus activations have been reported in such situations as spatial attention and orienting, language and semantic processing, and mathematical cognition.[32,33] On the basis of meta-analysis, Bludau et al[34] reported the involvement of the frontal pole in action selection, working memory, and perception. Each of the aforementioned functions of the 4 regions is critical for intelligence. Taken together, the present findings of significant/marginally significant spatial map–versus–FSIQ correlations in the PFNs (Fig 2 and Table) support the critical role of the PFNs for intelligence.

In this study, marginally significant spatial map–versus–IQ correlation was found in left cerebellum in the R.PFN of children (Fig 2*c* and Table). In addition to its critical role in motor control, the cerebellum has been repeatedly reported to be involved in some cognitive functions. As for IQ, Frangou et al[24] reported significant correlation between IQ and gray matter attenuation in cerebellum. Taki et al[35] reported that the regional gray matter volume of cerebellum, together with that in bilateral prefrontal and temporo-parietal regions, was significantly positively correlated with FSIQ. The present finding of marginally significant correlation in the cerebellums of children is consistent with the 2 reports.

Only positive (and no negative) spatial map–versus–FSIQ correlations were found in this study. Formerly, decreased coactivation in certain resting-state networks has been linked to Alzheimer disease,[36] obsessive-compulsive disorder,[37] and cocaine addiction,[38] and increased coactivation in certain resting-state networks has been linked to better performances in response inhibition[21] and motor skill learning.[39] In these studies, the extent of coactivation was deemed to represent the strength of functional interactions between the regions within the networks. If this were the case, the significant positive spatial map–versus–FSIQ correlations observed in this study may indicate that stronger functional interactions in the PFNs are advantageous for intelligence. According to the influential neural efficiency hypothesis of intelligence,[40] brighter individuals would display lower brain activa-

tion during cognitive task performance. Limited by datasets (no task data were available), the present results answered only the question about whether the PFN-IQ relationship exists at the 2 developmental stages. Further studies including both task and resting data may make it clear about how the PFN regions are involved in cognition.

The correlation in the R.PFN of children survived a family-wise error–corrected threshold of $P < .05$, whereas the correlation in the R.PFN of adolescents survived only a looser threshold of $P < .005$ (uncorrected) and cluster size >200 mm^3. This does not mean that the R.PFN-IQ relationship become weaker with development. It should be noted that the sample size of children was 84, and that of adolescents was 50 in this study. Because statistical power decreases with the decrease of sample size, the present finding of marginally significant correlations in adolescents may be interpreted, at least in part, by the smaller sample size of the group. Indeed, in this study, a correlation coefficient of 0.41 (right IFG in the R.PFN) in children corresponded to significant correlation, whereas a correlation of 0.43 (right frontal pole in the R.PFN) in adolescents only corresponded to marginally significant correlation (Table).

As has been mentioned, only a few studies have been performed specially for investigating the functional basis of IQ in children, and, to our knowledge, no study has been performed on the functional basis of IQ in adolescents, though numerous studies have been performed on that in adults. Langeslag et al[14] noticed that both the brain and IQ underwent significant development before adulthood and proposed the importance of analyzing whether the PFN-IQ relationship had been established in children. They analyzed the correlation between IQ and the parieto-frontal functional connectivity across children of 6–8 years old, on the basis of RS-fMRI. In their study, significant functional connectivity-versus-IQ correlation was observed only in the R.PFN at a relatively loose threshold ($P < .05$, false discovery rate–corrected for only 10 comparisons), and the correlation in the L.PFN was not significant ($P < .05$, false discovery rate–corrected for 3 comparisons). In the present study, the spatial map–versus–FSIQ correlations in the R.PFN of children (Fig 2a,-b and Table) and L.PFN of adolescents (Fig 2e and Table) were strong enough to survive an family-wise error–corrected threshold of $P < .05$ (threshold-free cluster enhanced, family-wise error–corrected for the number of voxels within the corresponding PFN mask). The present results bridge the gap between the findings that are based on adults and the results by Langeslag et al[14] by indicating that during late childhood, the PFN-IQ relationship in the right hemisphere has been well established, and that relationship in the left hemisphere was also established during adolescence.

Both the study by Langeslag et al[14] and the present study implicated a right-lateralized advantage in the development of PFN-IQ relationship. One speculative explanation for the findings is that the right hemisphere of a child's brain may develop earlier than its contralateral counterpart, and the left hemisphere may develop later to build a PFN-IQ relationship similar to that in adults. This speculation is consistent with former findings of rightward asymmetries of brain maturation in early developmental stages. For instance, the volume of the right hemisphere has been reported to be significantly larger than that of its left counterpart in children between 4–18 years old.[41] Zhu et al[42] reported that the FCs in the right hemisphere were stronger than those in the left hemisphere in children of 0–10 years old. Zhou et al[43] reported right-lateralized cortical thickness asymmetries in vision- and language-relevant areas in subjects of 5–14 years of age. Further studies are needed to provide a longitudinal view about the development of hemisphere-IQ relationship.

It should be noted that we investigated the PFN-IQ relationship based only on children of 8.00–11.99 years old and adolescents of 12.00–15.99 years old. These age ranges can provide only information about the extent of influences of resting-state coactivation in the PFN on IQ at the 2 developmental stages. To provide an overall view of the development of the PFN-IQ relationship, a study including samples covering a larger age range (eg, from 5 years old to adulthood) is needed. In addition, a larger sample size may enable a finer division of age ranges (eg, every 2 years rather than 4 years, as was used in the current study) and thus facilitate the acquisition of more detailed and precise understanding of the development of the PFN-IQ relationship. Furthermore, comparable sample size at each age range may provide an intuitive idea about the relative strength of the PFN-IQ relationship at different developmental stages.

CONCLUSIONS

We correlated FSIQ with the spatial maps of resting-state PFNs across 84 children and 50 adolescents to provide a better understanding of the development of the PFN-IQ relationship. The spatial map–versus–FSIQ correlations in the R.PFN of children and L.PFN of adolescents were strong enough to survive an family-wise error–corrected threshold of $P < .05$. The present findings not only supported the critical role of the PFNs for intelligence but bridged the gap between the results that were based on adults and those based on younger children (6–8 years old) by indicating that during late childhood, the PFN-IQ relationship in the right hemisphere has been well established, and that relationship in the left hemisphere was also established during adolescence. Further studies including a larger sample size and covering a larger age range are needed to better depict the developmental trajectory of the PFN-IQ relationship.

REFERENCES

1. Colom R, Jung RE, Haier RJ. **Distributed brain sites for the G-factor of intelligence.** *NeuroImage* 2006;31:1359–65
2. Jung RE, and Haier RJ. **The Parieto-Frontal Integration Theory (P-FIT) of intelligence: converging neuroimaging evidence.** *Behav Brain Sci* 2007;30:135–54
3. Haier RJ, Jung RE, Yeo RA, et al. **Structural brain variation and general intelligence.** *NeuroImage* 2004;23:425–33
4. Jung RE, Haier RJ, Yeo RA, et al. **Sex differences in N-acetylaspartate correlates of general intelligence: a 1H-MRS study of normal human brain.** *NeuroImage* 2005;26:965–72
5. Colom R, Haier RJ, Head K, et al. **Gray matter correlates of fluid,**

crystallized, and spatial intelligence: testing the P-Fit model. *Intelligence* 2009;37:124–35

6. Colom R, Burgaleta M, Roman FJ, et al. **Neuroanatomic overlap between intelligence and cognitive factors: morphometry methods provide support for the key role of the frontal lobes.** *NeuroImage* 2013;72:143–52

7. Song M, Zhou Y, Li J, et al. **Brain spontaneous functional connectivity and intelligence.** *NeuroImage* 2008;41:1168–76

8. van den Heuvel MP, Stam CJ, Kahn RS, et al. **Efficiency of functional brain networks and intellectual performance.** *J Neurosci* 2009;29:7619–24

9. Wang L, Song M, Jiang T, et al. **Regional homogeneity of the resting-state brain activity correlates with individual intelligence.** *Neurosci Lett* 2011;488:275–78

10. Cole MW, Yarkoni T, Repovs G, et al. **Global connectivity of prefrontal cortex predicts cognitive control and intelligence.** *J Neurosci* 2012;32:8988–99

11. Casey BJ, Tottenham N, Liston C, et al. **Imaging the developing brain: what have we learned about cognitive development?** *Trends Cogn Sci* 2005;9:104–10

12. Gogtay N, Giedd JN, Lusk L, et al. **Dynamic mapping of human cortical development during childhood through early adulthood.** *Proc Natl Acad Sci U S A* 2004;101:8174–79

13. Sowell ER, Thompson PM, Leonard CM, et al. **Longitudinal mapping of cortical thickness and brain growth in normal children.** *J Neurosci* 2004;24:8223–31

14. Langeslag SJ, Schmidt M, Ghassabian A, et al. **Functional connectivity between parietal and frontal brain regions and intelligence in young children: the generation R study.** *Hum Brain Mapp* 2013;34:3299–307

15. Beckmann CF, DeLuca M, Devlin JT, et al. **Investigations into resting-state connectivity using independent component analysis.** *Philos Trans R Soc Lond B Biol Sci* 2005;360:1001–13

16. Smith SM, Fox PT, Miller KL, et al. **Correspondence of the brain's functional architecture during activation and rest.** *Proc Natl Acad Sci U S A* 2009;106:13040–45

17. ADHD-200 Sample. http://fcon_1000.projects.nitrc.org/indi/adhd200/. Accessed Jan 26, 2013

18. Biswal BB, Mennes M, Zuo XN, et al. **Toward discovery science of human brain function.** *Proc Natl Acad Sci U S A* 2010;107:4734–39

19. Filippini N, MacIntosh BJ, Hough MG, et al. **Distinct patterns of brain activity in young carriers of the apoE-epsilon4 allele.** *Proc Natl Acad Sci U S A* 2009;106:7209–14

20. Beckmann C, Mackay C, Filippini N, et al. **Group comparison of resting-state fMRI data using multi-subject ICA and dual regression.** In: *15th Annual Meeting of Organization for Hum Brain Mapp, poster 441 SU-AM.* 2009

21. Tian L, Kong Y, Ren J, et al. **Spatial vs temporal features in ICA of resting-state fMRI: a quantitative and qualitative investigation in the context of response inhibition.** *PLoS One* 2013;8:e66572

22. Smith SM, Nichols TE. **Threshold-free cluster enhancement: addressing problems of smoothing, threshold dependence and localisation in cluster inference.** *NeuroImage* 2009;44:83–98

23. Fangmeier T, Knauff M, Ruff CC, et al. **FMRI evidence for a three-stage model of deductive reasoning.** *J Cogn Neurosci* 2006;18:320–34

24. Frangou S, Chitins X, and Williams SC. **Mapping IQ and gray matter density in healthy young people.** *NeuroImage* 2004;23:800–05

25. Schmithorst VJ, Wilke M, Dardzinski BJ, et al. **Cognitive functions correlate with white matter architecture in a normal pediatric population: a diffusion tensor MR imaging study.** *Hum Brain Mapp* 2005;26:139–47

26. Gray WD, Schoelles MJ, Bringsjord SA, et al. **SAGE: Five powerful ideas for studying and transforming the intelligence analyst's task environment.** In: *47th Annual Conference of the Human Factors and Ergonomics Society* 2003:1019–23

27. Langer N, Pedroni A, Gianotti LR, et al. **Functional brain network efficiency predicts intelligence.** *Hum Brain Mapp* 2012;33:1393–406

28. Knops A, Willmes K. **Numerical ordering and symbolic arithmetic share frontal and parietal circuits in the right hemisphere.** *NeuroImage* 2013;84C:786–95

29. Verbruggen F, Aron AR, Stevens MA, et al. **Theta burst stimulation dissociates attention and action updating in human inferior frontal cortex.** *Proc Natl Acad Sci U S A* 2010;107:13966–71

30. Bitan T, Cheon J, Lu D, et al. **Developmental changes in activation and effective connectivity in phonological processing.** *NeuroImage* 2007;38:564–75

31. MacSweeney M, Brammer MJ, Waters D, et al. **Enhanced activation of the left inferior frontal gyrus in deaf and dyslexic adults during rhyming.** *Brain* 2009;132:1928–40

32. Liang P, Wang Z, Yang Y, et al. **Three subsystems of the inferior parietal cortex are differently affected in mild cognitive impairment.** *J Alzheimers Dis* 2012;30:475–87

33. Esposito R, Mosca A, Pieramico V, et al. **Characterization of resting state activity in MCI individuals.** *Peer J* 2013;1:e135

34. Bludau S, Eickhoff SB, Mohlberg H, et al. **Cytoarchitecture, probability maps and functions of the human frontal pole.** *NeuroImage* 2014;93(Pt 2):260–75

35. Taki Y, Hashizume H, Sassa Y, et al. **Correlation among body height, intelligence, and brain gray matter volume in healthy children.** *NeuroImage* 2012;59:1023–27

36. Greicius MD, Srivastava G, Reiss AL, et al. **Default-mode network activity distinguishes Alzheimer's disease from healthy aging: evidence from functional MRI.** *Proc Natl Acad Sci U S A* 2004;101:4637–42

37. Cheng Y, Xu J, Nie B, et al. **Abnormal resting-state activities and functional connectivities of the anterior and the posterior cortexes in medication-naive patients with obsessive-compulsive disorder.** *PLoS One* 2013;8:e67478

38. Cisler JM, Elton A, Kennedy AP, et al. **Altered functional connectivity of the insular cortex across prefrontal networks in cocaine addiction.** *Psychiatry Res* 2013;213:39–46

39. Ma L, Narayana S, Robin DA, et al. **Changes occur in resting state network of motor system during 4 weeks of motor skill learning.** *NeuroImage* 2011;58:226–33

40. Neubauer AC, Fink A. **Intelligence and neural efficiency.** *Neurosci Biobehav Rev* 2009;33:1004–23

41. Giedd JN, Snell JW, Lange N, et al. **Quantitative magnetic resonance imaging of human brain development: ages 4–18.** *Cereb Cortex* 1996;6:551–60

42. Zhu C, Guo X, Jin Z, et al. **Influences of brain development and ageing on cortical interactive networks.** *Clin Neurophysiol* 2011;122:278–83

43. Zhou D, Lebel C, Evans A, et al. **Cortical thickness asymmetry from childhood to older adulthood.** *NeuroImage* 2013;83:66–74

Symptom Differences and Pretreatment Asymptomatic Interval Affect Outcomes of Stenting for Intracranial Atherosclerotic Disease

M.D. Alexander, P.M. Meyers, J.D. English, T.R. Stradford, S. Sung, W.S Smith, V.V. Halbach, R.T. Higashida,
C.F. Dowd, D.L. Cooke, and S.W. Hetts

ABSTRACT

BACKGROUND AND PURPOSE: Different types of symptomatic intracranial stenosis may respond differently to interventional therapy. We investigated symptomatic and pathophysiologic factors that may influence clinical outcomes of patients with intracranial atherosclerotic disease who were treated with stents.

MATERIALS AND METHODS: A retrospective analysis was performed of patients treated with stents for intracranial atherosclerosis at 4 centers. Patient demographics and comorbidities, lesion features, treatment features, and preprocedural and postprocedural functional status were noted. χ^2 univariate and multivariate logistic regression analysis was performed to assess technical results and clinical outcomes.

RESULTS: One hundred forty-two lesions in 131 patients were analyzed. Lesions causing hypoperfusion ischemic symptoms were associated with fewer strokes by last contact [χ^2 (1, $n = 63$) = 5.41, $P = .019$]. Nonhypoperfusion lesions causing symptoms during the 14 days before treatment had more strokes by last contact [χ^2 (1, $n = 136$), 4.21, $P = .047$]. Patients treated with stents designed for intracranial deployment were more likely to have had a stroke by last contact (OR, 4.63; $P = .032$), and patients treated with percutaneous balloon angioplasty in addition to deployment of a self-expanding stent were less likely to be stroke free at point of last contact (OR, 0.60; $P = .034$).

CONCLUSIONS: More favorable outcomes may occur after stent placement for lesions causing hypoperfusion symptoms and when delaying stent placement 7–14 days after most recent symptoms for lesions suspected to cause embolic disease or perforator ischemia. Angioplasty performed in addition to self-expanding stent deployment may lead to worse outcomes, as may use of self-expanding stents rather than balloon-mounted stents.

ABBREVIATIONS: BMS = balloon-mounted stent; ICAD = intracranial atherosclerotic disease; PTA = percutaneous transluminal angioplasty; SES = self-expanding stent

Intracranial atherosclerotic disease (ICAD) causes considerable morbidity and mortality, accounting for up to one-third of ischemic strokes in some series, particularly in certain populations.[1-3] Some lesions prove recalcitrant to first-line medical management, and, in recent decades, endovascular treatments have emerged and evolved as complementary therapies.[4,5] Early series demonstrated technical feasibility and acceptable safety for percutaneous transluminal angioplasty (PTA) and then stent placement of lesions in ICAD.[5-17] Initially, intracranial procedures were performed with devices designed and approved for coronary interventions, with subsequent release of angioplasty balloons specifically engineered for intracranial use.[5,12,17-33] In 2005, the Wingspan stent system with Gateway PTA balloon catheter (Stryker, Kalamazoo, Michigan) became the first stent approved for treatment of ICAD in the United States.[5,12,18-22,25,34] Numerous studies reported progressively improved outcomes and low complication rates, but randomized data proving efficacy were lacking.[5,12,18,20,24,25,35,36] In 2011, enrollment in the first randomized, controlled trial to evaluate stent placement versus medical management of ICAD, the Stent placement and Aggressive Medical Management for Preventing Recurrent Stroke in Intracranial Stenosis (SAMMPRIS) trial, was halted early due to

high complication rates in the stent placement group as compared with the medical management group.[4]

The results of SAMMPRIS have elicited strong responses from both proponents and detractors of stent placement, with clinical decisions now changing.[5] This current study retrospectively analyzes results of stent placement procedures performed for ICAD at 4 centers, with attention given to factors not specifically assessed in SAMMPRIS that may help guide further investigations of endovascular ICAD management.

MATERIALS AND METHODS

Under institutional review board–approved protocols, medical records were retrospectively examined by querying prospectively maintained procedure data bases at 2 large academic medical centers and 2 affiliated community hospitals, all of which have high-volume neurointerventional services. All patients who received stents for ICAD were evaluated. Patients with ICAD in whom stent placement was attempted but unsuccessful were included, as were patients with ICAD in whom PTA alone was planned but who received a stent to treat complications from PTA. Stent placement procedures performed during treatment of acute stroke were not included.

Information was gathered according to the guidelines of the Standards Committee of the Society for NeuroInterventional Surgery for investigations of endovascular treatment of ICAD.[5] Presenting symptoms were noted and, as appropriate, further classified as "hypoperfusion" if clear evidence existed that reduced perfusion elicited ischemic symptoms. Examples of sufficient evidence of hypoperfusion etiology included reduced flow demonstrated on perfusion imaging, infarcts clearly located in a watershed distribution, and symptom exacerbation during known hypotension or on application of positional stressors. Symptoms that were probably caused by mixed subtypes were classified as indeterminate, as were symptoms that could not be clearly classified as hypoperfusion or nonhypoperfusion. Among nonhypoperfusion lesions, further classification divided them according to the duration of symptom-free interval before treatment. Ischemic symptoms were classified as TIA or stroke, the latter designated with permanent deficits or restricted diffusion on MR imaging. Specific medical comorbidities were considered present if a patient was treated for that condition; in the absence of treatment, the absence of a diagnosis was confirmed with clinical or laboratory data. Pretreatment antiplatelet or anticoagulation therapy other than procedural loading doses was noted. Functional status was evaluated by use of mRS, with a value assigned by authors performing data review on the basis of descriptions of functional performance in the medical record if a value was not formally noted.

The date of stent placement procedure and anesthesia type were recorded. Lesions were classified by vessel and furthest downstream vessel segment treated, listed in On-line Table 1. Lesion features and technical success were recorded according to those reported by the primary interventionalist, if available. When not explicitly stated, these data were assessed by investigators conducting data review. The degree of stenosis was determined by use of the Warfarin-Aspirin Symptomatic Intracranial Disease Trial (WASID) technique.[5,37] Stenosis length was measured, and Mori classification was assigned.[38] The presence of tandem stenoses was noted, including stenoses in upstream extracranial vessel segments. Stent type, model, size, and number deployed were noted, as was performance of PTA during the same procedure. Postdeployment stenosis was measured in the same fashion as measurement before deployment. Technical success was defined as residual stenosis <50% without procedural complication.[5] Any procedural complications were noted, as well as means taken to treat them, if applicable, and whether such complications were symptomatic. Complications occurring after procedure completion within 30 and 90 days of treatment were classified as peri-procedural and postprocedural, respectively.

The duration for postprocedure treatment with aspirin and clopidogrel was noted, as were use of glycoprotein IIb/IIIa inhibitors or any combination antiplatelet agents. Follow-up interval and duration were determined by the primary interventionalist, as was the technique of any follow-up imaging; no formal protocol existed between practitioners. The most recent date of contact was determined for long-term follow-up. For those patients with available records, the Social Security Death Index was queried to screen for deaths among patients lost to follow-up.[39] In patients who died, death records were reviewed to evaluate cause of death.

End points evaluated were ischemic stroke, intraparenchymal hemorrhage, death, or other adverse event related to treatment at 30 days, 90 days, 1 year, 2 years, and point of last contact. Functional status was also assessed at these time points with the use of mRS. Data analysis was performed with the use of χ^2 tests and logistic regression analysis by use of IBM SPSS version 20 (IBM, Armonk, New York).

RESULTS

Between June 1998 and December 2011, 142 lesions in 131 patients met inclusion criteria and had sufficient medical records for review. All sites in this study participated in the SAMMPRIS trial, but the few enrolled patients did not have data sufficient for inclusion in this study. Patient demographics, symptom features, and lesion characteristics are summarized in On-line Table 1. Technical success was achieved in 124 (87.3%) procedures. Treatment details and angiographic results are summarized in Table 1. Procedural complications occurred during treatment of 13 (9.2%) lesions, with 2 complications occurring during 1 procedure for the same lesion. Of these complications, two (1.4%) caused neurologic symptomatic sequelae. No permanent non-neurologic morbidity occurred from procedural complications. Mean follow-up time was 949 days (standard deviation, 1187; median, 413). Follow-up time exceeded 90 days for 101 (71.1%) lesions and 1 year for 79 (55.6%) lesions. Eighteen complications occurred in the postprocedural period, of which 13 were symptomatic. Thus, overall postprocedural complications occurred in 34 (23.9%) cases, with complications causing permanent symptomatic sequelae in 16 (11.3%) cases, summarized in On-line Table 2.

No difference was noted in outcomes when comparing symptom types. Head-to-head comparison of hypoperfusion and nonhypoperfusion lesions showed correlation of the latter

Table 1: Treatment characteristics

No. of stents deployed			
0	6		
1	136		
2	10		
Stent modalities			
Balloon-mounted, bare metal	78		
Balloon-mounted, drug-eluting	21		
Self-expanding	47		
Total	146		
Anesthesia technique			
MAC	36		
GETA	106		
Stent types			
AVE Series	53		
Bx Velocity	11		
Driver	15		
Palmaz	2		
Wingspan	37		
Other[a]	28		
Total	146		
Stent-designed indications			
Coronary	95		
Neuro	40		
Peripheral	11		
Total	146		
Angiographic results			
Mori	Pretreatment stenosis	Posttreatment stenosis	Success
A ($n = 19$)	80.8%	3.9%	84.2%
B ($n = 73$)	80.2%	7.8%	89.0%
C ($n = 50$)	86.0%	13.8%	86.0%

Note:—MAC indicates monitors anesthesia care; GETA, general endotracheal anesthesia.
[a] Cypher, Enterprise, Herculink, Multi-Link, Neuroform, NIR Primo, Precise, Sprint, Taxus.

Table 2: Multivariate models

	OR	95% CI	P Value
mRS >2 at last contact			
Tandem	0.319	0.143–0.713	.005
Hyperlipidemia	3.158	1.220–8.173	.018
Antiplatelet	3.907	1.107–13.792	.034
Tobacco	0.437	0.197–0.968	.041
Death at last contact			
Tandem	0.297	0.111–0.799	.016
Antiplatelet	4.504	1.017–19.949	.047
Diabetes	0.432	0.175–1.065	.068
PTA SES	4.028	0.875–18.532	.074
Tobacco	0.451	0.185–1.099	.080
Sex	2.285	0.649–8.042	.198
Neuro stent	1.725	0.393–7.565	.470

with new or recurrent stroke by last contact [χ^2 (1, $n = 63$) = 5.41, $P = .019$]. Nonhypoperfusion lesions causing symptoms within 7 days of treatment were associated with stroke by last contact [χ^2 (1, $n = 136$), 4.21, $P = .047$]. When considering nonhypoperfusion lesions causing symptoms within 14 days, the association was stronger [χ^2 (1, $n = 136$) = 4.93, $P = .032$]. A trend was also noted for nonhypoperfusion lesions being correlated with complications occurring in the first 90 days after treatment, though this did not reach statistical significance [χ^2 (1, $n = 68$) = 3.68, $P = .051$].

The results of univariate analysis are summarized in On-line Tables 3–9. Adverse events were more likely to occur in women and patients with diabetes, history of stroke, history of tobacco use, no diagnosis of hyperlipidemia, or no preproce-

dural antiplatelet therapy. Lesion features associated with death, stroke, or mRS >2 included basilar artery location, involvement of any basilar segment or petrous ICA, tandem lesions, Mori C classification, treatment with self-expanding stent (SES), and PTA performed in addition to SES deployment. Use of stents designed for intracranial use was associated with stroke, whereas stents designed for use elsewhere were associated with death.

In multivariate analysis (Table 2), patients treated with stents designed for intracranial deployment were less likely to be stroke free by last contact (OR, 0.060; 95% CI, $0.004-0.812$; $P = .034$). This distinction did not predict rates of restenosis in this series. All 4 variables with statistically significant effects on mRS by last contact retained significance in the multivariate model. Absence of antiplatelet therapy and presence of tandem stenoses retained significance in prediction of death by last contact.

DISCUSSION

ICAD causes a significant burden worldwide, accounting for $10-15\%$ of strokes in series published from the United States and up to 33% in series from Asia.[3,5,40] Many high-risk characteristics were demonstrated in the WASID trial, which also established the role for dual antiplatelet therapy in ICAD treatment, findings confirmed in this current study.[37,40] Since the WASID trial, standard of practice in medical management has undergone a paradigm shift toward aggressive medical management that also includes lifestyle modifications, a shift that has now been accentuated by SAMMPRIS.[5]

Despite advances in medical therapy, some patients' symptoms recur. It is these patients for whom surgical and endovascular therapies were initially developed. Initial operative treatments showed promise, but subsequent examination in large trials showed no benefit of surgical intervention.[41,42] Early endovascular treatment typically involved PTA alone, but residual stenosis >50% was common, and many patients had dissections that required stent placement.[1,5,14,15,43] PTA also carries a risk for arterial perforation and is often counteracted acutely by vessel recoil.[5] Thus, development of stent placement for ICAD was pursued.[5]

Initial reports demonstrated that intracranial stent placement can involve serious complications, dictating that such stents be used only in high-risk patients with medically refractory disease.[9,10] However, with advances in stent placement technique and technology, both technical success rates and complication rates improved.[5,24,25,44,45] On the basis of data from procedures with the use of devices designed for use in coronary arteries, technical success rates appeared to plateau around 95% with complications within the first 30 days after stent deployment occurring in approximately 7% of cases.[5]

The Wingspan system is the first device granted Food and Drug Administration approval for treatment of ICAD. Multiple series using this stent have been reported.[12,18,24,25,35,36] The 2 largest nonrandomized, prospective series evaluating the device are the United States Wingspan registry, which reported a technical success rate of 98.8%, and the NIH Wingspan registry, which reported a rate of 96.7%.[18,25] Restenosis >50% occurred in 27.9% and 25% of patients in these studies, respectively.[18,25] In the current series, technical success occurred in 87.3% of cases, and restenosis >50% occurred in 13.4%.

The peri-procedural complication rates of the 2 registries (6.1% and 9.6%) approached that seen elsewhere for series that used other devices.[18,25] Because of inconsistency in follow-up scheduling for this current retrospective study, 30-day outcomes were not consistently available. However, the comparable 90-day rate of any stroke and death was 14.8%. Excluding radiographic infarcts with no permanent symptomatic sequelae to most closely mirror outcomes measured in registries, the postprocedural complication was 11.3% in our series. By comparison, WASID did not report 90-day complications, but these end points occurred within 1 year in 15% of patients in the aspirin group.[37]

Given that nonrandomized series had suggested improving stent safety and efficacy, SAMMPRIS was disappointing when the trial was halted short of its planned enrollment size because of an unexpectedly high rate of stroke or death within 30 days of treatment in the stent placement (14.7%) versus medical arm (5.8%).[4] No significant difference was noted between the groups beyond 30 days of enrollment, and the 1-year rate of stroke or death was 20.0% versus 12.2%, respectively.[4] SAMMPRIS helped identify the path forward to identifying a role for safe, efficacious interventional treatment of ICAD, namely the reduction of peri-procedural complications through factors such as device improvement, peri-procedural blood pressure management, anesthetic techniques, and use of combination antiplatelet drugs. Additionally, appropriate patient selection criteria must be identified. Multiple factors must be considered in the design of the SAMMPRIS trial and its implications for future investigation.[46]

The SAMMPRIS trial made no distinction between pathophysiologic causes of symptoms. Our series shows that nonhypoperfusion lesions have higher risk of death at the point of last contact after stent placement. Additionally, multiple prior studies demonstrated that complication rates increase the sooner intervention is performed with relation to most recent symptoms, probably related to stability of atherosclerotic plaques.[10,22,40,47] We posit that such concerns relate to unstable plaques that would be expected to cause primarily nonhypoperfusion symptoms, for example, embolization distal to the plaque or perforator occlusion adjacent to the plaque. In the current study, lesions causing nonhypoperfusion symptoms within 7 or 14 days of treatment were associated with stroke by point of last contact. Intervention timing, particularly for thromboembolic lesions, should be studied further. Optimum management also must be determined for lesions that do not afford sufficient asymptomatic windows. Additionally, stenosis caused by non-ICAD pathologies responds differently to endovascular treatment, shown by poor outcomes in patients without diagnosis of hyperlipidemia.

Before release of the Wingspan device, stent deployment to treat ICAD often required use of devices designed for coronary interventions.[5] Treatment with a balloon-mounted stent (BMS) carries concern for dissection, vessel rupture, and recoil after deployment.[1,43] With SES, wall stress persists longer than with BMS, causing more pronounced inflammation that causes neovascularization and neointimal hyperplasia.[48] This may account for the higher rates of recurrent stenosis seen after treatment with SES compared with BMS, and it probably explains the lower rates of restenosis in this mixed SES/BMS study rather than the larger purely SES Wingspan studies.[1,5,48-50]

The choice of intracranial stent has historically been driven by balancing potentially higher risks of BMS against greater residual stenosis and recurrence rates with SES. In this study, lesions treated with SES had worse rates of both stroke and death. Lesions treated with PTA in addition to SES had worse outcomes compared with treatment with BMS or SES without PTA. This could easily reflect bias, because more severe lesions may be more likely to be treated additionally with PTA. Severe lesions are also more likely to have poorer outcomes, as seen with Mori class C lesions in this series and elsewhere.[1] This certainly bears further examination given that the technique used in SAMMPRIS required PTA before SES deployment. Interestingly, devices specifically designed for intracranial deployment had less favorable outcomes than other types. This may reflect reported operator difficulty with the Wingspan system.[47,51,52] Future development of a BMS for intracranial use may affect results.

Limitations of this study result from its retrospective design. A lack of prospectively developed protocols for describing patient symptoms limited the analysis, particularly when attempting to discern treatment subtypes. Inadequate capture within early postprocedure periods limited direct comparison to other investigations. Although this study benefits from many years of data, it includes patients treated with methods formerly considered appropriate but not currently standard of care. Finally, all symptom and functional assessment was performed retrospectively by reviewing clinical follow-up documentation rather than formal standardized assessment, and follow-up was not standardized.

SAMMPRIS indicates that aggressive medical management should be the first-line treatment for ICAD. Further investigation must determine what treatments to offer for persistent symptoms and which patients are candidates for such treatment. Additionally, better metrics should be pursued that account for the nuances of symptoms from these lesions that can dramatically affect patients' lives but are not adequately captured by scales such as mRS.[53] Randomized, controlled trials should be sought, and novel designs should be considered, such as group crossover or Bayesian enrollment, and any treatment performed outside such trials should be included in multicenter registries with standardized protocols to best evaluate outcomes.

CONCLUSIONS

ICAD causes significant morbidity and mortality. Treatment must begin with medical management, but certain patients will remain symptomatic despite aggressive measures. In such cases, a role for endovascular treatment remains undefined. The current study demonstrates that lesions causing symptoms as the result of reduced perfusion have more favorable outcomes after stent

placement, and lesions causing nonhypoperfusion symptoms respond more favorably to stent placement when treated after a 7- to 14-day asymptomatic period. Currently available stents designed for intracranial use, SES deployment, and PTA in conjunction with SES deployment were associated with worse outcomes in the present study and warrant further examination.

REFERENCES

1. Jiang WJ, Cheng-Ching E, Abou-Chebl A, et al. **Multicenter analysis of stenting in symptomatic intracranial atherosclerosis.** *Neurosurgery* 2012;70:25–30
2. Sacco RL, Kargman DE, Gu Q, et al. **Race-ethnicity and determinants of intracranial atherosclerotic cerebral infarction: the Northern Manhattan Stroke Study.** *Stroke* 1995;26:14–20
3. Wong LK. **Global burden of intracranial atherosclerosis.** *Int J Stroke* 2006;1:158–59
4. Chimowitz MI, Lynn MJ, Derdeyn CP, et al. **Stenting versus aggressive medical therapy for intracranial arterial stenosis.** *N Engl J Med* 2011;365:993–1003
5. Hussain MS, Fraser JF, Abruzzo T, et al. **Standard of practice: endovascular treatment of intracranial atherosclerosis.** *J Neurointerv Surg* 2012;4:397–406
6. Lutsep HL. **Stenting of Symptomatic Atherosclerotic Lesions in the Vertebral or Intracranial Arteries (SSYLVIA): study results.** *Stroke* 2004;35:1388–92
7. Miao ZR, Feng L, Li S, et al. **Treatment of symptomatic middle cerebral artery stenosis with balloon-mounted stents: long-term follow-up at a single center.** *Neurosurgery* 2009;64:79–84
8. Mori T, Kazita K, Chokyu K, et al. **Short-term arteriographic and clinical outcome after cerebral angioplasty and stenting for intracranial vertebrobasilar and carotid atherosclerotic occlusive disease.** *AJNR Am J Neuroradiol* 2000;21:249–54
9. Levy EI, Horowitz MB, Koebbe CJ, et al. **Transluminal stent-assisted angioplasty of the intracranial vertebrobasilar system for medically refractory, posterior circulation ischemia: early results.** *Neurosurgery* 2001;48:1215–23
10. Gupta R, Schumacher HC, Mangla S, et al. **Urgent endovascular revascularization for symptomatic intracranial atherosclerotic stenosis.** *Neurology* 2003;61:1729–35
11. Jiang WJ, Wang YJ, Du B, et al. **Stenting of symptomatic M1 stenosis of middle cerebral artery: an initial experience of 40 patients.** *Stroke* 2004;35:1375–80
12. Bose A, Hartmann M, Henkes H, et al. **A novel, self-expanding, nitinol stent in medically refractory intracranial atherosclerotic stenoses: the Wingspan study.** *Stroke* 2007;38:1531–37
13. Gomez CR, Misra VK, Liu MW, et al. **Elective stenting of symptomatic basilar artery stenosis.** *Stroke* 2000;31:95–99
14. Marks MP, Marcellus ML, Do HM, et al. **Intracranial angioplasty without stenting for symptomatic atherosclerotic stenosis: long-term follow-up.** *AJNR Am J Neuroradiol* 2005;26:525–30
15. Marks MP, Wojak JC, Al-Ali F, et al. **Angioplasty for symptomatic intracranial stenosis: clinical outcome.** *Stroke* 2006;37:1016–20
16. Yu W, Smith WS, Singh V, et al. **Long-term outcome of endovascular stenting for symptomatic basilar artery stenosis.** *Neurology* 2005; 64:1055–57
17. Kim DJ, Lee BH, Kim DI, et al. **Stent-assisted angioplasty of symptomatic intracranial vertebrobasilar artery stenosis: feasibility and follow-up results.** *AJNR Am J Neuroradiol* 2005;26:1381–88
18. Fiorella D, Levy EI, Turk AS, et al. **US multicenter experience with the Wingspan stent system for the treatment of intracranial atheromatous disease: periprocedural results.** *Stroke* 2007;38:881–87
19. Fiorella DJ, Levy EI, Turk AS, et al. **Target lesion revascularization after Wingspan: assessment of safety and durability.** *Stroke* 2009; 40:106–10
20. Henkes H, Miloslavski E, Lowens S, et al. **Treatment of intracranial atherosclerotic stenoses with balloon dilatation and self-expanding stent deployment (WingSpan).** *Neuroradiology* 2005;47:222–28
21. Levy EI, Turk AS, Albuquerque FC, et al. **Wingspan in-stent restenosis and thrombosis: incidence, clinical presentation, and management.** *Neurosurgery* 2007;61:644–50
22. Nahab F, Lynn MJ, Kasner SE, et al. **Risk factors associated with major cerebrovascular complications after intracranial stenting.** *Neurology* 2009;72:2014–19
23. Turk AS, Levy EI, Albuquerque FC, et al. **Influence of patient age and stenosis location on Wingspan in-stent restenosis.** *AJNR Am J Neuroradiol* 2008;29:23–27
24. Yu SCH, Leung TWH, Lee KT, et al. **Angioplasty and stenting of atherosclerotic middle cerebral arteries with Wingspan: evaluation of clinical outcome, restenosis, and procedure outcome.** *AJNR Am J Neuroradiol* 2011;32:753–58
25. Zaidat OO, Klucznik R, Alexander MJ, et al. **The NIH registry on use of the Wingspan stent for symptomatic 70–99% intracranial arterial stenosis.** *Neurology* 2008;70:1518–24
26. Kessler IM, Mounayer C, Piotin M, et al. **The use of balloon-expandable stents in the management of intracranial arterial diseases: a 5-year single-center experience.** *AJNR Am J Neuroradiol* 2005;26: 2342–48
27. Hatano T, Tsukahara T, Ogino E, et al. **Stenting for vertebrobasilar artery stenosis.** *Acta Neurochirurgica Suppl* 2005;94:137–41
28. Lee TH, Kim DH, Lee BH, et al. **Preliminary results of endovascular stent-assisted angioplasty for symptomatic middle cerebral artery stenosis.** *AJNR Am J Neuroradiol* 2005;26:166–74
29. Chow MM, Masaryk TJ, Woo HH, et al. **Stent-assisted angioplasty of intracranial vertebrobasilar atherosclerosis: midterm analysis of clinical and radiologic predictors of neurological morbidity and mortality.** *AJNR Am J Neuroradiol* 2005;26:869–74
30. Lylyk P, Vila JF, Miranda C, et al. **Endovascular reconstruction by means of stent placement in symptomatic intracranial atherosclerotic stenosis.** *Neurol Res* 2005;27(Suppl 1):S84–88
31. Boulos AS, Agner C, Deshaies EM. **Preliminary evidence supporting the safety of drug-eluting stents in neurovascular disease.** *Neurol Res* 2005;27(Suppl 1):S95–S102
32. Abou-Chebl A, Bashir Q, Yadav JS. **Drug-eluting stents for the treatment of intracranial atherosclerosis: initial experience and midterm angiographic follow-up.** *Stroke* 2005;36:e165–e168
33. Abou-Chebl A, Krieger DW, Bajzer CT, et al. **Intracranial angioplasty and stenting in the awake patient.** *J Neuroimaging* 2006;16: 216–23
34. Costalat V, Maldonado IL, Vendrell JF, et al. **Endovascular treatment of symptomatic intracranial stenosis with the Wingspan stent system and Gateway PTA balloon: a multicenter series of 60 patients with acute and midterm results.** *J Neurosurg* 2011;115:686–93
35. Lanfranconi S, Bersano A, Branca V, et al. **Stenting for the treatment of high-grade intracranial stenoses.** *J Neurol* 2010;257:1899–908
36. Zhao ZW, Deng JP, He SM, et al. **Intracranial angioplasty with Gateway-Wingspan system for symptomatic atherosclerotic stenosis: preliminary results of 27 Chinese patients.** *Surg Neurol* 2009;72: 607–11
37. Chimowitz MI, Lynn MJ, Howlett-Smith H, et al. **Comparison of warfarin and aspirin for symptomatic intracranial arterial stenosis.** *N Engl J Med* 2005;352:1305–16

38. Mori T, Fukuoka M, Kazita K, et al. **Follow-up study after intracranial percutaneous transluminal cerebral balloon angioplasty.** *AJNR Am J Neuroradiol* 1998;19:1525–33

39. Quinn J, Kramer N, McDermott D. **Validation of the Social Security Death Index (SSDI): an important readily-available outcomes database for researchers.** *West J Emerg Med* 2008;9:6–8

40. Kasner SE, Chimowitz MI, Lynn MJ, et al. **Predictors of ischemic stroke in the territory of a symptomatic intracranial arterial stenosis.** *Circulation.* 2006;113:555–63

41. Powers WJ, Clarke WR, Grubb RL Jr, et al. **Extracranial-intracranial bypass surgery for stroke prevention in hemodynamic cerebral ischemia: the carotid occlusion surgery study randomized trial.** *JAMA* 2011;306:1983–92

42. Powers WJ, Grubb RL Jr, Raichle ME. **Clinical results of extracranial-intracranial bypass surgery in patients with hemodynamic cerebrovascular disease.** *J Neurosurg* 1989;70:61–67

43. Nguyen TN, Zaidat OO, Gupta R, et al. **Balloon angioplasty for intracranial atherosclerotic disease periprocedural risks and short-term outcomes in a multicenter study.** *Stroke* 2011;42:107–11

44. Chamczuk AJ, Ogilvy CS, Snyder KV, et al. **Elective stenting for intracranial stenosis under conscious sedation.** *Neurosurgery* 2010;67:1189–93

45. Samaniego EA, Hetzel S, Thirunarayanan S, et al. **Outcome of symptomatic intracranial atherosclerotic disease.** *Stroke* 2009;40:2983–87

46. Patel RD, Saver JL. **Evolution of reperfusion therapies for acute brain and acute myocardial ischemia: a systematic, comparative analysis.** *Stroke* 2013;44:94–98

47. Tarr RW, Albuquerque F, Hirsh J, et al. **The SAMMPRIS trial: the end or just the beginning.** *J Neurointerv Surg* 2011;3:310–11

48. Shofti R, Tio F, Beyar R. **Neointimal vascularization and intimal thickening in response to self-expanding stents: a swine model.** *Int J Cardiovasc Intervent* 2004;6:61–67

49. Fiorella D, Chow MM, Anderson M, et al. **A 7-year experience with balloon-mounted coronary stents for the treatment of symptomatic vertebrobasilar intracranial atheromatous disease.** *Neurosurgery* 2007;61:236–42

50. Groschel K, Schnaudigel S, Pilgram SM, et al. **A systematic review on outcome after stenting for intracranial atherosclerosis.** *Stroke* 2009;40:e340–347

51. Yu SC, Leung TW, Lee KT, et al. **Learning curve of Wingspan stenting for intracranial atherosclerosis: single-center experience of 95 consecutive patients.** *J Neurointerv Surg* 2014;6:212–18

52. Rahme RJ, Aoun SG, Batjer HH, et al. **SAMMPRIS: end of intracranial stenting for atherosclerosis or back to the drawing board?** *Neurosurgery* 2011;69:N16–N18

53. Rasmussen PA. **Stroke outcome measures: a tale of two trials.** *J Neurointerv Surg* 2013;5:393–94

Inter- and Intraobserver Agreement in Scoring Angiographic Results of Intra-Arterial Stroke Therapy

M. Gaha, C. Roy, L. Estrade, G. Gevry, A. Weill, D. Roy, M. Chagnon, and J. Raymond

ABSTRACT

BACKGROUND AND PURPOSE: Angiographic results are commonly used as surrogate markers of the success of intra-arterial therapies for acute stroke. Inter- and intraobserver agreement in judging angiographic results remain poorly characterized. Our goal was to assess 2 commonly used revascularization scales.

MATERIALS AND METHODS: A portfolio of 148 pre- and post treatment images of 37 cases of proximal anterior circulation occlusions was electronically sent to 12 expert observers who were asked to grade treatment outcomes according to recanalization (of arterial occlusive lesion) or reperfusion (TICI) scales. Three expert observers had to score treatment outcomes by using a similar portfolio of 32 patients or when they had full access to all angiographic data, twice for each method 3–12 months apart. Results were analyzed by using κ statistics.

RESULTS: Agreement among 9 responding observers was moderate for both the TICI ($\kappa = 0.45 \pm 0.01$) and arterial occlusive lesion ($\kappa = 0.39 \pm 0.16$) scales. Agreement was similar (moderate) when 3 observers had access to a portfolio ($\kappa = 0.59 \pm 0.06$ and 0.49 ± 0.07, respectively) or to the full angiographic data ($\kappa = 0.54 \pm 0.06$ and 0.59 ± 0.07, respectively). Intraobserver agreement was "fair to moderate" for both methods. Interobserver agreement became "substantial" (>0.6) when outcomes were dichotomized into "success" (TICI 2b, 3; arterial occlusive lesion II, III or "failure"; the results were judged more favorably when the arterial occlusive lesion rather than the TICI scale was used.

CONCLUSIONS: There is an important variability in the assessment of angiographic outcomes of endovascular treatments, invalidating comparisons among publications. A simple dichotomous judgment can be used as a surrogate outcome when treatments are assessed by the same observers in randomized trials.

ABBREVIATIONS: AOL = arterial occlusive lesion; IMS = Interventional Management of Stroke; TIMI = Thrombolysis in Myocardial Infarction

Current therapies of acute stroke aim at rapid restoration of blood flow or revascularization of the occluded territory to salvage ischemic brain tissue. A gamut of methods and devices has been introduced to accomplish revascularization.[1-4] While all may agree that the well-being of the patient at the end of treatment is the most important outcome,[5] we also need surrogate markers of mechanistic efficacy, directly linked to the effect we are aiming for, to more expediently determine which method or device should be selected to be tested in a more rigorous fashion, because the heterogeneity of presentations ensures that large trials will be needed to show differences in clinical outcomes. In addition, regulatory agencies approve devices according to their ability to restore blood flow.[6] Thus angiographic scoring systems and a new vocabulary (such as Thrombolysis in Myocardial Infarction [TIMI], TICI, arterial occlusive lesion [AOL], described below) are now used to adjudicate and compare angiographic results of acute stroke therapies.[7-12]

The precision of outcome scales must be assessed before their widespread use. Testing can be accomplished by asking various individuals to repeatedly but independently categorize the angiographic results of the same patients and by studying intra- and interobserver agreement of the resulting verdicts. Despite notes of concern[13,14] and except for small studies limited to 2–3 observers introducing unusual scales[15,16] or comparing 2 scoring systems obtained from consensus reading,[17] the inter- and intraobserver agreement among multiple observers for commonly used systems

has not been rigorously assessed. The aim of the present work was to assess the precision and reproducibility of 2 angiographic outcome scales of intra-arterial therapies, one for recanalization and one for reperfusion: The primary arterial occlusive lesion recanalization scoring method, initially proposed for the Interventional Management of Stroke (IMS) I analyses,[17] and the Thrombolysis in Cerebral Infarction perfusion categories, proposed by the Technology Assessment Committees of the American Society of Interventional and Therapeutic Neuroradiology and the Society of Interventional Radiology.[7] These scales (with or without some modifications) are being used in recent trials on intra-arterial stroke therapy, such as IMS II and III,[18] the Mechanical Retrieval and Recanalization of Stroke Clots Using Embolectomy (MR Rescue) trial,[19] and the Endovascular Treatment for Small Core and Anterior Circulation Proximal Occlusion with Emphasis on Minimizing CT to Recanalization Time (ESCAPE) trial (M. Hill, personal communication; May 2013) and others.[20]

MATERIALS AND METHODS

The primary aim of this work was to evaluate the intra- and interobserver variability in adjudicating outcomes of treatment according to 2 ordinal scales commonly used to assess angiographic results of intra-arterial thrombectomy. The evaluation comprised 3 parts, 2 by electronic surveys; the third evaluation was designed to resemble clinical work and to validate the results obtained by the electronic surveys: 1) an electronic survey to assess interobserver agreement among 9 different expert "external" readers regarding the angiographic outcomes of 37 cases; 2) a similar electronic survey, modified and reduced to match the 32 patients to be analyzed in part 3, to assess intra- and interobserver agreement independently twice, 12 months apart, by 3 expert "internal" readers; and 3) an intra- and interobserver study of the same 32 patients by the same 3 expert readers having access to the full set of angiographic data, directly on the hospital PACS, independently adjudicating results twice, 3–12 months apart, to be compared with the survey of part 2.

Part 1: Electronic Survey with 9 Observers

To minimize variability due to different angiographic equipment, number and type of projections, and selection of final images from various series and to ease the participation of external readers, we assembled a portfolio of 148 images that could be sent electronically to and easily assessed by multiple observers. All anonymized images were retrieved by one author (L.E.) from the PACS of one institution. The portfolio comprised paired (postero-anterior and lateral projections) selected pre- and post treatment late arterial phase angiograms of 37 cases. Cases included 32 consecutive patients who had been treated endovascularly for acute anterior circulation strokes in a single institution during 9 months (January to September 2011). For part 1, 5 additional cases were constructed by using intermediate-phase results of complex interventions in 5 patients already included, in an attempt to better balance the proportions of the marginal sums of the contingency tables and hopefully minimize paradoxes of κ statistics.[21] On each page of the electronic version sent to reviewers, 2 pretreatment and 2 post treatment images were displayed side by side. No clinical information was provided. There was no

training of observers. The part 1 electronic portfolio was sent to 12 expert interventional neuroradiologists, selected because they had designed studies or trials on transarterial stroke therapy. Nine, with 5–27 years of clinical experience, answered, working in 6 different centers; 4 were from Canada; 3, from the United States; and 2, from France. One observer answered the questionnaire twice 3 months apart. Observers were given the task of grading each pair of images according to the 4-value AOL scale[8] and the 5-value TICI scale.[7] The explicit definitions of the 2 scales appeared in explanatory boxes beside the answering boxes for each case.

Part 2: Electronic Survey with 3 Readers

The electronic questionnaire, modified to include only the 32 real patients (excluding the 5 "constructed cases" added to part 1), was administered twice, 12 months apart, to the 3 internal interventional neuroradiologists involved in the treatment of acute stroke who participated in part 3 of the study.

Part 3: Intra- and Interobserver Agreement Using All Angiographic Images

To verify that the artificial conditions imposed by the electronic survey did not affect results and to better assess intraobserver agreement, the same 3 observers were asked to grade the angiographic outcomes of the same 32 patients, by using the full set of angiographic data presented by 3 authors not participating in the evaluation of cases (L.E., C.R., M.G.) directly on the PACS, independently twice, 3–12 months apart.

Scores and Dichotomies

To assess intracranial reperfusion, readers were asked to use the TICI score as described by Higashida et al[7]: grade 0, no perfusion, no antegrade flow beyond the point of occlusion; grade 1, penetration with minimal perfusion; grade 2, partial perfusion; grade 2a, only partial filling (less than two-thirds) of the entire vascular territory visualized; grade 2b, complete filling of all of the expected vascular territory visualized but filling more slowly than normal; and grade 3, complete perfusion.

To assess arterial recanalization, readers were asked to use the AOL score[22]: score 0, no recanalization of the primary occlusive lesion; score I, incomplete or partial recanalization of the primary occlusive lesion with no distal flow; score II, incomplete or partial recanalization of the primary occlusive lesion with any distal flow; and score III, complete recanalization of the primary occlusion with any distal flow.

Because many reports providing results of treatments have used dichotomous "success-versus-failure" end points, we repeated κ statistics, lumping categories into "success" defined as TICI 2b, 3 or AOL II, III, versus "failure," defined as TICI 0, 1, 2a or AOL 0, I.[4,23-25]

Statistical Analyses

The multirater κ statistics were computed by using the macro MAGREE with SAS, Version 9.3 (SAS Institute, Cary, North Carolina). This macro implements the methodology of Fleiss et al,[27] measuring the agreement when the number of raters is >2. This method also allowed identifying, for each scale, the categories in

Table 1: Interobserver agreement using the TICI reperfusion scale

	Ob2	Ob3	Ob4	Ob5	Ob6	Ob6a	Ob7	Ob8	Ob9
Ob1	0.497 ± 0.098	0.411 ± 0.102	0.478 ± 0.103	0.544 ± 0.101	0.508 ± 0.104	0.315 ± 0.114	0.517 ± 0.100	0.580 ± 0.100	0.519 ± 0.094
Ob2		0.419 ± 0.100	0.286 ± 0.102	0.576 ± 0.096	0.506 ± 0.102	0.320 ± 0.115	0.458 ± 0.096	0.538 ± 0.099	0.330 ± 0.089
Ob3			0.197 ± 0.088	0.284 ± 0.100	0.513 ± 0.103	0.191 ± 0.096	0.339 ± 0.103	0.345 ± 0.105	0.404 ± 0.103
Ob4				0.510 ± 0.100	0.343 ± 0.103	0.352 ± 0.103	0.384 ± 0.098	0.583 ± 0.098	0.297 ± 0.087
Ob5					**0.602 ± 0.101**	0.594 ± 0.102	**0.712 ± 0.091**	**0.752 ± 0.082**	0.397 ± 0.094
Ob6						0.525 ± 0.107	0.465 ± 0.108	**0.610 ± 0.101**	0.425 ± 0.093
Ob6a							0.542 ± 0.096	0.421 ± 0.106	0.283 ± 0.085
Ob7								0.511 ± 0.102	0.442 ± 0.102
Ob8									0.423 ± 0.095
All observers				$\kappa = 0.44570 \pm 0.013176$; $P < 0.001$					

Note:—Inter-observer Kappa values $\geq$ 0.6 are highlighted in bold type.

Table 2: Interobserver agreement using the dichotomized TICI scale

	Ob2	Ob3	Ob4	Ob5	Ob6	Ob6a	Ob7	Ob8	Ob9
Ob1	**0.773 ± 0.104**	**0.634 ± 0.116**	0.546 ± 0.138	**0.674 ± 0.121**	**0.679 ± 0.117**	0.329 ± 0.156	**0.628 ± 0.122**	**0.727 ± 0.113**	0.578 ± 0.125
Ob2		0.452 ± 0.116	0.507 ± 0.151	**0.673 ± 0.116**	0.580 ± 0.119	0.291 ± 0.162	0.432 ± 0.128	**0.722 ± 0.111**	0.493 ± 0.118
Ob3			0.452 ± 0.116	0.517 ± 0.135	**0.724 ± 0.113**	0.337 ± 0.133	**0.665 ± 0.124**	0.576 ± 0.126	**0.717 ± 0.117**
Ob4				**0.673 ± 0.116**	0.580 ± 0.119	**0.645 ± 0.131**	0.536 ± 0.119	**0.722 ± 0.111**	0.493 ± 0.118
Ob5					**0.784 ± 0.101**	**0.674 ± 0.119**	**0.73 ± 0.111**	**0.946 ± 0.053**	**0.677 ± 0.118**
Ob6						0.575 ± 0.126	**0.727 ± 0.113**	**0.731 ± 0.110**	**0.780 ± 0.103**
Ob6a							**0.634 ± 0.116**	**0.614 ± 0.129**	0.483 ± 0.128
Ob7								**0.679 ± 0.117**	**0.723 ± 0.115**
Ob8									**0.734 ± 0.107**
All observers				$\kappa = 0.61569 \pm 0.024507$; $P < 0.001$					

Note:—Inter-observer Kappa values $\geq$ 0.6 are highlighted in bold type.

Table 3: Interobserver agreement using the AOL recanalization scale

	Ob2	Ob3	Ob4	Ob5	Ob6	Ob6a	Ob7	Ob8	Ob9
Ob1	0.132 ± 0.066	0.241 ± 0.103	0.288 ± 0.118	0.196 ± 0.096	0.425 ± 0.116	**0.607 ± 0.115**	0.199 ± 0.091	0.265 ± 0.086	0.382 ± 0.098
Ob2		0.420 ± 0.111	0.272 ± 0.084	**0.787 ± 0.103**	0.336 ± 0.093	0.065 ± 0.070	0.376 ± 0.110	**0.648 ± 0.101**	0.352 ± 0.106
Ob3			0.304 ± 0.102	0.553 ± 0.105	0.575 ± 0.106	0.258 ± 0.109	0.474 ± 0.108	0.535 ± 0.109	0.595 ± 0.104
Ob4				0.370 ± 0.095	0.424 ± 0.109	0.340 ± 0.121	0.366 ± 0.090	0.305 ± 0.089	0.467 ± 0.103
Ob5					0.514 ± 0.105	0.263 ± 0.095	0.461 ± 0.110	**0.733 ± 0.093**	0.533 ± 0.107
Ob6						0.290 ± 0.124	0.419 ± 0.111	0.509 ± 0.102	**0.633 ± 0.101**
Ob6a							0.264 ± 0.091	0.265 ± 0.086	0.445 ± 0.098
Ob7								**0.653 ± 0.110**	**0.623 ± 0.116**
Ob8									0.550 ± 0.111
All observers				$\kappa = 0.39434 \pm 0.015957$; $P < 0.001$					

Note:—Inter-observer Kappa values $\geq$ 0.6 are highlighted in bold type.

which the most frequent disagreements occurred. κ values were interpreted according to Landis and Koch,[27] with κ coefficients of 0 = poor; 0.01–0.20 = slight; 0.21–0.40 = fair; 0.41–0.60 = moderate; 0.61–0.80 = substantial; and 0.81–1.0 = almost-perfect agreement.

RESULTS

Patients

The portfolio included 32 consecutive patients (17 women; mean age, 63 ± 12). In addition to intra-arterial therapy, patients received IV-rtPA in 61% of the cases. The mean delay between symptoms and thrombectomy was 199 ± 47 minutes. The most frequent occlusions were located on the M1 segment of the middle cerebral artery ($n = 19$; 60%) or on the distal internal carotid artery (T-occlusion; $n = 10$; 32%). The most frequent thrombectomy methods used during this period were an aspiration system ($n = 13$; 41%) or a Stentriever (Trevo; Stryker, Kalamazoo, Michigan) system ($n = 14$; 43%). Characteristics of patients are summarized in the On-line Table.

Survey with 9 Observers

There were large discrepancies in the adjudication of angiographic outcomes, with, for example, complete perfusion (TICI 3) being attributed to a wide range (8%–49%) of patients or complete recanalization (AOL III) in 22%–65% of patients, depending on observers.

Table 1 summarizes the κ values obtained when the 9 observers scored angiographic outcomes according to the TICI reperfusion categories (overall agreement, $\kappa = 0.446 \pm 0.013$). Table 2 summarizes the κ values when the categories were dichotomized as success (2b, 3) versus failure (0, 1, 2a) (overall agreement, $\kappa = 0.616 \pm 0.025$). κ coefficients of pairs of observers that reached "substantial agreement" ($\kappa > 0.6$) increased from 9% to 60% with dichotomization. The TICI category that was the subject of most disagreements was 2b ($\kappa = 0.242 \pm 0.025$).

Table 3 summarizes the κ values when angiographic outcomes were categorized according to the AOL recanalization categories (overall agreement, $\kappa = 0.394 \pm 0.016$). Table 4 results were obtained when they were analyzed as success (II, III) or failure (0, I) (overall agreement, $\kappa = 0.762 \pm 0.025$). κ coefficients of pairs of observers that reached substantial agreement ($\kappa > 0.6$) increased from 16% to 91% with dichotomization. The AOL category that was the subject of most disagreements was II ($\kappa = 0.188 \pm 0.025$).

The endovascular intervention was successful in 68%–87% of patients according to various observers when success was defined in terms of recanalization (AOL II or III) but in only 32%–62% of

Table 4: Interobserver agreement using the dichotomized AOL scale

	Ob2	Ob3	Ob4	Ob5	Ob6	Ob6a	Ob7	Ob8	Ob9
Ob1	**0.646 ± 0.144**	0.593 ± 0.154	**0.613 ± 0.141**	**0.788 ± 0.117**	**0.64 ± 0.144**	**0.773 ± 0.122**	**0.726 ± 0.128**	**0.726 ± 0.128**	**0.726 ± 0.128**
Ob2		**0.65 ± 0.153**	**0.802 ± 0.107**	**0.853 ± 0.101**	**0.85 ± 0.101**	**0.682 ± 0.146**	**0.788 ± 0.117**	**0.788 ± 0.117**	**0.929 ± 0.070**
Ob3			0.491 ± 0.149	**0.654 ± 0.153**	**0.65 ± 0.153**	**0.802 ± 0.133**	0.593 ± 0.154	0.593 ± 0.154	0.593 ± 0.154
Ob4				**0.802 ± 0.107**	**0.802 ± 0.107**	**0.654 ± 0.135**	**0.742 ± 0.120**	**0.742 ± 0.120**	**0.871 ± 0.088**
Ob5					**0.853 ± 0.101**	**0.841 ± 0.108**	**0.929 ± 0.070**	**0.929 ± 0.070**	**0.929 ± 0.070**
Ob6						**0.682 ± 0.146**	**0.788 ± 0.117**	**0.788 ± 0.117**	**0.929 ± 0.070**
Ob6a							**0.773 ± 0.122**	**0.773 ± 0.122**	**0.773 ± 0.122**
Ob7								**0.863 ± 0.094**	**0.863 ± 0.094**
Ob8									**0.863 ± 0.094**
All observers				$\kappa = 0.76197 \pm 0.024507$; $P < 0.001$					

Note:—Inter-observer Kappa values ≥ 0.6 are highlighted in bold type.

Table 5: Intra- and interobserver agreement using TICI (3 observers)

	Intraobserver (All Images)			Interobserver Agreement		
	Observer 1	Observer 2	Observer 3	Questionnaire	All Images Session 1	All Images Session 2
Full TICI scale	0.488 ± 0.119	0.158 ± 0.122	0.095 ± 0.105	0.590 ± 0.060	0.364 ± 0.060	0.538 ± 0.060
Dichotomized TICI	**0.716 ± 0.132**	0.216 ± 0.179	0.246 ± 0.176	**0.699 ± 0.100**	0.489 ± 0.110	**0.678 ± 0.110**

Note:—Inter-observer Kappa values ≥ 0.6 are highlighted in bold type.

Table 6: Intra- and interobserver agreement using AOL (3 observers)

	Intraobserver (All Images)			Interobserver Agreement		
	Observer 1	Observer 2	Observer 1	Observer 2	Observer 1	Observer 2
Full AOL scale	**0.611 ± 0.126**	0.233 ± 0.149	0.302 ± 0.143	0.492 ± 0.070	0.238 ± 0.070	0.590 ± 0.070
Dichotomized AOL	**0.731 ± 0.145**	**0.790 ± 0.142**	**0.626 ± 0.168**	**0.787 ± 0.100**	0.561 ± 0.110	**0.870 ± 0.110**

Note:—Inter-observer Kappa values ≥ 0.6 are highlighted in bold type.

patients when success was defined in terms of reperfusion (TICI 2b or 3).

Intra- and Interobserver Agreement with Electronic or Full Datasets

The results of parts 2 and 3 are summarized in Tables 5 and 6.

Intraobserver agreement between 2 sessions for experts having access to the full set of angiographic data on 32 patients was only slight to fair (0–0.4) in most cases, with only 1 observer reaching substantial agreement for the AOL scores. The κ values of the interobserver agreement obtained by comparing answers to the electronic questionnaire and the verdicts of the first and second reading sessions when observers had access to all images were similar and always below 0.6 (less than substantial).

When results were dichotomized, intraobserver agreement remained fair for 2 of 3 observers assessing reperfusion with the TICI scale but reached substantial agreement for all 3 readers when they assessed recanalization with the AOL scale; the interobserver agreement improved to substantial or >0.6 with dichotomization of the results of the electronic survey for both scales and for one of the PACS sessions, but not the other.

The endovascular intervention was successful in 72%–79% of patients according to 3 observers having access to all images when success was defined in terms of recanalization (AOL II or III) but in only 35%–59% of patients when success was defined in terms of reperfusion (TICI 2b or 3).

DISCUSSION

The salient features of this work are the following: 1) Agreement in adjudicating angiographic results of endovascular interventions among multiple observers is, at best, fair to moderate; 2) this problem is not limited to divergent interpretations of the definitions of the various categories by various experts because intra-observer agreement was similarly poor when the same experts re-evaluated the same results twice on 2 independent occasions; 3) difficulties were not caused by the artificial and limited information provided by the survey we used to assess interobserver variations because similarly poor results were obtained when 3 observers were given access to all angiographic images; 4) κ coefficients reached more reassuring substantial agreement values when results were dichotomized into successes and failures; 5) the AOL recanalization scoring system seemed more repeatable than the TICI reperfusion scheme; and 6) the AOL II, III recanalization categories provided a more frequent verdict of success compared with the 2b, 3 TICI categories when dichotomization was used.

To evaluate our interventions, we had no choice but to reduce the variety and heterogeneity naturally found in clinical results to a (preferably small) number of categories and terms to name these categories that will determine what counts as a success or failure, in a common language that will allow tabulation of results and both valid comparisons between groups and communication of results among clinicians. When new categories (such as the TICI scale) are proposed, definitions can be provided as a sort of manual of translation, rules to translate the concrete results obtained in each particular case to a common language. As with any language, translation and communication by using our new terms may fail. If the meaning of such terms as TICI 2b or AOL II can be intentionally defined by explicit descriptions, whether these definitions and categories succeed in fixing the referents (ie, in re-identifying the same angiographic outcomes when they are seen by different observers or by the same observers at different time points) must be empirically tested to ensure that the new language does what it was designed to do, to allow valid comparisons and unambiguous communication. Both TICI and AOL scales had poor concordance when the same results were judged by different

observers or by the same observers on 2 different occasions. This finding suggests that results of various case series or registries should not be compared when angiographic outcomes have not been adjudicated by the same observer.[20,28]

κ statistics provide a measure of agreement that takes into account the role of chance in the occurrence of concordant verdicts when estimating agreement between observers.[29] Depending on prevalence, κ statistics are liable to paradoxes, such as high agreement but low κ values, when the distribution of the cases is imbalanced among categories.[21] This problem may partly explain the low κ values of the intraobserver study on the 32-patient sample, in which tables were asymmetric. We believe that paradoxes do not explain the poor precision found in the 37-patient sample assessed by the 9 reviewers, more balanced by the introduction of 5 "intermediate cases" and when agreement was low for each category.

Difficult questions arise when one tackles the problem of agreement regarding a treatment outcome. Surely there must be some reality regarding revascularization, but in the absence of a standard criterion, truth regarding the verdict of the test, its accuracy, is impossible to capture. To construct and assess our scales, we are left with "validity," a vague concept that attempts to secure the link between the measure and the phenomenon of interest, such as whether the scale makes intuitive sense (face validity), whether it conforms to theory (construct validity), and whether it allows the prediction of an important clinical outcome (predictive validity).[30] These considerations were taken into account when scales were designed. Revascularization can be conceived as angiographic recanalization of the primary arterial occlusive lesion (what the AOL attempts to capture) or by reperfusion in the arterial bed distal to the occlusion.[22] Reperfusion can be assessed by TIMI, originally used to estimate coronary blood flow after percutaneous angioplasty[31] and used in Prolyse in Acute Cerebral Thromboembolism II,[32] or by TICI, introduced by Higashida et al[7] to intuitively adapt the TIMI scheme to the cerebral circulation and used in IMS-II and III.[18] The results obtained with the AOL classification recanalization system in one study should not be compared with those obtained by using the TICI reperfusion scale in another, the former being more frequently associated with a verdict of success than the latter, at least in this study.

Interobserver disagreement in adjudicating treatment results may be caused by multiple problems: intrinsic ambiguities in the definitions of the classifications; discrepancies in the various ways the definitions are interpreted by various readers; and even if the definitions were understood in the same way, discrepancies in applying the definitions to individual cases. The current study cannot disentangle these various reasons for the discordance among observers. One way to improve agreement would be to modify the proposed classification and retest in a trial-and-error fashion the same portfolio to progressively improve repeatability. It was not feasible to independently test all classification systems and their various modifications in the same study by using the same portfolio and the same observers. Other scales could have been more repeatable than the ones we tested.

The TICI system has been criticized for internal inconsistencies, particularly regarding the 2a, 2b, 3 categories,[13] a problem clearly exposed by the present work, which confirms 2b as the category with the most frequent disagreements. The AOL recanalization categories, however, were also subject to discrepancies in interpretation; the contentious category was AOL II. It may be impossible to obtain consensus for these "gray zone" cases.

Modifications of the TICI scale have been proposed, for example, to get rid of the difficult 2b, 3 distinction between "complete" and "complete-but-slow" perfusion.[33] Others have proposed entirely different classifications.[16]

The interobserver agreement between 2 radiologists assessing angiographic results according to the TIMI classification scheme in 38 patients has shown low-weighted κ values (0.4; 95% CI, 0.2–0.6),[15] similar to those in our study. On the other hand, another report has previously shown better agreement among 3 observers by using the TIMI or a new Qureshi grading system in 15 randomly selected patients, with κ values in the range of 0.7.[16]

By adding statistical noise, variability or lack of precision may affect results of studies comparing 2 treatments. This will, by necessity, impose methodologic adjustments such as increasing the number of patients to be recruited in the study to show a difference between 2 groups. The variability we observed in judging the success of the procedure was probably underestimated because there are many other sources of discrepancies in a core lab context compared with the electronic survey: There are more images, from various series, by using various projections and diverse equipment from various centers. Legitimate strategies to enhance precision include standardization of angiographic projections and techniques, using an operation manual, refining criteria defining the score classes, and training (or even certifying) the observers. Repeating the measurements by a number of observers, with resolution of discrepancies by consensus, can succeed in achieving a precision that is artificial; it is unclear, however, if such verdicts are more valid.[34]

For sure, predictive validity is important; clinical outcomes have been correlated to revascularization in acute ischemic stroke,[9] though many other factors (collateral circulation, penumbra, eloquence of the vascular territory, and so forth) may also impact outcomes.[7] To attempt to incorporate all potential factors in a single, intuitively appealing but complex scale with multiple categories may increase the variability of interpretations and, consequently, decrease precision, when the time comes to assess interobserver agreement.[35] Various other scales have been described[15,16,36] in attempts to intuitively enhance validity. The real test for any scale, however, will eventually come with usage, if it is used. To propose yet another classification could only add to the confusion that already plagues this field.[14]

The present work suggests that it is possible to live with the current reperfusion and recanalization scales, provided a number of precautions are kept in mind. First, any comparison among revascularization methods or devices should be given credibility when performed within a randomized trial, by using predefined, simple ordinal scales adjudicated by an independent central laboratory staffed with experienced observers masked to treatment allocation. While the verdicts of various observers can be alarmingly divergent for the 2 scales we studied, κ values can reach satisfactory levels of agreement (0.6) when results are dichotomized as success or failure. Surrogate angiographic outcomes can serve a useful function if only to help explain or

understand reasons for disappointing clinical results. Clinical outcomes, typically translated into the modified Rankin Scale scores at 3 months, are probably better end points for major clinical trials.[5,18]

Limitations

The electronic survey was designed to ease the assessment by multiple interventional neuroradiologists. Nine of 12 potential observers responded. Readers had access to only 4 selected images to evaluate results according to the TICI and AOL scores. We can only speculate what the results would be if missing responses had been available. How seriously observers worked to come to verdicts can always be questioned, and the context of the assessment is certainly different from typical clinical work or from a core lab context. It may not be realistic to expect readers to assess perfusion on a few static images. The intra- or interobserver agreement was, however, no better when 3 neuroradiologists had access to all images. Posterior circulation strokes were not included, and this feature may have decreased variability in interpretations. New recommendations on angiographic revascularization grading scales have now been published.[36] They include a modified TICI scale, slightly different from the one we used, which is also subject to variability in interpretation.[37]

CONCLUSIONS

Recanalization or reperfusion scales are interpreted differently by different observers. Rather than yet another classification scheme, we propose to dichotomize results for analyses and comparisons.

ACKNOWLEDGMENTS

We are grateful to the 9 international experts who took time to respond to the survey. This work would not have been possible without their generous help.

REFERENCES

1. Penumbra Stroke Trial Investigators. **The Penumbra pivotal stroke trial: safety and effectiveness of a new generation of mechanical devices for clot removal in intracranial large vessel occlusive disease.** *Stroke* 2009;40:2761–68
2. Mourand I, Brunel H, Costalat V, et al. **Mechanical thrombectomy in acute ischemic stroke: catch device.** *AJNR Am J Neuroradiol* 2011;32:1381–85
3. Smith WS, Sung G, Saver J, et al. **Mechanical thrombectomy for acute ischemic stroke: final results of the multi Merci trial.** *Stroke* 2008;39:1205–12
4. Costalat V, Machi P, Lobotesis K, et al. **Rescue, combined, and stand-alone thrombectomy in the management of large vessel occlusion stroke using the Solitaire device: a prospective 50-patient single-center study: timing, safety, and efficacy.** *Stroke* 2011;42:1929–35
5. Kent TA, Mandava P. **Recanalization rates can be misleading.** *Stroke* 2007;38:e103, author reply e104
6. Felten RP, Ogden NR, Pena C, et al. **The Food and Drug Administration medical device review process: clearance of a clot retriever for use in ischemic stroke.** *Stroke* 2005;36:404–06
7. Higashida RT, Furlan AJ, Roberts H, et al. **Trial design and reporting standards for intra-arterial cerebral thrombolysis for acute ischemic stroke.** *Stroke* 2003;34:e109–137
8. Khatri P, Hill MD, Palesch YY, et al. **Methodology of the Interventional Management of Stroke III trial.** *Int J Stroke* 2008;3:130–37
9. Rha JH, Saver JL. **The impact of recanalization on ischemic stroke outcome: a meta-analysis.** *Stroke* 2007;38:967–73
10. Goyal M, Fargen KM, Turk AS, et al. **2c or not 2c: defining an improved revascularization grading scale and the need for standardization of angiography outcomes in stroke trials.** *J Neurointerv Surg* 2014;6:83–86
11. Almekhlafi MA, Menon BK, Freiheit EA, et al. **A meta-analysis of observational intra-arterial stroke therapy studies using the Merci device, Penumbra system, and retrievable stents.** *AJNR Am J Neuroradiol* 2013;34:140–45
12. Jauch EC, Saver JL, Adams HP Jr, et al. **Guidelines for the early management of patients with acute ischemic stroke: a guideline for healthcare professionals from the American Heart Association/American Stroke Association.** *Stroke* 2013;44:870–947
13. Kallmes DF. **TICI: if you are not confused, then you are not paying attention.** *AJNR Am J Neuroradiol* 2012;33:975–76
14. Tomsick T. **TIMI, TIBI, TICI: I came, I saw, I got confused.** *AJNR Am J Neuroradiol* 2007;28:382–84
15. Bar M, Mikulik R, Jonszta T, et al. **Diagnosis of recanalization of the intracranial artery has poor inter-rater reliability.** *AJNR Am J Neuroradiol* 2012;33:972–74
16. Qureshi AI. **New grading system for angiographic evaluation of arterial occlusions and recanalization response to intra-arterial thrombolysis in acute ischemic stroke.** *Neurosurgery* 2002;50:1405–14, discussion 1414–15
17. Khatri P, Neff J, Broderick JP, et al. **Revascularization end points in stroke interventional trials: recanalization versus reperfusion in IMS I.** *Stroke* 2005;36:2400–03
18. Broderick JP, Palesch YY, Demchuk AM, et al, for the Interventional Management of Stroke (IMS) III Investigators. **Endovascular therapy after intravenous t-PA versus t-PA alone for stroke.** *N Engl J Med* 2013;368:893–903.
19. Kidwell CS, Jahan R, Gornbein J, et al. **MR RESCUE Investigators: a trial of imaging selection and endovascular treatment for ischemic stroke.** *N Engl J Med* 2013;368:914–23
20. Broderick JP, Schroth G. **What the SWIFT and TREVO II trials tell us about the role of endovascular therapy for acute stroke.** *Stroke* 2013;44:1761–64
21. Feinstein AR, Cicchetti DV. **High agreement but low kappa. I. The problems of two paradoxes.** *J Clin Epidemiol* 1990;43:543–49
22. IMS II Trial Investigators. **The Interventional Management of Stroke (IMS) II study.** *Stroke* 2007;38:2127–35
23. Castaño C, Dorado L, Guerrero C, et al. **Mechanical thrombectomy with the Solitaire AB device in large artery occlusions of the anterior circulation: a pilot study.** *Stroke* 2010;41:1836–40
24. Roth C, Papanagiotou P, Behnke S, et al. **Stent-assisted mechanical recanalization for treatment of acute intracerebral artery occlusions.** *Stroke* 2010;41:2559–67
25. Stampfl S, Hartmann M, Ringleb PA, et al. **Stent placement for flow restoration in acute ischemic stroke: a single-center experience with the Solitaire stent system.** *AJNR Am J Neuroradiol* 2011;32:1245–48
26. Fleiss J, Levin B, Paik M. *Statistical Methods for Rates and Proportions.* New York: Wiley & Sons; 2003
27. Landis JR, Koch GG. **The measurement of observer agreement for categorical data.** *Biometrics* 1977;33:159–74
28. Saver JL, Liebeskind DS, Nogueira RG, et al. **Need to clarify thrombolysis in myocardial ischemia (TIMI) scale scoring method in the Penumbra pivotal stroke trial.** *Stroke* 2010;41:e115–16
29. Cohen J. **A coefficient of agreement for nominal scales.** *Educ Psychol Meas* 1960;20:27–46

30. Newman TB, Browner WS, Cummings SR. **Designing studies of medical tests.** In: Hulley SB, Cummings SR, Browner WS, et al, eds. *Designing Clinical Research: An Epidemiologic Approach.* 4th ed. Philadelphia: Lippincott, Williams & Wilkins; 2001:175–93

31. Chesebro JH, Knatterud G, Roberts R, et al. **Thrombolysis in myocardial infarction (TIMI) trial, phase I: a comparison between intravenous tissue plasminogen activator and intravenous streptokinase—clinical findings through hospital discharge.** *Circulation* 1987;76:142–54

32. Furlan A, Higashida R, Wechsler L, et al. **Intra-arterial prourokinase for acute ischemic stroke: the PROACT II study—a randomized controlled trial. Prolyse in Acute Cerebral Thromboembolism.** *JAMA* 1999;282:2003–11

33. Bankier AA, Levine D, Halpern EF, et al. **Consensus interpretation in imaging research: is there a better way?** *Radiology* 2010;257:14–17

34. Maclure M, Willett WC. **Misinterpretation and misuse of the kappa statistic.** *Am J Epidemiol* 1987;126:161–69

35. Noser EA, Shaltoni HM, Hall CE, et al. **Aggressive mechanical clot disruption: a safe adjunct to thrombolytic therapy in acute stroke?** *Stroke* 2005;36:292–96

36. Zaidat OO, Yoo AJ, Khatri P, et al. **Recommendations on angiographic revascularization grading standards for acute ischemic stroke: a consensus statement.** *Stroke* 2013;44:2650–63

37. Suh SH, Cloft HJ, Fugate JE, et al. **Clarifying differences among thrombolysis in cerebral infarction scale variants: is the artery half open or half closed?** *Stroke* 2013;44:1166–1168

Treatment of Multiple Intracranial Aneurysms with 1-Stage Coiling

P. Jeon, B.M. Kim, D.J. Kim, D.I. Kim, and S.H. Suh

ABSTRACT

BACKGROUND AND PURPOSE: Although multiple intracranial aneurysms are frequent, determining treatment strategy and methods for them is often complicated. The aim of this study was to evaluate the safety and effectiveness of 1-stage coiling for multiple intracranial aneurysms.

MATERIALS AND METHODS: All patients who underwent 1-stage coiling for ≥2 aneurysms were identified from a prospectively registered neurointerventional data base during 10 years. The patient characteristics and clinical and angiographic outcomes at discharge and follow-up were retrospectively evaluated.

RESULTS: One hundred sixty-seven patients (male/female ratio, 30:137; mean age, 58 years) with multiple aneurysms (418 aneurysms; mean, 2.5 aneurysms/patient) underwent attempted 1-stage coiling for ≥2 aneurysms (359 aneurysms; mean, 2.1 aneurysms/patient). In 131 patients (78.4%), all detected aneurysms were treated with coiling only. Treatment-related morbidity and mortality at discharge were 1.8% and 0.6% per patient, respectively. Of the 132 patients without subarachnoid hemorrhage, 129 (97.7%) had favorable outcomes (mRS 0–2) at discharge; of the 35 patients with SAH, 27 (77.1%) had favorable outcomes at discharge. Of the 162 patients (97%) for whom clinical follow-up was available (mean, 35.8 months), 154 patients (95.1%) had favorable outcomes. Immediate posttreatment angiography showed complete occlusion in 186 (51.8%) aneurysms, neck remnants in 134 (37.3%), sac remnants in 33 (9.2%), and failure in 6 (1.7%). Of the 262 (73.9%) aneurysms that underwent follow-up imaging (mean, 24.8 months), 244 (93.1%) showed a stable or improved state, with 12 (4.6%) minor and 6 (2.3%) major recurrences.

CONCLUSIONS: One-stage coiling of multiple aneurysms seems to be safe and effective, with low morbidity and mortality.

I ntracranial aneurysm is the most important cause of subarachnoid hemorrhage, resulting in 8%–20% dependent morbidity and 37%–57% mortality.[1] Strategies and methods for treating intracranial aneurysms have been extensively studied. Multiple intracranial aneurysms are frequent, with a reported incidence of 19%–34% of patients who present with SAH.[2-5] Determining treatment strategy and methods for multiple aneurysms is often complicated. Coiling is currently accepted as a standard treatment for ruptured or unruptured intracranial aneurysms and has been increasingly used, regardless of the location of the intracranial aneurysm.[6] Nevertheless, while many cases of clipping for multiple aneurysms have been reported,[7-12] there were only 2 small case series using coiling for multiple aneurysms.[13,14] The purpose of this study was to evaluate the safety and effectiveness of 1-stage coiling for multiple intracranial aneurysms.

MATERIALS AND METHODS

The institutional review board approved this retrospective analysis and waived patient informed consent due to the study design. All patients who underwent 1-stage coiling for ≥2 aneurysms were identified from a prospectively registered neurointerventional data base in 2 tertiary referral academic hospitals from January 2003 through December 2012. In patients with acute SAH with multiple aneurysms, the ruptured aneurysm was first treated; then, if feasible, the other aneurysms were treated in the same session. However, if it was not clear which aneurysm was ruptured, coiling was attempted only if it was feasible for all potentially ruptured aneurysms. In the patients with multiple unruptured aneurysms, neurointerventionists and vascular neurosurgeons determined, after diagnostic angiography, which aneurysms could be treated with 1-stage coiling. All procedures

Characteristics of patients and aneurysms, and immediate clinical and angiographic outcomes after treatment with 1-stage coiling[a]

Characteristics and Outcomes	
No. of patients (No. of aneurysms coiled)	167 (359)
Age (yr) (mean) (range)	57.7 ± 10.6 (30–83)
Male/female	30:137
Presentation with subarachnoid hemorrhage	35 (21.0%)
No. of aneurysms per patient (range)	2.5 ± 0.9 (2–7)
No. of coiled aneurysms per patient (range)	2.1 ± 0.4 (2–3)
No. of patients with all detected aneurysms coiled	131 (78.4%)
Location of aneurysms coiled (n = 359)	
ICA paraclinoid	135 (37.6%)
ICA–posterior communicating artery	56 (15.6%)
ICA–anterior choroidal artery	26 (7.2%)
ICA bifurcation	7 (1.9%)
Middle cerebral artery	58 (16.2%)
Anterior cerebral artery	44 (12.3%)
Vertebrobasilar artery	32 (8.9%)
Aneurysm size (mm) (mean) (range)	5.6 ± 2.7 (2–21)
<10 mm	326 (90.8%)
10–24.9 mm	33 (9.2%)
Neck size (mm) (mean) (range)	3.3 ± 1.3 (0.4–10.0)
Wide neck (neck size ≥4 mm or dome-to-neck ratio <1.5)	233 (64.9%)
Distribution of aneurysms coiled	
Unilateral anterior circulation	73 (43.7%)
Bilateral anterior circulation	66 (39.5%)
Posterior circulation	3 (1.8%)
Unilateral anterior + posterior circulation	20 (12.0%)
Bilateral anterior + posterior circulation	5 (3.0%)
Treatment-related morbidity (n = 167)	3 (1.8%; 95% CI, 0.24–3.83%)
Treatment-related mortality (n = 167)	1 (0.6%; 95% CI, 0.58–1.78%)
Immediate angiographic outcome	
Complete occlusion	186 (51.8%)
Neck remnant	134 (37.3%)
Sac remnant	33 (9.2%)
Coiling failure	6 (1.7%)

[a] Data are shown as number (%) except where otherwise noted.

were performed with the patient under general anesthesia. Coiling was performed by using a conventional single catheter, multicatheter, balloon-assisted, stent-assisted, or combined technique. For all unruptured aneurysms, preoperative dual antiplatelet medication (aspirin, 100–325 mg, and clopidogrel, 75 mg) was given at least 5 days before treatment for all patients starting in late 2010. Generally, dual antiplatelet medication was stopped after the treatment but was maintained for at least 3 months and then changed to aspirin monotherapy for patients who received stent-assisted coiling.

All clinical and radiographic data were prospectively registered into neurointerventional and neurosurgical data bases in each hospital at the time of treatment and then were retrospectively analyzed by the authors. All periprocedural complications during and after treatment were prospectively recorded and retrospectively evaluated for this study. For patients presenting with SAH, treatment-related morbidity was defined as treatment-related complications causing deterioration of the patient's neurologic condition. For patients without SAH, treatment-related morbidity was defined as any objective clinical symptom developing after coiling and remaining at discharge. Patients were regularly followed up on an outpatient basis, according to the protocol of each institution, typically 1 month after discharge and then every 3–6 months. Clinical outcome was evaluated at discharge and follow-up, according to the modified Rankin Scale score. The

mRS score at the latest clinical follow-up was defined as the final outcome. If the latest clinical follow-up was performed >3 months before the commencement of this study, a structured telephone interview was performed to evaluate clinical outcome.[15] If the patient's clinical condition deteriorated due to an event definitively unrelated to treatment or an intracranial aneurysm, the functional outcome at the follow-up just before that event was defined as the final outcome.

Immediate angiographic results were assessed according to the Raymond classification: complete, neck remnant, or sac remnant.[16] Follow-up imaging (conventional angiography and/or MR angiography) was performed initially at 6–12 months and then at 24–36 months. Imaging follow-up results were classified into 3 categories compared with immediate posttreatment control angiography: 1) stable or improved; 2) minor recurrence, when the recurrence did not require retreatment; and 3) major recurrence, when the recurrence required retreatment. If major recanalization was detected, retreatment was performed.

Statistical Analysis

All statistical analyses were performed by using the Statistical Package for the Social Sciences, Version 20 (IBM, Armonk, New York). All categoric variables are presented as a percentage and 95% confidence intervals. All continuous variables are presented as mean ± SD.

RESULTS

The characteristics of the patients and aneurysms as well as the clinical and angiographic outcomes are summarized in the Table. One-stage coiling was used to treat 167 patients with ≥2 aneurysms. The patients had 418 aneurysms (2.5 aneurysms per patient); 108 patients had two, 44 had three, 9 had four, 3 had five, 2 had 6, and 1 patient had 7 aneurysms. One-stage coiling was attempted on 359 aneurysms (2.1 aneurysms per patient). In 131 patients (78.4%), all detected aneurysms were treated with coiling only. Ninety-seven patients were treated with 1 type; 68 patients, with 2 types; and 2 patients, with 3 types of coiling techniques. Specifically, coiling was completed with a single catheter in 151 (42.1%), multicatheters in 60 (16.7%), balloon-assisted in 70 (19.5%), and stent-assisted in 78 (21.7%) aneurysms. Coiling was aborted in 6 (1.7%) aneurysms due to technical difficulties, but without complications.

The rate of any complication was 6.6% (11/167). Of the 11 complications, 2 occurred in patients with SAH, while the other 9 occurred in patients without SAH. All complications occurred during the treatment of the last aneurysm or were detected after completion of the embolization. Specifically, thromboembolic
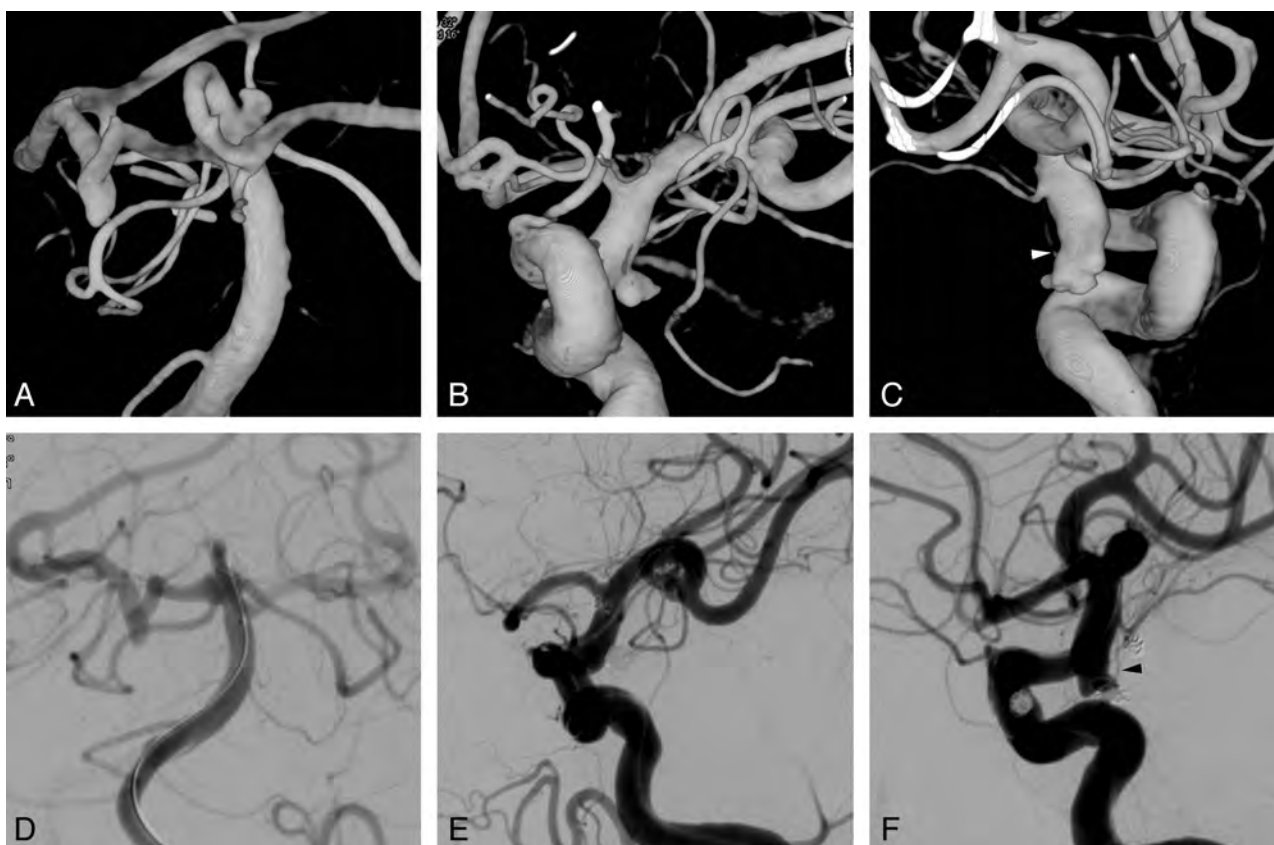
FIG 1. A 61-year-old woman presented with a Hunt and Hess scale grade 3 subarachnoid hemorrhage. Nonenhanced CT (not shown) showed a diffuse, nonlocalized, subarachnoid hemorrhage in the entire basal cistern. 3D reconstruction images of cerebral angiography reveal 3 similar-sized small aneurysms at the left superior cerebellar artery origin (*A*) and bilateral posterior communicating artery origin (*B* and *C*). Each of the 3 aneurysms also has an irregular shape with a daughter sac. The white arrowhead indicates a left tuberothalamic artery incorporated into the aneurysm sac. Postembolization control angiograms after balloon-assisted coiling for all 3 aneurysms show complete occlusion of the superior cerebellar artery (*D*) and the left posterior communicating artery (*E*) aneurysms, and an intentional neck remnant, from which a left tuberothalamic artery (*black arrowhead*) directly originated, of the right posterior communicating artery aneurysm (*F*).

events occurred in 6 patients, all of which resolved with intraarterial infusion of a glycoprotein IIb/IIIa inhibitor (tirofiban, 0.5–1.0 mg). Five of the 6 patients had no symptoms posttreatment, but 1 patient experienced morbidity at discharge (mRS 3) due to a small infarction in the midbrain. After completion of the treatment without any problems during the procedure, perforator infarctions (2 brain stem and 1 basal ganglia) were detected in 3 patients, resulting in morbidity at discharge in 2 patients (mRS 2 and 3, respectively). One patient had a puncture site pseudoaneurysm, requiring surgical repair. The final patient had an ICA rupture during balloon-assisted coiling for the last hypophyseal aneurysm after successful embolization of basilar artery tip and anterior choroidal aneurysms, resulting in mortality.

Treatment-related morbidity and mortality at discharge occurred in 3 (1.8%) and in 1 (0.6%) of the 167 patients, respectively. Favorable outcomes (mRS 0–2) at discharge occurred in 129 (97.7%) of 132 patients without SAH and in 27 (77.1%) of 35 patients with SAH. Of the 162 patients (97%) for whom clinical follow-up was available for a mean of 35.8 months, 154 patients (95.1%) had favorable outcomes. Immediate posttreatment angiography showed complete occlusion in 186 (51.8%) patients, neck remnant in 134 (37.3%), sac remnant in 29 (7.8%), and failure in 6 (1.7%). Of the 262 (73.9%) aneurysms that had available follow-up imaging for a mean of 24.8 months, 244 (93.1%)

showed a stable or improved state and there were 12 (4.6%) minor and 6 (2.3%) major recurrences. All major recurrent aneurysms were retreated with coiling without complications.

DISCUSSION

Multiple intracranial aneurysms occur in 19%–34% of patients who present with SAH.[2-5] Coiling as a treatment for multiple intracranial aneurysms has not been well studied. To our knowledge, only 2 small case series of 1-stage coiling for multiple intracranial aneurysms have been reported in the literature. Solander et al[13] treated 38 patients with 93 aneurysms with coiling ($n = 79$) and clipping ($n = 14$). Twenty-five patients underwent 1-stage coiling for >1 aneurysm at various distributions. No patient had treatment-related permanent morbidity. Xavier et al[14] treated 6 patients with 1-stage coiling for 13 aneurysms. No periprocedural complications were reported in that study. In the current study, 1-stage coiling was completed with 1–3 different types of coiling techniques in 353 (98.3%) of 359 aneurysms in 167 patients, with 1.8% morbidity and 0.6%. mortality. Furthermore, in 78.4% of patients, all detected aneurysms were treated with coiling only.

There have been many reported cases in which multiple aneurysms have been treated with clipping.[7-12] Clipping of multiple aneurysms, however, results in poorer outcomes than in a single aneurysm.[7-11] This can be explained by the increased manipula-

tion of cerebral arteries and brain tissue during multiple-aneurysm surgery.[8,11] Coiling for multiple aneurysms, however, does not require increased manipulation of cerebral arteries or brain tissue. Although the ruptured aneurysm should be treated first, in a patient with SAH who has multiple intracranial aneurysms, it is often difficult to determine which aneurysm is ruptured. In this case, all of the possibly ruptured aneurysms should be treated in the same session. One-stage clipping for multiple aneurysms may be limited in cases in which multiple aneurysms are distributed bilaterally or are in both the anterior and posterior circulations.[8] One-stage treatment of multiple aneurysms distributed bilaterally or in both the anterior and posterior circulations may be more feasible with coiling than with clipping.

In patients with SAH who had multiple aneurysms and in whom it was unclear which aneurysm was ruptured, 1-stage coiling for all of the possibly ruptured aneurysms, regardless of the distribution of multiple aneurysms, was an important advantage (Fig 1). In patients with unruptured aneurysms, multiplicity is associated with a greater risk of rupture compared with single aneurysms.[17] Which patients with unruptured aneurysms will experience SAH is often unpredictable, and it is even more difficult to determine which of the multiple unruptured aneurysms will rupture. In our institution, 3 patients had SAH from a remaining aneurysm after the most dangerous-looking aneurysms had been treated (data not shown). Therefore, it is our policy to treat, if feasible, all unruptured aneurysms in patients in good medical condition. Because coiling of unruptured aneurysms is associated with less morbidity and mortality than clipping,[18] it seems reasonable to treat as many aneurysms as possible with coiling.

Another advantage of 1-stage coiling of multiple intracranial aneurysms is that coiling avoids repeat general anesthesia and groin punctures compared with multiple separate procedures; 1-stage coiling may decrease the rate of complications associated with repeat general anesthesia and multiple femoral artery punctures. One-stage coiling of multiple aneurysms may prolong the time that patients remain under general anesthesia. Therefore, in terms of general anesthesia, one should balance the benefits and the risks of 1-stage coiling versus coiling in multiple separate sessions, considering each patient's medical condition.

Cost-effectiveness is also an expected advantage of coiling. Coiling was associated with significantly shorter lengths of hospital stay and significantly lower total hospital charges for patients with both ruptured and unruptured aneurysms, compared with clipping.[19] One-stage coiling of multiple aneurysms may further shorten the lengths of overall hospital stays and reduce overall total medical costs.

In addition to the retrospective nature, this study has several limitations. Because the treatment strategy was different between the 2 hospitals, case selection for 1-stage coiling was also different, which might affect our results. Coiling technique and perioperative medications have changed during the 10 years of the case-registration period; these changes might affect angiographic and clinical outcomes. Nonetheless, the results of this study may help determine treatment strategies for multiple intracranial aneurysms.

CONCLUSIONS

One-stage coiling of multiple intracranial aneurysms seems to be a safe and effective treatment with low morbidity and mortality.

REFERENCES

1. Nieuwkamp DJ, Setz LE, Algra A, et al. **Changes in case fatality of aneurysmal subarachnoid hemorrhage over time, according to age, sex, and region: a meta-analysis.** *Lancet Neurol* 2009;8:635–42
2. Kassell NF, Torner JC, Jane JA, et al. **The international cooperative study on the timing of aneurysm surgery. Part 2. Surgical results.** *J Neurosurg* 1990;73:37–47
3. Kaminogo M, Yonekura M, Shibata S. **Incidence and outcome of multiple intracranial aneurysms in a defined population.** *Stroke* 2003;34:16–21
4. Rinne J, Hernesniemi J, Puranen M, et al. **Multiple intracranial aneurysms in a defined population: prospective angiographic and clinical study.** *Neurosurgery* 1994;35:803–08
5. Juvela S. **Risk factors for multiple intracranial aneurysms.** *Stroke* 2000;31:392–97
6. Andaluz N, Zuccarello M. **Recent trends in the treatment of cerebral aneurysms: analysis of a nationwide inpatient database.** *J Neurosurg* 2008;108:1163–69
7. Mount LA, Brisma R. **Treatment of multiple intracranial aneurysms.** *J Neurosurg* 1971;35:728–30
8. Mizoi K, Suzuki J, Yoshimoto T. **Surgical treatment of multiple aneurysms: review of experience with 372 cases.** *Acta Neurochir (Wien)* 1989;96:8–14
9. Inagawa T. **Surgical treatment of multiple intracranial aneurysms.** *Acta Neurochir (Wien)* 1991;108:22–29
10. Vajda J. **Multiple intracranial aneurysms: a high risk condition.** *Acta Neurochir (Wien)* 1992;118:59–75
11. Rinne J, Hernesniemi J, Niskanen M, et al. **Management outcome for multiple intracranial aneurysms.** *Neurosurgery* 1995;36: 31–37, discussion 37–38
12. Hong T, Wang Y. **Unilateral approach to clip bilateral multiple intracranial aneurysms.** *Surg Neurol* 2009;72 (suppl 1):S23–28, discussion S28
13. Solander S, Ulhoa A, Vinuela F, et al. **Endovascular treatment of multiple intracranial aneurysms by using Guglielmi detachable coils.** *J Neurosurg* 1999;90:857–64
14. Xavier AR, Rayes M, Pandey P, et al. **The safety and efficacy of coiling multiple aneurysms in the same session.** *J Neurointerv Surg* 2012;4:27–30
15. Janssen PM, Visser NA, Dorhout Mees SM, et al. **Comparison of telephone and face-to-face assessment of the modified Rankin Scale.** *Cerebrovasc Dis* 2010;29:137–39
16. Roy D, Milot G, Raymond J. **Endovascular treatment of unruptured aneurysms.** *Stroke* 2001;32:1998–2004
17. Sonobe M, Yamazaki T, Yonekura M, et al. **Small unruptured intracranial aneurysm verification study: SUAVs study, Japan.** *Stroke* 2010;41:1969–77
18. Higashida RT, Lahue BJ, Torbey MT, et al. **Treatment of unruptured intracranial aneurysms: a nationwide assessment of effectiveness.** *AJNR Am J Neuroradiol* 2007;28:146–51
19. Hoh BL, Chi YY, Lawson MF, et al. **Length of stay and total hospital charges of clipping versus coiling for ruptured and unruptured adult cerebral aneurysms in the Nationwide Inpatient Sample database 2002 to 2006.** *Stroke* 2010;41:337–42

Phlebographic Study Does Not Show Differences Between Patients with MS and Control Subjects

M. Stefanini, S. Fabiano, F. Garaci, S. Marziali, A. Meschini, V. Cama, M. Fornari, S. Rossi, D. Centonze, R. Gandini, G. Simonetti, and R. Floris

ABSTRACT

BACKGROUND AND PURPOSE: Hypothetical correlation between chronic cerebrospinal venous insufficiency and MS has gained the attention of patients and the scientific community. Studies performed by echo-color Doppler ultrasonography have shown different results, and it is necessary to use more objective diagnostic techniques. The aim of our study was to evaluate the presence of stenoses affecting azygos veins and internal jugular veins by use of venography in patients with MS.

MATERIALS AND METHODS: We recruited 2 groups of subjects who underwent venography: the study group included 29 patients with MS and the control group included 15 healthy volunteers. The ileo-lumbar plexus, the azygos, and the internal jugular veins were selectively catheterized. We considered any cross-sectional area reduction of the venous lumen >50% to be a significant stenosis. Furthermore, blood pressure was measured in the studied vessels at the stenotic internal jugular veins.

RESULTS: Selective venography showed at least 1 significant venous stenosis in 84% of subjects examined, without significant difference between the study group and the control group. Positive venography chronic cerebrospinal venous insufficiency patterns were found in 50% of all subjects examined, without any significant difference between the 2 groups. The multivariate logistic regression analysis failed to assess any significant association between the presence of a positive venography and MS condition. The difference between the median blood pressure of stenotic and nonstenotic internal jugular veins was not statistically significant ($P = .46$).

CONCLUSIONS: Our data exclude any direct correlation between chronic cerebrospinal venous insufficiency and MS because venous abnormalities were equally present in both groups.

ABBREVIATIONS: AV = azygos vein; CCSVI = chronic cerebrospinal venous insufficiency; EDSS = Expanded Disability Status Scale; IJV = internal jugular vein; ILP = ileo-lumbar plexus

Chronic cerebrospinal venous insufficiency (CCSVI) is a nosological hypothesis that was discussed for the first time by the World Consensus Conference on Venous Malformations in Monte Carlo in September 2009. The CCSVI hypothesis suggests that inadequate blood flow from the CNS is caused by stenotic and/or malformative alterations of the main vessels draining blood from the brain and spine such as internal jugular veins (IJVs) and the azygos vein (AV). In this hypothesis, venous outflow is delayed or stopped; thus, toxic catabolites and iron cannot be removed and their deposition in the cerebral tissue is facili-

tated. This may cause a harmful effect, which may activate inflammatory response either in a direct and indirect way, leading to neuronal and oligodendrocytic damage.

MS is a chronic disease affecting the CNS with both neurodegeneration and inflammatory demyelination processes. The pathogenetic contribution of parenchymal iron deposition through proinflammatory action and oxidative damage has been hypothesized.[1-3]

A highly significant correlation between CCSVI and MS has been reported by Zamboni et al[4] in a cohort of patients evaluated by echo-color Doppler ultrasonography.

Moreover, Zamboni et al[5] led a pilot study enrolling 65 patients to assess the efficacy of percutaneous transluminal angioplasty of stenotic IJV and AV in the treatment of CCSVI. The authors of this study stated that the percutaneous treatment positively influenced the clinical condition and the quality of life of patients with MS when compared with the preoperative assessment.

At this time, several scientific endeavors examining the pres-

Table 1: Demographic and clinical characteristics

	Study Group	Control Group	P Value
No.	29	15	
Sex, M/F	10/19	11/4	.03
Age, y	46.4 ± 9.5	42.6 ± 7.1	.18
Disease duration, y	12.6 ± 6.7	NA	
Disease course (RR/SP/PP)	17/8/4	NA	
EDSS	3.6 ± 2.1 (1.0–7.0)	NA	

Note:—NA indicates not applicable; RR, relapsing-remitting; SP, secondary-progressive; PP, primary-progressive.

ence of CCSVI in MS are being undertaken, and other authors believe it is better for the health of patients to discourage potentially dangerous endovascular procedures until the question has been definitively clarified.[6]

Controversy exists to rule out whether the morphologic variability that occurs in the jugular veins should be considered a pathologic aspect or a normal anatomic variation, without any clinical consequences.

The aim of our study was to evaluate the presence of abnormalities and malformations affecting the IJV and AV by use of venography in patients with MS and to compare these findings with those from a control group of healthy volunteers.

MATERIALS AND METHODS

Subjects and Clinical Assessments

Between October 2011 and March 2012, we recruited 2 groups of subjects who underwent selective venography to evaluate the presence of morphologic and hemodynamic abnormalities involving the venous system. The study was approved by our institution's ethical committee, and all subjects signed a written informed consent for the procedure and personal data treatment.

The study group included 29 patients with MS free of relapse or steroid treatment in the 30 days before the study entry; the control group included 15 healthy volunteers who had no medical history of cerebrovascular or neurologic disorders.

The selection criteria used were age between 18–65 years, normal renal function, and diagnosis of MS according to 2005 McDonald Criteria.[7]

Exclusion criteria for both groups were pre-existing medical conditions known to be associated with neck pathology, history of cerebral congenital vascular malformations, cerebral venous thrombosis, and previous selective venous catheterization. Family members of patients with MS were not considered eligible as control subjects.

Demographic and clinical data of enrolled subjects are presented in Table 1.

Demographic and clinical information of patients with MS was derived from medical records. MS disease onset was defined as the first episode of focal neurologic dysfunction indicative of MS. Disease duration was estimated as the number of years from onset to the last assessment of disability. Disability was determined by a specially trained and certified examining neurologist by use of the Expanded Disability Status Scale (EDSS), a 10-point disease severity score derived from 9 ratings for individual neurologic domains.[8]

FIG 1. Selective catheterization of the azygos vein in a 37-year-old patient with secondary-progressive MS in which the injection of contrast medium showed the presence of a twisting of the AV associated with a shunt with the hemiazygous venous system. Note the opacification of the intraspinal venous plexus.

Phlebographic Procedures

All procedures were carried out in an angiographic suite by 2 interventional radiologists, a nurse, and an anesthesiologist. The patient was placed in the supine position; after a percutaneous transfemoral venous access was performed and a 5F sheath was introduced, the ileo-lumbar plexus (ILP), the AV, and the IJV were selectively catheterized by use of either a Vertebral or a Cobra 1 5F catheter (Terumo Europe, Leuven, Belgium). Contrast media was then injected at 3 mL/s at the origin of the ILP (10 mL of contrast media with the tip of the catheter at the level of the L5 vertebral body), at the confluence between the AV (10 mL of contrast) and the hemiazygous vein, and at the J3 level of the IJV corresponding to the upper part of the vein (10 mL of contrast media). The IJV was evaluated in the anterior-posterior oblique position to confirm the presence of alteration, whereas the AV was evaluated in the right posterior oblique projection (range, 10–15°). A 10-second phlebographic acquisition at 0.5 frames per second was performed with the patient holding his or her breath after a forced inspiration. In all patients, to confirm a normal contrast media outflow, we also performed a fluoroscopic visualization with the patient breathing normally. Furthermore, blood pressure was measured in the studied vessels at the J1 segment of the

FIG 2. Selective catheterization of the left and right internal jugular veins in a 35-year-old patient with relapsing-remitting MS. Venous stenosis at the level of the section J2 of the right IJV and of its origin is shown, with associated drainage in spinal venous plexus through a collateral branch. The left IJV does not present alterations in size and drainage.

FIG 3. Selective catheterization of the left internal jugular vein in a 41-year-old patient with primary-progressive MS. After injection of contrast medium, stenosis of segment J1 with reflux in both vertebral veins and opacification of the vertebral venous plexus is documented.

IJV, brachiocephalic trunk, superior vena cava, inferior vena cava, and transstenoses by use of a PrimeWire Prestige Pressure Guide Wire (Volcano Corporation, San Diego, California).

At the end of the procedure, manual compression was performed, and all patients were discharged at 4 hours after an ultrasonography evaluation of the puncture site.

In accordance with Zamboni et al,[5] we considered any cross-sectional area reduction of the venous lumen >50% to be a significant stenosis. We have also evaluated the presence of vascular malformations at the level of the AV and the IJV, such as twisting, septum, annulus, and atresia. Thus, we referred to the patterns of Zamboni et al to classify our findings and to consider as positive for the further analysis:

Type A was classified as a steno-obstruction of the proximal AV, associated with a closed stenosis of 1 of the 2 IJVs.

Type B was classified as significant stenoses of both IJVs and the proximal AV.

Type C was classified as bilateral stenosis in both IJVs, with a normal AV.

Type D was classified as multiple abnormalities of the AV.

Statistical Analysis

Clinical and demographic data are expressed, unless otherwise specified, as mean ± standard deviation. Comparisons between 2 groups of data were performed by the Student t test or by the Mann-Whitney test. The Fisher exact test was used for contingency analyses. The MS condition was analyzed as the dependent variable in logistic regressions with sex and age and either the presence of a positive venography or the presence of at least 1 significant stenosis as predictors. The associations between either the presence of a positive venography or the presence of at least 1 significant stenosis and disease severity were assessed by use of multivariate binary logistic regression models with dichotomous EDSS (cutoff point of 4.0) or progressive status (categorizing relapsing-remitting MS as nonprogressive) as outcome variables. The significance level was set at $P < .05$.

RESULTS

Selective venography showed at least 1 significant extracranial venous stenosis in 84% of all subjects examined (37/44), without any significant difference ($P > .5$) between the study group (25/29) and the control group (12/15).

Stenosis or malformations of the AV were observed in 9 subjects (Fig 1). Those of the right IJV were found in 19 subjects (Fig 2), stenosis or malformations of the left IJV in 17 subjects (Fig 3), and those of the ILP in 15 subjects (Fig 4).

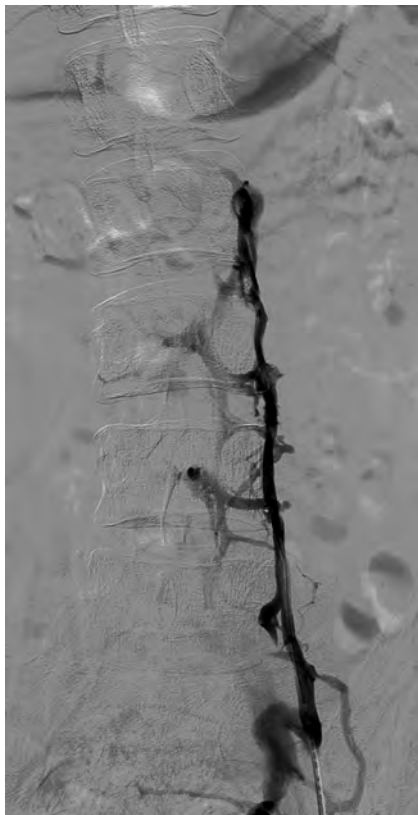Regression analysis confirmed the lack of association between

FIG 4. Selective catheterization of the ileo-lumbar plexus in a 33-year-old patient affected by relapsing-remitting MS. After injection of the contrast medium, opacification of the intraspinal venous plexus without opacification of the inferior vena cava is documented.

Table 3: Venographic pattern distribution

Type	Study Group	Control Group	RR MS	SP MS	PP MS
A	4	2	3	1	0
B	1	0	0	1	0
C	10	4	8	1	1
D	1	0	0	1	0

Note:—RR indicates relapsing-remitting; SP, secondary-progressive; PP, primary-progressive.

Table 4: Logistic regression (progressive MS as outcome variable)

	Coefficient	SE	OR	95% CI	P Value
Venography	−2.26	1.60	0.10	0.00–2.38	.15
Stenosis, n	0.76	0.76	2.14	0.48–9.56	.31
Age	0.10	0.05	1.12	1.00–1.24	.04
Sex, male	0.83	0.92	2.29	0.37–14.19	.37

Note:—SE indicates standard error.

$0.14-27.83$; $P = .61$). In the multivariate logistic regression analysis, including the presence of a positive venography and the number of significant stenoses among the independent variables, the only significant predictor of progressive status was age (Table 4). Furthermore, the probability of EDSS $\geq$4.0 was associated neither with the presence of at least 1 venous stenosis (OR = 0.48; 95% CI, 0.03–7.11; $P = .59$) nor with a positive venography (OR = 0.14; 95% CI, 0.00–3.36; $P = .22$) in logistic regressions correcting for age, sex, and disease duration. Finally, neither the number of venous stenoses nor the probability of having a positive venography differed significantly in patients treated with different immunomodulator agents during 2 years before the study entry or in never-treated patients (not shown).

The difference between the median blood pressure of stenotic IJVs (13.59 cm H$_2$O; range, 40.79–28.50 cm H$_2$O) and nonstenotic IJVs (16.314 cm H$_2$O; range, 8.57–28.55 cm H$_2$O) was not statistically significant ($P = .46$).

The difference between the mean blood pressure of stenotic AVs (19.03 cmH$_2$O; range, 10.87–27.19 cm H$_2$O) and nonstenotic AVs (18.35 cm H$_2$O; range, 9.51–38.06 cm H$_2$O) was not statistically significant ($P = .79$).

The mean procedural time was 28 minutes (range, 22–43 minutes).

No major or minor procedural and postprocedural complications were recorded, and patients were discharged 4 hours after the end of the percutaneous procedure.

DISCUSSION

CCSVI is a nosological hypothesis recently defined and characterized by abnormalities of the venous system of the neck and thorax causing defective blood drainage from the CNS.[4,5]

The recent description of CCSVI and its hypothesized strong correlation with MS has gained the attention of both the scientific community and patients, especially in consideration of the potential reversibility of this condition. This correlation appears to be confirmed by the studies of Zamboni et al,[5,9] who not only reported the presence of CCSVI in all patients affected by MS but also published a study on the feasibility of the endovascular treatment of this condition and its positive effects on MS progression. Despite several reports supporting this hypothesis,[10-14] in recent literature we found studies reporting disagreeing data and, in some cases, doubting the existence of CCSVI itself, all on the basis of echo-color Doppler ultrasonography evaluation.[2,15-20]

Table 2: Logistic regression (MS condition as outcome variable)

	Coefficient	SE	OR	95% CI	P Value
Venography	0.77	1.24	2.16	0.18–24.91	.53
Stenosis, n	−0.01	0.59	0.98	0.30–3.19	.98
Age	0.06	0.04	1.06	0.97–1.15	.16
Sex, male	−1.57	0.72	0.20	0.05–0.86	.03

Note:—SE indicates standard error.

the presence of MS condition and at least 1 significant venous stenosis (OR = 1.12; 95% CI, 0.17–7.07; $P = .89$), correcting for age and sex.

Positive venography patterns, as described by Zamboni et al,[4,5] were found in 50% of all subjects examined (22/44), without any significant difference ($P = .5$) between the study group (16/29) and the control group (6/15). In line with this, the multivariate logistic regression analysis, also including the number of significant stenoses as an independent variable, failed to assess any significant association between the presence of a positive venography and MS condition (Table 2).

Furthermore, type C was the more frequent hemodynamic pattern observed among positive subjects, without significant differences between study and control groups (10/16 versus 4/6, $P > .5$), as shown in Table 3, in which the 4 hemodynamic patterns were also stratified according to MS disease course.

We then assessed the association between the venographic findings and measures of disease severity among the MS group. The presence of at least 1 significant stenosis failed to predict progressive status, correcting for age and sex (OR = 1.97; 95% CI,
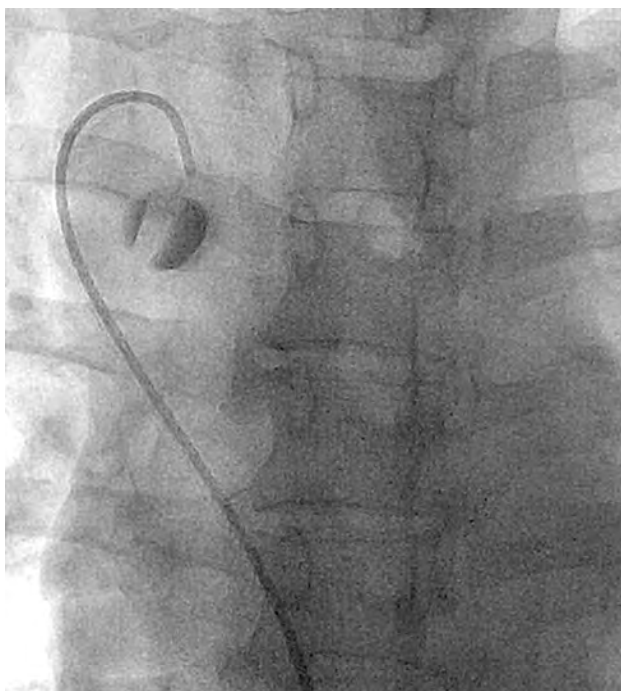
FIG 5. Selective catheterization of the azygos vein in a 45-year-old patient affected by relapsing-remitting MS. At the confluence of the azygos vein after administration of contrast medium, a valve is evident.
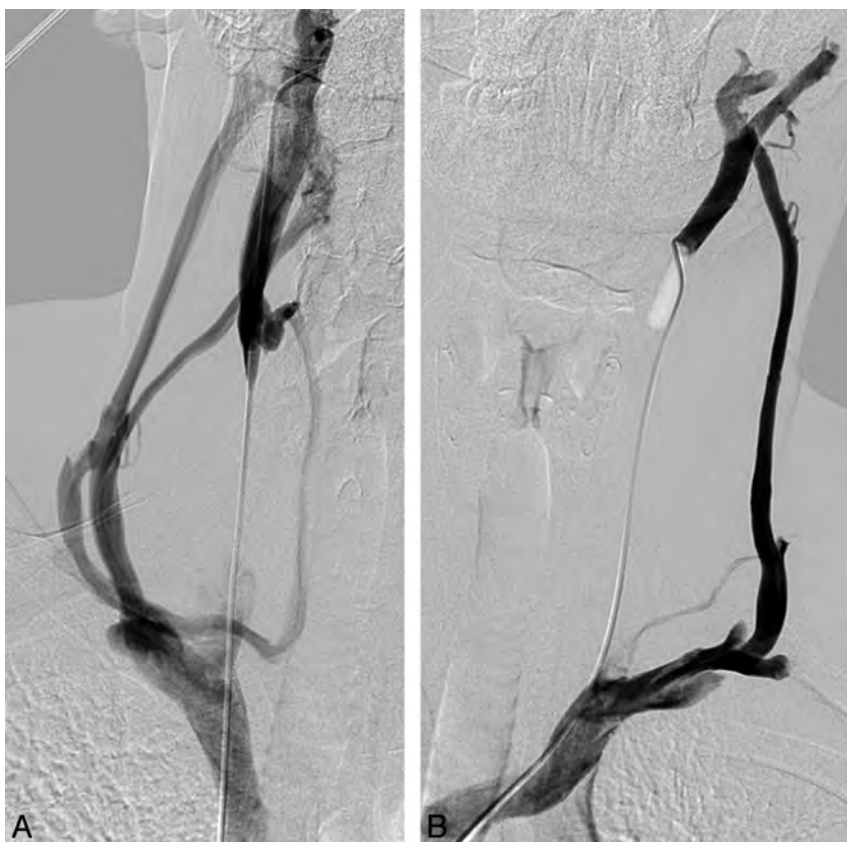

FIG 6. Selective catheterization of the internal jugular veins bilaterally (*A*, *-B*) in a 27-year-old control subject. Complete obstruction of the IJVs bilaterally with evidence of venous outflow through collateral circulation in the external jugular veins is shown.

Even recent studies, on the basis of MR imaging,[21-23] do not appear to demonstrate the association. The choice of a diagnostic method with high sensitivity and specificity is a key point. Nowadays, the most reliable techniques are compared with each other.[24]

We therefore decided to investigate the CCSVI hypothesis by use of venography, which is considered to be the reference standard[24] in evaluation of the venous system. The results of our study show significant discrepancies from those reported by Zamboni et al in terms of stenosis of the ILP (34% in our experience versus 9% of Zamboni et al[4]) and of the AV (20.5% versus 71%). Regarding the latter, the difference may be due to the fact that despite the evidence of what is defined by Zamboni et al as a "membranous obstruction at the junction of the AV with the superior vena cava" present in all patients (Fig 5), such finding never correlated with a reduced venous outflow or a significant abnormality in terms of intravenous pressure. Furthermore, these so-called "obstructions" were never associated with rachidian collaterals. In fact, AV arch valves have been reported to be common and should not necessarily be interpreted as pathologic findings.[25]

In 95% of the patients, IJV stenoses were found just above the termination of the IJVs. However, a reduced caliber of the vessel at such level was present in all patients and in all cases, and it did not correlate with a significant blood pressure gradient as reported by Zamboni et al. Because it has been demonstrated that the presence of jugular valves is very frequent, the reported reduction of caliber and/or stenosis of the IJVs, in the absence of collateral drainage vessels, probably should not be interpreted as a pathologic finding but as a physiologic condition caused by the valve's fibrous ring and contiguous anatomic structures (the collar bone and the sternocleidomastoid muscle).

Given our data, we believe that with venography it is not possible to define a pathologic condition characterized by the presence of a reduced blood drainage from the CNS as the result of stenotic alterations or venous malformations of the neck and thorax, which definitely correlates with MS. In our opinion, 1 of the major limitations of venography in the evaluation of CCSVI may be the lack of standardization in the interpretation of the images, which therefore tends to be operator-dependent, especially when no blood pressure gradient is associated with morphologic alterations. In our series, only 6 patients presented with the complete occlusion of 1 or both IJVs with the evidence of voluminous collateral drainage (Fig 6), and in only 1 case the stenosis of the AV was associated with rachidian drainage. However in all of these cases, no significant blood pressure gradient was recorded. In the remainder of our population, the interpretation of venograms could have been influenced not only by the operator's experience but also several parameters of contrast media injection

(volume, length, and site of injection) as well as patient breath dynamics.

We found no significant difference in terms of incidence of CCSVI between subjects with MS and control subjects; moreover, in both groups, the presence of at least 1 stenosis was higher, suggesting that these alterations are present in general population without a higher incidence in patients with MS. No significant association of single patterns of Zamboni et al venographic classification was found. Furthermore, considering single venographic type and MS forms, we are in line with Zamboni et al regarding the distribution of Type A (more frequent among relapsing-remitting MS), but we observed a different distribution of the other types.

The absence of any statistically significant correlations between extracranial venous stenosis and MS or disability progression may suggest that these alterations are unrelated to MS pathogenesis. This study, although with the statistical limitations of a small sample size, is the first to assess the relationship between CCSVI condition and MS, performing selective venography in both patients with MS and healthy volunteers.

CONCLUSIONS

Our data exclude any direct correlation between CCSVI and MS because venous stenosis was equally present in both groups. However, the possibility that they play a role in other pathologies cannot be excluded. Indeed, further studies are needed to standardize the evaluation of CCSVI, obtaining images from broader populations of patients and larger control groups, to assess definitive venographic features of this proposed clinical entity.

REFERENCES

1. Singh AV, Zamboni P. **Anomalous venous blood flow and iron deposition in multiple sclerosis.** *J Cereb Blood Flow Metab* 2009;29:1867–78
2. Worthington V, Killestein J, Eikelenboom MJ, et al. **Normal CSF ferritin levels in MS suggest against etiologic role of chronic venous insufficiency.** *Neurology* 2010;75:1617–22
3. Williams R, Buchheit CL, Berman NE, et al. **Pathogenic implications of iron accumulation in multiple sclerosis.** *J Neurochem* 2012;120:7–25
4. Zamboni P, Galeotti R, Menegatti E, et al. **Chronic cerebrospinal venous insufficiency in patients with multiple sclerosis.** *J Neurol Neurosurg Psychiatry* 2009;80:392–99
5. Zamboni P, Galeotti R, Menegatti E, et al. **A prospective open-label study of endovascular treatment of chronic cerebrospinal venous insufficiency.** *J Vasc Surg* 2009;50:1348–58
6. Khan O, Filippi M, Freedman MS, et al. **Chronic cerebrospinal venous insufficiency and multiple sclerosis.** *Ann Neurol* 2010;67:286–89
7. Polman CH, Reingold SC, Edan G, et al. **Diagnostic criteria for multiple sclerosis: 2005 revisions to the "McDonald Criteria."** *Ann Neurol* 2005;58:840–46
8. Kurtzke JF. **Rating neurologic impairment in multiple sclerosis: an expanded disability status scale (EDSS).** *Neurology* 1983;33:1444–52
9. Malagoni AM, Galeotti R, Menegatti E, et al. **Is chronic fatigue the symptom of venous insufficiency associated with multiple sclerosis? A longitudinal pilot study.** *Int Angiol* 2010;29:176–82
10. Al-Omari MH, Rousan LA. **Internal jugular vein morphology and hemodynamics in patients with multiple sclerosis.** *Int Angiol* 2010;29:115–20
11. Beggs C. **Multiple sclerosis appears to be associated with cerebral venous abnormalities.** *Ann Neurol* 2010;68:560–61
12. Hojnacki D, Zamboni P, Lopez-Soriano A, et al. **Use of neck magnetic resonance venography, Doppler sonography and selective venography for diagnosis of chronic cerebrospinal venous insufficiency: a pilot study in multiple sclerosis patients and healthy controls** *Int Angiol* 2010;29:127–39
13. Simka M, Zaniewski M. **Reinterpreting the magnetic resonance signs of hemodynamic impairment in the brains of multiple sclerosis patients from the perspective of a recent discovery of outflow block in the extracranial veins.** *J Neurosci Res* 2010;88:1841–45
14. Zivadinov R, Schirda C, Dwyer MG, et al. **Chronic cerebrospinal venous insufficiency and iron deposition on susceptibility-weighted imaging in patients with multiple sclerosis: a pilot case-control study.** *Int Angiol* 2010;29:158–75
15. Doepp F, Paul F, Valdueza JM, et al. **No cerebrocervical venous congestion in patients with multiple sclerosis.** *Ann Neurol* 2010;68:173–83
16. Centonze D, Floris R, Stefanini M, et al. **Proposed chronic cerebrospinal venous insufficiency criteria do not predict multiple sclerosis risk of severity.** *Ann Neurol* 2011;70:51–58
17. Garaci F, Marziali S, Meschini A, et al. **Brain hemodynamic changes associated with chronic cerebrospinal venous insufficiency are not specific to multiple sclerosis and do not increase its severity.** *Radiology* 2012;265:233–39
18. Floris R, Centonze D, Fabiano S, et al. **Prevalence study of chronic cerebrospinal venous insufficiency in patients with multiple sclerosis: preliminary data.** *Radiol Med* 2012;117:855–64
19. Mayer CA, Pfeilschifter W, Lorenz MW, et al. **The perfect crime? CCSVI not leaving a trace in MS.** *J Neurol Neurosurg Psychiatry* 2011;82:436–40
20. Valdueza JM, Doepp F, Schreiber SJ, et al. **What went wrong? The flawed concept of cerebrospinal venous insufficiency.** *J Cereb Blood Flow Metab* 2013;33:657–68
21. Sundström P, Wåhlin A, Ambarki K, et al. **Venous and cerebrospinal fluid flow in multiple sclerosis: a case-control study.** *Ann Neurol* 2010;68:255–59
22. Wattjes MP, van Oosten BW, de Graaf WL, et al. **No association of abnormal cranial venous drainage with multiple sclerosis: a magnetic resonance venography and flow-quantification study.** *J Neurol Neurosurg Psychiatry* 2011;82:429–35
23. Zivadinov R, Cutter G, Marr K, et al. **No association between conventional brain MR imaging and chronic cerebrospinal venous insufficiency in multiple sclerosis.** *AJNR Am J Neuroradiol* 2012;33:1913–17
24. Zaharchuk G, Fischbein NJ, Rosenberg J, et al. **Comparison of MR and contrast venography of the cervical venous system in multiple sclerosis.** *AJNR Am J Neuroradiol* 2011;32:1482–89
25. Yeh BM, Coakley FV, Sanchez HC, et al. **Azygos arch valves: prevalence and appearance at contrast-enhanced CT.** *Radiology* 2004;230:111–15

Phlebographic Study between Patients with MS and Control Subjects: The Ethical Profile

The term and the concept of chronic cerebrospinal venous insufficiency (CCSVI) were coined by the Italian vascular surgeon Paolo Zamboni, who proposed compromised blood drainage from the central nervous system in patients with MS, caused by strictures and valves in the major veins of the neck.

Very soon after the description in 2009 of CCSVI as the major, if not unique, causal factor of MS,[1] uncontrolled angioplastic or stent placement procedures in the jugular veins, initially termed "liberation therapies," were increasingly offered to patients with the disease. The "CCSVI community" grew rapidly on the Web and gained the attention of the media and of the general public. As a result of misunderstanding and oversimplification, not only patients with MS but also patients with other neurodegenerative disorders such as amyotrophic lateral sclerosis decided to undergo the angioplastic procedure, even if discouraged by their doctors.

In their first publication, Zamboni et al[1] described venous abnormalities, identified through combined transcranial and extracranial color Doppler high-resolution examination (TCCS-ECD) and confirmed by selective venography of the azygous and jugular venous system, to be dramatically associated with MS only because they were never detectable in healthy individuals or in subjects with other neurologic diseases. In response to criticisms coming from other research groups who failed to replicate the TCCS-ECD findings of Zamboni et al (including the authors of the study published in this issue of the *American Journal of Neuroradiology* and Centonze et al[2]), the CCSVI community proposed the argument that CCSVI detection through TCCS-ECD is a very tough task, requiring appropriate training and specific equipment. In the absence of specific training, operator abilities, and the proper TCCS-ECD machine, only objective venographic evaluations were claimed by Zamboni et al[1] to be suitable to detect CCSVI.

In this atmosphere, the proposal coming from the authors of this study to perform selective venography in patients with MS appeared to me and to the other members of the ethical committee of my institution crucial to provide a final answer to the CCSVI scientific debate, but only if combined with blind venographic studies in the appropriate control subjects. Proper controls were not investigated by Zamboni et al or by others, and in fact the 2009 study of Zamboni et al[1] only reported unblinded results in control subjects who underwent the phlebographic procedure but were not matched with the patients with MS.

In general terms, experimental science cannot do without experimentation due to intrinsic epistemologic requirements. In particular, experimentation is essential for the progress of medical science. As stated in *Human Rights and Biomedicine*[3], medical progress is based on research, an essential part of which is the realization of studies that include human subjects. In these studies, however, the interests and welfare of the human being will prevail over the sole interest of society or science.

The ethical values regarding experimentation on human beings are, in hierarchical order: the defense of life and of the person, which is the key point of ethics; the validity of the therapeutic principle; and the social theme connected to scientific progress. In accordance with the principle of social solidarity, it is legitimate to ask an individual to share in the risk for the good of the entire society of which he or she is a member, keeping in mind, however, that there is, in the individual, the global value and fundamental reason of existence of society itself.

In experimentation on healthy volunteers, such a principle is applied that legitimizes experimentation on the basis of the following conditions:

1) The first condition is that the consensus must be free, explicitly informed, and personal and regard a healthy (not presumed to be) individual who is not connected by work or position to the person conducting the experiment;
2) The risk that the volunteer is subjected to must not exceed the limit of the defense of the life and integrity of that person. Within these limits, the principle of proportionality between risks and benefits is always in force: clinical studies of insufficient or doubtful scientific validity cannot be ethically accepted. The experimenter must always be ready to interrupt the experiment in the event that the informed consensus is withdrawn or unforeseen risks arise.

The invasiveness of the phlebographic procedure for patients and healthy individuals was well taken into account when the

clinical research plan was approved by our institutional ethical committee. Nonetheless, the advancements in knowledge stemming from well-designed and conducted research on CCSVI were finally judged to beneficially affect the lives of thousands of patients with MS and of their doctors, who rely on scientific evidence to make their decisions.

REFERENCES

1. Zamboni P, Galeotti R, Menegatti E, et al. **Chronic cerebrospinal venous insufficiency in patients with multiple sclerosis.** *J Neurol Neurosurg Psychiatry* 2009;80:392–99

2. Centonze D, Floris R, Stefanini M, et al. **Proposed chronic cerebrospinal venous insufficiency criteria do not predict multiple sclerosis risk or severity.** *Ann Neurol* 2011;70:51–58

3. **Convention on Human Rights and Biomedicine.** Oviedo, Spain, April 4, 1997. http://conventions.coe.int/Treaty/en/Treaties/Html/164.htm

M. G. Marciani
Professor of Neurology and President of
Ethical Committee of the Fondazione
Policlinico Tor Vergata, Rome, Italy

MR Imaging Evolution of Endoscopic Cranial Defect Reconstructions Using Nasoseptal Flaps and Their Distinction from Neoplasm

K.O. Learned, N.D. Adappa, J.Y.K. Lee, J.G. Newman, J.N. Palmer, and L.A. Loevner

ABSTRACT

BACKGROUND AND PURPOSE: Endoscopic endonasal approach is the procedure of choice for the resection of ventral skull base neoplasms, with defect closure requiring multilayer reconstruction. This study evaluates the temporal MR imaging evolution of nasoseptal flaps and free grafts used in endoscopic skull base reconstruction.

MATERIALS AND METHODS: Sixty-nine follow-up brain MRIs of 22 patients who had endoscopic skull base reconstruction using 26 nasoseptal flaps combined with 8 collagen-matrix dural grafts, 10 fascia lata grafts, and 10 intracranial fat grafts were retrospectively reviewed. Temporal changes in signal intensity, enhancement, thickness, and the configuration of reconstructive layers were evaluated. Tissue with signal intensity or enhancement different from that of normal evolving reconstructive layers at the surgical bed was evaluated, and its association with clinically confirmed tumor was assessed with the Fisher exact test.

RESULTS: All normal reconstructive layers were retracted to cranial defects and showed maturation of imaging features within 2–6 months. The immediate postoperative T2-isointensity to brain and enhancement of nasoseptal flaps persisted, but the flap thickness was reduced by 20%–30% (average thickness, 4.5 ± 1.3 mm); additionally, the C shape and vascular pedicle of the nasoseptal flaps became indistinct, but the flap location remained unchanged. The initial appearance of the nonenhancing fascia lata with variable T2 signal intensity became enhancing with increasing T2-hypointensity and a graft-thickness reduction of ≥50% (average thickness, 3.5 ± 1.6 mm). All fat grafts showed progressive resorption. In 6 patients, abnormal tissue represented residual or recurrent tumor ($P = .0001$).

CONCLUSIONS: Maturation and stability of multilayer endoscopic skull base reconstructions on MR imaging occurs within 2–6 months postoperatively. Understanding of the normal imaging evolution of endoscopic skull base reconstructions is essential to distinguish them from neoplasms.

ABBREVIATIONS: ASB = anterior skull base; CSB = central skull base; EEA = endoscopic endonasal approach; ESBR = endoscopic skull base reconstruction; NSF = nasoseptal flap

The traditional open craniofacial surgical approach to the ventral skull base allows a wide exposure, but at the cost of craniotomy, brain and cranial nerve retraction, and facial incision. The endoscopic transsphenoidal adenohypophysectomy is the standard in pituitary surgery. More recently, the use of the endoscopic endonasal approach (EEA) has expanded beyond the sella, and it is now routinely used for the resection of a spectrum of sinonasal, ventral skull base, and intracranial pathologies.[1-6] Endoscopic skull base reconstruction (ESBR) with multilayer closure of the cranial base defect using vascularized tissues has become the repair method of choice in EEA, resulting in low CSF leak rates comparable with those in the open surgical approach.[7-10] The workhorse of ESBR in EEA is the vascularized pedicled nasoseptal flap (NSF), which is based on the nasoseptal branch of the sphenopalatine artery (Fig 1A, -B).[11,12] A combination of intradural fat graft, inlay subdural collagen matrix, and/or the fascia lata with onlay NSF is effective in repairing cranial defects (Fig 1C).[7-10] Most cranial defects are sufficiently closed by a single NSF elevated from one side of the nasal septum. Larger, extended cranial defects may require harvesting of bilateral nasoseptal flaps from both sides of the nasal septum and additional free mucosal grafts to cover the entire defect.

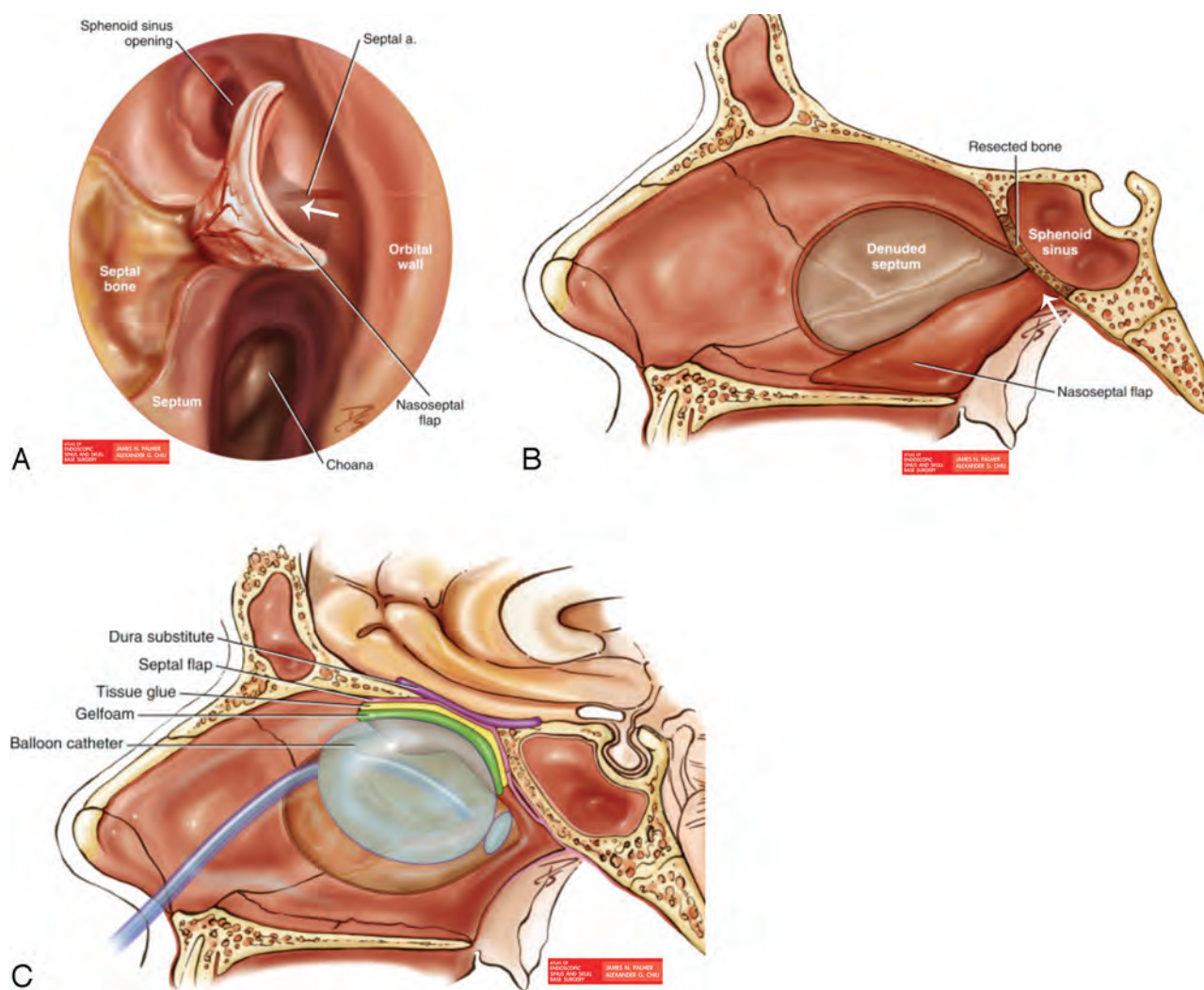Kang et al[13] described the MR imaging appearance of ESBR

FIG 1. Multilayer ESBR using NSF. *A*, Endoscopic coronal view of the nasal cavity illustrates harvesting of the NSF from the nasal septum with the preserved septal artery vascular pedicle (*arrow*) arising from the sphenopalatine artery. *B*, Sagittal view of the harvested NSF shows that the flap is anchored by its pedicle (*arrow*), leading toward the ipsilateral sphenopalatine foramen. *C*, Sagittal drawing of the ESBR shows inlay dura substitute (such as collagen matrix, fascia lata) and onlay mucosal closure with an NSF (labeled as a septal flap). Autologous fat graft may be placed above the dura substitute layer to fill the intracranial resection bed. The NSF is held in place by biologic tissue glue. Reconstruction is bolstered with nasal sponges and/or a balloon catheter to prevent dislodging during the immediate postoperative period. Reprinted with permission from *Atlas of Endoscopic Sinus and Skull Base Surgery*. Palmer JN, Chiu AG. Copyright Elsevier, 2013.[12]

using NSFs to repair the surgically created skull base defects in a small cohort of patients following transsphenoidal resection of pituitary adenomas.[13] Recently, Learned et al[14] reported the immediate postoperative MR imaging evaluation of ESBR utilizing NSFs in a spectrum of sinonasal and skull base tumors resected using EEAs with defects along the entire ventral skull base. In the immediate postoperative period, NSFs have a C-shaped configuration on coronal and/or sagittal planes and avid enhancement, with the associated free grafts closely abutting the NSFs and showing no enhancement.[13,14] Follow-up MR imaging is routinely performed for neoplastic surveillance in patients following EEA skull base resections and reconstructions. The normal evolution of the multilayer reconstructions following EEA is not well understood and can be mistaken for recurrent or persistent tumor. This study evaluates the temporal MR imaging appearances of grafts and NSFs used in ESBR.

MATERIALS AND METHODS
Subjects
Our institutional review board approved the retrospective review of our skull base surgery data base from January 2008 to May 2013 to identify 22 patients (13 men, 9 women; mean age, 54 years) who had undergone EEA skull base surgery, multilayer ESBR using NSFs, and brain MR imaging surveillance within 48 hours following surgery and thereafter for follow-up. The spectrum of pathologies included sinonasal tumors (36%), clival chordomas and chondrosarcomas (18%), and intracranial neoplasms (46%). Surgically created skull base defects included anterior skull base (ASB) (41%), central skull base (CSB) (36%), and clival defects (23%). In 22 ESBRs, 26 NSFs (18 single and 8 bilateral flaps) were used with a combination of 8 collagen matrix dural grafts (Dura-Gen; Integra Life Sciences, Plainsboro, New Jersey; Surgisis Biodesign Dural graft; Cook Medical, Bloomington, Indiana), 10

Table 1: Patient clinical data

Pathologies (No. of Patients and Average Tumor Size)	Skull Base Defects	ESBR Tissues (No. of Patients)	Length of MRI Follow-Up (mo)	Adjuvant Therapy (No. of Patients)
Esthesioneuroblastoma ($n = 6$; 2.5 cm)	ASB	F, FL, NSF, FM ($n = 1$) D, NSF ($n = 3$) D, NSF, FM ($n = 2$)	9–32	Radiation ($n = 4$), Chemoradiation ($n = 2$)
Sinonasal endocrine carcinoma ($n = 1$; 4.0 cm)	ASB	F, FL, NSF, FM ($n = 1$)	16	Chemoradiation ($n = 1$)
Sinonasal undifferentiated carcinoma ($n = 1$; 2.2 cm)	ASB	D, NSF ($n = 1$)	3	Chemoradiation ($n = 1$)
Chondrosarcoma ($n = 1$; 2.5 cm)	Clivus	D, NSF ($n = 1$)	21	Radiation ($n = 1$)
Chordoma ($n = 3$; 2.0 cm)	Clivus	NSF ($n = 2$) F, FL, NSF ($n = 1$)	9–21	Radiation ($n = 2$)
Meningioma ($n = 4$; 2.2 cm)	ASB CSB Clivus	D, NSF ($n = 1$) F, FL, NSF ($n = 2$) F, FL, NSF ($n = 1$)	3–41	Radiation ($n = 1$)
Craniopharyngioma ($n = 1$; 3.5 cm)	CSB	F, FL, NSF ($n = 1$)	6	
Pituicytoma ($n = 1$; 3.1 cm)	CSB	F, FL, NSF ($n = 1$)	13	Radiation ($n = 1$)
Pituitary macroadenoma ($n = 4$; 3.4 cm)	CSB	NSF ($n = 1$) F, NSF ($n = 1$) FL, NSF ($n = 1$) F, FL, NSF ($n = 1$)	6–27	Radiation ($n = 1$)

Note:—ASB indicates cribriform plates, crista galli, and/or ethmoid fovealis; CSB, planum sphenoidale, tuberculum sella, sella, and/or dorsum sella; D, collagen matrix dural graft; F, intracranial fat; FL, fascia lata; FM, free mucosa.
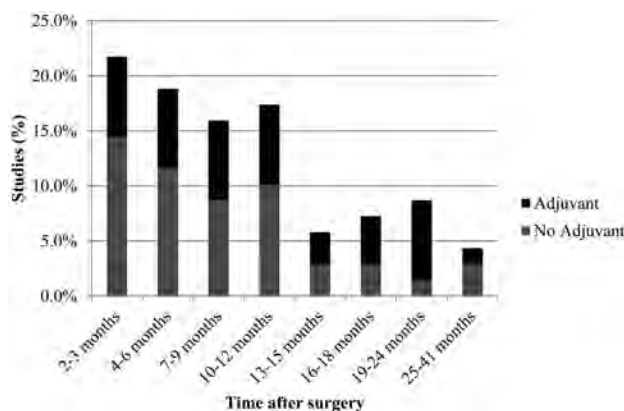

FIG 2. Graft shows the percentage of follow-up MR imaging studies performed before or without adjuvant treatment (*gray bar*) and after adjuvant treatment (*black bar*) versus postoperative time intervals.

autologous fascia lata grafts, 10 intracranial fat grafts, and 4 additional free mucosal grafts. Table 1 summarizes patient clinical data.

Imaging Methods

Sixty-nine follow-up MRIs were obtained at 2- to 6-month intervals, depending on tumor histology, adjuvant therapy, clinical status, and surveillance paradigm. The length of follow-up ranged from 3 to 41 months, with an average of 16.4 months. We categorized the follow-up MRIs of the entire cohort according to the time at which they were obtained after surgery: first follow-up at 2–3 months; subsequently, every 3-month-interval follow-up during the first 1–2 years after surgery; and every 6-month-interval follow-up thereafter. The graph in Fig 2 summarizes the percentage of serial follow-up MRIs after surgery and adjuvant treatment.

Brain MRIs were performed at 1.5T ($n = 55$) and 3T ($n = 14$) (Signa and Optima; GE Healthcare, Milwaukee, Wisconsin; and Espree, Avanto, Verio and Skyra; Siemens, Erlangen, Germany), including thin-section images of the sella turcica/ventral skull base with parameters detailed in On-line Tables 1 and 2. All patients received intravenous administration of 0.1-mmol/kg gadolinium (MultiHance; Bracco Diagnostics, Princeton, New Jersey).

Imaging and Statistical Analysis

All images were reviewed together in consensus by 2 neuroradiologists subspecialized in head and neck imaging. The NSFs and free grafts were evaluated for temporal changes in T2 signal intensity (in comparison with the gray matter and white matter of the brain parenchyma), the presence of enhancement, and the average thickness. The C-shaped configuration of enhancing NSFs in our cranial base reconstructions was best demonstrated on an enhanced sagittal and/or coronal plane. The free grafts were located above the enhancing NSFs in multilayer ESBRs. Therefore, the average of 2 maximal flap and graft thickness measurements at 2 different locations on enhanced sagittal and/or coronal planes was recorded. All studies of each patient were evaluated at the same time in our retrospective study to assess the temporal change of ESBRs. Imaging assessment was correlated with surgical techniques and clinical follow-up. The presence of tissue with signal-intensity or enhancement different from that of normal evolving reconstructive layers was also evaluated, and its MR imaging characteristics were compared with those of the neoplasm on preoperative MR imaging. The association of the abnormal tissue that was similar to the preoperative neoplasm and clinically confirmed tumor was assessed with the Fisher exact test, using the Statistical Package for the Social Sciences, Version 20.0 (IBM, Armonk, New York).

RESULTS

All normal reconstructions demonstrated retraction of the reconstructive layers to the cranial defects with reduction in thickness and showed maximal alterations of the imaging features within 2–6 months, with little or no further change on subsequent imaging. Fifty-five percent of follow-up MR imaging studies were performed before or without adjuvant treatment and 45%, af-
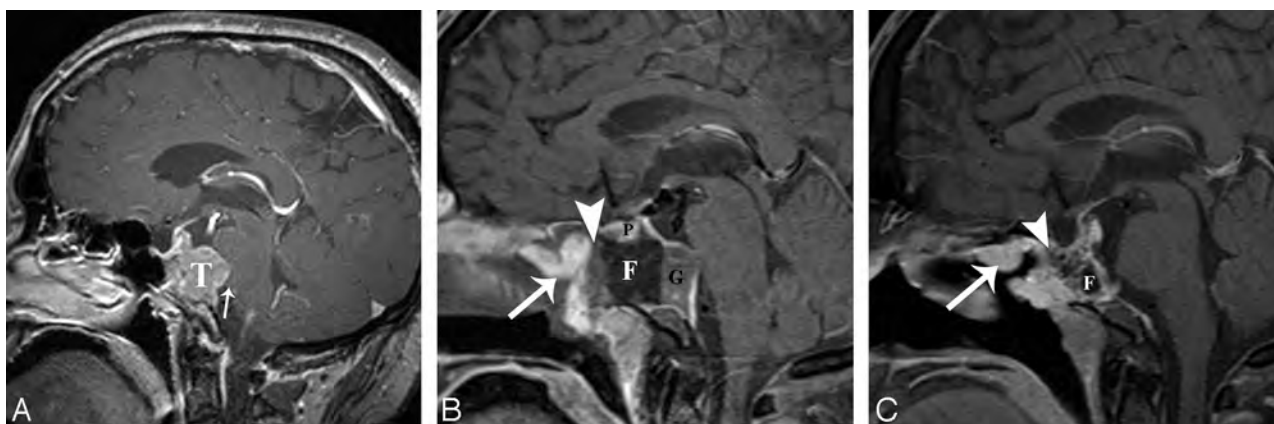
FIG 3. A 47-year-old man with normal evolution of the ESBR after EEA gross total resection and adjuvant radiation of a clival chordoma. *A*, Preoperative sagittal enhanced T1WI shows tumor (T) eroding the upper clivus and compressing the ventral pons (*arrow*). *B*, Immediate postoperative sagittal enhanced fat-saturated T1WI shows an enhancing C-shaped NSF covering the clival defect (*arrow*), abutting the nonenhancing fascia lata (*arrowhead*) and clivectomy fat packing (F). Nonenhancing Gelfoam (Phadia, Uppsala, Sweden) and blood (G), enhancing pituitary (P). *C*, Five-month follow-up sagittal enhanced fat-saturated T1WI shows a solidly enhancing slightly thinner NSF and retraction of the reconstruction with the enhancing fascia lata (*arrowhead*) inseparable from granulation tissue/resorbing fat (F). Marked nodularity along the anterior and inferior portions of the NSF relates to retraction and incorporation of the flap into the newly enhancing free grafts and granulation tissues.

ter adjuvant treatment (Fig 2). The patients' sinonasal inflammatory mucosal changes and adjuvant radiation or chemoradiation had no appreciable effect on the normal imaging evolution of ESBRs (Figs 3 and 4). The appearance of the different components of the flaps and their changes with time to become stable within 2–6 months are summarized in Table 2 and presented in detail below.

The immediate postoperative T2-isointensity to the brain (mostly similar to gray matter) and solid enhancement of 21 NSFs persisted, and the flap thickness was reduced by 20%–30% (average thickness, 4.5 ± 1.3 mm) (Figs 3 and 4). Their immediate postoperative distinctive C shape and vascular pedicle configurations became less well-defined on follow-up imaging as the NSFs incorporated into the newly enhancing free grafts and granulation tissues, but the flap location remained unchanged (Fig 3). The markedly nodular appearance of the NSF was noted in 4 of our patients (18%) who did not have tumor recurrence (Fig 3C).

Five NSFs without enhancement on immediate postoperative MR imaging demonstrated 1- to 5-mm-thick solid enhancing tissue on follow-up. Similarly, 4 free mucosal grafts without enhancement on immediate postoperative MR imaging showed 1- to 5-mm-thick solid enhancement on follow-up. Their enhancement correlated to clinically evident healing granulation tissue and/or mucosalization at the graft sites.

The immediate postoperative nonenhancing fascia lata with variable T2 signal intensity became mildly enhancing with increasing T2-hypointensity, and the graft thickness decreased by ≥50% (average thickness, 3.5 ± 1.6 mm) (Figs 3 and 4). The collagen matrix dural grafts remained nonvisible to ≤2 mm, and the immediate postoperative nonenhancing thin grafts became inseparable from enhancing granulation tissue at the reconstructed skull base on follow-up imaging (Fig 5). All fat grafts showed progressive resorption with ≥50% reduction in volume within 2–6 months and near disappearance by 14 months (Figs 3 and 4).

The nodular tissue with variable T2 signal intensity and en-

hancement different from the normal evolution of reconstructive layers was seen at the interface of the reconstruction and tumor bed in 6 patients (1 sinonasal carcinoma, 1 chordoma, 1 meningioma, and 3 pituitary tumors) (Fig 5). The MR imaging characteristics of the nodular tissue were similar to those of the primary neoplasm seen on the preoperative MR imaging. In the patients with sinonasal carcinoma, recurrence occurred at the margin of the radiation field. The presence of the abnormal tissue was associated with neoplastic residua in 5 patients and recurrence in 1 patient ($P = .0001$).

DISCUSSION
Endoscopic Skull Base Surgery and Cranial Defect Reconstruction
The endonasal approach provides a direct and less invasive surgical corridor to primarily midline sinonasal, skull base, and intracranial neoplasms along the ventral cranial base, with equivalent or better gross total resection compared with open surgery.[1-7] Open skull base surgery, classically in the form of combined craniotomy and a transfacial or endonasal endoscope-assisted approach, is repaired with the vascularized pericranial flap routinely sutured to the edge of the dural defect. Cranial defect closure in EEA has unique challenges, including the inability to suture the reconstructive layers and the difficulty in using a pericranial flap. A variety of biologic glues and temporary supportive nasal bolsters has been used to secure the ESBR layers to the cranial defect, while awaiting granulation and incorporation of the reconstructive tissues into the surgical bed.[8-10] The small dural defects have been successfully closed with nonvascularized free grafts such as seen in pituitary surgery. With the increasing size of cranial defects in EEA for resection of larger tumors and with deeper intra-arachnoid dissections and increased exposure to the cisterns, repair techniques using nonvascularized free grafts have shown unacceptable postoperative CSF leak rates.[7,8] To allow maximal resection with CSF leak rates similar to those in open surgical approaches, ESBR in the EEA routinely necessitates
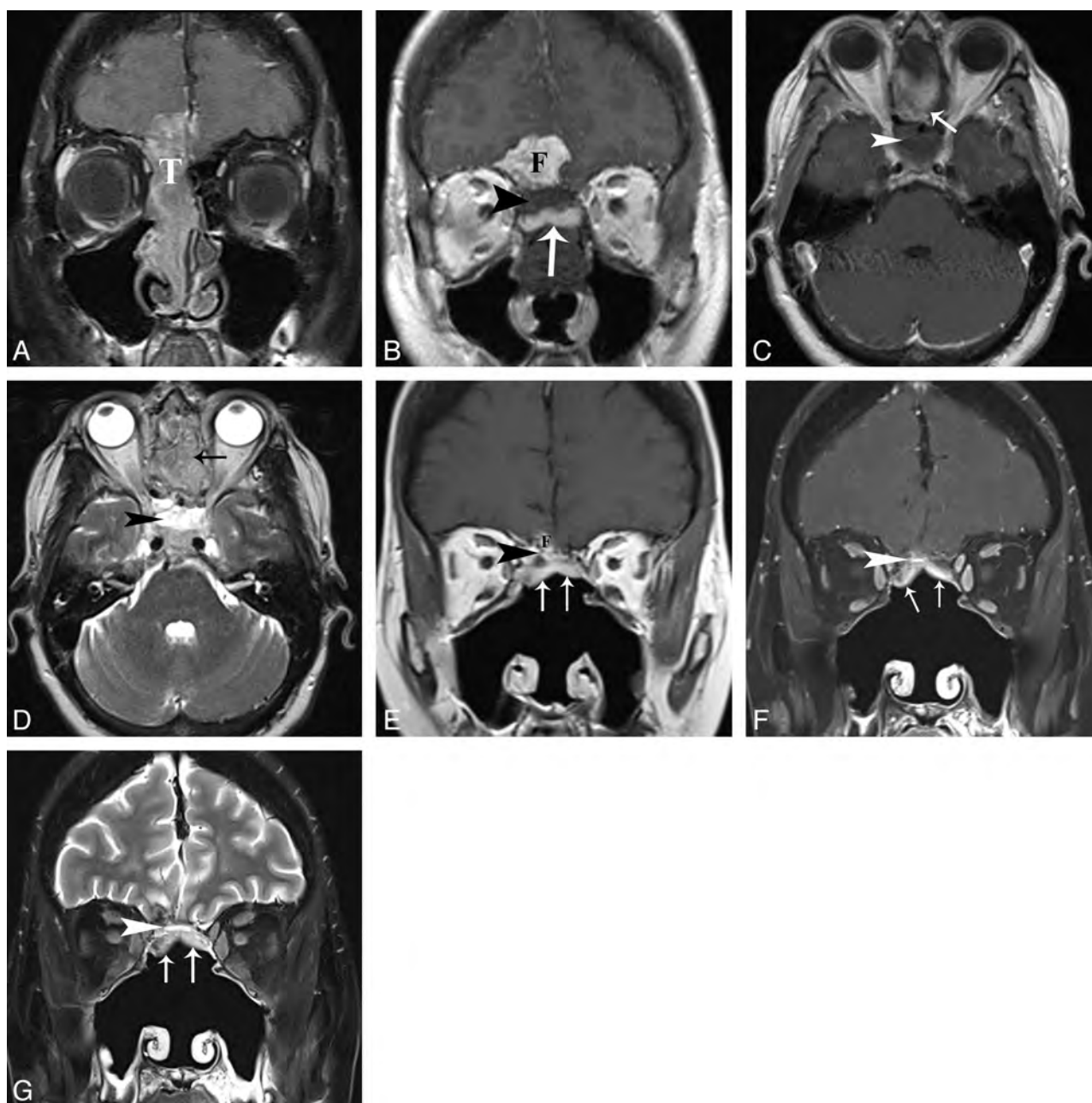
FIG 4. A 58-year-old woman status post transcribriform resection and adjuvant chemoradiation for sinonasal neuroendocrine carcinoma and NSF misinterpreted as a neoplasm. *A*, Preoperative coronal enhanced fat-saturated T1WI shows enhancing tumor (T) with intracranial extension. *B* and *C*, Immediate postoperative coronal and axial enhanced T1WI shows fat (F) in the subfrontal bed, nonenhancing T1-hypointense fascia lata (*arrowheads*) at the bone defect, and mucosal closure with enhancing NSF (*arrows*). *D*, Immediate postoperative axial T2WI shows T2-hyperintense fascia lata (*arrowhead*) and T2-isointense NSF (*arrow*). *E*, Three-month follow-up coronal enhanced T1WI shows normal evolution of the ESBR with retraction to the defect; significant resorption of intracranial fat graft (F); and a thin enhancing fascia lata (*arrowhead*) above the solidly enhancing NSF (*arrows*), mistaken for neoplasm in the official report. *F* and *G*, Sixteen-month follow-up (3 months after completion of chemoradiation) coronal fat-saturated enhanced T1WI and T2WI show little change of the enhancing fascia lata (*arrowheads*) and solidly enhancing T2-isointense NSF (*arrows*).

multilayer reconstruction using a vascularized NSF. The NSF is a pedicled vascular flap based on the posterior septal artery, a branch of the sphenopalatine artery.[11] This robust vascularized flap has become the mainstay in ESBR, with reported postoperative CSF leak rates in 5%–10% of cases, a range similar to that in open procedures.[7,8]

Our ESBRs were performed in a multilayer stepwise fashion, beginning intracranially and advancing out to the sinona-

sal mucosa, using a combination of autologous fat filling the intracranial surgical bed, subdural inlay collagen matrix underneath the edges of the dural defect and/or inlay-onlay fascia lata, and the final mucosal onlay closure with single or bilateral NSFs (Fig 1). Occasionally, additional free mucosal grafts taken from the nasal septum or turbinates were required to cover the far anterior edge of the cribriform defects, which were not reachable by the pedicled NSF (Table 1).

Table 2: MR imaging evolution of ESBR from the immediate postoperative period to stability on follow-up

|	Immediate Postoperative MRI	Follow-Up MRI at 2–6 Months
NSF	Solid enhancement, T2-isointensity to brain (mostly similar to gray matter), distinctive C shape and vascular pedicle configurations	Persistent solid enhancement, persistent T2-isointensity to brain (mostly similar to gray matter), thickness reduction by 20%–30%, average thickness of 4.5 mm Less well-defined C shape and vascular pedicle configurations, unchanged flap location
Fascia lata	Nonenhancing, variable T2 signal intensity	Mildly enhancing, increasing T2-hypointensity, thickness reduction by ≥50%, average thickness of 3.5 mm
Collagen matrix dural graft	Nonenhancing, nonvisible to ≤2 mm	Inseparable from enhancing granulation tissue at the reconstruction site, nonvisible to ≤2 mm
Fat graft	Fat signal intensity fills intracranial surgical bed	Fat signal intensity in retracted intracranial surgical bed, progressive resorption with volume reduction by ≥50%
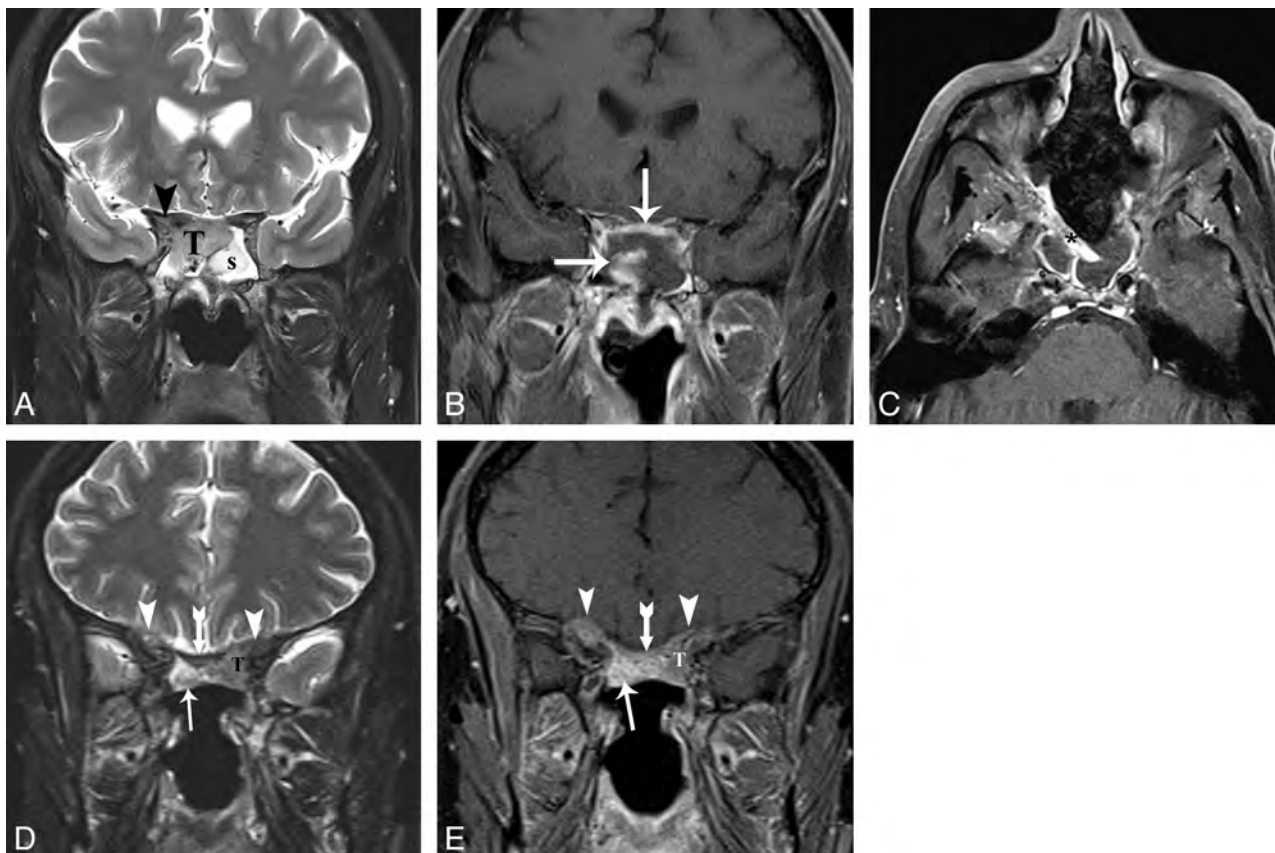
FIG 5. A 52-year-old man following transplanum resection and chemoradiation for sinonasal undifferentiated carcinoma has abnormal evolution of the ESBR, consistent with recurrent tumor. *A*, Preoperative coronal fat-saturated T2WI shows tumor (T) invading the planum sphenoidale and right optic canal (*arrowhead*). S indicates sinus secretions. *B* and *C*, Immediate postoperative coronal and axial enhanced fat-saturated T1WIs show an enhancing NSF (*arrows*) at the planum-sphenoidale defect with a right-sided vascular pedicle (*asterisk*). The thin nonenhancing collagen matrix dural inlay above the NSF is indiscernible. The nasal cavity is packed with sponge. *D* and *E*, Three-month follow-up coronal fat-saturated T2WI and enhanced T1WI show retraction of the enhancing NSF (*arrows*) into the skull base defect with a stable location of the right pedicle seen on the axial image (not shown) and mildly enhancing T2-hypointense dural graft/granulation (*bow arrows*). Nodular tumor recurrence at the edge of the reconstruction in the left sphenoid sinus (T) and along the supraorbital dura (*arrowheads*) has signal intensity and mild enhancement similar to that in preoperative tumor and different from that in the adjacent reconstructive layers.

MR Imaging Follow-Up of Endoscopic Skull Base Reconstruction

The imaging features of ESBR with the characteristic enhancing C shape and vascular pedicle configuration of the NSF and nonenhancing free grafts on immediate postoperative MR imaging have been described previously.[13,14] Kang et al[13] reported NSFs used to reconstruct defects following resection of pituitary adenomas and found stable signal intensity but variable changes in thickness and enhancement of NSFs on follow-up MRI at 3–7 months.[13] They described 2 flaps without enhancement in the immediate postop-

erative period that showed delayed enhancement on follow-up imaging and 8 flaps that enhanced in the immediate perioperative period with persistent enhancement in 7/8 flaps on follow-up imaging. Five of the initially enhancing NSFs became thinner; 2, thicker; and the average flap thickness varied from nonvisualization to 7 mm. They also noted reduction in the thickness of the multilayer reconstruction between the graft and defect. Their cohort of pituitary adenomas did not require adjuvant chemoradiation.

Our long-term follow-up (range, 3–41 months; average, 16.4 months) showed some differences from the published results of Kang et al.[13] None of our enhancing NSFs lost their immediate postoperative solid enhancement, and all demonstrated mild reduction in thickness. Our average flap thickness of 4.5 mm was comparable. None of our cases, including a similar cohort with a transellar approach without adjuvant treatment, had increases in flap thickness as seen in 2 patients in the study of Kang et al (an increase of 1 and 2 mm in flap thickness). This discrepancy may be explained by sampling error. During the immediate postoperative period, the NSF stood out as the only enhancing tissue among the nonenhancing free grafts and postoperative sinus contents. Therefore, its unique enhancing C-shaped configuration was easily delineated. Delayed enhancement of the free grafts, retraction and reduction in the thickness of the reconstructive layers, and integration of the enhancing NSF into the reconstruction site resulted in its less distinct configuration on follow-up MR imaging (Fig 3). The nonenhancing NSFs on immediate postoperative MR imaging probably compromised the vascular pedicles. Theoretically, they served as free mucosal grafts at the reconstructive site. Therefore, these nonenhancing NSFs behaved in a manner similar to those in the free mucosal grafts on follow-up; both appeared as thin enhancing granulation-mucosalization, radiographically and clinically.

The reduction in thickness of free grafts in our cohort varied. The fascia lata remained thicker than DuraGen, and its noticeable reduction in thickness probably reflects resolution of immediate postoperative swelling with increasing T2-hypointensity (Fig 4). Enhancement on follow-up reflects the incorporation of the fascia lata into the granulation tissue at the cranial defect. In reconstructions using only inlay subdural collagen matrix as the dural graft, the nonvisible to ≤2-mm nonenhancing collagen matrix became indistinguishable from the enhancing granulation at the defect (Fig 5).

In addition, the stabilization of the mature imaging features occurred within 2–6 months following surgery, with little or no further change on subsequent imaging. Seventy-four percent of our follow-up MRIs were obtained within the first year after surgery, because the initial follow-up intervals were generally closer, with a resulting higher number of studies, especially those for oncologic surveillance. Close to equal proportions of the imaging studies were performed in patients after they received adjuvant chemo- and/or radiation treatment (45%) and in patients who did not or have not received adjuvant treatment (55%). Notably, the adjuvant radiation or chemoradiation and the sinonasal inflammatory changes had no appreciable effect on the normal imaging evolution of ESBRs in our oncologic patients (Fig 4).

Imaging studies evaluating postoperative endoscopic pituitary surgery demonstrated the involution of surgical materials and identification of residual-recurrent adenoma by location, characteristic signal intensity, and nodular enhancing patterns that were identical to those of the corresponding preoperative adenoma.[15,16] Our evaluation of parasellar neoplasms following EEAs is concordant with those of MR imaging studies of transellar hypophysectomy. Our study also showed that the full-thickness enhancement of T2-isointense NSFs, which is different from the thin peripheral enhancement of the adjacent T2-hyperintense si-

nonasal mucosa, may mimic residual or recurrent tumor in patients with sinonasal neoplasms if the radiologist is not familiar with the normal appearance and evolution of these reconstructions (Fig 4). To avoid this pitfall, proper identification of the normal NSF on imaging and evaluation of the reconstructive margins for the presence of nodular tissue with signal characteristics and enhancement similar to that of preoperative neoplasm and different from that of the reconstructive layers are paramount (Fig 5).

Limitations and Implications for Patient Care

Limitations of our study include its retrospective nature and small sample size limited to an adult population with predominantly midline neoplasms. Even though the scanner variability makes our findings applicable to most practices, its effects on our results are uncertain, and that uncertainty may explain some of the minor differences in our results compared with those of Kang et al.[13] Our reported imaging features of free grafts were limited to collagen matrix dural grafts and the fascia lata, and different materials used at other institutions may appear different. However, these free tissue grafts are most commonly used at many centers.[8-10] The vascularized NSF, the workhorse of ESBR in EEA, is always present irrespective of the type of free grafts and reconstruction techniques.

With the ongoing evolution of surgical navigation, endoscopic instrumentation, and the growing success of EEA and ESBR in achieving gross total resection and reliable closure similar to that in the open approach, EEA is becoming a surgical standard for carefully selected cases in the minimally invasive surgical arena.[1] As these procedures are increasing across the country, neuroradiologists will increasingly face the challenge of postoperative surveillance following EEA and ESBR, which potentially have unique patterns of neoplastic residua and recurrence compared with those of traditional open surgery.

CONCLUSIONS

Understanding the normal imaging evolution of multilayer ESBR, specifically the persistent T2-isointensity with solid enhancement of the NSF and the maturation of the reconstructive layers within 2–6 month follow-up, is critical in the imaging assessment for tumor surveillance following an EEA to skull base neoplasms. Recognition of typical patterns of evolution should help the interpreting radiologist distinguish expected posttreatment change from tumor recurrence.

REFERENCES

1. Castelnuovo P, Dallan I, Battaglia P, et al. **Endoscopic endonasal skull base surgery: past, present and future.** Eur Arch Otorhinolaryngol 2010;267:649–63
2. Harvey RJ, Winder M, Parmar P, et al. **Endoscopic skull base surgery**

for sinonasal malignancy. *Otolaryngol Clin North Am* 2011;44: 1081–140

3. Komotar RJ, Starke RM, Raper DM, et al. **Endoscopic skull base surgery: a comprehensive comparison with open transcranial approaches.** *Br J Neurosurg* 2012;26:637–48

4. Koutourousiou M, Gardner PA, Tormenti MJ, et al. **Endoscopic endonasal approach for resection of cranial base chordomas: outcomes and learning curve.** *Neurosurgery* 2012;71:614–24

5. Leng LZ, Greenfield JP, Souweidane MM, et al. **Endoscopic, endonasal resection of craniopharyngiomas: analysis of outcome including extent of resection, cerebrospinal fluid leak, return to preoperative productivity, and body mass index.** *Neurosurgery* 2012;70:110–23

6. Dehdashti AR, Ganna A, Witterick I, et al. **Expanded endoscopic endonasal approach for anterior cranial base and suprasellar lesions: indications and limitations.** *Neurosurgery* 2009;64:677–87

7. Kassam AB, Prevedello DM, Carrau RL, et al. **Endoscopic endonasal skull base surgery: analysis of complications in the authors' initial 800 patients.** *J Neurosurg* 2011;114:1544–68

8. Harvey RJ, Parmar P, Sacks R, et al. **Endoscopic skull base reconstruction of large dural defects: a systematic review of published evidence.** *Laryngoscope* 2012;122:452–59

9. Liu JK, Schmidt RF, Choudhry OJ, et al. **Surgical nuances for nasoseptal flap reconstruction of cranial base defects with high-flow cerebrospinal fluid leaks after endoscopic skull base surgery.** *Neurosurg Focus* 2012;32:E7

10. Kassam AB, Carrau RL, Snyderman CH, et al. **Endoscopic reconstruction of the cranial base using a pedicled nasoseptal flap.** *Neurosurgery* 2008;63:ONS44–52, discussion ONS52–53

11. Hadad G, Bassagasteguy L, Carrau RL, et al. **A novel reconstructive technique after endoscopic expanded endonasal approaches: vascular pedicle nasoseptal flap.** *Laryngoscope* 2006;116:1882–86

12. Palmer JN, Chiu AG. *Atlas of Endoscopic Sinus and Skull Base Surgery.* Philadelphia: Elsevier; 2013

13. Kang MD, Escott E, Thomas AJ, et al. **The MR imaging appearance of the vascular pedicle nasoseptal flap.** *AJNR Am J Neuroradiol* 2009;30:781–86

14. Learned KO, Adappa ND, Loevner LA, et al. **MR imaging evaluation of endoscopic cranial base reconstruction with pedicled nasoseptal flap following endoscopic endonasal skull base surgery.** *Eur J Radiol* 2013;82:544–51

15. Steiner E, Knosp E, Herold CJ, et al. **Pituitary adenomas: findings of postoperative MR imaging.** *Radiology* 1992;185:521–27

16. Yoon PH, Kim DI, Jeon P, et al. **Pituitary adenomas: early postoperative MR imaging after transsphenoidal resection.** *AJNR Am J Neuroradiol* 2001;22:1097–104

High Variability in Radiologists' Reporting Practices for Incidental Thyroid Nodules Detected on CT and MRI

J.K. Hoang, A. Riofrio, M.R. Bashir, P.G. Kranz, and J.D. Eastwood

ABSTRACT

BACKGROUND AND PURPOSE: There are no guidelines for reporting incidental thyroid nodules seen on CT and MR imaging. We evaluated radiologists' current reporting practices for incidental thyroid nodules detected on these imaging modalities.

MATERIALS AND METHODS: Radiologists were surveyed regarding their reporting practices by using 14 scenarios of incidental thyroid nodules differing in size, patient demographics, and clinical history. Scenarios were evaluated for the following: 1) radiologists' most commonly selected response, and 2) the proportion of radiologists selecting that response (degree of agreement). These measures were used to determine how the patient scenario and characteristics of the radiologists affected variability in practice.

RESULTS: One hundred fifty-three radiologists participated. In 8/14 scenarios, the most common response was to "recommend sonography." For the other scenarios, the most common response was to "report in only body of report." The overall mean agreement for the 14 scenarios was 53%, and agreement ranged from 36% to 75%. Smaller nodules had lower agreement: 43%–51% for 8-mm nodules compared with 64%–75% for 15-mm nodules. Agreement was poorest for the 10-mm nodule in a 60-year-old woman (36%) and for scenarios with additional history of lung cancer (39%) and multiple nodules (36%). There was no significant difference in reporting practices and agreement when radiologists were categorized by years of practice, practice type, and subspecialty ($P > .55$).

CONCLUSIONS: The reporting practice for incidental thyroid nodules on CT or MR imaging is highly variable among radiologists, especially for patients with smaller nodules ($\leq$10 mm) and patients with multiple nodules and a history of cancer. This variability highlights the need for practice guidelines.

ABBREVIATIONS: ASNR = American Society of Neuroradiology; ITN = incidental thyroid nodule

Incidental thyroid nodules are seen in 16%–18% of CT and MR imaging studies that include the thyroid.[1,2] Although the prevalence of malignancy in incidental thyroid nodules (ITNs) is low and small thyroid cancers have an excellent prognosis, concern for missing malignancy may nevertheless lead to further evaluation for small nonspecific thyroid nodules. Initiating a work-up of an ITN seen on CT or MR imaging with diagnostic sonography can lead to further costly procedures, including fine-needle aspi-ration, follow-up sonography examinations, or even diagnostic thyroid lobectomy.

The Society of Radiologists in Sonography and other societies have published recommendations for biopsy of nodules seen on sonography,[3] but no medical organizations have specific published recommendations for the work-up of thyroid nodules seen on CT and MR imaging.[4] The Society of Radiologists in Sonography recommendations cannot be simply extrapolated to CT- and MR imaging–detected nodules because the sonographic signs of microcalcifications and solid composition cannot be reliably appreciated on CT and MR imaging.[5] Furthermore, CT and MR imaging allow a more comprehensive evaluation of neck nodes than is possible with the limited number of images captured during a thyroid sonography examination.

Without technique-specific guidelines, the reporting of ITNs seen on CT and MR imaging is likely to be nonuniform and influenced by radiologists' practice types or personal opinions. This variation leads to inconsistent practices and the potential for con-

Table 1: The 14 survey scenarios[a]

Scenario
8-mm nodule
12-year-old girl
30-year-old woman
30-year-old man
60-year-old woman
10-mm nodule
12-year-old girl
30-year-old woman
30-year-old man
60-year-old woman
15-mm nodule
12-year-old girl
30-year-old woman
30-year-old man
60-year-old woman
8-mm nodule in 60-year-old woman with history of treated lung cancer
10-mm nodule in 60-year-old woman with 7 thyroid nodules

[a] Radiologists were given an introduction that an indeterminate thyroid nodule was incidentally seen on CT or MRI with the above descriptions of nodule size and patient history.

fusion among clinicians who receive the radiology reports. In a retrospective study, Yousem et al[2] found that 61% of ITNs seen on CT and MR imaging of the neck were not reported by the radiologist issuing the clinical report, and they proposed that either the nodule was not seen or it was regarded as unimportant. A prior survey on incidental findings queried radiologists about the ITN, but the survey was limited to 1 scenario and was sent only to academic body imaging radiologists.[6]

The aim of this study was to survey radiologists' self-described reporting practices of hypothetic scenarios of ITNs detected on CT and MR imaging. We hypothesized that reporting practices for ITNs are highly variable and may depend on the radiologist's experience, practice type, and training.

MATERIALS AND METHODS

This study was approved by our institutional review board. The need for written informed consent was waived due to the design of this survey study and the anonymity of the survey respondents.

Survey and Study Group

A survey was designed to query radiologists about their reporting practices for 14 scenarios of ITN, differing in nodule size, age and sex of the patient, multiplicity of nodules, and presence of a history of treated lung cancer. The scenarios are listed in Table 1. The survey scenarios were designed to simulate the spectrum of ITNs encountered in clinical practice and to cover categories in the Duke 3-tiered system, which was devised for guiding work-up for ITNs detected on CT and MR imaging.[1,4] These criteria are divided into 3 mutually exclusive categories: Category 1 consists of nodules of any size with aggressive imaging findings, including associated suspicious lymph nodes, local invasion, or focal metabolic activity on PET. Nodules not meeting the criteria for category 1 are considered to have indeterminate imaging findings on CT and MR imaging and are grouped into categories 2 and 3. Category 2 nodules are those of any size in patients younger than 35 years of age, and category 3 is nodules ≥15 mm in patients 35

years of age or older. The 3 categories represent a descending risk of malignancy and need for work-up. ITNs that do not belong to any of the 3 categories are not selected for work-up. Younger patients are in category 2 because other studies have shown that there is a higher ratio of malignant-to-benign nodules in younger patients.[5,7-11]

Survey takers were given the following 5 response choices for each scenario: A) do not report, B) report in only body of report, C) report in impression without recommendation, D) recommend sonography ± biopsy, and E) I have no consistent practice. The survey also obtained information regarding the radiologists, including years in practice, current practice type, and subspecialty training.

The survey was created by using the Web site http://www.surveymonkey.com and was sent electronically to 3 groups: 1) radiologists in all subspecialties at a tertiary care academic institution (Duke University Medical Center), 2) radiologists attending the American College of Radiology head and neck radiology course, and 3) members of the American Society of Neuroradiology (ASNR). The survey was sent via e-mail lists to the first 2 groups. For ASNR members, the survey was featured in one of the monthly ASNR on-line newsletters that was e-mailed to all ASNR members. Only responses from board-certified radiologists were included. Responses were collected between September 18, 2012, and December 11, 2012.

Analysis of Survey Results

The results were evaluated for the following: 1) the most commonly selected response (A–E) for the 14 ITN scenarios, and 2) the degree of agreement for the most commonly selected response. The degree of agreement was the proportion of respondents who chose the most common response. A higher proportion would indicate high agreement and little variability in practice. The degree of agreement was categorized into high (≥75%), moderate (50%–74%), and low (<50%).

Response and Agreement by Scenario

The response and degree of agreement for all respondents were evaluated to determine how nodule size, patient demographics, multiplicity of nodules, and cancer history would affect the reporting practice and variability in practice.

Response and Agreement by Radiologist Groups

Response and degree of agreement were compared for radiologists with different years in practice, practice type, and subspecialty training to determine whether these characteristics would affect the reporting practice and variability in practice.

The mean agreement was calculated for radiologists of each group. The paired t test was used to compare differences in agreement between 2 groups of practices (academic versus private/hybrid). One-way ANOVA was used to compare differences in agreement for years in practice (fellow, attending of <10 years, and attending of >10 years) and differences in agreement in subspecialty training (neuroradiology, body imaging, and other).

Results from the on-line survey were exported on a spreadsheet for analysis (Excel; Microsoft, Redmond, Washington). Sta-

Table 2: Characteristics of survey respondents

Characteristics of Groups	No. of Respondents
Total	153
Years in practice	
Fellow	27 (18%)
Attending <10 years	76 (50%)
Attending ≥10 years	50 (33%)
Practice type	
Academic	108 (71%)
Private or hybrid	45 (29%)
Subspecialty training	
Neuroradiology	100 (65%)
Abdominal radiology	17 (11%)
Combinations or other	36 (24%)
Survey group	
Duke Radiology	41 (27%)
ACR CME course	28 (18%)
ASNR members	84 (56%)

Note:—ACR CME indicates the American College of Radiology Continuing Medical Education.

tistical analyses were performed by using SAS Enterprise (Version 4.2; SAS Institute, Cary, North Carolina).

RESULTS

Study Group
One hundred fifty-three radiologists participated in the study, including 41 from Duke Radiology, 28 from the American College of Radiology course, and 84 ASNR members. The response rates for these 3 groups were 41/67 (61%), 28/36 (78%), and 84/4552 (2%), respectively. Table 2 shows the characteristics of the respondents. Seventy-one percent of radiologists were in academic practice, and 65% had received subspecialty neuroradiology training.

Survey Results
The On-line Table shows the most commonly selected response for each scenario and the degree of agreement for the most commonly selected response.

Response and Agreement by Scenario
Although there were 5 reporting options, there were only 2 answers that were commonly selected responses when all radiologists were grouped together: "report only in body" (B) or "recommend sonography" (D). "Recommend sonography" was the most common response for 8/14 scenarios: all 4 scenarios of 15-mm nodules, 3 scenarios of 10-mm nodules in patients 12 years and 30 years of age, and 1 scenario of an 8-mm nodule in patients 12 years of age.

The degree of agreement represents the proportion of radiologists who chose the most commonly selected response and is an indicator of the most common practice. Agreement ranged from 36% to 75% (Fig 1), and the mean was 53%. This finding indicates that only 53% of radiologists had common reporting practices.

Agreement for the most commonly selected response was influenced by nodule size. There was lower agreement for smaller nodules, with 43%–51% agreement for 8-mm nodule scenarios compared with 64%–75% agreement for 15-mm nodule scenarios. When 15-mm nodule scenarios were excluded, the mean agreement was 46% and the range was 36%–56%.

Agreement was similar for scenarios with different ages except for the 10-mm nodule in the 60-year-old patient, which had 36% agreement compared with 53%–56% for the same size nodule in younger patients. The sex of the patient in the scenario did not influence the response or agreement as evidenced by the scenarios with the male and female 30-year-old patients. The 2 special scenarios of a patient with an additional history of lung cancer and a patient with multiple nodules had poor agreement (39% and 36%, respectively).

Response and Agreement by Radiologist Subgroups
The On-line Table shows that when comparing the 3 different groups of years in practice, there were 3 scenarios that had differences in the most commonly selected responses among the groups: 8-mm nodules in 30-year-old men, 10-mm nodules in 60-year-old women, and multiple nodules (footnote a on On-line Table). The mean agreement for fellows, attendings of <10 years, and attendings of ≥10 years was 52%, 51%, and 54%, respectively, and it was not significantly different ($P = .81$).

When practice type was considered, the most commonly selected responses differed between academic and private/hybrid practice radiologists for 2 scenarios in which the private/hybrid radiologists were more conservative, choosing "recommend sonography" and "report in impression without recommendation" rather than "report only in body" (On-line Table). These were 10-mm nodules in a 60-year-old woman and a patient with multiple nodules, respectively. The mean agreement for academic and private/hybrid for both was 52%, and it was not significantly different with the paired t test ($P = .55$).

The type of subspecialty training led to differences in the reporting for 4 scenarios. Radiologists with "other" training had "recommend sonography" rather than "report only in body" as the most commonly selected response for 8-mm nodules in male and female patients 30 years of age. Body-trained radiologists differed from the other subspecialties by choosing "report only in body" rather than "recommend sonography" for 10-mm nodules in 60-year-old women and patients with multiple nodules. The mean agreement for neuroradiology, body imaging, and other training was 52%, 54%, and 53%, respectively, and it was not significantly different ($P = .91$).

DISCUSSION
In contrast to thyroid nodules detected on sonography, there are presently no specific recommendations or guidelines offered by professional radiology organizations that deal specifically with the problem of ITNs discovered on CT or MR imaging.[3,4] This factor may contribute to confusion, inconsistent reporting, and even overinvestigation of small thyroid nodules. This study evaluates how radiologists claim to report thyroid lesions incidentally detected on CT and MR imaging and quantifies the variability in this self-described practice. We found that with the exception of relatively large nodules of 15 mm, there is substantial variability in reporting practices, with <50% of radiologists having the same practice of reporting ITNs. Additionally, variability is high even within groups similar in practice experience, practice type, and subspecialty.

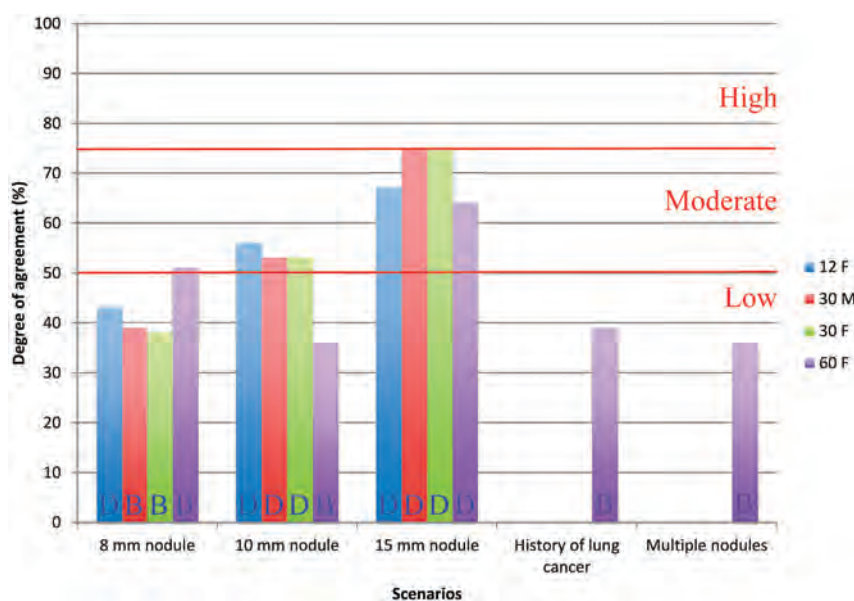Self-described reporting practices regarding incidental thy-

FIG 1. Degree of agreement for the most commonly selected response for all radiologists. Responses were the following: B = report only in body and D = recommend sonography. The degree of agreement was categorized into high (≥75%), moderate (50%–74%), and low (<50%). Scenarios included 12F = 12-year-old girl, 30M = 30-year-old man, 30F = 30-year-old woman, and 60F = 60-year-old woman.

guidelines. Such guidelines should have specific recommendations for patient age, nodule size, and the number of nodules.

A review by Hoang et al[4] proposed a set of criteria for reporting ITNs on CT, MR imaging, and PET. The work-up system, known as the Duke 3-tiered system, has since been evaluated in a retrospective study that compared the 3-tiered system with a ≥10-mm-sized threshold for consecutive ITNs detected on CT neck studies.[1] When the investigators applied the 3-tiered system to nodules of ≥10 mm, they found that the work-up of nodules could be reduced by 46%. In another study by Hobbs et al,[12] the Duke 3-tiered system was applied to a cohort of ITNs undergoing fine-needle aspiration and found that the system would have prevented biopsy in 35% of patients without missing any malignant nodules. Thus, guidelines such as the Duke 3-tiered system could reduce unnecessary ITN work-ups, improve consistency in reporting ITNs, and reduce the cost of medical care in this population.

roid nodules were previously investigated by Johnson et al,[6] who included a scenario of a 1-cm ITN in a 45-year-old woman in a survey, along with other incidental-finding scenarios seen on body CT. They concluded that there was good agreement in reporting practices for ITNs, with 81% of radiologists recommending sonography in that scenario. For similar scenarios in our study, notably of 10-mm nodules in a 30-year-old and a 60-year-old woman, the most common responses by radiologists were "recommend sonography" for the younger woman but "report only in body" for the older woman. Our study also found much greater variability in reporting practices as demonstrated by a lower degree of agreement for these responses (53% and 36%, respectively). The differences between our results and those of Johnson et al could be attributable to our larger sample size (153 versus 27) and a more heterogeneous group of radiologists. In their work, Johnson et al specifically surveyed academic radiologists who had prior fellowship training in body imaging, while our study surveyed radiologists from a variety of practice types and subspecialties. We believe that better representation of all types of radiologists is one of the strengths of our study.

The scenarios with the greatest agreement of reporting practices were 15-mm nodules, for which the most common reporting option was to recommend sonography, regardless of age or sex. In contrast, the agreement was as low as 36% for a 60-year-old woman with a 10-mm nodule and a 10-mm nodule in a patient with multiple thyroid nodules. An additional history of lung cancer in a 60-year-old woman with an 8-mm nodule also led to lower agreement (39%) than when there was no lung cancer history (51%). Low agreement in our survey reflects a small proportion of radiologists practicing in the same way. These inconsistent reporting practices could potentially result in confusion for the referring clinician and highlight the need for evidence-based or expert-opinion practice

When one is comparing our survey results with the results in the Duke 3-tiered system, it appears that the most commonly selected responses for scenarios by age and nodule size actually match the recommendations of the 3-tiered system. The exception is the 8-mm nodules in the 30-year-old patients, for which the survey respondents chose "report only in body," whereas the 3-tiered system does not specify a nodule size cutoff for the younger than 35-year age group. In clinical practice, the authors of the 3-tiered system use a 10-mm cutoff in adults younger than 35 years and no cutoff in children. These specifications were not described and used in the publications to simplify the guidelines for readers. Overall, the implication of the survey results is that the 3-tiered system is concordant with current practices and could be implemented in clinical practice.

This study had several limitations. Although we attempted to survey a diverse group of radiologists, these results may not be generalizable to all radiologists because of the predominance of academic radiologists and neuroradiologists in our study population. Second, the response from the ASNR members was low at 2%, though this is not surprising given that the survey was sent only once in an e-mailed newsletter. The absolute number of respondents from the ASNR was still large (86 radiologists), however, composing 56% of our study group. The response rate was higher from the other 2 groups of radiologists that received the survey. We also recognize that some radiology practices may have already developed guidelines within their groups for reporting thyroid nodules and that these groups may have already established high within-group agreement. In addition, there may be a nonresponse bias from radiologists who did not participate in the survey, which is inherent in survey studies. However, we do not believe that this would add systematic bias in favor of a particular

result. Finally, these are self-described reporting practices and may not reflect the true practice of the reporting radiologists.

CONCLUSIONS

The reporting practice of ITNs on CT or MR imaging is highly variable among radiologists, especially for patients with smaller nodules (≤10 mm) and for patients with multiple nodules and an additional history of cancer. This variability highlights the reality that there is no standard of practice and that there is a need for evidence-based or expert-opinion practice guidelines. Such guidelines could lead to greater reporting consistency and, potentially, decreased cost and medicolegal risk in the evaluation of low-risk ITNs.

REFERENCES

1. Nguyen XV, Choudhury KR, Eastwood JD, et al. **Incidental thyroid nodules on CT: evaluation of 2 risk-categorization methods for work-up of nodules.** *AJNR Am J Neuroradiol* 2013;34:1812–17
2. Yousem DM, Huang T, Loevner LA, et al. **Clinical and economic impact of incidental thyroid lesions found with CT and MR.** *AJNR Am J Neuroradiol* 1997;18:1423–28
3. Frates MC, Benson CB, Charboneau JW, et al. **Management of thyroid nodules detected at US: Society of Radiologists in Ultrasound Consensus Conference Statement.** *Radiology* 2005;237:794–800
4. Hoang JK, Raduazo P, Yousem DM, et al. **What to do with incidental thyroid nodules on imaging? An approach for the radiologist.** *Semin Ultrasound CT MR* 2012;33:150–57
5. Shetty SK, Maher MM, Hahn PF, et al. **Significance of incidental thyroid lesions detected on CT: correlation among CT, sonography, and pathology.** *AJR Am J Roentgenol* 2006;187:1349–56
6. Johnson PT, Horton KM, Megibow AJ, et al. **Common incidental findings on MDCT: survey of radiologist recommendations for patient management.** *J Am Coll Radiol* 2011;8:762–67
7. Belfiore A, La Rosa GL, La Porta GA, et al. **Cancer risk in patients with cold thyroid nodules: relevance of iodine intake, sex, age, and multinodularity.** *Am J Med* 1992;93:363–69
8. Fowler CL, Pokorny WJ, Harberg FJ. **Thyroid nodules in children: current profile of a changing disease.** *South Med J* 1989;82:1472–78
9. Kirkland RT, Kirkland JL, Rosenberg HS, et al. **Solitary thyroid nodules in 30 children and report of a child with a thyroid abscess.** *Pediatrics* 1973;51:85–90
10. Machens A, Holzhausen HJ, Dralle H. **The prognostic value of primary tumor size in papillary and follicular thyroid carcinoma.** *Cancer* 2005;103:2269–73
11. Rago T, Fiore E, Scutari M, et al. **Male sex, single nodularity, and young age are associated with the risk of finding a papillary thyroid cancer on fine-needle aspiration cytology in a large series of patients with nodular thyroid disease.** *Eur J Endocrinol* 2010;162:763–70
12. Hobbs H, Bahl M, Nelson RC, et al. **Incidental thyroid nodules detected on imaging: can workup be reduced by using the Society of Radiologists in Ultrasound recommendations and the three-tiered system?** *AJR Am J Roentgenol* 2014;202:18–24

Surgical and Clinical Confirmation of Temporal Bone CT Findings in Patients with Otosclerosis with Failed Stapes Surgery

J. Whetstone, A. Nguyen, A. Nguyen-Huynh, and B.E. Hamilton

ABSTRACT

BACKGROUND AND PURPOSE: Prior descriptions of imaging after failed stapes procedures for otosclerosis predated currently available CT technology and/or failed to assess commonly used metallic implants. The purpose of this study was to correlate temporal bone CT findings with clinically and intraoperatively determined causes of surgical failure.

MATERIALS AND METHODS: All patients with otosclerosis undergoing stapedectomy between December 1999 and December 2010 were identified from a search of neurotology clinical records. Patients presenting because of failed stapes surgery and having temporal bone CT scans at the time of revision surgery or clinical evaluation were included. Imaging and clinical records were retrospectively evaluated by a medical student, radiology resident, and senior neuroradiologist. Stapes prosthesis complications and relevant anatomic CT findings were correlated to clinical and intraoperative findings.

RESULTS: Twenty-two of 340 patients met inclusion criteria. Temporal bone CT findings were correlated to intraoperative findings in 17 of 22 patients and to clinical findings in 5 of 22 patients. Surgically confirmed abnormalities included 7 of 7 incus erosions, 3 of 6 piston re-sizings, 3 of 5 granulation tissues, 3 of 5 prosthesis disconnections, 3 of 4 obliterative otosclerosis, 2 of 2 oval window dislocations, and 1 labyrinthine ossificans. Clinically confirmed abnormalities included 2 cases each of superior semicircular canal dehiscence, and wrong piston size, and 1 each of piston disconnection, labyrinthine ossificans, and intravestibular footplate.

CONCLUSIONS: CT evaluation in the setting of failed stapes surgery is challenging. Many postoperative complications such as piston migration, incus necrosis, and overt vestibular penetration are well recognized on temporal bone CT. Of particular note, superior semicircular canal dehiscence is an important contraindication to stapes surgery.

ABBREVIATIONS: CHL = conductive hearing loss; SNHL = sensorineural hearing loss; MHL = mixed hearing loss; SSCD = superior semicircular canal dehiscence; OW = oval window; OtoO = obliterative otosclerosis

Otosclerosis affects approximately 1% of the population (more common in whites but rare in African Americans, Asians, and Native Americans) and usually presents early as conductive hearing loss (CHL) and later as mixed CHL and sensorineural hearing loss (SNHL) in young adults.[1-3] CHL occurs early on as the result of mechanical fixation of the stapes footplate within the oval window (OW) that prevents normal mobility. This limits transmission of energy as a fluid wave within the inner ear fluid and manifests as CHL. Surgical management of otosclerosis includes stapedectomy, which involves the creation of a small hole in the stapes footplate within the OW and removal of portions or all of the stapes and implantation of a prosthesis to restore mechanical sound conduction.

Surgical treatment of CHL is evaluated postoperatively with 4-frequency air-bone gap. Closure of the air-bone gap to 10 dB or less reflects surgical success and was achieved in 94.2% of patients in the largest prospective data base of stapedotomies for otosclerosis.[4] If CHL persists after surgery, then revision surgery is usually indicated but is more challenging.[5]

High-resolution temporal bone CT is an important technique that can identify many causes of stapedectomy failure, particularly for recurrent or persistent CHL, and provides a roadmap for revision surgery. Although 2 prior excellent studies delineated many common causes of failed otosclerosis surgery, better CT technology and an improved understanding of other conditions contributing to hearing loss have intervened since their publication.[6,7] One study, for example, addressed only fluoroplastic implants rather than the metallic implants that are typically used in the United States,[6] whereas the other study is in part outdated

Table 1: Temporal bone CT findings compared with intraoperative findings and clinical presentation in patients with revision stapedectomy

Patient	CT Oto	Age, y	Sex	Presentation	CT	Surgery
1	B OtoF	55	F	R MHL, vest	R LPS with incus erosion, gas in vestibule?	R LPS with incus necrosis, fistula not mentioned
2	B neg	44	F	R SNHL, vest	Neg	R long piston
3	R OtoF	35	F	L CHL, tinnitus	L prosthesis dislocation from OW	L long piston, loosening
4	B OtoC	68	M	R MHL	R LPS with disconnection, scar, incus erosion, OW dislocation	R LPS with disconnection, scar, incus necrosis, OW dislocation
5	R OtoF	56	F	R SNHL, vest	R long piston	R long piston, incus medialized
6	B OtoF	80	M	L SNHL	L long piston	L CI (piston length unconfirmed) Clinical notes limited
7	B OtoC	56	M	L MHL, vest R MHL	L LO, B OtoC, B OtoO	L OtoO prior surgery R CI limited notes; HL thought in part caused by OtoC
8	B neg	44	M	L CHL	L short piston	L short piston
9	B OtoF	61	M	R CHL	Neg	R OW dislocation, bone ingrowth
10	B neg	15	F	R CHL	R OW dislocation	R OW dislocation, scar, OtoO
11	B OtoC	51	F	R MHL	R OtoO	R OtoO prior surgery R CI; HL probably caused by OtoC
12	B neg	54	F	R CHL	R incus erosion	R piston loose, incus necrosis, scar
13	R OtoF	30	F	R CHL	R incus erosion	R stapes not crimped and scarred to incus with incus necrosis
14	B OtoF	31	F	R CHL	R incus erosion and disconnection, OtoO	R incus erosion and disconnection, OtoO
15	R OtoF	67	F	R CHL, vest	Neg	R nonmobile piston surrounded by scar
16	B neg	53	F	R vest	R long piston, incus erosion	R long piston, scar, incus necrosis
17	R OtoF	52	F	L vest	L incus erosion, prosthesis disconnection, OW dislocation	L piston medialized, disconnection, incus necrosis

Note:—LPS indicates lateralized piston syndrome; CHL, conductive hearing loss; SNHL, sensorineural hearing loss; MHL, mixed hearing loss; R, right; L, left; B, bilateral; OtoF, fenestral otosclerosis; OtoC, cochlear otosclerosis; OtoO, obliterative otosclerosis; neg, negative; vest, vestibular symptoms; CI, cochlear implantation; OW, oval window; LO, labyrinthine ossificans; HL, hearing loss.

because of technological advancements in CT technology and because anatomic considerations such as superior semicircular canal dehiscence (SSCD), labyrinthine ossificans, and obliterative otosclerosis (OtoO) were not recognized at that time as potential causes of surgical failure.[7] The particular limitations of CT evaluation of metallic-type prostheses were also not described at that time.[7]

We sought to perform a more contemporary evaluation of a series of consecutive patients with otosclerosis presenting for failed stapedectomy to better evaluate the potential role of preoperative temporal bone CT performed with the use of current technology.

MATERIALS AND METHODS

Patients undergoing stapes or stapes revision surgery at our institution between December 1999 and December 2010 were identified from a search of the department of neuro-otology clinical records. Patients presenting because of failed stapes surgery (those with new or persistent hearing and/or balance complaints after prior stapes surgery) and having temporal bone CT at the time of surgical or clinical evaluation were included in this retrospective review. Institutional review board approval was obtained with waiver of informed consent for this retrospective imaging and chart review. Temporal bone CT studies were reviewed in consensus in an unblinded fashion by a medical student, radiology resident, and neuroradiologist with a Certificate of Added Qualification in neuroradiology to identify imaging findings that could be correlated to surgical and clinical findings. The imaging and intraoperative reports were also discussed with a senior neurotologist.

Temporal bone CT protocol at our institution includes helically acquired 0.75-mm-thick axial images on 1 of 2 16-section MDCT scanners from the top of the temporal bones through the tip of mastoids obtained without intravenous contrast. Images are routinely reconstructed in axial and coronal increments in bone and soft tissue algorithms. Postprocessing by use of oblique sagittal (Stenvers and Poschl views) type reformats and 3D volume-rendered reconstructions were performed in selected cases when possible to better demonstrate abnormalities. High-quality multiplanar reformations and 3D reconstructions were not routinely possible in all cases in this retrospective study, given that the original dataset is not saved after a short period of time at our institution. Older studies in 4 cases included 1-mm-thick direct axial and coronal images by use of a single-section CT scanner.

CT images were reviewed to assess the location and position of the stapes prosthesis, appearance of the OW and round window, otic capsule attenuation, cochlea, vestibule, semicircular canals, ossicles, and tympanic cavity. Areas of abnormal soft tissue attenuation, abnormal bone formation, and ossicular fixation were assessed.

RESULTS

A total of 340 patients who had stapes surgery were initially identified from the department of neurotology clinical records. Sixty of 340 (17.6%) had temporal bone CT examinations available in our digital PACS. A total of 22 of 60 (36.7%) poststapedectomy patients (7 male, 15 female), ranging in age from 16–87 years (mean, 48 years) formed the basis of this review. Seventeen of these 22 patients had presurgical temporal bone CT studies that could be correlated with subsequent
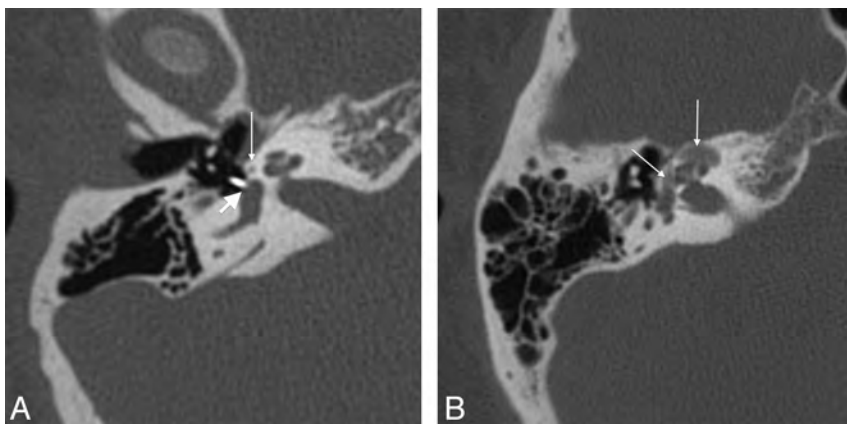
FIG 1. *A,* Axial CT in a 15-year-old girl with persistent conductive hearing loss poststapedectomy shows a small lucency in the left fissula antefenestrum (*thin arrow*), consistent with fenestral otosclerosis. Her piston prosthesis appeared short (*thick arrow*), without intravestibular penetration (surgically confirmed). *B,* Axial CT in a 56-year-old man with sensorineural hearing loss after stapedectomy shows extensive lucency surrounding the cochlea (*arrows*), consistent with cochlear otosclerosis.
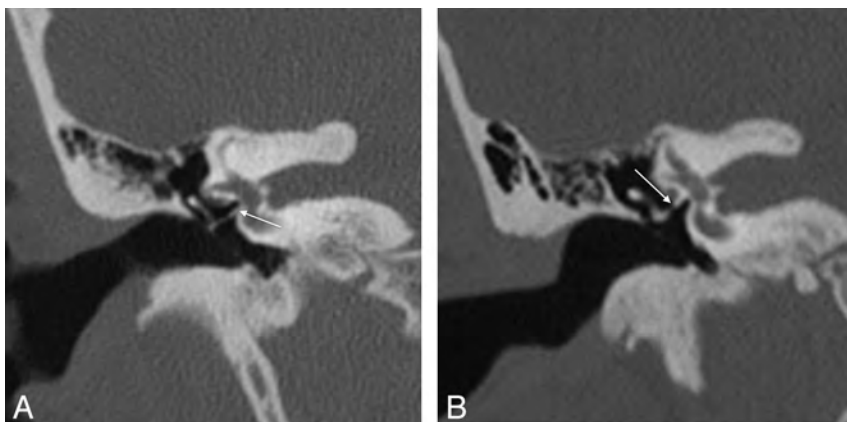

FIG 2. *A,* Coronal CT in a 40-year-old woman with recurrent right conductive hearing loss after stapedectomy shows inferior dislocation of the prosthesis (*arrow*) with respect to the oval window. *B,* Coronal CT in a 15-year-old girl with CHL shows superior dislocation of the stapes prosthesis from the OW (*arrow*).
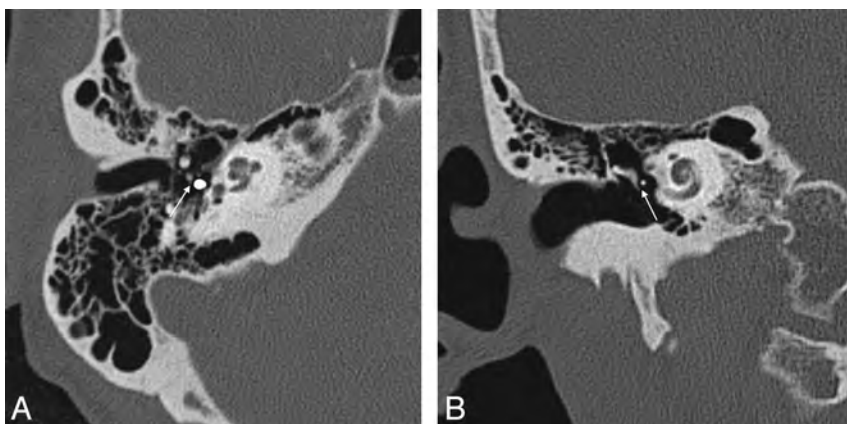

FIG 3. *A,* Axial CT in a 31-year-old woman with right conductive hearing loss after stapedectomy shows a gap (*arrow*) consistent with disconnected prosthesis. *B,* Coronal CT (same patient as in *A*) shows slender incus erosion and disconnection (*arrow*). This patient had intraoperatively confirmed disconnection and incus necrosis.

intraoperative findings. Fourteen of 17 had revision stapedectomies, whereas 3 of 17 had cochlear implant surgery in conjunction with prior stapes surgical reports plus clinical

correlation. Five additional poststapedectomy patients (3 male, 2 female; mean age, 42 years) with 6 postoperative ears have not undergone revision surgery to date but had temporal bone CT studies that were reviewed and correlated to clinical follow-up only.

Persistent hearing or balance complaints in the 17 patients with stapedectomy that prompted revision stapes surgery in 14 and cochlear implantation in 3 included CHL in 8 patients, SNHL and/or vestibular symptoms in 5 patients, and mixed hearing loss (MHL) in 4 patients. The primary intraoperative findings correlated to clinical presentation in the 17 patients with revision stapedectomy are detailed in Table 1.

Otosclerosis was visible radiographically in 12 of 17 (70.6%) of the surgical group and 3 of 5 (60%) of the clinically confirmed group. Fenestral otosclerosis was visible at CT in 9 of 17 (52.9%) of the surgical group and 3 of 5 (60%) of the clinically confirmed group (Fig 1*A*). Cochlear otosclerosis was present in 3 of 17 (17.6%) of the surgically confirmed and none of the clinically confirmed patients (Fig 1*B*).

CT Findings in Surgically Confirmed Patients

Preoperative temporal bone CT findings correlating to intraoperative findings included 2 of 2 cases of OW dislocation (Fig 2); 3 of 5 cases of prosthesis disconnection (Fig 3); 7 of 7 cases of incus erosion, 2 as part of the lateralized piston syndrome (Figs 4 and 5); 1 of 1 short piston (Fig 6); 2 of 5 long pistons (Fig 7); 3 of 5 with granulation tissue; and 3 of 4 surgically confirmed cases of OtoO (Fig 8). Three patients with no definite CT abnormality had the following intraoperative findings explaining surgical failure: 1 each of non-mobile piston encased in scar, piston dislocation from OW with new bone formation, and long piston. Additional incompletely seen CT findings at surgery included a case of prosthesis uncrimping with scar, though the CT did confirm incus erosion in this case that supported loosening.

CT findings identified but not mentioned in surgical notes included the following possible postoperative complications: 1 suspected long piston that received cochlear implant with limited intraoperative description, 1 piston
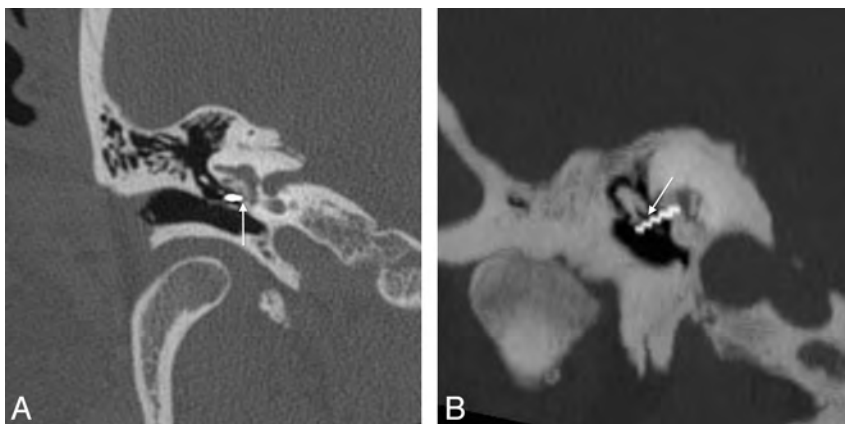
FIG 4. *A,* Axial CT in a 68-year-old man with recurrent mixed hearing loss shows findings suggesting the lateralized piston syndrome: prosthesis displacement inferior to the OW (*arrow*). Piston tip is encased in new otosclerotic bone. *B,* Coronal oblique multiplanar reformation (same patient as in *A*) shows incus erosion (*arrow*). Intraoperative findings confirmed scar tissue surrounding the stapes piston, causing prosthesis extrusion.
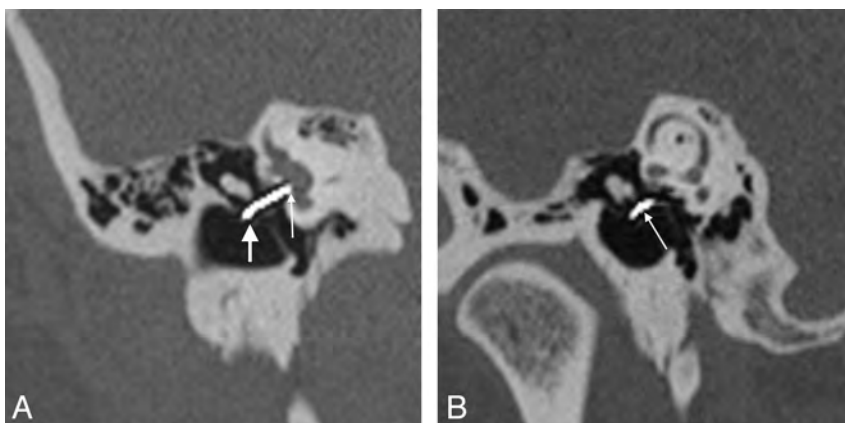

FIG 5. *A,* Stenver multiplanar reformation CT in a 55-year-old woman with mixed hearing loss shows findings of lateralized piston syndrome. The piston is in the oval window, but no vestibular penetration (*thin arrow*) is noted. Note piston lateralization to the tympanic membrane (*thick arrow*). *B,* Poschl MPR (same patient as in *A*) shows the piston traversing the expected location of the incus long process, which is eroded (*arrow*).
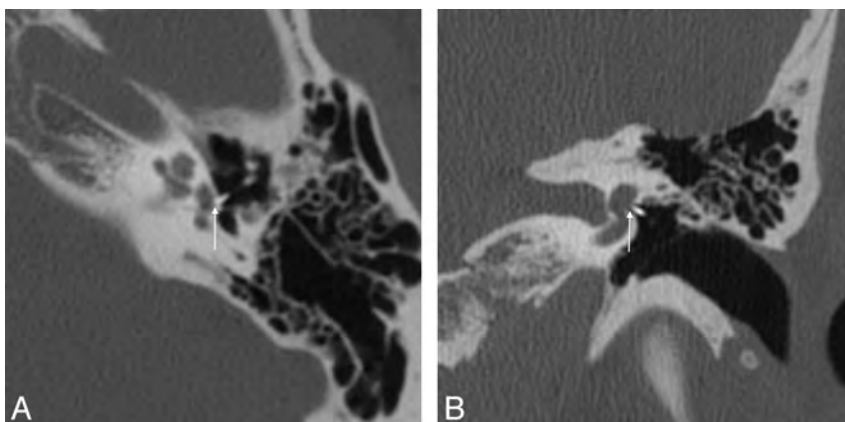

FIG 6. *A,* Axial CT in a 44-year-old woman with conductive hearing loss demonstrates no vestibular penetration (*arrow*) by the piston prosthesis. *B,* Coronal CT multiplanar reformation in the same patient as in *A* also shows no vestibular penetration (*arrow*), suggesting short piston. Intraoperative findings confirmed inadequate piston depth.

dislocation from the OW (in which concurrent incus erosion and prosthesis disconnection were seen and did correlate with CT), 1 possible intravestibular gas (in a patient with vestibular symptoms) without surgically confirmed labyrinthine fistula, and 1

prosthesis disconnection from the ossicular chain in which the only finding in this case at surgery was a suspected long piston, not evident at CT. Two additional CT anatomic findings were SSCD in a patient with ipsilateral CHL and labyrinthine ossificans in a patient with ipsilateral MHL that may have in part explained surgical failures.

CT Findings in Patients with Clinical Confirmation Only

The 5 patients evaluated having only clinical correlation showed abnormalities on temporal bone CT in 6 poststapedectomy ears (Table 2). One patient with postoperative SNHL had a long prosthesis with excessive vestibular penetration as a presumed cause. One patient with prior bilateral stapedectomies showed prosthesis disconnection and incus erosion correlating to MHL on 1 side and a "dead" ear (complete sensorineural deafness) on the contralateral side as the result of an intravestibular foreign body caused by footplate dislocation (Fig 9). Prosthesis dislocation from the OW and short piston probably explained CHL in 2 cases, respectively, whereas concurrent SSCD and labyrinthine ossificans could explain MHL in another (Fig 10). Interestingly, the patient with suspected short piston also had SSCD in addition to findings consistent with fenestral otosclerosis on her symptomatic but unoperated contralateral ear.

DISCUSSION

Otosclerosis is a genetically inherited osteodystrophy that affects the otic capsule of the temporal bone. Although autopsy series suggest a prevalence of 10%, approximately 1% of the population is affected clinically.[2] The inheritance pattern is autosomal dominant but with incomplete penetrance of 40% and variable clinical expression.[8]

Surgical treatment of otosclerosis has a high success rate, but revision stapedectomy is more challenging and prone to more surgical complications. Temporal bone CT is particularly useful for preoperative planning in such cases because it may reveal the suspected cause of surgical failure and/or may identify anatomic abnormalities that may alter the treatment plan.

Prior description of temporal bone CT in poststapedectomy patients was based on polytetrafluoroethylene implants in France[6] that are not commonly used in the United States and on an
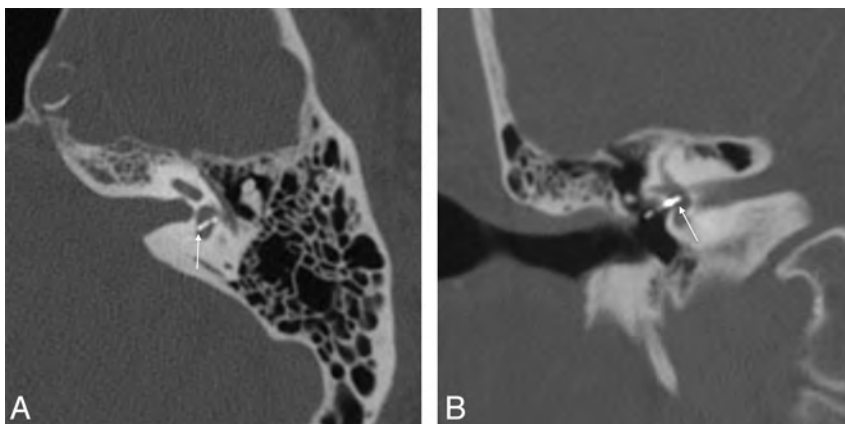
FIG 7. *A*, Axial CT in an 80-year-old man with sensorineural hearing loss shows deep intrusion into the vestibule (*arrow*). *B*, Coronal CT multiplanar reformation in a 68-year-old man with vestibular symptoms suggests deep intravestibular position of the stapes prosthesis (*arrow*). Long prosthesis and small labyrinthine fistula were confirmed intraoperatively.
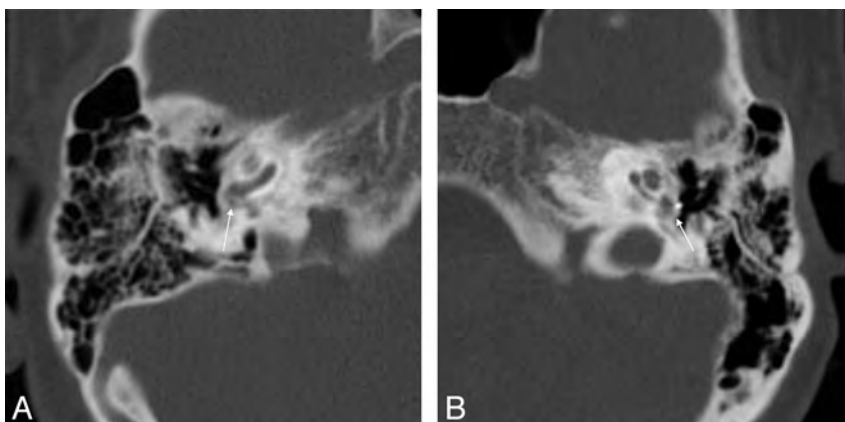

FIG 8. *A*, Axial CT in a 56-year-old man with persistent mixed hearing loss after stapedectomy demonstrates heaped-up lucent bone formation at the right round window consistent with obliterative otosclerosis (OtoO) (*arrow*). This patient also had probable superior semicircular canal dehiscence (not shown). *B*, Axial CT in the contralateral ear in the same patient as in *B* also shows OtoO. Note tip of prior stapes piston embedded within otosclerotic new bone (*arrow*).

Table 2: Temporal bone CT findings in patients after stapedectomy with clinical confirmation only

Patient	Age, y	Sex	CT Oto	Presentation	CT Findings
1	40	F	B OtoF	R CHL, tinnitus	R prosthesis dislocation from OW
2	67	M	B neg	R MHL	R SSCD, R LO
3	11	F	B OtoF	R CHL	R short piston
				SNHL	L SSCD (contralateral to operated ear)
4	41	M	B neg	B MHL, vertigo	L intravestibular foreign body (footplate)
					R disconnection of prosthesis-incus, incus erosion, OW dislocation
5	58	M	B OtoF	L SNHL	L long piston

Note:—CHL indicates conductive hearing loss; SNHL, sensorineural hearing loss; MHL, mixed hearing loss; OW, oval window; SSCD, superior semicircular canal dehiscence; LO, labyrinthine ossificans; R, right; L, left; B, bilateral; OtoF, fenestral otosclerosis; neg, negative.

most metallic prostheses were easy to evaluate in this study, a few were difficult to visualize, probably because of smaller prosthesis size and technical factors. It remains worthwhile commenting on suspected piston sizing abnormalities because most patients presenting with persistent CHL or other postoperative complications require surgical re-exploration, and preoperative CT findings improve surgical planning. Despite inaccurate size estimation on CT, excessive vestibular penetration caused by migration or length seemed reasonable to suggest in this study if the piston tip depth exceeded 50% of the (normal) vestibule width.

Persistent or recurrent CHL after primary stapes surgery occurs in approximately 5.8% of cases,[4] on the basis of residual air-bone gap >10 dB after surgery. This most often results from prosthesis migration or dislocation (>80%).[12,14] The prosthesis may become disconnected or loose and may be evidenced by a gap in the ossicular chain–stapes structure. MPR and/or 3D reconstruction may best demonstrate the gap. The "lateralized piston syndrome" was seen in 2 of our cases, and it is characterized by lateral piston extrusion out of the OW that is often associated with incus necrosis. The piston itself may contact the tympanic membrane in more than half of cases,[15] and was present in 1 of our cases.

Ossicular necrosis or resorption, evident by erosion on CT, may also lead to CHL. The incus long process is most often involved because it is typically the point of prosthesis attachment. Erosion is potentiated by excessive piston length or insufficient crimping, which may transmit undue stress, though nonsurgical cases of incus erosion are also reported, thought to be related to ischemic resorption.[16]

Granulation tissue or new bone formation may result in recurrent CHL. Granulation tissue is seen as soft tissue

older study from 1986 with the use of 1.5-mm-thick sections that predated MDCT.[7] Many conditions such as SSCD are now only visualized because better spatial resolution and thinner section collimation is available with MDCT.[9] MDCT further allows excellent MPR and 3D reformations that optimize detection of relevant pathology.[10]

Metallic stapes prostheses are more challenging to evaluate with CT because attenuation artifacts limit accurate evaluation of prosthesis size and intravestibular penetration.[11-13] Although

attenuation, though small size, suboptimal technique, and/or motion may limit visualization. Intraoperatively identified functional immobility and prosthesis uncrimping were additional sources of false-negative CT that illustrate the fact that some complications may not be detectable with any anatomic imaging technique.

Other findings that may contribute to poststapedectomy CHL are OtoO and ossicular fixation. OtoO reflects progression of otosclerosis and is seen as patchy lucent new bone formation. Bony
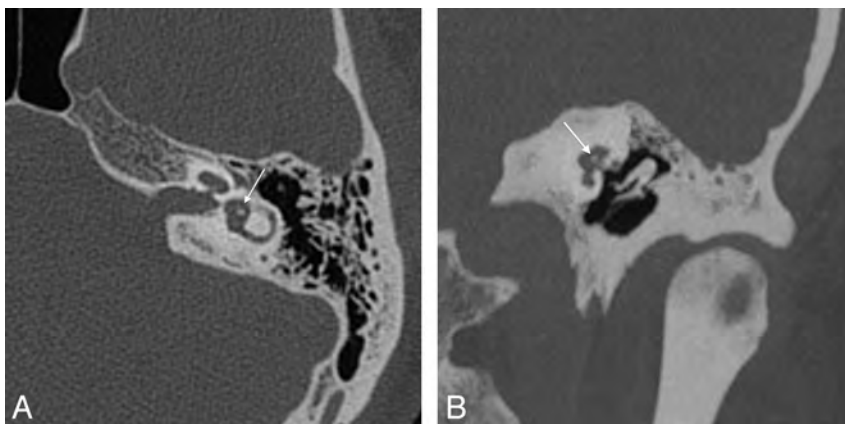
FIG 9. *A,* Axial CT in a 41-year-old man with vertigo and complete sensorineural hearing loss in the left ear after prior stapedectomy show focal hyperattenuation in the vestibule (*arrow*), consistent with intravestibular footplate dislocation. *B,* Coronal multiplanar reformation in the same patient as in *A* shows intravestibular footplate dislocation (*arrow*).
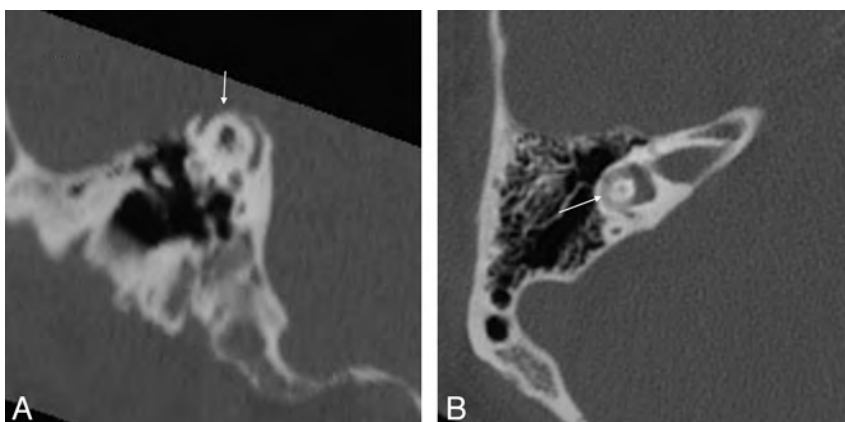

FIG 10. *A,* Poschl multiplanar reformation CT in a 67-year-old man with mixed hearing loss in the right ear after prior stapedectomy shows ipsilateral superior semicircular canal dehiscence (*arrow*) that probably explains surgical failure. *B,* Axial CT demonstrates ipsilateral labyrinthine ossificans (*arrow*) in the same patient as in *A* that might also have contributed to his surgical failure.

round window or OW obliteration prevents normal mechanical conduction and affects surgical planning. Although not an absolute contraindication, surgery is more complex and overall results are worse if OtoO is present.[6]

Two of 3 patients had SSCD that explained surgical failure (the third remains unoperated). This probably occurred in our series because SSCD was not well recognized as a cause of failed otosclerosis surgery with persistent CHL until the past decade. SSCD may be present in 5% of patients presenting for surgical treatment of otosclerosis.[17] SSCD acts as a "third window" mechanism, allowing dissipation of the mechanical fluid wave through an additional opening rather than transmission to the round window.[18,19] Any labyrinthine dehiscence should be reported because a case of posterior semicircular canal dehiscence causing CHL is also reported.[20-22]

Progressive SNHL and/or vestibular symptoms occur in 0.6–3% of primary and up to 14% of revision stapes surgeries.[23] Causes include serous or infectious labyrinthitis, labyrinthine fistula, reparative granuloma, and intravestibular foreign body. These are often less well evaluated with temporal bone CT, and

enhanced MR imaging may be indicated. Three patients with sensorineural deafness and/or vestibular symptoms had CT findings that could explain their findings: 2 pistons with excessive vestibule penetration and 1 stapes footplate dislocation into the vestibule. Progressive cochlear otosclerosis in 2 patients may have contributed to SNHL on the basis of natural disease progression because most poststapedectomy patients have late development of SNHL (30 years out) in the course of their disease.[24] Two patients also had labyrinthine ossificans as a suspected contributing cause of SNHL.

Limitations of this study include the occasionally incomplete nature of the electronic medical record and clinical correlation in 5 nonsurgical patients and 3 patients with cochlear implant surgery. There is also the possibility that pertinent intraoperative findings were not fully documented in the surgical reports. Furthermore, the prospective diagnostic capability of preoperative temporal bone CT was not assessed in this unblended, retrospective review. We were also unable to discriminate among patients with more than 1 potential contributing cause of persistent hearing and balance complaints.

CONCLUSIONS

Surgery is a mainstay of treatment for otosclerosis. Anatomic conditions that predispose to surgical failure include SSCD, OtoO, and labyrinthine ossificans. After initial surgery, temporal bone CT before revision surgery for persistent CHL may demonstrate prosthesis dislocation or disconnection, incus necrosis, granulation tissue, and inappropriate prosthesis size. SNHL and/or vestibular symptoms warrant assessment for suspected deep vestibular penetration or foreign body.

REFERENCES

1. Cummings CW, Fredrickson JM, Harker LA, et al, eds. *Otolaryngology-Head and Neck Surgery.* 2nd ed. St Louis: Mosby; 1993
2. Declau F, van Spaendonck M, Timmermans JP, et al. **Prevalence of histologic otosclerosis: an unbiased temporal bone study in Caucasians.** *Adv Otorhinolaryngol* 2007;65:6–16
3. Sakihara Y, Parving A. **Clinical otosclerosis, prevalence estimates and spontaneous progress.** *Clin Otosc Prev Acta Otol* 1999;199:468–72
4. Vincent R, Sperling, N, Oates, J, et al. **Surgical findings and long-term hearing results in 3,050 stapedotomies for primary otosclerosis: a prospective study with the Otology-Neurotology Database.** *Otol Neurotol* 2006;27(Suppl 2):S25–47

5. Ozuer MZ, Olgun L, Gultekin G. **Revision stapes surgery.** *Otolaryngol Head Neck Surg* 2012;146:109–13

6. Williams MT, Ayache D, Elmaleh M, et al. **Helical CT findings in patients who have undergone stapes surgery for otosclerosis.** *AJR Am J Roentgenol* 2000;174:387–92

7. Swartz JD, Lansman AK, Berger AS, et al. **Stapes prosthesis: evaluation with CT.** *Radiology* 1986;158:179–82

8. Moumoulidis I, Axon P, Baguley D, et al. **A review on the genetics of otosclerosis.** *Clin Otolaryngol* 2007;32:239–47

9. Curtin HD. **Superior semicircular canal dehiscence syndrome and multi–detector row CT.** *Radiology* 2003;226:312–14

10. Fatterpekar GM, Doshi AH, Dugar M, et al. **Role of 3D CT in the evaluation of the temporal bone.** *Radiographics* 2006;26(Suppl 1):S117–32

11. Bozzato A, Struffert T, Hertel V, et al. **Analysis of the accuracy of high-resolution computed tomography techniques for the measurement of stapes prostheses.** *Eur Radiol* 2010;20:566–71

12. Lesinski SG. **Causes of conductive hearing loss after stapedectomy or stapedotomy: a prospective study of 279 consecutive surgical revisions.** *Otol Neurotol* 2002;23:281–88

13. Warren FM, Riggs S, Wiggins RH. **Computed tomographic imaging of stapes implants.** *Otol Neurotol* 2008;29:586–92

14. Puxeddu R, Ledda GP, Pelagatti CL, et al. **Revision stapes surgery for recurrent transmissional hearing loss after stapedectomy and stapedotomy for otosclerosis.** *Acta Otorhinolaryngol Ital* 2005;25:347–52

15. Lagleyre S, Calmels MN, Escude B, et al. **Revision stapes surgery: the "lateralized piston syndrome."** *Otol Neurotol* 2009;30:1138–44

16. Choudhury N, Kumar G, Krishnan M, et al. **Atypical incus necrosis: a case report and literature review.** *J Laryngol Otol* 2008;122:1124–26

17. Picavet V, Govaere E, Forton G. **Superior semicircular canal dehiscence: preview in a population with clinically suspected otosclerosis-type hearing loss.** *B-ENT* 2009;5:83–88

18. Mikulec AA, McKenna MJ, Ramsey MJ, et al. **CHL without vertigo: superior semicircular canal dehiscence presenting as conductive hearing loss without vertigo.** *Otol Neurotol* 2004;25:121–29

19. Hope A, Fagan P. **Latent superior canal dehiscence syndrome unmasked by stapedotomy for otosclerosis.** *J Laryngol Otol* 2010;124:428–30

20. Gopen Q, Zhou G, Poe D, et al. **Posterior semicircular canal dehiscence: first reported case series.** *Otol Neurotol* 2012;33:1368–74

21. Merchant SN, Rosowski JJ, McKenna MJ. **Superior semicircular canal dehiscence mimicking otosclerotic hearing loss.** *Adv Oto-Rhino-Laryngol* 2007;65:137–45

22. Nakashima T, Ueda H, Furuhashi A, et al. **Air-bone gap and resonant frequency in large vestibular aqueduct syndrome.** *Am J Otol* 2000;21:671–74

23. Yehudai, N, Luntz M. **Resolution of delayed sudden sensorineural hearing loss after stapedectomy: a case report and review of the literature.** *Med J Otol* 2006;3:156–60

24. Redfors YD, Moller C. **Otosclerosis: thirty-year follow-up after surgery.** *Ann Otol Rhinol Laryngol* 2011;120:608–14

High-Resolution Secondary Reconstructions with the Use of Flat Panel CT in the Clinical Assessment of Patients with Cochlear Implants

M.S. Pearl, A. Roy, and C.J. Limb

ABSTRACT

SUMMARY: Radiologic assessment of cochlear implants can be limited because of metallic streak artifacts and the high attenuation of the temporal bones. We report on 14 patients with 18 cochlear implants (17 Med-El standard 31.5-mm arrays, 1 Med-El medium 24-mm array) who underwent flat panel CT with the use of high-resolution secondary reconstruction techniques. Flat panel CT depicted the insertion site, cochlear implant course, and all 216 individual electrode contacts. The calculated mean angular insertion depth for standard arrays was 591.9° (SD = 70.9; range, 280°). High-resolution secondary reconstructions of the initial flat panel CT dataset, by use of a manually generated field of view, Hounsfield unit kernel type, and sharp image characteristics, provided high-quality images with improved spatial resolution. Flat panel CT is a promising imaging tool for the postoperative evaluation of cochlear implant placement.

ABBREVIATIONS: CI = cochlear implant; EE = edge enhancement; FPCT = flat panel CT; HU = Hounsfield units; MSCT = multisection CT; RW = round window

Cochlear implants (CIs) can provide functional restoration of hearing in individuals with profound hearing impairment. Clinical outcomes after implantation vary considerably, however, in the degree and quality of hearing recovery. To assess factors potentially related to CI outcomes, much attention has been devoted to characterizing the CI electrode location,[1,2] insertion depth,[3] scalar localization,[4] and relationship to the facial nerve canal.[2,5] These data carry important prognostic information and have implications for surgical approaches, insertion techniques, and programming strategies for optimal auditory nerve stimulation. Although CT is considered the current reference standard method for characterizing CI position,[6] metallic artifact significantly limits the postoperative imaging evaluation of the electrode array and cochlear anatomy.

Flat panel CT (FPCT) is a relatively new imaging technique that provides CT-like images acquired with a C-arm x-ray system with the use of flat panel image detectors. This technique provides excellent visualization of high-contrast structures with superior spatial resolution in comparison to multisection CT (MSCT).[7] Furthermore, secondary reconstruction of the initial FPCT dataset by use of a smaller field of view produces higher-resolution images than can be obtained by standard FPCT reconstructions.

We sought to determine the effectiveness of high-resolution secondary reconstructions of initial FPCT datasets for postoperative CI imaging. We compared 4 different types of image characteristics (very smooth, normal, auto, and sharp) and 2 different kernel types (Hounsfield units [HU] and edge enhancement [EE]) used in the creation of secondary reconstructions to identify the specific reconstruction parameters that lead to optimal CI visualization.

Subjects

A total of 14 patients with sensorineural hearing loss who underwent previous cochlear implantation with 17 Med-El standard 12-electrode contact arrays (31.5-mm linear insertion length, 2.4 mm between contacts) and 1 Med-El medium 12-electrode contact array (24-mm linear insertion length, 1.9 mm between contacts) (Med-El, Innsbruck, Austria) were included (Table 1). Subjects included 8 men and 6 women with a mean age of 53 years (range, 21–62 years). A standard posterior tympanotomy approach was used in all cases. The implantation approaches were mixed and included pure round window (RW) insertions as well as cochleostomies just anterior to the RW with or without extension into the RW.

All patients gave written informed consent to participate in this institutional review board–approved study.

Table 1: Demographic information for patients with cochlear implants

Subject	Sex	Age, y	Etiology	Implant Device	Implant Side	Fig 5	RW Insertion
1	F	59	Meniere	Med-El Sonata, Standard Array	Right	B	
2	F	48	Autoimmune	Med-El Sonata, Standard Array	Right	H	RW
3	M	62	Meniere	Med-El Sonata, Standard Array	Left	R	RW
4[a]	M	51	Idiopathic	Med-El Concert, Standard Array	Right	F	RW
				Med-El Concert, Standard Array	Left	L	
5	F	54	Hereditary	Med-El Concert, Standard Array	Left	Q	
6	F	21	Idiopathic	Med-El Sonata, Standard Array	Left	P	
7[a]	M	59	Meniere	Med-El Concert, Standard Array	Right	D	
				Med-El Sonata, Standard Array	Left	M	
8[a]	M	62	Idiopathic	Med-El Sonata, Standard Array	Right	C	RW
				Med-El Sonata, Standard Array	Left	J	
9	F	51	Idiopathic	Med-El Concert, Standard Array	Right	G	RW
10	M	61	Meniere	Med-El Concert, Standard Array	Left	O	
11[a]	M	57	Idiopathic	Med-El Sonata, Standard Array	Right	E	
				Med-El Sonata, Standard Array	Left	K	
12	M	49	Meningitis	Med-El Concert, Standard Array	Right	A	
13	M	61	Viral	Med-El Sonata, Standard Array	Left	N	
14	F	50	Idiopathic	Med-El Concert, Medium Array	Right	I	

Note:—Demographic information for all 14 patients with cochlear implants include sex, age, etiology of hearing loss, type of CI, laterality, and corresponding image in Fig 5. Round window insertions are designated by RW.
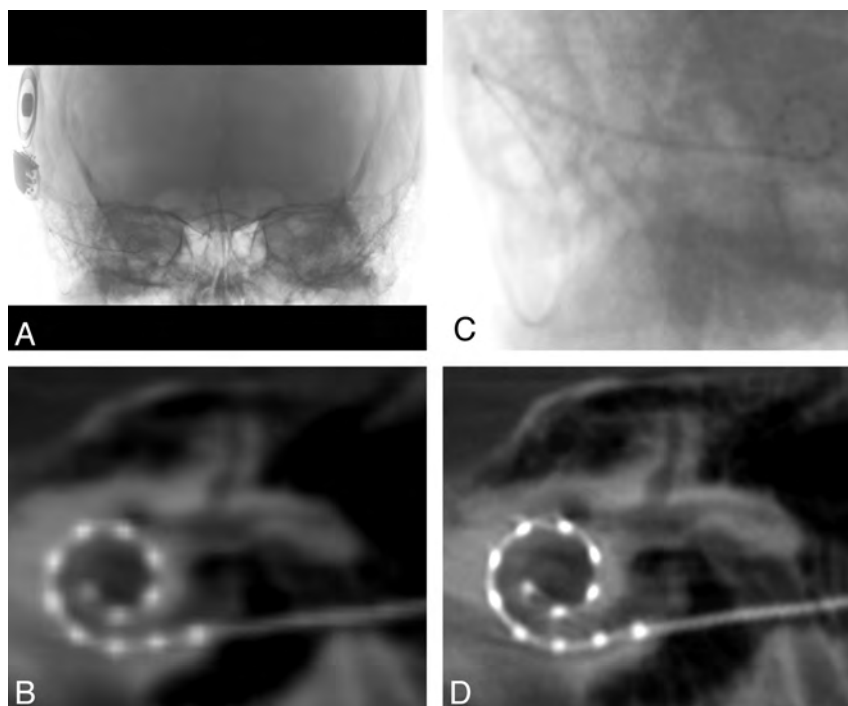
[a] Subjects with bilateral CIs.

FIG 1. Flat panel CT of a right-sided cochlear implant. *A,* Collimated fluoroscopic acquisition for a 20-second FPCT of a right-sided CI. The skull above and below is excluded from the initial acquisition. *B,* Example of a coronal oblique image acquired after the default reconstruction. *C,* Secondary reconstruction by use of a manually generated voxel of interest is created to include only the electrode array. *D,* Higher-resolution coronal oblique image is generated after the secondary reconstruction.

FPCT Imaging Protocol

All subjects underwent FPCT (DynaCT; Siemens, Erlangen, Germany) evaluation on a flat-panel angiography system (Axiom Artis Zee, Siemens) with the use of commercially available software (Syngo DynaCT, Siemens). A collimated 20-second FPCT of the head (Fig 1*A*) was performed by use of the following parameters: 109 kV, small focus, 200° degree rotation angle, and 0.4° degree/frame angulation step. Postprocessing was performed on a commercially available workstation (Leonardo DynaCT, InSpace 3D software; Siemens). High-resolution secondary reconstructions (Fig 1*C–D*) were created with the use of the following parameters: manually generated voxels of interest to include only the electrode array; voxel size, 0.07–0.08 mm, 512 × 512 section matrix; HU and EE kernel types; and very smooth, normal, auto, and sharp image characteristics.

An interventional neuroradiologist with fellowship training and subspecialty certification in diagnostic neuroradiology (M.S.P.) performed the postprocessing. All images were evaluated by all 3 authors: an interventional neuroradiologist with subspecialty certification in diagnostic neuroradiology (M.S.P.); a neuroscientist with >4 years of research dedicated to CIs (A.R.); and a neurotologist who is a CI specialist and has >15 years of experience in the field of CI (C.J.L.).

Reconstruction Parameters

The secondary reconstruction parameters available for postprocessing included kernel type (HU and EE) and image characteristic (very smooth, normal, auto, and sharp). Each kernel type was paired with each type of image characteristic to create the secondary reconstructions by use of a smaller manually generated VOI.

For each reconstruction, 2D multiplanar images were created. Coronal oblique images in the plane of the array were generated by aligning the multiplanar reconstruction axes on the axial and sagittal planes parallel to the basal turn and perpendicular to the modiolus (Fig 2). The section thickness was set to 3 mm to include all electrode contacts on one image. The
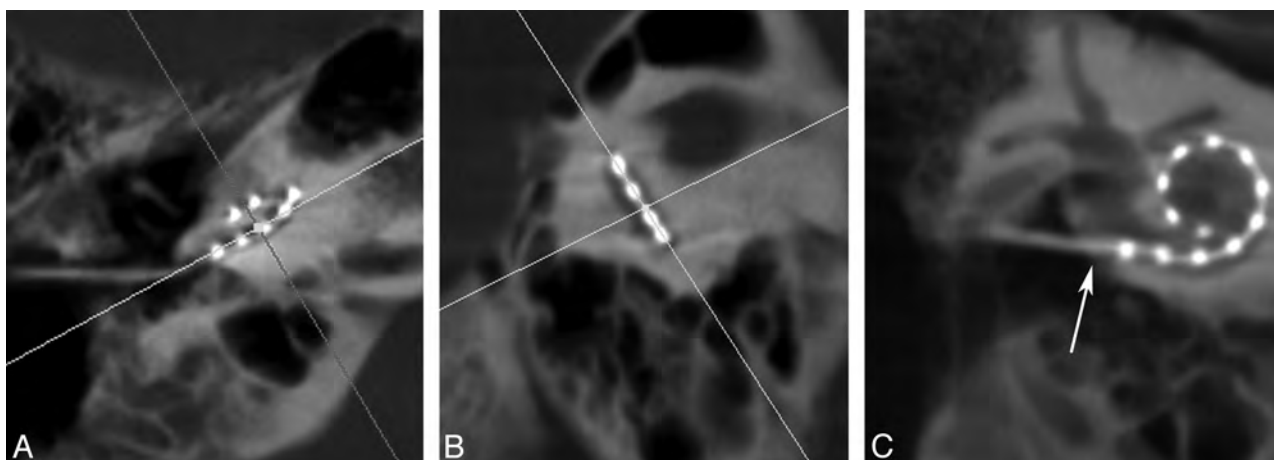
FIG 2. Multiplanar reconstruction images of a right-sided cochlear implant. Multiplanar reconstruction axes are aligned parallel to the basal turn on the axial *(A)* and sagittal *(B)* planes to generate a coronal oblique *(C)* image of the CI. This image is rotated slightly to visualize the vestibule and superior semicircular canal. Arrow in *(C)* denotes the insertion point.
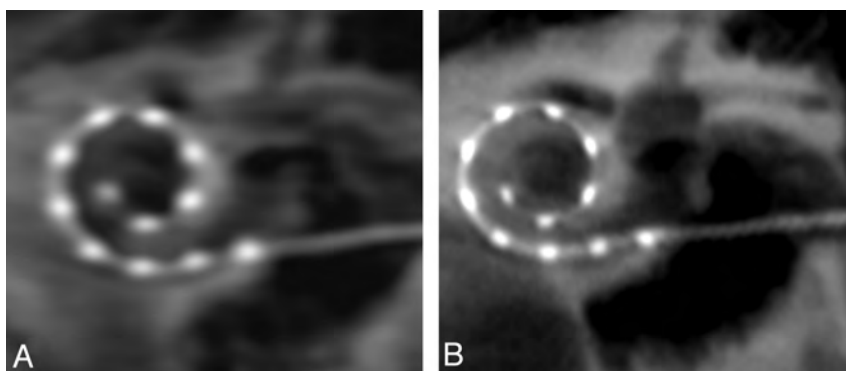

FIG 3. Secondary reconstructions comparing edge enhancement *(A)* and Hounsfield unit (HU) *(B)* kernel type show more distinct individual electrode contacts and osseous structures on the image generated by HU kernel type.

window width and contrast level were adjusted until both the individual electrode contacts and surrounding labyrinthine structures were visualized.

The individual electrode contacts appeared less distinct by use of the EE kernel type in comparison to the HU kernel type (Fig 3). All individual electrode contacts could be identified by means of all 4 types of image characteristics; however, the very smooth and normal types created images whose electrodes and surrounding osseous structures were blurry. More distinct contacts and osseous structures were apparent with the auto and sharp image characteristics. The combination of reconstruction parameters that produced the clearest depiction of the electrode array and surrounding labyrinthine structures were HU kernel type and sharp image characteristics (Fig 4).

Visualization of Insertion Point and Individual Electrode Contacts

FPCT depicted all 18 insertion points and distinguished all 216 individual electrode contacts for all 14 patients (Fig 5*A–R*). This includes 1 patient (Fig 5*I*) with a Med-El medium 12-electrode contact array. A standard posterior tympanotomy approach was used in all subjects. Five of the 18 CIs were pure RW insertions (Table 1).

Measuring Angular Insertion Depth

The 2D MPR section thickness was reduced to 0.1 mm to determine the electrode array insertion point, defined by the entrance of the electrode array from the middle ear into the lumen of the scala tympani. This was determined in the axial images at the air-to-bone interface along the outer margin of the electrode and then confirmed in the sagittal and coronal planes. The insertion point was designated in the coronal images and used as the first reference point for measuring angular insertion depth. With the use of a 3-mm section thickness, the 3 most apical electrodes were identified and used to create a circle depicting their course. A line drawn from the insertion point to the center of this circle served as the reference (zero degree) line. The angle θ between the most apical electrode and the reference line was calculated (Fig 6). This angle was subtracted from or added to 360 or 720, depending on the relationship between the apical electrode and the number of turns across the reference line (Table 2).

The mean apical electrode insertion depth for the standard 31.5-mm array was 519.1° (SD = 70.8; range, 468.8–749.0°). The apical insertion depth for the medium 24-mm array was 424.0° (Fig 7). There was no significant difference in the angular insertion depth between male (mean = 593.3; SD = 67.3) and female patients (mean = 541.9; SD = 47.9), $t(11) = 1.81$, $P = .10$, 2-tailed; however, this observation may be limited because of the small sample size in each group. Given the idiopathic etiology for hearing loss in 43% of our subjects (6 of 14; not an uncommon finding in this patient population) we did not specifically compare etiology with implant depth.

DISCUSSION

Advances in CI design and implantation have been limited by the inability to assess individual electrode contact placement, reliably calculate angular insertion depth, and accurately determine the
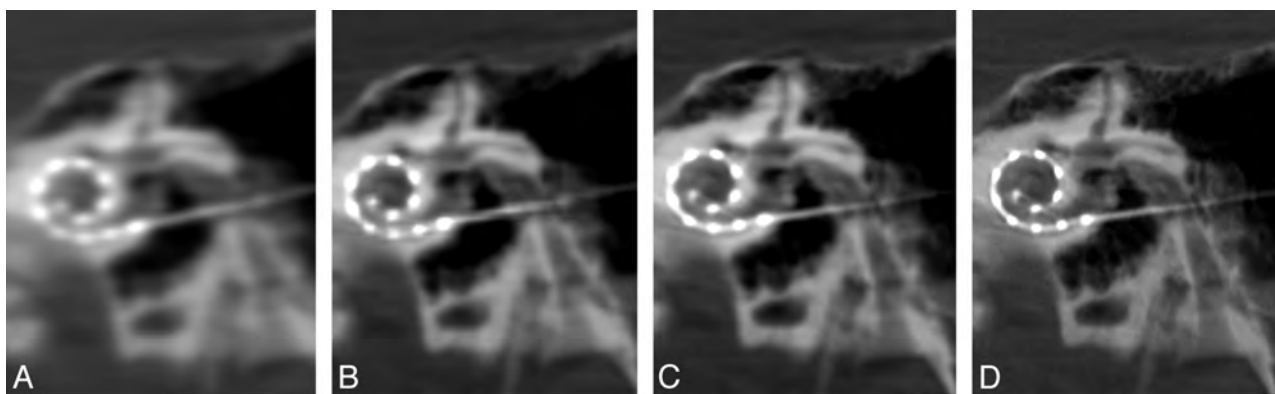
FIG 4. Coronal oblique secondary reconstructions of the same patient with cochlear implants. These images illustrate the variable image quality obtained with identical 3-mm section thickness, window width (3681), contrast (1246), and kernel type (HU). Note the blurring and poor visualization of the electrode contacts with the very smooth (A) setting. A sharp (D) parameter produces optimal images with well-defined osseous structures and individual electrode contacts. (A) Very smooth, (B) normal, (C) auto, (D) sharp.

relationship of the electrode array to adjacent labyrinthine structures. These data provide important prognostic information and may play a critical role in CI outcomes.[8]

Imaging evaluation of postoperative CI placement was initially performed with plain radiographs in the Stenvers projection.[9,10] MSCT replaced this method and has since become the reference standard imaging technique for assessing the electrode array location relative to intracochlear scalae, the electrode-modiolar interval, and the proximity of the electrode to the fallopian canal.[6] CT offers the ability to provide 3D positional information and excellent contrast for different tissue types.[11] Despite these advantages, however, attenuated bone structures within the acquisition field[12] and metallic artifacts severely limit the visibility of electrode contacts and adjacent structures.[10,13,14]

FPCT is a relatively new imaging technique that creates less streak artifacts and offers higher spatial resolution than MSCT (cubic voxel size of approximately 0.07 mm versus 0.4–0.6 mm, respectively).[7] These CT-like images can discern individual electrode contacts, often not possible on MSCT.[2,7] In addition, FPCT has demonstrated improved imaging of the cochlea and facial nerve canal, enabling identification of electrode contacts in close proximity to the fallopian canal and therefore most prone to induce inadvertent stimulation of the facial nerve.[2,15]

Initial studies with the use of FPCT in the evaluation of CIs were performed with the use of cadaveric-implanted temporal bones.[2,6,7] The authors noted potential limitations caused by the use of temporal bone specimens rather than whole skulls, which were thought to be more challenging for imaging purposes.[2] Only recently have patients with CIs been evaluated by FPCT.[3,16] Our study represents one of the larger series to date of CI assessment with FPCT (14 patients, 18 electrode arrays), and the only one to explore optimal reconstruction parameters, including secondary reconstruction techniques. In our series, FPCT was able to identify all 18 insertion points and all 216 individual electrode contacts as well as to identify surrounding labyrinthine structures that were not degraded by streak artifact. Secondary reconstructions of the initial FPCT dataset by use of a VOI to include only the electrode array created voxel sizes of 0.07–0.08 mm, allowing for higher-resolution images than initial reconstructions (Fig 1B–D). These datasets were optimized by use of an HU kernel type and

sharp image characteristic, which enabled the distinct identification of individual electrode contacts and surrounding osseous and soft tissue structures. Figure 4 highlights the range of image quality obtained with different postprocessing algorithms and shows the advantages of the "sharp" algorithm, with better delineation of osseous structures and less blurring of the image.

FPCT could not clearly detect the basilar membrane to designate exact scalar location, which is consistent with previous reports.[2] CT methods for this designation use oblique coronal images reconstructed perpendicular to the basal turn and parallel to the modiolus. The scalar position, however, is inferred in relation to the cochlear walls[17] because the image resolution is insufficient to visualize the osseous spiral lamina and basilar membrane.[18] Although we could infer the scalar position on the basis of the relative location of the CI in the cochlear chamber, this was not specifically attempted because definitive location could not be made or compared with any other standard. Additionally, given that an electrode may penetrate the basilar membrane and traverse >1 scalae, it is difficult to assume true location without visualizing distinct landmarks. Scalar localization will be the subject of future research as reconstruction algorithms and other advanced postprocessing techniques continue to improve. Whereas some reports cite the ability to clearly detect scalar position of the CI, the assessment of positioning within the scala tympani was primarily demonstrated in ex vivo specimens.[16]

The limitations of our report include the evaluation of only 1 CI manufacturer (Med-El; chosen for consistency during development of the imaging protocol), and the predominant assessment of CIs with electrode contacts spaced 2.4 mm apart (Med-El standard array), which are farther apart than some arrays currently available through other manufacturers. The distinct identification of individual electrode contacts was easily achievable, suggesting that this method should also distinguish more closely spaced contacts. Patient 14 (Fig 5I), implanted with the Med-El medium 12-electrode contact array, demonstrates the feasibility of visualizing electrode contacts spaced 1.9 mm apart. Currently planned studies will apply the FPCT technology with high-resolution secondary reconstruction algorithms to investigate other electrode designs and CI manufacturers.
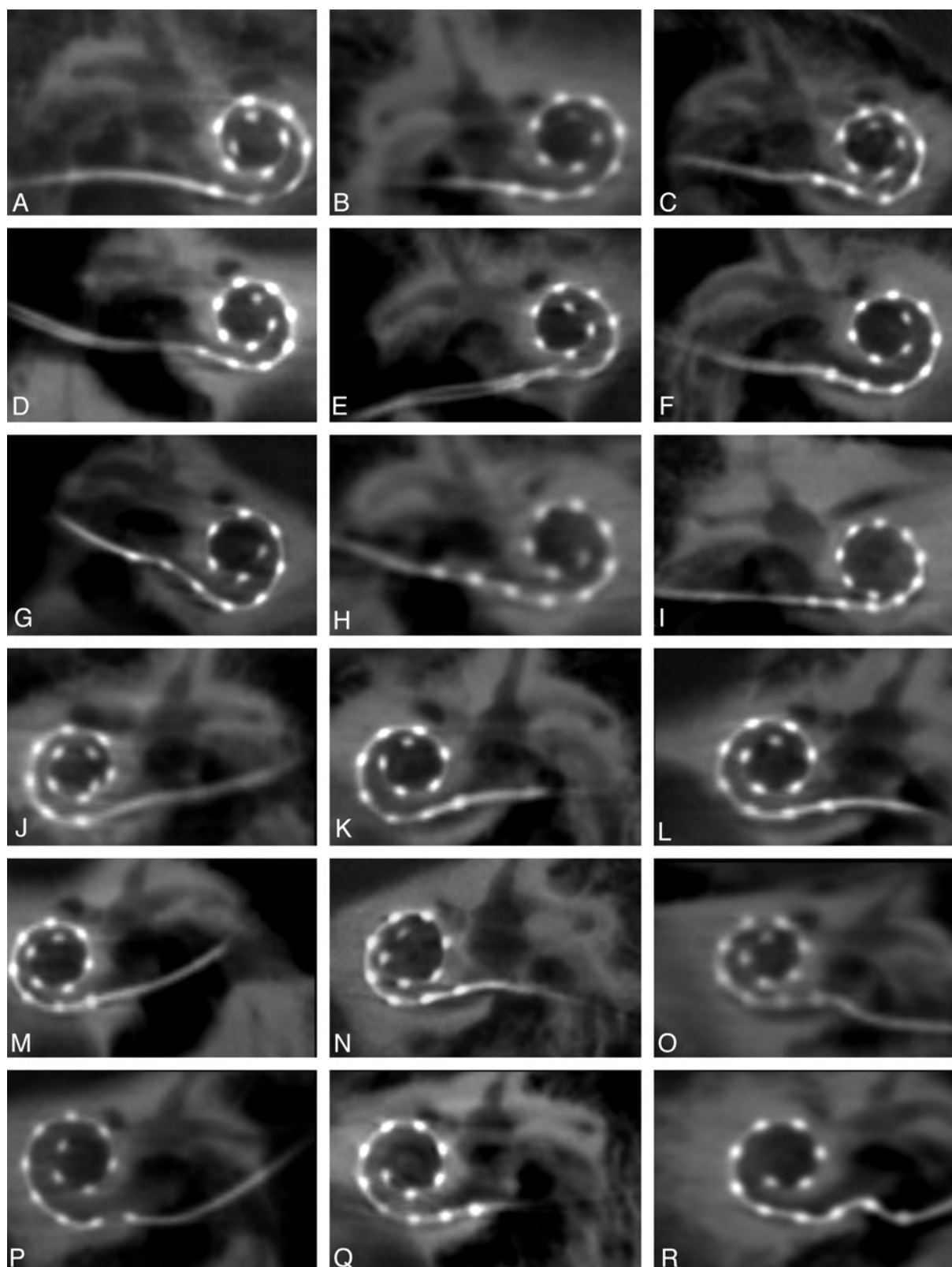
FIG 5. High-resolution secondary reconstructions of all 14 patients and 18 cochlear implants (CIs). *A–I,* Nine right-sided CIs, including 1 patient *(I)* with an implanted medium array, are shown in the coronal oblique plane. *J–R,* Nine left-sided CIs are depicted, all of which are the standard length array. Images are arranged in order of descending angular insertion depth. All 216 individual electrode contacts are clearly visualized in all patients.
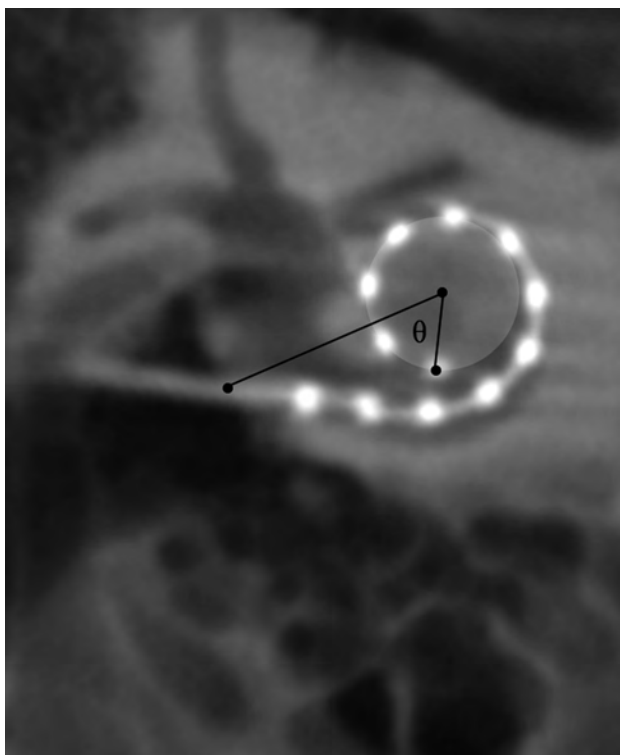
FIG 6. Method for calculating the angular insertion depth of the most apical electrode. The insertion point, as determined by the axial and sagittal images (not shown) is designated in the coronal oblique image. A circle whose outer circumference represents the trajectory of the 3 most apical electrodes is drawn. A reference line is drawn between the insertion point and the center of this circle. The most apical electrode is then identified and the angle θ is calculated between the electrode and the reference line. In this example, angular insertion depth is calculated by $360 \pm \theta$.

Table 2: Method for calculating angular insertion depth

No. of Complete Turns	Angular Insertion Depth
<1	$360 - \theta$
>1, <1.5	$360 + \theta$
>1.5, <2	$720 - \theta$
>2	$720 + \theta$

Note:—Angular insertion depth calculations: The angular insertion depth for apical electrodes coursing <1 complete turn in relation to the zero degree line is calculated by $360 - \theta$; for >1 turn but <540° (1.5 turns), insertion depth equals $360 + \theta$; for >1.5 turns but <2 turns, insertion depth equals $720 - \theta$. For >2 turns, insertion depth equals $720 + \theta$.

CONCLUSIONS

FPCT evaluations of postoperative CIs are easy to perform, produce high-resolution images, and are able to depict all individual electrode contacts, thus enabling measurement of the angular insertion depth of the most apical electrode contacts. Optimal imaging methods use a high-resolution secondary reconstruction algorithm with a manually generated small VOI (voxel size, 0.07–0.08 mm), HU kernel type, and sharp image characteristic. These advances in CI imaging may lead to a better understanding of the relationship between cochlear anatomy, CI electrode placement, and auditory performance.
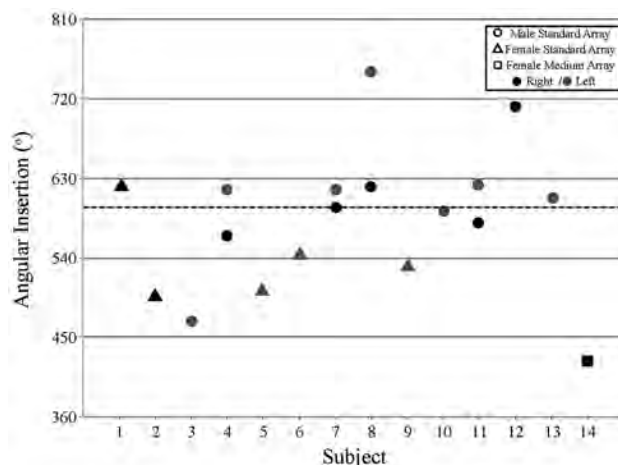
FIG 7. Measured angular insertion depth of the most apical electrodes. Circles and triangles depict angular insertion depth for male and female patients with Med-El 31.5-mm standard array, respectively. Square refers to the single Med-El 24-mm medium array patient. Black filled shapes depict a right implanted ear; gray filled shapes depict a left implanted ear.

REFERENCES

1. Teymouri J, Hullar TE, Holden TA, et al. **Verification of computed tomographic estimates of cochlear implant array position: a micro-CT and histologic analysis.** *Otol Neurotol* 2011;32:980–06
2. Bartling SH, Gupta R, Torkos A, et al. **Flat-panel volume computed tomography for cochlear implant electrode array examination in isolated temporal bone specimens.** *Otol Neurotol* 2006;27:491–98
3. Trieger A, Schulze A, Schneider M, et al. **In vivo measurements of the insertion depth of cochlear implant arrays using flat-panel volume computed tomography.** *Otol Neurotol* 2011;32:152–57
4. Lane JI, Driscoll CL, Witte RJ, et al. **Scalar localization of the electrode array after cochlear implantation: a cadaveric validation study comparing 64-slice multidetector computed tomography with microcomputed tomography.** *Otol Neurotol* 2007;28:191–94
5. Vanpoucke F, Zarowski A, Casselman J, et al. **The facial nerve canal: an important cochlear conduction path revealed by Clarion electrical field imaging.** *Otol Neurotol* 2004;25:282–89
6. Zeitler DM, Wang KH, Prasad RS, et al. **Flat-panel computed tomography versus multislice computed tomography to evaluate cochlear implant positioning.** *Cochlear Implants Int* 2011;12:216–22
7. Struffert T, Hertel V, Kyriakou Y, et al. **Imaging of cochlear implant electrode array with flat-detector CT and conventional multislice CT: comparison of image quality and radiation dose.** *Acta Otolaryngol* 2010;130:443–52
8. Finley CC, Holden TA, Holden LK, et al. **Role of electrode placement as a contributor to variability in cochlear implant outcomes.** *Otol Neurotol* 2008;29:920–28

9. Cohen LT, Xu J, Xu SA, et al. **Improved and simplified methods for specifying positions of the electrode bands of a cochlear implant array.** *Am J Otol* 1996;17:859–65

10. Xu J, Xu SA, Cohen LT, et al. **Cochlear view: post-operative radiography for cochlear implantation.** *Am J Otol* 2000;21:49–56

11. Skinner MW, Ketten DR, Vannier MW, et al. **Determination of the position of nucleus cochlear implant electrodes in the inner ear**. *Am J Otol* 1994;15:644–51

12. Whiting BR, Holden TA, Brunsden BS, et al. **Use of computed tomography scans for cochlear implants.** *J Digit Imaging* 2008;21:323–28

13. Whiting BR, Bae KT, Skinner MW. **Cochlear implants: three-dimensional localization by means of coregistration of CT and conventional radiographs.** *Radiology* 2001;221:543–49

14. van Wermeskerken GK, van Olphen AF, Graamans K. **Imaging of electrode position in relation to electrode functioning after cochlear implantation.** *Eur Arch Otorhinolaryngol* 2009;266:1527–31

15. Bigelow DC, Kay DJ, Rafter KO, et al. **Facial nerve stimulation from cochlear implants.** *Am J Otol* 1998;19:163–69

16. Arweiler-Harbeck D, Monninghoff C, Greve J, et al. **Imaging of electrode position after cochlear implantation with flat panel CT.** *ISRN Otolaryngol* 2012;2012:728205

17. Ruivo J, Mermuys K, Bacher K, et al. **Cone beam computed tomography, a low-dose imaging technique in the post-operative assessment of cochlear implantation.** *Otol Neurotol* 2009;30:299–303

18. Verbist BM, Frijns JH, Geleijns J, et al. **Multisection CT as a valuable tool in the post-operative assessment of cochlear implant patients.** *AJNR Am J Neuroradiol* 2005;26:424–29

High-Resolution MRI Evaluation of Neonatal Brachial Plexus Palsy: A Promising Alternative to Traditional CT Myelography

D. Somashekar, L.J.S. Yang, M. Ibrahim, and H.A. Parmar

ABSTRACT

BACKGROUND AND PURPOSE: Despite recent improvements in perinatal care, the incidence of neonatal brachial plexus palsy remains relatively common. CT myelography is currently considered to be the optimal imaging technique for evaluating nerve root integrity. Recent improvements in MR imaging techniques have made it an attractive alternative to evaluate nerve root avulsions (preganglionic injuries). We aim to demonstrate utility of MR imaging in the evaluation of normal and avulsed spinal nerve roots.

MATERIALS AND METHODS: All study patients with clinically diagnosed neonatal brachial plexus palsy underwent MR imaging by use of a high-resolution, heavily T2-weighted (driven equilibrium) sequence. MR imaging findings were reviewed for presence of nerve root avulsion from C5–T1 and for presence of pseudomeningocele. The intraoperative findings were reviewed and compared with the preoperative MR imaging findings.

RESULTS: Thirteen patients (9 male, 4 female) underwent MR imaging; 6 patients underwent nerve reconstruction surgery, during which a total of 19 nerve roots were evaluated. Eight avulsions were noted at surgery and in the remainder, the nerve injury was more distal (rupture/postganglionic injury). Six of the 8 nerve root avulsions identified at surgery were at C5–6 level, whereas 1 nerve root avulsion was identified at C7 and C8 levels, respectively. The overall sensitivity and specificity of MR imaging for nerve root avulsions was 75% and 82%, respectively.

CONCLUSIONS: Our preliminary results demonstrate that high-resolution MR imaging offers an excellent alternative to CT myelography for the evaluation of neonatal brachial plexus palsy with similar sensitivity compared with CT myelography.

ABBREVIATIONS: NBPP = neonatal brachial plexus palsy; CTM = CT myelogram

Neonatal brachial plexus palsy (NBPP) results from insult to the brachial plexus during the perinatal period.[1] NBPP can result when the upper shoulder of the infant becomes blocked by the pubic symphysis of the mother.[2,3] Nerve injury can occur anywhere along the brachial plexus but generally occurs in the supraclavicular brachial plexus at the nerve roots/trunks levels, resulting in varied neurologic deficits. Damage to the nerve roots arising from the ventral aspect of the spinal cord results in motor function disability. The most common lesions occur within the C5 and C6 spinal nerves (80% of patients), with a smaller group of patients having more extensive lesions ranging from C5–C7 and

from C5–T1 (pan-plexopathy).[1,3] Collectively, the clinical presentation resulting from these lesions is referred to as NBPP.

NBPP occurs with an incidence of up to 3 per 1000 live births.[1] The most severe forms of injury result from complete axonal disruption (neurotmesis or severe axonotmesis), either at the level of the proximal nerve roots or trunks of the brachial plexus (ruptures, postganglionic injury), or when 1 or more of the spinal nerves of the brachial plexus are torn out of the spinal cord (root avulsion, preganglionic injury).[4] In these cases, the likelihood of spontaneous recovery is low and surgical intervention is generally thought to be reasonable.[5] Less severe injuries such as simple stretching of the nerves (neurapraxia) or rupture of a few axons (mild axonotmesis) can result in spontaneous functional recovery[3] (Fig 1). The clinical treatment of patients with NBPP can be difficult and depends on the specific type of lesion involved. Early on, it is often difficult to characterize the lesion type because patients may clinically present with similar apparent deficiencies regardless of the levels involved. This presents a diagnostic and management dilemma because patients with neurapraxia/mild
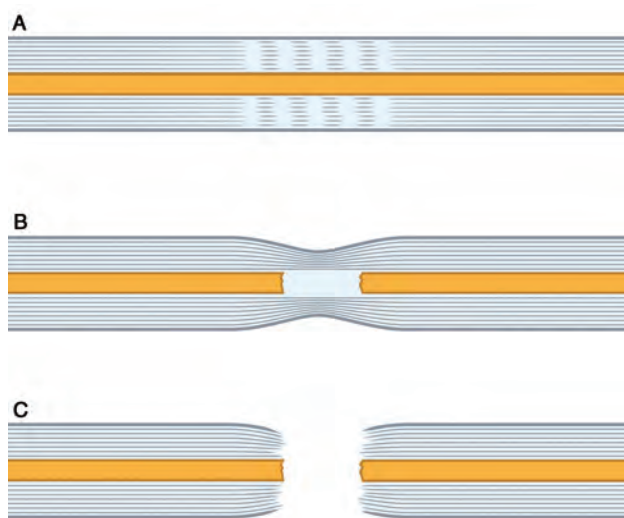
FIG 1. Schematic diagram showing different patterns of injuries affecting the nerve, including neuropraxia (A), mild axonotmesis (B), and neurotmesis (C).

axonotmesis will demonstrate spontaneous recovery over time, whereas the effectiveness of surgical intervention for neurotmesis or nerve root avulsion decreases with time. The typical practice at this time is to allow the patient a 3-month period in which to exhibit spontaneous recovery.[4,5] If recovery does not occur or is incomplete, further evaluation is recommended to determine the extent of injury. Perhaps there is a role for imaging earlier after birth because patients with minor injuries could be given a more favorable prognosis without the waiting period, at the admitted increased medical costs. However, it is possible that early imaging can save medical costs downstream by identifying patients who do not need more extensive follow-up and evaluation in the future.

Although direct surgical exploration may be considered the reference standard for lesion characterization, it carries significant morbidity and would require laminectomy to observe the intradural nerve roots. For this reason, CT myelography (CTM) and electrodiagnostic studies have been used as less invasive techniques and comprise the standard preoperative assessment for establishing preganglionic nerve root avulsion and postganglionic nerve ruptures in neonatal, pediatric, and adult populations.[4,6] CTM is most useful for detection of root avulsions (72% sensitivity), whereas electrodiagnostic studies are best at detecting postganglionic nerve ruptures, especially in the upper plexus (93% sensitivity).[6] These 2 tests are generally used in combination with one another to provide the neurosurgeon with supplemental preoperative information.[6]

Although CTM is currently the most widely used imaging method for evaluating nerve root avulsion, there are drawbacks. It requires an invasive lumbar puncture, instillation of iodinated contrast into the thecal sac, and the use of radiation, all of which carry unfavorable risks, particularly within the infant and pediatric populations. Nevertheless, CTM continues to be recommended in every preoperative assessment for NBPP at many specialty centers.[4,6] Recent improvements in MR imaging techniques have made MR imaging an attractive alternative to conventional CT. MR imaging is noninvasive, does not require the use of intrathecal contrast, and does not use ionizing radiation. This technique, if effective at diagnosing nerve root avulsion, can emerge as an alternative technique to CTM in the pediatric population. To date, however, there are only a few reports contained in the literature examining the utility of MR imaging for nerve root avulsions and none looking specifically at NBPP.[7-11] The reports contain scant imaging examples of nerve root avulsion, and many of the images are not convincingly diagnostic.[12] Most of the reports focus on the use of a heavily T2-weighted 3D sequence, referred to under various names on the basis of the specific manufacturer, such as 3D CISS (constructive interference in steady state), 3D True-FISP (fast imaging with steady-state precession), FIESTA (fast imaging employing steady-state acquisition), and DRIVE (driven equilibrium) sequences.[7] The end goal of these sequences is the same: to create a sequence with very high CSF-to-tissue contrast with elimination of pulsation artifact, to optimally visualize the exiting cervicothoracic nerve roots.[13] Until now, however, there are no studies that unequivocally and consistently demonstrate high-quality images of nerve root avulsion. Some propose that it lacks the requisite spatial resolution to provide the neurosurgeon with necessary diagnostic information,[14] though more recent advances in high-resolution 3T MR challenge this proposition.[15] Our aim was to use high-resolution MR imaging in evaluation of ventral nerve root avulsions in NBPP and to demonstrate that it is an excellent noninvasive and nonirradiating alternative to CTM.

MATERIALS AND METHODS

Institutional review board approval was obtained, and patient consent was waived for this Health Insurance Portability and Accountability Act–compliant prospective study. Patients were referred to our institution for evaluation of NBPP. All patients were given an obligatory observation period of 3–4 months to assess for spontaneous recovery. If clinical improvement was not forthcoming, they were referred for additional evaluation including MR imaging. MR imaging examination was performed on a 3T magnet (Ingenia; Philips Healthcare, Best, the Netherlands). We used a high-resolution 3D T2 DRIVE sequence with TR/TE/ of 1500/100 ms, TSE factor of 40, uniform voxel size of 0.6 mm with field of view of 80 mm, and reconstruction matrix of 320 × 320. A sensitivity encoding factor (parallel imaging) of 1.6 was used. Total scan time for this sequence was 8 minutes, 43 seconds. Sagittal and coronal reformatted images on both right and left sides were obtained in all patients and reviewed. All imaging studies were independently reviewed by 2 board-certified and pediatric neuroradiology–trained radiologists. Findings of presence or absence of ventral nerve root avulsions were recorded by consensus. At the time of writing, 6 of the 13 patients had proceeded to surgery. The findings at the time of surgery were recorded. The initial radiologic diagnoses were then compared with the surgical findings for any discrepancy (Table).

RESULTS

Thirteen patients (9 male, 4 female) with clinically diagnosed NBPP underwent MR imaging evaluation. Average age at the time of imaging was 6 months. MR imaging was successful and able to visualize the individual ventral and dorsal nerve roots in all patients (Fig 2A–C). We used axial images as primary images for our analysis; sagittal and coronal reformatted images complemented

Comparison of MRI and surgical findings at each cervical level

		Cervical Level									
		C5		C6		C7		C8		T1	
Patient	Affected Side	MRI	Surgery	MRI	Surgery	MRI	Surgery	MRI	Surgery	MRI	Surgery
1	Right	N	N	N	N	N	N	N	N/A	N	N/A
2	Left	N	N	N	A	N	N	N	N/A	N	N/A
3	Right	A	A	A	A	A	N	A	N/A	N	N/A
4	Left	N	N	N	A	N	N	N	N/A	N	N/A
5	Right	N	N	A	A	A	A	A	A	N	N
6	Right	N	N	A	A	A	N	N	N/A	N	N/A

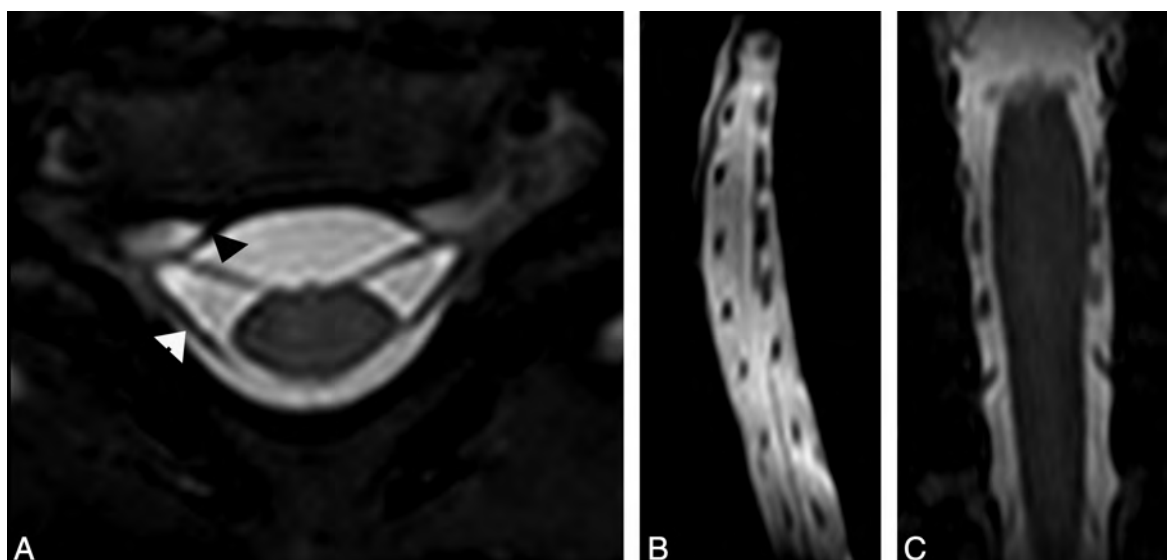**Note:**—N indicates normal; A, avulsion.

FIG 2. *A,* Axial high-resolution MR imaging in a 6-month-old girl with clinically suspected right-sided brachial plexus palsy showing intact right ventral (*arrowhead*) and dorsal nerve roots on both sides. Compare with normal left-sided nerve roots. Sagittal *(B)* and *(C)* coronal reformatted images from the axial data again show normal ventral and dorsal nerve roots at each vertebral level.

the axial images by showing multiple nerve roots at the same time. Of the 13 patients, 6 underwent brachial plexus exploration and nerve reconstruction, from which a total of 19 nerve roots were evaluated. At surgery, 8 ventral nerve root avulsions were noted. Overall, MR imaging was 75% sensitive and 83% specific in the preoperative detection of these ventral nerve root avulsions. The positive and negative predictive values were also 75% and 83%, respectively. A more in-depth, level-by-level analysis demonstrated that 6 of 8 surgically confirmed avulsions occurred at the C5 and C6 levels (Fig 3*A–F*). At C5, there was 1 avulsion, which was correctly identified by means of MR imaging (100% sensitive and specific). At C6, there were 5 surgically proved avulsions. Of these, MR imaging was successful in detecting 3 of the lesions (60% sensitive, 100% specific). Interestingly, the remaining 2 avulsions that were not detected did not have any evidence of associated pseudomeningocele, either on imaging or at surgery. The C6 level nerve roots were reanalyzed again in light of surgical data, but no obvious technical issues on MR images were noticed to explain this discordance. At C7, there was 1 surgically confirmed avulsion that was detected by MR imaging; however, there were 2 additional false-positive C7 avulsions (100% sensitive, 60% specific, 33% positive predictive value). MR imaging correctly identified 1 avulsion at C8. An additional C8 avulsion was detected, but this level was not explored surgically and thus there was no confirmation. At the T1 level,

MR imaging did not detect any abnormalities. Only 1 of these T1 levels was surgically confirmed to be normal, whereas none of the other T1 roots were explored, and thus confirmation of whether these roots were actually intact was not possible. MR imaging detected 5 pseudomeningoceles (Fig 4) occurring in 3 patients, all of which were associated with nerve root avulsions. Of note, no MR imaging avulsions were identified in the absence of a pseudomeningocele. Interestingly, however, there were 2 surgically confirmed C6 avulsions. In both of these cases, there was no evidence of pseudomeningocele.

DISCUSSION

NBPP includes a wide array of injuries, primarily to the exiting nerve roots and trunks of the brachial plexus. Identification of avulsion (preganglionic) injuries is critical for maximizing outcomes by early surgical intervention and for operative planning: the nerve reconstruction strategy for avulsion injuries significantly differs from that of rupture (postganglionic injuries). In the case of ruptured nerve roots or trunks, autologous nerve grafting is usually used. A harvested nerve, often the sural nerve, is used to bridge the gap between the disrupted elements of the brachial plexus.[3] This provides a physical pathway as well as neurotrophic factors to stimulate axonal outgrowth. This surgery is often accomplished by means of a supraclavicular approach.[5] Brachial plexus root avulsion provides an additional challenge because
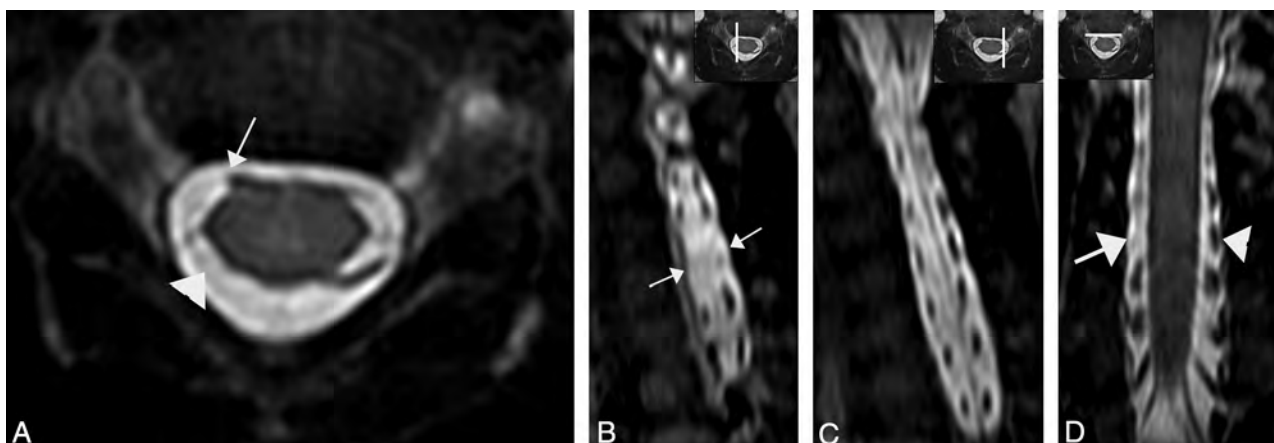
FIG 3. *A*, Axial high-resolution MR imaging in a 5-month-old girl with clinically suspected right-sided brachial plexus palsy shows avulsion injury of the right C5 ventral nerve root (*arrow*). The right dorsal nerve root is also avulsed (*arrowhead*). Sagittal *(B)* reformatted images on the right side show absent ventral and dorsal C5 nerve roots (*arrows*), compared with the normal nerve roots on left side *(C)*. Coronal reformatted image *(D)* at the level of ventral nerve roots show absent right C5 ventral nerve root from avulsion (*arrow*), compared with the normal left-sided nerve root (*arrowhead*).
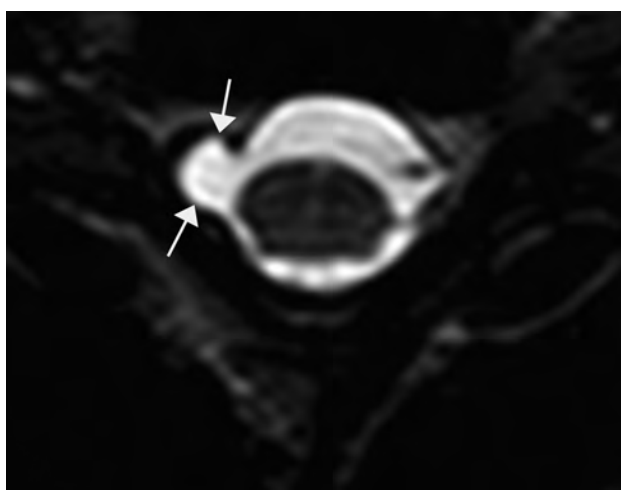

FIG 4. Axial high-resolution MR imaging in a 4-month-old boy with clinically suspected right-sided brachial plexus palsy shows a pseudomeningocele at right C5–6 level (*arrow*). Note absent nerve roots on right side suggestive of nerve root avulsion injury. Compare with normal ventral and dorsal nerve roots on the left side.

currently there is no feasible way in which to reattach the avulsed root to the spinal cord. The solution is a nerve transfer, in which an extra-plexus exiting nerve is cut and coapted to the denervated brachial plexus terminal nerve.[3]

In the present study, we evaluated a total of 13 patients by use of high-resolution MR imaging, of which 6 went on to surgery for confirmation and repair. In terms of overall performance, MR imaging demonstrated a sensitivity of 75% and specificity of 83%, both of which are comparable to the results published on CTM. Vanderhave et al[6] found the sensitivity of CTM as compared with surgical exploration to be 50% at levels C5 and C6, 83.3% at C7, and 75% at C8 and T1. There were 2 instances in which MR imaging failed to detect nerve root avulsion, both at the C6 level in different patients. These avulsions were detected at surgery, and these patients had no other roots that were avulsed. Curiously, no secondary findings such as pseudomeningocele were identified, either on imaging or at surgery. Isolated root avulsion without

such secondary findings of trauma is quite unusual, and no satisfactory anatomic explanation exists; perhaps there was scarring of the pseudomeningocele in the interval from time of injury to the time of imaging. Nonetheless, these 2 cases provide excellent examples in which nerve root avulsions can exist at surgery without the presence of pseudomeningocele formation. Therefore, it is imperative that MR and CT emphasize the imaging of actual nerve roots and that the neuroradiologist should not rely solely on the detection of pseudomeningoceles to confirm or discount the existence of a root avulsion. Our results demonstrate that MR imaging offers an excellent alternative to CT myelography in the evaluation of complete brachial plexus nerve root avulsion(s). The high-resolution MR imaging technique provides unambiguous visualization of intact nerve roots and accurate assessment of nerve root avulsions. MR imaging is also able to clearly show dorsal and ventral nerve roots in all 3 planes. It is important to differentiate the dorsal and ventral nerve roots and assess whether they are intact or avulsed because an intact dorsal nerve root can be used as a donor for an avulsed ventral nerve root by the neurosurgeon.

There are limitations to this study. First and foremost, the sample size is small, with 13 patients included in the study, only 6 of whom went on to surgery. Nevertheless, this is the first study of its kind to compare MR imaging findings with the reference standard of surgical exploration in the setting of NBPP. Another limitation stems from the lack of comparison CTM within this study group. Ideally, CTM and MR imaging would have been obtained in all patients to allow for a one-to-one comparison of the accuracy of the tests, but, obviously, given the ethical considerations, this was not deemed possible. Thus, the sensitivities and specificities for MR imaging were compared with those of CTM in the already published literature. The third limitation is that with the exception of 1 patient, the remaining C8 and T1 levels were never surgically observed. This in part had to do with the alternate, more in-depth surgical approach necessary to access these levels. This resulted in 1 C8 avulsion being detected on MR but never undergoing surgical confirmation. This was an isolated, nonsurgically confirmed avulsion. All other avulsions were surgically confirmed or refuted.

CONCLUSIONS

By prospectively examining 13 patients with clinically diagnosed NBPP, we have demonstrated the potential utility of MR imaging for providing reliable preoperative diagnoses of the type and extent of injury. It has proven value and has supplanted the use of CTM at our institution. Given that it is both noninvasive and nonirradiating while still providing all of the diagnostic information necessary to aid our neurosurgical colleagues, MR imaging should be the recommended technique in evaluating nerve root avulsion injuries in patients with NBPP.

REFERENCES

1. Doumouchtsis SK, Arulkumaran S. **Are all brachial plexus injuries caused by shoulder dystocia?** *Obstet Gynecol Surv* 2009;64:615–23
2. Alfonso DT. **Causes of neonatal brachial plexus palsy**. *Bull NYU Hosp Jt Dis* 2011;69:11–16
3. Malessy MJ, Pondaag W. **Nerve surgery for neonatal brachial plexus palsy.** *J Pediatr Rehabil Med* 2011;4:141–48
4. Steens SC, Pondaag W, Malessy MJ, et al. **Obstetric brachial plexus lesions: CT myelography.** *Radiology* 2011;259:508–15
5. Chung KC, Yang LJS, McGillicuddy JE. *Practical Management of Pediatric and Adult Brachial Plexus Palsies.* Philadelphia: Elsevier Health; 2011:35–46
6. Vanderhave KL, Bovid K, Alpert H, et al. **Utility of electrodiagnostic testing and computed tomography myelography in the preoperative evaluation of neonatal brachial plexus palsy.** *J Neurosurg Pediatr* 2012;9:283–89
7. Vargas MI, Viallon M, Nguyen D, et al. **New approaches in imaging of the brachial plexus.** *Eur J Radiol* 2010;74:403–10
8. Du R, Auguste KI, Chin CT, et al. **Magnetic resonance neurography for the evaluation of peripheral nerve, brachial plexus, and nerve root disorders.** *J Neurosurg* 2010;112:362–71
9. van Ouwerkerk WJ, Strijers RL, Barkhof F, et al. **Detection of root avulsion in the dominant C7 obstetric brachial plexus lesion: experience with three-dimensional constructive interference in steady-state magnetic resonance imaging and electrophysiology.** *Neurosurgery* 2005;57:930–40
10. Doi K, Otsuka K, Okamoto Y, et al. **Cervical nerve root avulsion in brachial plexus injuries: magnetic resonance imaging classification and comparison with myelography and computerized tomography myelography.** *J Neurosurg* 2002;96:277–84
11. Hayes CE, Tsuruda JS, Mathis CM, et al. **Brachail plexus: MR imaging with a dedicated phased array of surface coils.** *Radiology* 1997;203:286–89
12. Smith AB, Gupta N, Strober J, et al. **Magnetic resonance neurography in children with birth-related brachial plexus injury.** *Pediatr Radiol* 2008;38:159–63
13. Hingwala D, Chatterjee S, Kesavadas C, et al. **Applications of 3D CISS sequence for problem solving in neuroimaging.** *Indian J Radiol Imaging* 2011;21:90–97
14. Yoshikawa T, Hayashi N, Yamamoto S, et al. **Brachial plexus injury: clinical manifestations, conventional imaging findings, and the latest imaging techniques.** *Radiographics* 2006;26:S133–43
15. Chhabra A, Thawait GK, Soltados T, et al. **High-resolution 3T MR neurography of the brachial plexus and its branches, with emphasis on 3D imaging.** *AJNR Am J Neuroradiol* 2013;34:486–97

Prenatal Diagnosis of Fetal Ventriculomegaly: Agreement between Fetal Brain Ultrasonography and MR Imaging

S. Perlman, D. Shashar, C. Hoffmann, O.B. Yosef, R. Achiron, and E. Katorza

ABSTRACT

BACKGROUND AND PURPOSE: Accurate measurement of the lateral ventricles is of paramount importance in prenatal diagnosis. Possible conflicting classifications caused by their measurement in different sectional planes by sonography and MR imaging are frequently raised. The objective of our study was to evaluate the agreement between ultrasonography and MR imaging in the measurement of the lateral ventricle diameter in the customary sectional planes for each technique.

MATERIALS AND METHODS: Measurement of both lateral ventricles was performed prospectively in 162 fetuses from 21 to 40 weeks of gestational age referred for evaluation due to increased risk for cerebral pathology. The mean gestational age for evaluation was 32 weeks. The measurements were performed in the customary plane for each technique: axial plane for sonography and coronal plane for MR imaging.

RESULTS: The 2 techniques yielded results in substantial agreement by using intraclass correlation and κ coefficient score tests. When we assessed the clinical cutoff of 10 mm, the κ score was 0.94 for the narrower ventricle and 0.84 for the wider ventricle, expressing almost perfect agreement. The Bland-Altman plot did not show any trend regarding the actual width of the ventricle, gestational week, or interval between tests. Findings were independent for fetal position, sex, and indication for examination.

CONCLUSIONS: Our study indicates excellent agreement between fetal brain ultrasonography and MR imaging as to the diagnosis of fetal ventriculomegaly in the customarily used sectional planes of each technique.

Ventricular dilation is one of the most common, prenatally diagnosed cerebral abnormalities.[1,2] "Ventriculomegaly" is defined as an atrial diameter exceeding 10 mm.[3,4] The prognosis of ventricular dilation depends on the degree of dilation and the presence of associated cerebral or extracerebral abnormalities.[5] Thus, accurate measurement of the lateral ventricles is of paramount importance in prenatal diagnosis. Recently, guidelines for the assessment of the diameter of the lateral ventricles by using the axial transventricular plane as part of routine fetal sonographic evaluation have been suggested.[6,7]

MR imaging of the fetal CNS is a complementary tool and is performed following detection of abnormalities identified by sonography. The common belief is that fetal CNS MR imaging is more accurate than sonography, particularly when evaluation for associated anomalies is required, when the mother is obese, or when more precise measurement of the ventricular diameter is required.[8]

Measurement of lateral ventricle diameter by using MR imaging is performed on a coronal plane.[9] Measurement of lateral ventricle diameter by using ultrasound is performed on an axial plane.[6] This variation may raise possible conflicting classifications due to different sectional planes or use of different tools. The aim of our study was to evaluate the agreement between ultrasonography and MR imaging in the measurement of the lateral ventricle diameter in the customary sectional planes for each technique in prenatal diagnosis.

MATERIALS AND METHODS

This prospective study was performed in a single tertiary center from January 2011 to December 2012. During this period, 162 singleton fetuses were examined between the ages of 21 and 40 weeks of gestation for increased risk of cerebral pathology. The study was approved by the local institutional ethics committee. Informed consent was obtained from all patients.

The mean and median gestational age when performing MR

imaging was 32.4 ± 2.8 and 32 weeks, respectively (range, 21–40 weeks). The SD and median time lag between ultrasonographic and MR imaging examinations was 6 ± 14 days.

The distribution of the number of fetuses as a function of gestational age is represented in Fig 1. Patients were referred to our department for neurosonographic evaluation and cerebral MR imaging following the detection of ventricular dilation or ventricular asymmetry ($n = 54$, 33.3%) on sonographic examination or suspected cerebral abnormality. Distribution of the number of fetuses as a function of the indication for neurosonographic evaluation is presented in Table 1. There was no difference in the mean gestational age in regard to the indication.

Fetal presentation was recorded in 147 cases: cephalic in 113 (77%), breech in 32 (21.7%), and transverse in 2 cases (1.3%). Fetal sex was recorded in 128 cases: 79 males (62%) and 49 females (38%).

Sonographic examinations were performed by using the Voluson E-8 (GE Medical Systems, Zipf, Austria) sonography platforms, equipped with a transabdominal, multifrequency (4- to 8-MHz) probe. In our institution, we perform fetal brain MR imaging by using a 1.5T system (GE Healthcare Technologies, Milwaukee, Wisconsin). Single-shot fast spin-echo T2-weighted sequences in 3 orthogonal planes were performed by using the following parameters: section thickness, 3–4 mm; no gap; flexible coil (8-channel cardiac coil); matrix, 320/224; TE, 90 ms; and TR, 1298 ms. The FOV was determined by the size of the fetal head: 24 cm for the smaller fetuses and ≤30 cm for the larger fetuses. T1 fast-spoiled gradient-echo sequences were performed only in the

axial plane with a larger FOV (400 mm), with section thickness, 4 mm; gap, 0.5 mm; TR, 160 ms; and TE, 2.3 ms.

For each fetus, both lateral ventricles were measured by ultrasonography and MR imaging by using the same customarily used sectional plane for each technique.

Sonographic measurements were performed in the axial plane as recommended by the International Society of Ultrasound in Obstetrics and Gynecology guidelines for sonographic examination of the fetal central nervous system.[6] Calipers were positioned inside the echoes generated by the ventricular walls (Fig 2A). For MR imaging, measurements were obtained on the coronal plane at the level of the ventricles (with good visibility of the choroid plexuses) (Fig 2B).[9]

Sonography is a dynamic, real-time examination, necessitating the presence of the patient; therefore, a single observer performed all measurements. On the other hand, MR imaging results can be accessed as needed. The reproducibility of measurements of the lateral ventricles in MR imaging was assessed as well. Two radiologists (radiologist 1 and radiologist 2) evaluated the entire study sample. Each radiologist was unaware of the results obtained by the other.

Ventricle (a) was defined as narrower and ventricle (b), as wider. We matched the ventricles relatively according to the measurements obtained by MR imaging.

Statistical Analysis

The width of the measured ventricles in the different planes was compared and statistically analyzed by using the Statistical Package for the Social Sciences software, Version 18.0 (IBM, Armonk, New York).

Quantitative variables are described as median (range), and qualitative variables, as frequency (percentage).

Reproducibility of the sonography and MR imaging measurements of both ventricles was assessed by using Bland-Altman analysis and the intraclass correlation coefficient. "Ventriculomegaly" was defined as an atrial diameter exceeding 10 mm (>4 SDs). The measure of agreement between ultrasonography and MR imaging to define ventriculomegaly was calculated by using the κ coefficient. Agreement was considered slight when $\kappa \leq 0.2$; fair when $0.2 > \kappa \leq 0.4$; moderate when $0.4 < \kappa \leq 0.6$; ex-
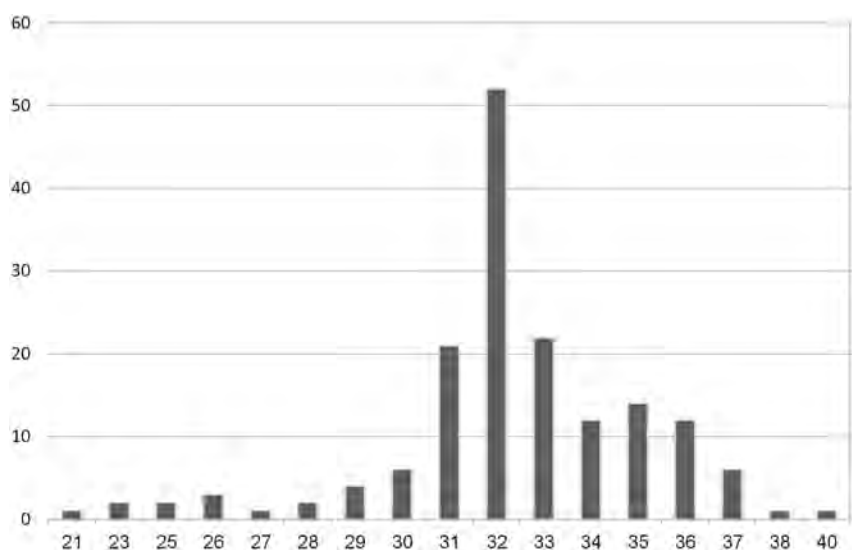
FIG 1. Distribution of number of fetuses providing data as a function of gestational age ($n = 162$).

Table 1: Distribution of numbers of fetuses providing data as a function of the indication for neurosonography

Indication	No.	Mean Gestational Week	Min	Max	Median
CMV seroconversion	35	33.63	30	40	33
Ventricular asymmetry	54	31.78	21	37	32
Abnormal head circumference	15	34.27	29	38	35
Abnormal posterior fossa	10	31.60	26	35	32
Cystic lesions	8	33.75	31	37	33
Family history of CNS illness	6	32.33	31	34	32
Midline abnormalities	6	31.67	23	37	32
Obstetric complications and extra-CNS anatomic findings	28	31.00	23	36	32

Note:—Min indicates minimum; Max, maximum; CMV, cytomegalovirus.

cellent when $0.6 < \kappa \le 0.8$; and almost-perfect when $\kappa > 0.8$.

RESULTS

The reproducibility of ventricular measurements between sonographic examination and MR imaging was fairly good, as demonstrated by estimates of the mean differences, 95% limit of agreement, and the intraclass correlation coefficient (Table 2).

There was no particular trend in the Bland-Altman plot for either the narrower (a) or the wider (b) ventricle (Fig 3). When we assessed the clinical cutoff of 10 mm, the κ score was 0.94 for axial and coronal planes of the narrower ventricle and 0.84 for the

wider ventricle—almost perfect agreement for both evaluating radiologists.

Indeed, when we compared sonographic with MR imaging measurements, 37 cases (radiologist 1) and 35 cases (radiologist 2) of disagreement were observed in the determination of ventriculomegaly (ie, when 1 value was above 10 mm and the other, below 10 mm). In 18 cases, the discrepancy between the 2 measurements was <1.9 mm. In 15 cases, obesity or previous multiple cesarean deliveries were responsible for poor visibility of the ventricular walls by sonographic examination. In 2 cases, no explanation was found for the disagreement between measurements (Table 3). No specific trend was found when estimating the agreement between measurements in the 2 modalities in relation to gestational age.

When estimating the agreement between sonography and MR imaging measurements as a function of the time interval between tests, the Bland-Altman plot did not indicate any particular trend (Fig 4). Three cases demonstrated great differences between the 2 modalities. In the first, the ventricles were measured as very narrow on MR imaging, most likely below the measurement resolution by sonography (5 mm). In the second case, the ventricles were very wide (>20 mm) in both modalities. Both cases represent the extremes of the norm, and measurement differences did not have an impact on clinical decisions. The third case represents a rare case of disagreement between sonography and MR imaging. The time lag between these examinations was a few days; therefore, progressive ventricular dilation could not explain the differences.

The reproducibility of measurements of the lateral ventricles on MR
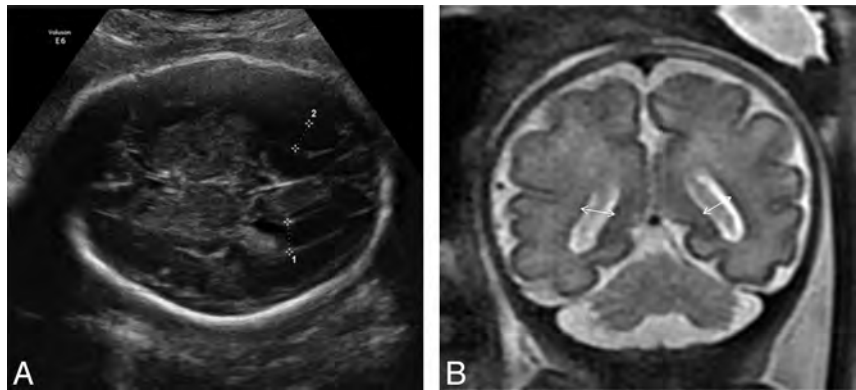
FIG 2. *A*, Sonographic measurement of the fetal lateral ventricles in the axial transventricular plane. *B*, Measurement of the fetal lateral ventricles in a T2-weighted MR image (coronal plane) at the level of the ventricles; ventricular diameter is measured at the midheight of the ventricle.

Table 2: Reproducibility of measurements of the lateral ventricles for ultrasound and MRI

	Differences in Measurement of Ventricles, Ultrasound-MRI (mm)			Definition of Ventriculomegaly κ Coefficient
	Mean	95% Limits of Agreement	ICC (95% CI)	
MRI radiologist 1				
Ventricle (a)	0.33 ± 1.58	(−2.76–1.58)	0.91 (0.88–0.94)	93.8
Ventricle (b)	−0.26 ± 1.58	(−3.35–1.58)	0.94 (0.91–0.95)	83.4
MRI radiologist 2				
Ventricle (a)	−0.88 ± 1.52	(−3.86–1.52)	0.9 (0.78–0.95)	93.8
Ventricle (b)	−1.09 ± 1.5	(−4.05–1.5)	0.92 (0.75–0.96)	84.2

Note:—ICC indicates intraclass correlation coefficient.

FIG 3. Plots of the difference between sonographic and MR imaging ventricular measurements against their mean (*A*, narrower ventricle; *B*, wider ventricle).

Table 3: Comparison between ultrasonography and MRI data in the evaluation of ventricular diameter below and above the clinical cutoff of 10 mm

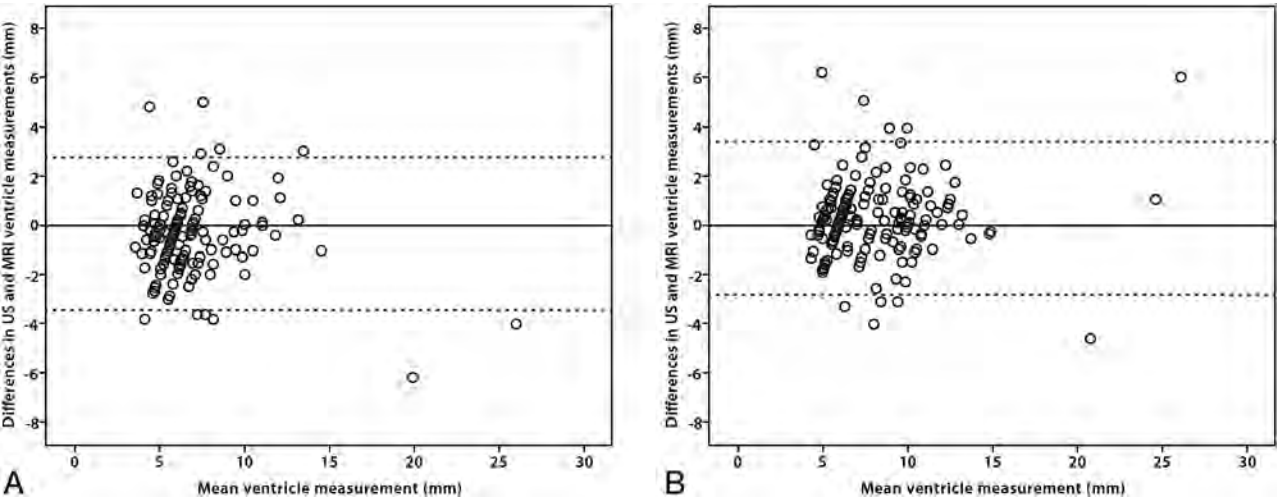| | Ultrasonography Axial Plane | | | |
| | Ventricle (a) | | Ventricle (b) | |
	<10 mm	≥10 mm	<10 mm	≥10 mm
MRI coronal plane, radiologist 1				
<10 mm	138	5*	103	14*
≥10 mm	5*	14	13*	32
MRI coronal plane, radiologist 2				
<10 mm	134	1**	108	20**
≥10 mm	9**	18	5**	25

* Cases of disagreement for the diagnosis of ventriculomegaly (ventricular width ≥ 10 mm) between ultrasound and MRI for radiologist 1, total of 37 cases.
** Cases of disagreement for the diagnosis of ventriculomegaly between ultrasound and MRI for radiologist 2, total of 35 cases.
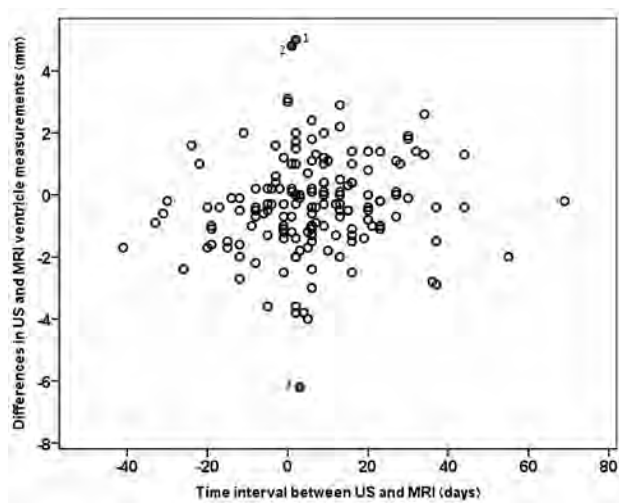

FIG 4. Plots of the difference between sonography and MR imaging ventricular measurements against the time interval between sonography and MR imaging. Cases of great differences between the 2 modalities: 1) very narrow ventricles on MR imaging, most likely below the measurement resolution by sonography (5 mm); 2) very wide ventricles (>20 mm) in both modalities; and 3) a rare case of disagreement between sonography and MR imaging.

Table 4: Interobserver agreement: MRI

	Mean	95% Limits of Agreement	ICC	95% CI
Ventricle (a)	−1.20 ± 1.11	−3.39–0.97	0.91	0.41–0.97
Ventricle (b)	−0.82 ± 1.03	−2.84–1.19	0.96	0.84–0.98

Note:—ICC indicates intraclass correlation coefficient.

imaging was fairly good. The limits of agreement were considered acceptable for clinical purposes, and the intraclass correlation coefficient showed almost perfect agreement (Table 4).

Our findings were independent for fetal sex, presentation, gestational age, and the indication for conducting the neurosonography. The Bland-Altman plot did not indicate any trend regarding the actual width of the ventricle or the time interval between tests.

DISCUSSION

A great deal of attention has been given to the importance of measuring the fetal lateral ventricular diameter as a pivotal find-

ing for prenatal diagnosis of CNS pathologies.[1,10,11] Ventriculomegaly is one of the most common sonographically detectable fetal cerebral abnormalities.[12]

More than 20 years ago, it was established that the normal fetal ventricular diameter remains relatively constant throughout gestation.[10,13] Since these reports, 10 mm is considered the upper limit of the normal range for lateral ventricle diameter measured in the axial plane. The 10-mm cutoff was derived from serial studies that established this cutoff as +3 or +4 SDs, depending on the series.[3,14,15]

The prognosis of ventricular dilation depends on the degree of the dilation and the presence of associated cerebral or extracerebral abnormalities.[16,17] Thus, accurate measurement of the lateral ventricles is of paramount importance in prenatal diagnosis. Measuring the ventricle diameter reliably is particularly problematic when the ventricular measurement is close to the standard 10-mm threshold. Measurement of the proximal lateral ventricle is frequently difficult due to near-field artifacts.[7]

It is now accepted that fetal brain MR imaging plays an important role in the prenatal detection of associated cerebral anomalies.[8] The common understanding is that MR imaging is more accurate than sonographic imaging, particularly in cases of maternal obesity, in identifying or excluding associated anomalies, or in cases in which a more precise measurement of the ventricular diameter is required.[18]

Questions of possible conflicting classifications caused by measurement of the fetal lateral ventricles in different sectional planes by sonography and MR imaging are frequently raised. Usually in sonographic examinations, the fetal ventricle diameter is measured on an axial plane at the level of the thalami as a line perpendicular to the atrium at the level of the posterior margin of the choroid plexus.[6] Measurement of the lateral ventricle diameter by using MR imaging is performed on a coronal plane.[9]

Good agreement between fetal sonography and MR imaging in the measurement of the lateral ventricle diameter was previously reported when comparing the same coronal planes.[19] However, the coronal plane is not frequently used as a customary practice in the sonographic examination of the fetal CNS; neither is it mentioned as part of the "fetal neurosonogram" in the International Society of Ultrasound in Obstetrics and Gynecology guidelines.[6] Others have compared measurements in the axial plane for both imaging modalities, reporting that MR imaging mean ventricular measurements were slightly smaller than sonographic measurements.[20] However, the axial plane is not commonly used for assessment of the fetal lateral ventricles when using MR imaging.

The aim of our study was to evaluate the agreement between ultrasonography and MR imaging in the measurement of the diameter of the lateral ventricles in the routinely used sectional planes for each technique. Our results indicate that when the fetal lateral ventricles are measured on an axial plane by using ultrasonography and on the coronal plane by using MR imaging, the 2 modalities are in close agreement. Two radiologists assessed the reproducibility of MR imaging measurements of the fetal lateral ventricles in our study. Previous reports have reported moderate-to-substantial agreement among MR imaging radiologists in the measurements of the lateral ventricles.[9] Our study shows high

agreement between our 2 radiologists in the measurement of both ventricles. Our results showed no influence as to fetal presentation, sex, gestational age, indication for neurosonography, or time lag between tests.

As reported by others,[19] when the ventricles are very narrow, sonographic evaluation tends to overestimate the ventricular diameter. Our results show that when the fetal ventricular diameter is within normal limits or mildly dilated, ultrasonography and MR imaging are in close agreement. However, in cases of severe ventricular dilation, we found greater discrepancies between sonography and MR imaging. These differences usually do not have significance in clinical decision-making.

MR imaging has a better contrast resolution and is less dependent on maternal body habitus. These features most probably account for most cases with strong disagreement between sonography and MR imaging. This also raises the question as to whether poor visibility of the fetal lateral ventricular walls when conducting prenatal sonography is an indication for prenatal fetal brain MR imaging.

CONCLUSIONS

Accurate measurement of the lateral ventricles is of paramount importance in prenatal diagnosis, particularly when the ventricular measurement is close to the standard 10-mm threshold of fetal ventriculomegaly. It is now accepted that fetal brain MR imaging plays an important role in the prenatal diagnosis of ventriculomegaly. Possible conflicting classifications caused by measurement of the fetal lateral ventricles in different sectional planes by sonography and MR imaging are frequently found. Our study reveals that in the customarily used sectional planes for sonography and MR imaging, measurements of the fetal lateral ventricles are in close agreement.

REFERENCES

1. Garel C. **Ventricular dilatation.** In: Garel C, ed. *MRI of the Fetal Brain: Normal Development and Cerebral Pathologies.* Berlin: Springer-Verlag; 2004:201–16
2. Leitner Y, Goez H, Gull I, et al. **Antenatal diagnosis of central nervous system anomalies: can we predict prognosis?** *J Child Neurol* 2004;19:435–38
3. Almog B, Gamzu R, Achiron R, et al. **Fetal lateral ventricular width: what should be its upper limit?** *J Ultrasound Med* 2003;22:39–43
4. Salomon LJ, Bernard JP, Ville Y. **Reference ranges for fetal ventricular width: a non-normal approach.** *Ultrasound Obstet Gynecol* 2007;30:61–66
5. Gaglioti P, Oberto M, Todros T. **The significance of fetal ventriculomegaly: etiology, short- and long-term outcomes.** *Prenat Diagn* 2009;29:381–88
6. International Society of Ultrasound in Obstetrics & Gynecology Education Committee. **Sonographic examination of the fetal central nervous system: guidelines for performing the 'basic examination' and the 'fetal neurosonogram.'** *Ultrasound Obstet Gynecol* 2007;29:109–16
7. Guibaud L. **Fetal cerebral ventricular measurement and ventriculomegaly: time for procedure standardization.** *Ultrasound Obstet Gynecol* 2009;34:127–30
8. Girard N, Ozanne A, Chaumoitre K, et al. **MRI and in utero ventriculomegaly.** *J Radiol* 2003;84(12 pt 1):1933–44
9. Tilea B, Alberti C, Adamsbaum C, et al. **Cerebral biometry in fetal magnetic resonance imaging: new reference data.** *Ultrasound Obstet Gynecol* 2009;33:173–81
10. Cardoza JD, Goldstein RB, Filly RA. **Exclusion of fetal ventriculomegaly with a single measurement: the width of the lateral ventricular atrium.** *Radiology* 1988;169:711–14
11. Filly RA, Cardoza JD, Goldstein RB, et al. **Detection of fetal central nervous system anomalies: a practical level of effort for a routine sonogram.** *Radiology* 1989;172:403–08
12. Kelly EN, Allen VM, Seaward G, et al. **Mild ventriculomegaly in the fetus, natural history, associated findings and outcome of isolated mild ventriculomegaly: a literature review.** *Prenat Diagn* 2001;21:697–700
13. Siedler DE, Filly RA. **Relative growth of the higher fetal brain structures.** *J Ultrasound Med* 1987;6:573–76
14. Farrell TA, Hertzberg BS, Kliewer MA, et al. **Fetal lateral ventricles: reassessment of normal values for atrial diameter at US.** *Radiology* 1994;193:409–11
15. Patel MD, Goldstein RB, Tung S, et al. **Fetal cerebral ventricular atrium: difference in size according to sex.** *Radiology* 1995;194:713–15
16. Beeghly M, Ware J, Soul J, et al. **Neurodevelopmental outcome of fetuses referred for ventriculomegaly.** *Ultrasound Obstet Gynecol* 2010;35:405–16
17. Melchiorre K, Bhide A, Gika AD, et al. **Counseling in isolated mild fetal ventriculomegaly.** *Ultrasound Obstet Gynecol* 2009;34:212–24
18. Browning PD, Laorr A, McGahan JP, et al. **Proximal fetal cerebral ventricles: description of ultrasound technique and initial results.** *Radiology* 1994;192:337–41
19. Garel C, Alberti C. **Coronal measurement of the fetal lateral ventricles: comparison between ultrasonography and magnetic resonance imaging.** *Ultrasound Obstet Gynecol* 2006;27:23–27
20. Twickler DM, Reichel T, McIntire DD, et al. **Fetal central nervous system ventricle and cisterna magna measurements by magnetic resonance imaging.** *Am J Obstet Gynecol* 2002;187:927–31

Choice of Diffusion Tensor Estimation Approach Affects Fiber Tractography of the Fornix in Preterm Brain

A. Plaisier, K. Pieterman, M.H. Lequin, P. Govaert, A.M. Heemskerk, I.K.M. Reiss, G.P. Krestin, A. Leemans, and J. Dudink

ABSTRACT

BACKGROUND AND PURPOSE: Neonatal DTI enables quantitative assessment of microstructural brain properties. Although its use is increasing, it is not widely known that vast differences in tractography results can occur, depending on the diffusion tensor estimation methodology used. Current clinical work appears to be insufficiently focused on data quality and processing of neonatal DTI. To raise awareness about this important processing step, we investigated tractography reconstructions of the fornix with the use of several estimation techniques. We hypothesized that the method of tensor estimation significantly affects DTI tractography results.

MATERIALS AND METHODS: Twenty-eight DTI scans of infants born <29 weeks of gestation, acquired at 30-week postmenstrual age and without intracranial injury observed, were prospectively collected. Four diffusion tensor estimation methods were applied: 1) linear least squares; 2) weighted linear least squares; 3) nonlinear least squares, and 4) robust estimation of tensors by outlier rejection. Quality of DTI data and tractography results were evaluated for each method.

RESULTS: With nonlinear least squares and robust estimation of tensors by outlier rejection, significantly lower mean fractional anisotropy values were obtained than with linear least squares and weighted linear least squares. Visualized quality of tract reconstruction was significantly higher by use of robust estimation of tensors by outlier rejection and correlated with quality of DTI data.

CONCLUSIONS: Quality assessment and choice of processing methodology have considerable impact on neonatal DTI analysis. Dedicated acquisition, quality assessment, and advanced processing of neonatal DTI data must be ensured before performing clinical analyses, such as associating microstructural brain properties with patient outcome.

ABBREVIATIONS: LLS = linear least squares; WLLS = weighted linear least squares; NLLS = nonlinear least squares; RESTORE = robust estimation of tensors by outlier rejection; FA = fractional anisotropy

DTI enables in vivo assessment of WM microstructure and has become essential for quantification of brain abnormalities because it has been suggested to provide early biomarkers of neurodevelopment.[1] Fiber tractography has the unique property to delineate specific WM pathways and is rapidly gaining in popularity because it may reveal substantial insights into disturbed brain connectivity and functionality of infants born preterm.[2-4]

There are many technical issues that may complicate the analysis of DTI data, including scanner type, hardware setup, acqui-

sition parameters, and processing methodology.[5,6] In addition, DTI applied in preterm infants is especially challenging because of specific clinical factors, such as the increased risk of subject motion, hemodynamic vulnerability, smaller head sizes, and higher heart and breathing rates compared with healthy adults. Therefore, before associations between tractography results and neurodevelopmental outcome can be established, it is of paramount importance that acquisition and processing of DTI data are performed with the highest standards possible.[7,8] For example, different algorithms to estimate the diffusion tensor have been developed. These methods differ considerably in processing speed and dealing with data outliers. For instance, the linear least squares (LLS) method is widely used to estimate diffusion parameters but may lead to inaccuracy as it incorrectly assumes that data outliers are homogeneously distributed. Furthermore, there seems to be no consensus on how to practically define and handle data outliers. Awareness of these matters is essential because improper use may lead to inaccuracy; especially if data are compared when different estimation methods have been used. Unfortu-

nately, however, most studies using preterm brain DTI data have hardly focused on these important aspects, calling for a thorough investigation.

In the present study, trajectories of the fornix were reconstructed with fiber tractography for 28 preterm infants and compared when different diffusion tensor estimation approaches were used. Our hypothesis was that the chosen tensor estimation methodology significantly affects results of fiber tractography. This would demonstrate that an informed choice of diffusion tensor estimation is crucial for a reliable tractography analysis, which is especially relevant when artifact-sensitive DTI data of the preterm brain are involved.

MATERIALS AND METHODS

This study was approved by the institutional review board. Written informed parental consent was obtained for all subjects.

Patients

Between February 2011 and December 2012, preterm infants born before a gestational age of 29 weeks were recruited prospectively. MR imaging data were acquired at a postmenstrual age of 30 weeks (29 4/7 to 30 4/7 weeks). To avoid unnecessary data heterogeneity, infants with evidence of intracranial injury (intraventricular or cerebellar hemorrhage, WM abnormalities) observed with conventional MR imaging (see T1WI and T2WI protocols below) were excluded. Of the 217 eligible infants, 36 died before 30-week postmenstrual age; in 82 infants, the MR imaging scan could not be performed at 30-week postmenstrual age because of hemodynamic instability or logistic circumstances; and informed parental consent was not obtained for 20 infants. Of the remaining 79 infants, 36 had intracranial abnormalities, and 15 others were excluded from further analysis because different DTI acquisition settings were applied. This eventually resulted in 28 usable datasets.

MR Imaging

MR imaging procedures were carried out according to protocol[9]: all infants were accompanied by trained staff only and were positioned in an MR imaging–compatible incubator (Lammers Medical Technology, Luebeck, Germany) that provided controlled temperature and humidity, MR-compatible pulse oximetry, and MR-compatible ventilation. Moldable earplugs and neonatal earmuffs protected the infants from auditory noise; no sedation was given.

Imaging data were acquired with a 1.5T EchoSpeed scanner (GE Healthcare, Milwaukee, Wisconsin). Axial T2WI FSE was obtained with the following parameter settings: TR: 13,100 ms; TE: 139 ms; flip angle: 90°; section thickness: 1.2 mm; FOV: 190 × 190 mm^2; acquisition matrix: 256 × 224; reconstruction matrix: 256 × 256 (voxel size: 0.74 × 0.74 × 1.23 mm^3); acquisition time was 2:58 minutes. Axial 3D T1-spoiled gradient-echo MR imaging data were acquired by use of: TR: 9 ms; TE: 3 ms; flip angle: 15°; section thickness: 1.6 mm; FOV: 150 × 150 mm^2; acquisition matrix: 224 × 224; reconstruction matrix 256 × 256 (voxel size: 0.59 × 0.59 × 1.6 mm^3); acquisition time was 3:10 minutes. DTI was performed with the use of a single-shot EPI sequence with diffusion gradients in 25 noncollinear directions, TR: 11,725 ms;

TE: 85.6 ms; section thickness: 3 mm; FOV: 220 × 220 mm^2; acquisition matrix: 128 × 64; reconstruction matrix 256 × 256 (voxel size: 0.86 × 0.86 × 3 mm^3); b value: 750 seconds/mm^2; number of non–diffusion-weighted images: 3; acquisition time was 5:17 minutes.

DTI Data Processing

DTI data were analyzed with the use of ExploreDTI (http://www. exploredti.com)[10] version 4.8.3. The diffusion-weighted images were first corrected for eddy currents, EPI distortion, and patient movement.[11,12] The diffusion tensor was then estimated according to 4 different methods: 1) LLS; 2) weighted linear least squares (WLLS); 3) nonlinear least squares (NLLS), and 4) robust estimation of tensors by outlier rejection (RESTORE).[13-15] Next, whole-brain tractography was performed for all datasets with the following parameters: fractional anisotropy (FA) threshold: 0.08; fiber length range: 15–500 mm; angle threshold 30°; and step size: 1 mm.[16] Without loss of generality of this work, a single WM structure was investigated. Because of its important relation to cognition[17,18] and high tracking reproducibility as the result of its unique shape, we performed tractography of the fornix. ROI placement was performed on the color-coded FA maps[19]: 1) 1 "OR" ROI was placed in the axial plane at the level of the bilateral columns of the fornix, above the mammillary bodies; 2) 2 "AND" ROIs were placed: in the coronal plane to encompass the corpus of the fornix and in the axial plane to include both crura of the fornix in the same section where the "OR" ROI was placed, and 3) 2 "NOT" ROIs were placed in the sagittal plane laterally to the seed region to exclude fibers from the anterior commissure[20] (Fig 1). For each subject, tractography was repeated for each method of tensor estimation while the same subject-specific ROIs were used.

Data Analysis

Quality of the diffusion-weighted images was assessed with the outlier profiles of each dataset, after diffusion tensor estimation by use of RESTORE (Fig 2). The mean percentage of outliers per dataset was calculated by averaging the percentage artifacted voxels across the diffusion gradient orientations.[6] In addition, tract parameters, including mean FA, mean diffusivity, mean fiber trajectory length (in mm), and number of fiber trajectories were computed for each dataset.

The quality of tractography was visually and systematically evaluated (Table) by 2 authors independently. Both reviewers were blinded to the method of tensor estimation. The final score was the average of both total scores and ranged from 0–10 (Table). Statistical analysis was performed by use of SPSS version 20.0.0.1 (IBM, Armonk, New York). Intraclass correlations between both observers were calculated by use of a 2-way mixed model. Coefficients <0 were considered as no agreement; 0–0.20 as slight; 0.21–0.40 as fair; 0.41–0.60 as moderate; 0.61–0.80 as substantial; and 0.81–1 as almost perfect agreement.[21] The Spearman correlation coefficient was used to investigate the correlation between the visualized quality of tract reconstruction and the mean outlier percentage per dataset. Independent-sample t tests served to test differences in visualized quality of tract reconstruction between data with <10% and >10% data outliers. Repeated-

measures ANOVA served to test differences in tract parameters between the diffusion tensor estimation methods, respectively. Difference in variability of tract parameters between the estimation techniques was tested with the Levene test for equality of variances. A value of $P < .05$ (2-sided) was considered statistically significant.

FIG 1. Placement of ROIs. Tractography of the fornix was performed by placing 1 "OR" ROI (in blue), 2 "AND" ROIs (in green), and 2 "NOT" ROIs (in red) on color-coded fractional anisotropy maps.

RESULTS

Descriptive Statistics

Twenty-eight infants (15 boys) were included in this study. Mean gestational age and birth weight were 27.7 weeks (SD: 1.1 weeks) and 1053 g (SD: 256 g), respectively. Mean postmenstrual age at image acquisition was 30.0 weeks (SD: 0.3 weeks). The mean percentage of outliers per dataset was 10.1% (SD: 1.3%).

Outlier Evaluation

Figures 3 and 4 are characteristic representations of data with poor and good quality of data, respectively. Interclass correlation between observers showed excellent agreement with high significance (intraclass correlation coefficient: 0.87; 95% confidence interval: 0.82–0.91; $P < .01$). Although there was some overlap among the methods of tensor estimation, visualized quality of reconstruction of the fornix was significantly higher with the use of the RESTORE algorithm, particularly in datasets with a high percentage (>10%, $n = 13$) of data outliers (Fig 5). Furthermore, visualized quality of tract reconstruction across all tensor estimation methods depended also on the presence of data artifacts because tract quality
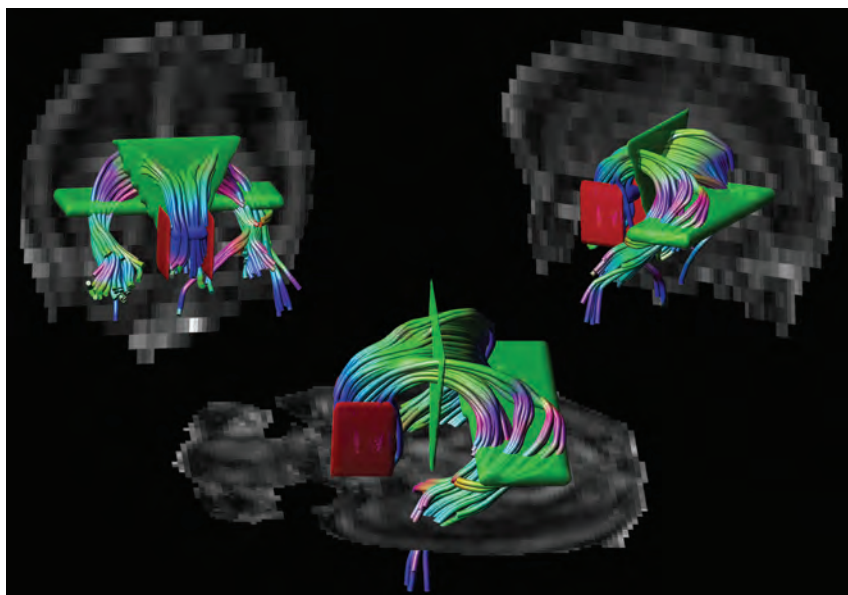

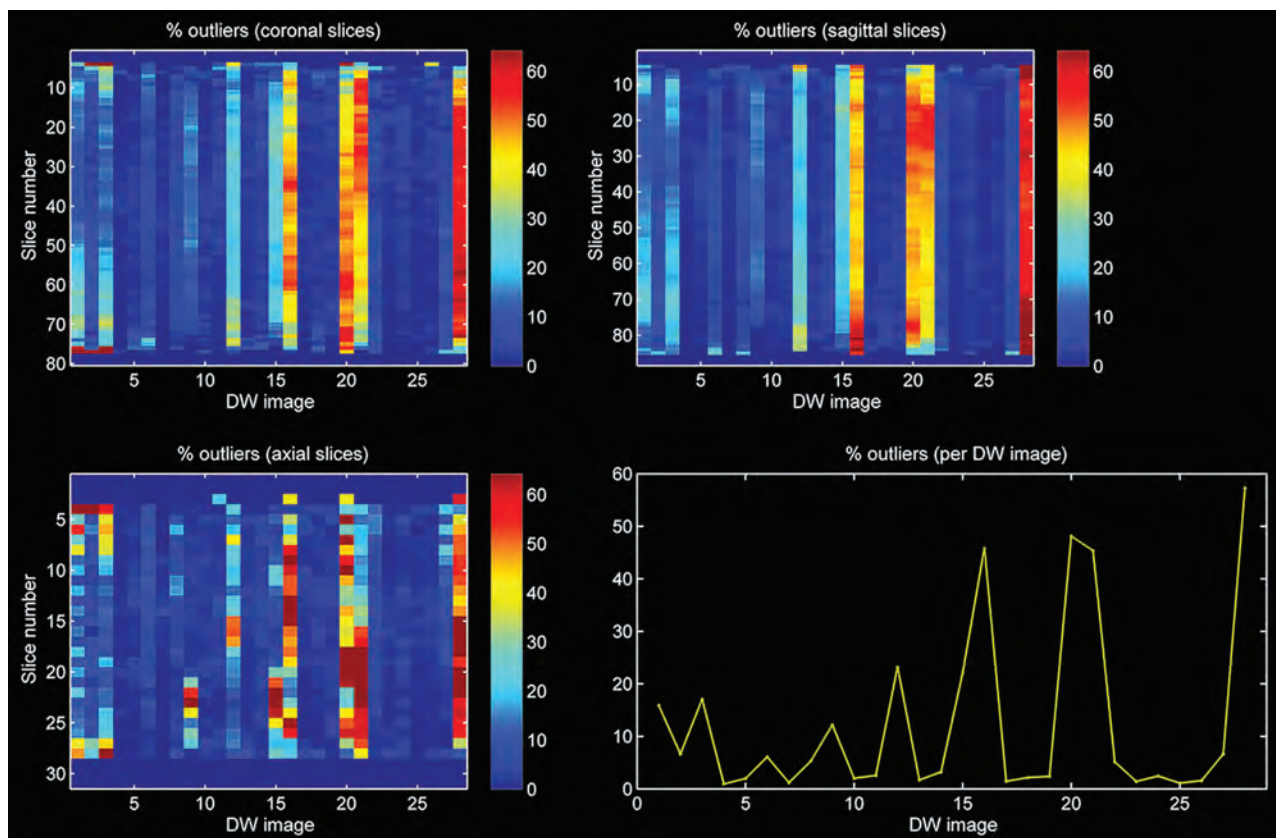**FIG 2.** Outlier profile of DTI data with high percentage of outliers.

Scoring system for visual evaluation of tract reconstruction of the fornix

	0 Points	1 Point	2 Points
Shape of the fornix[a]	No recognition of shape	Partially abnormal shape	Normal shape
Orientation of fibers[a]	Complete disorientation	Partially abnormal orientation	Normal orientation
Symmetry of crura	One missing crus	Partially asymmetric	Normal symmetry
Presence of non-realistic fibers[a]	Outweighing the total number of fibers	Less than the number of realistic fibers	None
No. of fiber trajectories	<10	10–100	>100

[a] Shape, orientation, and presence of non-realistic fibers with regard to description of anatomy by Nieuwenhuys et al, *The Human Central Nervous System,* 2008.[20]
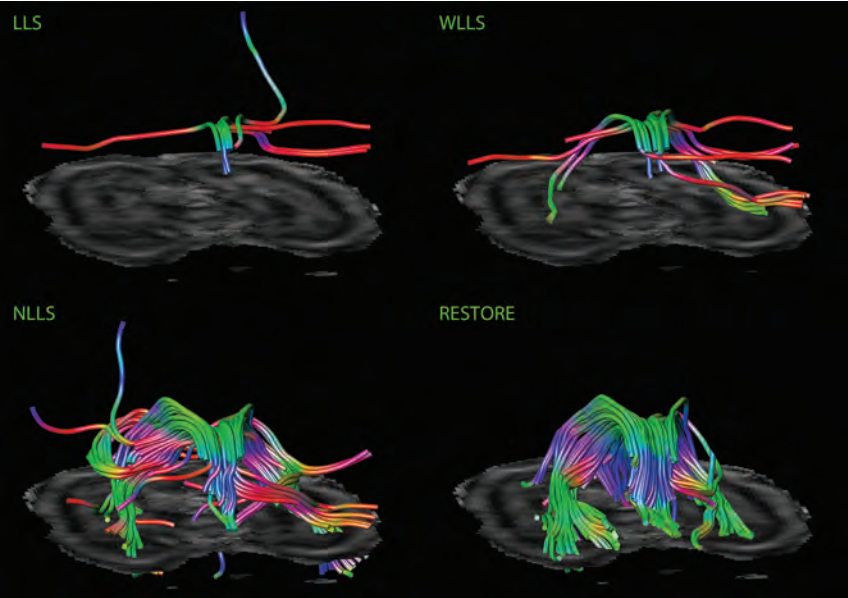

FIG 3. Impact of diffusion tensor estimation method on tract reconstruction of poor-quality DTI data. Characteristic representations illustrate the effect of tensor estimation methodology on reconstruction of the fornix with high percentage of data outliers (>10%). Note that reconstruction is not possible with the use of the linear least squares (LLS) and weighted linear least-squares (WLLS) methods and appears to be slightly possible with nonlinear least squares (NLLS) but is very well performed if the robust estimation of tensors by outlier rejection (RESTORE) approach is used.

RESTORE, there was no difference in variability of mean FA values with regard to the quality of the diffusion-weighted images (Fig 7).

DISCUSSION

This study emphasizes the paramount importance of quality assessment and dedicated use of processing methodology of neonatal DTI data before performing analysis. With our work, we demonstrated that 1) tract parameters are significantly affected by the chosen tensor estimation method and are estimated more reliably if data outliers are handled carefully; 2) robust estimation of the diffusion tensor results in significantly improved visualized quality of fiber reconstruction; 3) the mean percentage of data outliers of the diffusion-weighted images correlates significantly to visualized quality of tract reconstruction; and 4) data outliers are common and significantly affect subsequent DTI analysis if they are not taken into account.

Although the incidence of destructive types of brain injury with subsequent serious deficits is decreasing, preterm infants remain at considerable risk to develop cognitive and socio-emotional disabilities that persist into adolescence.[22,23] Advanced MR imaging techniques, such as DTI, have already provided important valuable insights into WM microstructural properties of these "subtle" types of brain injury.[1] Still, the neuropathologic correlates show high variation and inconsistency,[23] and their workings are not completely understood.[24] Moreover, preterm infants are vulnerable to respiratory and hemodynamic instability and movement artifacts.[7,9] Therefore, acquisition and processing of DTI data must be handled with dedicated care, which is essential to avoid misinterpretation. This is appropriately described in technical DTI reports,[5-7,25,26] but, paradoxically, such work receives little attention in clinical research. This could be because of their emphasis on clinical results, or, more importantly, because of the lack of awareness that the choice of diffusion tensor estimation approach may affect the subsequent reconstruction of fiber pathways.

As shown in the present study, the choice of tensor estimation algorithms can significantly affect DTI tractography results, which may complicate the interpretation of specific findings. In this context, study populations can only be compared reliably when identical processing pipelines have been applied, necessitating

was significantly correlated to the mean outlier percentage per dataset (Spearman correlation coefficient: −0.46; $P < .01$). This correlation was also tested for each tensor estimation method separately. The following Spearman coefficients were found: LLS: −0.48 ($P = .01$); WLLS: −0.47 ($P = .01$); NLLS: −0.57 ($P < .01$), and RESTORE: −0.36 ($P = .06$).

Tract Parameters

The impact of the diffusion tensor estimation method used on tract parameters is shown in Fig 6. There was a significant difference in mean FA value through the use of different diffusion estimation algorithms. Significantly lower mean FA values were obtained with NLLS and RESTORE than with LLS and WLLS. Furthermore, application of the RESTORE approach resulted in the lowest standard deviation of the mean FA value; LLS: 0.059; WLLS: 0.054; NLLS: 0.052; RESTORE: 0.051 (repeated-measures ANOVA, $P < .05$). Although not statistically significant, there was a trend toward an increased number of fiber trajectories in the following order of tensor estimation approaches: LLS, WLLS, NLLS, and RESTORE (Spearman correlation coefficient: 0.10; $P = .32$).

With the use of LLS, variability of mean FA values was significantly higher in datasets with more than 10% outliers compared with datasets with less than 10% outliers. With WLLS, NLLS, or
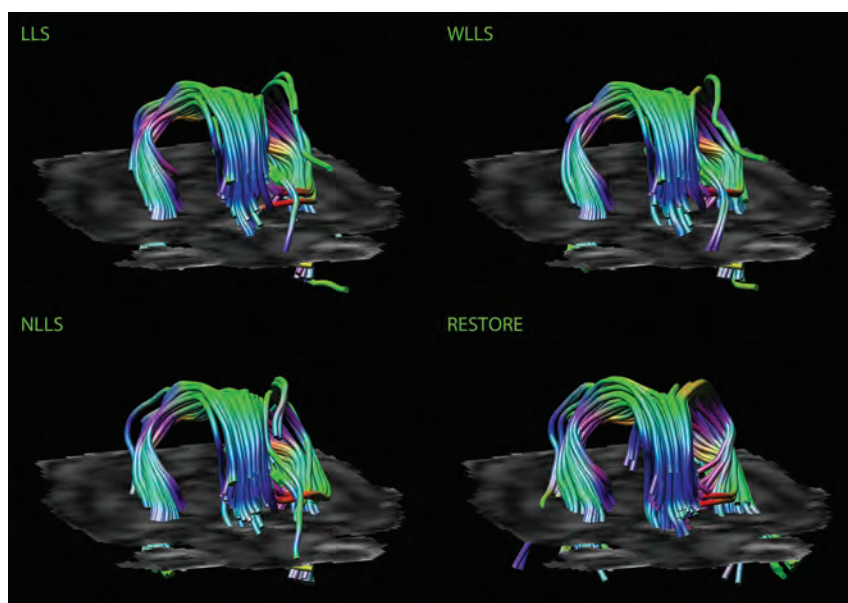
FIG 4. Impact of diffusion tensor estimation method on tract reconstruction of good-quality DTI data. Characteristic representations illustrate the effect of the tensor estimation on fiber tracking of the fornix with low percentage of data outliers (<10%). Note the more accurate tract reconstruction with the use of the robust estimation of tensors by outlier rejection approach.
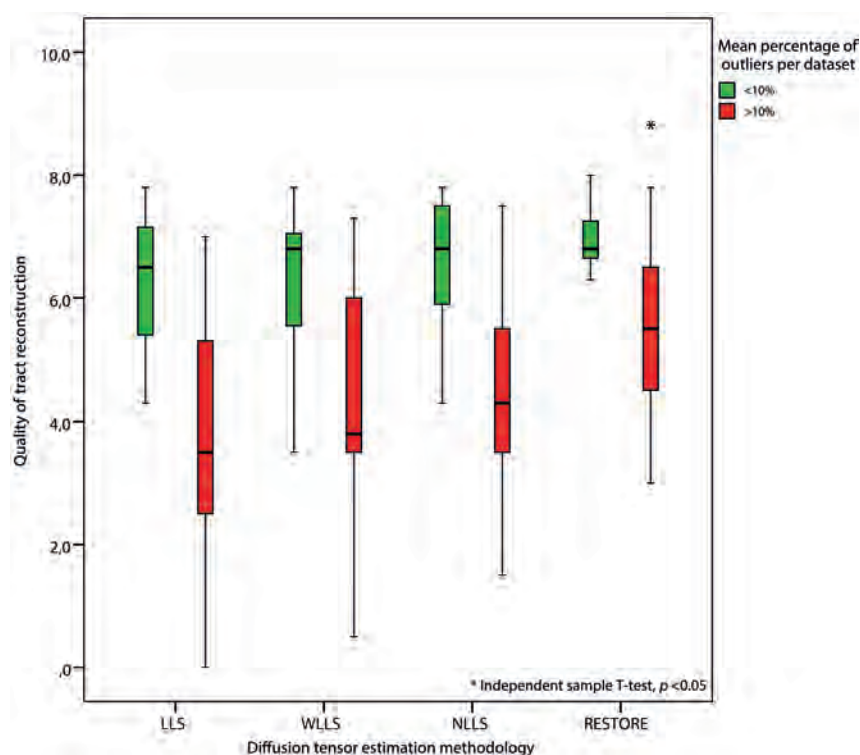

FIG 5. Impact of DTI data quality on tract reconstruction of the fornix. Quality of the reconstructed fornix was significantly higher by use of the robust estimation of tensors by outlier rejection technique; this was particularly evident for datasets with high percentages of outliers in the diffusion-weighted images (>10%).

shortening diffusion time, applying stronger gradients, or by use of lower b-values[7]; 3) oversampling gradient-sensitizing directions and removing corrupted diffusion-weighted images[6]; and 4) applying more advanced tensor estimation methods.[5] Because diffusion tensor estimation techniques differ considerably in principle, speed, and accuracy,[29] awareness of the benefits and pitfalls is essential: the LLS method is fast and mostly used but assumes that errors are identically distributed, which can result in inaccurate estimation of the tensor.[30] The WLLS method is slightly slower but provides more accurate results because it considers errors to be heterogeneously distributed.[31] NLLS iteratively minimizes errors and results in more reliable estimation but needs considerably longer processing time and may get stuck in local optima during optimization.[5,14] The RESTORE approach automatically detects and removes outliers before tensor estimation. This avoids manual and subjective identification of corrupted diffusion-weighted images and appears to be particularly valuable for data with frequent motion corruption.[13,26] In summary, the reliability of DTI analyses is drastically improved when handling data outliers in an appropriate way. However, additional research is needed to determine what types of data processing can reliably be performed without affecting data quality. This report presses the need for careful data handling because corrupted data can significantly affect the final result. Although this will require longer processing time and perhaps the need to remove datasets completely, it will probably decrease the spread in the final analysis and therefore improve statistical significance and reduce sample size.

Limitations of this study are important and must be addressed. First, only datasets without evidence of injury were used, and this may have resulted in a selection bias. Although this policy provided a homogeneous study population, we did not investigate the impact of processing datasets with brain injury. Second, we applied an arbitrary boundary to define "good-quality" and "poor-quality" data: 10% data outliers. We used this threshold solely to illustrate the impact of poor data quality on DTI analysis; hence, we do not suggest that this 10% level should be used as a threshold for future studies to define poor data quality.

the use of standardized guidelines before drawing conclusions with regard to outcome. Thus, strategies to limit image corruption should be incorporated into setups to acquire neonatal DTI data[27]; this includes 1) prevention of motion by comforting the infant and promoting natural sleep[28]; 2) adjustment of parameter settings, by
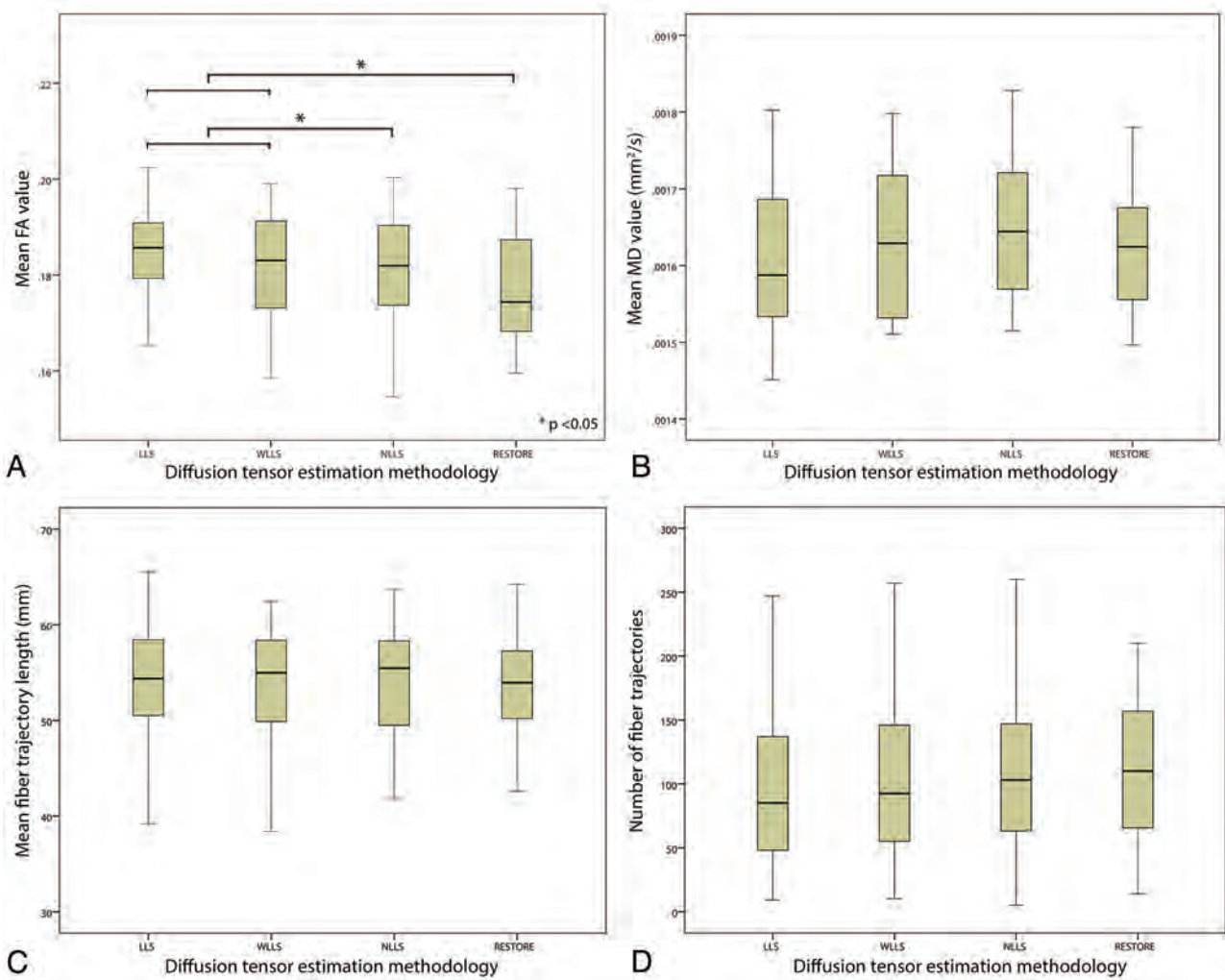
FIG 6. Impact of diffusion tensor estimation method on tract parameters. Tract parameters, such as fractional anisotropy (FA) *(A)*, mean diffusivity *(B)*, mean fiber trajectory length *(C)*, and number of fiber trajectories *(D)* were affected by the tensor estimation method; mean FA value was significantly lower with use of the nonlinear least squares and robust estimation of tensors by outlier rejection techniques (paired sample *t* test, $P < .05$).
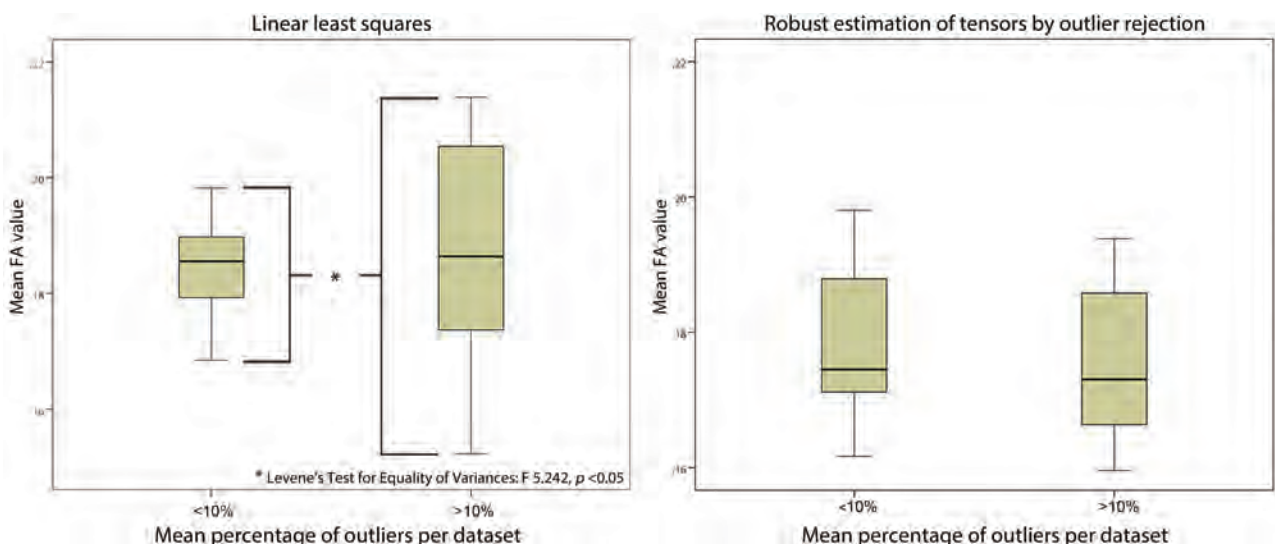
FIG 7. Impact of data quality on variability of tract parameters. Diffusion-weighted images with high outlier percentages ($>$10%) resulted in a significantly increased variability of mean fractional anisotropy values compared with data with fewer data outliers ($<$10%) if linear least squares was used (Levene test for equality of variances, $P < .05$). With application of robust estimation of tensors by outlier rejection, there was no difference in variability with regard to data quality.

CONCLUSIONS

As demonstrated with our tractography analysis of the fornix in the preterm brain, it is clear that the choice of diffusion tensor estimation methodology is crucial and that it has a considerable impact on subsequent analyses for studying microstructural brain properties. Given the insufficient attention in most clinical studies to date, this work raises the urgency to comply with the requirements to include state-of-the-art standardized research methodology wherever and whenever possible. Future studies should apply dedicated acquisition setups, standardized evaluation of data quality, and reliable processing of neonatal DTI data before performing analyses, such as associating microstructural brain properties with outcome.

REFERENCES

1. Ment LR, Hirtz D, Huppi PS. **Imaging biomarkers of outcome in the developing preterm brain.** *Lancet Neurol* 2009;8:1042–55
2. Bassi L, Ricci D, Volzone A, et al. **Probabilistic diffusion tractography of the optic radiations and visual function in preterm infants at term equivalent age.** *Brain* 2008;131:573–82
3. Ball G, Boardman JP, Aljabar P, et al. **The influence of preterm birth on the developing thalamocortical connectome.** *Cortex* 2013;49: 1711–21
4. van der Aa NE, Leemans A, Northington FJ, et al. **Does diffusion tensor imaging-based tractography at 3 months of age contribute to the prediction of motor outcome after perinatal arterial ischemic stroke?** *Stroke* 2011;42:3410–14
5. Jones DK, Cercignani M. **Twenty-five pitfalls in the analysis of diffusion MRI data.** *NMR Biomed* 2010;23:803–20
6. Tournier JD, Mori S, Leemans A. **Diffusion tensor imaging and beyond.** *Magn Reson Med* 2011;65:1532–56
7. Heemskerk AM, Leemans A, Plaisier A, et al. **Acquisition guidelines and quality assessment tools for analyzing neonatal diffusion tensor MRI data.** *AJNR Am J Neuroradiol* 2013;34:1496–1505
8. Kozak LR, David S, Rudas G, et al. **Investigating the need of triggering the acquisition for infant diffusion MRI: a quantitative study including bootstrap statistics.** *Neuroimage* 2013;69:198–205
9. Plaisier A, Raets MM, van der Starre C, et al. **Safety of routine early MRI in preterm infants.** *Pediatr Radiol* 2012;42:1205–11
10. Leemans A, Jeurissen B, Sijbers J, et al. **ExploreDTI: a graphical toolbox for processing, analyzing, and visualizing diffusion MR data.** 17th Annual Meeting of the International Society of Magnetic Resonance Medicine, Honolulu, Hawaii. April 18–24, 2009;3537
11. Leemans A, Jones DK. **The B-matrix must be rotated when correcting for subject motion in DTI data.** *Magn Reson Med* 2009;61: 1336–49
12. Irfanoglu MO, Walker L, Sarlls J, et al. **Effects of image distortions**

13. Chang LC, Jones DK, Pierpaoli C. **RESTORE: robust estimation of tensors by outlier rejection.** *Magn Reson Med* 2005;53:1088–95
14. Jones DK, Basser PJ. **"Squashing peanuts and smashing pumpkins": how noise distorts diffusion-weighted MR data.** *Magn Reson Med* 2004;52:979–93
15. Veraart J, Sijbers J, Sunaert S, et al. **Weighted linear least squares estimation of diffusion MRI parameters: strengths, limitations, and pitfalls.** *Neuroimage* 2013;81C:335–46
16. Basser PJ, Pajevic S, Pierpaoli C, et al. **In vivo fiber tractography using DT-MRI data.** *Magn Reson Med* 2000;44:625–32
17. Nagy Z, Ashburner J, Andersson J, et al. **Structural correlates of preterm birth in the adolescent brain.** *Pediatrics* 2009;124:e964–72
18. Zhuang L, Sachdev PS, Trollor JN, et al. **Microstructural white matter changes, not hippocampal atrophy, detect early amnestic mild cognitive impairment.** *PLoS One* 2013;8:e58887
19. Catani M, Thiebaut de Schotten M. **A diffusion tensor imaging tractography atlas for virtual in vivo dissections.** *Cortex* 2008;44: 1105–32
20. Nieuwenhuys R, Voogd J, van Huijzen C. *The Human Central Nervous System.* Berlin: Springer-Verlag; 2008
21. Landis JR, Koch GG. **The measurement of observer agreement for categorical data.** *Biometrics* 1977;33:159–74
22. Volpe JJ. **Brain injury in premature infants: a complex amalgam of destructive and developmental disturbances.** *Lancet Neurol* 2009; 8:110–24
23. Plaisier A, Govaert P, Lequin MH, et al. **Optimal timing of cerebral MRI in preterm infants to predict long-term neurodevelopmental outcome: a systematic review.** *AJNR Am J Neuroradiol* 2014;35: 841–47
24. Dyet LE, Kennea N, Counsell SJ, et al. **Natural history of brain lesions in extremely preterm infants studied with serial magnetic resonance imaging from birth and neurodevelopmental assessment.** *Pediatrics* 2006;118:536–48
25. Mukherjee P, Chung SW, Berman JI, et al. **Diffusion tensor MR imaging and fiber tractography: technical considerations.** *AJNR Am J Neuroradiol* 2008;29:843–52
26. Morris D, Nossin-Manor R, Taylor MJ, et al. **Preterm neonatal diffusion processing using detection and replacement of outliers prior to resampling.** *Magn Reson Med* 2011;66:92–101
27. Malamateniou C, Malik SJ, Counsell SJ, et al. **Motion-compensation techniques in neonatal and fetal MR imaging.** *AJNR Am J Neuroradiol* 2013;34:1124–36
28. Mathur AM, Neil JJ, McKinstry RC, et al. **Transport, monitoring, and successful brain MR imaging in unsedated neonates.** *Pediatr Radiol* 2008;38:260–64
29. Veraart J, Rajan J, Peeters RR, et al. **Comprehensive framework for accurate diffusion MRI parameter estimation.** *Magn Reson Med* 2013;70:972–84
30. Koay CG, Chang LC, Carew JD, et al. **A unifying theoretical and algorithmic framework for least squares methods of estimation in diffusion tensor imaging.** *J Magn Reson* 2006;182:115–25
31. Salvador R, Pena A, Menon DK, et al. **Formal characterization and extension of the linearized diffusion tensor model.** *Hum Brain Mapp* 2005;24:144–55

originating from susceptibility variations and concomitant fields on diffusion MRI tractography results. *Neuroimage* 2012;61:275–88

Focal Compression of the Upper Left Thoracic Intersegmental Arteries as a Potential Cause of Spinal Cord Ischemia

P. Gailloud, A. Ponti, L. Gregg, C.A. Pardo, and J.H.D. Fasel

ABSTRACT

BACKGROUND AND PURPOSE: This study was prompted by recurrent angiographic observations of focal stenoses involving the proximal segment of the left upper thoracic intersegmental arteries, a few centimeters distal to their origin. The purpose was to investigate the nature and prevalence of this anomaly.

MATERIALS AND METHODS: The existence of non-ostial thoracic intersegmental artery stenoses was evaluated in 50 angiograms; the contribution of stenosed branches to the anterior spinal artery was recorded. Angiograms performed in 3 patients with right-sided aortas were also reviewed. The topographic relationships of the upper thoracic intersegmental artery with surrounding structures were investigated in 3 cadavers.

RESULTS: Thirty-seven non-ostial stenoses were found in 26 patients (52%), predominantly on the left side (92%), between T3 and T8, most frequently at T4 and T5 (54%). Severe lesions were observed in 10% of cases. Patients with stenoses had fewer detectable anterior radiculomedullary arteries between T3 and T5 (35% versus 54%). Upper intersegmental artery stenoses, documented on the left side of all 3 specimens, appeared to be caused by the recurrent path of these intersegmental arteries related to the leftward position of the thoracic aorta, and by their course around reinforced paramedian longitudinal strands of the endothoracic fascia.

CONCLUSIONS: Upper thoracic intersegmental artery stenoses are frequent. They result from the leftward deviation of the descending aorta and the existence of a fixed point along the course of the intersegmental arteries related to the endothoracic fascia. Because contributors to the spinal vascularization often originate at similar levels, these stenoses may play a role in the susceptibility of the upper and midthoracic spinal cord to ischemia.

ABBREVIATIONS: ISA = intersegmental artery; RMA = radiculomedullary artery

This study was prompted by the recurrent observation made during spinal DSA of focal narrowings of variable severity involving the proximal segment of the left upper thoracic intersegmental arteries (ISAs), a few centimeters distal to their point of origin from the aorta (Fig 1). These stenoses can be severe and may result in the occlusion of the involved ISAs, in a manner reminiscent of the stenoses related to the passage of lumbar ISAs through the pillar of the diaphragm.[1,2] The purpose of our study,

conducted on clinical angiographic material as well as anatomic specimens, was to establish the angiographic prevalence of these focal narrowings, and discuss their etiology and potential clinical implications.

MATERIALS AND METHODS
Radiologic Data
The clinical data reviewed for this investigation were collected in institutional review board–approved databases; additional permission was granted for publication. The data were collected prospectively and stored in a dedicated workstation. All the studies were performed in a single-center by use of a biplanar neuroangiography suite (Artis zee; Siemens, Erlangen, Germany). To be considered, a spinal angiogram had to include bilateral evaluation of the ISA between T3–T12 and be free of pathologies involving the region of interest (eg, large vascular tumors). Fifty of a total of 132 spinal studies satisfying these criteria were performed between July 2011 and March 2013 in 21 women and 29 men, with age ranging from 3–80 years (average, 44; median, 47). Indica-
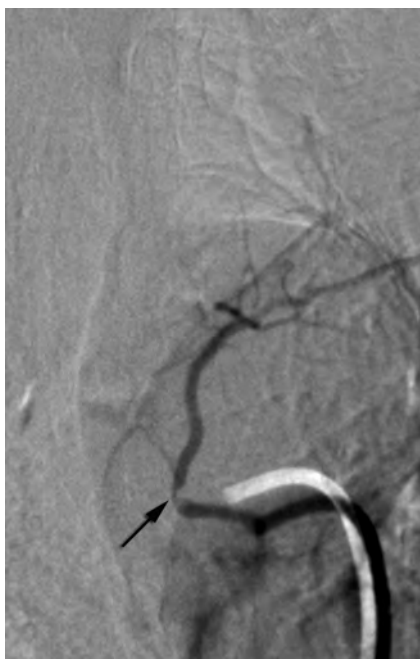
FIG 1. Non-ostial proximal intersegmental artery stenosis at left T4 in a 60-year-old woman (*arrow*).

tions for angiography in these 50 cases included progressive myelopathy (58%), acute myelopathy (26%), a known vascular malformation (6%), and spinal cord hemorrhage or tumor (10%).

Patients were logged in a normal group or a stenosis group on the basis of the presence of proximal narrowings, which were either categorized as 1) mild/moderate stenoses or 2) severe stenoses (including occlusions) (Fig 2A–D). Images were analyzed by use of a commercially available DICOM software (OsiriX 64, http://www.osirix-viewer.com), both in subtracted and native modes to assess for the presence of osseous changes potentially associated with arterial anomalies, for example, vertebral osteophytes. Available noninvasive imaging (CT and/or MR imaging) obtained in the patients with a stenosis was also reviewed.

The prevalence of upper thoracic radiculomedullary arteries (RMAs) has previously been analyzed in the same patient cohort and reported separately. However, radiculomedullary contributions coming from ISAs with a proximal stenosis were recorded, as well as the total number of anterior RMAs found between T3–T8 in both patient groups.

In addition, the presence of proximal stenoses was evaluated in 3 spinal angiograms performed by 1 of the authors in patients with right-sided aortic arches.

Anatomic Data

The topographic relationships of the upper thoracic ISA with surrounding structures were investigated in 3 cadavers.

RESULTS
Radiologic Data

Complete bilateral documentation of the ISAs between T3–T12 was achieved in 41 of the 50 reviewed angiograms (82%). One upper thoracic ISA was not identified in 8 instances (left T3 in 6 cases, right T3 and right T4 once each) and 2 in 1 instance (left T3
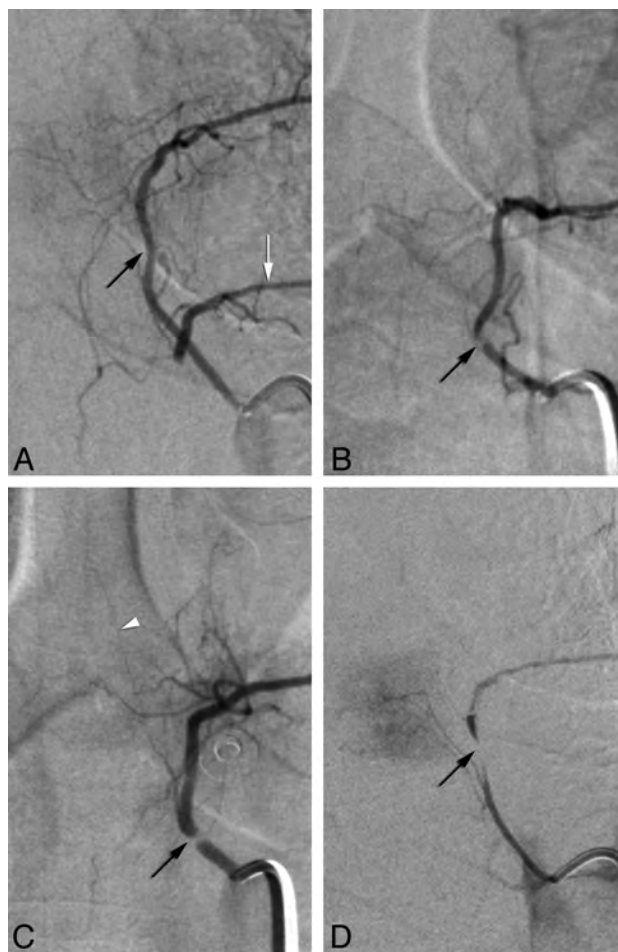
FIG 2. Categorization of stenoses as mild/moderate (*A* and *B*) or severe (*C* and *D*) (from studied cohort). *A*, Mild stenosis at left T5 in a 69-year-old woman (*black arrow*) illustrates the mildest form of recorded narrowing. Note collateral flow to left T6 (*white arrow*), which harbors a near-occlusive lesion. *B*, Moderate stenosis at left T5 in a 41-year-old woman (*arrow*); a continuous column of contrast is seen across the narrowing. *C*, Severe stenosis at left T5 in a 40-year-old woman (*arrow*); although close in severity to the case shown in *B*, this narrowing shows a completely unopacified segment. White *arrowhead* points to an anterior radiculomedullary artery. *D*, Near-occlusion at left T6 in the patient shown in *A* (*arrow*).

and T4). Angiographic diagnoses included ischemic lesion (eg, diaphragmatic crus syndrome, spinal artery thrombosis) (28%), a vascular malformation (14%), and spine or spinal cord tumor (8%); 50% of the angiograms were unremarkable.

Thirty-seven proximal non-ostial stenoses were noted in 26 of the 50 patients reviewed (52%); 34 stenoses (92%) were found on the left side and 3 (8%) on the right. The level of origin of the stenosed ISAs ranged between T3–T8, most commonly T4 and T5 (54%). Twenty-nine stenoses were of a mild/moderate degree (78%), whereas 8 were severe (22%); these severe stenoses were documented in 5 patients (10% of all patients), all on the left side. The Table summarizes our findings. The demographic characteristics of the 2 groups of patients were comparable: the 26 patients with stenoses included 12 women and 14 men, with an average age of 45 years (range, 3–80; median, 44), whereas the patients without stenoses included 9 women and 15 men, with an average age of 43 years (range, 8–66; median, 48).

Angiographic severity of proximal (non-ostial) stenoses affecting the upper thoracic intersegmental arteries

Levels	Left		Right	
	Mild/Moderate	Severe/Occlusions	Mild/Moderate	Severe/Occlusions
T3	3	1		
T4	8	1	1	
T5	7	3		
T6	3	2		
T7	1	1	2	
T8	4			

No evidence of osseous anomalies (eg, osteophytes) was noted in the review of nonsubtracted angiographic images. The analysis of noninvasive studies (CT or MR imaging) in all 26 patients with stenoses showed no associated lesion and/or mass effect at the involved levels.

A stenosed ISA provided an anterior RMA in 5 instances (mild/moderate = 3, severe = 2) and a posterior RMA in 2 cases (mild/moderate = 1, severe = 1).

Sixty-six anterior RMAs were found between T3 and T8, with at least 1 anterior RMA found in 47 of the 50 patients (94%). Thirty-two anterior RMAs were documented in the group without stenoses, with 23 of the 24 patients having at least 1 RMA (96%). In the stenosis group, 34 anterior RMAs were seen, with 23 patients having at least 1 RMA (92%). When considering only the branches found between T3 and T5, the number of patients with at least 1 anterior RMA was 9 in the stenosis group (35%) and 13 in the normal group (54%).

Proximal stenoses were found on neither side of the 3 patients with right-sided descending aorta.

Anatomic Data

Macroscopic investigations performed in 3 human specimens showed that the upper left thoracic ISAs initially adopt a medial course before sharply bending laterally and posteriorly in the vicinity of the vertebral column to pass along the posterior thoracic wall. This recurrent course and proximal curve was observed in all 3 specimens but not below the seventh thoracic vertebra or on the right side. To appreciate the anomaly, the thoracic aorta had to be gently dextroversed; the proximal portion of the ISAs could then be observed passing under bandlike reinforcements of the endothoracic fascia, mostly oriented longitudinally, some in a paramedian position, close to the medial aspect of the aorta (Fig 3A). The proximal portion of the ISA was bared by gentle blunt dissection of the endothoracic fascia. On both sides, the fascia tightly placated the arteries over the lateral aspect of the vertebral column. On the right side, the ISAs had a smooth course over the vertebral body before passing under the longitudinal reinforcements of the endothoracic fascia without noticeable curve or impingement. On the left side, the ISAs had an initial medial course that brought them to the fascia reinforcements, around which they took a sharp turn before continuing laterally and posteriorly within the intercostal space. The initial medial angulation of the artery and the sharpness of the turn around the edge of the fascia were most significant at the highest thoracic levels, correlating with a more lateral position of the aorta. Once freed
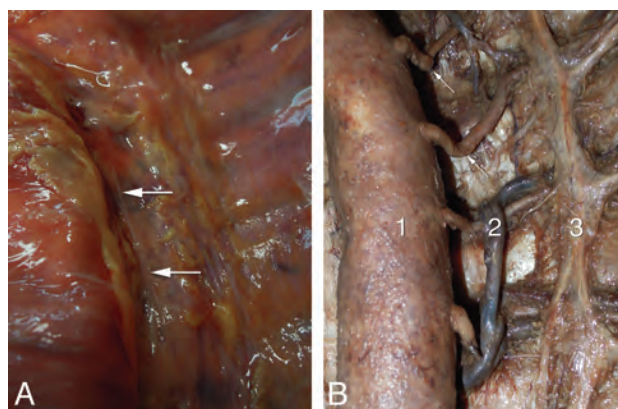
FIG 3. Anatomic observations in 2 human specimens. *A,* Anterior view of the endothoracic fascia in a fresh specimen after resection of the pleura; note the predominantly longitudinal bands of reinforcements (*arrows*) near the vertebral column. *B,* Anatomic dissection of an embalmed specimen documenting the proximal kinking of the left upper thoracic intersegmental arteries (*arrows*); 1, aorta (gently retracted to the right); 2, accessory hemiazygos vein; 3, sympathetic trunk.

from the attachment to the fascia, the proximal arterial segments showed a persistent bend, sometimes as severe as a kink (Fig 3B).

DISCUSSION

Angiographic Findings

The investigation of the spinal vasculature, first by nonselective and then by selective catheter spinal angiography, was pioneered in the mid-1960s by the teams of René Djindjian in France and John Doppman in the United States.[3-6] Since then, the normal and pathologic angiographic appearance of the spine and spinal cord vessels has been extensively studied.[5-13] Yet, a thorough review of the relevant anatomic and radiologic literatures, both past and current, did not yield specific information concerning the angiographic findings that prompted our investigation, for example, the observation of focal stenoses involving the proximal segment of the upper left thoracic ISAs. These non-ostial stenoses were found in 52% of our patients, mostly on the left side (92%), without being influenced by age or sex. The most commonly involved levels were T4 and T5 (54%). Eight of these stenoses (22%) were severe, that is, preocclusive or occlusive; they were found in 5 of the 50 patients reviewed (10%).

In a study examining the location of the aorta relative to the thoracic spine, Qiu et al[14] observed the maximum deviation from the midline (in the normal control group) at T5, T6, and T7. This finding was confirmed by Cronin et al,[15] who found the vertebral-aortic angle (defined as the angle between the center of the vertebral body and the center of the aorta) to be at its highest value (approximately 239°) at T3, T4, T5, and T6, then progressively decreasing to reach its lowest value at the lumbar level (approximately 195°). The vertebral levels showing the highest deviation correspond to the sites of origin of the ISAs from T3–T7,[16] levels at which were documented 33 of the 37 stenoses (89%) seen in our patients. This correlation speaks strongly in favor of a relationship between the leftward deviation of the thoracic aorta and the prevalence of proximal ISA stenoses. The 3 mild right-sided stenoses found in our series showed a different pattern than the left-sided
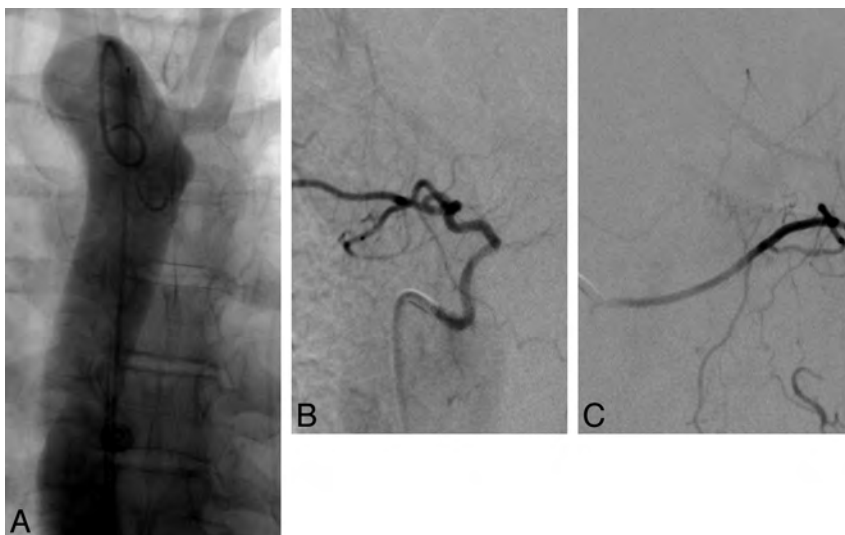
FIG 4. Mirror intersegmental anatomy in a 50-year-old woman with a right-sided aortic arch. *A,* Arch aortograms, postero-anterior projection; note that the deflection of the descending aorta from the midline is much less pronounced than in patients with a left-sided arch. *B,* Right T6 injection shows the typical course of a "normal" left-sided upper thoracic intersegmental artery (ISA), with a short recurrent course followed by a lateral bend. *C,* Left T6 injection shows the typical course of a "normal" right-sided upper thoracic ISA, with a smooth course across the midline, over the vertebral column.

FIG 5. Thoracic CT angiography in a 54-year-old woman, axial image through the T5 level, illustrates the difference in trajectories between left and right upper thoracic intersegmental arteries, whereas the right-sided artery smoothly curves around the vertebral body to cross the midline; the left one, after a short initial recurrent segment, sharply bends dorsally to continue its course along the corresponding rib. This "fixed" point in the vessel path (arrow), which results from the obligatory turn the artery must take around the medial attachment of the endothoracic fascia, corresponds to the site of stenosis.

ones, that is, a short irregular segment rather than stenosis at a bend. We do not have a specific explanation for these three narrowings. On the other hand, it might be assumed that "bend" stenoses should be seen on the right side of patients with a right-sided aortic arch and descending aorta. None was found on either side in 3 such patients included in this report. This finding appears consistent with our hypothesis: the mirror anatomy of the upper thoracic ISAs explains the lack of stenoses on the left side, whereas the fact that right-sided thoracic aortas lie closer to the spine than left-sided ones renders them less likely to stretch right-sided ISAs and participate in stenosis formation (Fig 4).

Of note, in a few patients, selective angiography of an ISA harboring a proximal stenosis was performed during full inspiration and expiration; these maneuvers did not reveal a significant impact of the breathing pattern on the appearance and severity of the stenoses.

The low proportion of vascular malformations (14%) included in the reviewed cohort of 50 cases (of a total of 132) probably reflects a selection bias, with patients with such a lesion being less likely to fulfill the inclusion criterion of having complete bilateral documentation of their thoracic ISAs.

Anatomic Findings

We initially postulated that upper thoracic ISA stenoses were caused by an extrinsic compressive mechanism, for example, by the sympathetic chain running alongside the vertebral column. Our anatomic investigations disproved this hypothesis because the sympathetic chain was too lateral to account for the stenoses observed angiographically. In addition, at the point in which the structures cross each other, the ISAs already lie in-between the ribs and appear well protected from potential compression by the sympathetic chain. On the other hand, focal bends of the upper left ISAs were seen in all 3 specimens investigated when the vessels were followed medially, near their site of origin from the dorsal aortic wall. The bends, visible only after gentle dextroversion of the aorta, resulted from the initial recurrent course of the upper thoracic ISAs and the sharp turn they assume around the medial reinforcements of the endothoracic fascia before continuing their course along the posterior thoracic wall. The severity of this bend was accentuated by the leftward position of the aorta at the upper thoracic level. The endothoracic fascia, reinforced by longitudinal strands of connective tissue, was found to act as a fixed point in the course of the ISAs, which were stretched by the lateral displacement of the aorta (Figs 5 and 6). The topography and appearance of the curves observed in the anatomic specimens correlated with most stenoses documented by means of spinal DSA in our patients.

Clinical Implication

Severe ISA stenoses were found in 10% of our patients, with anterior or posterior RMAs coming from these branches in 3 instances. Although our study is not large enough to provide meaningful statistical data, the fact that anterior RMAs were less often documented between T3 and T5 in the group of patients with stenoses (35% versus 54%) is also interesting because it may suggest a relationship between proximal ISA lesions and impairment of the spinal cord blood supply. The lower angiographic prevalence of anterior RMAs in the stenosis group could be related either to suboptimal opacification or to thrombo-occlusive complications.

The upper and midthoracic regions of the spinal cord have been considered as a zone at risk for ischemia. Postulating a lack of adequate blood supply to that area, several authors introduced the concept of a thoracic arterial "watershed zone,"[17,18] believed to
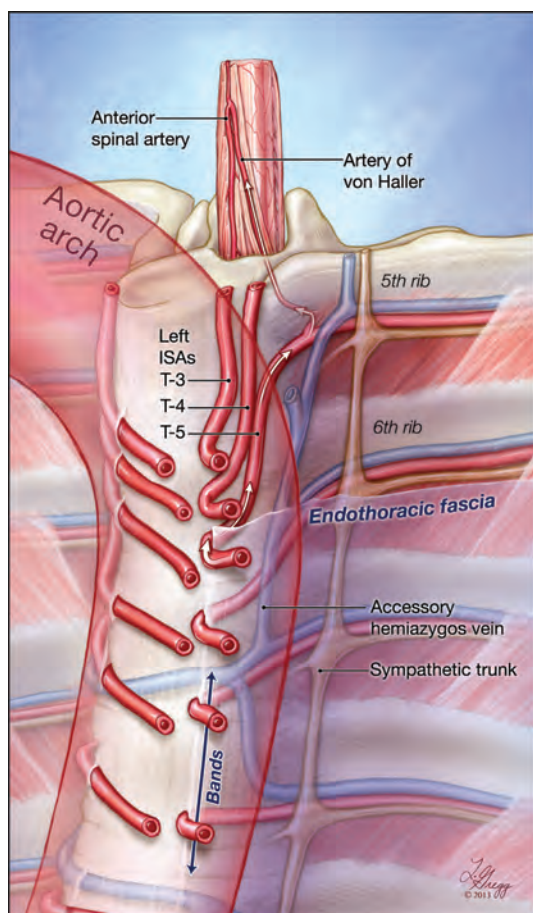
FIG 6. Graphic representation of the study findings. This illustration depicts the course of the upper thoracic intersegmental arteries (ISAs) in relation to the vertebral column, the endothoracic fascia, and the position of the thoracic aorta. Note the difference in trajectory between the right-sided ISAs, smoothly curving around the spine to pass under the fascia, and the left-sided ones, which have to adopt a recurrent course to reach the fixed paramedian points imposed by the attachment of the fascia to the lateral aspect of the vertebral column. The reinforced bands of connective tissue found within the paramedian endothoracic fascia are indicated by an arrow at T7 and T8. Note that the length of the recurrent segments and the sharpness of the bends increase with the leftward deviation of the upper thoracic aorta. In this example, the fifth thoracic ISA provides a prominent anterior radiculomedullary branch, the artery of von Haller.

FIG 7. Angiographic findings investigating for progressive myelopathy in a 52-year-old woman. *A,* Non-ostial occlusion of the left T6 intersegmental artery. *B,* Left T7 injection shows collateral supply to left T6 distal to the site of occlusion (*arrow*), with opacification of the anterior spinal artery (*arrowhead*) through a left T6 anterior radiculomedullary artery (artery of von Haller, *small arrow*).

result either from the transition of the spinal cord supply from the subclavian artery to the aorta,[17] or from the smaller number and size of the thoracic anterior RMAs.[19] Yet, this notion disregards the fact that if contributions to the spinal cord vascularization are indeed less conspicuous in the upper thoracic region than at the cervical or lumbosacral levels, the thoracic spinal cord is also of a lesser size, with a smaller volume of parenchyma to supply. Overall, as Gillilan[20] observed, "the blood supply to the thoracic cord is entirely adequate for the volume of gray matter present, and it is relatively as good as for any other cord segment." Moreover, the presence of a constant anterior radiculomedullary artery at the upper or midthoracic level, playing a role similar to the arteries of the cervical and lumbosacral enlargements, has been suggested for some time.[21-24] In a recent angiographic study, this artery, for which the eponym of artery of von Haller was proposed, was found between left T3 and left T7 in approximately 70% of
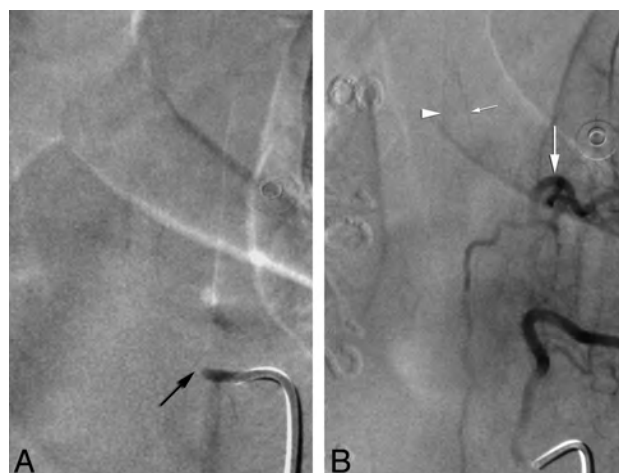
patients, weakening further the hypothesis that the thoracic spinal cord sensitivity to ischemia results from a "watershed" mechanism.

The findings reported in our study appear to provide an alternate explanation for the occurrence of upper and midthoracic spinal cord ischemia. The dominant anterior RMA at the upper thoracic level, or artery of von Haller, originates most commonly from the ISAs with the highest prevalence of proximal stenoses, that is, left T3–T7. The conjunction of these 2 anatomic conditions suggests the possibility that proximal stenoses impact the supply of the spinal cord by impairing the flow to the artery of von Haller (Fig 7). This mechanism would be very similar to the situation encountered at the lumbar level, in which the passage of upper lumbar ISAs through the crus of the diaphragm[2] occasionally results in extrinsic compression, leading to spinal cord ischemia when the involved vessel provides a significant spinal artery contributor.[1,25] Although surgical treatment can be offered at the lumbar level, with the compression being relieved by section of the pillar of the diaphragm, there is at this time no straightforward method addressing the upper thoracic ISA stenoses described in the present report. Several patients presenting with progressive or recurrent myelopathies of unclear etiologies, and in whom a stenosis or occlusion was shown to involve an ISA providing a prominent anterior RMA, were placed on prophylactic antiplatelet therapy with aspirin and/or clopidogrel.

CONCLUSIONS

Proximal non-ostial ISA stenoses were found at the upper thoracic level in approximately half the reviewed angiograms, in particular between T3–T8, almost exclusively on the left side. Severe stenoses or occlusions were observed in 10% of the patients investigated. These stenoses appear to result from the combination of the leftward deviation of the proximal descending aorta and the existence of a fixed paramedian point along the course of the ISAs, related to the attachment of the endothoracic fascia over the lateral aspect of the vertebral column. Because an important con-

tributor to the spinal cord vascularization commonly originates from the ISAs with the highest prevalence of proximal stenoses (left T4 and T5), we suggest a potential role of this anatomic configuration in the susceptibility of the upper and midthoracic spinal cord regions to ischemia.

REFERENCES

1. Rogopoulos A, Benchimol D, Paquis P, et al. **Lumbar artery compression by the diaphragmatic crus: a new etiology for spinal cord ischemia.** *Ann Neurol* 2000;48:261–64
2. Kauppila LI. **Blood supply of the lower thoracic and lumbosacral regions: postmortem aortography in 38 young adults.** *Acta Radiologica* 1994;35:541–44
3. Djindjian R, Faure C. [**Neuro-radiological investigations (arteriography and phlebography) in vascular malformations of the spinal cord**]. *Roentgen Eur Radiodiagnostic Clinique Européen* 1963;158: 171–95
4. Djindjian R, Houdart R, Hurth M. **Acquisitions récentes en angiographie médullaire.** *Revure Neurologique* 1966;115:1068–69
5. Doppman JL, Di Chiro G, Ommaya AK. *Selective Arteriography of the Spinal Cord.* St Louis: Green; 1969
6. Di Chiro G, Doppman J, Ommaya AK. **Selective arteriography of arteriovenous aneurysms of spinal cord.** *Radiology* 1967;88:1065–77
7. Djindjian R. *Angiography of the Spinal Cord.* Baltimore: University Park Press; 1970
8. Lazorthes G, Gouaze A, Djindjian R. *Vascularisation et Circulation de la Moelle Épinière.* Paris: Masson & Cie; 1973
9. Launay M, Chiras J, Bories J. **Angiography of the spinal cord: venous phase: normal features: pathological application.** *J Neuroradiol* 1979;6:287–315
10. Di Chiro G, Wener L. **Angiography of the spinal cord: a review of contemporary techniques and applications.** *J Neurosurg* 1973;39: 1–29
11. Merland JJ, Riche MC, Chiras J. **Intraspinal extramedullary arteriovenous fistulae draining into the medullary veins.** *J Neuroradiol* 1980;7:271–320
12. Chiras J, Morvan G, Merland JJ. **The angiographic appearances of the normal intercostal and lumbar arteries: analysis and the anatomic correlation of the lateral branches.** *J Neuroradiol* 1979; 6:169–96
13. Chiras J, Morvan G, Merland JJ. **Blood supply to the thoracic (dorsal) and lumbar spine.** *Anat Clin* 1982;4:23–31
14. Qiu Y, He YX, Wang B, et al. **The anatomical relationship between the aorta and the thoracic vertebral bodies and its importance in the placement of the screw in thoracoscopic correction of scoliosis.** *Eur Spine J* 2007;16:1367–72
15. Cronin P, Williams DM, Vellody R, et al. **The normal distribution of thoracoabdominal aorta small branch artery ostia.** *Eur J Radiol* 2011;80:e563–70
16. Shimizu S, Tanaka R, Kan S, et al. **Origins of the segmental arteries in the aorta: an anatomic study for selective catheterization with spinal arteriography.** *AJNR Am J Neuroradiol* 2005;26:922–28
17. Mettler FA. *Neuroanatomy.* 2nd ed. St Louis: CV Mosby Co; 1948
18. Zülch KJ. **Mangeldurchblutung als Ursache ungeklärter Rückenmarksschädigungen.** *Deutsche Zeitschrift Nervenheilkunde* 1954;172: 81–101
19. Dommisse GF. *The Arteries and Veins of the Human Spinal Cord From Birth.* Edinburgh/New York: Churchill Livingstone; 1975
20. Gillilan LA. **The arterial blood supply of the human spinal cord.** *J Comp Neurol* 1958;110:75–103
21. Von Haller A. *Iconum anatomicarum quibus aliquae partes corporis humani delineatae traduntur. Fasciculus VII: Arteriae cerebri Medullae spinalis Oculi.* Göttingen: Widow of Abram Vandenhoeck; 1754
22. Corbin JL. *Anatomie et Pathologie Artérielles de la Moelle.* Paris: Masson & Cie; 1961
23. Suh T, Alexander L. **Vascular system of the human spinal cord.** *Arch Neurol Psychiatry* 1939;41:659–77
24. Djindjian R. **Arteriography of the spinal cord.** *Am J Roentgenol Radium Ther Nucl Med* 1969;107:461–78
25. Batt M, Rogopoulos A, Benchimol D, et al. **Paraplegia with lumbar artery compression by the diaphragmatic crus.** *J Vasc Surg* 2008;48: 1017–21

Familial Adhesive Arachnoiditis Associated with Syringomyelia

V. Pasoglou, N. Janin, M. Tebache, T.J. Tegos, J.D. Born, and L. Collignon

ABSTRACT

SUMMARY: Adhesive arachnoiditis is a rare condition, often complicated by syringomyelia. This pathologic entity is usually associated with prior spinal surgery, spinal inflammation or infection, and hemorrhage. The usual symptoms of arachnoiditis are pain, paresthesia, and weakness of the low extremities due to the nerve entrapment. A few cases have had no obvious etiology. Previous studies have reported one family with multiple cases of adhesive arachnoiditis. We report a second family of Belgian origin with multiple cases of arachnoiditis and secondary syringomyelia in the affected individuals.

Adhesive arachnoiditis is a relatively scarce condition. This pathology refers to an inflammation of the arachnoid matter, which becomes thick and adherent and is often associated with syringomyelia. Common etiologies are spinal surgery, inflammation and/or infection such as tuberculous meningitis, hemorrhage, trauma, and injection of anesthetic agents. During the past decades, this entity (syndrome) has been particularly related to an oil-based contrast agent used for myelographic studies. However, a few cases with no obvious cause have also been reported in the literature. In this regard, adhesive arachnoiditis is a sporadic condition, except for a single family of Japanese origin comprising 9 affected individuals. Part of this family immigrated to Canada and was reported by Duke and Hashimoto in 1974.[1] Adding new cases from part of the same family in Japan, Nagai et al[2] published an update in 2000 and drew a pedigree showing an apparent vertical transmission of the disease over 3 generations. We report here a second family with multiple cases of arachnoiditis and secondary syringomyelia in the affected individuals.

CASE SERIES

The pedigree of the Belgian family is shown in Fig 1.

Case 1

In 1979, a 35-year-old woman without a history of trauma, infection, and spinal operation presented to a local emergency department with flaccid paraparesis and complete sensory loss of all modalities below the level T6 (Fig 1, II.7). A myelographic examination was performed and revealed a blockage at the level of the dorsal spine. Surgery revealed the presence of attenuated arachnoidal adhesions at the levels T5–T6. The patient was treated by lysis of the adherent tissue. Postoperatively, the patient reported a slight amelioration of the symptoms, but 1 year later, she presented with walking difficulty, a right-sided Babinski sign, and complete sensory loss below the T6 level. CT of the brain and myelographic findings were normal; however, her symptoms worsened with time. In 1985, a routine MR imaging examination of the cervical and dorsal spine was performed and revealed a syringomyelic cavity from the C5 to T5 levels, just above where the surgeon had found the arachnoid adherences.

Case 2

In the early 80s, the brother of case 1, a 50-year-old man, was diagnosed with syringomyelia (Fig 1, II.1). The patient underwent surgery for this condition but died due to perioperative complications. This information was disclosed by the family because no official documentation was available.

Case 3

The son of case 2 and brother of case 4 was neurologically impaired and presented with walking difficulties. No official diagnosis or documentation was available (Fig 1, III.6).

Case 4

A 49-year-old woman (daughter of case 2, sister of case 3, cousin of cases 5 and 6) without a history of trauma, infection, or spinal
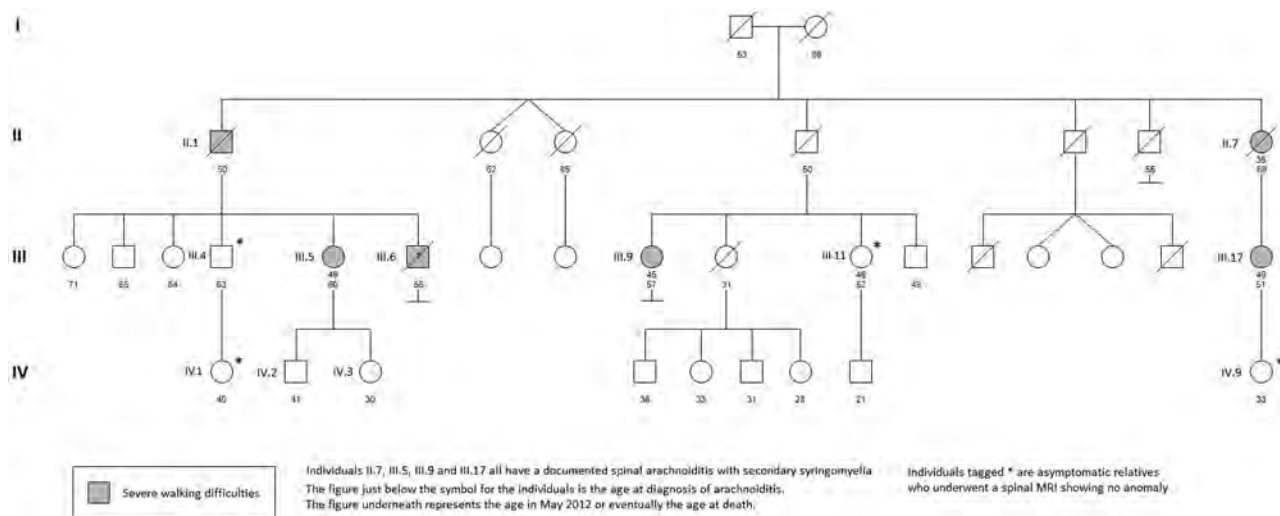
FIG 1. The pedigree of the Belgian family with spinal arachnoiditis and secondary syringomyelia. Squares and circles represent males and females, respectively. Solid symbols represent the affected family members.

operation presented in 2001 with walking difficulty and instability (Fig 1, III.5). The symptoms first appeared in 2000 when she reported paresthesia and bilateral dysesthesias below the knee, as well as chronic back pain. During the present neurologic examination, the patient could hardly lift her legs (flaccid paralysis). The examination revealed loss of pain and hot-cold sensation below the T3 level on both sides. The light-touch sensation and the vibration sensation in both medial malleoli were preserved. The Babinski sign was absent bilaterally. The routine serologic study findings were normal, including C-reactive protein levels. The CSF contained <5 white blood cells/mm^3. CT of the brain revealed hydrocephalus. MR imaging using sagittal T2-weighted turbo spin-echo, T1-weighted TSE, a myelographic sequence, and a gadolinium-enhanced T1-weighted turbo spin-echo sequence of the whole spine, completed by a transverse T2-weighted TSE at the level of the detected anomalies, was performed and revealed the presence of a syringomyelic cavity at the T3–T8 levels. No arachnoid adhesions were detected by the examination. There was no anomaly in the rest of the spine, and the administration of contrast material confirmed the absence of a causative tumoral lesion. The neurosurgeon mentioned the presence of thick and adherent arachnoid matter just below the level of the tubular syringomyelic cavity; nevertheless, MR imaging did not depict this arachnoid web. The pathologic examination of the extracted specimen confirmed the fibrous nature of the meningeal tissue sample with meningoepithelial cells and lymphocyte infiltration. The diagnosis of adhesive arachnoiditis was made. Follow-up MR imaging examinations showed the regression of the transverse size of the spinal cord and syrinx.

Case 5

A 45-year-old woman (cousin of cases 3, 4, and 6) presented in 2007 with dorsal pain, walking difficulty, and paresthesias at the thoracic dermatomes (Fig 1, III.17). The neurologic examination revealed hyperesthesia at the T5 level. The routine serologic study findings were normal, including the C-reactive protein level. The CSF contained 1 white blood cell/mm^3. All other CSF data were within normal ranges. The MR imaging examination included

the same sequences as those used in case 4 and demonstrated the presence of a syringomyelic cavity extending from the T2 to T7 levels and the presence of low-signal arachnoid adhesions at the T3–T4 level (On-line Fig 1). The rest of the spine was normal. After administration of contrast material, the arachnoid webs did not enhance and the presence of a causative tumoral lesion was excluded. The neurosurgeon confirmed the presence of thick and adherent arachnoid matter. The pathologic examination findings alluded to an adhesive arachnoiditis without signs of tumoral infiltration.

Case 6

In 2010, a 49-year-old woman (cousin of cases 3, 4, and 5) without any predisposing factors for arachnoiditis presented with left-sided numbness from level T4 to T10 (Fig 1, III.9). Light-touch sensation was decreased between the T4 and T8 levels, but the vibration sensation was normal. The deep tendon reflexes were normal in the upper and lower limbs. The Babinski sign was absent bilaterally. She also had walking difficulty and urinary incontinence. The routine serologic study findings were normal, including C-reactive protein. The CSF contained <5 white blood cells/mm^3. CT of the brain revealed hydrocephalus. MR imaging examination of the spine included a sagittal T2 (TR/TE, 1900/100 ms), sagittal T1 (TR/TE, 330/7.4 ms), sagittal short-TI inversion recovery (TE/TR, 60/2500 ms and inversion recovery delay, 170 ms) of the whole spine completed by axial balanced turbo-field echo (TR/TE: 6.2/3.1 ms) at the level of the detected anomalies. We also used a midline sagittal cardiac-gated phase-contrast MR imaging (10-mm-thick sagittal section, a 250 × 250 mm FOV, acquisition matrix of 252 × 185, TR of 21 ms, TE of 6.4 ms, phase-contrast velocity set at 10 cm/s). Finally, a gadolinium-enhanced T1-weighted turbo spin-echo encompassing the whole spine was performed.

We observed the presence of a syringomyelic cavity extending from T4 to T8 with thickening of the meninges at the T5–T6 levels (Fig 2). The rest of the spine was normal, and the administration of contrast material confirmed the absence of a causative tumoral lesion. The arachnoid adhesion did not enhance. In our case, cine

FIG 2. Sagittal T2-weighted MR image. Note enlargement of the spinal cord with a syringomyelic cavity extending from levels T4 to T8 (*arrow*). At the T5–T6 levels, posterior to the cord, a band-like low-signal-intensity structure represents a fibrous thickening of the arachnoid matter (*arrowhead*). The superior half of the cavity, just above the arachnoid thickening, is much more dilated than the inferior half.
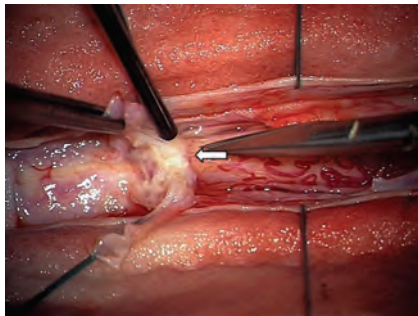

FIG 3. Intraoperative photograph confirming the presence of a thick and adherent arachnoid web (*arrow*), depicted by MR imaging.

MR imaging proved to be of little diagnostic value because the motion of the heart and great vessels produced significant artifacts in the thoracic spine (it did not help in identifying the site of CSF blockage). During surgery, the neurosurgeon confirmed the presence of thick and fibrous arachnoid matter (Fig 3 and On-line Video). The pathologic examination findings of the resected tissue confirmed the presence of adhesive arachnoiditis (Fig 4). The follow-up MR imaging examination showed that the transverse size of the spinal cord had regressed and the syrinx was less expansive.

Asymptomatic Members of the Family

All the living first-degree relatives of the affected individuals are asymptomatic. An MR imaging of the whole spine was recommended to exclude the possibility of an asymptomatic arachnoid-
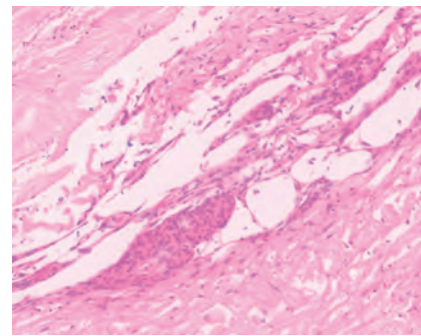
FIG 4. The pathologic examination demonstrated a thick membrane, rich in collagen limited by meningoepithelial cells. There is no evidence of inflammation, infection, or old hemorrhage (H&E stain).

itis in these family members. The MR imaging examination included sagittal T2- and T1-weighted TSE sequences of the whole spine and a transverse balanced turbo-field echo sequence of the lower cervical and upper dorsal spine. The MR imaging showed no anomaly in the following individuals: III.4, III.11, IV.1, and IV.9.

DISCUSSION

Spinal adhesive arachnoiditis is an inflammation inside the dura, affecting the arachnoid layer of the meninges, resulting in fibrosis. As a consequence, the arachnoid becomes firm, adherent, and thick and gets attached to the pia and dura mater.[3] The causes of spinal arachnoiditis include trauma, tumors, infections, spinal surgery, and spinal injection of substances such as anesthetics or oil-based myelographic contrast materials, which are no longer used clinically.[4,5]

Adhesive arachnoiditis is a chronic inflammatory condition causing neurologic impairment. It usually presents with diverse symptoms such as persistent back pain, weakness, and dissociated sensory loss. This condition is notably underdiagnosed, even though there is a high and well-known association between adhesive arachnoiditis and failed back surgery syndrome. On the other hand, there have been reports suggesting that spinal arachnoiditis is a coincidental finding rather than a disease.[6] Quencer et al[7] described a number of patients in whom arachnoiditis was totally asymptomatic.

The complications of adhesive arachnoiditis include the formation of arachnoid cysts, spinal cord damage (ischemia possibly due to obliterative angiopathy), and syringomyelia.[7-10] Jenik et al[11] highlighted, for the first time, the possible relationship between adhesive arachnoiditis and syringomyelia. Syringomyelia is an eccentric cavity within the spinal cord, which contains extracellular fluid (identical or similar to CSF). The most widely accepted theory regarding the etiology of syringomyelia is that the perturbation of CSF flow in the subarachnoid space modifies the fluid velocity, leading to a reduction of the fluid pressure and a passive distension of the spinal cord.[12,13]

The pathophysiology of syringomyelia is still unknown despite numerous and thorough efforts.[13-15] Older studies reported that CSF enters the syrinx via the fourth ventricle through the central canal.[16] On the other hand, Ball and Dayan[17] proposed that CSF enters the syrinx through the spinal perivascular space of Virchow-Robin. The studies of Heiss et al[18] and Stoodley et al[19] used

this hypothesis as a basis for explaining the pathophysiology of syringomyelia. According to Chang and Nakagawa,[20,21] the formation of the syrinx is caused by CSF pressure gradients inside and outside the spinal cord. This hypothesis could explain the association of syringomyelia with both Chiari malformation and adhesive arachnoiditis. Concerning the relationship between arachnoiditis and syrinx formation, the authors support a pressure drop in the subarachnoid space distal to the blockage. As a result, the pressure inside the spinal cord becomes superior to the perimedullar pressure. The cyclic pressure gradient at each CSF pulse leads to the formation of a syrinx.

The symptoms of syringomyelia are usually progressive and worsen during a long period. The most usual clinical manifestation of syringomyelia is a dissociated suspended sensory loss (impaired pain and temperature sensation but preserved light touch, vibration, and position sense), motor deficit, dysesthesias, and pain. When occurring outside of the context of arachnoiditis, syringomyelia is commonly associated with extramedullar malformations, such as Chiari or Dandy-Walker malformation. Isolated syringomyelia, with no history of Chiari malformation, trauma, or infection, can also occur, but it should always raise the suspicion of an intramedullary tumor. When a syrinx has been diagnosed, a contrast-enhanced MR imaging study is, therefore, mandatory to exclude an associated expansive intramedullary lesion.

To the best of our knowledge, reports about familial cases of arachnoiditis in humans are limited to the articles of Duke and Hashimoto[1] and Nagai et al,[2] which deal with the same family of Japanese origin. There was no relation between the Japanese family and the family of native Belgians described here. Furthermore, all family members involved in the case study live in the same area of Belgium within a 50-km range. Nothing in our medical records or in our knowledge suggests the exposure of the family to toxic substances, endemic organisms, and so forth. Available data from our cases and the Japanese family suggest that arachnoiditis may sometimes be very strongly influenced by a very rare inherited genetic anomaly. A major gene with incomplete penetrance could explain the family data. Of course, multigenic inheritance is also a possibility. A genetic study of this family will be undertaken to look for a major gene.

Regarding syringomyelia, in 2002 a review by Yabe et al[22] reported 21 cases of familial syringomyelia since 1899. Two more cases of familial syringomyelia were published since 2002.[23,24] Almost all the published cases of familial syringomyelia (whether associated or not with Chiari malformation) entail only 2 affected individuals who often belong to the same sibship, but they sometimes stand in a parent-child relationship or in a more remote degree of relationship. Although a highly penetrant Mendelian transmission seems very unlikely, these published cases are consistent with the hypothesis that genetic factors might play a role in the development of sporadic syringomyelia and/or the development of the Chiari malformation. Consistent with this hypothesis, Newman et al[25] reported, 30 years ago, an association between human leukocyte antigen A9 and syringomyelia in a series of 53 cases (40 of which were associated with a Chiari malformation).

The CSF pulsates in the craniocaudal direction due to the cerebral blood volume variations during the cardiac cycle. Normal and pathologic CSF pressure pulse has been extensively studied

and recorded as waveforms.[26,27] In their study, Enzmann et al[28] demonstrated that the most significant and consistent finding within preoperative syrinx cavities is the presence of fluid that pulsates in a similar way to subarachnoid CSF. The larger syringes demonstrated more important pulsations than the smaller ones. Nonpulsating syringes were usually the smaller ones. The postoperative studies of the syrinx showed a complete elimination of the pulsations in 3 of 5 patients. Furthermore, when narrowing of the subarachnoid space was observed, there were no CSF pulsations. There was no pulsation in patients with cystic formation associated with a tumor. More recent studies confirmed the pulsatility of the cyst and of the pericystic subarachnoid space.[29] Additionally, the occurrence of the systolic peak is earlier in the cyst than in the pericystic subarachnoid space. In patients with Chiari I malformation associated with syringomyelia, Koç et al[30] demonstrated that at the level of the foramen magnum, the flow pattern demonstrates a heterogeneous pattern, which was ameliorated after surgical decompression. Regarding the syrinx, the preoperative flow pattern was heterogeneous, but after the operation for decompression, there was an impressive decrease in CSF flow.

Mauer et al[31] showed that cardiac-gated phase-contrast CSF flow studies are more reliable than invasive conventional myelography to detect the site of spinal CSF blockage in idiopathic syringomyelia. Concerning the imaging of adhesive arachnoiditis associated with syringomyelia, according to Inoue et al,[32] the most striking MR imaging findings are the deformity of the cord at the level of the arachnoid thickening, blurring of a part of a syrinx wall, and the focal signal void within the syrinx.

For imaging of the subarachnoid space and arachnoid pathology, T2-weighted imaging is the method of choice. Nevertheless, there are some inconveniences arising from the loss of signal due to CSF flow provoking a loss of contrast within the arachnoid space. According to Roser et al,[33] 3D constructive interference in steady state MR imaging is an ideal method for the diagnosis of subarachnoid space disorders and syringomyelia due to the degradation of the flow-void artifacts compared with T2-weighted imaging and the amelioration of contrast within the subarachnoid space. Moreover, this method provides the possibility of producing multiplanar reconstruction images. Nevertheless, this sequence is very sensitive to motion caused by swallowing and breathing.[34] Gottschalk et al[34] suggested that cardiac-gated cine steady-state free precession MR imaging has a certain value in the evaluation of idiopathic syringomyelia and the detection of the arachnoid membranes.

For the imaging of future patients, we would suggest the use of sagittal T2, T2*, T1, and postgadolinium T1-weighted sequences from C0 to the cauda equina, a midline sagittal cardiac-gated phase-contrast MR imaging completed by axial balanced turbofield echo at the level of the anomalies.

Regarding the treatment of adhesive arachnoiditis associated with syringomyelia, the first aim should be lysis of the adhesions, to resolve the pathologic factor. Drainage of the syrinx by myelotomy or by shunting is performed. Nonetheless, Klekamp et al[35] reported that recurrence of the syrinx after shunting occurs in 92% of cases for focal and 100% for extensive arachnoid scarring. The same authors reported that for long-term management of the

syrinx, microsurgical lysis of the arachnoid adherences and decompression of the subarachnoid space with a fascia lata can lead to an improved outcome.

REFERENCES

1. Duke RJ, Hashimoto SA. **Familial spinal arachnoiditis: a new entity.** *Arch Neurol* 1974;30:300–03
2. Nagai M, Sakuma R, Aoki M, et al. **Familial spinal arachnoiditis with secondary syringomyelia: clinical studies and MRI findings.** *J Neurol Sci* 2000;177:60–64
3. Benner B, Ehni G. **Spinal arachnoiditis: the postoperative variety in particular.** *Spine (Phila Pa 1976)* 1978;3:40–44
4. Caplan LR, Norohna AB, Amico LL. **Syringomyelia and arachnoiditis.** *J Neurol Neurosurg Psychiatry* 1990;53:106–13
5. Brammah TB, Jayson MI. **Syringomyelia as a complication of spinal arachnoiditis.** *Spine (Phila Pa 1976)* 1994;19:2603–05
6. Mooij JJ. **Spinal arachnoiditis: disease or coincidence?** *Acta Neurochir (Wien)* 1980;53:151–60
7. Quencer RM, Tenner M, Rothman L. **The postoperative myelogram: radiographic evaluation of arachnoiditis and dural/arachnoidal tears.** *Radiology* 1977;123:667–79
8. Lee HJ, Cho DY. **Symptomatic spinal intradural arachnoid cysts in the pediatric age group: description of three new cases and review of the literature.** *Pediatr Neurosurg* 2001;35:181–87
9. Jain AK, Jena A, Dhammi IK. **Correlation of clinical course with magnetic resonance imaging in tuberculous myelopathy.** *Neurol India* 2000;48:132–39
10. Benini A, Blanco J. **Chronic fibroplastic leptomeningitis of the spinal cord and cauda equina** [in German]. *Schweiz Arch Neurol Psychiatr* 1990;141:293–343
11. Jenik F, Tekle-Haimanot R, Hamory BH. **Non-traumatic adhesive arachnoiditis as a cause of spinal cord syndromes: investigation of 507 patients.** *Paraplegia* 1981;19:140–54
12. Greitz D, Franck A, Nordell B. **On the pulsatile nature of intracranial and spinal CSF-circulation demonstrated by MR imaging.** *Acta Radiol* 1993;34:321–28
13. Greitz D. **Unraveling the riddle of syringomyelia.** *Neurosurg Rev* 2006;29:251–63, discussion 264
14. Elliott NS, Lockerby DA, Brodbelt AR. **The pathogenesis of syringomyelia: a re-evaluation of the elastic-jump hypothesis.** *J Biomech Eng* 2009;131:044503
15. Mallucci C, Brodbelt A. **The enigma of syringomyelia.** *Br J Neurosurg* 2007;21:423–24
16. Gardner WJ. **Hydrodynamic mechanism of syringomyelia: its relationship to myelocele.** *J Neurol Neurosurg Psychiatry* 1965;28:247–59
17. Ball MJ, Dayan AD. **Pathogenesis of syringomyelia.** *Lancet* 1972;2:799–801
18. Heiss JD, Patronas N, DeVroom HL, et al. **Elucidating the pathophysiology of syringomyelia.** *J Neurosurg* 1999;91:553–62
19. Stoodley MA, Brown SA, Brown CJ, et al. **Arterial pulsation-dependent perivascular cerebrospinal fluid flow into the central canal in the sheep spinal cord.** *J Neurosurg* 1997;86:686–93
20. Chang HS, Nakagawa H. **Hypothesis on the pathophysiology of syringomyelia based on simulation of cerebrospinal fluid dynamics.** *J Neurol Neurosurg Psychiatry* 2003;74:344–47
21. Chang HS, Nakagawa H. **Theoretical analysis of the pathophysiology of syringomyelia associated with adhesive arachnoiditis.** *J Neurol Neurosurg Psychiatry* 2004;75:754–57
22. Yabe I, Kikuchi S, Tashiro K. **Familial syringomyelia: the first Japanese case and review of the literature.** *Clin Neurol Neurosurg* 2002;105:69–71
23. Mavinkurve GG, Sciubba D, Amundson E, et al. **Familial Chiari type I malformation with syringomyelia in two siblings: case report and review of the literature.** *Childs Nerv Syst* 2005;21:955–59
24. Koç K, Anik I, Anik Y, et al. **Familial syringomyelia in two siblings: case report.** *Turk Neurosurg* 2007;17:251–54
25. Newman PK, Wentzel J, Foster JB. **HLA and syringomyelia.** *J Neuroimmunol* 1982;3:23–26
26. Cardoso ER, Rowan JO, Galbraith S. **Analysis of the cerebrospinal fluid pulse wave in intracranial pressure.** *J Neurosurg* 1983;59:817–21
27. Matsumoto T, Nagai H, Kasuga Y, et al. **Changes in intracranial pressure (ICP) pulse wave following hydrocephalus.** *Acta Neurochir (Wien)* 1986;82:50–56
28. Enzmann DR, O'Donohue J, Rubin JB, et al. **CSF pulsations within nonneoplastic spinal cord cysts.** *AJR Am J Roentgenol* 1987;149:149–57
29. Brugières P, Idy-Peretti I, Iffenecker C, et al. **CSF flow measurement in syringomyelia.** *AJNR Am J Neuroradiol* 2000;21:1785–92
30. Koç K, Anik Y, Anik I, et al. **Chiari 1 malformation with syringomyelia: correlation of phase-contrast cine MR imaging and outcome.** *Turk Neurosurg* 2007;17:183–92
31. Mauer UM, Freude G, Danz B, et al. **Cardiac-gated phase-contrast magnetic resonance imaging of cerebrospinal fluid flow in the diagnosis of idiopathic syringomyelia.** *Neurosurgery* 2008;63:1139–44, discussion 1144
32. Inoue Y, Nemoto Y, Ohata K, et al. **Syringomyelia associated with adhesive spinal arachnoiditis: MRI.** *Neuroradiology* 2001;43:325–30
33. Roser F, Ebner FH, Danz S, et al. **Three-dimensional constructive interference in steady-state magnetic resonance imaging in syringomyelia: advantages over conventional imaging.** *J Neurosurg Spine* 2008;8:429–35
34. Gottschalk A, Schmitz B, Mauer UM, et al. **Dynamic visualization of arachnoid adhesions in a patient with idiopathic syringomyelia using high-resolution cine magnetic resonance imaging at 3T.** *J Magn Reson Imaging* 2010;32:218–22
35. Klekamp J, Batzdorf U, Samii M, et al. **Treatment of syringomyelia associated with arachnoid scarring caused by arachnoiditis or trauma.** *J Neurosurg* 1997;86:233–40

Rebound Intracranial Hypertension: A Complication of Epidural Blood Patching for Intracranial Hypotension

P.G. Kranz, T.J. Amrhein, and L. Gray

ABSTRACT

SUMMARY: Rebound intracranial hypertension is a complication of epidural blood patching for treatment of intracranial hypotension characterized by increased intracranial pressure, resulting in potentially severe headache, nausea, and vomiting. Because the symptoms of rebound intracranial hypertension may bear some similarity to those of intracranial hypotension and literature reports of rebound intracranial hypertension are limited, it may be mistaken for refractory intracranial hypotension, leading to inappropriate management. This clinical report of 9 patients with confirmed rebound intracranial hypertension reviews the clinical characteristics of patients with this condition, emphasizing factors that can be helpful in discriminating rebound intracranial hypertension from refractory spontaneous intracranial hypotension, and discusses treatment.

ABBREVIATIONS: SIH = spontaneous intracranial hypotension; RIH = rebound intracranial hypertension; EBP = epidural blood patching; LP = lumbar puncture

Epidural blood patching (EBP) is considered by many authors to be the treatment of choice in cases of spontaneous intracranial hypotension (SIH).[1-3] Prior investigations have predominantly focused on the diagnostic evaluation of spontaneous intracranial hypotension, optimal methods for localizing the CSF leak, and various approaches to performing epidural blood patching. Relatively less attention has been paid, however, to the postprocedural care of patients with intracranial hypotension, including recognition and management of posttreatment complications.

Rebound intracranial hypertension (RIH) is a potential complication of epidural blood patching characterized by a postprocedural elevation of CSF pressure.[4] Although RIH has been reported previously, reports are limited to only a few patients. The mechanism underlying this phenomenon remains unknown and the onset of symptoms has been reported over a wide timeframe, ranging from days to years after EBP. Despite the small number of reported cases in the literature, our experience has been that this phenomenon is not uncommon. It is likely, in our opinion, that RIH often goes unrecognized.

The primary clinical manifestation of RIH is headache, which may be accompanied by nausea, emesis, and blurred vision. Because patients with SIH typically also have headache as their primary complaint, and because experience with treating these patients is limited at many centers, the headaches associated with RIH might be mistakenly attributed to refractory SIH. As a consequence, treatment aimed at increasing CSF pressure, such as repeat EBP, will be unhelpful for patients with RIH and could even exacerbate the condition. Awareness of this complication is therefore important.

The purpose of this case series is to describe the presentation of a series of patients with confirmed RIH, with an emphasis on common features that may suggest the diagnosis, as well as potential treatment strategies.

MATERIALS AND METHODS

Case Series

This investigation is a retrospective case series of patients with confirmed RIH after EBP. The investigation was approved by our local institutional review board and is Health Insurance Portability and Accountability Act–compliant. A waiver of informed consent was obtained for this retrospective review.

Cases were identified from the investigators' cohort of patients previously treated for intracranial hypotension. Inclusion criteria were history of intracranial hypotension confirmed by a combination of clinical symptoms, brain imaging, and/or decreased CSF pressure; treatment with epidural blood and/or fibrin glue patching with subsequent development of new complaints clinically suspected to be caused by increased intracranial pressure; and repeat lumbar puncture (LP) with a documented opening pressure of >20 cm H_2O. Patients with clinically suspected RIH with-

Pre- and post-EBP characteristics of patients with RIH

Patient	Opening Pressure (cm H_2O)		Time from EBP to Repeat LP	Headache Location		Post-EBP N/V[a]	Post-EBP Blurred Vision	Patching Agent	Patch Volume	Duration of Acetazolamide Treatment
	Pre-EBP	Post-EBP		Pre-EBP	Post-EBP					
1	6.8	25.5	6 hours	Occipital	Frontal	Yes	Yes	Fibrin glue	6 mL	5 days
2	N/A	28.0	3 weeks	Retro-orbital	Peri-orbital	No	No	Blood	18 mL	—[b]
3	12.3	31.0	2 hours	Retro-orbital	Retro-orbital	Yes	No	Blood + fibrin glue	16 mL	5 days
4	7.8	31.0	24 hours	Occipital	Holocephalic	Yes	Yes	Blood	18 mL	6 weeks
5	1.0	>55.0	2 hours	Holocephalic	Holocephalic	Yes	Yes	Blood	6 mL	2 weeks
6	15.0	32.0	7 days	Occipital	Frontal	Yes	Yes	Blood	5 mL	3+ years
7	10.8	24.2	24 hours	Occipital	Frontal and peri-orbital	Yes	Yes	Blood	18 mL	4 weeks
8	7.0	22.0	48 hours	Occipital	Frontal	Yes	Yes	Blood	20 mL	6 weeks
9	8.0	22.0	12 months	Occipital	Occipital	Yes	Yes	Blood	42 mL	6 months

Note:— N/A indicates data not available.
[a] Nausea/vomiting.
[b] Received follow-up care at another institution.

out a confirmatory opening pressure measurement were not included.

Pretreatment (ie, before EBP) and post-EBP clinical symptoms, CSF pressure measurements, and treatment details were recorded. In all cases, LP was performed by use of imaging (fluoroscopic or CT fluoroscopic) guidance, and opening pressures were measured with the patient in the lateral decubitus position, with legs extended, resting quietly without talking.

A total of 9 cases were identified that met inclusion criteria. These patients included 6 men and 3 women, with an average age of 44 years (range, 21–61). One patient (patient 8) received an epidural blood patch for post-LP headache after work-up of nonpositional migraine headaches. The remaining 8 patients were treated for SIH. Pre-EBP and post-EBP patient characteristics are summarized in the Table.

Characteristics before Blood Patching

Pre-EBP MR imaging was available in 7 of 8 patients with SIH; 1 of these pretreatment MRIs was performed without contrast. No MR imaging was performed before EBP in the patient with post-LP headache. Among the patients with pretreatment brain MR imaging, diffuse dural enhancement was present in 3 of 6 (50%), brain sagging in 5 of 7 (71%), cerebellar tonsillar ectopia in 5 of 7 (71%), subdural collections in 1 of 7 (14%), and venous distention sign[5] in 5 of 7 (71%). All patients, with the exception of 1 (patient 2), underwent patching with blood and/or fibrin glue (Tisseel; Baxter BioSurgery, Deerfield, Illinois) at our institution. Because we routinely measure opening pressure as part of the diagnostic evaluation of intracranial hypotension, pre-EBP opening pressures were available in all except this 1 patient. The average pre-EBP opening pressure was 8.6 cm H_2O (range, 1.0–15.0). A pre-EBP CT myelogram was available on all patients with SIH and showed active CSF leakage in 3 of 8 (38%) patients. No patients in this case series underwent MR myelography with intrathecal gadolinium. The total volume of autologous blood and/or fibrin glue used for patching varied widely, with as little as 5 mL for 1 patient with a localized leak (patient 6), to as much as 42 mL (patient 9).

All patients had positional headache before blood patching. Pretreatment headache location was most commonly occipital ($n = 6$), with retro-orbital ($n = 2$) and holocephalic ($n = 1$) headaches less commonly present. Symptoms of intracranial hypotension had been present for an average of 12 months (range, 1 week to 2 years) before EBP.

Characteristics after RIH Development

The median time to repeat LP for confirmation of RIH after EBP was 1 day (range, 2 hours to 1 year). Six of 9 (66%) patients had symptoms of RIH within 48 hours of blood patching. Headache location associated with RIH was different compared with the location of the pretreatment headache in 6 of 9 (66%) patients, with the most common locations described being frontal (44%) and peri- or retro-orbital (33%). Eight of 9 (89%) patients had new nausea and/or vomiting. New blurred vision was present in 7 of 9 (78%) patients.

The average opening pressure among patients who had RIH symptoms was 30 cm H_2O (range, 22–55). Notably, 1 patient (patient 5) had an opening pressure of >55 cm H_2O only 2 hours after blood patching, despite a pretreatment opening pressure of 1 cm H_2O and a patch volume of only 6 mL.

All patients demonstrated symptomatic improvement after removal of CSF. In 8 of 9 cases, patients were started on oral acetazolamide and were treated for variable periods of time, ranging from 5 days to 3+ years.

DISCUSSION

Although RIH is sparsely reported, in our experience it is not an uncommon complication of epidural blood patching. Although this case series was limited to patients with elevated opening pressure confirmed by lumbar puncture and therefore probably represents a subset of patients with a more severe spectrum of disease, we commonly encounter patients with similar, less severe symptoms after EBP. Although often self-limited and minor, RIH symptoms can at times be severe or persist well beyond the immediate posttreatment period. Lack of familiarity with this complication can result in misdiagnosis, including an incorrect attribution of symptoms to refractory intracranial hypotension.

The lack of more widespread recognition of this condition is probably caused by a superficial similarity of presenting features: headache is the predominant symptom experienced by patients with RIH and patients with intracranial hypotension.[4] This case series highlights several typical features that are useful for discriminating persistent intracranial hypotension from RIH.

First, patients who have RIH typically describe a change in headache phenotype. In contrast to the headaches of intracranial hypotension, which are commonly occipital in location,[6] we found that headaches in RIH are most commonly frontal or peri-orbital in location (Fig 1). Additionally, headaches in intracranial hypotension are exacerbated with upright positioning, whereas those associated with RIH are typically worse when recumbent. Some patients report
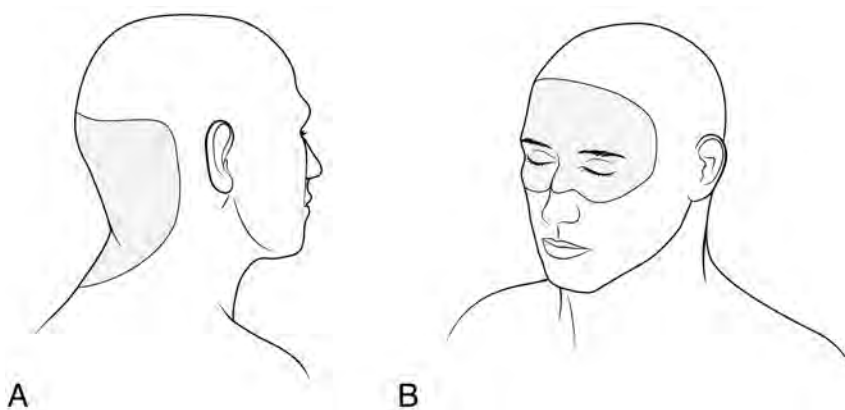
FIG 1. *A*, Patients presenting with intracranial hypotension most commonly — although not exclusively — complain of headaches in the occipital region. *B*, Patients who develop rebound intracranial hypertension often have a change in headache location, most commonly having headaches in a frontal, peri-orbital, or retro-orbital location.

that the headaches associated with RIH are worse in the morning. These symptoms mirror features of those patients with raised intracranial pressure caused by other etiologies.[7,8] Jugular venous outflow is impaired in the recumbent position,[9] which probably accounts for the worsening of symptoms in some patients with RIH while lying down. Prolonged recumbent positioning at night may contribute to morning headaches, though other proposed mechanisms such as a rise in pCO_2 at night, decreased CSF reabsorption, and increased CSF production modulated by chemical factors such as melatonin, for example, may also play a role.[7,10] By contrast, headaches more prominent in the later part of the day are seen in some patients with intracranial hypotension.[11]

Second, patients with acute RIH frequently have nausea, vomiting, and blurred vision, which are symptoms commonly found with elevated intracranial pressure. Whereas mild manifestations of these symptoms can occasionally be present at presentation in patients with intracranial hypotension, severe or continuous nausea, vomiting, and blurred vision are not common with low CSF pressure. The development of such symptoms immediately after blood patching should therefore raise suspicion for RIH.

Third, symptoms often develop in close proximity to the time of blood patching. Onset within 24–48 hours of treatment is common, and patients should be monitored most closely during this time period. In our series, onset even within several hours of EBP was not rare. In some cases, patients may even begin to have symptoms during the patching procedure itself while still on the procedure table. Nevertheless, not all patients in our series developed symptoms acutely, and a more delayed onset of symptoms should therefore not exclude the possibility of RIH. In our experience, patients who have development of symptoms over a more prolonged time period generally complain of less severe symptoms than those who have RIH more acutely, though the overall course of their symptoms may be more protracted.

Literature reports of RIH have been limited, with only 8 cases previously described, to our knowledge. The largest previous case series by Mokri[4] reported 4 patients. Three of those patients had CSF pressure confirmed by lumbar puncture; the other patient was diagnosed by the presence of papilledema. Symptom

onset in that series ranged from 1 week to 9 months. Other authors have reported cases of RIH in which symptom onset was more rapid (ranging from immediate to 3 days).[12-14] A single case report described a much more delayed onset of symptoms, occurring 2 years after blood patching.[15] CSF pressure measurements in these series, when measured, ranged from 20–28 cm H_2O. In general, the onset of symptoms in our series was more rapid, with a median time to onset of symptoms of 1 day, and the degree of CSF pressure elevation more severe, with an opening pressure of >25 cm H_2O in 66% of patients. This may be caused in part by sampling bias; patients in our series only underwent lumbar puncture if symptoms were severe, whereas many patients clinically suspected of having mild RIH were treated empirically without a confirmatory lumbar puncture. Thus, patients with milder CSF pressure elevations and/or more gradual symptom onset would not have been likely to be included in this investigation. We used 20 cm H_2O as the threshold for inclusion both because it replicates the criteria of prior reports of the condition and because it is a generally accepted upper limit of normal for CSF pressure in nonobese patients.[16] It is possible, however, that the relative change in CSF pressure contributes to the development of symptoms independent of the absolute CSF pressure.

The mechanism behind the development of RIH is unknown. One potential explanation could be the immediate displacement of CSF from the enclosed confines of the spinal canal caused by the addition of patching material in the epidural space, resulting in increased pressure. Although this mechanism probably exists to some degree in all patients undergoing epidural patching, the degree of pressure increase caused by this mechanism would be expected to be proportional to the volume of patching material used; this was not always seen in our series. For example, 3 patients in our series had development of RIH despite the use of <10 mL patching material, and yet many other patients who receive EBP by use of volumes of 20–30 mL or more do not have RIH. An additional mechanistic possibility could be considered: physiologic mechanisms are engaged in patients with intracranial hypotension to compensate for decreased CSF volume, such as distention of venous structures in the head (as demonstrated by the "venous distention sign") or in the cervical spinal canal.[5,17] When CSF volume is acutely returned to normal, failure of these compensatory mechanisms to immediately reverse could result in increased intracranial pressure. This explanation does not satisfactorily explain cases of delayed development of RIH, however. Mokri[4] proposed several other possible mechanisms for RIH including upregulation of CSF production or disrupted CSF reabsorption in the setting of prolonged CSF leak, or return to a preexisting state of (previously unrecognized) idiopathic intracranial hypertension. All of these potential mechanisms, he concluded, were vulnerable to criticism for various reasons. Ultimately, it is possible that multiple different pathways exist that result in raised

intracranial pressure and that variable engagement of 1 or more of these pathways may influence the time to onset and severity of symptoms among different patients.

Treatment of RIH in our series consisted of CSF drainage at the time of lumbar puncture, which immediately reduced, and in some cases eliminated, symptoms in all patients. Because the effect of CSF drainage is temporary, most patients were subsequently started on acetazolamide. Acetazolamide is an inhibitor of carbonic anhydrase that decreases CSF production through the inhibition of sodium-hydrogen ion exchange across the choroid plexus.[18] We typically use an oral starting dose of 250 mg twice per day and increase as necessary to control symptoms. Some patients may not be able to tolerate the side effects of acetazolamide, which include paresthesias of the digits, fatigue, and nausea.[19] If patients cannot tolerate acetazolamide, we have used topiramate as an alternative because it also demonstrates carbonic anhydrase inhibitory effect and has been studied as an alternative to acetazolamide in cases of idiopathic intracranial hypertension.[20,21] Acetazolamide should be used cautiously in patients with sulfa allergy, though our experience is that it is well tolerated by most patients with a history of reaction to other sulfa drugs, a finding that agrees with previous reports of the use of acetazolamide in sulfa-allergic patients.[22] Other reported strategies for the treatment of RIH include the use of IV glycerol and the need for CSF shunting.[1,13,14] Although we do not routinely admit patients overnight after their procedure, we do explicitly counsel patients on the symptoms that might suggest RIH and follow-up with them frequently by telephone after the procedure, in addition to providing them with emergency contact information should symptoms of RIH develop.

There are several limitations to this investigation. First, by only including patients with an opening pressure of >20 cm H_2O, we probably have excluded some patients with milder, but nonetheless symptomatic, elevations in CSF pressure. These patients may have a relatively increased CSF pressure compared with their pretreatment baseline but with opening pressures that still fall in the normal range. Second, because most patients who undergo epidural blood patching do not undergo routine subsequent CSF pressure evaluation, asymptomatic rises in CSF pressure in some patients could occur. Finally, and perhaps most importantly, we included only patients with symptoms severe enough to warrant repeat lumbar puncture. It is possible that RIH may present with different, less severe, clinical characteristics in patients with less dramatic elevations in CSF pressure.

CONCLUSIONS

RIH is a potential complication of epidural blood patching that should be considered in patients who report headache after treatment. Particularly suggestive features include change in headache phenotype, development of new nausea, vomiting, or blurred vision, and symptom development in close relationship to blood patching. Patients should be monitored closely for development of these symptoms, and can be treated with CSF drainage and/or oral acetazolamide.

REFERENCES

1. Mokri B. **Spontaneous low pressure, low CSF volume headaches: spontaneous CSF leaks.** *Headache* 2013;53:1034–53
2. Sencakova D, Mokri B, McClelland RL. **The efficacy of epidural blood patch in spontaneous CSF leaks.** *Neurology* 2001;57:1921–23
3. Berroir S, Loisel B, Ducros A, et al. **Early epidural blood patch in spontaneous intracranial hypotension.** *Neurology* 2004;63:1950–51
4. Mokri B. **Intracranial hypertension after treatment of spontaneous cerebrospinal fluid leaks.** *Mayo Clinic Proc* 2002;77:1241–46
5. Farb RI, Forghani R, Lee SK, et al. **The venous distension sign: a diagnostic sign of intracranial hypotension at MR imaging of the brain.** *AJNR Am J Neuroradiol* 2007;28:1489–93
6. Schievink WI. **Spontaneous spinal cerebrospinal fluid leaks and intracranial hypotension.** *JAMA* 2006;295:2286–96
7. Dunn LT. **Raised intracranial pressure.** *J Neurol Neurosurg Psychiatry* 2002;73(Suppl 1):i23–27
8. Sergott RC. **Headaches associated with papilledema.** *Curr Pain Headache Rep* 2012;16:354–58
9. Valdueza JM, von Munster T, Hoffman O, et al. **Postural dependency of the cerebral venous outflow.** *Lancet* 2000;355:200–01
10. Nilsson C, Ståhlberg F, Gideon P, et al. **The nocturnal increase in human cerebrospinal fluid production is inhibited by a beta 1-receptor antagonist.** *Am J Physiol* 1994;267:R1445–48
11. Leep Hunderfund AN, Mokri B. **Second-half-of-the-day headache as a manifestation of spontaneous CSF leak.** *J Neurol* 2012;259:306–10
12. Cestari DM, Rizzo JF. **Intracranial hypertension following epidural blood patch.** *Neurology* 2003;61:1303
13. Lin W-C, Lee M-H, Kao Y-F, et al. **Monitoring rebound intracranial hypertension by cine MRI after treatment of spontaneous intracranial hypotension in a patient with notable subdural hemorrhage.** *Eur J Radiol Extra* 2009;69:e1–e4
14. Tsui H, Wu S, Kuo H, et al. **Rebound intracranial hypertension after treatment of spontaneous intracranial hypotension.** *Eur J Neurol* 2006;13:780–82
15. Philipps J, Busse O. **From low to high: late-onset intracranial hypertension after treatment of spontaneous intracranial hypotension.** *J Neurol* 2007;254:956–57
16. Whiteley W, Al-Shahi R, Warlow CP, et al. **CSF opening pressure: reference interval and the effect of body mass index.** *Neurology* 2006;67:1690–91
17. Medina JH, Abrams K, Falcone S, et al. **Spinal imaging findings in spontaneous intracranial hypotension.** *Am J Roentgenol* 2010;195:459–64
18. Johanson CE, Murphy VA. **Acetazolamide and insulin alter choroid plexus epithelial cell [Na+], pH, and volume.** *Am J Physiol* 1990;258:F1538–46
19. Ball AK, Clarke CE. **Idiopathic intracranial hypertension.** *Lancet Neurol* 2006;5:433–42
20. Celebisoy N, Gökçay F, Sirin H, et al. **Treatment of idiopathic intracranial hypertension: topiramate vs acetazolamide, an open-label study.** *Acta Neurol Scand* 2007;116:322–27
21. Shah VA, Fung S, Shahbaz R, et al. **Idiopathic intracranial hypertension.** *Ophthalmology* 2007;114:617.e611–617.e612
22. Lee AG, Anderson R, Kardon RH, et al. **Presumed "sulfa allergy" in patients with intracranial hypertension treated with acetazolamide or furosemide: cross-reactivity, myth or reality?** *Am J Ophthalmol* 2004;138:114–18

American Society of Neuroradiology: Gordon Sze

The American Society of Neuroradiology (ASNR) is lucky to have Dr. Gordon Sze as its new President. Gordon, an accomplished academic neuroradiologist, is also a warm-hearted human being capable of gently leading even in the most complex situations. A graduate of Harvard Medical School, he completed his radiology residency and neuroradiology training at the University of California at San Francisco. After 2 years as an attending neuroradiologist at Cornell University, he moved to Yale, where he is currently Professor of Radiology and Chief of Neuroradiology. Gordon has filled many important committee positions in ASNR, including Treasurer, Secretary, and Vice President as well as being an American Society of Spine Radiology Past President. He has authored nearly 130 peer-reviewed articles and 26 book chapters. A proficient researcher, he has served as a principal investigator on 9 grants and as coinvestigator on another 12. Gordon is an excellent speaker and educator and has delivered more than 300 invited lectures and has trained more than 130 fellows in neuroradiology. His abilities and dedication as a manuscript reviewer have led him to become a member of 9 editorial boards. Those of us who have worked with him never cease to be impressed with his calm and rational demeanor and the breadth of his knowledge. As ASNR enters an era of challenges, we are fortunate to have Gordon help us navigate through them.

American Society of Head and Neck Radiology: Yoshimi Anzai

Dr. Yoshimi Anzai is Professor of Radiology and Neuroradiology Chief at the University of Washington in Seattle. Originally from Japan where she graduated from medical school, she completed her residency at the University of Michigan and her fellowship at the University of California at Los Angeles. Yoshimi is particularly well-suited to lead the American Society of Head and Neck Radiology (ASHNR), not only because of her stellar academic credentials but also because she trained in clinical otolaryngology. Her service experience and committee memberships are impressive, and outside of ASHNR, it is well worth mentioning that she is Vice President of the American Association for Women Radiologists, has served on 14 ASNR committees, and is President-Elect of the Radiology Alliance for Health Services Research. Despite these activities, she is an active coinvestigator in 7 grants and is a principal investigator on 2. She has published more than 140 peer-reviewed articles and 25 book chapters and has given close to 200 abstract presentations. Under her experienced guidance, ASHNR will continue to grow and assert its place as one of our most important subspecialty scientific societies.

American Society of Functional Radiology: David Mikulis

With degrees in physics and medicine from Tufts University, Professor David Mikulis is ideally suited to head the American Society of Functional Radiology (ASFNR). Currently a Professor of Radiology at the University of Toronto and a senior scientist at the Toronto Western Research Institute, David completed his radiology residency at the New England Deaconess Hospital and his neuroradiology training at Massachusetts General Hospital. His research achievements are impressive: a principal investigator on 16 grants and a coinvestigator on 37 others. He has published 175 peer-reviewed articles and given multiple invited lectures. His teaching abilities have led him to obtain, on 4 consecutive occasions, the Excellence in Teaching Award from his institution. For ASFNR, he has previously been Treasurer, Secretary, and Vice President, and he is a Past President of the Eastern Neuroradiological Society.

American Society of Pediatric Radiology: Thierry A.G.M. Huisman

Dr. Thierry Huisman is the new President of the American Society of Pediatric Radiology (ASPNR). Thierry obtained his MD from Erasmus University in Rotterdam, his radiology training from the University Hospital Zurich, and his pediatric neuroradiology fellowship at the University Children's Hospital also in Zurich, and he is currently Professor of Radiology at Johns Hopkins University School of Medicine. He has authored more than 200 original articles and 37 book chapters, participated in 240 invited lectures, and presented 175 abstracts at meetings, yet he still finds the time to be a manuscript reviewer for 31 journals. With his considerable experience and leadership, ASPNR will continue to thrive.

American Society of Spine Radiology: Adam E. Flanders

After completing his radiology training at the University of Illinois, Dr. Adam Flanders was a neuroradiology fellow at Thomas Jefferson University, where he is now Professor of Radiology and Rehabilitation Medicine. He has authored more than 140 articles, 22 book chapters, and 2 books and has presented 280 abstracts at meetings. Adam has also been a principal investigator on 3 grants and a coinvestigator on 15 others. His service record includes membership on 8 ASNR committees and terms as Treasurer and Vice President of American Society of Spine Radiology. He serves as Associate Editor for *Neurographics* and *RadioGraphics* and is a manuscript reviewer for 12 other journals.

SOCIAL MEDIA

PUBLICATION METRICS
AMERICAN JOURNAL OF NEURORADIOLOGY

AJNR BLOG
EST January 2009

ajnrblog.org

Posts
919

Hits
391,312

Per Day
201

facebook
EST March 2009

facebook.com/amjneuroradiol

Fans
5,637

Reach
573 per post

Clicks
67 per post

twitter
EST January 2013

@amjneuroradiol

Followers
437

Tweets
1,272

Klout
41

© Choose Chicago

ASNR 2015 – 53rd ANNUAL MEETING

April 25-30 • Sheraton Chicago Hotel & Towers • Chicago, Illinois

ASNR 2016 – 54th ANNUAL MEETING

May 21-26 • Washington Marriott Wardman Park • Washington, DC

ASNR 2017 – 55th ANNUAL MEETING

April 22-27 • Long Beach Convention & Entertainment Center • Long Beach, California

ASNR 2018 – 56th ANNUAL MEETING

June 2-7 • Vancouver Convention Centre • Vancouver, B.C., Canada

ASNR 2019 – 57th ANNUAL MEETING

May 18-23 • Hynes Convention Center • Boston, Massachusetts

TO REQUEST MORE INFORMATION ON UPCOMING MEETINGS, CONTACT:

American Society of Neuroradiology
800 Enterprise Drive, Suite 205, Oak Brook, Illinois 60523-4216
Phone: 630-574-0220 • Fax: 630-574-0661
Website: www.asnr.org • Email: meetings@asnr.org

Simplify
the MOC Process

Manage
your CME Credits Online

CMEgateway.org

It's Easy and Free!

Log on to CME Gateway to:

- View or print reports of your CME credits from multiple societies from a single access point.

- Print an aggregated report or certificate from each participating organization.

- Link to SAMs and other tools to help with maintenance of certification.

American Board of Radiology (ABR) participation!

By activating ABR in your organizational profile, your MOC–fulfilling CME and SAM credits can be transferred to your own personalized database on the ABR Web site.

Sign Up Today!

go to CMEgateway.org

Available to Members of Participating Societies

American Board of Radiology (ABR)

American College of Radiology (ACR)

American Roentgen Ray Society (ARRS)

American Society of Neuroradiology (ASNR)

Commnission on Accreditation of Medical Physics Educational Programs, Inc. (CAMPEP)

Radiological Society of North America (RSNA)

Society of Interventional Radiology (SIR)

SNM

The Society for Pediatric Radiology (SPR)

DOTAREM® (gadoterate meglumine) injection, for intravenous use
Initial U.S. Approval: 2013

BRIEF SUMMARY OF PRESCRIBING INFORMATION
CONSULT PACKAGE INSERT FOR FULL PRESCRIBING INFORMATION

WARNING: NEPHROGENIC SYSTEMIC FIBROSIS (NSF)
Gadolinium-based contrast agents (GBCAs) increase the risk for NSF among patients with impaired elimination of the drugs. Avoid use of GBCAs in these patients unless the diagnostic information is essential and not available with non-contrasted MRI or other modalities. NSF may result in fatal or debilitating fibrosis affecting the skin, muscle and internal organs.
- **The risk for NSF appears highest among patients with:**
  - **Chronic, severe kidney disease (GFR < 30 mL/min/1.73m²), or**
  - **Acute kidney injury.**
- **Screen patients for acute kidney injury and other conditions that may reduce renal function. For patients at risk for chronically reduced renal function (e.g. age > 60 years, hypertension, diabetes), estimate the glomerular filtration rate (GFR) through laboratory testing (5.1).**
- **For patients at highest risk for NSF, do not exceed the recommended DOTAREM dose and allow a sufficient period of time for elimination of the drug from the body prior to any re-administration *[see Warnings and Precautions (5.1)]*.**
---

1   INDICATIONS AND USAGE
DOTAREM is a gadolinium-based contrast agent indicated for intravenous use with magnetic resonance imaging (MRI) in brain (intracranial), spine and associated tissues in adult and pediatric patients (2 years of age and older) to detect and visualize areas with disruption of the blood brain barrier (BBB) and/or abnormal vascularity. (1)

4   CONTRAINDICATIONS
History of clinically important hypersensitivity reactions to DOTAREM. (4)

5   WARNINGS AND PRECAUTIONS
5.1   Nephrogenic Systemic Fibrosis
Gadolinium-based contrast agents (GBCAs) increase the risk for nephrogenic systemic fibrosis (NSF) among patients with impaired elimination of the drugs. Avoid use of GBCAs among these patients unless the diagnostic information is essential and not available with non-contrast MRI or other modalities. The GBCA-associated NSF risk appears highest for patients with chronic, severe kidney disease (GFR < 30 mL/min/1.73m²) as well as patients with acute kidney injury. The risk appears lower for patients with chronic, moderate kidney disease (GFR 30 - 59 mL/min/1.73m²) and little, if any, for patients with chronic, mild kidney disease (GFR 60 - 89 mL/min/1.73m²). NSF may result in fatal or debilitating fibrosis affecting the skin, muscle and internal organs. Report any diagnosis of NSF following DOTAREM administration to Guerbet LLC (1-877-729-6679) or FDA (1-800-FDA-1088 or www.fda.gov/medwatch).
Screen patients for acute kidney injury and other conditions that may reduce renal function. Features of acute kidney injury consist of rapid (over hours to days) and usually reversible decrease in kidney function, commonly in the setting of surgery, severe infection, injury or drug-induced kidney toxicity. Serum creatinine levels and estimated GFR may not reliably assess renal function in the setting of acute kidney injury. For patients at risk for chronically reduced renal function (e.g., age > 60 years, diabetes mellitus or chronic hypertension), estimate the GFR through laboratory testing.
Among the factors that may increase the risk for NSF are repeated or higher than recommended doses of a GBCA and the degree of renal impairment at the time of exposure. Record the specific GBCA and the dose administered to a patient. For patients at highest risk for NSF, do not exceed the recommended DOTAREM dose and allow a sufficient period of time for elimination of the drug prior to re-administration. For patients receiving hemodialysis, physicians may consider the prompt initiation of hemodialysis following the administration of a GBCA in order to enhance the contrast agent's elimination. The usefulness of hemodialysis in the prevention of NSF is unknown *[see Dosage and Administration (2) and Clinical Pharmacology (12)]*.

5.2   Hypersensitivity Reactions
Anaphylactic and anaphylactoid reactions have been reported with DOTAREM, involving cardiovascular, respiratory, and/or cutaneous manifestations. Some patients experienced circulatory collapse and died. In most cases, initial symptoms occurred within minutes of DOTAREM administration and resolved with prompt emergency treatment *[see Adverse Reactions (6)]*.
- Before DOTAREM administration, assess all patients for any history of a reaction to contrast media, bronchial asthma and/or allergic disorders. These patients may have an increased risk for a hypersensitivity reaction to DOTAREM.
- Administer DOTAREM only in situations where trained personnel and therapies are promptly available for the treatment of hypersensitivity reactions, including personnel trained in resuscitation.
- During and following DOTAREM administration, observe patients for signs and symptoms of hypersensitivity reactions.

5.3   Acute Kidney Injury
In patients with chronically reduced renal function, acute kidney injury requiring dialysis has occurred with the use of GBCAs. The risk of acute kidney injury may increase with increasing dose of the contrast agent; administer the lowest dose necessary for adequate imaging. Screen all patients for renal impairment by obtaining a history and/or laboratory tests. Consider follow-up renal function assessments for patients with a history of renal dysfunction.

5.4   Extravasation and Injection Site Reactions
Ensure catheter and venous patency before the injection of DOTAREM. Extravasation into tissues during DOTAREM administration may result in tissue irritation *[see Nonclinical Toxicology (13.2)]*.

6   ADVERSE REACTIONS
GBCAs have been associated with a risk for NSF *[see Warnings and Precautions (5.1)]*. NSF has not been reported in patients with a clear history of exposure to DOTAREM alone. For hypersensitivity reactions and acute kidney injury see Warnings and Precautions *(5.2) and (5.3)*.

6.1   Clinical Studies Experience
Because clinical trials are conducted under widely varying conditions, adverse reaction rates observed in the clinical trials of a drug cannot be directly compared to rates in the clinical trials of another drug and may not reflect the rates observed in clinical practice.
The data described below reflect DOTAREM exposure in 2813 patients, representing 2672 adults and 141 pediatric patients. Overall, 55% of the patients were men. In clinical trials where ethnicity was recorded the ethnic distribution was 74% Caucasian, 12% Asian, 4% Black, and 10% others. The average age was 53 years (range from 0.1 to 97 years).
Overall, 3.9% of patients reported at least one adverse reaction, primarily occurring immediately or several days following DOTAREM administration. Most adverse reactions were mild or moderate in severity and transient in nature.
Table 1 lists adverse reactions that occurred in ≥ 0.2% patients who received DOTAREM.

Table 1: Adverse Reactions in Clinical Trials

Reaction	Rate (%) n = 2813
Nausea	0.6%
Headache	0.5%
Injection Site Pain	0.4%
Injection Site Coldness	0.2%
Burning Sensation	0.2%

Adverse reactions that occurred with a frequency < 0.2% in patients who received DOTAREM include: feeling cold, rash, somnolence, fatigue, dizziness, vomiting, pruritus, paresthesia, dysgeusia, pain in extremity, anxiety, hypertension, palpitations, oropharyngeal discomfort, serum creatinine increased and injection site reactions, including site inflammation, extravasation, pruritus, and warmth.
Adverse Reactions in Pediatric Patients
During clinical trials, 141 pediatric patients (7 aged < 24 months, 33 aged 2 - 5 years, 58 aged 6 - 11 years and 43 aged 12 -17) received DOTAREM. Overall, 6 pediatric patients (4.3%) reported at least one adverse reaction following DOTAREM administration. The most frequently reported adverse reaction was headache (1.5%). Most adverse events were mild in severity and transient in nature, and all patients recovered without treatment.

6.2   Postmarketing Experience
The following additional adverse reactions have been identified during postmarketing use of DOTAREM. Because these reactions are reported voluntarily from a population of uncertain size, it is not always possible to reliably estimate their frequency or establish a causal relationship to drug exposure.
- bradycardia, tachycardia, arrhythmia
- hypersensitivity / anaphylactoid reactions including cardiac arrest, respiratory arrest, cyanosis, pharyngeal edema, laryngospasm, bronchospasm, angioedema, conjunctivitis, ocular hyperemia, eyelid edema, lacrimation increased, hyperhidrosis, urticaria

- coma, convulsion, syncope, presyncope, parosmia, tremor
- muscle contracture, muscle weakness
- diarrhea, salivary hypersecretion
- malaise, fever
- NSF, in patients whose reports were confounded by the receipt of other GBCAs or in situations where receipt of other GBCAs could not be ruled out. No unconfounded cases of NSF have been reported with DOTAREM.
- superficial phlebitis

7   DRUG INTERACTIONS
DOTAREM does not interfere with serum and plasma calcium measurements determined by colorimetric assays. Specific drug interaction studies with DOTAREM have not been conducted.

8   USE IN SPECIFIC POPULATIONS
8.1   Pregnancy
Pregnancy Category C
There are no adequate and well-controlled studies with DOTAREM conducted in pregnant women. Limited published human data on exposure to other GBCAs during pregnancy did not show adverse effects in exposed neonates. No effects on embryo fetal development were observed in rats or rabbits at doses up to 10 mmol/kg/day in rats or 3 mmol/kg/day in rabbits. The doses in rats and rabbits were respectively 16 and 10 times the recommended human dose based on body surface area. DOTAREM should be used during pregnancy only if the potential benefit justifies the potential risk to the fetus.
While it is unknown if DOTAREM crosses the human placenta, other GBCAs do cross the placenta in humans and result in fetal exposure.
Reproductive and developmental toxicity studies were conducted with gadoterate meglumine in rats and rabbits. Gadoterate meglumine was administered intravenously in doses of 0, 2, 4 and 10 mmol/kg/day (or 3.2, 6.5 and 16.2 times the recommended human dose based on body surface area) to female rats for 14 days before mating throughout the mating period and until gestation day (GD) 17. Pregnant rabbits were intravenously administered gadoterate meglumine at the dose levels of 0, 1, 3 and 7 mmol/kg/day (or 3.3, 10 and 23 times the human doses based on body surface area) from GD6 to GD19. No effects on embryo fetal development were observed in rats or rabbits at doses up to 10 mmol/kg/day in rats or 3 mmol/kg/day in rabbits. Maternal toxicity was observed in rats at 10 mmol/kg/day (or 16 times the human dose based on body surface area) and in rabbits at 7 mmol/kg/day (23 times the human dose based on body surface area).

8.3   Nursing Mothers
It is not known whether DOTAREM is excreted in human milk. Limited case reports on use of GBCAs in nursing mothers indicate that 0.01 to 0.04% of the maternal gadolinium dose is excreted in human breast milk. Because many drugs are excreted in human milk, exercise caution when DOTAREM is administered to a nursing woman. Nonclinical data show that gadoterate meglumine is excreted into breast milk in very small amounts (< 0.1% of the dose intravenously administered) and absorption via the gastrointestinal tract is poor.

8.4   Pediatric Use
The safety and efficacy of DOTAREM at a single dose of 0.1 mmol/kg have been established in pediatric patients from 2 to 17 years of age. No dosage adjustment according to age is necessary in this population *[See Dosage and Administration (2.1) and Clinical Studies (14)]*. The safety and efficacy of DOTAREM have not been established in pediatric patients below 2 years of age. GFR does not reach adult levels until 1 year of age *[see Warnings and Precautions (5.1)]*.

8.5   Geriatric Use
In clinical studies of DOTAREM, 900 patients were 65 years of age and over, and 312 patients were 75 years and over. No overall differences in safety or efficacy were observed between these subjects and younger subjects. In general, use of DOTAREM in elderly patients should be cautious, reflecting the greater frequency of impaired renal function and concomitant disease or other drug therapy. No age-related dosage adjustment is necessary.

8.6   Renal Impairment
No DOTAREM dosage adjustment is recommended for patients with renal impairment. Gadoterate meglumine can be removed from the body by hemodialysis *[see Warnings and Precautions (5.1) and Clinical Pharmacology (12.3)]*.

10   OVERDOSAGE
DOTAREM administered to healthy volunteers and to patients at cumulative doses up to 0.3 mmol/kg was tolerated in a manner similar to lower doses. Adverse reactions to overdosage with DOTAREM have not been reported. Gadoterate meglumine can be removed from the body by hemodialysis *[See Clinical Pharmacology (12.3)]*.

13   NONCLINICAL TOXICOLOGY
13.1   Carcinogenesis, Mutagenesis, Impairment of Fertility
Long-term animal studies have not been performed to evaluate the carcinogenic potential of gadoterate meglumine.
Gadoterate meglumine did not demonstrate mutagenic potential in *in vitro* bacterial reverse mutation assays (Ames test) using Salmonella typhimurium, in an *in vitro* chromosome aberration assay in Chinese hamster ovary cells, in an *in vitro* gene mutation assay in Chinese hamster lung cells, nor in an *in vivo* mouse micronucleus assay.
No impairment of male or female fertility and reproductive performance was observed in rats after intravenous administration of gadoterate meglumine at the maximum tested dose of 10 mmol/kg/day (16 times the maximum human dose based on surface area), given during more than 9 weeks in males and more than 4 weeks in females. Sperm counts and sperm motility were not adversely affected by treatment with the drug.

13.2   Animal Toxicology and/or Pharmacology
Local intolerance reactions, including moderate irritation associated with infiltration of inflammatory cells were observed after perivenous injection in rabbits suggesting the possibility of local irritation if the contrast medium leaks around the veins in a clinical setting *[see Warnings and Precautions (5.4)]*.

17   PATIENT COUNSELING INFORMATION
17.1   Nephrogenic Systemic Fibrosis
Instruct the patients to inform their healthcare provider if they:
- have a history of kidney disease, or
- have recently received a GBCA.
GBCAs increase the risk for NSF among patients with impaired elimination of the drugs. To counsel patients at risk for NSF:
- Describe the clinical manifestations of NSF.
- Describe procedures to screen for the detection of renal impairment.
Instruct the patients to contact their physician if they develop signs or symptoms of NSF following DOTAREM administration, such as burning, itching, swelling, scaling, hardening and tightening of the skin; red or dark patches on the skin; stiffness in joints with trouble moving, bending or straightening the arms, hands, legs or feet; pain in the hip bones or ribs; or muscle weakness.

17.2   Common Adverse Reactions
Inform patients that they may experience:
- Reactions along the venous injection site, such as mild and transient burning or pain or feeling of warmth or coldness at the injection site.
- Side effects of headache, nausea, abnormal taste and feeling hot.

17.3   General Precautions
Instruct patients receiving DOTAREM to inform their physician if they:
- Are pregnant or breastfeeding.
- Have a history of allergic reaction to contrast media, bronchial asthma or allergy.
- Are taking any medications.

Rx Only

Guerbet
Guerbet LLC
120 W 7th Street. Suite 108
Bloomington, IN 47404

Pre-filled syringes manufactured by Catalent, Belgium for Guerbet
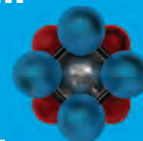Vials manufactured by Recipharm, France for Guerbet

GU06131043
Revised 06/2013

DOTAREM®
(gadoterate meglumine) Injection

Macrocyclic and Ionic...

DOTAREM

...There is only One.

The first and only macrocyclic and ionic gadolinium agent in its class.[1]

Global clinical experience with over **43 million doses** administered outside the US.[2]

INDICATION[1]

DOTAREM is a gadolinium-based contrast agent indicated for intravenous use with magnetic resonance imaging (MRI) in brain (intracranial), spine and associated tissues in adult and pediatric patients (2 years of age and older) to detect and visualize areas with disruption of the blood brain barrier (BBB) and/or abnormal vascularity.

IMPORTANT SAFETY INFORMATION[1]

WARNING: NEPHROGENIC SYSTEMIC FIBROSIS (NSF)

Gadolinium-based contrast agents (GBCAs) increase the risk for NSF among patients with impaired elimination of the drugs. Avoid use of GBCAs in these patients unless the diagnostic information is essential and not available with non-contrasted MRI or other modalities. NSF may result in fatal or debilitating fibrosis affecting the skin, muscle and internal organs.

- **The risk for NSF appears highest among patients with:**
  - **Chronic, severe kidney disease (GFR < 30 mL/min/1.73m^2), or**
  - **Acute kidney injury.**
- **Screen patients for acute kidney injury and other conditions that may reduce renal function. For patients at risk for chronically reduced renal function (for example, age > 60 years, hypertension or diabetes), estimate the glomerular filtration rate (GFR) through laboratory testing [*see Warnings and Precautions*].**
- **For patients at highest risk for NSF, do not exceed the recommended DOTAREM dose and allow a sufficient period of time for elimination of the drug from the body prior to any re-administration [*see Warnings and Precautions*].**

Contraindicated in patients with a history of clinically important hypersensitivity reactions to DOTAREM.

The possibility of serious or life-threatening anaphylactoid/anaphylactic reactions with cardiovascular, respiratory or cutaneous manifestations, ranging from mild to severe, including death, should be considered. Monitor patients closely for need of emergency cardiorespiratory support.

In patients with chronically reduced renal function, acute kidney injury requiring dialysis has occurred with the use of GBCAs. The risk of acute kidney injury may increase with increasing dose of the contrast agent; administer the lowest dose necessary for adequate imaging. Screen all patients for renal impairment by obtaining a history and/or laboratory tests. Consider follow-up renal function assessments for patients with a history of renal dysfunction.

Ensure catheter and venous patency before the injection of DOTAREM. Extravasation into tissues during DOTAREM administration may result in tissue irritation.

The most common adverse reactions associated with DOTAREM in clinical studies were nausea, headache, injection site pain, injection site coldness, and burning sensation.

For more information about DOTAREM, including Boxed WARNING, please see the Full Prescribing Information.

Please see adjacent Brief Summary of Prescribing Information.

DOTAREM is a registered trademark of Guerbet and is available by prescription only.

GU02141011

References: 1. Dotarem [package insert]. Bloomington, IN: Guerbet LLC; 2013. **2.** Data on file, Guerbet LLC.

www.guerbet-us.com

Guerbet | Contrast for Life